Karlsruhe Institute of Technology

Hybrid Polymer Electrolytes for Li-Metal Batteries

Zur Erlangung des akademischen Grades eines

DOKTORS DER NATURWISSENSCHAFTEN

(Dr. rer. nat.)

von der KIT-Fakultät für Chemie und Biowissenschaften
des Karlsruher Instituts für Technologie (KIT)

genehmigte

DISSERTATION

von

M.Sc. Daniel Alexander Döpping

aus Brettorf

1. Referent: Prof. Dr. Patrick Théato
2. Referent: Prof. Dr. Dominic Bresser

Tag der mündlichen Prüfung: 07.05.2025

Declaration of Authorship

Die vorliegende Arbeit wurde im Zeitraum von Februar 2022 bis Januar 2025 am Institut für Technische Chemie und Polymerchemie (ITCP) am Karlsruher Institut für Technologie (KIT) unter der wissenschaftlichen Betreuung von Prof. Dr. Patrick Théato angefertigt.

Hiermit erkläre ich, dass die vorliegende Arbeit im Rahmen der Betreuung durch Prof. Dr. Patrick Théato selbstständig verfasst und keine anderen als die angegebenen Quellen und Hilfsmittel verwendet wurden. Sämtliche wörtlichen oder sinngemäßen Übernahmen und Zitate, sowie alle Abschnitte wurden gekennzeichnet. KI-basierte Tools wurden zur Unterstützung genutzt, jedoch ausschließlich zur sprachlichen Überarbeitung, Fehlerkorrektur oder Formatierung, nicht jedoch zur eigenständigen Erstellung wesentlicher Inhalte oder Argumentationsstrukturen. Die Satzung des Karlsruher Instituts für Technologie (KIT) zur Sicherung guter wissenschaftlicher Praxis wurde beachtet. Des Weiteren erkläre ich, dass ich mich derzeit in keinem laufenden Promotionsverfahren befinde, und auch keine vorausgegangenen Promotionsversuche unternommen habe. Die elektronische Version der Arbeit stimmt mit der schriftlichen Version überein und die Primärdaten sind gemäß Abs. A (6) der Regeln zur Sicherung guter wissenschaftlicher Praxis des KIT beim Institut abgegeben und archiviert.

Karlsruhe, den 03.07.2025

_____

Daniel Döpping

Abstract

Hybrid electrolytes have emerged as a promising solution to address the limitations of purely inorganic and polymer-based electrolytes in solid-state batteries. While inorganic electrolytes offer high ionic conductivity, they suffer from poor mechanical flexibility and interfacial compatibility. Conversely, polymer electrolytes provide flexibility and ease of processing but generally exhibit lower ionic conductivity. Hybridization seeks to combine the advantages of both classes, mitigating interfacial resistance, improving mechanical stability, and enhancing electrochemical performance. However, achieving an optimal balance between these properties remains challenging due to complex interactions between the polymer and inorganic particles. The present thesis explores multiple strategies for optimizing hybrid electrolytes, focusing on hydrogenated nitrile butadiene rubber (HNBR)-based composite polymer electrolytes (CPEs), sulfur-containing polymers for argyrodite-based CPEs, the coating of lithium aluminum titanium phosphate (LATP) and lithium lanthanum zirconium oxide (LLZO) particles for poly(vinylidene fluoride-*co*-hexafluoropropylene) (PVDF-HFP) CPEs, and self-crosslinking oxide-based CPEs.

The first project investigates the use of HNBR as a polymer matrix for CPEs, incorporating LATP and Li_6PS_5Cl to enhance the poor ionic conductivity of HNBR. Ionic conductivity measurements showed that adding pristine LATP slightly improved conductivity at elevated temperatures, while polyacrylonitrile (PAN) coated LATP exhibited reduced ionic conductivity. The coating of LATP with PAN was systematically optimized through a model system utilizing SiO_2 nanoparticles. Additionally, a mixed and a layered HNBR-Li_6PS_5Cl system were evaluated. While the layered system achieved an ionic conductivity improvement by a factor of 5.8, overall performance remained insufficient for practical applications due to poor reproducibility and low conductivity at ambient temperatures.

In a second project sulfur-containing polymers as an alternative to oxygen-based polymer matrices for argyrodite-based CPEs are explored. The high oxophilicity of phosphates in argyrodites leads to degradation in the presence of oxygen-rich polymers, limiting their long-term stability. Sulfur-based polymers such as polytrithiocarbonates and polythioethers are synthesized and characterized. These polymers demonstrated improved chemical compatibility with argyrodites while maintaining mechanical flexibility, potentially enabling higher polymer content in CPEs

without compromising performance. It was found that the nucleophilicity of the argyrodite surface is able to attack polytrithiocarbonates leading to depolymerization. Polythioethers on the other hand are stable in contact with argyrodites but do decrease ionic conductivity. Thermogravimetric analysis (TGA) and differential scanning calorimetry (DSC) were employed to evaluate the thermal properties and stability of the synthesized polymers. Electrochemical impedance spectroscopy (EIS) demonstrated that these sulfur-based polymers exhibited enhanced chemical compatibility with argyrodites while maintaining mechanical flexibility.

The third project focuses on the optimization of surface coatings of LATP and LLZO particles to enhance their dispersion and stability in polymer matrices. A grafting-to approach was applied using alkoxy silane-modified poly(ethylene glycol) methyl ethers (mPEG) of different chain lengths, leading to improved particle distribution. For LLZO, mPEG-silane (M_n = 1,000 g mol^{-1}) coatings successfully prevented agglomeration and degradation of poly(vinylidene fluoride-*co*-hexafluoropropylene) (PVDF-HFP), resulting in CPEs with significantly enhanced cycling stability. Electrochemical impedance spectroscopy (EIS) and rate capability tests confirmed lower interface resistance and prolonged cycle life in lithium iron phosphate (Li||LFP) cells.

The fourth and last project builds upon the alkoxy silane modified polymers and translates the findings into self-crosslinking oxide-CPEs as a solvent-free alternative to conventional hybrid electrolytes. Systematically, the properties of oxide particles, polymers, and processing are optimized resulting in a novel and simple toolbox for thin high-performance CPEs. This approach not only reduces manufacturing complexity but also improves mechanical stability and ion transport by preventing particle sedimentation. The resulting CPEs are characterized regarding mechanical, thermal and electrochemical properties. By utilizing roll-to-roll press manufacturing, thin poly(ethylene oxide) (PEO)-LLZO CPEs of 30 µm are made and show superior performance in Li||LFP cells compared to similar systems.

In summary, the findings of this thesis highlight multiple strategies for optimizing hybrid electrolytes. The use of sulfur-based polymers for argyrodite-CPEs demonstrated superior chemical compatibility, while surface modification of oxide particles significantly improved interfacial stability and electrochemical performance. Self-crosslinking oxide-CPEs provided an innovative approach for solvent-free fabrication, simplifying processing while maintaining high ionic conductivity. Overall, these advancements contribute to the development of commercially viable hybrid solid-state

electrolytes, bridging the gap between fundamental research and practical application in next-generation lithium-metal batteries.

Kurzzusammenfassung

Hybride Elektrolyte haben sich als vielversprechende Lösung erwiesen, um die Einschränkungen rein anorganischer und polymerbasierter Elektrolyte in Festkörperbatterien zu überwinden. Anorganische Elektrolyte bieten zwar eine hohe Ionenleitfähigkeit, leiden aber unter ihrer geringen mechanischen Flexibilität und Grenzflächenkompatibilität. Umgekehrt bieten Polymerelektrolyte Flexibilität und einfache Verarbeitung, weisen aber im Allgemeinen eine geringere Ionenleitfähigkeit auf. Durch Hybridisierung wird versucht, die Vorteile beider Klassen zu kombinieren, indem der Grenzflächenwiderstand verringert, die mechanische Stabilität verbessert und die elektrochemischen Eigenschaften gesteigert werden. Aufgrund der komplexen Wechselwirkungen zwischen dem Polymer und den anorganischen Partikeln ist es jedoch nach wie vor schwierig, ein optimales Gleichgewicht zwischen diesen Eigenschaften herzustellen. In der vorliegenden Arbeit werden mehrere Strategien zur Optimierung von polymeren Hybridelektrolyten untersucht, wobei der Schwerpunkt auf hydriertem Nitrilbutadienkautschuk (HNBR) basierenden Kompositpolymerelektrolyten (CPEs) und schwefelhaltigen Polymeren für CPEs auf Argyroditbasis liegt. Darüber hinaus werden die Beschichtung von Lithium-Aluminium-Titan-Phosphat (LATP) und Lithium-Lanthan-Zirkonium-Oxid (LLZO) für Poly(vinylidenfluorid-*co*-hexafluoropropylen) (PVDF-HFP) CPEs und selbstvernetzende Oxid-basierte CPEs untersucht.

Im ersten Projekt wird die Verwendung von HNBR als Polymermatrix für CPEs untersucht, wobei LATP und Li_6PS_5Cl zugesetzt werden, um die schlechte Ionenleitfähigkeit von HNBR zu verbessern. Messungen der Ionenleitfähigkeit zeigten, dass die Zugabe von unbehandeltem LATP die Leitfähigkeit bei erhöhten Temperaturen leicht verbesserte, während mit Polyacrylnitril (PAN) beschichtetes LATP eine geringere Ionenleitfähigkeit aufwies. Die Beschichtung von LATP mit PAN wurde anhand eines Modellsystems mit SiO_2-Nanopartikeln systematisch optimiert. Zusätzlich wurden ein gemischtes und ein geschichtetes HNBR-Li_6PS_5Cl-System untersucht. Während das geschichtete System eine Verbesserung der Ionenleitfähigkeit um den Faktor 5.8 erzielte, blieb die Gesamtleistung aufgrund der schlechten Reproduzierbarkeit und der geringen Leitfähigkeit bei Umgebungstemperaturen für praktische Anwendungen unzureichend.

In einem zweiten Projekt werden schwefelhaltige Polymere als Alternative zu sauerstoffbasierten Polymermatrizen für CPEs auf Argyroditenbasis erforscht. Die

hohe Oxophilie der Thiophosphate in Argyroditen führt zu Nebenreaktionen in Gegenwart von sauerstoffreichen Polymeren, was die Langzeitstabilität von hybridisierten Systeme einschränkt. Als Alternative werden Polymere auf Schwefelbasis wie Polytrithiocarbonate und Polythioether synthetisiert und charakterisiert. Diese Polymere zeigen eine verbesserte chemische Kompatibilität mit Argyroditen bei gleichzeitiger Beibehaltung der mechanischen Flexibilität, was einen höheren Polymeranteil in CPEs ohne Leistungseinbußen ermöglichen könnte. Es wurde festgestellt, dass die Nukleophilie der Argyrodit-Oberfläche in der Lage ist, Polytrithiocarbonate anzugreifen, was zur Depolymerisation führt. Polythioether hingegen sind im Kontakt mit Argyroditen stabil, verringern jedoch die Ionenleitfähigkeit. Die thermogravimetrische Analyse (TGA) und die Differential-Scanning-Kalorimetrie (DSC) werden eingesetzt, um die thermischen Eigenschaften und die Stabilität der synthetisierten Polymere zu bewerten. Die elektrochemische Impedanzspektroskopie (EIS) zeigt, dass diese Polymere auf Schwefelbasis eine verbesserte chemische Kompatibilität mit Argyroditen aufweisen und gleichzeitig ihre mechanische Flexibilität beibehalten.

Das dritte Projekt befasst sich mit der Optimierung von Oberflächenbeschichtungen von LATP- und LLZO-Partikeln, um deren Dispersion und Stabilität in Polymermatrizen zu verbessern. Es wurde ein Pfropfverfahren mit Alkoxysilan-modifizierten Poly(ethylenglykol)methylethern (mPEG) unterschiedlicher Kettenlänge angewandt, was zu einer verbesserten Partikelverteilung führte. Bei LLZO verhindert die mPEG-Silan-Beschichtungen (M_n = 1,000 g mol^{-1}) erfolgreich die Agglomeration und den Abbau von Poly(vinylidenfluorid-*co*-hexafluorpropylen) (PVDF-HFP), was zum Einsatz in CPEs mit deutlich verbesserter Zyklenstabilität führt. Elektrochemische Impedanzspektroskopie (EIS) und Ratenfähigkeitstests bestätigen einen geringeren Grenzflächenwiderstand und eine verlängerte Zyklenlebensdauer in Lithium-Eisenphosphat-Zellen (Li||LFP).

Das vierte und letzte Projekt baut auf den mit Alkoxysilan modifizierten Polymeren auf und setzt die gewonnen Erkenntnisse anderweitig in selbstvernetzende Oxid-CPEs als lösungsmittelfreie Alternative zu herkömmlichen Hybridelektrolyten um. Systematisch werden die Eigenschaften der Oxidpartikeln, Polymeren und Verarbeitung optimiert, was zu einem neuartigen und einfachen System für dünne Hochleistungs-CPEs führt. Dieser Ansatz reduziert nicht nur die Komplexität der Herstellung, sondern verbessert auch die mechanische Stabilität und den Ionentransport, indem er die Sedimentation

der Partikel verhindert. Die resultierenden CPEs werden hinsichtlich ihrer mechanischen, thermischen und elektrochemischen Eigenschaften charakterisiert. Durch den Einsatz von Rolle-zu-Rolle-Pressen werden dünne Poly(ethylenoxid) (PEO)-LLZO-CPEs von 30 µm hergestellt, die in Li||LFP-Zellen im Vergleich zu ähnlichen Systemen eine überlegene Leistung zeigen.

Zusammenfassend lässt sich sagen, dass die Ergebnisse dieser Arbeit mehrere Strategien zur Optimierung von Hybridelektrolyten aufzeigen. Die Verwendung von schwefelbasierten Polymeren für Argyrodit-CPEs zeigt eine hervorragende chemische Kompatibilität, während die Oberflächenmodifikation von Oxidpartikeln die Grenzflächenstabilität und die Leistung in Batteriezellen deutlich verbessert. Selbstvernetzende Oxid-CPEs bieten einen innovativen Ansatz für die lösungsmittelfreie Herstellung, der die Verarbeitung vereinfacht und gleichzeitig eine hohe Ionenleitfähigkeit gewährleistet. Insgesamt tragen diese Fortschritte zur Entwicklung kommerziell nutzbarer hybrider Festkörperelektrolyte bei, die die Kluft zwischen Grundlagenforschung und praktischer Anwendung in Lithium-Metall-Batterien der nächsten Generation überbrücken.

Table of Content

1 Introduction

The transition to sustainable energy sources is one of the most pressing global challenges of the 21st century. As fossil fuel-based energy systems give way to renewable alternatives such as solar and wind power, the need for efficient, high-capacity energy storage solutions becomes increasingly critical.[1] Among various energy storage technologies, rechargeable batteries play a pivotal role in enabling this transition, particularly in electric vehicles (EVs) and grid storage applications.[2] Lithium-ion (Li-ion) batteries, which have dominated the energy storage market for the past three decades, have facilitated significant advancements in portable electronics, transportation, and renewable energy integration. However, as the demand for higher energy densities and safer battery chemistries grows, Li-ion technology is approaching its theoretical limits, necessitating the exploration of the next-generation battery architectures.[3]

Li-ion batteries rely on intercalation-type electrodes and liquid electrolytes (LEs), which inherently limit their energy density and introduce safety concerns due to the flammability and instability of organic solvents. With the increasing energy demands of modern applications, the limitations of Li-ion batteries, such as finite specific capacity, risk of thermal runaway, and cycle life constraints, become more apparent. In response to these challenges, lithium-metal (Li-metal) batteries have emerged as a promising alternative due to their significantly higher theoretical energy density. Li-metal anodes, with a specific capacity of 3,860 mAh g^{-1}, far surpass conventional graphite anodes, which are limited to approximately 372 mAh g^{-1}. This dramatic increase in capacity, if successfully implemented in a stable electrochemical system, could lead to a new era of energy storage technology and enable various new technologies like electric passenger planes.[4]

Despite their potential, Li-metal batteries have faced critical hurdles, primarily associated with the formation of lithium dendrites, which compromise battery lifespan and safety. The use of solid-state electrolytes (SSEs) has been identified as a key strategy to mitigate these challenges. SSEs offer intrinsic safety advantages by eliminating flammable liquid electrolytes and providing mechanical suppression of dendrite growth. However, conventional solid-state electrolytes, such as ceramic and polymer-based materials, each present their own set of limitations. Ceramic electrolytes, while highly conductive, suffer from brittleness and poor interfacial contact

with lithium metal,[5] whereas polymer electrolytes exhibit improved flexibility but often lack sufficient ionic conductivity at ambient temperatures.[6]

To address these limitations, hybrid solid-state electrolytes (HSSEs) have emerged as a compelling research focus, combining the benefits of both ceramic and polymer components. By strategically integrating inorganic fillers with polymer matrices, HSSEs aim to achieve an optimal balance of ionic conductivity, mechanical stability, and interfacial compatibility with lithium metal.[7]

Among the various polymer matrices explored for HSSEs, hydrogenated nitrile butadiene rubber (HNBR),[8–10] poly(vinylidene fluoride-*co*-hexafluoropropylene) (PVDF-HFP),[11–15] and poly(ethylene oxide) (PEO)[16–22] have garnered significant attention. HNBR is known for its exceptional mechanical strength and thermal stability, making it a suitable candidate for enhancing the durability of hybrid electrolytes.[8] Whereas, PVDF-HFP, with its high dielectric constant and flexibility, facilitates improved lithium-ion transport while maintaining mechanical integrity.[23] PEO, a widely studied polymer electrolyte, enables effective lithium-ion conduction through solvation with lithium salts but often requires optimization to achieve high conductivity at room temperature.[24–26] By incorporating inorganic fillers such as $Li_{1.5}Al_{0.5}Ti_{1.5}(PO_4)_3$ (LATP),[27,28] $Li_7La_3Zr_2O_{12}$ (LLZO),[29–31] or Li_6PS_5Cl,[32–34] into a polymer matrix the main disadvantage of polymer electrolytes, the comparatively low ionic conductivity, could be overcome while maintaining the facile processing of polymers.[2]

However, current research indicates that a simple mixing of polymers and inorganic fillers does not increase electrochemical performance as much as necessary due to incompatible interfaces.[22,35–37] By finetuning the surface properties of inorganic fillers with specifically designed coatings, the interaction between the polymer matrix and the filler can be enhanced.[22,38] Accordingly, this dissertation explores the design, synthesis, and electrochemical performance of novel hybrid solid-state electrolytes for Li-metal batteries with the objective of enhancing their energy density, safety, and long-term stability.

2 Theoretical Background

2.1 Step Polymerization

Step polymerization is one of the two principal methods for polymer synthesis, the other being chain polymerization. In contrast to chain polymerization, where polymerization occurs through the successive addition of monomers to an active center (e.g., free radicals, cations, or anions), step polymerization involves the reaction of bifunctional or multifunctional monomers containing two or more reactive groups.[39] In the case of a polycondensation reaction these monomers react in a stepwise fashion, forming covalent bonds and producing small molecules, a condensate, such as water, methanol, or other byproducts. For another type of step polymerization, the polyaddition, no small molecules are released during the polymerization process.[40]

Step polymerization involves the gradual joining of monomers or oligomers through covalent bonds, where any molecule (monomer, dimer, or oligomer) may react with another molecule that contains the appropriate reactive group. The fundamental reaction mechanism involves the interaction of complementary functional groups, which may include amines, alcohols, carboxyls, isocyanates, or epoxides.[39]

Often, step polymerizations differentiate between AA+BB and AB monomers, with A and B depicting compatible complementary functional groups. AA+BB-type reactions use two different monomers which contain two of each functional group. An example would be, on the one hand, the synthesis of Nylon-6,6 from hexamethylene diamine and adipic acid. AB-type monomers on the other hand, have both functional groups in one monomer. An example for AB-type monomers are amino acids that contain a primary amine and a carboxylic acid, which can polymerize into polypeptids.[41,42] In **Scheme 1,** a simplified reaction scheme of AA+BB-type and AB-type monomers for polycondensation and polyaddition reactions is depicted.

For step polymerizations, the process begins when two complementary functional groups (e.g., a hydroxyl group and a carboxyl group in polyester synthesis, releasing a water molecule) react to form a dimer. These dimers can then react with other monomers or oligomers to form larger species, and the polymerization proceeds through the random linking of the intermediates.

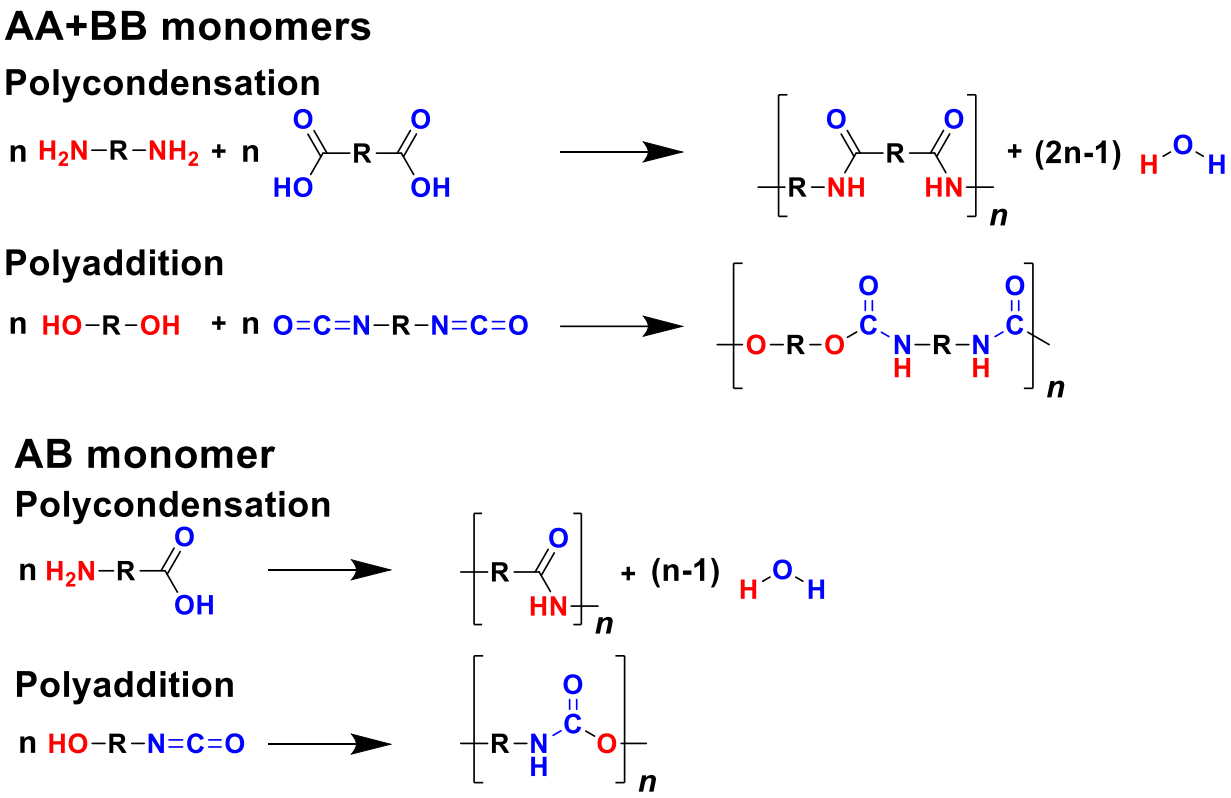

Scheme 1 Simplified reaction scheme of AA+BB (up) and AB (bottom) type polycondensation and polyaddition reactions, respectively. R can be any, under polymerization conditions, unreactive, group of aliphatic or aromatic nature.

The resulting polymers grow until the polymerization reaction reaches a high degree of conversion (i.e., 99 %), at which point the polymer chains become sufficiently long, and high molecular weight products are achieved. Through addition of different monomers with suitable functional groups, multifunctional moieties and/or linkers for orthogonal reactions, a platitude of polymer architectures, such as copolymers, block polymers, radial/star polymers, graft polymers, and dendrimers could be synthesized.[41] The kinetics of step polymerization follow a second-order reaction mechanism, where the rate of polymerization is dependent on the concentration of reactive functional groups in the system. For a simple system with two reactants (AA+BB), the reaction rate can be expressed following **Equation 1**:

$$rate\ of\ polymerization = k * [A][B] \qquad \textbf{Equation 1}$$

where k is the rate constant, and [A] and [B] are the concentrations of the reactive functional groups on the two different monomers. This equation reflects the fact that polymerization proceeds through the random collision of reactive groups. As the reaction progresses and monomers are consumed, the concentration of reactive groups decreases, leading to a reduction in the rate of polymerization over time.[43]

As a result of this decrease in the concentration of functional groups, the polymerization rate declines progressively as the reaction approaches completion. Unlike chain polymerization, where the polymerization rate remains relatively constant throughout the process, step polymerization exhibits a progressively decreasing reaction rate as the number of available functional groups declines.[44]

A key feature of step polymerization is the direct correlation between the conversion of monomers and the molecular weight of the resulting polymer, with high values of the molecular weight forming only at very high conversions. This relationship is described by Carothers equation. For a simple step polymerization involving bifunctional monomers, the Carothers equation is following **Equation 2**:

$$X_n = \frac{1}{1-p} \qquad \textbf{Equation 2}$$

where X_n is the number-average degree of polymerization and p is the conversion, i.e., the fraction of the functional groups that have reacted. This equation demonstrates that as the conversion increases, the molecular weight of the polymer increases significantly. However, the relationship is not linear, and molecular weight only rises sharply after a significant portion of the monomers have reacted, typically around 90% conversion. At lower conversions, the polymer consists mostly of oligomers with low molecular weights. At higher conversions, polymerization becomes more efficient, and larger polymer chains form as larger oligomers are combined. Therefore, step polymerization is inherently slow in terms of molecular weight development, and high molecular weights are generally achieved only near the completion of the reaction.[43,45] This is a fundamental difference from chain polymerization, where the polymerization rate and molecular weight increase continuously as monomers are added to the growing polymer chain.[40]

Several factors influence the efficiency and outcome of step polymerization. The reactivity of the functional groups involved in the polymerization is one of the most important factors. For example, in polyester synthesis, the reactivity of the hydroxyl and carboxyl groups determines how efficiently the polymerization proceeds. Similarly, in polyurethanes, the reactivity of the isocyanate groups with hydroxyl groups is critical in controlling the rate of polymerization. Temperature also plays a significant role, as increasing temperature generally accelerates the reaction by increasing the kinetic energy of the molecules, thus enhancing the frequency of collisions between reactive groups. However, excessively high temperatures can lead to side reactions or the degradation of monomers.[46]

Solvent choice is another important consideration in step polymerization, particularly in condensation reactions, where solvents can aid the removal of the byproducts, such as water, and drive the equilibrium toward polymer formation. The use of solvents can also influence the viscosity of the reaction mixture, which in turn affects the diffusion rates of the monomers and oligomers. Furthermore, catalysts are often employed to increase the rate of polymerization, especially when dealing with functional groups that have low reactivity.[46]

Step polymerization is widely used in the synthesis of a range of commercially important polymers. Polyesters, such as polyethylene terephthalate (PET), are produced through polycondensation reactions between diols and dicarboxylic acids, making them essential in the manufacturing of fibers, films, and bottles. Polyamides, such as nylon, are formed through similar condensation reactions between diamines and dicarboxylic acids. Polycarbonates, which are commonly used in optical lenses and engineering plastics, can be synthesized through the polycondensation of bisphenol A and phosgene.[41,47]

Polyaddition reactions are also critical for producing high-performance polymers such as polyurethanes and epoxy resins, which find applications in adhesives, coatings, automotive parts, foams, and electronic devices.[48,49]

While step polymerization is typically slower than radical polymerization and requires high conversion rates to achieve high molecular weights, it offers significant versatility in the production of polymers with a broad range of properties through a plethora of available monomers.

2.2 Anionic Ring Opening Polymerization

Anionic ring-opening polymerization (AROP) is an ionic polymerization where the polymerization process involves the opening of a cyclic monomer (typically a lactone, lactam, epoxide, siloxanes, or cyclic ether) through the nucleophilic attack of an anionic initiator, following a chain-growth mechanism. This process leads to the formation of linear or branched polymers with well-defined structures and controlled molecular weights. AROP is particularly useful for synthesizing polymers with high stereoregularity, such as polyesters,[50] polyamides,[51] and polyethers,[52] as well as for the preparation of functional materials,[53] biodegradable plastics,[54] and block copolymers.[55]

The mechanism of AROP closely resembles that of traditional living anionic polymerization but differs in that the initiator first attacks a monomer that is cyclic rather than linear. The attack on the monomer results in the opening of the ring and the formation of an active anionic center at the chain end. This active species can then propagate the polymerization by reacting with additional monomer units, causing the cycle to open and extend the polymer chain. Importantly, because AROP does not typically involve the formation of any side products, the process can produce high-purity polymers with narrow molecular weight distributions.[56] Exemplary, the main steps of an AROP on ε-caprolactone are shown in a simplified manner in **Scheme 2**.

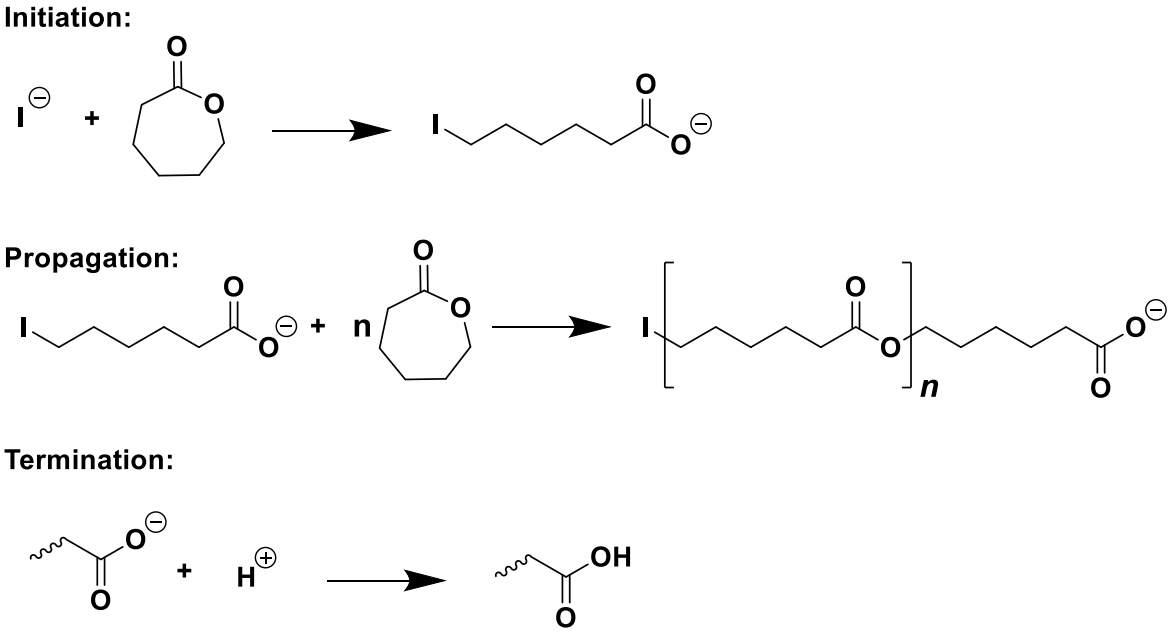

Scheme 2 The three steps of an AROP exemplary on ε-caprolactone as monomer. First, the nucleophilic Initiator I opens the ring and forms the reactive propagating species. Second, the active species propagates by opening other monomers and extending the chain. Third, termination by recombination is impossible due to the coulombic repulsion of the anionic species. Hence, termination typically occurs by transfer of a proton to terminate the active species. The proton can be transferred from monomers or solvent molecules (rare) or by addition of protic molecules at the end of the reaction, such as, acids, water, or methanol.

The initiation of AROP can occur using a variety of initiators, including alkali metals (e.g., lithium or sodium),[52] metal alkoxides,[57,58] strong organic bases,[59] and organometallic compounds.[53] The choice of initiator depends on the monomer being used and the employed polymerization conditions. For example, in the case of the polymerization of cyclic esters like lactones, an alkoxide initiator is commonly employed,[57] while for epoxide polymerization, a metal-based initiator, such as an

organolithium compound, is often preferred.[52] Depending on the choice of initiator, and monomer, the addition of complexing agents like crown ethers can be beneficial to obtain higher molecular weights, as the cations are complexed and the active species anions gain higher reactivity towards polymerization.[56]

One of the key advantages of AROP is its ability to produce polymers with controlled topologies, such as block copolymers, by sequentially adding different monomers. The living nature of the polymerization allows for the precise control over the block sequence and the molecular weight of each block. Additionally, AROP enables the creation of polymers with functional end groups that can be further modified or used for subsequent reactions, making it a versatile tool for the design of complex polymer architectures, e.g., star polymers.[60]

Factors that influence the rate and control of AROP include the monomer structure, the polarity of the solvent, the temperature, the type of counter cation and the concentration of the initiator.[61] For example, less reactive monomers, such as cyclic ethers, may require higher temperatures or more aggressive initiators to initiate polymerization.[62] A main driving force of ring-opening polymerizations is the ring strain of the monomer. Stable ring conformations with low ring strain, e.g., 5 and 6 membered rings are often thermodynamically favored over polymers due to their higher entropy especially at elevated temperatures. These monomers often require catalysts to achieve high molecular weights.[63] Thermodynamic considerations are crucial, as polymerization is only possible when the free energy change is negative under given conditions. The ceiling temperature, above which polymer formation is thermodynamically unfavorable, and the equilibrium monomer concentration are important factors.[64]

AROP can also be used to implement comonomers into the chain. Especially with 3-membered heterocycles, such as epoxides[65] and thiiranes,[63] this technique is used to obtain polymer structures that would be difficult to synthesize otherwise, e.g., aliphatic 5-membered repeating units, which favor cyclisation over polymerization.[66] In particular, the reaction of epoxides with CO_2 to polycarbonates is interesting as it can be used for carbon capture and produce polymers at the same time (**Scheme 3**).[67]

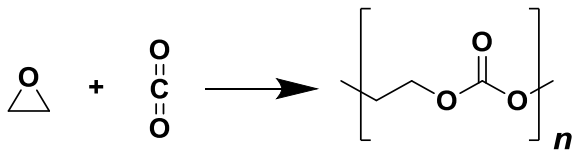

Scheme 3 Reaction of ethylene oxide and carbon dioxide to poly(ethylene carbonate). This reaction is able to capture and convert carbon dioxide into usable polymers.

Overall, anionic ring-opening polymerization offers exceptional control over polymer molecular weight, architecture, and functionality, making it an important method for synthesizing high-performance materials with tailored properties.

2.3 Free Radical Polymerization

Free Radical polymerization (FRP) is a widely used method for synthesizing polymers, characterized by the generation of reactive radical species that initiate the polymerization process, following a chain-growth mechanism.

Similar to the AROP, the radical polymerization process involves three main steps:

1. initiation
2. propagation
3. termination

In the initiation step, free radicals are formed through the thermal decomposition of initiators (e.g., azo compounds, peroxides) or via photochemical processes. These initiators generate radicals that react with monomers, leading to the formation of an initiating radical. During the propagation phase, the active radical reacts with monomer units, adding them to the growing polymer chain. Each addition generates a new propagating radical, allowing the chain to continue growing rapidly. The process concludes in the termination step, where two radical chain ends combine to form a stable polymer or through disproportionation, where one radical transfers a hydrogen atom to another, resulting in two stable polymer chains.[68] In **Scheme 4** a simplified FRP of styrene as the monomer with azobisisobutyronitrile (AIBN) as initiator to yield poly(styrene) (PS) is illustrated.

Opposed to the step polymerization, the radical polymerization generally generates polymers with large molecular weights even at low conversions.[69] The aforementioned disproportion reaction to terminated growing chains can also occur with solvent molecules. Other reactive species, such as oxygen or water can also terminate the propagating radical and form, for polymerization reactions unreactive, radical species or recombine. This has significant impact on the dispersity *Đ* which is defined as **Equation 3**

$$Đ = \frac{M_w}{M_n} \qquad \textbf{Equation 3}$$

with M_w being weighted average molecular weight and M_n number average molecular weight. Due to the random nature of radical formation and termination processes, along

with potential chain transfer reactions there is a significant variation in chain lengths, ultimately resulting in a broad molecular weight distribution of approximately 2 in a free radical polymerization but can vary widely depending on polymerization kinetics and conditions.[70]

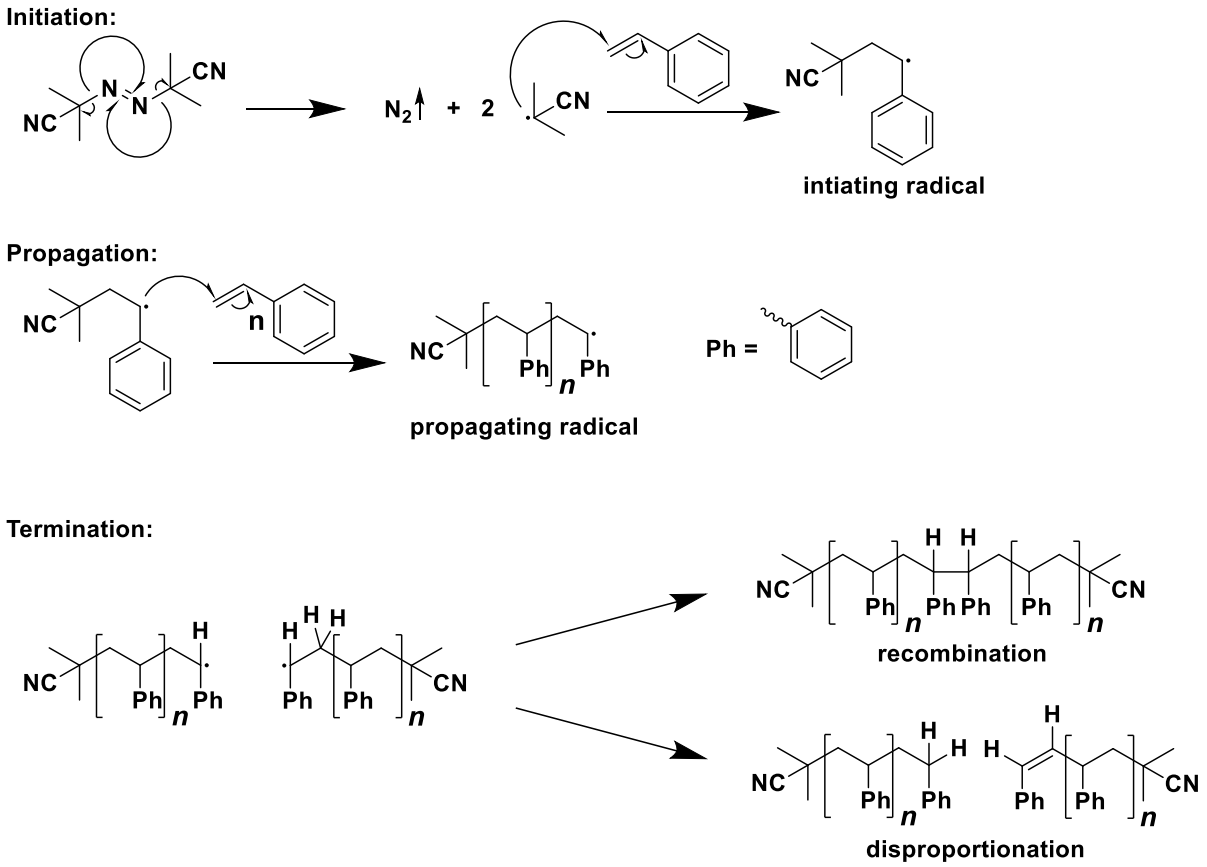

Scheme 4 Simplified depiction of the polymerization of styrene with AIBN. First, decomposition of AIBN into two radicals and nitrogen gas. The radical attacks a double bond and leads to the formation of the initiating radical. Second, the initiating radical propagates the chain-growth by attacking further styrene double bonds, extending the chain through the propagating radical. Lastly, either two radical chains recombine to terminate the reaction or through disproportionation a proton is transferred from one propagating radical to another.

FRP is utilized in the synthesis of numerous commercial polymers. Key applications include acrylate[71] and methacrylate[72] derived polymers, which are used in paints,[73] adhesives,[74] superabsorbents,[75] and synthetic glas[76] for their durability and versatility. Styrene-based polymers, such as polystyrene and styrene-butadiene rubber, are widely used in packaging,[77] insulation,[78] and construction.[79] The production of synthetic rubbers through radical polymerization is also critical in the tire industry.[80] Moreover, various copolymers of rubbers like acrylonitrile-butadiene rubber (NBR) are synthesized on an industrial scale using emulsion polymerization. Their application are highly important in electrical insulation and sealing under harsh conditions.[81]

The versatility of radical polymerization allows for the synthesis of diverse polymer architectures, including copolymers and branched structures, establishing it as a cornerstone of modern polymer chemistry and industry.[82]

2.3.1 Chain Transfer Polymerization

As aforementioned, the most common mechanism of radical polymerization proceeds via the initiation, propagation, and termination steps. However, a crucial side reaction that influences molecular weight distribution and the final properties of the polymer is the process named chain transfer (**Scheme 5**).

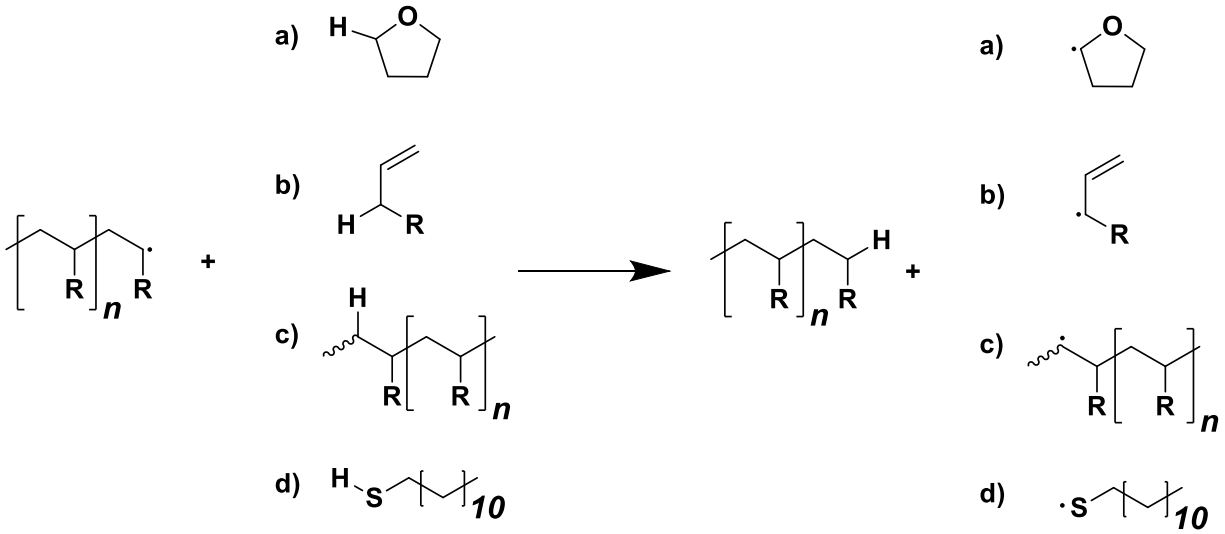

Scheme 5 Schematic representation of different chain transfer types. In all cases, the active radical abstracts a hydrogen atom which terminates the growing polymer chain and moves the active radical to the position of the hydrogen atom. The transferred hydrogen atom is highlighted. a) Transfer of the active radical to a solvent molecule (THF). b) Transfer to a monomer, the monomer radical may undergo rearrangements. c) Transfer to a polymer chain, this can occur inter- or intramolecular. d) Transfer to a chain-transfer agent (1-dodecanethiol). Thiols and halogenated molecules are frequently used for this purpose.

Chain transfer refers to the process in which the active radical center of a growing polymer chain is transferred to another molecule or polymer chain, leading to the formation of new active radical species and a terminated polymer chain. This phenomenon plays a significant role in controlling the molecular weight, dispersity and the polymerization kinetics.[68]

Chain transfer reactions can occur through several pathways, depending on the nature of the transfer agent and the conditions of the polymerization.[83]

One of the most common forms of chain transfer occurs when the growing polymer radical abstracts a hydrogen atom from the solvent (**Scheme 5** a) or monomer

(**Scheme 5** b). This process leads to the formation of a new polymer chain while simultaneously generating a new free radical, which can initiate further polymerization, rearrange, or recombine.[83,84]

For example, in the case of polymerizations using methyl methacrylate (MMA), chain transfer can occur between the growing radical and an MMA monomer molecule, resulting in the formation of a new active MMA radical. This reduces the overall polymer chain length, thus affecting the molecular weight and dispersity.[85]

Chain transfer can also occur between the growing polymer radical and an existing polymer chain either inter- or intramolecular (**Scheme 5** c). This type of transfer is commonly seen in systems with high polymer concentration, where the probability of interaction between growing polymer chains is elevated. The active radical is transferred to the polymer chain, creating a new polymer radical while terminating the original growing chain. Especially but not limited to polyethylene, intramolecular chain transfer, leads to so called “back-biting” leading to short chain branches (**Scheme 6**).

Scheme 6 Schematic representation of a favored “chair”-conformation of the propagating chain of polyethylene leading to the intramolecular chain transfer due to the vicinity of the hydrogen atom and active radical. Chain propagation continues from the new radical position leading to short sidechains and branching.

The propagating chain may form a cyclic intermediate close to e.g., the chair conformation of cyclohexane as it is thermodynamically favored. In this formation, the active radical is close to a hydrogen atom of the polymer backbone. The vicinity facilitates a reaction and the active radical transfers to the backbone, which then propagates and forms a branching point. Polyethylene where this effect is not suppressed by catalysts or chain-transfer agents (CTA) is called low-density polyethylene (LDPE) and is often used in packaging and “one use” plastics. It exhibits lower degrees of crystallization and therefore mechanical stability, due to the increased branching.[86]

A more deliberate approach to control the molecular weight in radical polymerization involves the use of chain transfer agents (**Scheme 5** d). These agents are compounds that react with growing polymer radicals, transferring the radical to themselves, and thus limiting the growth of the polymer chain, while initiating a new one. This process reduces the overall polymerization rate and results in the formation of polymers with a

more controlled molecular weight distribution. CTAs can be classified based on their chemical structure, which influences their efficiency and reactivity in the polymerization process. Common examples include thiols, halogenated compounds, and certain solvents.[87]

The use of CTAs allows for the manipulation of polymer properties, such as viscosity, strength, and solubility, which are highly dependent on the molecular weight of the polymer. By selecting an appropriate CTA, it is possible to fine-tune the polymerization to produce materials with specific characteristics, making this technique valuable in applications ranging from coatings[88] to adhesives[89] and biomedical devices.[90] Despite the advantages of using CTAs, challenges remain in selecting the optimal agent, as the choice can significantly affect the efficiency of polymerization and the final product's properties.[91]

Several factors influence the rate and extent of chain transfer reactions, and understanding these factors is crucial for controlling the polymerization process.

The reactivity of the monomer with the growing radical significantly influences the chain transfer rate. Monomers with weak C-H bonds or those capable of forming stable radicals, such as styrene, acrylates, and methacrylates, are more prone to participate in chain transfer reactions. In contrast, monomers with strong C-H bonds or lower reactivity reduce the likelihood of chain transfer.[92,93]

Additionally, the selection of the CTA is critical in governing the extent of chain transfer. Key factors affecting CTA reactivity include bond dissociation enthalpy, steric hindrance, and electronic properties. For example, thiols (R-SH) are highly reactive due to the weak S-H bond, making them effective targets in H-abstraction through radical processes. Further, CTA concentration influences chain transfer frequency: higher concentrations promote more frequent transfer events and lower molecular weights, while lower concentrations allow for larger polymer chains.[83,94]

Temperature significantly affects chain transfer rates by increasing radical formation and the kinetic energy of monomer and CTA molecules, thus enhancing chain transfer likelihood. However, this can also lead to broader molecular weight distributions if not carefully controlled. Pressure, particularly in gas-phase or supercritical fluid polymerizations, impacts the solubility of CTAs in the monomer phase, affecting the chain transfer rate as well.[95,96]

Moreover, the solvent plays a crucial role in the rate of chain transfer by influencing the diffusion of radicals and CTAs. Polar solvents may stabilize free radicals, reducing

the chain transfer rate, while non-polar solvents can enhance radical diffusion, thereby increasing the likelihood of chain transfer.[97]

One of the primary applications of chain transfer in radical polymerization is controlling the molecular weight of the polymer. By selecting appropriate CTAs and adjusting their concentration, desired molecular weights and dispersities can be achieved.[98]

2.3.2 Reversible-Deactivation Radical Polymerization

The chain transfer plays an integral role in reversible-deactivation radical polymerization (RDRP), also called controlled radical polymerization (CRP), techniques, such as nitroxide-mediated polymerization (NMP), atom transfer radical polymerization (ATRP), and reversible addition-fragmentation chain transfer (RAFT) polymerization. In these processes, chain transfer reactions are used to regenerate the active species, thus allowing for the growth of the polymer chains in a controlled manner. The ability to control the polymerization process enables the synthesis of polymers with narrow molecular weight distributions, specific architectures, and functional end groups, which are crucial for a variety of advanced materials and applications.[99]

The inherent problem of free radical polymerizations RDRP techniques solve is that the propagation and termination of growing chains is significantly faster than the initiation. Since the effectivity of a polymerization is dependent on several factors, especially monomer concentration and viscosity, chains, that are initiated at the start of the reaction, and chains that are initiated at the end of the reaction, have vastly different polymerization conditions because of lower monomer concentration and increased viscosity towards the end. Due to the different environments the propagating chains are subjected to, the molecular weights differ, and polydispersity is increased. NMP, ATRP, and RAFT use different techniques to reduce the propagation rate through the addition of a controlling agent. The controlling agent can reversibly transform propagating chains into a dormant species, thus decreasing the propagation rate and enabling more homogenous conditions for all propagating chains. Consequently, since most growing chains experience similar conditions throughout their propagation, the dispersity is significantly reduced.[99]

Nitroxide-mediated polymerization is one of the earliest controlled radical polymerization techniques developed. NMP employs a stable nitroxide radical as a

controlling agent that can reversibly interact with the growing polymer chains. The nitroxide radical, typically an alkoxyamine (R-N-O•), can act as both a chain transfer agent and a radical scavenger, helping to control the initiation and termination steps of the polymerization. The deactivation prevents the chain from undergoing further polymerization, but the chain can be reactivated by breaking the bond between the polymer chain and the nitroxide group, typically through thermal or chemical means. This equilibrium between active and dormant species results in a controlled growth of the polymer chain (**Scheme 7**).

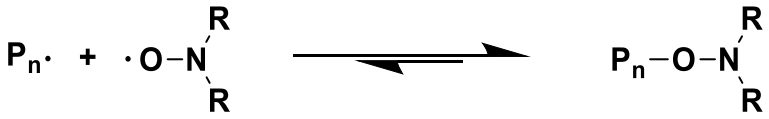

Scheme 7 Simplified mechanism of the active-dormant species equilibrium during NMP. The active species on the left has a propagating polymer chain (P_n•), while the predominant dormant species (R-N-O-P_n) on the right is not able to insert monomers.

At high temperatures, the C-O-N bond in the alkoxyamine is cleaved, generating a carbon-centered radical (P_n•) that can react with vinyl monomers, along with a stable nitroxide radical (R-N-O•). The propagating radicals can recombine with the nitroxide radicals, resulting in the formation of a dormant alkoxyamine species (R-N-O-P_n). The homolysis of the C-O-N bond is influenced by both the temperature and the specific structure of the alkoxyamine. Hence, depending on monomer and desired reaction conditions, the synthesis of different alkoxyamine derivatives is necessary.
However, NMP is limited by the requirement for high temperatures to initiate the process, which also promotes frequent side reactions involving the nitroxide, which can lead to the formation of undesired by-products.[100]

Atom-transfer radical polymerization is another widely used controlled radical polymerization method that relies on the reversible activation and deactivation of a dormant species through a redox process. In ATRP, a transition metal complex, often a copper or iron-based complex, coordinates with a halogen atom attached to the polymer chain end, forming a dormant species. The activation step involves the transfer of the halogen atom from the dormant chain to a metal complex, generating a free radical that can propagate the polymerization (**Scheme 8**).

Scheme 8 Simplified mechanism of the active-dormant species equilibrium during ATRP with a copper complex. The active species on the left has a propagating polymer chain (P_n•), which is deactivated by a halogen (X) transfer from a metal complex (CuL, L is the ligand) to the active radical.

ATRP operates through an equilibrium between these active (P_n•) and dormant (P_n-X) species. The metal complex facilitates the transfer of the halogen atom by change of oxidative state, which is a reversible process that controls the rate of polymerization. The key to ATRP is maintaining a low concentration of radicals, which prevents the formation of excessive side products and leads to the synthesis of polymers with controlled molecular weights and low polydispersities.[101]
The efficiency of ATRP can be significantly affected by the choice of metal catalyst, ligand, solvent, and temperature. Copper-based catalysts are commonly used because of their low cost and efficiency. The advantages of ATRP include its versatility, as it can be used to polymerize commonly used monomers, including styrenes, acrylates, and methacrylates, and its ability to produce well-defined polymers with controlled architectures, such as block copolymers and star polymers.[102] However, ATRP is sensitive to impurities, particularly oxygen, which oxidize the catalyst and lower polymerization efficiency.[103]

Both NMP and ATRP are widely employed in the synthesis of well-defined polymers. However, due to their distinct disadvantages regarding polymerizable monomers, sensitivity to oxygen, and strict reaction condition requirements, RAFT polymerization emerged as another technique to obtain control over radical polymerizations.[104,105] RAFT polymerization is adaptive to the thiol-based chain-transfer mechanism and is the only technique, that does not suppress the free radical concentration.[101]

RAFT polymerization utilizes a chain transfer agent to mediate the radical polymerization process, facilitating the control of chain growth through a reversible addition-fragmentation mechanism. This technique is applicable to a wide range of monomers, including functional and challenging monomers that are difficult to polymerize using other RDP methods, such as ATRP and NMP.[101]
RAFT polymerization is a widely used CRP technique that enables the synthesis of well-defined polymers with precise molecular weights and narrow distributions. It relies

on a chain transfer agent (CTA), typically a thiocarbonyl compound, to mediate radical polymerization through a reversible addition-fragmentation mechanism. This process allows control over chain growth and can polymerize a broad range of monomers, including those challenging for other CRP methods like ATRP and NMP.[101]

A schematic representation of the RAFT mechanism is shown in **Scheme 9**. The RAFT mechanism begins with a free radical initiator that generates radicals, which then react with monomers to form growing polymer chains. The key feature is the reversible chain transfer process, where the polymer radical interacts with the CTA, forming an equilibrium that regulates polymerization. The side-group (Z) in the CTA significantly influences reaction rates and must be carefully selected based on the monomer and reaction conditions. Termination occurs via recombination or disproportionation but is minimized due to the reversible nature of the RAFT process.

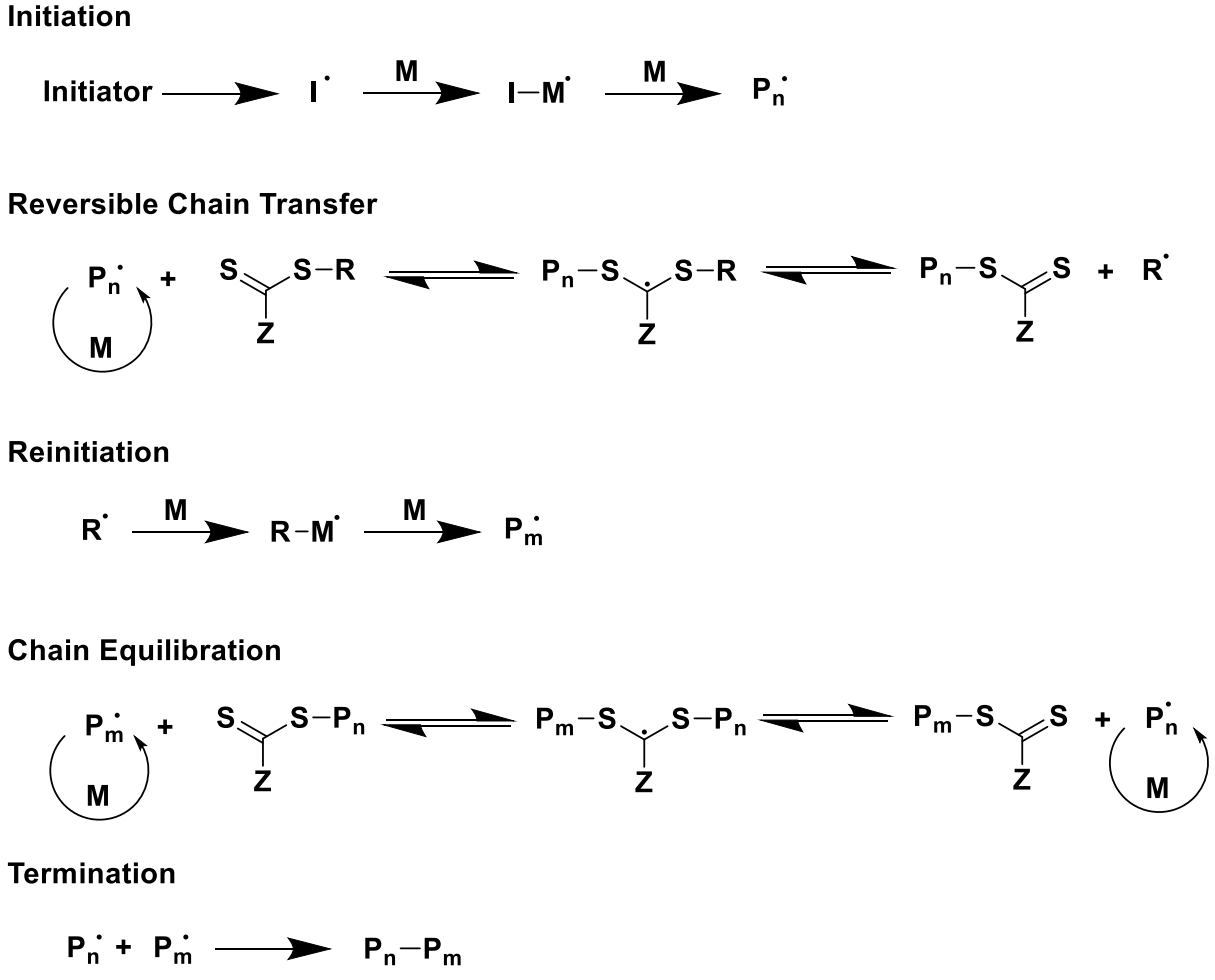

Scheme 9 Mechanism of RAFT polymerization. I is the initiator radical, M are monomers, Z is the side-group controlling addition-fragmentation rates, R is a free radical leaving group. Adapted from Handbook of RAFT Polymerization.[106]

A major advantage of RAFT polymerization is its versatility, enabling the synthesis of various polymer architectures such as block copolymers, graft polymers, and star-shaped polymers. Additionally, RAFT polymerization is less sensitive to oxygen and moisture than ATRP, making it easier to handle. However, limitations include potential side reactions, challenges in achieving very high molecular weights, and the sensitivity of CTAs to strong nucleophiles, which can degrade their effectiveness. Despite these challenges, RAFT polymerization remains a valuable tool for designing advanced materials with controlled properties.[106]

2.4 Post-Polymerization Modification

While traditional polymerization methods are crucial for the synthesis of a broad range of polymer materials, the ability to further manipulate the properties and functionalities of polymers after their initial synthesis is equally significant. This concept, known as post-polymerization modification (PPM), has emerged as a powerful tool for tailoring the physical, chemical, and mechanical properties of polymers. By introducing modifications at specific sites of the polymer chain or by altering the molecular architecture, PPM allows to design polymers with enhanced properties for specialized applications.[107]

Post-polymerization modification involves chemical changes to a polymer after its initial polymerization. Unlike copolymerization or other methods that involve adding monomers during the polymerization process, PPM typically takes place after the polymer backbone has been formed. The primary goal of PPM is to introduce new functional groups, alter the polymer's structure, or modify its physical properties without compromising the integrity of the polymer chain.[108]

In essence, PPM can be divided into two main categories:

1. Functional Group Modification: This involves the introduction of new functional groups to the polymer which may not be available through standard polymerization procedures, such as amines, alcohols, carboxylic acids and derivatives, or alkyl chains. These groups can modify the polymer’s reactivity, solubility, or interaction with other substances.[109]

2. Structural Modification: Structural modifications alter the polymer’s architecture, such as changing the molecular weight, branching, or crosslinking, to enhance

mechanical or thermal properties. These changes may also impact the crystallinity, the glass transition temperature (T_g), or the polymer morphology.[110]

Various strategies can be employed to carry out PPM, and the choice of method depends on the desired modification and the type of polymer. These methods can generally be divided into two main approaches: chemical modification and physical modification.

Chemical modifications are typically achieved through reactions that either attach new functional groups or alter the existing ones on the polymer chain. Common chemical post-polymerization techniques include click reactions, thiol-disulfide exchange, cycloadditions, Michael-additions, or chemistries based on, active esters, isocyanates, and epoxides.[107,108,110]

A click reaction is characterized by several key features: modularity, insensitivity to solvent parameters, high chemical yields, and resilience to the presence of oxygen and water. Additionally, these reactions exhibit both regiospecificity and stereospecificity. A crucial aspect is a large thermodynamic driving force, which ensures that the reaction favors the formation of a single product. This exothermic nature drives the reaction towards completion. Typical reactions include but are not limited to: copper-catalyzed azide-alkyne cycloaddition (CuAAC), strain-promoted azide-alkyne cycloaddition (SPAAC), thiol-ene, nucleophilic ring-opening, and isourea formation.[111,112]

For all chemical modifications of polymers, high yields and selectivity are crucial as they ensure efficient, cost-effective modifications without unwanted by-products since, steric hindrance can present challenges, especially when modifying polymers with bulky side groups or dense structures. This can result in lower reaction rates, incomplete modifications, or the need for harsher conditions (e.g., higher temperature or pressure), which may risk degrading the polymer.[113] PPMs may be used to target the repeating units of a polymer but are also useful to modify end-groups to enable chemistries which are not accessible during polymerization conditions (**Scheme 10**).

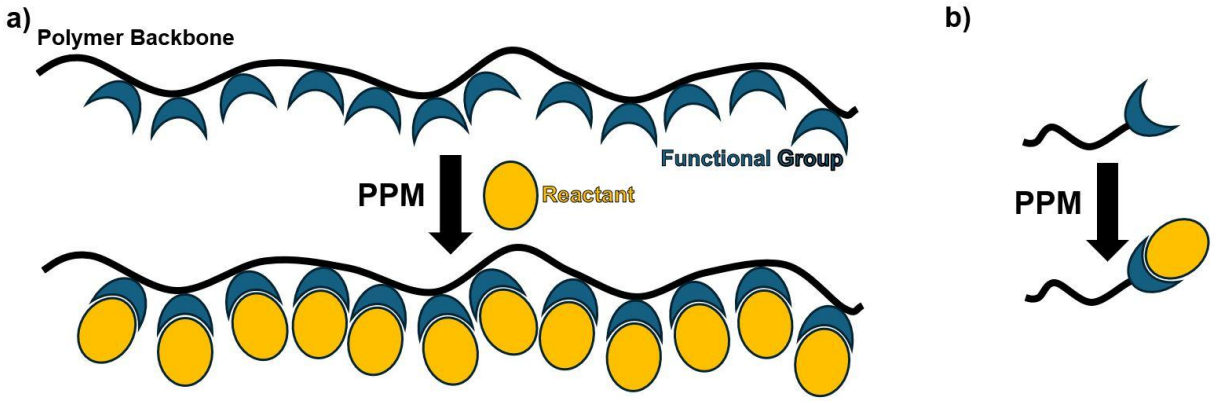

Scheme 10 a) The reactant of a PPM is used to modify/attach to a functional group of the repeating unit along the backbone. b) The reactant is used to modify/attach to the end-group of a polymer.

Exemplary, poly(glycidyl methacrylate) exhibits a reactive epoxide in its repeating unit, which can be ring-opened by nucleophiles such as, thiols or amines(**Scheme 11** a). However, if an RDRP method like RAFT is employed to control the molecular weight and dispersity, modifying the monomer before polymerization can be harmful to the CTA. Hence, a PPM would be the preferable synthetic pathway. Similarly, polyethers such as, poly(ethylene oxide) (PEO) often have hydroxy end-groups which can be used for chemical PPM. A simple and quantitative option is the addition of isocyanates (**Scheme 11** b) which have further functional groups for applications like coating[114] and crosslinking.[115]

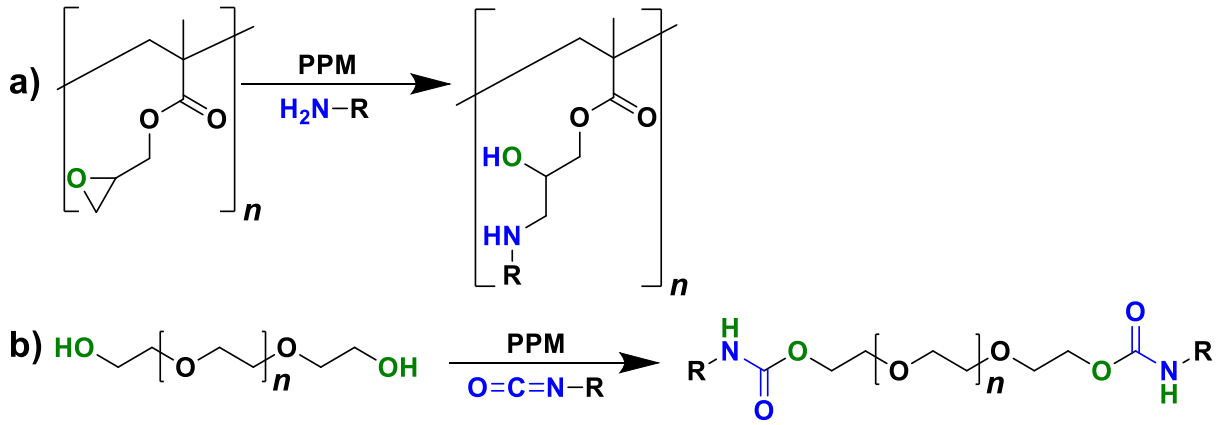

Scheme 11 a) PPM of poly(glycidyl methacrylate) with a primary amine on each repeating unit along the backbone. b) End-group PPM of PEO with an isocyanate.

Physical modifications, on the other hand, typically involve changes to the polymer morphology or architecture without altering the chemical composition. These changes include processes like crosslinking and self-assembly.

Post-polymerization crosslinking involves the formation of covalent bonds between polymer chains, which can enhance the mechanical strength and thermal stability of

the material. Crosslinking can be achieved through thermal, photochemical, or chemical methods, and it is commonly used to produce materials such as hydrogels, elastomers, and coatings. It is also one of the oldest forms of PPM as the vulcanization of natural rubber with elemental sulfur is known since the 1840s.[107]

Self-assembly is the process by which individual polymer chains spontaneously organize into higher-order structures such as nanoparticles, micelles, or films.[116] This can be facilitated by block copolymers, which have distinct segments with different solubility or reactivity. Self-assembly can be triggered by solvents, thermal or photochemical activation. PPMs can further control or fine-tune the self-assembly process by incorporating specific interactions such as hydrogen bonding, ionic interactions, or metal-ligand coordination.[117]

2.5 Particle Coating

Particle coating is a highly versatile technique used in numerous fields, including materials science,[118] biotechnology,[119] and pharmaceuticals.[120] Typically done through applying a thin, uniform layer of material to the surface of particles to modify their properties, improve stability, or enable specific functionality. Although there are a plethora of different organic[121] and inorganic[122] coating materials available, this chapter will focus on polymers as coating materials for particles. In polymer science, particle coating plays a key role in the design of advanced materials with tailored functionalities.[123]

At the core of particle coating chemistry is the interaction between the coating material and the particle surface. This interaction is critical to ensure that the coating adheres strongly to the particle without compromising the particle's integrity. For efficient coating, adhesion forces such as van der Waals forces, hydrogen bonding, and covalent bonds must be strong enough to ensure stability.[124] Additionally, the solubility of the coating material in the chosen solvent and its ability to uniformly spread across the particle surface are essential for achieving a consistent and effective layer.[125]

To further enhance adhesion and tailor the properties of the coating, surface modification of the particles is often required. This can include the introduction of reactive functional groups that facilitate better interactions between the particle and the coating material. For example, the use of catechol-based[126] and silane-based[127]

coatings has gained significant attention due to their strong bonding properties, particularly in aqueous environments.[128]

Grafting is a widely used strategy in particle coating, as it allows the attachment of polymers or other materials to the particle surface. There are three primary approaches for grafting, namely, grafting-from, grafting-to, and grafting-through, each with distinct chemical mechanisms and advantages (**Scheme 12**).[129] Often it is necessary, to activate the surface to be reactive enough for these grafting approaches. Activating the surface include chemical and physical techniques such as plasma discharge, UV irradiation, ozone treatment, acidification/basification, and attachment of functional surface-ankers.[130,131]

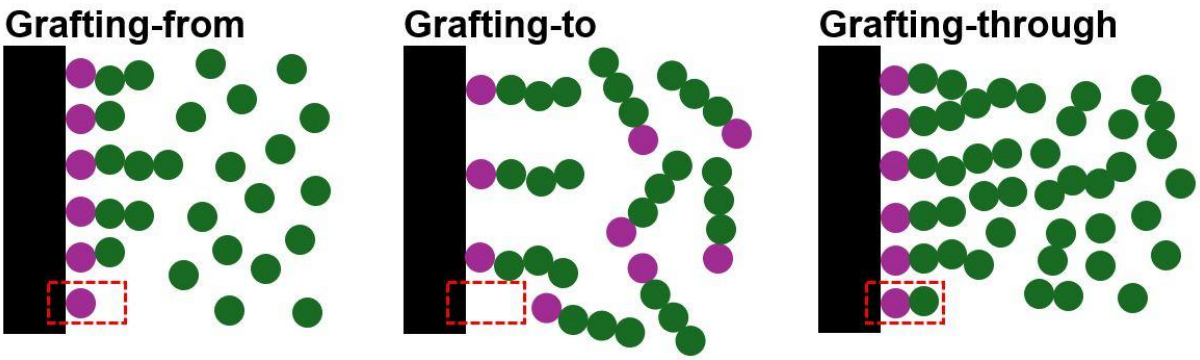

Scheme 12 Schematic representation of grafting strategies for surface modification with polymers. black: particle surface; violet: surface-anker; green: monomers. The red box shows the (pre-treated) surface before the polymer coating reaction begins

Grafting-from involves growing polymer chains directly from the particle surface by initiating polymerization at reactive sites on the particle. This method typically employs surface-initiated polymerization techniques, such as ATRP,[132] RAFT,[129] or NMP[133] methods. The key advantage of the grafting-from approach is the ability to control the polymer architecture, such as chain length and density, directly on the particle surface. However, the method requires careful control of polymerization conditions to avoid unwanted crosslinking or aggregation of the grafted chains. Further, often it is necessary to synthesize the surface-ankers, which increases cost and can be challenging depending on the intended use.[129]

Grafting-to involves attaching pre-synthesized polymer chains to reactive groups on the particle surface. This method is generally simpler and faster than grafting-from, as it does not require initiating polymerization on the particle itself. However, the process can be limited by steric hindrance, especially when long polymer chains are involved. This can lead to incomplete attachment or difficulty in achieving a uniform coating. To

overcome these limitations, the particle surface can be modified with smaller functional groups that allow for efficient attachment of the polymers.[131,134]

Grafting-through combines aspects of both grafting-from and grafting-to. In this approach, monomers are polymerized in the presence of particles with monomers attached to the surface, resulting in the formation of polymer chains that are covalently bond to the particle surface. This method allows for more control over the length and density of the grafted polymer, similar to grafting-from, while also allowing for the use of pre-formed polymerizable monomers, similar to grafting-to.[131]

2.5.1 Silane-based Coatings

Silane-based coatings are another popular choice for particle coating, particularly for silica-based particles or other materials that can react with alkoxy silane functional groups. Alkoxy silanes are compounds that contain silicon atoms bonded to organic groups, typically with the general formula R-Si(OR')$_3$, where R is an organic group (often a functional group such as an amine or thiol) and OR' is an alkoxy group (e.g., methoxy or ethoxy).[135]

The chemistry behind silane-based coatings involves the hydrolysis of the alkoxy groups to form silanol (Si-OH) groups, which then condense with other silanol or hydroxy groups to form siloxane (Si-O-Si) and metal-silane (M-O-Si) bonds. This reaction results in the formation of a strong, covalent bond between the silane molecule and the particle surface, providing a durable coating (**Scheme 13**).[136]

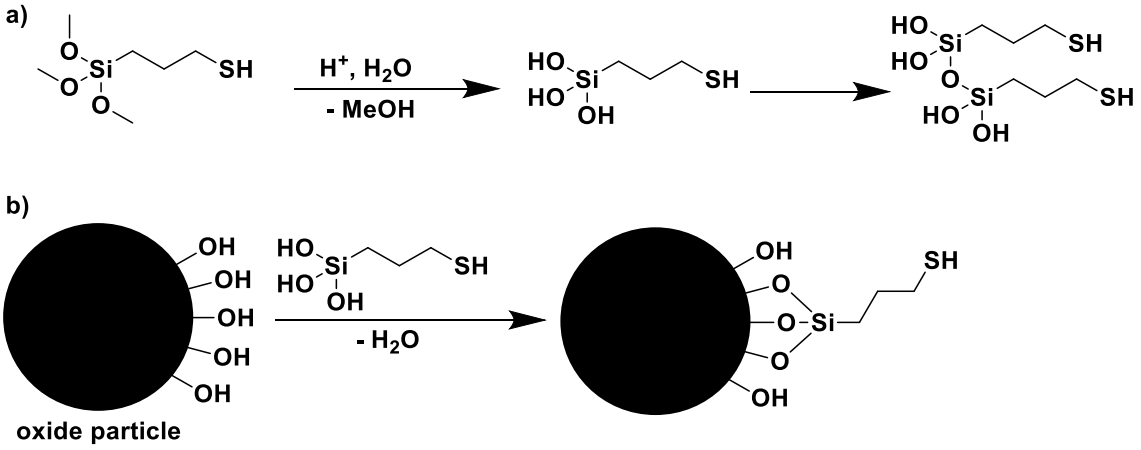

Scheme 13 Schematic reaction steps in particle coating utilizing alkoxysilanes. a) Hydrolysis of alkoxy groups to yield silanol. Silanol can homocondense into siloxanes. b) Silanols react with hydroxy groups at an oxide particle surface to yield a covalently bond silane with a functional group attached to the particle surface.

The ratio of homocondensation versus surface grafting depends on the pH-value, concentration, and the surface properties. Due to this behavior, it is possible to coat particles and surfaces in a single layer of silane. Usually, pH 4 is necessary to suppress the formation of siloxanes in solution.[136,137]

Silane-based coatings are particularly effective in modifying surfaces to increase their hydrophobicity,[138] improve dispersion in polymer matrices,[139] or impart specific chemical functionalities such as RAFT agents.[140] Further, silanes can be used to functionalize silica nanoparticles for drug delivery,[141] sensors,[142] or as catalyst supports.[143] The versatility of silane chemistry allows for fine-tuning of the particle surface, enabling specific interactions with biological systems or enhancing the mechanical properties of composite materials. Hence, many alkoxysilanes with various functional groups are commercially available and also employed in industrial processes.[144,145]

2.6 Lithium-Ion Batteries

Lithium-ion (Li-ion) batteries have revolutionized energy storage technology since their commercialization in the early 1990s. Li-ion batteries were and are of significant importance in the development of advanced technologies such as portable electrical devices (e.g., smartphones, laptops, tablets), electrical vehicles, and stationary energy storage.

With their higher energy densities compared to other battery chemistries, they play an important role in the energy transition and the implementation of renewable energies.

The development of the Li-ion battery by John B. Goodenough, M. Stanley Whittingham, and Akira Yoshino was awarded with the Nobel Prize in Chemistry in 2019 underlining the high impact of their invention for society.[146]

Like all batteries, Li-ion batteries work through a reversible redox reaction (reduction-oxidation reaction), where one material loses electrons (oxidation) and another material gains electrons (reduction). During discharge this reaction occurs between two electrodes: the anode (where oxidation happens) and the cathode (where reduction takes place). As the redox reaction happens, electrical energy is generated by the movement of electrons through an external circuit from the anode to the cathode through current collectors. Meanwhile during charging the process is reversed and electrical energy is converted to chemical energy which is stored in the battery's

materials. To prevent direct contact between the anode and cathode, a separator keeps them apart while still allowing ions to move through an electrolyte, maintaining the flow of charge needed for the battery to function.[147]
The underlined components are the core parts of a battery cell and essential for its operation.

They are explained more in-depth in the following:

Anode: In LIBs, the anode is typically made from graphite. Novel developments also aim to employ silicon, alloys, and Li-metal in the anode.[148] During discharge, lithium ions migrate from the anode to the cathode through the electrolyte, releasing electrons. Charging reverses the direction of ion and electron flow.

Cathode: The cathode of LIBs is typically composed of a lithium metal oxide. Several different chemistries with their own advantages and disadvantages are used such as lithium cobalt oxide (LCO), lithium manganese oxide (LMO), lithium nickel cobalt aluminum oxide (NCA), lithium nickel manganese cobalt oxide (NMC), and lithium iron phosphate (LFP). It serves as the destination for lithium ions during discharge and the source of lithium ions during charging.[149]

Electrolyte: The electrolyte is a liquid or gel-like substance that facilitates the movement of (lithium) ions between the anode and cathode. In a LIB, it usually consists of a lithium salt (e.g., $LiClO_4$, $LiPF_6$) dissolved in an organic solvent, such as ethylene carbonate, propylene carbonate or dimethyl carbonate.[150]

Separator: The separator is a porous, insulating material (often polymers such as polyethylene or polypropylene placed between the anode and cathode to prevent direct contact between the electrodes, thus avoiding short circuits. It also allows the passage of lithium ions during charging and discharging.[151]

Current Collectors: The current collectors, typically made from copper (for the anode) and aluminum (for the cathode), serve to collect and transport electrons from the external circuit to the electrodes.[152]

Lithium-ion batteries operate based on the intercalation and de-intercalation of lithium ions into the graphite anode and cathode materials during charging and discharging cycles.

During discharge, when the battery is supplying power to a load, lithium ions move from the anode to the cathode through the electrolyte. This movement occurs because of the electrochemical potential difference between the anode and cathode. The electrochemical reactions for a typical commercial Li-ion battery can be summarized as follows:[153]

Anode Reaction (Graphite):

$$LiC_6 \rightarrow Li^+ + e^- + C_6$$

Lithium ions (Li^+) are released from the graphite structure and move through the electrolyte towards the cathode, while electrons (e^-) flow through the external circuit, generating electrical energy.

Cathode Reaction (LCO):

$$LiCoO_2 + Li^+ + e^- \rightarrow Li_2CoO_2$$

At the cathode, lithium ions combine with the cobalt oxide, incorporating electrons from the external circuit.

During charging, when an external voltage is applied to the battery, lithium ions are forced to move from the cathode back to the anode, where they are intercalated into the graphite. The reactions are reversed from the discharging process (**Scheme 14**).[154]

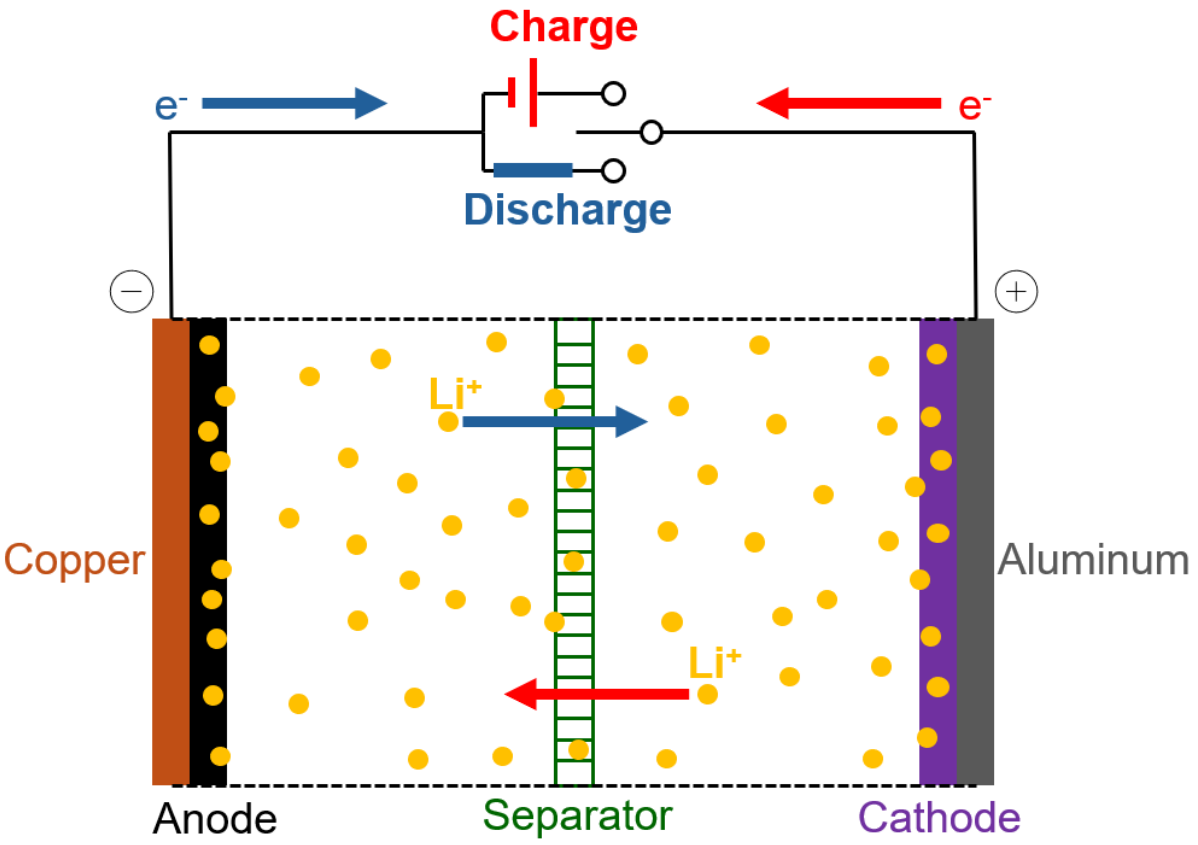

Scheme 14 Simplified scheme of a Li-ion battery with a liquid electrolyte (LE) (not shown). Lithium ion and electron flow direction is depicted in red during charge and blue during discharge.[156]

The energy density of a battery is one of its most critical performance metrics and is defined as the amount of energy that can be stored per unit of mass or volume. Li-ion batteries typically exhibit an energy density ranging from 100 to 250 Wh kg^{-1}, significantly higher than older battery technologies, such as nickel-cadmium (NiCd) and lead-acid batteries. Additionally, the nominal voltage of a lithium-ion cell is usually around 3.7 V, which is higher than that of most other rechargeable batteries contributing to the widespread adoption of Li-ion technology.[155]

Other factors which are of high importance for batteries and especially in their application are cycle life, C-rate capability, temperature sensitivity, and safety.

Cycle life refers to the number of charge and discharge cycles a battery can undergo before its capacity drops below a specified percentage of its original capacity (typically 80%). The cycle life of Li-ion batteries can range up to 10000 cycles under ideal conditions.[157]

The C-rate (**Equation 4**) at which a battery is charged or discharged is critical to its performance. Higher charge and discharge rates generally result in greater power

output but can also lead to increased heat generation, reduced efficiency, and increased degradation rates.

$$\text{C-rate} = \frac{I}{C_{max}} \qquad \textbf{Equation 4}$$

with I (in A) being the current of charge or discharge and C_{max} (in Ah) the maximum capacity of the battery cell.[158]

Temperature plays a crucial role in the performance and longevity of lithium-ion batteries. High temperatures can increase the rate of side reactions within the battery, potentially leading to capacity degradation, overheating, or even thermal runaway, which can result in dangerous situations such as fires. On the contrary, extremely low temperatures can reduce the battery's efficiency and available capacity, as the movement of lithium ions is slower in colder environments.[159]

The stability of the voltage during both charge and discharge cycles is critical to battery performance. Overcharging or discharging a lithium-ion battery beyond a specific voltage range (typically below 3.0 V or above 4.2 V per cell) can significantly reduce its lifespan or cause safety hazards.[160] Battery management systems (BMS) are used to monitor and control voltage levels, temperature, and charge/discharge speed to prevent harmful conditions. All properties of a Li-ion battery are depending on factors such as the specific chemistry used, depth of discharge, cycling behavior, and operating temperature.

The main benefits of Li-ion batteries compared to other cell chemistries are the high energy density, long cycle life, low self-discharge, and no memory effect. However, there are still many limitations which need to be lifted to enable more applications such as long-distance electric vehicles or electric air and nautical travel. The main concerns are the relatively high cost, safety concerns due to fires and explosions, and environmental impact of the required materials like cobalt.[161,162]

2.7 Solid-State Batteries

The development of solid-state batteries (SSBs) promises to reduce many drawbacks of the current Li-ion technology. One of the most notable benefits is their higher energy density. SSBs may utilize a lithium metal anode rather than the graphite anodes used in conventional lithium-ion batteries. Lithium metal has a much higher theoretical capacity (3,860 mAh g^{-1}) compared to graphite (372 mAh g^{-1}), which allows for a higher

energy density. This results in increased volumetric and gravimetric energy densities. Additionally, these batteries may operate at higher voltages, further boosting their performance.[163]

Improved safety is another significant advantage of solid-state lithium metal batteries. Unlike liquid electrolytes, which are flammable and prone to leaks, solid-state batteries use non-flammable solid electrolytes. These solid electrolytes provide better thermal stability, which reduces the risk of battery fires and leaks. Moreover, solid-state batteries help mitigate dendrite formation, a challenge in conventional lithium-ion batteries. Lithium dendrites are tree-like structures of lithium metal that can penetrate the separator and cause short circuits. Solid-state electrolytes (SSE) can help prevent dendrite growth, leading to safer operation and longer cycle life.[164]

The development of solid-state lithium metal batteries is driven by several key technologies. One of the most important points is the advancement of high-performance SSEs. In general, SSEs must possess high ionic conductivity, stability at room temperature, and mechanical properties that prevent dendrite penetration. A schematic representation of the requirements of SSEs is shown in **Scheme 15**.

Currently, there are three main SSE categories: polymers, oxides, and sulfides which will be explained in more detail in Chapter 2.7.1, 2.7.2, and 2.7.3, respectively.[163]

Another critical area of focus is the lithium metal anode. Although lithium metal provides a higher energy density than traditional graphite anodes, it is more prone to dendrite formation. Depending on the SSE employed this issue varies widely as e.g., oxide SSEs are harder and therefore dendrite penetration is suppressed compared to soft polymers. Techniques to mitigate this issue, such as using protective coatings on the lithium metal anode or incorporating solid electrolytes that prevent dendrite growth are being developed.[165]

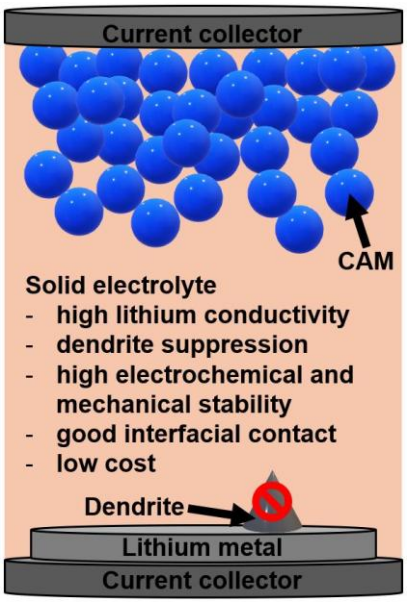

Scheme 15 Ideal solid-state electrolyte for Lithium metal batteries. The cathode active material (CAM) is the Li-ion intercalating material on the cathode side.[163]

The interface between the solid electrolyte and the lithium metal anode also requires attention. A stable interface is essential to prevent delamination and reduce degradation, which can reduce battery efficiency and lifespan. Different strategies such as the use of protective layers or special processing techniques to improve the adhesion and stability of these interfaces are under investigation.[166,167]

In addition to the anode and electrolyte, the development of high-energy cathodes is also crucial. Materials such as lithium-rich layered oxides and sulfur are being investigated as potential candidates for high-capacity cathodes that pair well with lithium metal anodes in SSBs.[168,169]

Manufacturing techniques also play a vital role in the commercialization of solid-state lithium metal batteries. Scaling-up production is challenging due to the delicate nature of solid electrolytes, which require advanced deposition, lamination, and sintering processes. Achieving cost-effective mass production methods is essential to make SSBs more affordable and scalable for widespread use.[170]

2.7.1 Polymer Electrolytes

Polymer electrolytes (PEs) have emerged as a favorable choice due to their processability, flexibility, low cost, and the ability to form stable interfaces with lithium metal, making them an ideal candidate for lithium metal solid-state batteries.[171]

In general, polymer electrolytes consist of a polymer matrix in which lithium salts are dissolved, providing the ionic conductivity necessary for battery operation. The most

common types of PEs used in SSBs are based on polyethers, polyesters, polycarbonates, halogenated polymers and their derivatives. Polymers for SSEs need to have polar groups that can dissociate the lithium salt.[172] Single-ion conducting polymers, which incorporate the anion of the dissociating lithium salt into their structure, are also explored.[173] These materials offer varying combinations of mechanical flexibility, processability, electrochemical stability, and electrochemical performance.[4]

The ability to conduct lithium ions (Li^+) is crucial for efficient battery operation. The ionic conductivity of PEs is highly dependent on the polymer's amorphous nature, dielectric constant, the concentration of the lithium salt, and temperature.[172]

Nevertheless, the ionic conductivity of PEs is typically lower than that of liquid electrolytes, which has limited their widespread adoption. However, various strategies, such as increasing the lithium salt concentration, incorporating plasticizers, or developing composite electrolytes with inorganic fillers, have been used to enhance the conductivity and thermal stability of PEs.

The transport of lithium ions in PEs is a critical aspect of their performance in solid-state batteries. Understanding the ion transport mechanism is essential for optimizing the ionic conductivity and enhancing the overall performance of SSBs.

Lithium ions move through the polymer matrix via a process of diffusion. The polymer chains undergo motion, allowing lithium ions to hop between available sites in the polymer backbone. The driving force is the electric field originating from the electrodes. There are three main Li^+ diffusion mechanisms in PEs: interchain hopping, intrachain hopping, and segmental motion (**Scheme 16**). The Lithium-ion transport in inter- and intrachain hopping occurs through the breaking and new formation of Li^+ coordination from the polar groups of the polymer along the same or different polymer chains. This is the main transport mechanism in crystalline phases or at low temperatures.[16] At elevated temperatures above the melting point T_m the segmental motion of polymer chain segments with the coordinated Li-ions amplifies the other two transport mechanisms and adds to a strongly increased ion transport.[174]

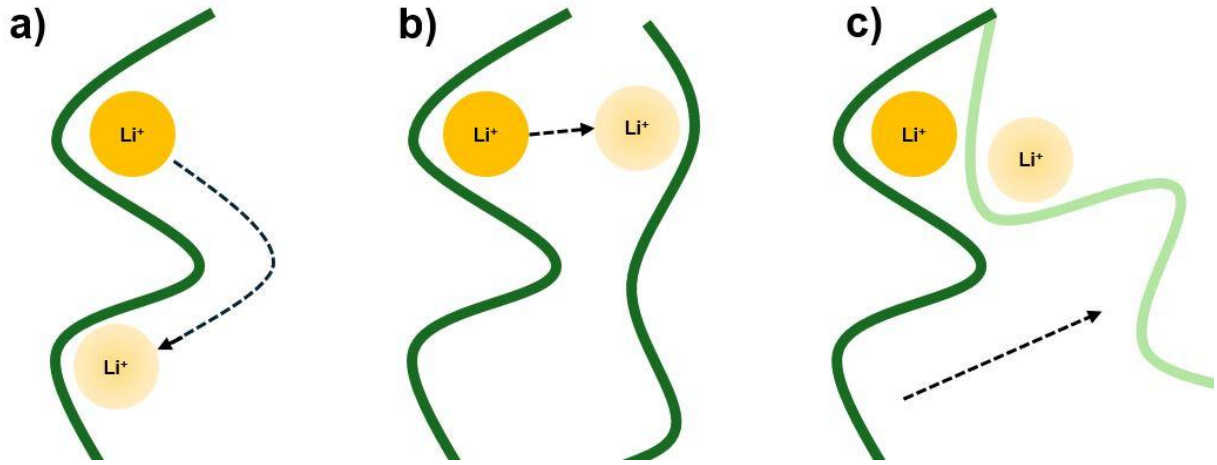

Scheme 16 Schematic depiction of: a) interchain hopping b) intrachain hopping c) segmental motion.

The overall ionic conductivity σ of the polymer electrolyte is governed by the number density of free lithium ions and their mobility, which depends on the polymer chain dynamics. There are two main models that can be applied to the ion transport in polymers. If inter- and intrachain hopping is the main contributor, the ionic conductivity follows Arrhenius behavior:

$$\sigma = \sigma_0 * e^{\frac{-E_a}{RT}} \qquad \textbf{Equation 5}$$

σ_0 is the pre-exponential factor, E_a is the activation energy for ion migration, R is the molar gas constant, T is the temperature.[175]

If the segmental motion has a significant contribution, the Vogel-Tamman-Fulcher (VTF) model includes ion-hopping and segmental motion:

$$\sigma = \sigma_0 * T^{\frac{1}{2}} * e^{\frac{-B}{T-T_0}} \qquad \textbf{Equation 6}$$

Here B is a pseudoactivation energy and T_0 the equilibrium glass transition temperature (approximated by T_g-50 K).[176]

In general, at lower temperatures, the polymer matrix becomes more rigid, which reduces ion mobility and, consequently, ionic conductivity. Conversely, higher temperatures provide more polymer chain mobility, increasing the ion conduction. However, there is a trade-off, as excessive temperatures may cause the decomposition of the electrolyte or increase the risk of lithium dendrite formation.

The role of the lithium salt is essential in the ion conduction process. Common salts such as lithium bis(trifluoromethanesulfonyl)imide (LiTFSI), lithium hexafluorophosphate ($LiPF_6$), lithium perchlorate ($LiClO_4$), lithium triflate (LiTf), and lithium tetraborate (LiBOB) are typically used in polymer electrolytes.[177] These salts dissociate into lithium ions and counterions in the electrolyte. The dissociation is not

always complete, and salt clusters of Li^+ and the anions can form depending on concentration. The transport mechanisms for the clusters are identical to completely dissociated salts, but may reduce the ionic conductivity due to the generally bulky anions.[178] Fluorinated salts are generally preferred as they stabilize the anion through the strong electron withdrawing effect which increases acidity. Further, they tend to form a more stable solid electrolyte interface (SEI) between the anode and the electrolyte. In the SEI, the formation of LiF is generally preferred as it is Li^+ conductive while simultaneously passivating the anode.[179,180]

2.7.2 Oxide Electrolytes

Oxide electrolytes for lithium metal batteries (LMB) are typically made from inorganic materials that possess high ionic conductivity and electrochemical stability, essential for stable and safe operation of LMBs. The most widely studied classes of ceramic and oxidic electrolytes include: NaSICON-type, Garnet-type, Perovskite-type, and LiSICON-type.[181]

NaSICON (Sodium (Na) Super Ionic Conductor) type solid-state electrolytes, known for their high ionic conductivity, are increasingly explored in LMBs, particularly for their ability to enable safe and efficient ion transport. They typically have a framework structure composed of interconnected polyhedra (such as phosphate or silicate groups), allowing for easy movement of sodium/lithium ions through the material and therefore exhibit enhanced safety by preventing dendrite growth in lithium metal anodes. A well-known example of a lithium-based NaSICON electrolyte is $Li_{1.5}Al_{0.5}Ti_{1.5}(PO_4)_3$ (LATP), which exhibits high ionic conductivity and stability.[182] LATP will be explained in more detail in Chapter 2.7.2.1.

Garnet-type solid-state electrolytes are named after the garnet crystal structure, which is a cubic structure typically. For Li containing garnets the general structure is $Li_xA_3B_2O_{12}$, with A and B being other metals. This three-dimensional network facilitates the efficient movement of lithium ions. One of the most well-known garnet-type SSEs is $Li_7La_3Zr_2O_{12}$ (LLZO), which has gained significant attention due to its high ionic conductivity and excellent stability at room temperature.[183] LLZO will be explained in more detail in Chapter 2.7.2.2.

Perovskite-type SSEs are an important class of materials for LMBs, primarily due to their unique crystal structure and stability. The perovskite structure is characterized by an ABO_3 arrangement, where *A* and *B* are cations, forming a 3D-network where Li-

ions hop through octahedral channels inside a generally tetragonal crystal structure. Perovskite-type Li-ion SSEs are *A* site deficient, which enables spacious vacancies facilitating Li-ion hopping. Perovskite SSEs are notable for their ability to maintain structural integrity when in contact with lithium metal, preventing dendrite formation. A well-known example is $Li_{3x}La_{(2/3)-x}TiO_3$ (LLTO), where titanium ions are surrounded by oxygen octahedra, forming a stable lattice structure with deficient La layers. These materials although promising, have some drawbacks as they exhibit poor stability against lithium metal and high interface resistance.[184]

LiSICON (Lithium Super Ionic Conductor) solid-state electrolytes are another class of SSEs. The LiSICON structure typically consists of a network of lithium ions interspersed with other metal or non-metal ions, arranged in a framework that allows for fast ion migration. They are structurally similar to γ-Li_3PO_4 and are based on XO_4 (X = P, Al, Si, Ge, S, and Ti) tetrahedral and Li-O polyhedral groups. This highly ordered framework provides excellent stability, particularly when in contact with lithium metal. Further, substituting oxygen for sulfur expands this group of SSEs into the thiophosphate Li-ion conductors, which often have significantly increased ionic conductivity compared to their phosphate counterparts.[185] Thiophosphates will be explained in more detail in Chapter 2.7.3.

Other oxide SSE types include the anti-perovskite-type and amorphous oxides. They are not as commonly utilized in current research but interested readers may find more information here: anti-perovskite-type,[186–188] amorphous oxides.[189–193]

Ionic conductivity in ceramic and oxidic solid-state electrolytes depends on several factors, including the crystallographic structure, the types of defects or vacancies in the material, and the interaction between lithium ions and the electrolyte lattice.

In ceramic electrolytes, lithium ions typically migrate through the crystal lattice by hopping between available sites or vacancies within the material.

In crystalline structures, cationic vacancies or interstitials act as the mobile charged species. The three primary migration mechanisms, depicted in **Scheme 17**, are: (left) vacancy diffusion, where an ion moves into an adjacent vacant site, (middle) the direct interstitial mechanism, where ions migrate between partially filled sites, and (right) the concerted or correlated interstitialcy (knock-on) mechanism, where the migrating interstitial ion displaces a neighboring lattice ion to an adjacent site.[194]

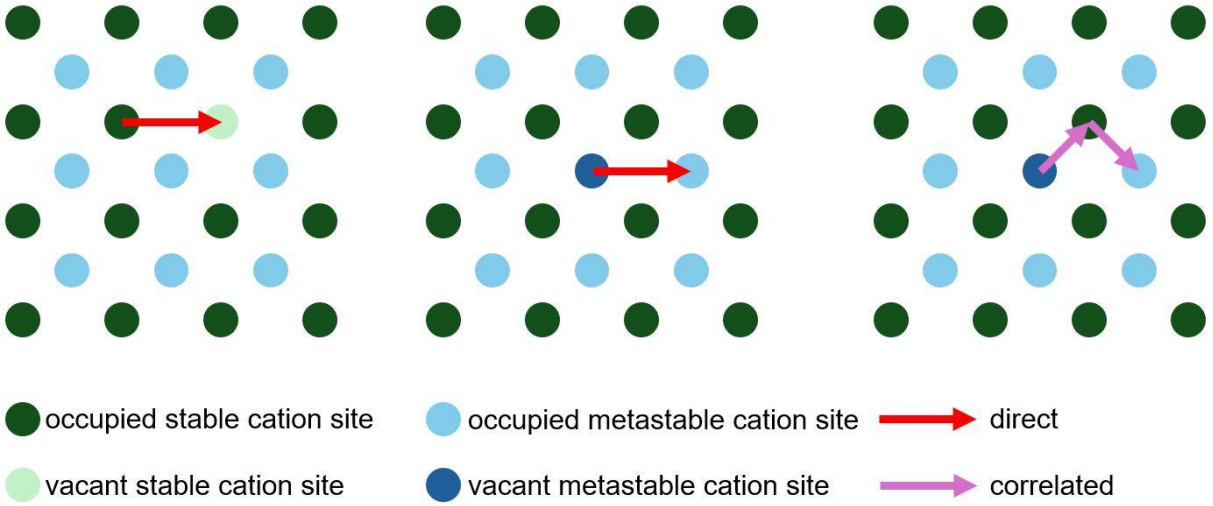

Scheme 17 Migration mechanisms for cations in latices. Left: vacancy diffusion from an occupied to a vacant lattice position. Middle: direct interstitial mechanism of no fully occupied positions. Right: concerted or correlated interstitialcy mechanism. The migrating ion pushes a neighboring ion into a vacant position.[194]

For garnet-type materials like LLZO, lithium conduction is facilitated by vacancies in the structure. The ionic conductivity of ceramic electrolytes is often enhanced by doping with various elements to create vacancies or to increase the lattice parameters, thereby improving ion diffusion. In garnet-type electrolytes, doping with elements such as Al, Ga, or Ta increases the number of available lithium sites, facilitating faster ion migration. The type and concentration of dopants play a crucial role in tuning the ionic conductivity and stability of these materials.[195]

One of the most significant challenges with ceramic electrolytes is ensuring stable contact with the lithium metal anode. The interface between the electrolyte and lithium metal can form a passivating layer that inhibits ion conduction, leading to an increase in interfacial resistance and the potential for dendrite formation. This problem is exacerbated in the case of oxide-based electrolytes, where the formation of a stable SEI layer is difficult to achieve.[196]

Recent research has focused on modifying the electrolyte surface or introducing interlayers between the lithium metal and electrolyte to improve interfacial stability. Thin lithium-based interlayers or the application of buffer layers protective coatings, has been shown to help mitigate these issues.[196]

Ceramic electrolytes, particularly those made from garnet or oxide materials, often exhibit brittleness, which poses challenges during the cycling of lithium metal batteries. Mechanical failure, such as cracking or delamination, can significantly degrade battery performance.[197]

Further, many ceramic electrolytes, such as garnet-based and perovskite-type materials, require high-temperature sintering (above 1000°C) to achieve optimal ionic conductivity. This high-temperature requirement makes the production process costly and energy-intensive, which limits the scalability of these materials for commercial applications.[182,198]

2.7.2.1 LATP

First reported in the late 1980s, LATP is a highly promising solid-state electrolyte SSE as it provides high ionic conductivity and uses no critical elements.[199] Additionally, phosphates are stable against air and water which for oxides often leads to chemical degradation.[200]

LATP is typically synthesized using a variety of solid-state and sol-gel techniques. The most common approach involves the high-temperature solid-state reaction of stoichiometric amounts of lithium phosphate (Li_3PO_4), titanium dioxide (TiO_2), and aluminum oxide (Al_2O_3). The precursors are mixed in a ball mill and subsequently densified by calcination and sintering. This method allows for the formation of the crystalline LATP phase at temperatures typically ranging from 700 to 1200°C.[27,201–203]

A similar method is melt quenching. The precursors are molten at even higher temperatures (1500 °C) and quenched at room temperature to obtain an amorphous glass. The glass is sintered for crystallization.[204,205]

An alternative solution method is the sol-gel synthesis, which allows to produce LATP with improved homogeneity and lower sintering temperatures. In this process, metal alkoxides or aqueous solutions of metal salts are used to create a gel-like precursor, which is then heated to form the desired LATP phase. This method can reduce the formation of impurities and control the particle size distribution, potentially improving the ionic conductivity of the final product.[206–208]

Coprecipitation is also possible. The precursors are dissolved and precipitated through pH adjustment followed by calcination.[209]

Additionally, other approaches, such as hydrothermal[210] or microwave-assisted synthesis,[211,212] have been explored to produce LATP at lower temperatures, enhancing process efficiency and reducing energy consumption. These techniques are still being developed and refined to optimize the properties of LATP for large-scale applications.

The main phase of LATP is $LiTi_2(PO_4)_3$ (LTP) in a NaSICON-type structure with partial substitution of Ti^{4+} with Al^{3+}. LTP forms a 3D network from TiO_6 octahedra and PO_4 tetrahedra. Li^+ fully occupies the Li1 sites in between the octahedra but also partially fills other sides (Li3) (**Scheme 18**).[213]

The lattice parameters and the degree of crystallinity significantly influence the ionic conductivity of LATP, which is typically in the range of 10^{-6} to 10^{-3} S cm^{-1} at room temperature, depending on the synthesis method, density, and material purity. The structure also allows for the incorporation of various dopants.[182]

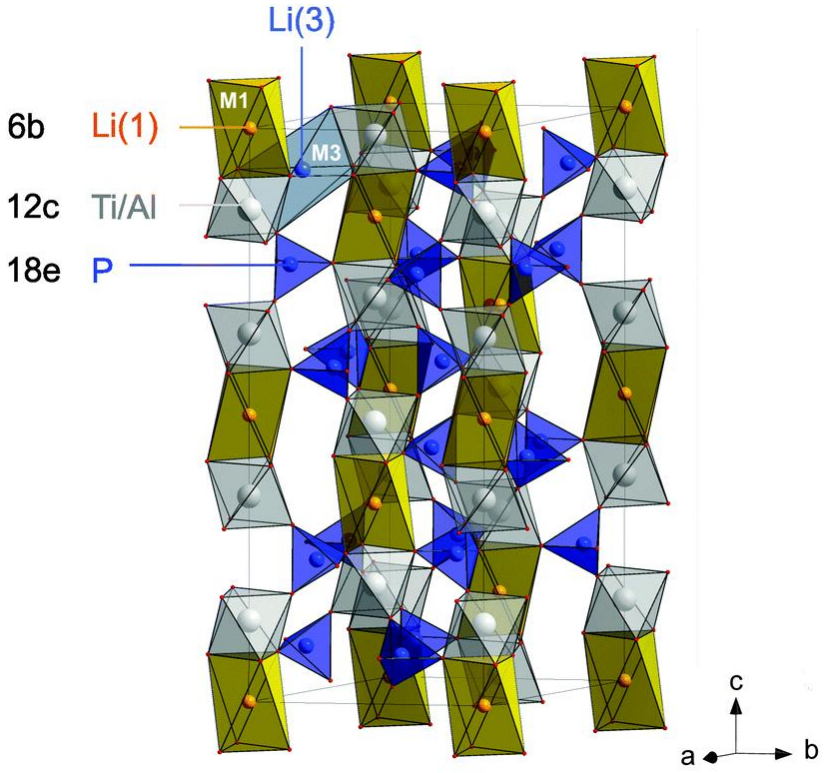

Scheme 18 Crystal lattice of LATP. Reproduced from Epp et al. with permission from the Royal Society of Chemistry.[213]

LATP has a wide electrochemical stability window (between 2 V and 6 V vs. $Li|Li^+$), making it suitable for use with a variety of electrodes, including high-voltage cathodes. This stability is critical for preventing unwanted side reactions and enhancing the overall safety of the battery system.[214]

Further, it is mechanically strong, with a relatively high modulus, making it more resilient to the mechanical stresses that arise during the cycling of solid-state batteries. This property reduces the risk of cracking or failure during charge and discharge cycles.[215] Also, LATP exhibits good thermal stability, retaining its properties at elevated temperatures.[216]

One of the major challenges in the development of solid-state batteries is the stability of the electrolyte against lithium metal, which is commonly used as the anode material. LATP's stability against lithium is influenced by several factors, including the grain boundary structure, the presence of impurities, and the operating temperature. In some cases, small amounts of reaction with lithium can occur at the interface, leading to the formation of SEI layers, which can impact the overall performance.[217] LATP has demonstrated some degree of stability against lithium metal, but ultimately fails to form a stable SEI in long term cycling. Artificial SEI formation,[218] protective layers,[219] and interface engineering[220] seem to be effective methods to reduce or mitigate this problem.

2.7.2.2 LLZO

LLZO ($Li_7La_3Zr_2O_{12}$) has emerged as another highly promising SSE due to its high ionic conductivity and high stability against lithium metal.

LLZO has an ionic conductivity typically in the range of 10^{-4} to 10^{-3} S cm^{-1} at room temperature,[221,222] which is higher than LATP. Further, LLZO's electrochemical stability window is wider than LATP's, typically ranging from 0 V to > 6 V vs. $Li|Li^+$ depending on the specific dopants and synthesis conditions.[223] This wide voltage window allows LLZO to be compatible with a broader range of high-voltage cathodes, which is beneficial for advancing solid-state batteries, particularly those aimed at high-energy applications and allows direct contact with the Li-metal anode.

The synthesis of LLZO uses a lot of the same techniques[224] as aforementioned for LATP (2.7.2.1) with the addition of some methods like spark plasma sintering,[225] pulsed laser deposition,[226] or chemical vapor deposition.[227,228]

One of the major challenges for LLZO, compared to LATP, is its instability when exposed to air. Unlike LATP, which is stable under ambient conditions, LLZO is highly reactive with moisture and CO_2 in the atmosphere. When exposed to air, LLZO the forms lithium carbonate (Li_2CO_3) at the surface which significantly reduces its ionic conductivity and leads to dendrite penetration of the SSE.[229,230] This air instability poses significant challenges in both its synthesis and handling, as precautions must be taken to prevent degradation during processing and storage.[231] To improve the air compatibility, LLZO can be coated with different organic and inorganic compounds to reduce the formation of Li_2CO_3 at the surface and in grain boundaries.[229,232–234]

Another issue is the high hardness of LLZO. Powders or pellets are highly abrasive to machinery leading to contamination and accelerated mechanical degradation.[30]

LLZO has a tetragonal and a cubic garnet structure consisting of ZrO_6 octahedra with LaO_8 dodecahedra. The cubic phase has the higher ionic conductivity (~ 10^{-4} to 10^{-3} S cm^{-1}) compared to the tetragonal phase (~ 10^{-6} S cm^{-1}) and is therefore the preferred phase.[31,235] Increased ionic conductivity is caused by more empty Li^+ positions available in the cubic phase.[236] Li1 and Li2 Li-coordination sites are located in between the octa- and dodecahedra. The cubic structure is depicted in **Scheme 19**.

LLZO is often doped to improve its electrochemical performance. Various dopants, such as Al^{3+},[237] Ga^{3+},[237] Ce^{4+},[238] Ta^{5+},[239] and Nb^{5+},[240] are introduced to modify the crystal structure and increase lithium ion mobility. For instance, doping with Al^{3+} or Ga^{3+} typically leads to the substitution of La^{3+} or Zr^{4+} sites, which can create additional lithium ion conduction pathways, thereby enhancing the ionic conductivity of LLZO.[236]

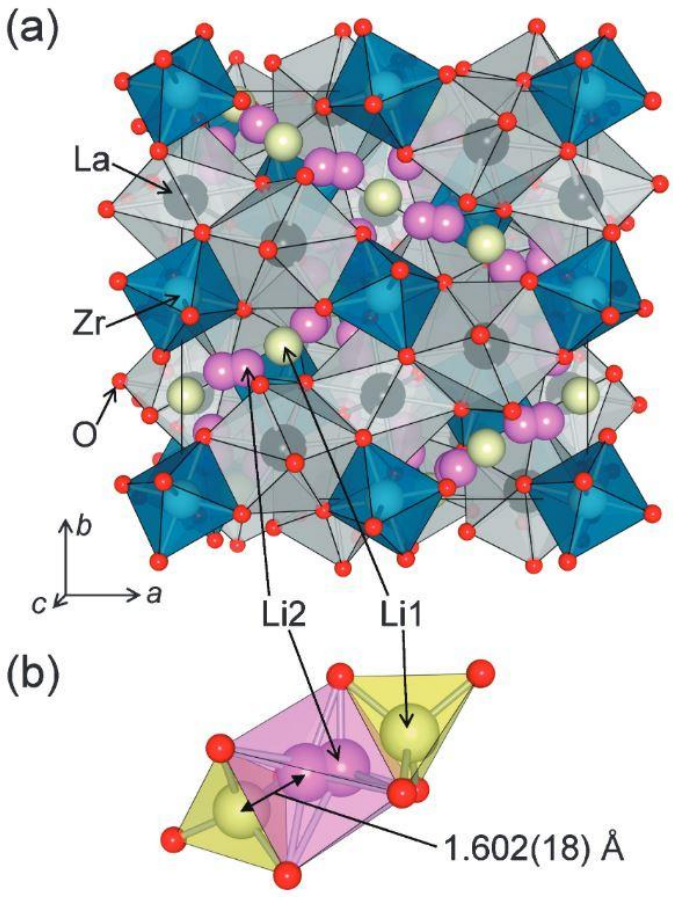

Scheme 19 a) Crystal structure of cubic LLZO. b) L1 and L2 coordination sites in the polyhedra. Reproduced from Awaka et al. with permission from the Chemical Society of Japan.[241]

Additionally, these dopants help stabilize the crystal structure, which is crucial for maintaining the high ionic conductivity at elevated temperatures. Elements like Ta^{5+} or

Nb^{5+} can enhance the overall stability of the garnet structure and reduce the grain boundary resistance, further improving the material's ionic conductivity and long-term cycling performance.[242] Doping not only optimizes the ionic conductivity but also enhances the stability of LLZO in contact with lithium metal, helping mitigate issues related to dendrite formation and interface stability. However, the precise control of doping concentration is essential, as excessive doping can lead to defects or instability that might negate the benefits of doping.[239]

2.7.3 Sulfide Electrolytes

As aforementioned, sulfide-based compounds have emerged as a promising class of materials due to their high ionic conductivity and wide electrochemical stability window. Sulfide-SSEs can be categorized into different classes depending on their chemical composition: thiophosphates, halide thiophosphates, sulfides without phosphorous, and glassy sulfides.[243]

Thiophosphates generally only contain the elements Li-X-P-S (X = Sn, Ge, Al, Y, Si or nothing) but can have a wide range of molar ratios. Lithium thiophosphate (Li_3PO_4) was the discovered in 1984 as a sulfide-based crystalline Li-ion conductor.[244] Since then, many iterations and optimizations of the simple structure lead to a stark increase in ionic conductivity at room temperature from $3 \cdot 10^{-7}$ S cm^{-1} to 10^{-3} S cm^{-1}.[245] This is mainly due to the optimized molar ratio and synthesis procedures as the $Li_7P_3S_{11}$ exhibits a ionic conductivity up to 10,000 times higher.[245]

The structure of thiophosphate electrolytes is typically characterized by a framework that consists of tetrahedral $[PS_4]^{3-}$ units, where the phosphorus atoms are surrounded by sulfur atoms. The lithium ions are intercalated into the structure and can move through the crystal lattice, primarily via a vacancy-mediated mechanism. The ionic conductivity of thiophosphate-based materials depends heavily on the structural features, such as the size and connectivity of the channels through which lithium ions migrate. Additionally, the presence of sulfur in the structure significantly affects the material's electronic properties, helping to mitigate issues related to electronic conduction.[246]

Introducing other elements like Sn, Ge, Al, Y, or Si changes the crystal structure into different thio-LiSICONs. Moreover, these additions often aim to increase ionic conductivity and lower the ion-migration activation energy.[243]

However, thiophosphates suffer from challenges such as low mechanical strength, which can result in poor interface contact with electrodes, which require high stack pressures for battery operation and limited processability at large scales.[247] Additionally, thiophosphates tend to degrade in contact with air and water while releasing toxic H_2S.[248]

The introduction of halides into the thiophosphate structure leads to the formation of argyrodites. They will be explained in Chapter 2.7.3.1.

Another class of sulfide-based electrolytes that has attracted attention for lithium metal batteries is phosphorus-free sulfides. These materials consist of lithium and sulfur, and other metal sulfides, but lack the phosphorus component found in thiophosphates. Some examples are Li_2GeS_3,[249] Li_4SnS_4[250] or Li_3SbS_4.[251] Similar to the thiophosphates, optimizing the molar ratios of the elements can improve their performance. It is also reported that these non-phosphor based SSEs are less susceptible to hydrolysis and oxidation.[252]

Phosphorus-free sulfide-based electrolytes typically suffer from a lack of structural stability, which can lead to issues such as reduced performance overtime or during cycling. Their relatively high reactivity with lithium metal can lead to the formation of detrimental interphase layers that degrade performance. Additionally, these materials often require precise synthesis conditions, and the cost and toxicity of the raw materials (e.g., antimony or arsenic) can pose challenges for scalability.[253]

The main advantage of glassy sulfides is the absence of grain boundaries due to their amorphous nature. Further, they exhibit isotropic ionic conduction and usually are easy to fabricate through a wide range of compositions.

Glassy sulfides lack the long-range order seen in crystalline sulfide electrolytes, but they retain many of the desirable ionic conductivity characteristics. The absence of grain boundaries in amorphous materials can reduce resistance to ion flow and enhance overall conductivity. Glassy sulfides are often composed of lithium sulfide (Li_2S) or lithium thiolates in combination with other glass-forming materials such as germanium, boron, or phosphorus. Most research in this field is focused on Li_2S-P_2S_5 and Li_2S-SiS_2 doped with various compounds such as LiI or Li_3PO_4.[254–256]

One of the key advantages of glassy sulfides is their ability to be processed into thin films or complex shapes, which is essential for the development of flexible and high-performance solid-state batteries. These materials also tend to have relatively low

activation energy for ionic conduction, allowing them to operate efficiently at room temperature or even slightly lower temperatures.[257]

Although glassy sulfides offer improved ionic conductivity and processability, they often face challenges related to mechanical stability and long-term cycling performance. The amorphous structure can result in reduced stability under prolonged electrochemical cycling, and these materials may suffer from high reactivity with lithium metal. Additionally, glassy sulfides are typically brittle and prone to hydrolysis and oxidation, which can lead to cracking during battery operation and affect their mechanical integrity.[258]

2.7.3.1 Argyrodites

Among the various sulfide-based solid-state electrolyte materials mentioned above, argyrodite-type sulfide compounds, specifically those with the general formula LiPSX (where X represents a halide such as Cl, Br, or I), have emerged as highly promising candidates for LMBs. These materials offer exceptional ionic conductivity, wide electrochemical stability windows, and compatibility with lithium metal anodes, making them particularly attractive for next-generation battery technologies.[259]

Argyrodite-type sulfides are a unique class of materials that feature a distinctive crystal structure. The general formula LiPSX refers to lithium phosphorus sulfide halides, where free sulfide (S^{2-}) halide (X^{-}) ions are integrated into a framework of $[PS_4]^{3-}$ tetrahedra, with lithium ions occupying interstitial sites within the lattice (**Scheme 20**).[260]

The ionic conductivity of LiPSX electrolytes is generally in the range of 10^{-3} to 10^{-2} S cm^{-1} at room temperature, with some compositions exceeding these values at elevated temperatures. This high ionic conductivity is critical for enabling fast charge and discharge rates, which are essential for high-performance lithium metal batteries. This high conductivity is attributed to the relatively low activation energy for Li-ion migration in the crystal structure, as well as the well-defined pathways for lithium ions to travel through the framework.[259,261]

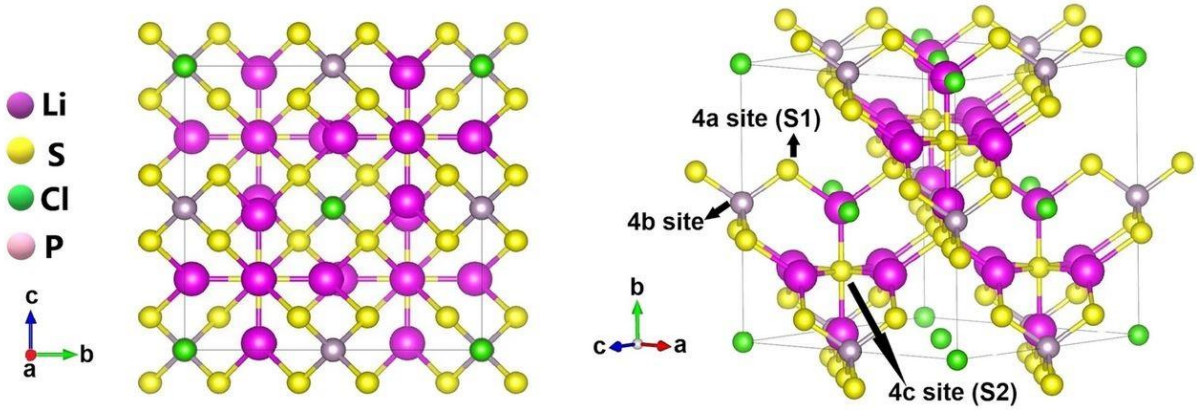

Scheme 20 Crystal structure of Li_6PS_5Cl. Reproduced from Baktash et al. with permission from Springer Nature.[261]

In addition to their high ionic conductivity, argyrodite-type electrolytes also exhibit relatively high stability against lithium metal, which is a significant advantage in preventing the formation of dendrites.[262] To further improve the Li-metal-argyrodite interface, Li-In alloys are often used as anodes to reduce side reactions.[263] The ability of these electrolytes to support stable cycling and mitigate dendrite growth is one of the key factors driving their potential in lithium metal battery applications.

Another critical property of LiPSX electrolytes is their electrochemical stability window. These materials are typically stable within a voltage range of 0.5 to 3.0 V versus $Li|Li^+$, which makes them incompatible with a wide range of cathode materials, like NCM, and other high-energy-density materials. However, in practice the window is wider as the (de)lithiation in full cells is favored compared to the decomposition of the argyrodite.[264] Further, the degradation products passivate the cathode and do not lead to continuous decomposition as was confirmed by Auvergniot et al.[265]

The synthesis of argyrodite LiPSX-type electrolytes requires careful control of composition, stoichiometry, and processing conditions. Several synthesis methods have been explored for the preparation of these materials, each influencing the microstructure and ionic conductivity of the final product.

The most common method for synthesizing LiPSX argyrodite electrolytes is solid-state synthesis, in which stoichiometric amounts of Li_2S, phosphorus pentasulfide (P_4S_{10}), and halide salts (e.g., LiCl, LiBr, or LiI) are mixed or ball milled and heated at high temperatures. This approach typically requires temperatures in the range of 400–600°C, depending on the specific composition and desired properties. The solid-state method is relatively straightforward and cost-effective, but it may result in the formation

of unwanted phases or poor control over the final particle size and morphology. Post-annealing and sintering can help to improve the ionic conductivity of the argyrodites.[266] In order to improve the homogeneity of the precursor materials and the overall quality of the final product, solution-based methods such as sol-gel or precipitation techniques are increasingly being explored. These methods involve dissolving the precursors in a solvent, followed by gelation and subsequent precipitation or heat treatment to form the argyrodite electrolyte. This approach allows for better control over the stoichiometry, morphology, and microstructure of the resulting materials, and it has the potential to yield higher ionic conductivity compared to solid-state synthesis.[267–270]

One of the significant challenges for solid-state electrolytes is maintaining mechanical integrity during cycling. While argyrodite LiPSX electrolytes offer good mechanical properties relative to other sulfide-based SSEs, they are still relatively brittle compared to liquid electrolytes. However, their high ionic conductivity, coupled with the ability to form dense, uniform thin films, can help improve their mechanical stability, especially when used in combination with appropriate electrolyte composite structures.[271]

Cycling stability is a crucial factor in determining the long-term performance of lithium metal batteries. LiPSX electrolytes have demonstrated excellent cycling stability, particularly in combination with lithium-indium metal anodes. The materials are able to maintain high ionic conductivity and stable electrochemical performance over many charge and discharge cycles but usually require high pressure (> 25 - 50 MPa) to maintain contact and stable electrochemical performance.[272]

Argyrodite LiPSX-type sulfide electrolytes represent a promising class of solid-state materials for lithium metal batteries, offering high ionic conductivity, excellent electrochemical stability, and compatibility with lithium metal anodes. While challenges related to mechanical fragility, interface stability, and scalability remain, continued research into these materials is likely to yield solutions that make LiPSX electrolytes a key component of future high-energy-density, safe, and long-lasting lithium metal batteries. With further advancements in synthetic techniques and materials engineering, LiPSX-type argyrodite electrolytes hold the potential to play a significant role in the next generation of energy storage technologies.[266]

2.7.4 Hybrid Electrolytes

As aforementioned, one of the primary challenges facing SSBs is the development of a suitable electrolyte that can effectively support the use of lithium metal as the anode. Lithium metal, while offering high energy density, is prone to dendrite formation, which can cause short circuits and failure of the battery especially in polymer electrolytes. Furthermore, such polymer-based materials often struggle with low ionic conductivity at room temperature. Oxides and sulfides, however, often have issues related to interface stability between the electrolyte and the electrodes in addition to high pressure requirements for stable cyclisation. Further, processing and scalability of polymers is significantly easier than it is for oxides and sulfides.[4] In **Table 1** the main advantages and disadvantages of oxides, sulfides, and polymers for application in SSBs are summarized. In summary, all the currently employed SSEs of oxides, sulfides, and polymers have significant drawbacks, hindering the industrialization and adoption of the SSB.

To solve some of these issues and mitigate the weaknesses of the different concepts, hybrid systems gain more and more attention as they are a logical step towards improving the performance and applicability of SSBs.

Table 1 List of main strengths and drawbacks of oxide, sulfide, and polymer solid state electrolytes. Adapted from Pacios et al.[4]

	oxides	sulfides	polymers
strengths	high voltage compatibility	high ionic conductivity	facile processing
	safety	decent electrode compatibility	mass production feasibility
	stability		
drawbacks	high interface resistance	high cost	high operation temperature
	unfavorable mechanical properties	air sensitive	dendrites cause short circuits
	mass production feasibility	toxicity of H_2S	stability
	conductivity	stability	ion conductivity
	difficult to make large capacity batteries	mass production feasibility	

The term “hybrid electrolyte” is not clearly defined yet in the scientific literature. For this thesis, the definition of a “hybrid electrolyte” will follow Passerini’s et al. definition of a hybrid electrolyte:[273]

Hybrid electrolytes contain at least two lithium-ion conductive phases, which can be inorganic, polymeric and/or liquid phases.

A comprehensive overview of the classification and types of hybrid electrolytes from Passerini et al. is depicted in **Scheme 21**.

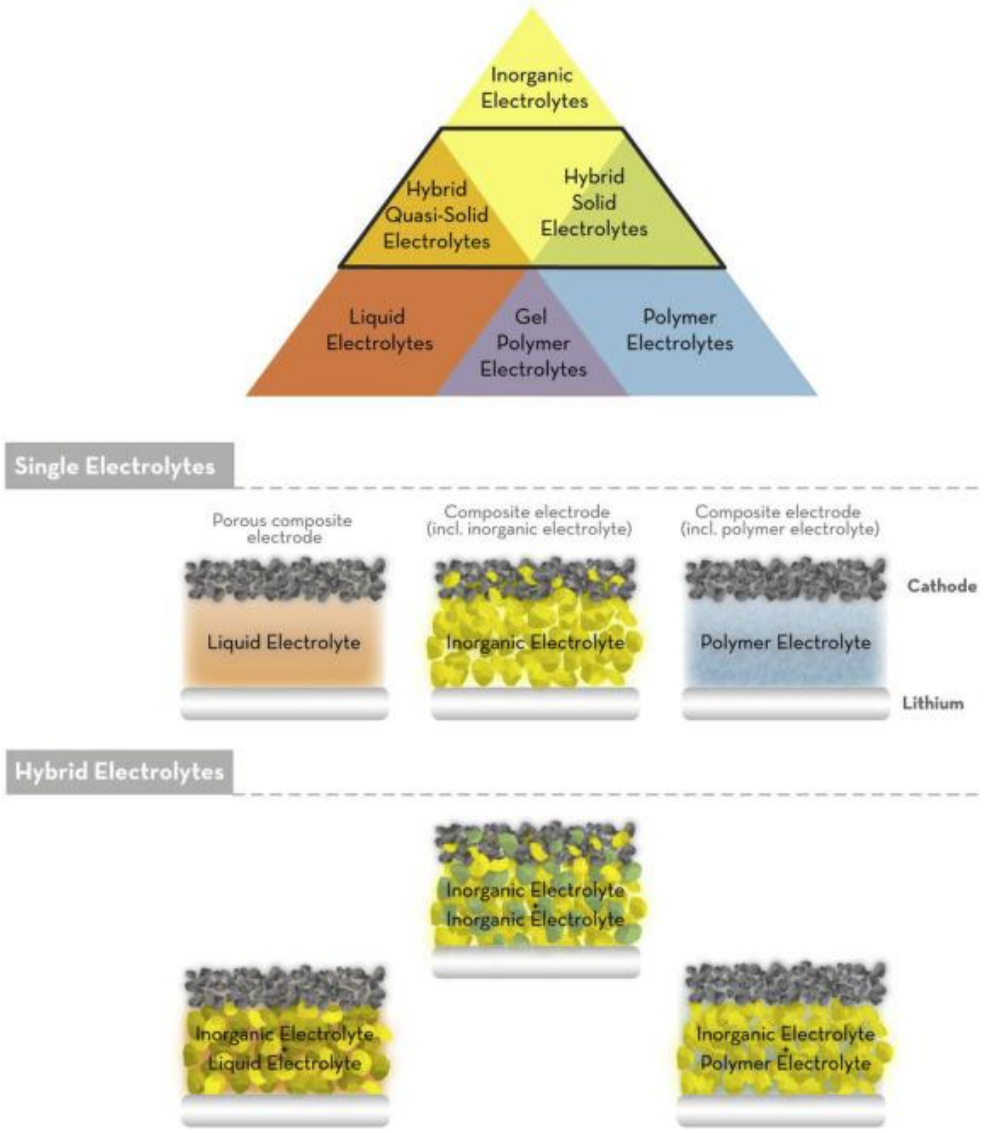

Scheme 21 Classification of hybrid electrolytes. Oxides and sulfides are combined as inorganic electrolytes. Reprinted from Passerini et al. with permission from Elsevier.[273]

With this definition, hybrid electrolytes combine aspects of solid, polymeric, and liquid phases, aiming to mitigate the drawbacks of each. Since there are a plethora of different SSEs available, and the possible combinations are nearly endless, categorization is difficult. However, current research shows that some combinations seem to have more potential than others:[274]

1. layered hybrid electrolytes
2. inorganic mixed hybrid electrolytes
3. liquid-oxide hybrid electrolytes
4. polymer-inorganic hybrid electrolytes

A simplified overview of the four categories of hybrids is shown in **Scheme 22**. Note that all hybrid concepts may also be combined, and constituents may be swapped.

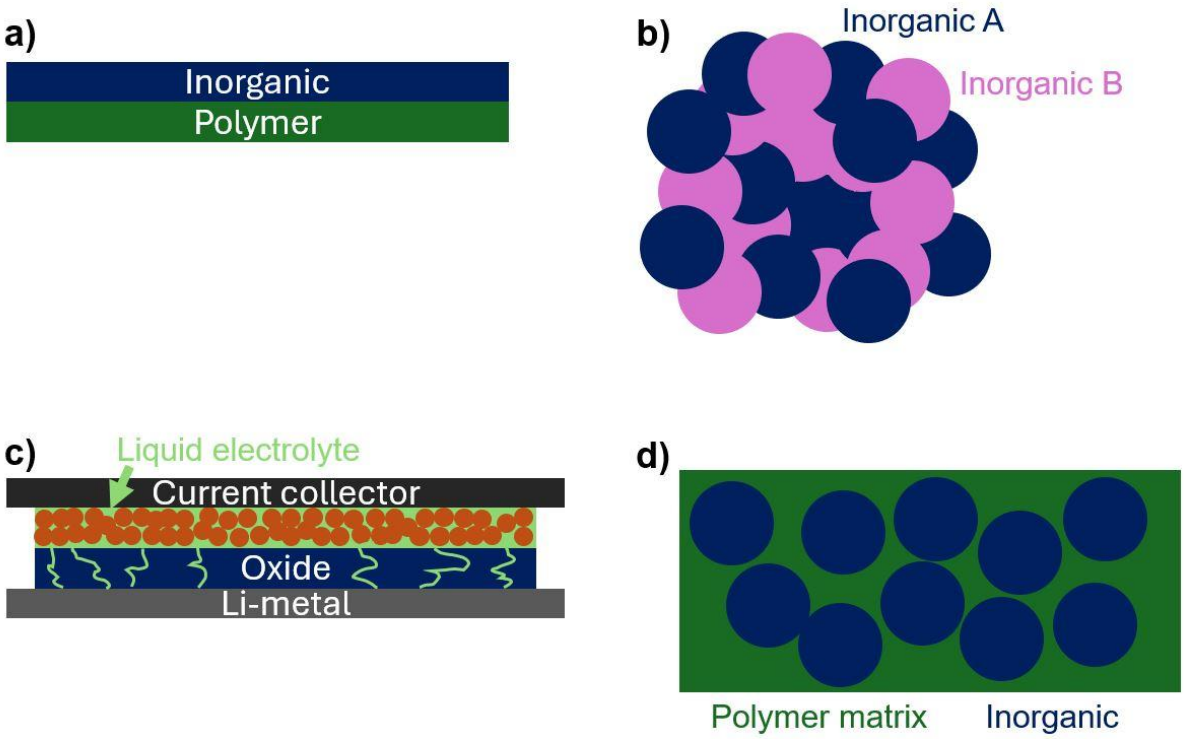

Scheme 22 Schematic representation of different hybrid categories. a) layered electrolyte of a polymer and an inorganic layer. b) mixed inorganic electrolytes from two different inorganic electrolytes. c) a liquid-oxide hybrid electrolyte where the liquid electrolyte provides ion transport into the porous cathode (orange) and infiltrates the oxide separator. d) a polymer-inorganic electrolyte where an inorganic particle is dispersed in a polymer matrix. Note that these concepts may be combined, and components can be exchanged for other materials as well. Often, a strict definition of a hybrid system is not possible.

Layered hybrid electrolytes typically consist of layers of different materials, each engineered to address specific challenges in lithium-metal SSBs. For instance, one layer may be designed to provide high ionic conductivity, while another offers robust mechanical properties to suppress dendrite growth.[275] A common configuration involves a solid inorganic layer combined with a polymeric or gel phase at the electrode interfaces. The inorganic layer, often composed of materials such as lithium garnets (e.g., LLZO)[276] or sulfides,[277] ensures excellent ionic transport and chemical stability. The polymeric layer, in contrast, provides flexibility and an intimate interface with the lithium-metal anode, reducing interfacial resistance and accommodating volume changes during cycling.[278]

The layered structure enables a synergetic effect, overcoming limitations inherent to single-phase electrolytes. For example, while purely inorganic electrolytes exhibit high

stiffness and ionic conductivity, they often suffer from poor interfacial contact with the lithium-metal anode. Conversely, polymer electrolytes, though mechanically soft and chemically compatible, typically have lower ionic conductivities. By integrating these phases into a layered hybrid design, it is possible to leverage the strengths of both materials while mitigating their drawbacks. Layers of inorganic layers are also possible. Hüttl et al. showed, that a layered system of LLZO and $Li_7P_3S_{11}$ could reduce interface resistance drastically while improving cycling stability without accelerating degradation.[279] Combining two polymeric phases can also be beneficial. Goodenough's research group could increase Li-metal battery performance by layering one low and one high voltage stable PE and orienting them accordingly to anode and cathode.[280]

Recent advancements in layered hybrid electrolytes have focused on improving interfacial stability and scalability. Techniques such as atomic layer deposition[281] and layer-by-layer assembly have been employed to precisely control the thickness and composition of each layer.[7] Furthermore, the incorporation of lithium salts and ceramic fillers into polymeric layers has been shown to enhance ionic conductivity and lithium-ion transference number.[282] Some studies have also explored the use of gradient structures, where the composition and properties vary gradually across the layers to minimize delamination and improve mechanical integrity.[283]

Inorganic mixed hybrid electrolytes are materials that combine multiple inorganic phases to create a composite structure with synergistic properties. These hybrids are designed to address key challenges such as ionic conductivity, mechanical stability, and interfacial compatibility with lithium metal. Currently, there are few examples of inorganic-inorganic mixtures. Both available studies use Li_3PS_4 to mitigate the high hardness of oxides such as LLZO,[284] Al_2O_3, SiO_2, and $Li_6ZnNb_4O_{14}$[285] to ease processing, increase the ionic conductivity and improve interfacial contact.

Liquid-oxide hybrid electrolytes combine the advantages of both liquid and solid electrolytes. These hybrid electrolytes are designed to take advantage of the high ionic conductivity of liquid electrolytes, while leveraging structural stability and dendrite-suppressing properties of oxide materials. One approach towards a liquid-oxide hybrid is a quasi-solid slurry as was shown by Park et al.[286] By adding an ionic liquid to LATP powder they obtained a clay that achieved an ionic conductivity of 1.6 mS cm^{-1} while

facilitating processing of the SSE. For LLZO, Kim et al. could confirm similar behavior.[287] Alternatively, the research group of Archer showed that nanoporous Al_2O_3 can be infiltrated with LEs to obtain LE-like ionic conductivities while suppressing dendrite penetration.[288] Similar, a study by Cheng et al. showed that ionic liquids were used to infiltrate a flexible LLZO sheet to boost interface contact.[289] Other studies include the infiltration of metal-organic-frameworks[290] or porous oxide monoliths.[291]
More common however, is the use of LEs, ionic liquids, or other organic liquids, to improve the wettability of oxide pellets with the anode but even more importantly the cathode.[292–294] The oxides are usually of high hardness and therefore quickly lose contact to the porous cathode under cycling as the battery cell expands and shrinks. Liquid electrolytes help to mitigate the contact and capacity loss.[295,296]

Polymer-inorganic hybrid electrolytes are commonly referred to as Composite Polymer Electrolytes (CPE) and will be explained in the next Chapter 2.7.4.1.

2.7.4.1 Composite Polymer Electrolytes

For this thesis, any system where a polymer and any form of inorganic material are combined to form the separator will be considered a CPE. Inorganic materials can be Li-ion conduction but may also be inert materials. As there are technically not two Li-ion conducting phases, if inactive inorganic materials are used, they would not be covered by the definition given for hybrid electrolytes in the last Chapter 2.7.4.
Composite polymer electrolytes have emerged as a promising class of materials for lithium metal batteries, addressing some of the limitations of traditional liquid and solid-state electrolytes. By combining polymers and inorganic fillers, these materials aim to improve the generally poor ionic conductivity and mechanical strength of polymer electrolytes while maintaining their superior processing and scalability.[297] Often, polymers such as PEO,[28,298] PVDF,[14] PAN,[299] PMMA,[300] and their derivatives,[301] copolymers[13] and blends[19] are employed in the fabrication of CPEs. For inorganic fillers there are two main classes of materials: active and inactive.[302] Active fillers directly participate in Li-ion transport by providing fast-conducting pathways. Prominent examples include LLZO[21] and LATP.[303] Inactive fillers, on the other hand, do not exhibit inherent ionic conductivity but enhance the electrolyte's mechanical properties, reduce polymer crystallinity, or modify the microstructure to facilitate ion transport.[304] Common inactive fillers include inert materials like Al_2O_3,[305] TiO_2,[306] and SiO_2,[307] which improve

the electrolyte's dimensional stability and suppress dendrite growth on the lithium anode.[308] Although inactive fillers themselves are incapable of Li-ion transport, some, such as MoO_3, form an interface with polymers and Li-salts that exhibit higher ionic conductivity than the polymer itself.[309]

Usually, ceramic fillers are used as sulfides tend to react with polymers, especially oxygen containing polymers.[310] Nevertheless, there are some examples of sulfide-based CPEs with PEO and PMMA derivatives.[32,311–313] For argyrodites specifically, butadiene-rubber derivatives and are often used as a binder to improve flexibility and contact. They are not or only slightly ion conductive and therefore usually only small amounts are used.[34,314]

Two key architectures dominate the field: polymer-in-ceramics (PIC) and ceramics-in-polymer (CIP). The exact definitions are unclear yet but in general, CIP contain less than 50 wt% ceramics while the opposite is true for PIC. The differentiation is important as the transport mechanisms of Li-ions are dependent on the dominant phase.[315]

Fabrication of CPEs varies widely. Physical mixing through ball milling[316] or extrusion[317] of particles and polymers is possible and often used in larger scales. On the lab scale, techniques such as solvent-casting,[318] electrospinning,[319] hot-pressing,[320] or roll-pressing[321,322] are frequently used.

Depending on the fabrication method and surface energy of the fillers, particle agglomeration is a pervasive issue. Inadequate dispersion techniques or high filler concentrations exacerbate this problem, creating hotspots of conductivity and mechanical stress.[36] Surface modification of ceramic particles using functional groups or coatings has been explored to mitigate agglomeration and improve polymer compatibility.[323,324] For instance, surface grafting of salts[325] and polymers[18,22] onto ceramics can enhance ionic conductivity and promote better dispersion within the polymer matrix.

Particle alignment, size, proportion, morphology, and tortuosity are of high importance in CPEs.[326] Together with coatings they define the interface between polymer and filler. Usually, this interface has a high resistance for Li-ion reducing the overall performance of the CPE. Hence, interface engineering emerged as a highly relevant topic to the success of CPEs.[36]

In summary, CPEs represent a synergistic approach to overcoming the limitations of individual polymer or inorganic electrolytes. While the architectures of polymer-in-

ceramics and ceramics-in-polymer each offer distinct benefits regarding electrochemical and mechanical performance, their practical application in lithium metal batteries is hindered by challenges such as particle agglomeration and interface resistance. Advances in material synthesis, surface engineering, and processing techniques are essential to fully exploit the potential of CPEs in next-generation energy storage systems.

3 Motivation and Goal

The research across all projects was conducted in close collaboration with universities and research institutes within Germany as part of the FestBatt 2 Cluster of Competence (FB2), founded by the Federal Ministry of Education and Research (BMBF). FestBatt 2 (03XP0428C) aims to bridge research and industry in the development of solid-state lithium metal batteries.

This dissertation is motivated by the urgent need to address the challenges in developing high-performance solid-state electrolytes (HSSEs) by optimizing polymer-particle interactions, creating scalable synthesis methods, and enhancing the fundamental understanding of interface behavior. By collaborating closely with both industrial and academic partners, this work seeks to explore the potential of integrating oxide- and sulfide-based Li-ion conductive particles into polymer matrices to achieve superior ionic conductivity, mechanical stability, and electrochemical performance. The primary goal is to develop practical, cost-effective, and scalable strategies for the fabrication of HSSEs to ensure their successful implementation in real-world battery applications.

The motivation behind this research is further strengthened by the demand for commercially viable solutions that bridge the gap between fundamental materials science and industrial feasibility. In particular, active filler materials, e.g., LATP and LLZO, need improved interaction with polymers in mixed systems to reduce agglomeration and interfacial Li-ion transport. For this purpose, polymeric coatings need to be developed that improve the polymer-particle interface compatibility. Moreover, the processing of hybrid materials is challenging and difficult to implement into existing factories. Hence, developing “drop-in” concepts, that can be included into already established streamlined processes would be highly beneficial for the commercialization of SSBs.

By leveraging innovative polymer chemistries, surface modification techniques, and advanced coating strategies, this work aims to address the key limitations of current HSSEs. Novel sulfur-based polymers compatible with argyrodites need to be developed and cheap, efficient, and controllable coatings for ceramic electrolytes for different polymer matrices are essential to improve the performance of hybrid electrolytes. The development of thin, flexible, and high-performance hybrid solid-state electrolytes that can operate under ambient conditions without complex processing steps would represent a significant step forward in solid-state battery technology.

4 Results and Discussion

4.1 Evaluation of HNBR for CPEs

Hydrogenated Nitrile Butadiene Rubber (HNBR) is a synthetic elastomer synthesized by hydrogenating nitrile rubber (NBR) (**Scheme 23**), which improves its thermal stability, chemical resistance, and mechanical properties. It is produced on an industrial scale and is used in automotive applications, construction, and in sealing.[327]

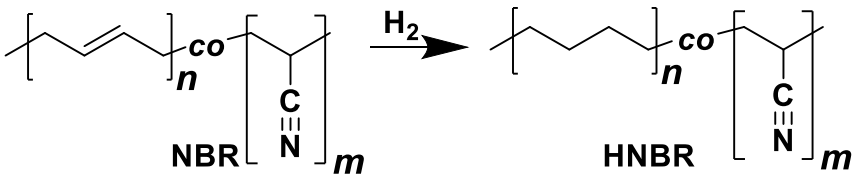

Scheme 23 PPM of NBR to obtain HNBR.

HNBR is highly resistant to high temperatures (e.g., > 300 °C), while having great film forming properties making it a suitable polymer for high safety SSEs. Since it does not contain oxygen atoms and therefore exhibits high stability for sulfide-based SSEs, it is used as a binder for argyrodites.[9,314] Through a collaboration with ARLANXEO, they supplied Therban 4367, a HNBR with 43 wt% acrylonitrile content and a low viscosity, which facilitates improved film formation. In this chapter, Therban 4367 is used in combination with LATP and Li_6PS_5Cl to assess the viability of HNBR rubbers as a Li-ion conducting phase in a CPE.

As a basis, a publication from Li et al.[8] shows that HNBR with 40 wt% acrylonitrile has desirable properties for polymer electrolytes: completely amorphous, oxidative stability > 5 V, t^+ of 0.56, high thermal stability > 100 °C, and good dissociation of LiTFSI. Nevertheless, the main drawback is the comparatively low ionic conductivity of $3.1 \cdot 10^{-7}$ S cm^{-1} at 25 °C. By the addition of a highly ionic conductive phase such as LATP or Li_6PS_5Cl this disadvantage might be circumvented while maintaining the favorable properties and facile processing.

Parts of this chapter, along with the corresponding sections in the experimental part, were adapted with permission from a publication written by the author (Daniel Döpping).[328]

4.1.1 Strategy

To take advantage of the excellent film forming properties of HNBR, LATP powder can be incorporated through solvent-casting. The general procedure of Li et al. was adapted to add LATP powder as a dispersion.[8] LATP with the elemental distribution $Li_{1.5}Al_{0.5}Ti_{1.5}P_3O_{12}$ and an average size of 0.24 µm was kindly provided by Forschungszentrum Jülich within the FB2-Hybrid platform by Dr. Martin Finsterbusch and M.Sc. Xiaochen Liu. Additional data of the provided LATP is available in the Appendix (**Figure 111** and **Table 23**).

Solvent-casting however, is not applicable to Li_6PS_5Cl, as Li_6PS_5Cl degrades quickly in contact with solvents capable of dissolving HNBR, namely acetone.[329] Hence, alternative membrane preparation methods are necessary for Li_6PS_5Cl-HNBR CPEs. For this purpose, a hot-press was purchased and placed inside a glovebox. Through repeatedly mixing and pressing HNBR with Li_6PS_5Cl powder, a composite can be achieved without the utilization of solvents. Alternatively, layered structures of HNBR-Li_6PS_5Cl-HNBR may protect Li_6PS_5Cl against degradation by air/water during processing while boosting contact at the electrolyte-electrode interface by incorporating the flexible polymer layer and therefore reducing the required stack pressure.

According to Li et al., HNBR has the highest ionic conductivity at a [N]:[Li] ratio of 5:1. As a baseline, the ionic conductivity of Therban 4367 with LiTFSI at the aforementioned ratio in a temperature window form 20 - 70 °C was measured (**Figure 1**).

Compared to the reported value from Li et al. of $3.1 \cdot 10^{-7}$ S cm^{-1} at 25 °C, the recorded value for 30 °C is slightly lower at $1.3 \cdot 10^{-7}$ S cm^{-1}. This difference may be due to slightly different acrylonitrile content (Li et al. 40 wt%, Therban 4367 43 wt%), polymer synthesis procedure, or varying sample preparations.

The measured baseline of Therban 4367 is used to assess the CPE's performance in regard to their influence on the ionic conductivity.

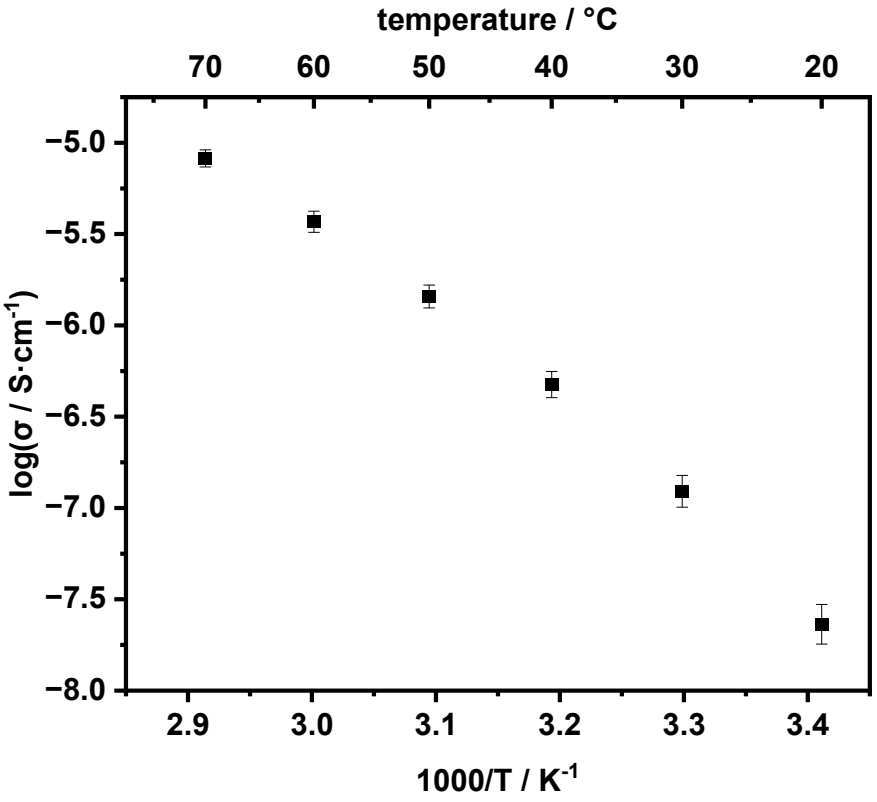

Figure 1 Ionic conductivity of pure Therban 4367 with a LiTFSI concentration of [N]:[Li]=5:1 from 20 - 70 °C. The film preparation is described in 6.3.1.1.

4.1.2 LATP-CPEs

As the supply of LATP was limited to approximately 5 g, the number and quantity of available experiments was limited. First, it was necessary to determine the influence of pristine LATP on the ionic conductivity of HNBR films. Hence, a film with 12 wt% of LATP (**Figure 2**) was made to compare the ionic conductivity to the pure HNBR-LiTFSI film (picture in Appendix **Figure 112**, the film preparation is described in 6.3.1.2). The films are labeled according to their composition (e.g., HNBR-12wt%LATP means the film is composed of the default HNBR-LiTFSI matrix with an LATP concentration of 12wt% of total mass added). 12 wt% were chosen, as this is close to common oxide content (10-15%) that provide the highest ionic conductivity in various polymer-oxide CPEs.[330–334] The direct comparison in ionic conductivity to HNBR-LiTFSI is depicted in **Figure 3**.

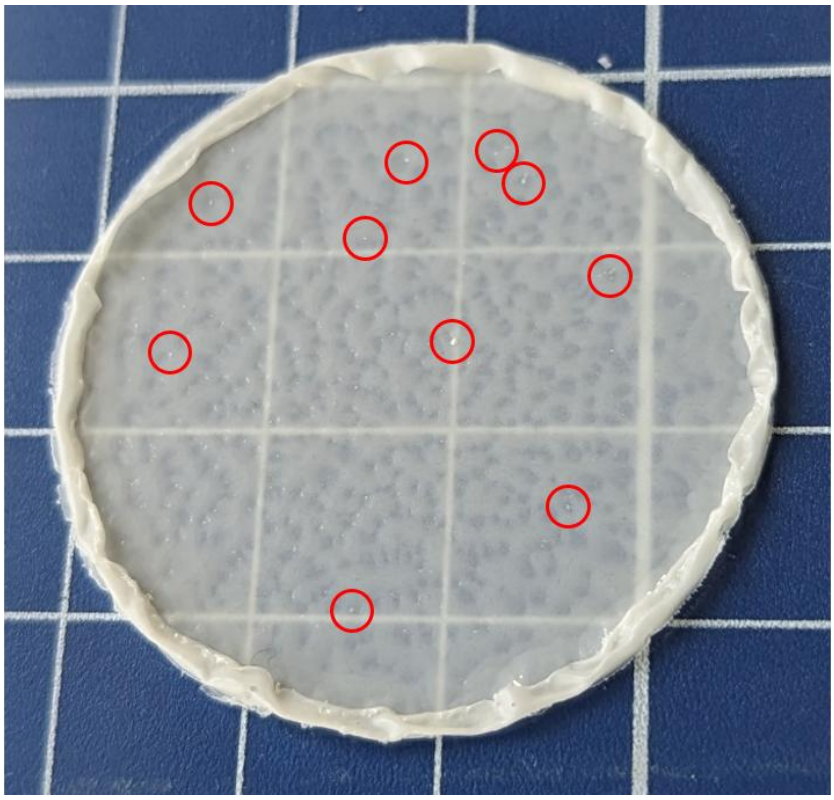

Figure 2 Picture of the HNBR-12wt%LATP film. Red circles mark visible agglomerates of LATP nanoparticles. The surface is slightly uneven.

Visually, the HNBR-LATP films had a slightly irregular surface which may be due to surface tension during drying or uneven solvent evaporation. More importantly, the films showed agglomerates of LATP powder, which indicated a high surface energy of the nanoparticles. The issues arising from uneven filler distributions are explained in Chapter 2.7.4. Nevertheless, the determined ionic conductivity showed a clear trend.
At 20 °C no difference could be observed between the pristine and LATP containing HNBR film with an ionic conductivity of $2.33 \cdot 10^{-8}$ S cm^{-1}. However, with increasing the temperature, the HNBR-12wt%LATP film exhibited a continuously higher ionic conductivity than the pure HNBR film with an ionic conductivity of $1.02 \cdot 10^{-5}$ S cm^{-1} at 70 °C compared to $8.21 \cdot 10^{-6}$ S cm^{-1} of the pure HNBR film.
The findings of uneven LATP distribution in the HNBR matrix and increased ionic conductivity at elevated temperatures strongly indicate that the LATP-polymer interface is the main limiting factor of the CPE. The mismatch in chemical potential between particle surface and polymer hinders the Li-ion conduction through the LATP particles. At higher temperatures the interface resistance can be overcome by Li-ions and therefore slightly boost the ionic conductivity.

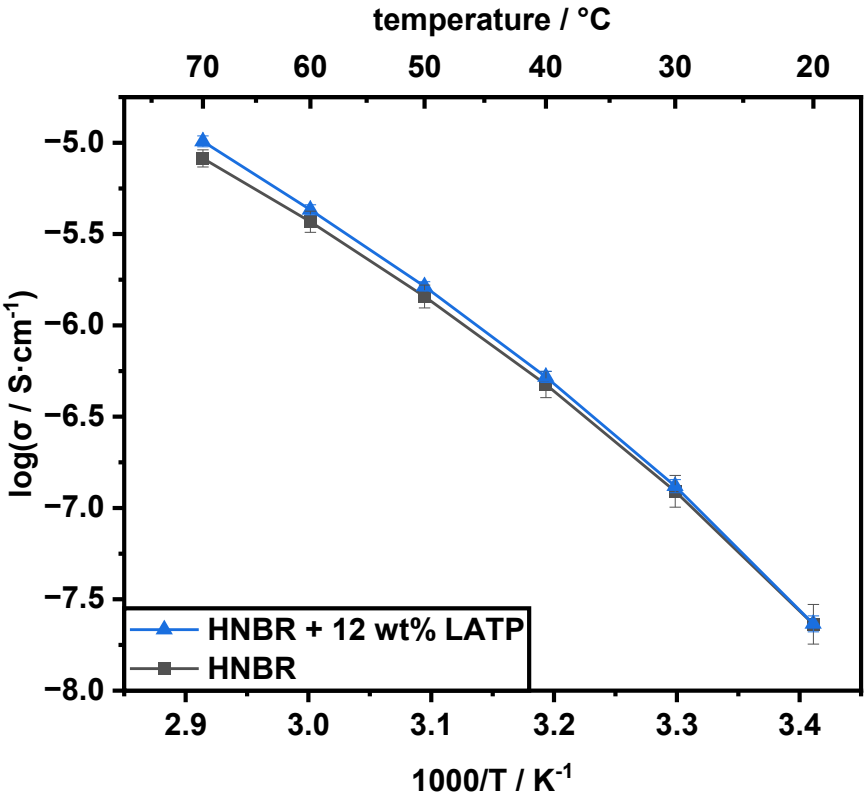

Figure 3 Comparison of the ionic conductivity of pure HNBR+LiTFSI films with HNBR-12wt%LATP CPE from 20 - 70 °C.

To further assess the viability of LATP-HNBR CPEs, a novel approach of PAN surface coating of LATP was theorized. The formation of space-charge layers in between the LATP and HNBR matrix may be a reason for the high interface resistance at the LATP particle surface as was shown for PEO-LLZO composites.[335]

By covalently binding PAN to the LATP particles a better mixing with the HNBR should be possible as HNBR also contains PAN segments and consequently may reduce the interface resistance to Li-ion migration.

To achieve thin, scalable, and controllable polymer coatings, a method by Zhou et al. was adapted.[88] The surface was coated by a thin layer of CTA and in a second step a radical polymerization functionalized the surface with the desired polymer. Finding suitable synthesis parameters for a homogenous, thin coating was challenging and required multiple attempts. Due to the limited amount of LATP available, the coating behavior was systematically studied on silica nanoparticles of similar size (200 - 400 nm average diameter). The results of this study on silica nanoparticles were published in *Polymer Chemistry*. The study included PMMA coatings, however, since they are not the targeted coating material for the LATP particles, this chapter will only

consider the results for PAN coatings and focus on the important results for thin, homogeneous PAN coatings on LATP.[328]

The general coating strategy is based on a surface modification of oxide particles with a commercially available alkoxy silane, (3-mercaptopropyl)-trimethoxysilane (SH-TMS). SH-TMS subsequently acts as a chain transfer agent in a radical polymerization leading to thin polymer coatings at the particle surface. A schematic of the two-step coating process can be found in **Scheme 24**.

The method of Zhou has a distinct advantage over other coating strategies. First, SH-TMS is considerably more affordable than other surface-active CTAs, which often need to be synthesized in multi-step processes (e.g., RAFT-agents, etc.). Second, in theory, any radically polymerizable monomer can be used, circumventing the monomer limitations of controlled radical mechanisms. Third, although to a lesser degree compared to CRP, control over chain length and dispersity is given. Lastly, as there are free polymer chains forming in solution, indirect characterization of the particle coating is possible without the need to cleave polymer chains off the particle surface.

The first step of tethering the CTA agent to the silica particle surface was adapted from literature to favor monolayer coating of SH-TMS.[336] After drying the SH-TMS coated silica (SH@SiO_2), TGA (6.3.1.3, **Figure 62**), ATR-IR (6.3.1.3, **Figure 63**), and Cryo-TEM analysis was performed on the sample. In TGA and ATR-IR no differences were found between pristine and SH-TMS coated silica nanoparticles, still the Cryo-TEM micrographs showed a coating of less than 1 nm with slightly thicker coating at the contact points between particles (**Figure 4**).

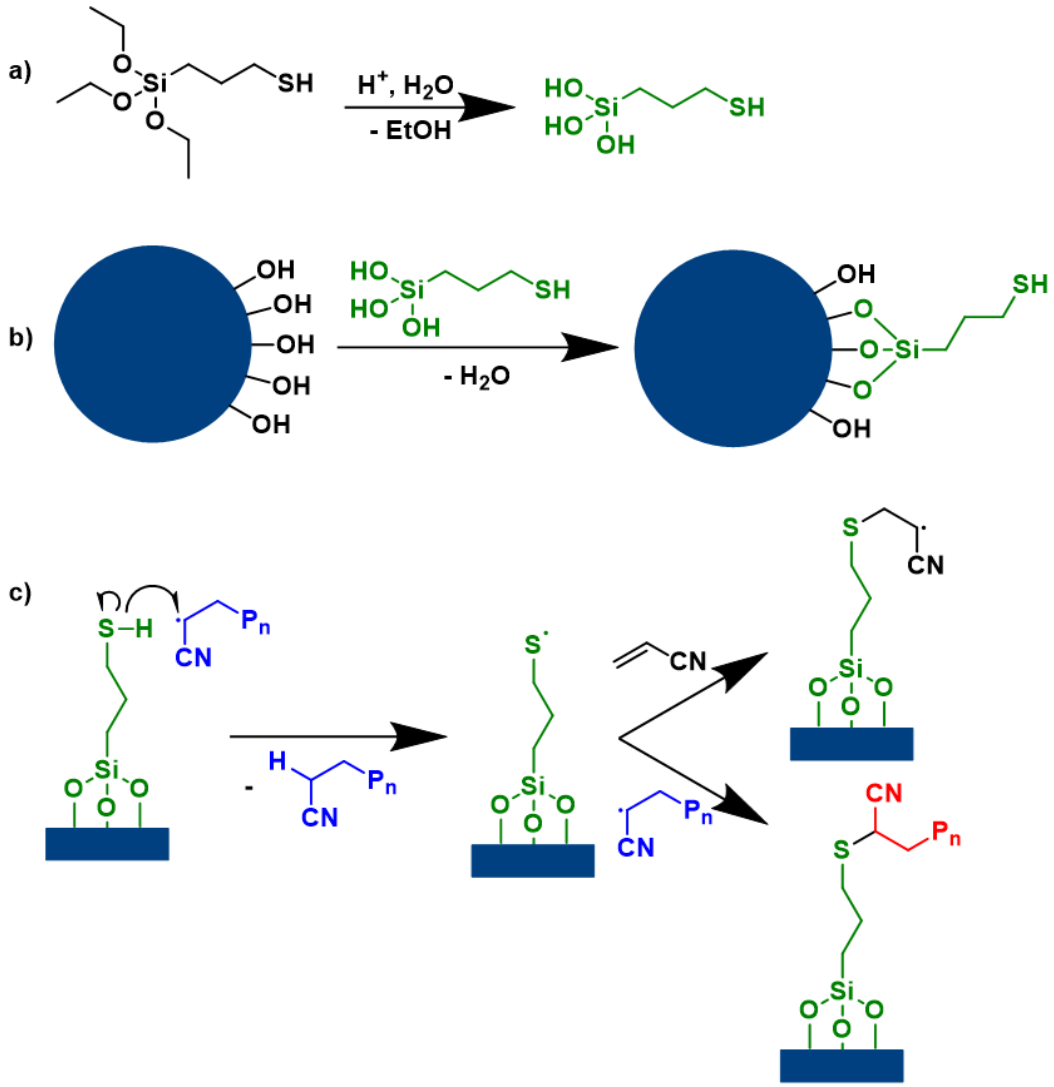

Scheme 24 a) Reaction scheme of the hydrolyzation of (3-mercaptopropyl)-trimethoxysilane (SH-TMS) to (3-mercaptopropyl)-silanetriol under acidic conditions. b) Surface modification of oxide particles (dark blue) with (3-mercaptopropyl)-silanetriol (green) via condensation. Additional condensation products were omitted for clarity. The (3-mercaptopropyl)-silanetriol can have 1 to 3 condensations with the surface or react with other silanetriols to an amorphous network at the surface or in solution. The thiol-surface acts as a chain-transfer agent in the subsequent radical polymerization. c) Simplified chain transfer mechanism of PAN to the SH-TMS at the silica particle surface. P_n represents the polymer chain of PAN, the dark blue bars represent the silica particle. Growing and terminated polymer chains in solution (light blue) and polymer chains bound via SH-TMS (red) to the silica nanoparticle surface are mechanistically linked. Therefore, the chain length in solution and coating thickness of PAN should be correlated. The upper path depicts a "grafting-from" reaction path while the lower path depicts "grafting-to" which simultaneously happens during the coating. Note that for simplification several competing reaction pathways are not depicted. The most important alternative reaction path does not include a CTA and therefore reacts according to a classical free radical polymerization.[328]

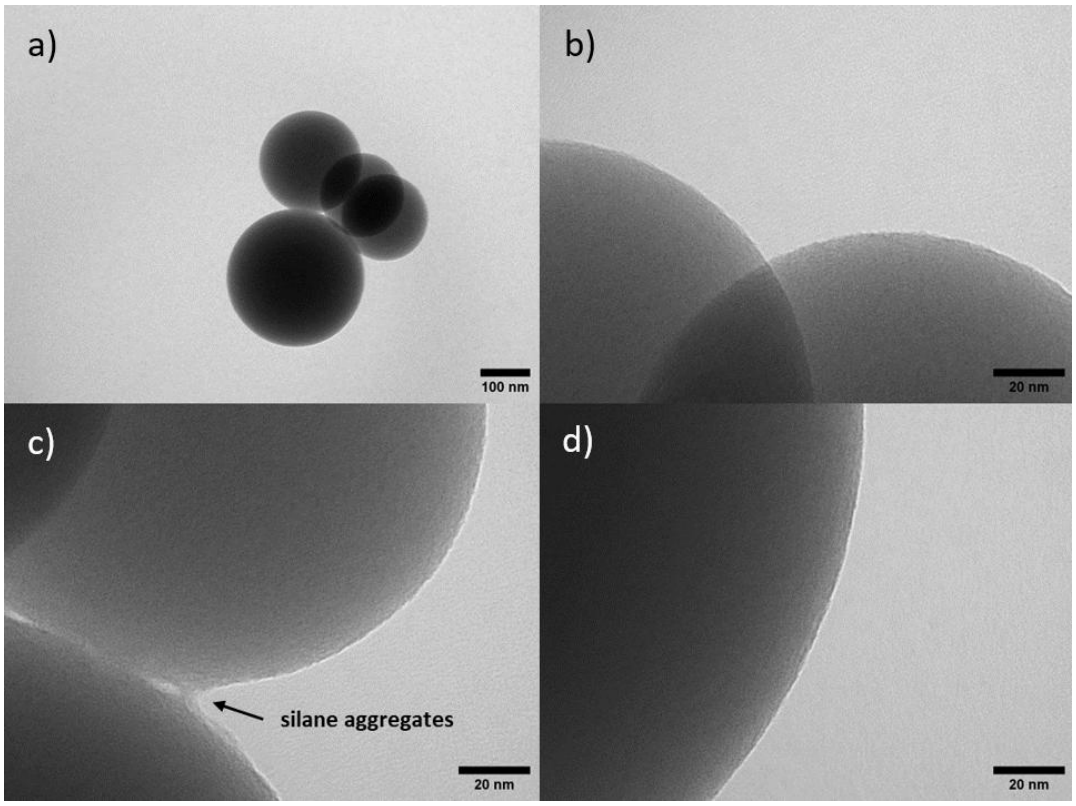

Figure 4 TEM micrographs of SH@SiO_2. Silica particles are spherical with a diameter of > 150 nm (a). The SH-TMS coating is hard to discern from the amorphous silica particle (b, d). At contact points between particles, small agglomerates of silane are visible (c).[328]

To assess the coating behavior of PAN on SH@SiO_2 particles, a wide range of monomer concentrations was tested. As it is crucial to maintain the same CTA concentration between samples, the mass of SH@SiO_2 was used as a reference and the mass ratio of monomer increased from 1:0.1, 1:0.5, 1:1, 1:2, to 1:5 (m(SH@SiO_2):m(acrylonitrile)), respectively. All other parameters were kept identical (procedure in Chapter 6.3.1.4). Upon the polymerization, SEC samples were withdrawn in specific intervals from the crude reaction mixture which showed a steady increase in the values of the number average molecular weight and dispersity correlating to monomer concentration increase, indicating, that the CTA on the silica surface successfully participated in the polymerization (**Figure 5**, **Table 2**). The only outlier was 1:5 as the high monomer concentration probably led to the Trommsdorff-Norrish-effect accelerating the polymerization rate. This was also evident from the PAN coated silica nanoparticles (PAN@SiO_2) after washing and drying being off-white powders for all concentrations but 1:5 where thick polymeric chunks were obtained instead (6.3.1.4, **Figure 64**).

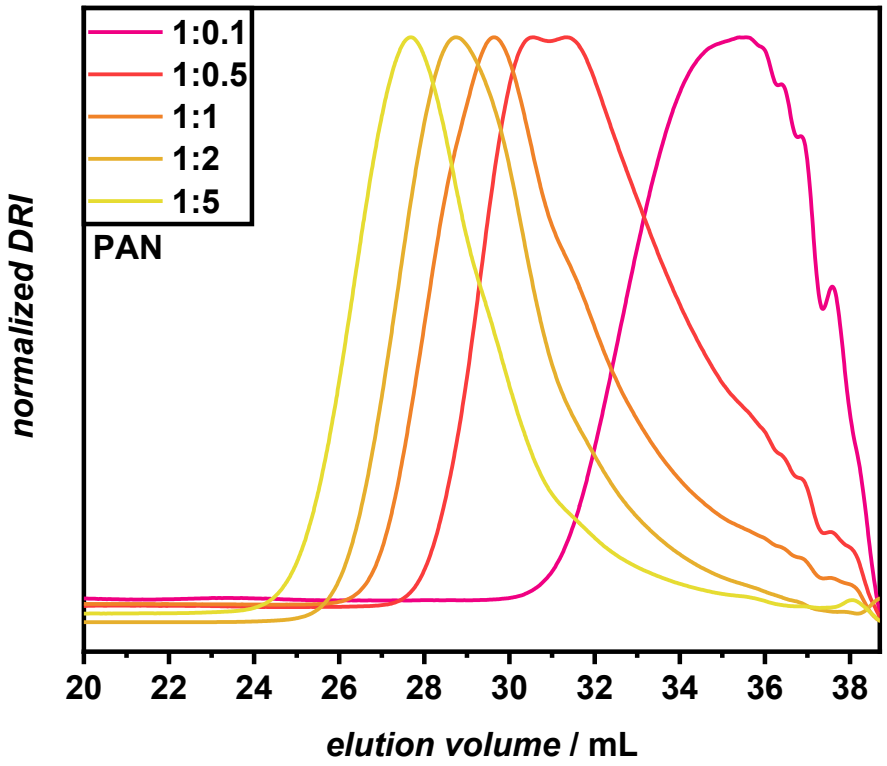

Figure 5 DMAC-SEC elugram of all tested concentrations of PAN in the crude reaction mixture against a PMMA standard.[328]

Table 2 M_n and dispersity, *Đ,* values for PMMA and PAN from the crude reaction mixture after the particle coating. Increasing the monomer concentration increases both, the number average molecular weight M_n and the dispersity *Đ* for both polymers. The values in italics are omitted from the fits due to skewed values from the gel effect.

Ratio	M_n / g mol^{-1}	*Đ*
1:0.1	900	3.82
1:0.5	2,400	4.38
1:1	4,000	5.19
1:2	4,900	7.02
1:5	*9,500*	*6.75*

Further, the dried PAN@SiO_2 particles were analyzed via TGA (6.3.1.4, **Figure 65**), ATR-IR (6.3.1.4, **Figure 66**), Cryo-TEM (**Figure 6**), and High-angle annular dark-field (HAADF) scanning transmission electron microscopy (STEM) with Energy-dispersive X-ray spectroscopy (EDX) (**Figure 7**).

In the TGA measurements, omitting 1:5, the mass loss correlated strongly with the monomer concentration (Appendix, **Figure 113**) indicating control over the coating thickness by varying the monomer concentration. ATR-IR revealed no difference to pristine silica nanoparticles except for 1:5 where weak bands corresponding to CH_2 and CN were identified (6.3.1.4, **Figure 66**).

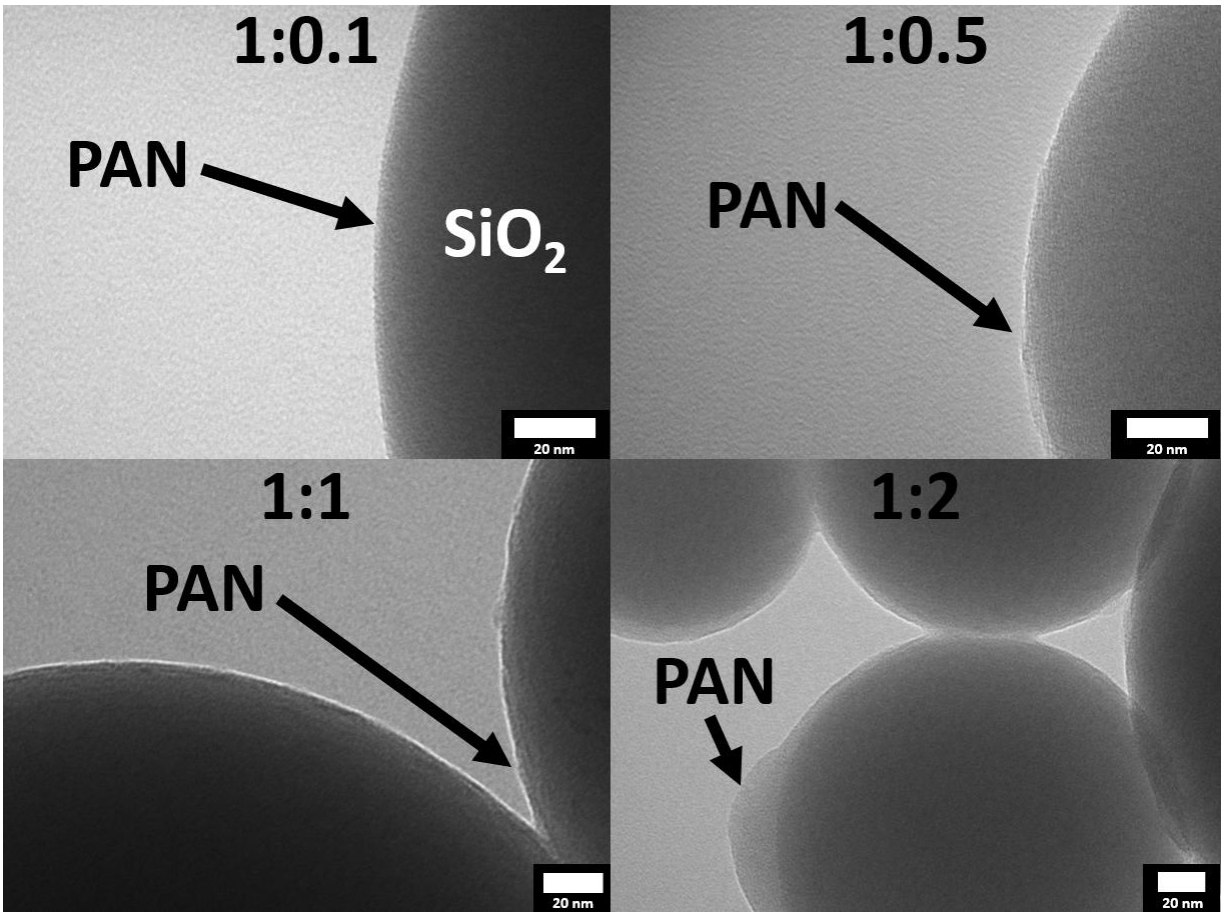

Figure 6 TEM micrographs PAN coatings on SiO_2-NPs at the respective monomer concentration in solution. Dark gray spherical shapes are the SiO_2-NPs with the lighter gray edges showing the amorphous polymer coating. 1:5 could not be measured.[328]

Through Cryo-TEM micrographs, a homogeneous coating layer could be identified as a thin light gray layer atop the silica surface. Increasing the acrylonitrile concentration led to increased inhomogeneity and irregularities/agglomerates at the particle surface. Additional TEM micrographs of PAN@SiO_2 corroborating these findings are shown in the Appendix (**Figure 114** - **Figure 117**).

For clear identification of the structure of the coating, an EDX scan on a single particle of PAN@SiO_2 1:2 was performed. The EDX scan confirmed the core-shell structure through the elemental composition across a three-layer structure consisting of PAN, a CTA, and the silica nanoparticle core. The outermost layer, corresponding to the PAN

coating, was clearly identifiable by the presence of nitrogen (N, green) signals in the EDX data. The scan shows that the polymer layer was approximately 8 nm thick on one side and 12 nm on the other, which formed the outer boundary of the structure. This consistent elemental profile suggests that the polymer coating was evenly applied around the silica nanoparticle core, but as already observed in the TEM micrographs can have varying thickness.

Beneath the polymer coating lies the chain-transfer agent (CTA) layer, which is composed of sulfur-containing thiol groups. The EDXS scan reveals a distinct sulfur (S, orange) peak, confirming the presence of the CTA. The sulfur signal is confined to a very thin layer, approximately less than 2 nm thick, positioned between the polymer coating and the silica nanoparticle core. This sharp sulfur peak highlights the thin, interfacial nature of the CTA layer, suggesting that it plays a key role in the polymerization process without significantly extending beyond the interface region.

The innermost layer, representing the silica nanoparticle core, is characterized by strong silicon (Si, blue) and oxygen (O, red) signals in a 1:2 ratio, which is expected of silica. The EDX data shows a clear transition to a homogenous intensity of silicon and oxygen peaks as the scan moves towards the core. The absence of significant sulfur or nitrogen signals in this region confirms that the coating along the scan axis is thin and no large PAN or SH-TMS agglomerates are formed.

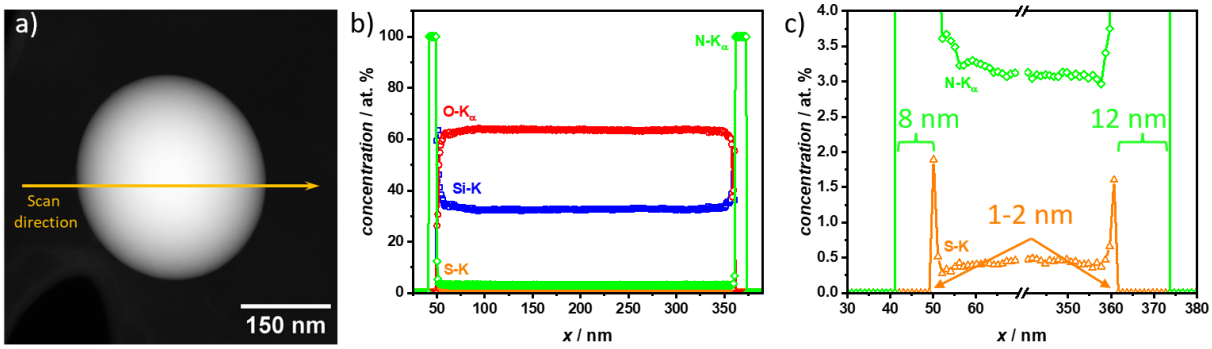

Figure 7 a) High-angle annular dark-field (HAADF) scanning transmission electron microscopy (STEM) of PAN@SiO_2 1:2. The Si-, O-, S- and N-distributions within the single SiO_2 core-shell nanoparticle are determined from the EDX line profile, which is recorded along the orange line in the HAADF-STEM image. The particle has a diameter of 320 nm. b) Elemental distribution along the EDX scanning line for PAN@SiO_2 1:2. Si-, O-, S-, and N-distributions are shown in blue, red, orange, and green, respectively. Si and O show the position of the SiO_2-NP. S indicates the SH-TMS CTA coating layer. N represents the PAN coating attached to the CTA. c) Elemental distribution along the EDX scanning line magnified to better visualize the interface. S- and N-distributions are shown in orange, and green, respectively. The coating thickness of the nitrogen containing PAN is 8 nm on the left side and 12 nm on the right side. The thickness of the sulfur layer is 1-2 nm within the range of the resolution limit of the EDX scan.[328]

After confirming the viability of visual identification of the coating layer in TEM micrographs, all coated particles were assessed for their average coating thickness by measuring the visible coating layer in ImageJ. For each sample, about 40 - 80 values were measured in even intervals wherever the coating layer was clearly identifiable. The arithmetic mean and standard derivation of the coating thickness of all samples was calculated and plotted against the M_n obtained from the crude solution (**Figure 8**).

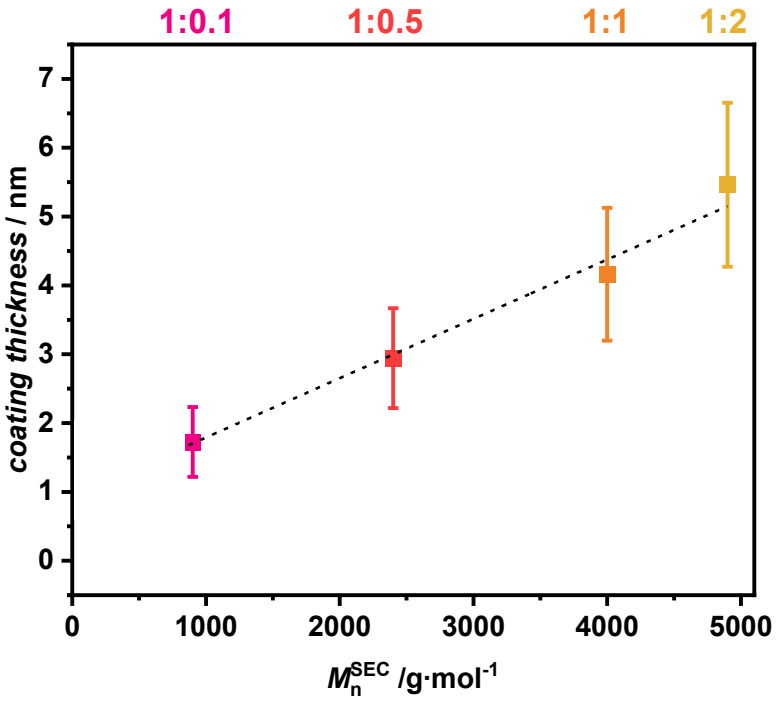

Figure 8 M_n in solution plotted against the coating thickness of PAN on SiO_2-NPs. Values for the coating thickness are derived from ImageJ. Depicted is the arithmetic mean with one standard deviation as error. The dotted line is the linear fit of the M_n-coating thickness data points indicating a strong correlation (R^2=0.99) between polymer chain length in solution and coating thickness on the surface of SiO_2-NPs. All values used for calculation are available in Chapter 6.3.1.4.[328]

The strong correlation between molecular weight in solution and coating thickness indicates substantially good control over the coating behavior through SH-TMS as a surface bound CTA. Furthermore, it was shown that the two-step coating approach is suitable for thin, homogeneous coatings of PAN to a nanoparticle surface.

After evaluating the average coating thickness and homogeneity, the conditions for PAN@SiO_2 1:1 seemed to have the best properties for PAN coatings of LATP. The PAN layer was on average about 4 nm thick, allowing for entanglement with the HNBR matrix while not showing excessive polymer agglomerates as were observed for 1:2. Hence, first SH@LATP and afterwards PAN@LATP was synthesized according to the

procedure for PAN@SiO_2 with a monomer mass ratio of 1:1 (6.3.1.3 and 6.3.1.4). As a first characterization a TGA measurement revealed an increased mass loss with each subsequent synthesis step (**Figure 9**) indicating a successful coating. The maximum mass loss of PAN@LATP was smaller than 3% and therefore a definitive proof of coating with PAN was impossible through TGA. The low difference is within the weight drift range of ~10 µg, and adsorbed water/gas can lead to measurement errors in a similar range as is mentioned in the handbook of the utilized TA Instruments TGA 5500.[337] Nevertheless, the indication of additional degradation steps in PAN@LATP over SH@LATP at 270 °C and 330 °C implies a chemical difference between the two samples.

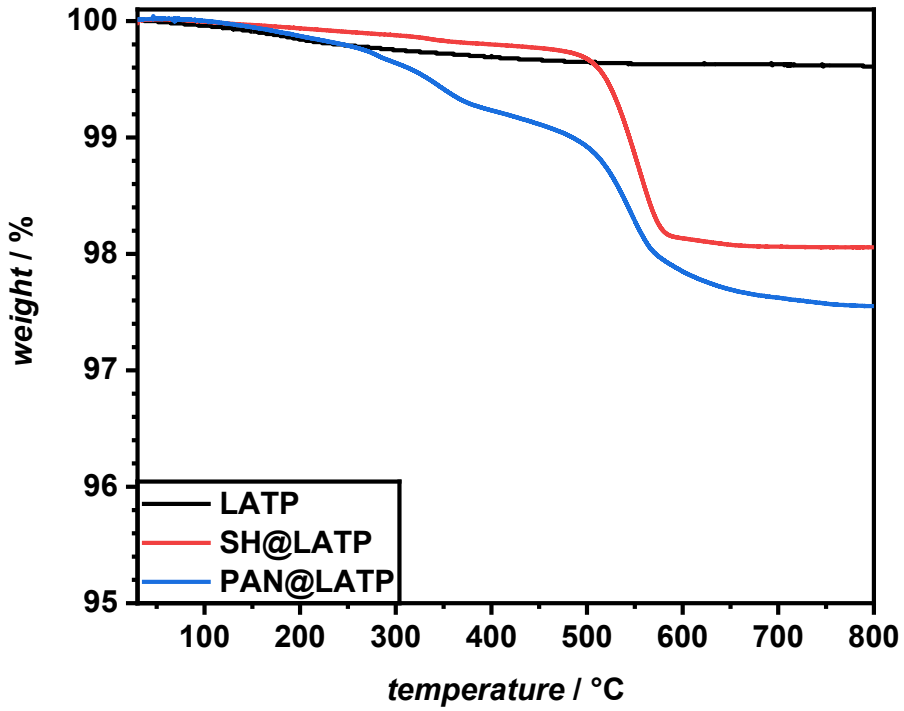

Figure 9 TGA measurements of pristine LATP, SH@LATP, and PAN@LATP from 30 - 800 °C at a heating rate of 10 K min^{-1}.

To confirm the successful surface modification, Cryo-TEM micrographs of all particles were taken as well. In the micrographs LATP expectedly had a highly different morphology than SiO_2. While SiO_2 exhibits an almost perfectly spherical shape with a smooth surface, LATP has a rough and edgy surface with small crevices (**Figure 10** a) assumably due to the pressing and sintering during the synthesis of LATP. Moreover, TEM micrographs revealed a large particle size distribution with some particles

exceeding several µm and widely varying particle shapes. Still, upon coating with SH-TMS the surface was visually similar to SH@SiO_2 with a smooth edge denoting a silane coating filling crevices and leveling the rough boundaries (**Figure 10** b).

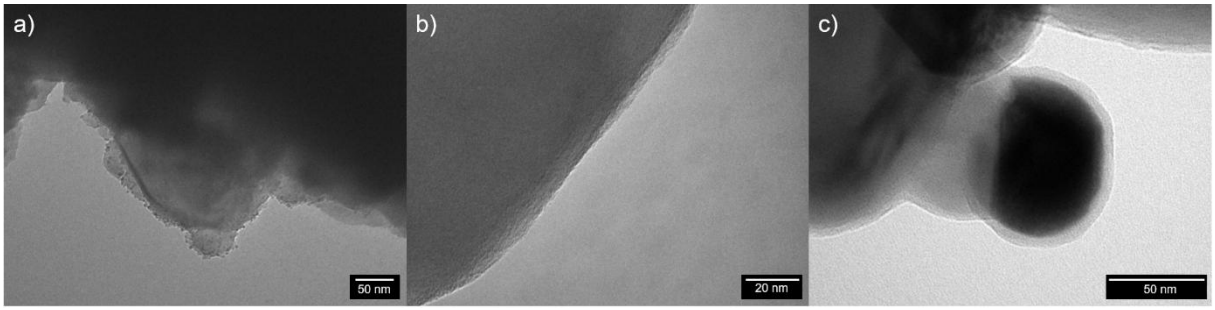

Figure 10 TEM micrographs of a) pristine LATP, b) SH@LATP, and c) PAN@LATP. The rough surface of pristine LATP is smoothened by coating with SH-TMS.

Furthermore, after coating with PAN, an amorphous layer of about 5 nm thickness was visible revealing the successful synthesis of PAN@LATP (**Figure 10** c). The coating layer of PAN@LATP 1:1 was about 1 nm thicker than PAN@SiO_2 1:1 which is probably due to the different particle morphologies and the resulting differences in contact area between particles and solution affecting the reaction rates. Additionally, the diffusion properties change due to the crevices and inhomogeneous distribution of particle sizes. Further TEM micrographs of LATP, SH@LATP, and PAN@LATP are available in the Appendix **Figure 118**, **Figure 119**, and **Figure 120**, respectively.

Upon the conformation of the homogeneous and thin PAN coating, HNBR films containing the newly synthesized PAN@LATP particles were made following the same procedure as for the HNBR-12wt%LATP films (6.3.1.2). The resulting HNBR-12wt%PAN@LATP (**Figure 11**) film was visually identical to HNBR-12wt%LATP. The coating with PAN did not suppress the formation of LATP agglomerates. Larger agglomerates of PAN@LATP particles were observed in TEM micrographs and may be a result of the polymeric coating “glueing” particles together. Hence, the exact cause of the agglomeration, whether due to the high surface energy of the particles or adhesion from the coating, could not be definitively determined. Nonetheless, the ionic conductivity of HNBR-12wt%PAN@LATP was measured and compared to that of the previous films, HNBR-LiTFSI and HNBR-12wt%LATP (**Figure 12**).

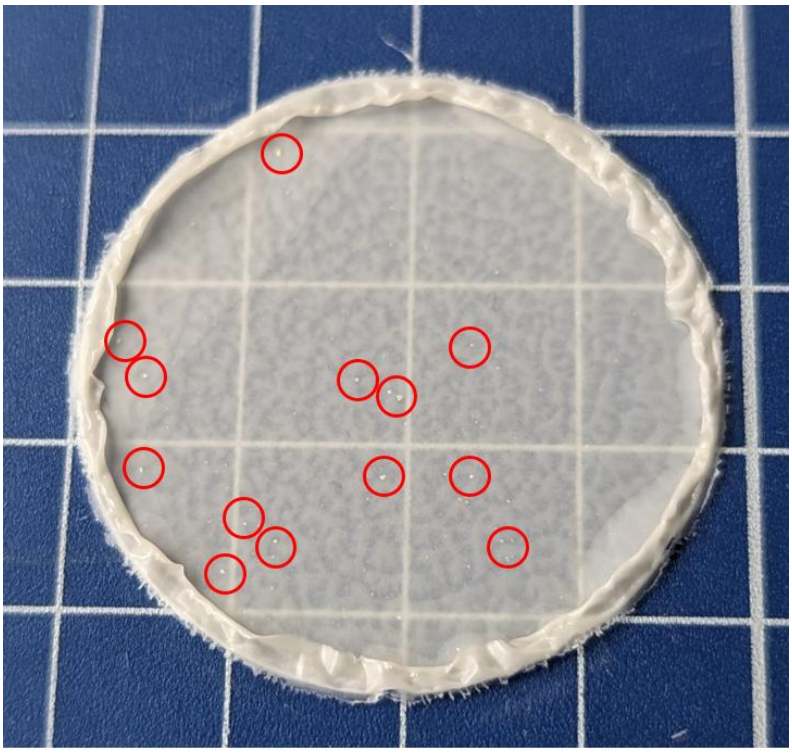

Figure 11 Picture of the HNBR-12wt%PAN@LATP film. Red circles mark visible agglomerates of LATP nanoparticles. The surface is slightly uneven.

Interestingly, the film with PAN-coated LATP exhibited poorer performance across all temperatures compared to the pure HNBR-LiTFSI film. The difference was highest at 20 °C. HNBR-12wt%PAN@LATP exhibited an ionic conductivity of $1.81 \cdot 10^{-8}$ S cm^{-1} compared to the HNBR-LiTFSI film's $2.33 \cdot 10^{-8}$ S cm^{-1}. With increasing temperature, the difference between the pure HNBR film and the PAN coated LATP CPE became negligible with the HNBR-12wt%PAN@LATP film having an ionic conductivity of $8.10 \cdot 10^{-6}$ S cm^{-1} at 70 °C. Following this trend, the PAN-coated LATP appeared to inhibit the Li-ion conduction compared to the pure LATP, rather than enhancing it, and even further decreased the overall ionic conductivity of the HNBR matrix at room temperature. This behavior could be attributed to the high rigidity of PAN, which limits the number of polymer chains at the LATP surface available for Li-ion coordination and transport, as such processes rely on the segmental motion of the polymer chains. Furthermore, the entanglement with the HNBR matrix would also be restricted, contributing to the observed agglomeration. Overall, the addition of LATP particles, whether coated and uncoated, had negligible impact on the inherently low ionic conductivity of HNBR.

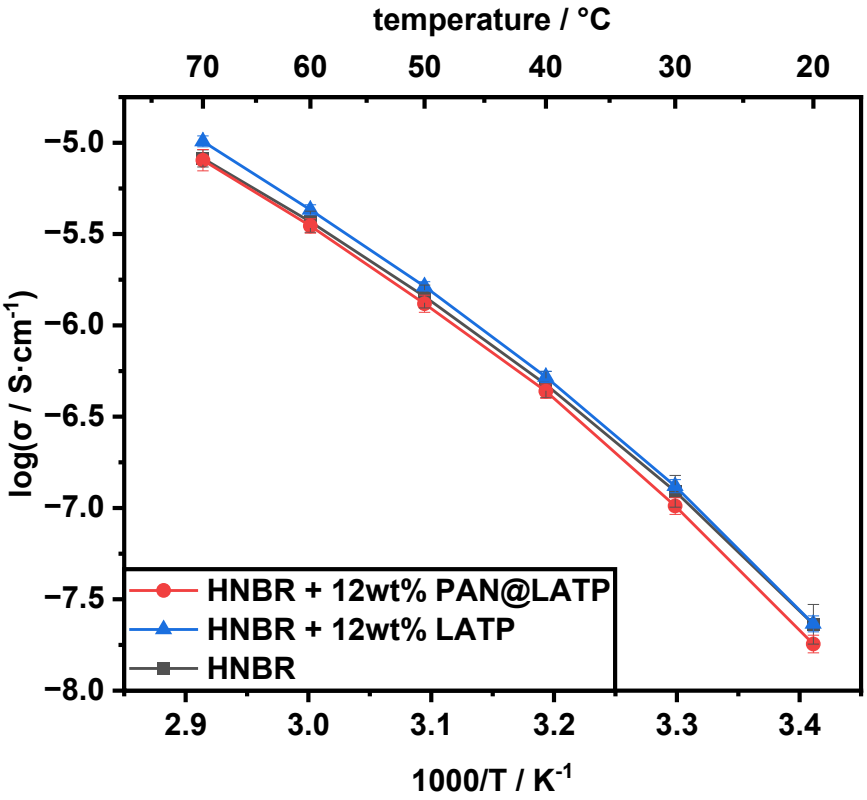

Figure 12 Comparison of the ionic conductivity of pure HNBR+LiTFSI films with HNBR-12wt%LATP and HNBR-12wt%PAN@LATP CPE from 20 - 70 °C.

Consequently, it was concluded that HNBR CPEs with LATP additives are unsuitable for application in Li-metal solid-state batteries, as the Li-ion conduction through the HNBR matrix could not sufficiently be enhanced. It is unlikely that the ceramic-in-polymer approach of incorporating LATP to HNBR can achieve ionic conductivity in the range of 10^{-4} S cm^{-1}, even at elevated temperatures. Therefore, a more promising filler with higher ionic conductivity, namely Li_6PS_5Cl was explored.

4.1.3 Li_6PS_5Cl CPEs

As previously mentioned, Li_6PS_5Cl is highly unstable and degrades upon contact with most solvents, except for xylenes and acetonitrile (MeCN).[329,338] As HNBR is insoluble in both acetonitrile and *p*-xylene, solvent-casting is not a viable method for membrane preparation. However, incorporating a Li-salt into the HNBR matrix is essential to enable Li-ion conduction. To achieve a homogeneous distribution of salt within the HNBR matrix, it is preferable to solubilize HNBR and the salt, followed by vigorous mixing, and subsequent drying of the HNBR-salt mix. Another significant challenge in utilizing Li_6PS_5Cl is the requirement for all synthesis steps to be carried out under an inert atmosphere to prevent degradation and, more critically, to avoid the formation of toxic H_2S gas. Hence, all synthesis procedures including Li_6PS_5Cl are performed within a specialized sulfur glovebox (6.1.12.2).

To reiterate, the primary goal of hybridizing Li_6PS_5Cl with HNBR is to improve safety by limiting exposure to air/water, while also reducing the high-pressure requirements for stable cyclization. Therefore, two different hybridization approaches were evaluated. The first approach involved synthesizing a mixed CPE membrane by repeatedly pressing and kneading a preformed HNBR-LiTFSI film with Li_6PS_5Cl until a homogenous mass was obtained (**Scheme 25** a). This method effectively minimizes the exposed surface of Li_6PS_5Cl by encapsuling the ~10 µm particles within an inert HNBR matrix. Additionally, the soft and flexible nature of HNBR improves the wettability of the electrodes, which is expected to reduce the required pressure needed for stable cell operation.

The second approach involved creating, a layered system composed of HNBR-LiTFSI|Li_6PS_5Cl|HNBR-LiTFSI, designed to specifically protect the surface of the film while encapsulating the highly ionically conductive Li_6PS_5Cl layer (**Scheme 25** b). In this configuration, the outer HNBR-LiTFSI layers not only shield the Li_6PS_5Cl from direct exposure but also enhance the wettability at the electrode–electrolyte interface. This improved interfacial contact is expected to further reduce the pressure requirements for stable cell operation. After processing, the two films were visually different. The mixed HNBR-Li_6PS_5Cl hybrid displayed a uniform color and consistent thickness throughout, indicating a homogeneous distribution of the components (**Figure 13** a). In contrast, the layered HNBR-Li_6PS_5Cl hybrid showed a visibly higher concentration of Li_6PS_5Cl in the central region, with a gradual decrease towards the outer regions (**Figure 13** b). This uneven distribution is attributed to the hot-pressing,

during which the interlocking nature of. the Li_6PS_5Cl particles hindered their even spread towards the edges of the film. This effect is further evident by the marble-like structure of films punched out near the outer parts of the layered film (**Figure 13** c), where cracks formed within the Li_6PS_5Cl layer, clearly showing interlocked particle agglomerates with higher mechanical strength. Additionally, the mixed HNBR-Li_6PS_5Cl has maintained a thickness of approximately 120 µm across all measured samples, while layered HNBR-Li_6PS_5Cl has exhibited significant thickness variation, with the central region reaching about 290 µm, while areas near the edges were reduced to around 90 µm. Since the HNBR-LiTFSI films have an initial thickness of 50 µm, it is evident that the polymer in the layered system was compressed significantly more and spread thinner towards the edges during the hot-pressing process.

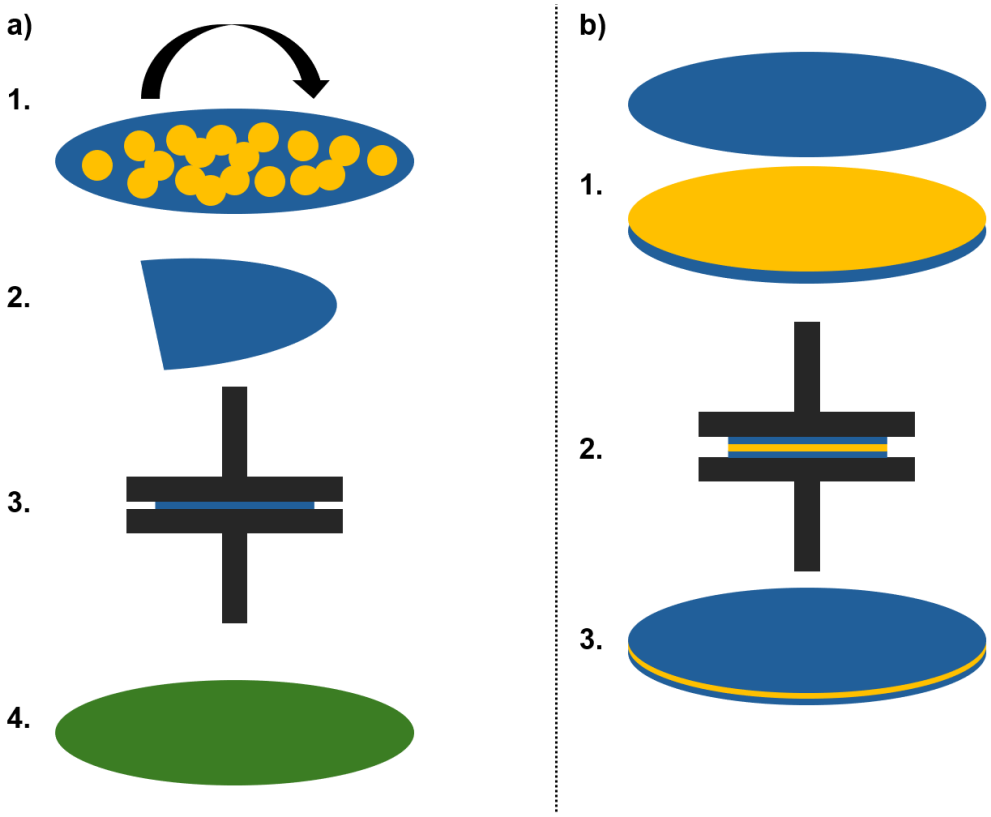

Scheme 25 Synthesis procedure for HNBR-Li_6PS_5Cl hybrids. Premade HNBR-LiTFSI films (blue) are used for both systems. a) For the mixed system Li_6PS_5Cl is spread evenly atop the HNBR-LiTFSI film and the film is folded to encapsule the Li_6PS_5Cl (1.+ 2.). The mix is hot-pressed to obtain a film (3.). this process is repeated 10 times until a homogeneous film is achieved (4.). b) For the layered system Li_6PS_5Cl is spread evenly atop one HNBR-LiTFSI film and the Li_6PS_5Cl layer is covered with another HNBR-LiTFSI film (1.). The stack is hot-pressed (2.) to obtain a layered hybrid (3.).

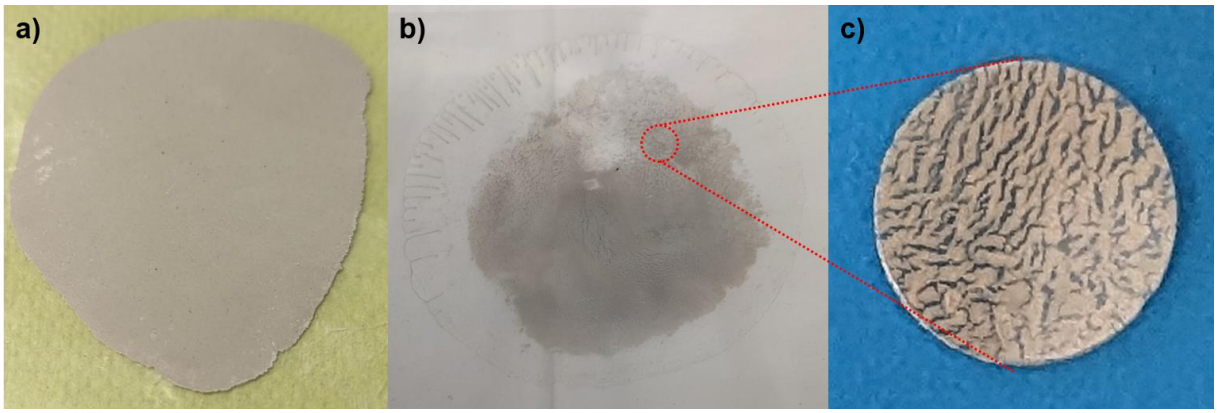

Figure 13 a) Mixed HNBR-Li_6PS_5Cl hybrid after kneading and hot-pressing 10 times. b) Layered HNBR-Li_6PS_5Cl hybrid after hot-pressing. An uneven distribution of Li_6PS_5Cl is visible. No Li_6PS_5Cl is visible in the peripheral regions. c) 10 mm punched out film from an off-center area. The Li_6PS_5Cl has a marble-like pattern with cracks in between.

The exact thickness of the polymer and Li_6PS_5Cl layers in the layered hybrid could not be precisely determined. However, it is assumed that in the center of the layered hybrid the Li_6PS_5Cl layer was considerably thicker compared to the edges. In contrast, the polymer layer was likely thinner in the center compared to the edges.

From the mixed film, three 10 mm membranes were punched out, while for the layered film, three 10 mm membranes from the center and three from the edges were punched out. Additionally, small pieces from both films were cut off and transferred out of the glovebox for ambient exposure testing. These samples were stored inside a fume hood under ambient conditions for a week. The mixed film emitted a noticeable sulfuric odor, indicating degradation of the Li_6PS_5Cl, while the layered film showed no such odor, suggesting an improved stability. However, both films displayed visible changes after a week, implying that the HNBR matrix provided at least partial protection of the Li_6PS_5Cl against ambient conditions.

The punched-out films were then dried in an oven, and their ionic conductivity was measured at 60 °C. The results from the measurements were averaged to assess the performance differences between the mixed and layered hybrid films. (**Table 3**).

The results clearly indicated that the addition of Li_6PS_5Cl in the mixed sample negatively impacted the overall ionic conductivity, even compared to the pure HNBR-LiTFSI film. This decline in performance is likely due to the prolonged and repeated hot-pressing, which may have degraded both the argyrodite (Li_6PS_5Cl) and HNBR matrix, ultimately leading to reduced ion mobility.

Table 3 Average ionic conductivity of HNBR-LiTFSI compared to HNBR- Li_6PS_5Cl hybrids at 60 °C.

Film	Average σ at 60 °C / S cm^{-1}
pure HNBR-LiTFSI	$3.72 \cdot 10^{-6}$
mixed	$2.23 \cdot 10^{-6}$
layered (center)	$2.16 \cdot 10^{-5}$
layered (edge)	$6.74 \cdot 10^{-6}$

Furthermore, the ionic conductivity measurements were performed using CR2032 coin cells, which exhibit a pressure of about 4 bar on the electrolyte film. However, Li_6PS_5Cl typically requires pressures of 250 bar or higher to ensure stable performance and achieve high ionic conductivities.[272] Due to the high Li_6PS_5Cl content in the mixed film, the low stack pressure may have hindered Li-ion hopping at the grain boundaries, a limitation that could not be compensated by the addition of HNBR-LiTFSI. Given these findings, it was concluded that hot-press mixing is an inadequate solution for incorporating Li_6PS_5Cl into the HNBR matrix. As a result, no further experiments were conducted using this approach.

In the layered system, the enhancement in ionic conductivity resulting from the addition of Li_6PS_5Cl was more pronounced in the central region compared to the edges. As previously stated, this is likely due to a higher Li_6PS_5Cl to HNBR layer thickness ratio in the center is significantly higher compared to the edges, providing a greater volume of the highly ionically conductive material. Further, the center has a more homogenous distribution of Li_6PS_5Cl, free from the cracks observed in the peripheral regions, which likely contributed to improved ionic transport.

Hence, the longer Li-ion migration pathway through the less conductive HNBR-LiTFSI layer at the edges further impeded ionic transport. Therefore, the observed difference in ionic conductivity between the center and edges of the layered film can be primarily attributed to these structural variations and the differing thicknesses of the conductive and insulating layers (**Scheme 26**).

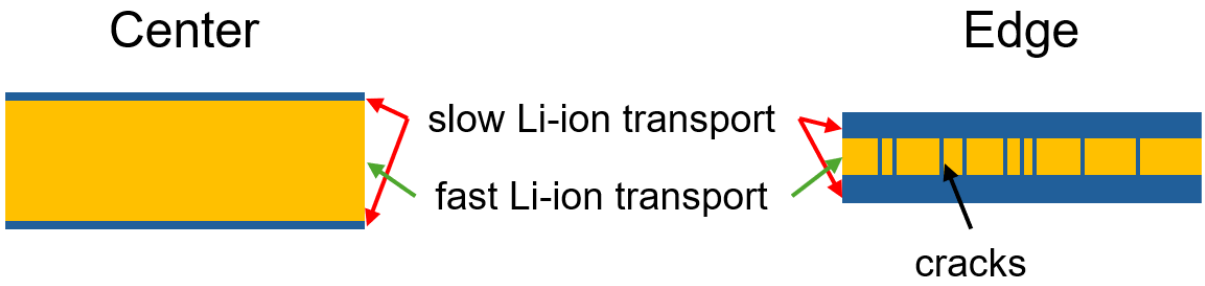

Scheme 26 Schematic representation of the assumed cross-section of the layered HNBR-Li_6PS_5Cl hybrid and the ion-transport properties of the layers. The HNBR-LiTFSI layer (blue) is thinner in the center than at the edges. Additionally, the Li_6PS_5Cl layer (yellow) is more homogeneous and thicker in the center leading to overall faster ion conduction in the center compared to the edges.

Overall, the ionic conductivity at the edges of the layered film was about 1.8 times higher than the pure HNBR-LiTFSI film, while at the center the ionic conductivity was boosted by a factor of 5.8. These are considerable increases, however, the ionic conductivity is still below the required 10^{-4} S cm^{-1}, even though the supplied Li_6PS_5Cl has an ionic conductivity of ~$4 \cdot 10^{-3}$ S cm^{-1} at a.t. according to MSE supplies.[339] By virtue of the stark difference in ionic conductivity of the pure Li_6PS_5Cl and the hybrids it can be assumed that the HNBR-LiTFSI is the limiting factor along with the low pressure. Also, the preparation method of a layered system through hot-pressing does not produce homogenous and reproducible films. Therefore, it was concluded that a HNBR-Li_6PS_5Cl hybrid is not a suitable system as it is severely hindered by the low ionic conductivity of the HNBR matrix/layer.

4.1.4 Recapitulation

In summary, four different CPEs containing HNBR were fabricated and characterized in regards to their electrochemical properties. For LATP based CPEs one membrane with pristine LATP and one membrane with thin PAN surface coated LATP was synthesized. To optimize the polymer coating a systematic study on silica nanoparticles was performed and the findings could be transferred successfully to the LATP particles. Adding pristine LATP to an HNBR-matrix slightly increased the ionic conductivity at elevated temperatures. In contrary, adding PAN@LATP to an HNBR-matrix led to a decrease in ionic conductivity at ambient temperature, and the previously observed agglomeration of LATP during synthesis was not suppressed by the PAN coating. It was concluded that an LATP-HNBR CPE does not provide sufficient ionic conductivity for application in Li-metal solid-state batteries.

In a consecutive study, the addition of Li_6PS_5Cl was evaluated. For this purpose, a mixed and a layered hybrid system were synthesized, and their ionic conductivity was determined. It was found that the mixed system decreased the ionic conductivity, while the layered system could boost it up to a factor of 5.8. Nevertheless, the synthesis of the layered system led to inhomogeneous and irreproducible films. Although the ionic conductivity could be significantly increased, it remained too low overall for practical application.

By virtue of these results, it was concluded that Li_6PS_5Cl is not suitable for CPEs with HNBR either as the ionic conductivity of the hybrids is dominated by the comparatively low ionic conductivity of HNBR.

4.2 Sulfur-Containing Polymers for Argyrodite-CPEs

As previously mentioned, argyrodites are highly reactive and degrade rapidly when exposed to various solvents and reagents. This reactivity is primarily due to the high oxophilicity of the phosphate, as the formation of a PO_4-structure is energetically favored over PS_4. Many polymers utilized in solid-state electrolytes, such as polyethers, polyesters, polycarbonates, and polyacrylates, contain oxygen within their functional groups, in order to coordinate with Li-ions. However, this oxygen content makes these polymers incompatible with argyrodites over extended periods, leading to degradation. As a result, the polymer content in argyrodite-based composite polymer electrolytes is typically limited to single-digit percentages to mitigate degradation. To overcome this limitation, alternative polymers with similar properties in regards to Li-ion coordination, ionic conductivity, and mechanical properties but higher tolerance for argyrodite contact are needed. Such alternatives may allow an increase in polymer content and facilitate CPE production on larger scales. A possible solution involves using polymers such as PVDF and its derivatives but due to the uncertain regulatory future of polyfluorinated polymers alternatives are preferred. However, the uncertain regulatory future surrounding polyfluorinated polymers encourages the exploration of non-fluorinated alternatives. In this context, one possible solution is the use of sulfur-based polymer, offering enhanced chemical compatibility with argyrodites while maintaining suitable electrochemical and mechanical properties for solid-state battery applications.

4.2.1 Strategy

Sulfur is abundant, polar enough for ion dissociation, and is often employed in polymer science.[340] Furthermore, the oxygen-based functional groups commonly utilized in battery applications, such as ethers and carbonates, have sulfur analogues that can also be incorporated into polymers. These sulfur-containing functional groups offer similar Li-ion coordination capabilities while providing improved chemical compatibility with argyrodites. In particular, trithiocarbonates and thioethers are of significant interest.

Trithiocarbonates serve as sulfur-based analogues to carbonates, while thioethers mirror the structure of polyethers, such as poly(ethylene oxide) (PEO), one of the most extensively studied polymers for solid-state batteries. By employing these sulfur-based

functional groups in polymer backbones, it may be possible to achieve high ionic conductivity and effective Li-ion coordination while enhancing chemical stability in contact with argyrodite materials.

This approach not only preserves the desirable electrochemical properties needed for battery applications but also broadens the range of compatible polymers, potentially enabling higher polymer content in composite polymer electrolytes and improving scalability for solid-state battery production (**Scheme 27**).

Polytrithiocarbonate **Polythioether**

Scheme 27 General structure of polytrithiocarbonates and polythioethers.

All polymers were characterized, whenever possible, in regard to their solubility, molecular weight, dispersity, thermal stability, structure, and electrochemical properties.

The following polymers were synthesized through different polymerization techniques (**Table 4**).

For the argyrodite, a close collaboration with Universität Münster within FB2-Hybrid was held. M.Sc. Philip Heuer from the working group of Prof. Dr. Wolfgang Zeier kindly synthesized and provided $Li_{5.5}PS_{4.5}Cl_{1.5}$ (procedure and characterization in 6.3.2.8). The argyrodite exhibits an ionic conductivity at room temperature of 8.2 mS cm^{-1} at a pressure of 50 MPa.

Table 4 List of the synthesized sulfur-decorated polymers with their respective polymerization techniques.

Polymer	Polymer structure	Polymerization
P1	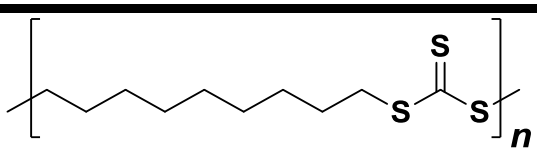	polycondensation
P2	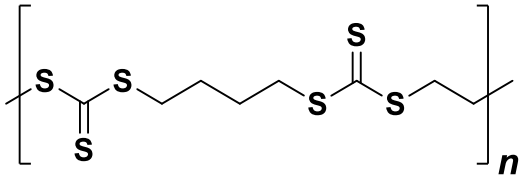	polycondensation
P3	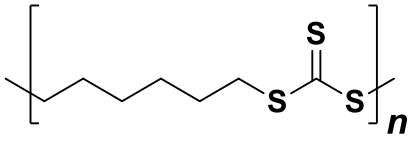	polycondensation
P4	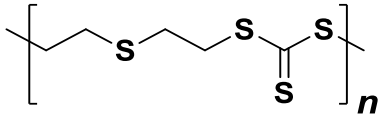	polycondensation
P5	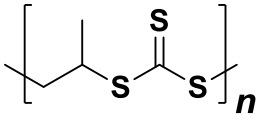	anionic ring-opening
P6	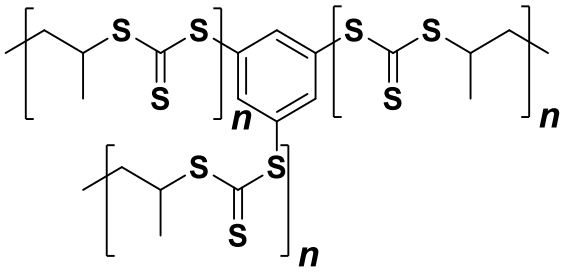	anionic ring-opening
P7	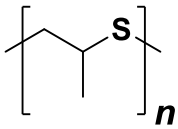	anionic ring-opening

4.2.2 Synthesis

The primary challenge with sulfur polymers lies in their poor solubility in common solvents, which significantly hinders their synthesis, characterization and processing. In the context of polymer electrolytes, it is essential to use polymers that are soluble, flexible, and highly stable. Aromatic polymers, despite their potential advantages, generally tend to have high glass transition temperatures, which result in rigidity and reduced flexibility, thus they were excluded from consideration. Hence, the focus

shifted toward synthesizing aliphatic sulfur polymers that exhibit properties suitable for polymer electrolyte applications, such as low T_g for enhanced flexibility, high (electro-) chemical stability for long-term performance, high thermal stability, and low production costs to support scalability and commercial feasibility.

First, a simple aliphatic polytrithiocarbonate was conceptualized. The polymer, referred as **P1,** was synthesized by adapting a known procedure for RAFT-agents (**Scheme 28** a).[341] Through the utilization of bifunctional starting materials, namely 1,9-dithiononan, 1,9-dibromononan, and carbon disulfide, a polytrithiocarbonate with a C9 methylene spacer was synthesized (Chapter 6.3.2.1). However, a significant challenge was encountered early in the process, as the polycondensation resulted in **P1** precipitating directly from the crude reaction mixture, exhibiting only slight solubility in toluene with no alternative solvent identified for effective dissolution. This poor solubility rendered **P1** unsuitable for use as a polymer electrolyte, as it cannot be characterized and efficiently processed or blended with Li-salts through conventional dissolution methods. Additionally, the T_g of 44 °C was relatively high compared to existing polymer electrolytes (T_g below freezing point e.g., PEO ~ -33 °C[342] and PVDF ~ -40 °C[343]). This elevated T_g limits the segmental motion of the polymer at room temperature, thereby restricting ion conduction and reducing its potential as an affective solid-state electrolyte.

Therefore, to address the limitations observed with **P1**, the starting materials were modified, replacing 1,9-dithiononane and 1,9-dibromononane with 1,4-dithiobutane and 1,2-dibromoethane, respectively. This adaptation led to the synthesis of a new polytrithiocarbonate, **P2**, featuring the same repeating unit length but incorporating two trithiocarbonate units within each repeating unit. The intention behind this structural modification was to introduce irregular spacing of the trithiocarbonate units, aiming to hinder the crystallization of **P2**, increase solubility, and promote amorphous behavior. However, these objectives were not achieved. During polymerization, also **P2** precipitated out of the reaction mixture and was found to be completely insoluble in common solvents, further limiting its potential for use in polymer electrolyte applications.

Consequently, the synthesis strategy was further refined to overcome the solubility challenges encountered with previous polymers. Therefore, **P3** was synthesized using an AA-BB type polycondensation, employing thiocarbonyldiimidazole and 1,6-dithiohexane (**Scheme 28** b) as monomers. The elimination of using carbon

disulfide (which has a low boiling point of 46 °C) allowed for using higher reaction temperatures. By increasing the reaction temperature to 80 °C, **P3** has remained in solution throughout the polymerization, however following precipitation, **P3** exhibited limited solubility, with only two solvents identified as suitable: DMSO (at 80 °C) and chloroform (at 50 °C). While this represented an improvement over previous attempts, the restricted solubility still posed challenges for further processing and potential applications in polymer electrolytes.

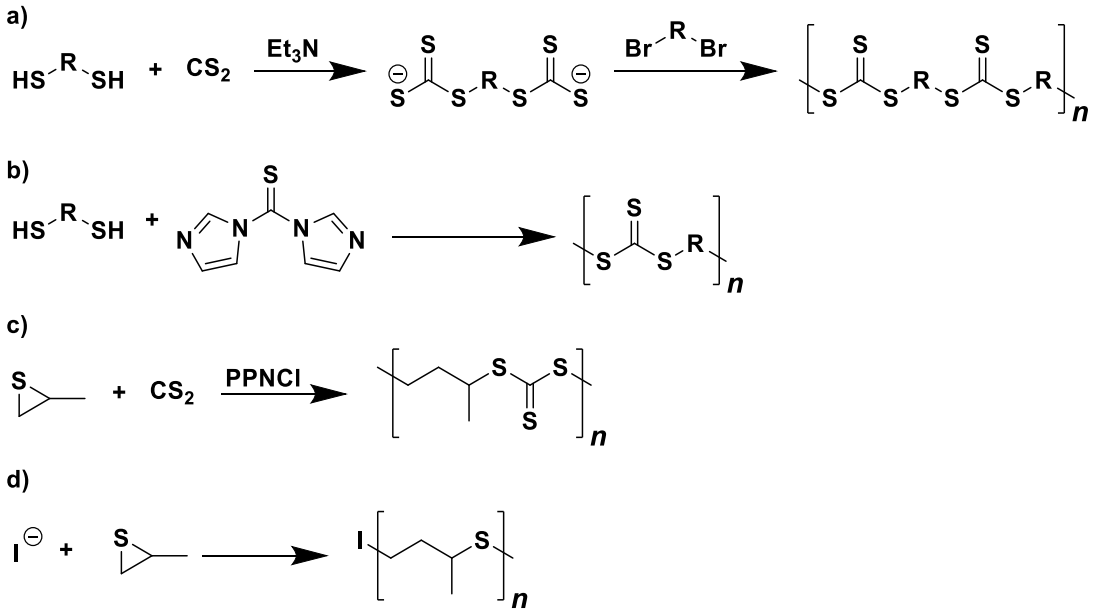

Scheme 28 Synthesis strategies for sulfur-based polymer electrolytes. a) An adapted procedure for the synthesis of trithiocarbonates, commonly used for RAFT-agents.[344] b) An AA-BB type step polymerization. c) Anionic ring-opening copolymerization of propylene sulfide and carbon disulfide catalyzed by bis(triphenylphosphoranylidene)ammonium chloride (PPNCl). d) Anionic ring-opening polymerization of propylene sulfide for the formation of polythioether-based polymers.

The incorporation of a thioether into the aliphatic repeating unit was intended to enhance the flexibility and solubility of the polymer. However, **P4** exhibited the same solubility issues as similar to those of **P3**. Additionally, the polymerization of **P4** was extremely exothermic, making it unsuitable for scale-up.

Since the previously employed synthesis techniques failed to produce polymers with the desired properties, a novel approach was utilized. Following a recently published procedure from Chen et al.,[63] an anionic ring-opening polymerization was conducted to synthesize polytrithiocarbonates decorated with methyl side-groups(**Scheme 28** c). These atactic methyl side-groups of **P5** significantly reduced crystallization, resulting in a polymer with enhanced solubility in a plethora of solvents, including *p*-xylene. Hence, **P5** was the first sulfur-based polymer which was considered viable as a

polymer electrolyte. To address the low mechanical stability of **P5**, a modified polymer, **P6,** was synthesized by adding a trifunctional initiator. This modification promoted increased chain entanglement and therefore improving mechanical strength and making **P6** more suitable for solid-state electrolyte applications.

Lastly, **P7** was synthesized as a polythioether, which have a higher chemical stability compared to polytrithiocarbonates. However, the sulfur-based PEO analogue, poly(ethylene sulfide), is insoluble and rigid. Therefore, the atactic methyl side-group was implemented once again to increase solubility and flexibility (**Scheme 28** d). However, the polymerization of **P7** proceeded very rapidly and posed significant challenges due to potentially explosive reaction, which was due to the high ring-strain of the monomer, propylene sulfide. To ensure safety and control, the reaction conditions were optimized iteratively. Additionally, propylene sulfide was synthesized in-house for the polymerization of **P7**, as the commercially available propylene sulfide is stabilized with butyl mercaptan which acts as an unintended initiator if a base is added, hence complicating accurate control over the initiator-to-monomer ratio. To avoid this issue, unstabilized propylene sulfide was synthesized according to established literature protocol.[63]
Comprehensive and detailed synthesis procedures are available in Chapter 6.3.2.

4.2.3 Characterization

All polymers **P1-7** were characterized by NMR, DSC, TGA, and SEC; however, certain measurements were omitted for polymers with limited solubility (6.3.2). Furthermore, the solubility of each polymer in common solvents was evaluated to assess their suitability for argyrodite CPE manufacturing. As *p*-xylene is one of the few solvents known to not degrade argyrodites upon contact, Special emphasis was placed on *p*-xylene solubility. In **Table 5** the most important characteristics of **P1-7** are summarized. Polymers **P1-4** exhibited poor solubility, rendering them unsuitable as polymer electrolytes. Further, when mixed with LiTFSI in a mortar, no interaction or salt dissociation was observed, further limiting their applicability. An interesting observation was observed for the glass transition temperatures, while the symmetrical aliphatic polytrithiocarbonates **P1** and **P3** had high glass transition temperatures above room temperature, adding an irregularly spaced trithiocarbonate functionality into the backbone of **P2** significantly reduced the T_g to -28 °C.

Table 5 List of all known solvents for all synthesized polymers, glass transition temperatures determined from DSC, degradation temperature determined from TGA at 5% mass loss, and number average molecular weight determined from SEC (smallest and largest measured).

Polymer	Solubility	T_g / °C	$T_{d,5\%}$ / °C	M_n / g mol^{-1}
P1	toluene (slightly)	44	214	insoluble
P2	-	-28	193	insoluble
P3	DMSO (80 °C) chloroform (50 °C)	136	198	insoluble
P4	chloroform (50 °C, slightly)	-	-	insoluble
P5	THF, chloroform, DMSO, DMAC, *p*-xylene, MeCN, DCM	8	171	8,500 - 10,000
P6	THF, chloroform, DMSO, DMAC, *p*-xylene, MeCN, DCM	8	171	5,700 - 6,300
P7	THF, chloroform, DMSO, DMAC, *p*-xylene, MeCN, DCM	-40	281	7,600 - 9,000

Polymers were measured against PMMA standards in SEC measurements. The M_n values do not represent absolute values but rather apparent values.

Nevertheless, the insolubility issue persisted although this improvement in flexibility. Further, the degradation temperature of polymers employed in Li-metal batteries is of high importance. During a thermal runaway event, the polymer may quickly degrade and possibly accelerate damage through release of flammable or toxic gases. This concern is particularly relevant for sulfur-based polymers, which tend to release SO_2 during oxidative degradation, which in turn is harmful to both humans and the environment.[345] **P1-4** exhibited degradation temperatures of approximately 200 °C under a nitrogen atmosphere close. In current Li-ion batteries, the separator melts between 120 - 150 °C and accelerates the thermal runaway by internal short circuit.[346] Therefore, a degradation temperature of 200 °C is an improvement, although achieving even higher degradation thresholds would further improve safety and performance.

P5-7 are well soluble in a wide range of common solvents, significantly enhancing their potential for use in polymer electrolytes. Especially, acetonitrile and *p*-xylene are of high importance, as acetonitrile is commonly used for the preparation of solvent-casted polymer electrolytes with LiTFSI, while *p*-xylene is notable for its chemical compatibility, as it does not degrade argyrodites upon contact. The T_g of **P5** and **P6** is both below room temperature, suggesting a high degree of segmental mobility at room

temperature and may be reduced further by the addition of LiTFSI into the polymer matrix. For **P5** and **P6** the degradation temperature is 171 °C, however their degradation is akin to a fast depolymerization pathway rather than gradual thermal breakdown. This behavior is linked to the structural characteristics of the propylene trithiocarbonate units within the polymer chain. The 5-membered ring of propylene trithiocarbonate is significantly more stable at elevated temperatures than the polymeric chain as was shown by Chen et al. for this specific polymer and by Zhen et al. for polytrithiocarbonates with stable cyclic repeating units in general.[63,347] These findings highlight the balance between processability, thermal stability, and mechanical properties in **P5–P7**, positioning them as promising candidates for solid-state electrolyte applications, especially in systems requiring chemical compatibility with sensitive materials like argyrodites.

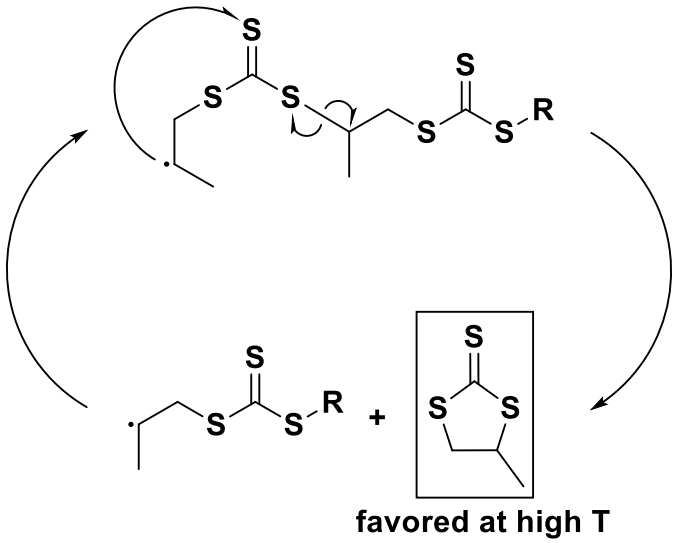

Scheme 29 Simplified radical depolymerization of polypropylene trithiocarbonate (**P5** and **P6**) at elevated temperatures. For a detailed description of the mechanism refer to Chen et al.[63]

The rapid depolymerization of **P5** is further underlined by the almost instantaneous mass loss observed in the TGA measurements (6.3.2.5 **Figure 79**), confirming the susceptibility of the polymer to fast thermal degradation.

The synthesis of **P7** deviates from conventional anionic ring-opening polymerizations as propylene sulfide propagates explosively in a highly exothermic reaction due to the high ring strain of propylene sulfide. This highly exothermic reaction, combined with the comparatively slow initiation rate, prevents the polymerization from exhibiting the characteristics of a living polymerization, as it would be the case for most anionic reactions. Due to these complications multiple attempts to reduce the propagation

kinetics by varying solvents, temperature, and initiator:monomer ratios were undertaken. Despite these attempts, including cooling the reaction flask and using low initiator concentrations, no full control over the polymerization reaction could be achieved. These results align with findings by Rumyantsev, who utilized the rapid propagation in combination with crown-ether/potassium xanthate catalyst system to achieve predictable polymer chain lengths.[348] However, due to the intended use as a polymer electrolyte, the use of metal-ion and crown-ether based catalysts was rejected as they most likely interact with Li-salts and skew ionic conductivity. Instead, a fully organic initiator system comprising benzyl mercaptan and 1,8-diazabicyclo(5.4.0)undec-7-ene (DBU) was selected. To assess the polymerization properties of this system, several polymerizations were performed under different conditions. First, the solvent was varied with other factors being kept constant. Interestingly, the reactions in solution (**P7-1**, MeCN and **P7-3**, THF) resulted in a bimodal distribution, while the reaction in bulk (**P7-2**) led to a broader monomodal distribution (**Figure 14**). In contrast, changing the solvent to chloroform (**P7-4**) or increasing the intiator:monomer ratio (**P7-5**) led to an explosion of the crimp vial in which the reaction was conducted. Hence, a bulk polymerization while cooling the reaction mixture in an ice bath was adapted (**P7-6**) to reduce the propagation rate and stop the boiling of propylene sulfide in the highly exothermic reaction. This proved to be the most successful attempt resulting in the largest molecular mass (M_n = 9,000 g mol^{-1}) while reducing the dispersity to its lowest observed value (1.16). To produce larger quantities of the polymer for CPEs fabrication and to supply FB2 project partners, the synthesis of **P7-6** was up-scaled, resulting in **P7-7**. Given the inherent risks associated with the highly exothermic nature of the polymerization, the initiator concentration was reduced in **P7-7** to mitigate the risk of explosive propagation. The initiator-to-monomer ratio was adjusted from 1:200 (initiator:monomer) in **P7-6** to 1:500 in **P7-7.** Despite this, the polymerization reaction still exhibited strong exothermic characteristics. As a result, the properties of **P7-7** differed from its precursor in terms of molecular weight and dispersity. The final polymer achieved a number-average molecular weight (M_n) of 8,900 g mol^{-1} and a dispersity ($Đ$) of 1.32, reflecting the impact of scale-up and altered initiation rates on polymer characteristics.

These variations highlight the complexities of scaling up propylene sulfide polymerization while maintaining consistent material properties, particularly in managing exothermicity and reaction kinetics.

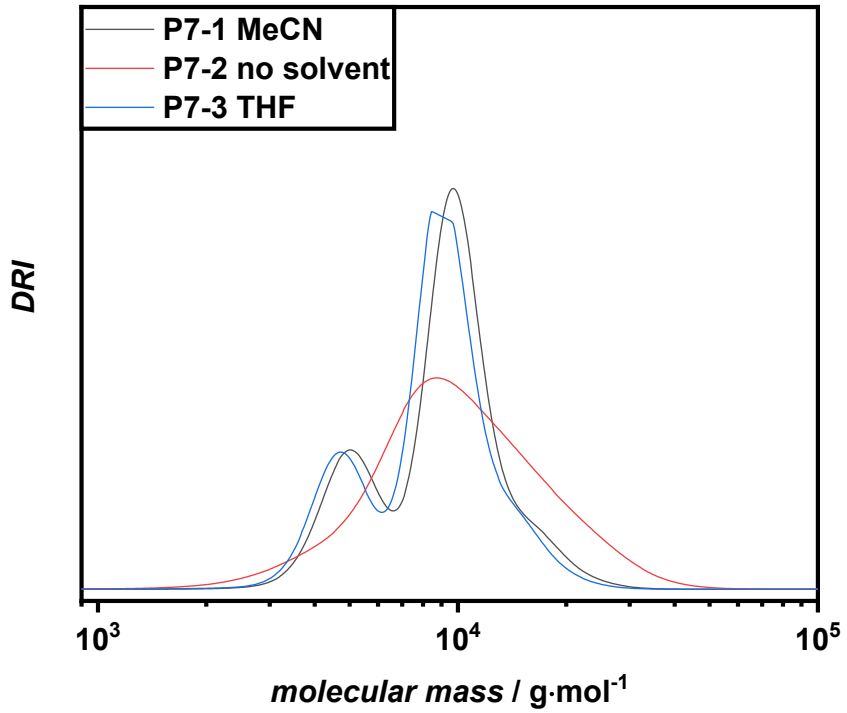

Figure 14 THF-SEC curves of P7-1/2/3 against a PMMA standard. Bulk reactions without a solvent have broad monomodal distributions while polymerizations in solution have a narrower bimodal distribution.

The polythioether **P7-7** (referred to as **P7** from this point forward) was selected for an in-depth characterization. It demonstrated similar solubility properties to **P5 and P6,** making it compatible for processing with argyrodites and Li-salts. However, **P7** differed significantly in its physical properties. While **P5** and **P6** formed amorphous solids, **P7** was obtained as a translucent sticky liquid with honey-like viscosity, offering greater flexibility during processing is. Furthermore, **P7** exhibited the lowest glass transition temperature of -40 °C, among all synthesized polymers, which in turn is also comparable to commonly utilized polymer electrolytes such as PEO and indicates significant segmental motion at room temperature, a key factor for efficient Li-ion transport.

P7 also had the highest thermal stability, with a degradation temperature of 281 °C and no evidence of depolymerization reaction during thermal analysis. This superior stability, combined with its favorable physical and electrochemical properties, positions **P7** as the most promising candidate for use as a polymer electrolyte (PE) or in the development of solid-state battery systems.

4.2.4 Argyrodite CPEs

P5 was chosen first for the preparation of a polymer electrolyte film. Due to its high surface tension, it could not be solvent-casted. Instead, **P5** was mixed with LiTFSI in MeCN, followed by drying, and hot-pressing to form a film (procedure in 6.3.2.9). Upon hot-pressing, the film was removed from the protective Mylar® foil, resulting in a flexible and soft membrane (**Figure 15**). 10 mm circles were punched out for ionic conductivity measurements. However, during testing, all cells immediately short circuited. Repeated multiple attempts to resolve the issue have failed even when foregoing the preconditioning step. No consistent impedance measurements could be obtained across at any tested temperatures, ultimately rendering **P5** unsuitable for use as a polymer electrolyte in its current form.

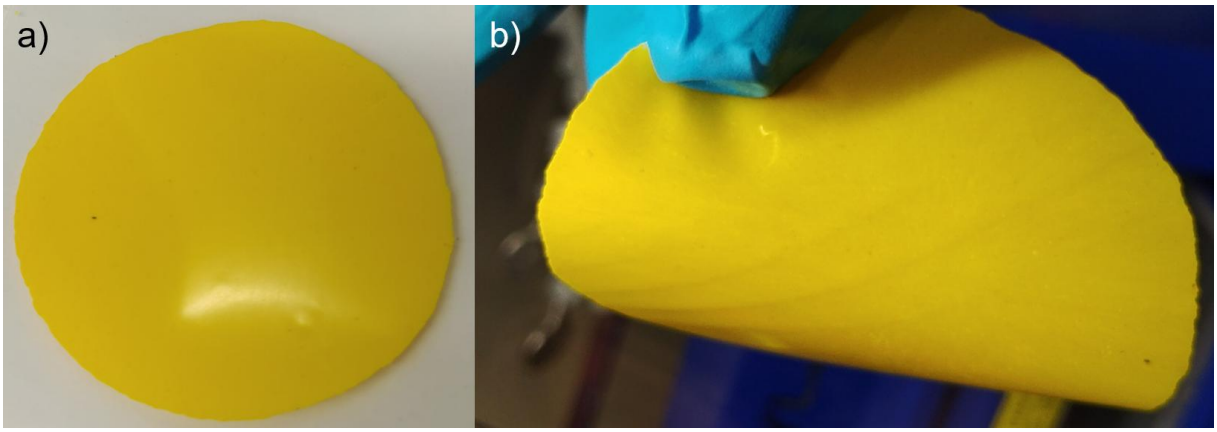

Figure 15 a) P5+LiTSI film after hot-pressing sandwiched between Mylar® foil. b) P5+LiTFSI film after removing from Mylar® foil. The film shows slight adhesion to the foil and is soft.

The softness of the **P5** film likely caused continuous compression and a reduction in thickness, ultimately leading to a short circuit. To mitigate this issue, the process was repeated using **P6**, which was expected to offer a higher resistance to creep due to its 3-arm branched nature. However, the same phenomenon was observed. Upon disassembling the cells, the **P6** film was found to be damaged by compressive stress, similar to the outcome with **P5**. This indicates that despite the structural modification, **P6** was still unable to withstand the mechanical stresses during operation, leading to the same short-circuiting issue.

Alternatively, to increase mechanical resistance against compression, equal mass ratio CPEs of the **P5** and $Li_{5.5}PS_{4.5}Cl_{1.5}$ with LiTFSI were prepared by combining all components in *p*-xylene in a glovebox (procedure in 6.3.2.10). The addition of

interlocking argyrodite particles should drastically increase compressive strength and reduce creep. However, efforts to measure the ionic conductivity were unsuccessful due to high variance in impedance readings across the cells. Upon opening the CPE cells, a brown-orange liquid leaked, and the CPE film was completely degraded. The complete absence of the distinctly yellow polymer indicated that a reaction was occurring during the measurements in the climate chamber, thus explaining the varying impedance measurements. Hence, pure **P5**, a pristine part of the **P5**-LiTFSI PE, and a pristine part of the **P5**-$Li_{5.5}PS_{4.5}Cl_{1.5}$ CPE were placed in a vial in the glovebox and observed over an extended period of three months to identify the trigger of the degradation. While the pure **P5** and the **P5**-LiTFSi PE remained visually the same, the argyrodite CPE gradually shifted in color from yellow to brown, suggesting chemical degradation. Subsequent NMR analysis revealed a depolymerization of the polytrithiocarbonate was occurring upon contact with the $Li_{5.5}PS_{4.5}Cl_{1.5}$ (**Figure 16**).

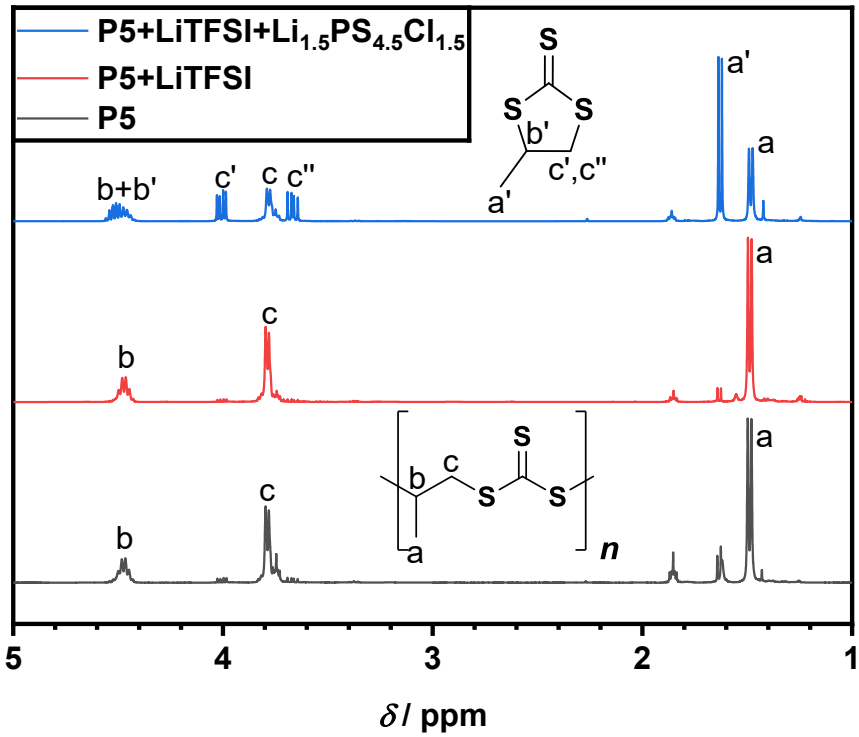

Figure 16 ^{1}H-NMR (400 MHz, $CDCl_3$) of **P5**, **P5**-LiTFSI PE, and **P5**- $Li_{5.5}PS_{4.5}Cl_{1.5}$ CPE after 3 months of storage under inert conditions in a glovebox. The depolymerization of the trithiocarbonate polymer to cyclic propylene trithiocarbonate can be identified by the shift of a to a' and the split of c to c' and c''. The ratio of a:a' in the CPE is 1:1 indicating that approximately half of the polymer degraded in 3 months under inert conditions.

While there was no change in between pure **P5** and the **P5**-LiTFSI PE after 3 months of storage under inert conditions, the **P5**-$Li_{5.5}PS_{4.5}Cl_{1.5}$ CPE showed peaks corresponding to cyclic propylene trithiocarbonate.

The shift of the doublet *a* corresponding to the methyl group and the splitting of *c* peak corresponding to -C*H*$_2$- into two peaks align with the report of Chen et al. about the radical degradation of polypropylene trithiocarbonate.[63] As the integral ratio of *a* to *a'* in the CPE is 1:1, it can be concluded that within three months, about half of the polymer depolymerized under inert atmosphere, in the absence of UV exposure, and at room temperature. These conditions make a radical process unlikely, hence, an alternative depolymerization mechanism is proposed based on the nucleophilic character of the thiophosphate groups present on the surface of the argyrodite (**Scheme 30**).

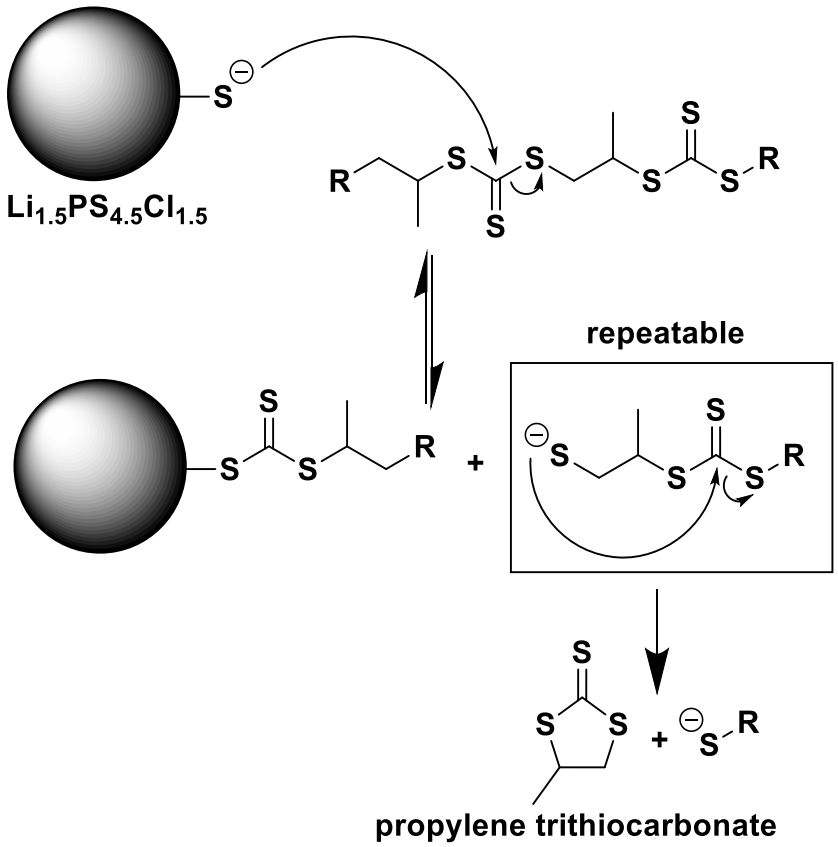

Scheme 30 Proposed depolymerization mechanism of polypropylene trithiocarbonate in contact with argyrodite surfaces. The thiolate of the thiophosphate (PS_4^{3-}) in a nucleophilic attack at the carbon of the trithiocarbonate opens the polymer chain and transfers the thiolate onto the polymer. The thiolate at the chain end attacks its neighboring trithiocarbonate unit and forms the stable cyclic propylene trithiocarbonate. This process repeats until the polymer is completely depolymerized. Increasing the temperature favors the formation of the cyclic propylene trithiocarbonate.

Trithiocarbonates are known for their susceptibility to nucleophilic attacks leading to fast degradation of the trithiocarbonate unit, a well-documented limitation in RAFT polymerizations.[341] Given that the surface of the argyrodite contains thiophosphates, which can generate thiolate anions, it is proposed that these thiolates act as nucleophiles, initiating the attack on the trithiocarbonate unit which is opening the polymer chain. The thiolate anion forming at the end of the newly cleaved polymer chain can repeat the nucleophilic attack at its neighboring trithiocarbonate unit thus forming a stable and thermodynamically favored cyclic propylene trithiocarbonate.
This step can be repeated continuously until the polymer is completely depolymerized. Moreover, the depolymerization process may be assisted by the presence of salts, as they may catalyze the reaction and further form solvate shells with the newly formed cyclic propylene trithiocarbonate, shifting the chemical equilibrium. Elevated temperature further favors the formation of cyclic propylene trithiocarbonate, accelerating the depolymerization**,** process and increasing the rate of polymer breakdown.
Since the depolymerization is most likely triggered by the argyrodite, polytrithiocarbonates are unsuitable as polymers for CPEs containing argyrodites. Consequently, no further experiments were conducted with **P5** or **P6**.

The utilization of **P7** as a polymer electrolyte in a CPE with $Li_{5.5}PS_{4.5}Cl_{1.5}$ was limited by its honey-like viscosity, which resulted in poor mechanical stability at room temperature, making it unsuitable as a matrix polymer. Hence, a different approach was theorized. To increase the resistance of $Li_{5.5}PS_{4.5}Cl_{1.5}$ particles against air and water, a thin coating layer of polymer is sufficient. Further, a thin polymeric coating layer with liquid properties may increase electrode wettability and reduce the pressure requirements during cell assembly. To implement this approach, $Li_{5.5}PS_{4.5}Cl_{1.5}$ particles were coated by mixing **P7**, LiTFSI, and a small amount of *p*-xylene were mixed in a mortar inside a glovebox (procedure in 6.3.2.11). Through continuous mixing, a paste was obtained, which dried as the solvent evaporated slowly. The paste was transferred to an oven and dried at 40 °C under a vacuum of 10^{-3} mbar, resulting in lumps of coated argyrodite (**Figure 17**). Visually, the argyrodite powder maintained its color, suggesting no degradation occurred during the process. The lumps indicated that the polymer coating promoted adhesion between $Li_{5.5}PS_{4.5}Cl_{1.5}$ particles.

Figure 17 Picture of P7+LiTFSI coated $Li_{5.5}PS_{4.5}Cl_{1.5}$ after drying in a vacuum oven.

The coated $Li_{5.5}PS_{4.5}Cl_{1.5}$ was sent to Universität Münster for analysis of H_2S evolution following the coating process and to assess any changes in ionic conductivity. However, due to instrument failure, the measurement of H_2S evolution could not be completed. The ionic conductivity of pristine and coated $Li_{5.5}PS_{4.5}Cl_{1.5}$ was determined by impedance measurements under a pressure of 50 MPa at 25 °C (**Figure 18**). The detailed procedure for these measurements is described in 6.1.8.2.

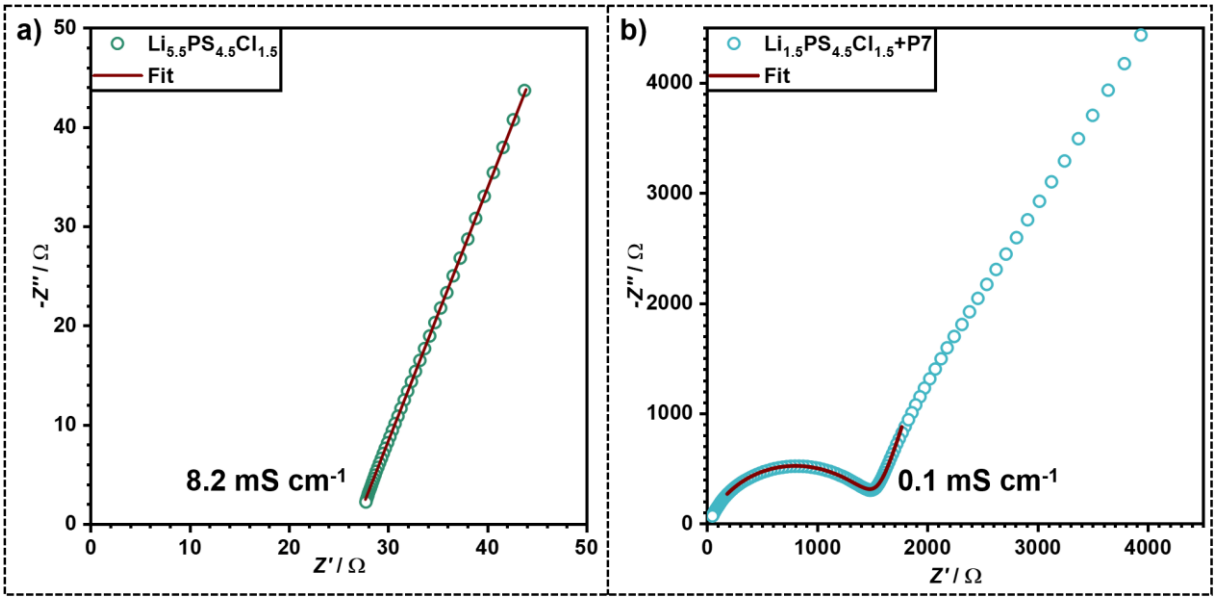

Figure 18 Nyquist plots of a) pristine $Li_{5.5}PS_{4.5}Cl_{1.5}$ and b) $Li_{5.5}PS_{4.5}Cl_{1.5}$ coated with P7 and LiTFSI. Both measurements were performed at 50 MPa and 25 °C.

The pristine $Li_{5.5}PS_{4.5}Cl_{1.5}$ exhibited an ionic conductivity of $8.2 \cdot 10^{-3}$ S cm^{-1}, while application of the coating of **P7** and LiTFSI significantly inhibited the ionic conductivity to $0.1 \cdot 10^{-3}$ S cm^{-1}. Nevertheless, the ionic conductivity of coated $Li_{5.5}PS_{4.5}Cl_{1.5}$ remains within an acceptable range for use in solid-state Li-metal batteries. However, due to

time constraints, further measurements of the ionic conductivity at lower pressures, across a broader temperature range, and assessments o H_2S evolution under the applied coating were not possible. As a result, a definitive statement about the suitability of poly(propylene sulfide)+LiTFSI coatings for $Li_{5.5}PS_{4.5}Cl_{1.5}$ in practical applications cannot be made at this stage, yet, among all investigated sulfur polymers, **P7** seems to be the most promising candidate.

4.2.5 Recapitulation

In summary, seven aliphatic polymers consisting exclusively of carbon, hydrogen, and sulfur, including six polytrithiocarbonates and one polypropylene sulfide, were synthesized and characterized regarding their possible application in argyrodite-based hybrid solid-state electrolytes. The polytrithiocarbonates were mostly insoluble, limiting their processability. However, the incorporation of an atactic methyl side group into polypropylene trithiocarbonate, the solubility was improved. Despite this enhancement, the resulting polymer electrolytes were too soft for use as a self-standing film in coin cells. Through the addition of $Li_{5.5}PS_{4.5}Cl_{1.5}$ to the polymer electrolyte, it was aimed to increase resistance against compression; thus, to improve the mechanical stability, however, it was found that the addition of the argyrodite triggered a depolymerization of the polytrithiocarbonate. As a result, polytrithiocarbonates were deemed unsuitable for hybrid systems containing argyrodites.

As the implementation of an atactic methyl side-group significantly improved solubility in polytrithiocarbonates, a polythioether with the similar structural features was synthesized, i.e., polypropylene sulfide. Although the good solubility properties could be transferred, polypropylene sulfide is a liquid at room temperature and therefore unsuitable as a matrix polymer. Alternatively, $Li_{5.5}PS_{4.5}Cl_{1.5}$ was coated in poly(propylene sulfide) and LiTFSI to improve wettability, reduce pressure requirements, and protect the argyrodite particles against moisture and air.

A reduction in the ionic conductivity in a reasonable range to 10^{-4} S cm^{-1} at room temperature was observed for the poly(propylene sulfide)+LiTFSI coated $Li_{5.5}PS_{4.5}Cl_{1.5,}$ however, due to time constraints, an in depth characterization, such as the evaluation of H_2S and the pressure-ionic conductivity relationship, were not completed. Further investigations are necessary to fully assess the viability of this approach and to determine the long-term stability and performance of poly(propylene sulfide)-coated argyrodite in solid-state electrolytes.

4.3 Coating of LATP/LLZO Particles for Oxide-CPEs

Initially, the coating of LATP with various alkoxy silane-modified poly(ethylene glycol) methyl ethers (mPEG) was proposed to evaluate the feasibility of a "grafting-to" approach. This method was explored as a potentially simpler, faster, more controllable, and scalable alternative to the coating approach described in Chapter 4.1. However, during the fabrication of LLZO mixed with poly(vinylidene fluoride-*co*-hexafluoropropylene) (PVDF-HFP) CPEs by M.Sc. Xioachen Liu from Forschungszentrum Jülich, degradation of PVDF-HFP was observed. The interaction between LLZO and PVDF-HFP triggered a dehydrofluorination, as La atoms on the particle surface form complexes with N and C=O units from the solvent (DMF), creating an alkaline environment.[349,350] This dehydrofluorination resulted in a brown discoloration and degradation of the originally white compounds (**Figure 19**).

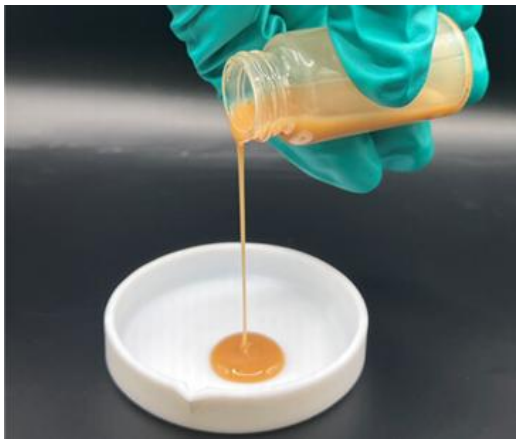

Figure 19 Degraded PVDF-LLZO slurry after dehydrofluorination.

The degradation resulted in increased interfacial resistance and reduced Li-ion transport. Furthermore, LLZO particles agglomerated during film preparation, leading to inhomogeneous distribution within the PVDF-HFP matrix. To solve both the degradation and agglomeration challenges, a collaboration was established between Forschungszentrum Jülich and Karlsruhe Institute of Technology (KIT) within the FB2-Hybrid cluster. The expertise gained from mPEG-LATP coatings was transferred into a new collaborative project. In this initiative, LLZO powder was synthesized by Xiaochen Liu, then sent to KIT for polymer coating before being returned to Forschungszentrum Jülich for the fabrication of CPEs and their subsequent characterization.

Parts of this chapter and the corresponding parts in the experimental section were adapted with permission from a prepared publication written by the authors (Daniel Döpping, Xiaochen Liu) [Publications within this Dissertation [3] in 9 List of Publications].

4.3.1 Strategy

Two approaches were investigated to stabilize the LLZO-PVDF interface, drawing from initial data obtained from mPEG-based LATP coatings. A simplified synthesis path is shown in **Scheme 31**.

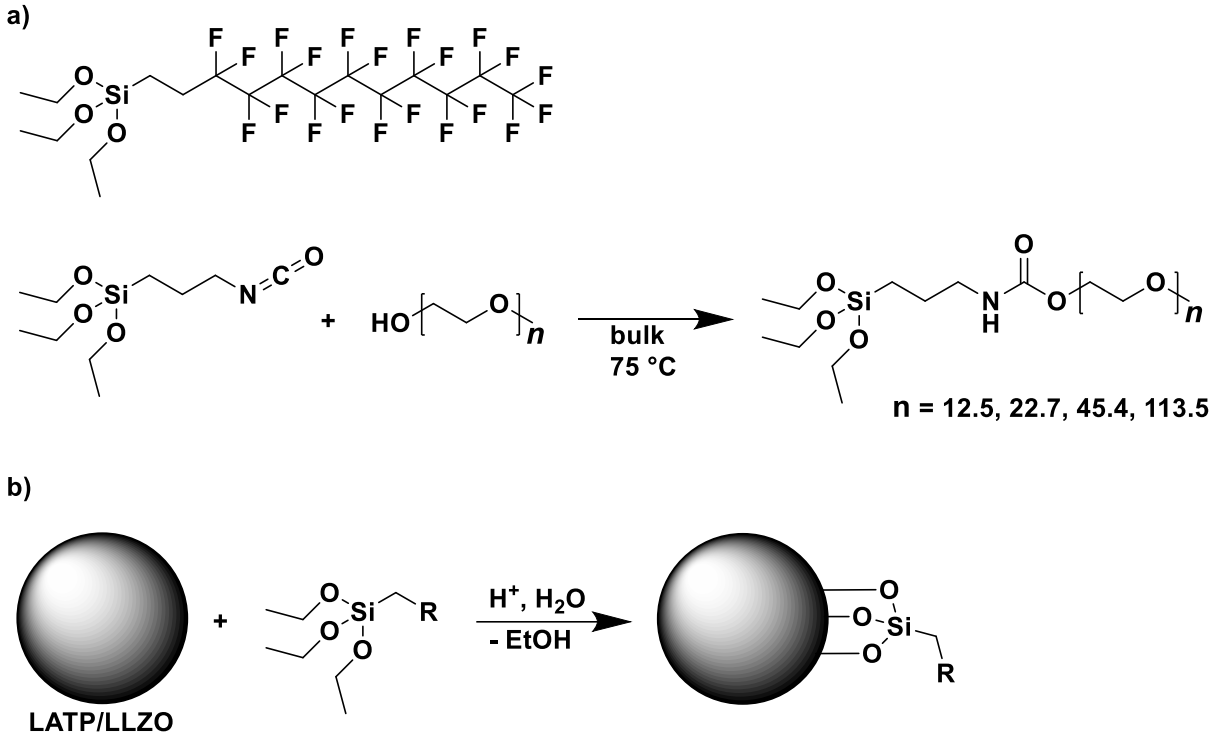

Scheme 31 Synthetic approach for coated LATP/LLZO-particles. a) 1*H*,1*H*,2*H*,2*H*-Perfluorodecyl triethoxy silane (commercially available) and the bulk synthesis of alkoxy silane modified mPEG. b) Acid catalyzed coating of the alkoxy silanes onto the surface of LATP/LLZO particles.

The first approach involved coating the LLZO with 1*H*,1*H*,2*H*,2*H*-perfluorodecyl triethoxy silane to mimic the properties of the PVDF-HFP matrix, therefore enhancing stability and reducing agglomeration. The second approach utilized an alkoxy silane modified mPEG coating to enable a Li-ion coordinating surface layer. Both approaches followed a “grafting-to” concept, which is known to have limits by grafting density as the polymer chain length increases.

While this limitation is negligible for the relatively small 1*H*,1*H*,2*H*,2*H*-perfluorodecyl triethoxy silane, it imposes a challenge on mPEG polymers, with a maximum effective chain length of approximately 1,000 g mol^{-1} (~23 repeating units), as determined in previous mPEG-LATP coating studies. Consequently, LLZO powder was coated with 1*H*,1*H*,2*H*,2*H*-perfluorodecyl triethoxy silane and mPEG1000 alkoxy silane and subsequently analyzed using TGA and Cryo-TEM to evaluate coating homogeneity. Following this, membranes incorporating PVDF-HFP were fabricated at Forschungszentrum Jülich and characterized for their suitability as coated LLZO-PVDF CPEs in Li-metal solid-state batteries.

4.3.2 Synthesis and Characterization

4.3.2.1 mPEG-silanes

First, the mPEG was directly modified with 3-(triethoxysilyl)propyl isocyanate (IPTES) to introduce a surface active alkoxy silane functionality through a highly efficient one-step process. This reaction was adapted and optimized from a procedure developed by Lin and Zhou.[114,351] By eliminating the use of solvents and instead utilizing a bulk reaction with a 1:2 molar ratio of mPEG to IPTES full conversion of the mPEG hydroxy functionality was achieved. Additionally, this bulk reaction approach enhances scalability, enabling synthesis of batches up to 150 g at the laboratory scale. The detailed procedure is available in 6.3.3.1.

The four synthesized mPEG-silanes were characterized using ^{1}H-NMR (6.3.3.1 **Figure 91** - **Figure 94**) and SEC (**Figure 20**). The ^{1}H-NMR showed all expected peaks in the correct proton ratio, suggesting a successful modification with full or near-complete conversion. For SEC measurements, both the purchased mPEGs and the IPTES-modified mPEG-silanes were measured against a PEO standard for comparison (**Table 6**). All mPEGs exhibited a narrow dispersity (*Đ*) ranging from 1.04 - 1.18, both before and after modification, and their molecular weight values closely matched supplier specifications prior to IPTES addition. After modification with IPTES, the M_n of the mPEGs increased by 100 to 400 g mol^{-1}. Given that IPTES has a molecular weight of 247.4 g mol^{-1}, this increase further confirmed a successful modification.

Table 6 List of THF-SEC measurements for all synthesized mPEGs (M_n = 550, 1,000, 2,000, and 5,000 g mol^{-1}) and the respective IPTES-modified mPEG-silane. Measured against PEO standards, values rounded to 50.

mPEG	unmodified		IPTES-modified	
	M_n / g mol^{-1}	$Đ$	M_n / g mol^{-1}	$Đ$
550	550	1.08	900	1.07
1,000	1,000	1.06	1,350	1.16
2,000	2,100	1.04	2,300	1.05
5,000	5,700	1.13	5,800	1.18

In the SEC graphs (**Figure 20**), a small shoulder was observed for all samples, which were more pronounced following IPTES-modification.

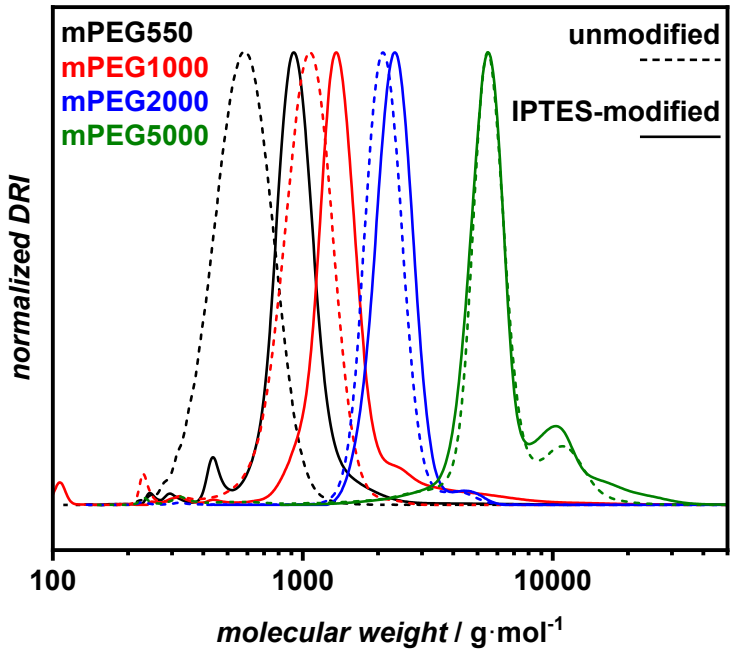

Figure 20 THF-SEC of unmodified compared to the IPTES-modified mPEG (M_n = 550, 1,000, 2,000, and 5,000 g mol^{-1}). Measured against PEO standards.

The increased shoulders at higher or approximately double the molecular weight in the SEC graphs were attributed to the homocondensation of alkoxy silanes, resulting in the formation of dimers and oligomers (**Scheme 32**).

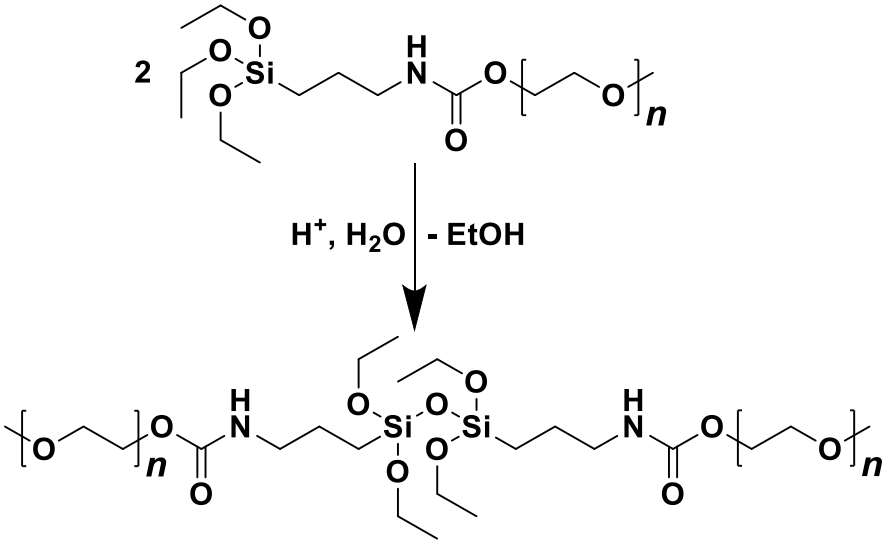

Scheme 32 Oligomerization of mPEG-silanes during drying in a vacuum oven. Moisture from the air triggers the homocondensation of the alkoxy silane end-groups.

During the drying process, the combination of reduced pressure and elevated temperature led to homocondensation of the alkoxy silane end-groups catalyzed by moisture from the air. To suppress this phenomenon and preserve the highest possible reactivity towards hydroxy groups on surfaces, the drying protocol was set optimized to 35 °C at 600 mbar, staying below the boiling point of ethanol, which is eliminated during the homocondensation. This adjustment significantly reduced the formation of shoulders in SEC graphs. However, complete removal of solvents, particularly THF, from the IPTES-modified mPEGs remained challenging. Nevertheless, a facile, fast, and efficient synthesis procedure for the modification of mPEG was successfully established.

4.3.2.2 mPEG@LATP

The alkoxy silane functionalized mPEGs were used to coat LATP (Appendix **Table 23**, **Figure 111**) by modifying the procedure for SH-TMS coating of LATP (6.3.1.3). In this process, LATP and the corresponding mPEG-silane were mixed in a 2:1 mass ratio and stirred under acidic conditions for 18 h. The crude LATP particles were then centrifuged, washed, dried, and analyzed using TGA (6.3.3.2 **Figure 95** - **Figure 98**) and TEM. A detailed procedure is provided in 6.3.3.2. The coated LATP samples were labelled based on the mPEG-silane used, following the format “mPEGXXXX@LATP”, where XXXX denotes the M_n provided by the supplier.

TGA measurements revealed varying mass loss, which appeared to be independent of the M_n of the mPEG-silane (**Table 7**).

Table 7 Mass loss of coated LATP particles after heating from 30 - 800 °C at 10 K min^{-1}. TGA graphs are available in 6.3.3.2.

Coated LATP	TGA mass loss / %
mPEG550@LATP	1.9
mPEG1000@LATP	4.0
mPEG2000@LATP	3.9
mPEG5000@LATP	2.3

The highest mass loss was observed for mPEG1000@LATP with 4.0 %, followed closely by mPEG2000@LATP (3.9 %), indicating that the “grafting-to” approach is constrained by the utilized polymer chain length. From mPEG550@LATP to mPEG1000@LATP, the mass loss approximately doubles, mirroring the increase in M_n of the mPEG, suggesting a similar grafting density. However, when M_n doubles again from mPEG1000 to mPEG2000, the mass loss remains nearly constant, implying mPEG1000-silane is about twice as reactive to the particle surface as mPEG2000-silane. This trend was further supported by mPEG5000-silane, which resulted in an even lower mass loss, reinforcing that increasing the molecular weight of the mPEG-silanes beyond 1000 g mol^{-1} resulted in a lower grafting density.

To confirm the coating of LATP, cryo-TEM micrographs of all four mPEG@LATP particles were captured (**Figure 21**). The images revealed that with increasing M_n of the mPEG-silane, the coating became thicker and more inhomogeneous. To quantify the coating thickness, measurements were taken at regular intervals using ImageJ and the values were averaged, with a standard deviation of error (**Table 8**).

Table 8 Average coating thickness with one standard deviation as error of all four mPEG@LATP particles synthesized.

Coated LATP	Coating Thickness / nm
mPEG550@LATP	5.3±1.2
mPEG1000@LATP	10.9±1.1
mPEG2000@LATP	15.2±2.5
mPEG5000@LATP	19.3±4.1

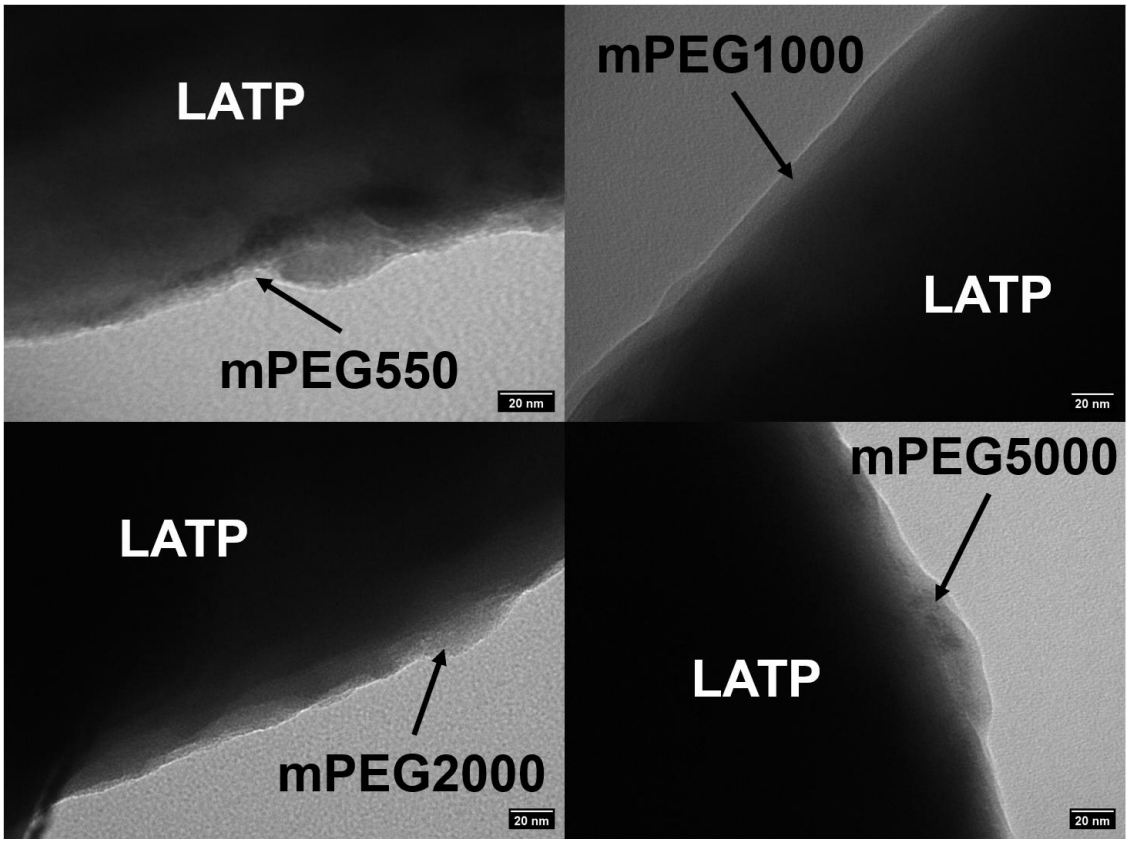

Figure 21 TEM micrographs of mPEG550@LATP (top left), mPEG1000@LATP (top right), mPEG2000@LATP (bottom left), and mPEG5000@LATP (bottom right). The coating gets increasingly thicker and more inhomogeneous with increasing M_n of the mPEG coating.

The findings of the TGA measurements were confirmed through TEM micrographs. While increasing the M_n of the mPEG-silane used in the coating from 550 to 1,000 g mol^{-1}, the coating thickness approximately doubled while maintaining similar homogeneity, as indicated by a consistent standard deviation in coating thickness. However, for M_n values above 1,000 g mol^{-1}, the increase in coating thickness became non-linear and led to more inhomogeneous coatings. Notably, in mPEG5000@LATP, condensed agglomerates of mPEG with sizes up to 1 µm were found (Appendix **Figure 124**).

Considering both TGA measurements and TEM micrographs, the optimal mPEG M_n for achieving a homogeneous coating with maximum grafting density in an alkoxy silane-based grafting-to approach was determined to be 1,000 g mol^{-1}.

4.3.2.3 PF@LLZO

Forschungszentrum Jülich supplied two batches of LLZO (Appendix **Figure 121** - **Figure 123**, **Table 24**), both synthesized using the same synthesis procedure, with one batch undergoing wet ball milling after sintering, followed by sieving. The smaller LLZO particles, with an average particle size of 350 nm, were selected for this project as their size closely matched that of LATP particles (254 nm).

For the coating of LLZO, the synthesis had to be adapted. While LATP exhibited only slight reactivity with the alkoxy silanes, resulting in thin surface coatings, LLZO demonstrated a significantly higher affinity towards alkoxy silanes, as evidenced by increased mass loss in TGA measurements. By virtue of the higher reactivity of LLZO with alkoxy silane, the mass ratio of LLZO to alkoxy silane was adjusted from 2:1 (used for LATP) to 10:1, ensuring a controlled and uniform coating process.

In the following, 1*H*,1*H*,2*H*,2*H*-perfluorodecyl triethoxy silane coated LLZO will be referred to as “PF@LLZO”. The TGA measurements (6.3.3.3 **Figure 99**) of PF@LLZO revealed a mass loss of 9.2 %, indicating that almost all of the 1*H*,1*H*,2*H*,2*H*-perfluorodecyl triethoxy silane successfully reacted with the LLZO surface, confirming the coating process with the perfluorated alkoxy silane. However, initial tests of mixing PF@LLZO with PVDF-HFP demonstrated that the coating did not prevent the degradation of PVDF-HFP in contact with PF@LLZO. As a result, no further analysis was performed, and the project proceeded with coating LLZO using with mPEG1000-silane instead.

4.3.2.4 mPEG@LLZO

As previously mentioned, LLZO and alkoxy silanes have a significantly higher reactivity compared to LATP and alkoxy silanes. Hence, the mass ratio of LLZO to mPEG1000-silane was also adjusted to 10:1. The resulting mPEG1000@LLZO particles were characterized by TGA (6.3.3.4 **Figure 100**), TEM (**Figure 23** a - d), before sent to Forschungszentrum Jülich for the fabrication of mPEG1000@LLZO+PVDF CPEs.

The TGA results showed a mass loss of 12.2 % exceeding the relative mass of the added as mPEG1000-silane. This indicates that the coating reaches full or near-full conversion of alkoxy silanes, while also absorbing solvents or moisture. To mitigate this, mPEG1000@LLZO was dried in an oven before being used as an active filler for PVDF-HFP CPEs.

The coated particles were sent to Forschungszentrum Jülich and used as active fillers for PVDF-HFP CPEs by M.Sc. Xiaochen Liu. The following data is derived from the collaborative publication.

First, mixing the coated mPEG1000@LLZO particles with DMF and PVDF-HFP did not lead to discoloration or decomposition (**Figure 22**). This simple test immediately highlighted the benefit of the mPEG coating, as it enabled stable slurry preparation at temperatures of 80 °C and above.

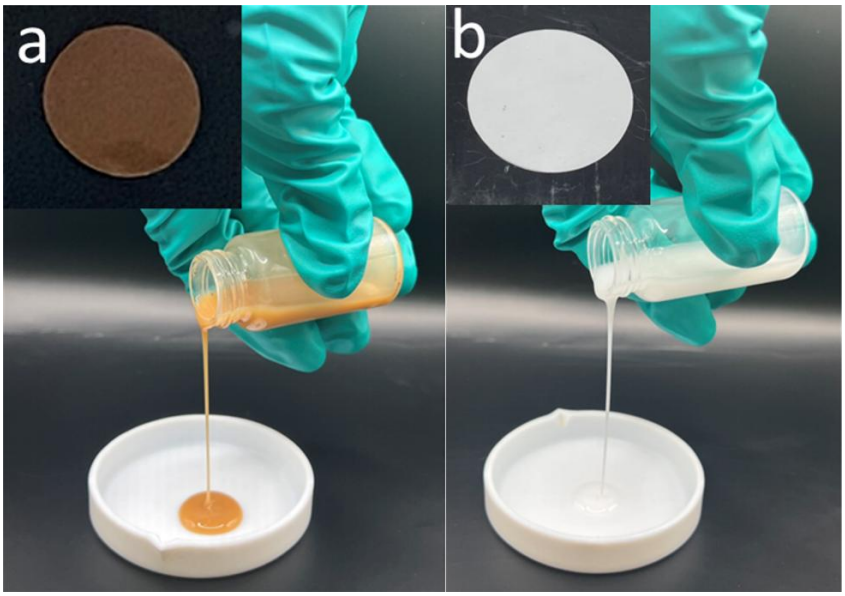

Figure 22 a) Decomposed slurry and film of pristine LLZO with PVDF-HFP and b) stable slurry and film of mPEG1000@LLZO after stirring at 80 °C. The white color indicates successful suppression of dehydrofluorination.

The mPEG1000@LLZO particles were further characterized by using TEM, Raman Spectroscopy, ATR-IR, and XRD.

The TEM micrographs (**Figure 23** a - d) revealed an even distribution of mPEG1000-silane on the LLZO surface, comparable to the coatings observed for mPEG@LATP. The polymer layer had a thickness of ~14 nm, closely matching the ~11 nm thickness found mPEG1000-silane coatings on LATP.

Raman Spectroscopy confirmed the presence of a characteristic Li_2CO_3 band at 1090 cm^{-1} in pristine LLZO, which forms due to exposure of LLZO surface with H_2O and CO_2. This band could be identified for the uncoated LLZO (**Figure 23** e), but was absent when coated with mPEG1000-silane, indicating that the mPEG coating effectively suppressed Li_2CO_3 formation. Instead, a band at 947 cm^{-1} corresponding to the protective Li_3PO_4 coating applied after synthesis was clearly identified. Moreover, the characteristic ether vibrations at 1050, 1410, and 1590 cm^{-1} were observed in ATR-

IR measurements (**Figure 23** f). As expected, the XRD patterns showed no deviations, confirming that the coating process preserved the cubic garnet phase of LLZO, ensuring that the bulk crystal structure remained intact beneath the coating. (**Figure 23** g).

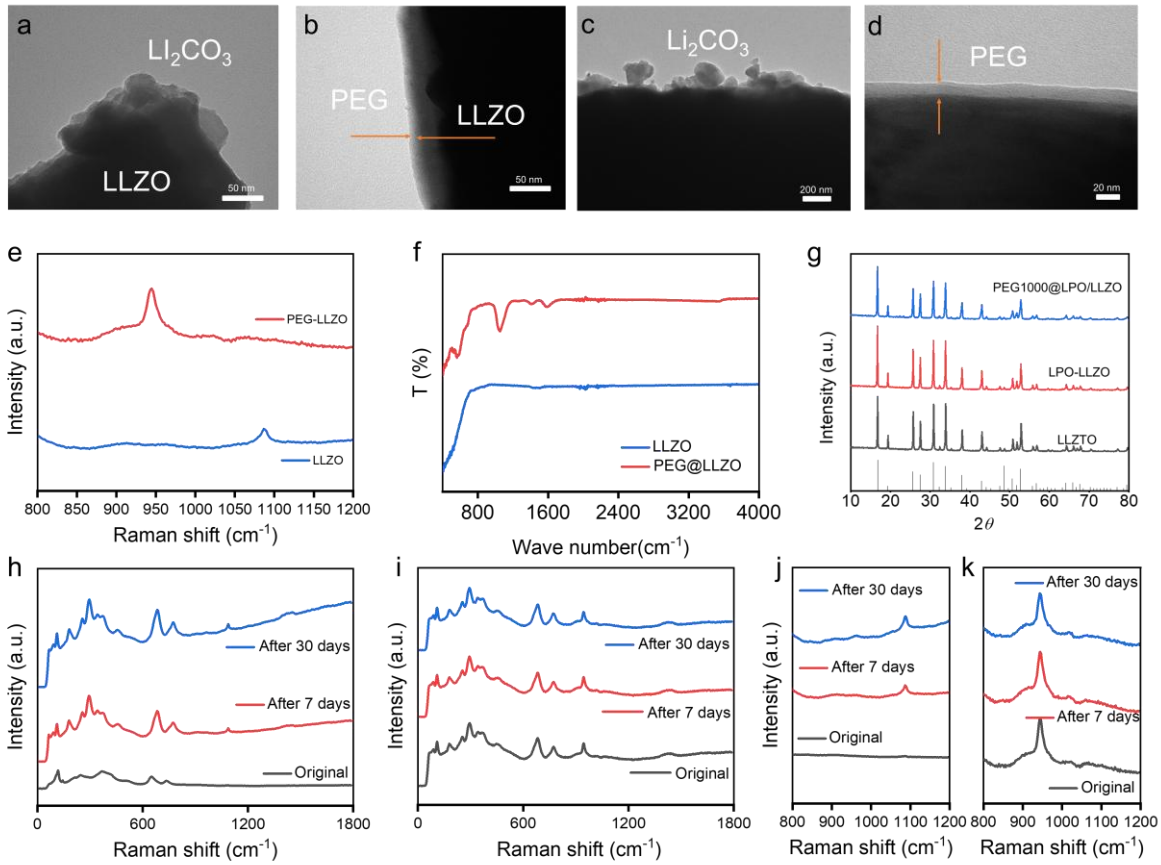

Figure 23 Characterization of pristine LLZO and mPEG1000@LLZO. TEM micrographs of pristine LLZO (a,c) and mPEG1000@LLZO (b,c). Raman spectroscopy of pristine LLZO and mPEG1000@LLZO from 800 to 1200 cm^{-2} (e) and 400 to 4000 cm^{-2} (f). XRD of pristine LLZO, Li_3PO_4 coated LLZO, and mPEG1000@LLZO. Comparison of Raman spectroscopy of pristine LZZO over 30 days (h,j) and mPEG1000@LLZO (i,k).

To assess the protective properties of the mPEG1000-silane coating, both pristine LLZO and mPEG1000@LLZO were stored under ambient conditions for 30 days. Raman spectroscopy revealed that the characteristic Li_2CO_3 band at 1090 cm^{-1}, which forms due to the exposure to moisture and CO_2 was absent in the mPEG1000@LLZO particles (**Figure 23** i and j). In contrast, this band was clearly visible in the pristine LLZO sample (**Figure 23** h and j) and increased in intensity over time, confirming that the mPEG1000 coating effectively inhibited Li_2CO_3 formation.

Comprehensive characterization using Raman and Infrared Spectroscopy, TEM, and XRD clearly proved the successful coating of the core-shell structure of the

mPEG1000@LLZO particles and highlighted the superior protective properties of the coating.

To evaluate its performance in solid-state battery applications, CPEs containing both pristine LLZO and mPEG1000@LLZO were prepared and characterized. The mPEG1000@LLZO containing CPEs exhibited a high room temperature ionic conductivity of $1.9 \cdot 10^{-4}$ S cm^{-1} with a Li^+ transference number of 0.61, indicating efficient Li-ion transport. Furthermore, no particle agglomeration of coated LLZO particles was observed in the CPEs indicating superior interface stability.

After detailed characterization of the electrochemical properties of the novel mPEG1000@LLZO-PVDF-HFP and comparison to the uncoated LLZO-PVDF-HFP CPEs, full cells with NMC622 and LFP were successfully assembled (**Figure 24**).

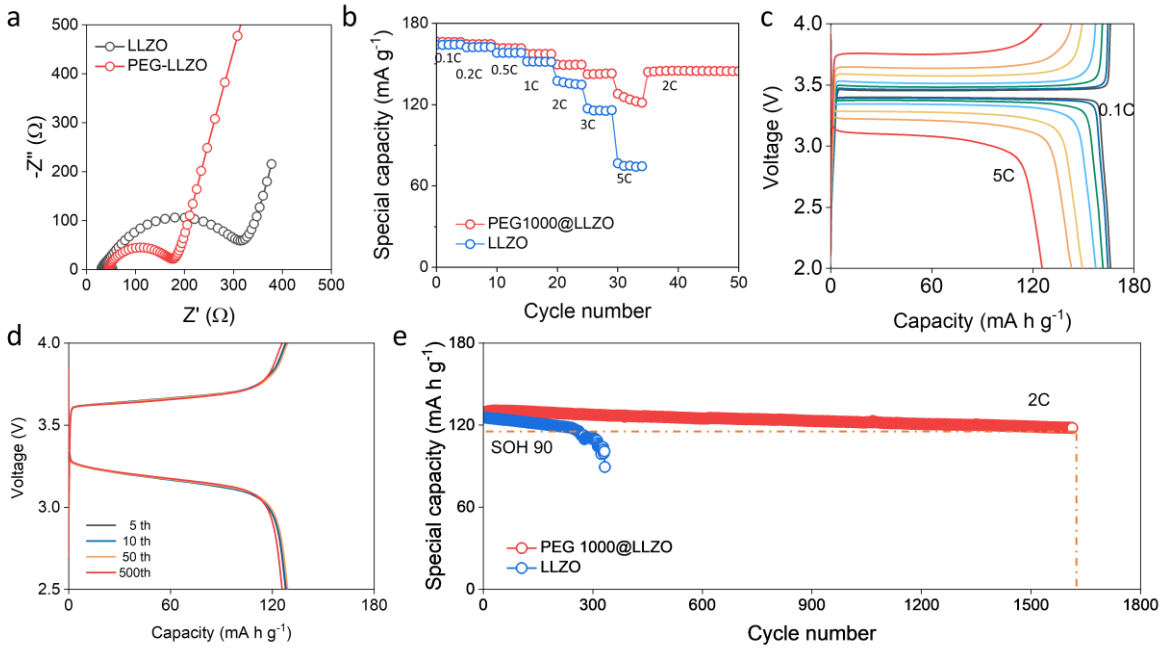

Figure 24 Electrochemical characterization of PVDF-HFP CPEs in Li||LFP 1.5 mg cm^{-2} mass loading cells. a) Impedance Spectroscopy of pristine and mPEG1000@LLZO CPEs. b) Rate capability tests. c) Charge/Discharge curves of mPEG1000@LLZO CPEs from 0.1 C to 5 C. d) Charge/Discharge curves of mPEG1000@LLZO CPEs at 2 C up to 500 cycles. e) Constant current cycling of Li||LFP cells at 2 C (2.5 - 4.0 V).

In particular, Li||LFP cells performed excellent with high rate capabilities and stable cycling performance at elevated C-rates, further validating the effectiveness of the mPEG1000@LLZO coating in solid-state battery applications.

The impedance of the mPEG coated CPEs was significantly lower compared to the uncoated CPEs (**Figure 24** a), a trend that persisted across all measurements. In terms of rate capability, the maintained capacity of coated LLZO (95 % at 1 C) surpassed the

uncoated LLZO (82 % at 1 C) counter part by a wide margin (**Figure 24** b and c). Furthermore, mPEG1000@LLZO CPEs exhibited exceptionally stable cycling performance at 2 C (1.5 mg cm^{-2} LFP mass loading) maintaining a state of health (SOH) above 90 % for over 1600 cycles. In contrast, the uncoated LLZO CPEs failed after roughly 330 cycles.

Undeniably, the coating of LLZO with mPEG1000-silane significantly improved air stability, mechanical properties, and most importantly electrochemical performance of the CPEs, highlighting the dramatic improvement in long-term durability. These results undeniably confirm that coating LLZO with mPEG1000-silane not only enhanced air stability and mechanical properties but, most importantly, significantly boosted the electrochemical performance of the CPEs.

4.3.3 Recapitulation

In summary, a facile and scalable synthesis for surface active mPEGs utilizing 3-(triethoxysilyl)propyl isocyanate was successfully developed and optimized. For assessing the efficiency of the grafting-to approach, four different M_n values were tested for the coating of LATP particles with an average particle size of 254 nm. It was found that M_n = 1000 g mol^{-1} has the best coating behavior and highest grafting density, resulting in homogeneous coatings with about 11 nm thickness. In contrast, increasing the polymer chain length reduces grafting density and leads to inhomogeneous polymer distribution at the particle surface. For LLZO (350 nm average particle size), a coating with 1*H*,1*H*,2*H*,2*H*-perfluorodecyl triethoxy silane, a perfluorinated alkoxy silane, was initially tested but showed no suppression of PVDF degrading in contact with the PF@LLZO particles. Hence, mPEG1000-silane was used to coat the LLZO particles, which successfully suppressed PVDF-HFP degradation and agglomeration of particles. The mPEG1000@LLZO particles were then used to fabricate CPEs with PVDF and compared to PVDF CPEs containing uncoated LLZO. Coating LLZO with mPEG1000-silane proved to be highly beneficial for CPE performance. Coated LLZO particles could be stored for over 30 days exposed to moisture and air without forming performance hindering Li_2CO_3. Moreover, the cycling stability in Li||LFP cells was excellent with 90 % SOH for over 1600 cycles at 2 C compared to the rapid cell failure after ~330 cycles for uncoated LLZO.

These findings demonstrate that mPEG1000-silane coating significantly enhances the stability, compatibility, and electrochemical performance of LLZO-based CPEs, making it a promising strategy for high-performance solid-state batteries.

4.4 Self-Crosslinking Oxide-CPEs

During the optimization of the synthesis of the coated LLZO in the previous Chapter 4.3, a high reactivity between triethoxy silanes and LLZO was observed. This led to the hypothesis that this high reactivity of specific oxides could be leveraged to create a self-crosslinking film, eliminating the need for additional solvents. Such an approach is crucial for the industrialization of CPEs, as the removal of solvent is an energy intensive step increasing production costs. Furthermore, a solvent-free system offers the advantage of higher viscosity, which helps to reduce particle sedimentation during drying, promoting more homogenous particle distribution.

Given the need for extensive parameter optimization and the lack of parallel electrochemical characterization capabilities at KIT, the project was carried out at in close collaboration with Dr. Annika Buchheit from PD Dr. Gunther Brunklaus' workgroup at Helmholtz-Institut Münster (HI MS). The workflow involved that LLZO powder was synthesized by M.Sc. Xiaochen Liu (Forschungszentrum Jülich) and sent to KIT. At KIT, the CPE films were manufactured, optimized, and characterized with respect to their chemical, thermal, and mechanical properties. Selected films were sent to HI MS for electrochemical characterization, ensuring a comprehensive evaluation of their performance

Parts of this chapter and the corresponding parts in the experimental section were adapted with permission from an accepted publication in *Small* written by the authors (Daniel Döpping, Annika Buchheit) [Publications within this Dissertation [2] in 9 List of Publications]. A patent (DE102024112955.7: „Verfahren zur Herstellung einer Kompositpolymerelektrolytmembran sowie eine durch das Verfahren erhältliche Kompositpolymerelektrolytmembran“) for the outlined preparation of thin CPE films is filed.

4.4.1 Strategy

To obtain self-crosslinking slurries, three main components are required: a polymer, a Li-salt, and an oxide-based filler. First, a polymer with two triethoxy silane functionalities, one at each chain end is necessary to enable crosslinking. This can be achieved by modifying the synthesis procedure for mPEG-silane to PEO, polytetrahydrofuran (PTHF), and poly(ε-caprolactone)-diol (PCL). All three polymers are commercially available with hydroxy-end-groups, making them suitable for efficient

triethoxy silane modification using IPTES. Additionally, to eliminate the need for a solvent, these polymers need to become flowable upon mixing with the Li-salt, ensuring a solvent-free processing approach. The general synthesis approach is depicted in **Scheme 33**.

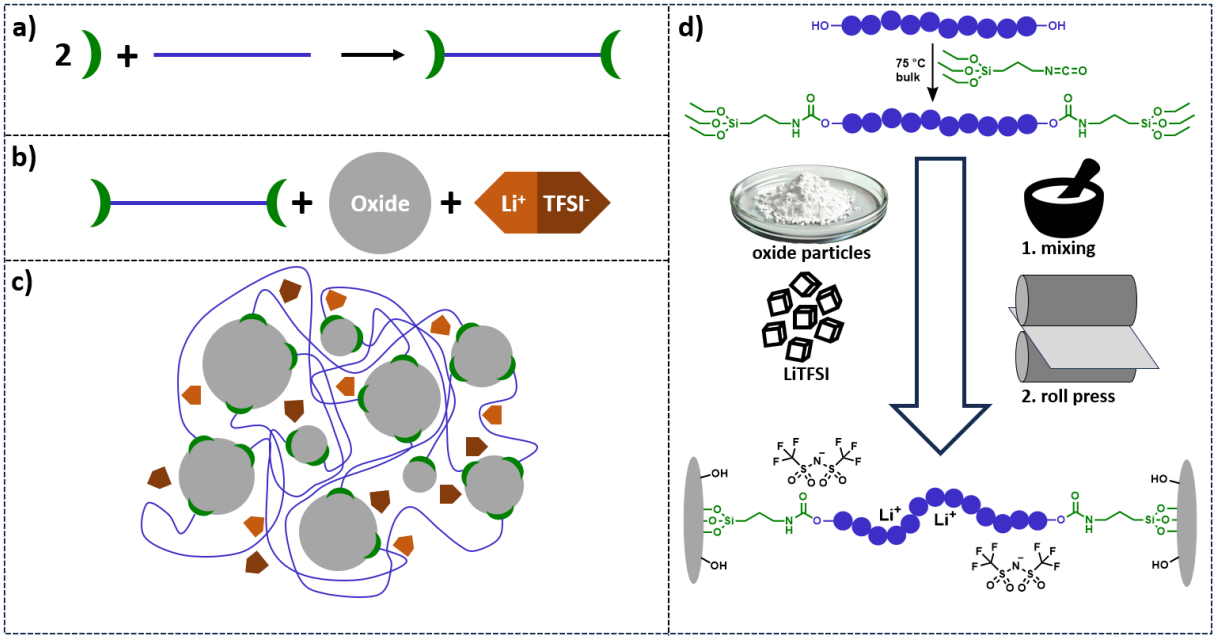

Scheme 33 Schematic depiction of the fabrication of self-crosslinking CPEs. a) IPTES (green) is used to modify the ends of a hydroxy-terminated polymer (PEO, PTHF, PCL, blue) to obtain a surface-active precursor polymer. b) The three components, a modified polymer, oxide nanoparticles (grey), and LiTFSI (orange) are mixed. c) LiTFSI dissociates and plasticizes the polymer resulting in a viscous slurry. After processing the silane-end-groups of the polymer react with the surface of the oxide nanoparticles to obtain a crosslinked film. d) Overview of the synthetic reaction and processing steps.

LiTFSI was chosen as the Li-salt due to its ability to dissolve in all three polymers, forming a high viscosity polymer-salt slurry upon mixing in a mortar. Additionally, an oxide-based filler with high affinity towards triethoxy silane was necessary. For this purpose, MoO_3 and LLZO were chosen as inactive and active fillers, respectively. MoO_3 nanoparticles (100 nm) are commercially available and studies showed the formation of a high Li-ion conducting interface with PEO in CPEs.[352] As aforementioned, LLZO has a high reactivity with triethoxy silanes, making it a suitable active filler.

Given the complexity of this system, which involves multiple parameters, including molecular weight and dispersity of the polymers and their blends, Li-salt concentration, particle size, possible additives, and processing parameters, a wide variety of CPEs were manufactured and characterized. TGA, DSC, Scanning Electron Microscopy (SEM), EDX, shear rheology, tensile strength of selected CPEs were conducted at KIT,

while ionic conductivity, transference number measurements, plating-stripping experiments, fast-charge capability, and charge/discharge cycling were conducted at HI MS.

4.4.2 Synthesis and Characterization

Since the synthesis of CPEs following the outlined procedure allows for a wide range of polymers, LiTFSI-concentrations, nanoparticles and additives, a systematic naming convention is implemented to clearly identify each CPE formulation. Within the respective chapters, CPEs are labelled according to a structured format to clearly indicate the composition of each sample:

POLYMER$_{[O]:[Li]\ ratio}$OXIDE MASS RATIO in % + ADDITIVE

For example, PEO$_{15}$100+SbF_3 shows the CPE is made from PEO-silane with LiTFSI concentration corresponding to an [O]:[Li] ratio of 15 (calculated based on ether oxygen content for PEO and PTHF, or ester concentration for PCL), 100 % of the mass of PEO is added in oxide nanoparticles (maintaining a 1:1 mass ratio between polymer and oxide) and SbF_3 was added as an additive into the slurry.

4.4.2.1 PEO-MoO_3-CPEs

As previously mentioned, the addition of MoO_3 offers significant benefits for PEO-based solid electrolytes, as it promotes the formation of fast Li-ion conducting channels form at the interface[352] and enhances the dissociation of LiTFSI.[309] Given that MoO_3 is commercially available as nanoneedles (100 nm) with a high surface area and comparatively affordable, it was chosen as an inactive filler for PEO-silane based CPEs.

To assess the viability of the proposed CPE, PEO (M_n = 6,000 g·mol^{-1}) was modified with IPTES to obtain PEO6k-silane (procedure in 6.3.4.1). The PEO6k-silane was then mixed with LiTFSI and MoO_3 nanoneedles in a mortar (PEO$_{12}$100, exact composition in **Table 9**). The [O]:[Li] ratio was arbitrarily set to 12, as previous studies have shown that this ratio provides a high ionic conductivity in PEO-LiTFSI based PEs.[353]

Table 9 Absolute and relative mass of slurry components for $PEO_{12}100$.

	PEO6k-silane	LiTFSI	MoO_3	combined
mass / mg	1500	752.8	1500	3752.8
wt%	39.9	20.1	39.9	100

After a few seconds of mechanical mixing, PEO and LiTFSI formed a sticky slurry that effectively incorporated the MoO_3 nanoneedles. The resulting slurry mixture was doctor bladed onto Mylar® foil and dried in a fume hood at ambient conditions (**Figure 25**), resulting in a rubbery film. Once it was confirmed a self-crosslinking slurry could be successfully formed using the theorized method, the film was further characterized using TGA (**Figure 26**).

The TGA revealed an initial mass loss of ~4%, between 100 and 290 °C, which was attributed to the hygroscopic properties of PEO and LiTFSI, as they readily absorb and retain moisture from ambient air.

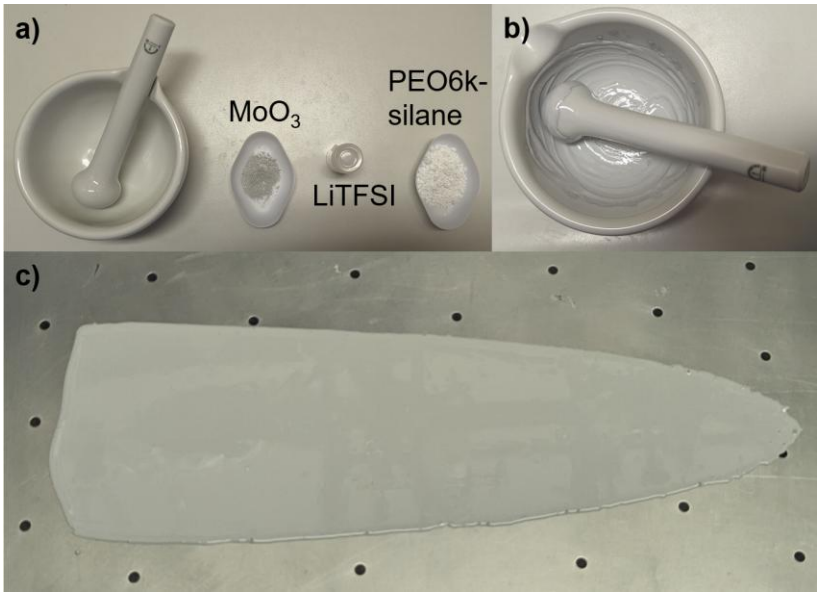

Figure 25 a) All components for CPE-slurry synthesis. b) Slurry after mixing components in a mortar for 3 min. c) Doctor bladed slurry on top of Mylar® foil.

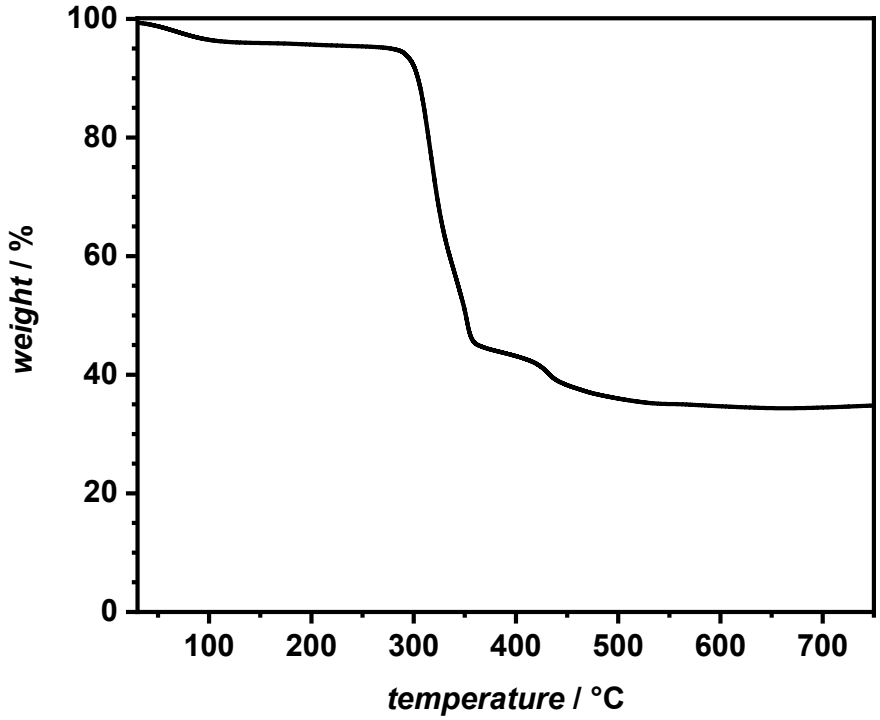

Figure 26 TGA of $PEO_{12}100$, a PEO6k-silane, LiTFSI, and MoO_3 CPE after drying under ambient conditions. Measurement from 30 - 750 °C at 10 K min^{-1}.

To minimize the influence of moisture, the films were dried after crosslinking and before electrochemical characterization.

Moreover, TGA analysis further revealed that the thermal degradation of PEO and LiTFSI started at 290 °C equilibrated at 500 °C with a residual mass of ~35.5 %. Since the total wt% of MoO_3 was calculated to be 39.9 wt%, and considering the ~4% mass loss due to evaporation of moisture, the TGA measurements confirmed the successful synthesis of $PEO_{12}100$ with the expected composition ratios.

To assess the effect of varying MoO_3 ratios on the ionic conductivity, films containing 0, 25, 50, 100, and 200 % of MoO_3 were fabricated and sent to HI-MS for ionic conductivity and transference number measurements (**Figure 27**). Adding no MoO_3 to the slurry for $PEO_{12}0$ underlined the importance of the oxide surface for the self-crosslinking process. Specifically, in the absence of MoO_3 ($PEO_{12}0$), the slurry failed to unless five drops of glacial acetic acid were added to catalyze the homocondensation of the triethoxy silane end-groups. Additionally, the MoO_3-free film exhibited significant air pockets and voids, further indicating poor film formation. In

contrast, all other slurries containing MoO_3 successfully crosslinked into homogeneous, self-standing films within 18 h, confirming that oxide surfaces play a crucial role in enabling solvent-free crosslinking and improving film integrity.

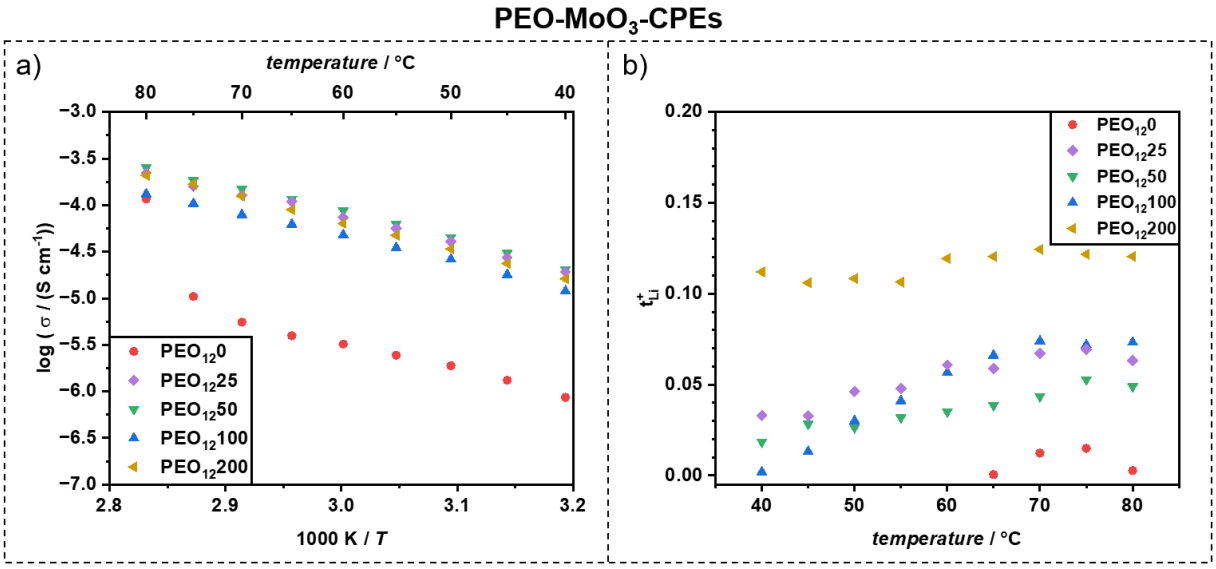

Figure 27 Characterization of PEO-MoO_3-CPEs with 0, 25, 50, 100, 200 % of MoO_3. a) Ionic conductivity from 40 - 80 °C. b) Li-transference number from 40 - 80 °C.

The ionic conductivity measurements revealed that all PEO-MoO_3-CPEs had a similar ionic conductivity trend across all temperatures. However, $PEO_{12}50$ demonstrated the highest ionic conductivity, at all temperatures, increasing from $2.0 \cdot 10^{-5}$ S cm^{-1} at 40 °C to $2.5 \cdot 10^{-4}$ S cm^{-1} at 80 °C. In contrast, $PEO_{12}100$ had the lowest ionic conductivity, ranging from $1.2 \cdot 10^{-5}$ S cm^{-1} at 40 °C to $1.3 \cdot 10^{-4}$ S cm^{-1} at 80 °C. $PEO_{12}25$ and $PEO_{12}200$ were in between those values, indicating a non-linear relationship between the MoO_3 content and the ionic conductivity of the CPEs. Despite these variations, the ionic conductivity of all films surpassed the threshold of 10^{-4} S cm^{-1} only at 80 °C, indicating that their ionic conductivity remains too low for practical application in solid-state Li-metal batteries at room temperature.

The CPE without MoO_3, $PEO_{12}0$, showed significantly lower ionic conductivity in the 40 - 75 °C range, with ionic conductivity of $8.6 \cdot 10^{-7}$ S cm^{-1} at 40 °C. However, at 80 °C, there was a sudden increase to $1.2 \cdot 10^{-4}$ S cm^{-1}, bringing it close to values observed for $PEO_{12}100$. Typically, PEO-LiTFSI systems with similar [O]:[Li] ratios have higher ionic conductivity in this temperature range.[354,355] The discrepancy in ionic conductivity was attributed to the pores and voids, formed during synthesis of the $PEO_{12}0$ film. Those pores and voids likely disrupted Li-ion transport, highlighting the importance of MoO_3 in facilitating a more uniform and conductive film structure.

Since the CPEs contained Li^+ and $TFSI^-$ ions, the lithium transference number was determined, as ionic conductivity measures the transport of all ions. For Li-batteries, however, only the transport of Li^+ ions is relevant for importance.

The Li^+ transference numbers of the films showed different behavior compared to their ionic conductivity. $PEO_{12}200$ had the highest t_{Li^+} with 0.124 at 70 °C, followed by $PEO_{12}100$, $PEO_{12}25$, and $PEO_{12}50$ with 0.074, 0.067, and 0.043, respectively. While the value for $PEO_{12}200$ was comparable to pure PEO-LiTFSI[355] systems, all other CPEs had significantly lower transference numbers. Further, $PEO_{12}0$ had no measurable t_{Li^+} from 40 - 60 °C and had a maximum t_{Li^+} at 75 °C of only 0.015 which is almost 10 times lower than expected. The reduced lithium transference number and low ionic conductivity are likely attributed to the inhomogeneous nature of the films without MoO_3, further emphasizing the role of MoO_3 in improving film uniformity and ion transport properties.
The lithium transference number results suggested that a higher MoO_3 content was beneficial for Li-ion conduction, although this effect was not pronounced in the ionic conductivity measurements. Though, the results were not comparable to the findings of Wang et al.[352] who reported a significant improvement in ionic conductivity when mixing PEO and MoO_3. This discrepancy led to the hypothesis that the silane bond at the particle surface might be hindering the formation of the highly Li-ion conductive PEO-MoO_3 interface. Consequently, it was concluded that PEO-MoO_3-CPEs were not suitable for the solvent-free CPE preparation system, as the interaction between the triethoxy silane and the MoO_3 interface likely disrupted the intended Li-ion transport pathways.

4.4.2.2 PCL-LLZO-CPEs

Since PCL has been successfully utilized in hybrid systems,[356] commercially available PCL-diol (M_n = 2,000 g mol^{-1}) was modified with IPTES (6.3.4.1) for use as a crosslinking polymer for LLZO CPEs. Given that LLZO was supplied by Forschungszentrum Jülich in two different average particle sizes (6.09 µm and 350 nm D(v,0.5)), both were evaluated for their impact on film formation and performance. The [ester]:[Li] ratio was set to 5:1, as previous studies identified this ratio as optimal for achieving the highest ionic conductivity.[356,357]

During the fabrication of films with PCL-silane, LiTFSI, and LLZO, several key observations were made, such as that films below a 1:1 mass ratio of PCL-silane:LLZO did not crosslink into solid films. Interestingly, increasing the LLZO content beyond 1:1 resulted in brittle films, making further processing impractical. By virtue of these complications, two films with a 1:1 mass ratio of PCL-silane to LLZO were successfully fabricated (**Table 10**) for further characterization.

Table 10 Absolute and relative mass of slurry components for two PCL_5100, one with LLZO with an average diameter of 6.09 µm and a second with LLZO with an average diameter of 350 nm.

	PCL-silane	LiTFSI	LLZO	combined
mass / mg	1,000	403.3	1,000	2,403.3
wt%	41.6	16.8	41.6	100

The slurry was again doctor bladed and dried under ambient conditions in a fume hood for 72 h. Afterwards, TGA of the film with 350 nm LLZO was measured (**Figure 28**).

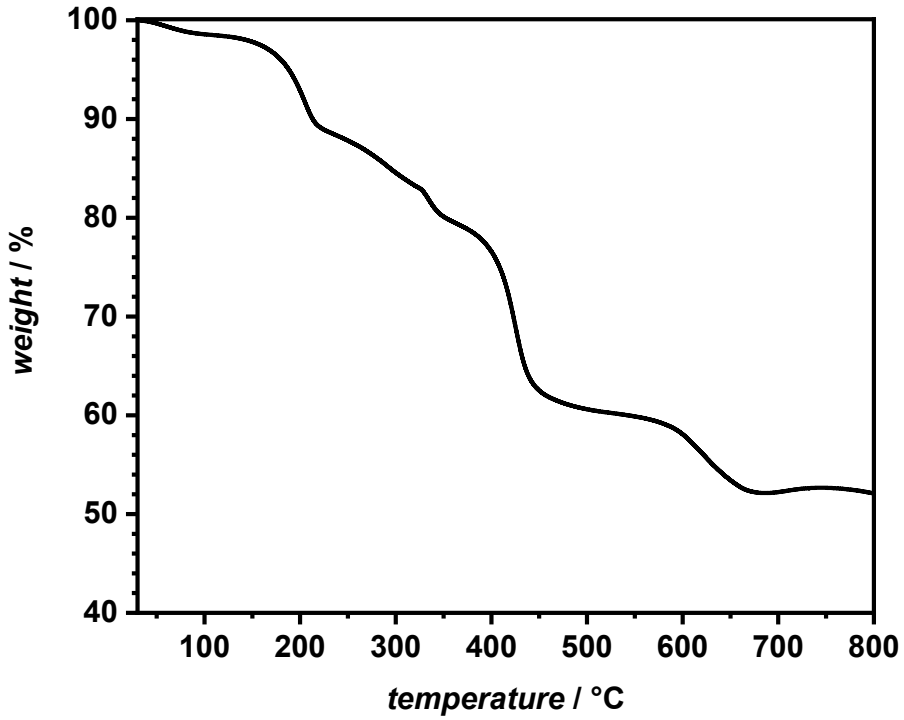

Figure 28 TGA of PCL_5100, a PCL-silane, LiTFSI, and LLZO (350 nm) CPE after drying under ambient conditions. Measurement from 30 - 800 °C at 10 K min^{-1}.

The TGA revealed an initial mass loss of ~1.55 %, due to moisture evaporation. Thereafter, multiple decomposition steps were observed, beginning at 190 °C, with the mass stabilizing at 52.3 % at 700 °C. This final mass was slightly higher than the calculated wt% of LLZO, which may be due to incomplete degradation of silicon moieties from the crosslinking process.

Following drying under high vacuum, both films were characterized regarding their ionic conductivity and transference number (**Figure 29**) to assess their electrochemical performance.

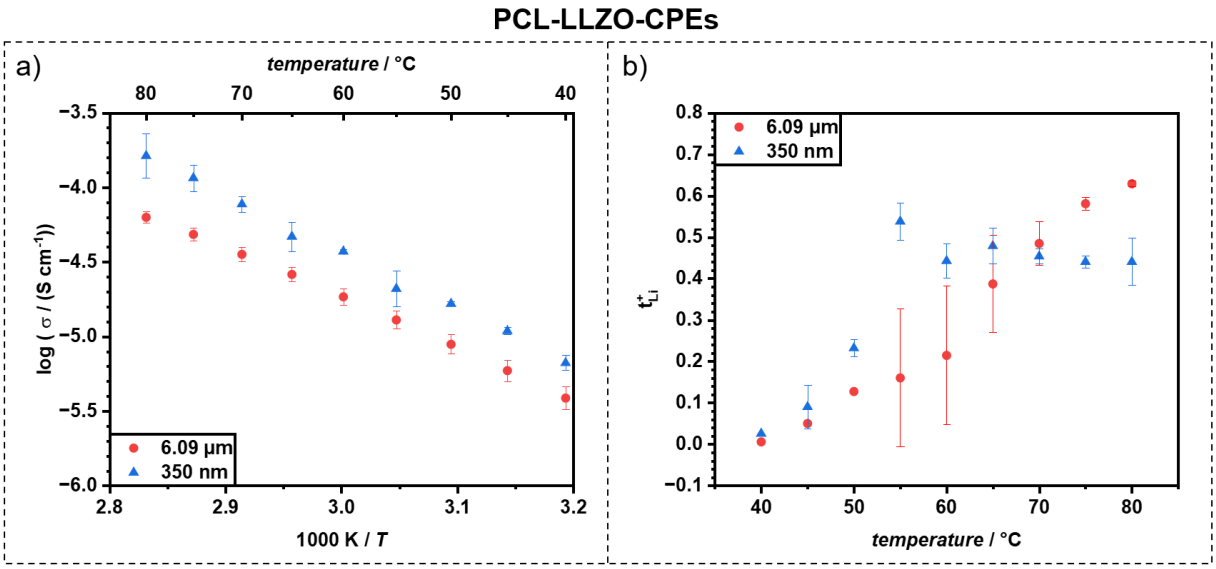

Figure 29 Characterization of PCL_5100 CPEs with LLZO of 6.09 µm and 350 nm average diameter. Comparison of a) Ionic conductivity from 40 - 80 °C. b) Li-transference number from 40 - 80 °C.

PCL_5100 with 350 nm LLZO particle size had an ionic conductivity of $6.7 \cdot 10^{-6}$ S cm^{-1} at 40 °C, which increased to $1.6 \cdot 10^{-4}$ S cm^{-1} at 80 °C. However, the film with the LLZO particle size of 6.09 µm, only increased from $3.9 \cdot 10^{-6}$ S cm^{-1} to $6.3 \cdot 10^{-5}$ S cm^{-1}. Hence, smaller particles are beneficial for the ionic conductivity in a PCL-silane crosslinked system. At 60 °C the film containing 350 nm LLZO particles exhibited an ionic conductivity of $3.7 \cdot 10^{-5}$ S cm^{-1}, being only slightly lower than published ionic conductivity of a hybrid PCL-Al_2O_3-LiTFSI ($5 \cdot 10^{-5}$ S cm^{-1})[356] at the same temperature. These findings suggested that LLZO did not participate in the Li-ion conduction because an inert filler (Al_2O_3) surpassed the ionic conductivity of the PCL-LLZO system.

Additionally, the lithium transference number steadily increased for the film with larger LLZO particles from 0.007 at 40 °C to 0.629 at 80 °C, with large error in the measurement, which indicated interfacial instability between the electrolyte and Li-

metal surface. For the smaller LLZO particles, a similar behavior was observed up to 55 °C, where the transference number plateaued around 0.479. While the film containing larger LLZO particles achieved transference numbers comparable to published values for PCL-Al_2O_3-LiTFSI systems (0.65)[356] and PCL-LLZO-LiTFSI CPEs (0.71),[358] the smaller particles appeared to contribute less effectively to overall Li-ion conduction.

Moreover, it was observed that both $PCL_5$100 films became brittle after being stored in a dry room for more than a week. This issue may arise by virtue of the comparatively low molecular weight of PCL-silane (M_n = 2,000 g mol^{-1}), leading to a densely crosslinked network. The prolonged drying time of $PCL_5$100 films (72 h) compared to PEO-MoO_3 (18 h) indicated a slower crosslinking reaction, which may not have been fully completed, leading to brittleness over time. Furthermore, the unstable Li-metal-electrolyte interface observed during transference number measurements might be explained by chemical side reactions. Ultimately, neither extended drying protocols nor modifications to the synthesis procedure were able to resolve these issues. To mitigate film brittleness, synthesizing longer PCL-diol with molecular weights of exceeding 6,000 g mol^{-1}, similar to PEO-MoO_3-CPEs, could be a potential solution. However, due to time constraints, the synthesis of suitable PCL-diol was not pursued. Consequently, PCL2k-diol was determined to be unsuitable for the application in the self-crosslinking CPE system.

4.4.2.3 Polyether-LLZO-CPEs

The polyethers polytetrahydrofuran (PTHF) and poly(ethylene oxide) (PEO) were selected as polymer crosslinkers for LLZO particles. PTHF is commercially available only with a molecular weight of M_n = 2,900 g mol^{-1}. In contrast, PEO is available in a wider range of molecular weights. However, to ensure liquefication upon mixing with LiTFSI and to avoid excessive viscosity, only lower number average molecular weights M_n (6,000, 10,000, and 20,000 g mol^{-1}) were evaluated.

The modification of PTHF with IPTES followed the established procedure and PTHF2.9k-silane was characterized by SEC and NMR (6.3.4.1 **Figure 104**, **Figure 109**). For PEO with 10,000 g mol^{-1}, the synthesis was identical to the previously reported synthesis of PEO6k-silane. However, for PEO with 20,000 g mol^{-1}, the high viscosity of the molten polymer required mechanical stirring. Nevertheless, all three

PEO-silanes were synthesized successfully and characterized (6.3.4.1 **Figure 101** - **Figure 103**, **Figure 108**).

The initial test of mixing PTHF2.9k-silane with LiTFSI and LLZO particles produced a comparatively low viscosity slurry that crosslinked into a self-standing film within 24 hours after doctor blading. A similar behavior was observed for PEO6k-silane and PEO10k-silane, with curing times ranging from 30 minutes to 4 hours, depending on ambient temperature and humidity. As expected, PEO10k-silane was slightly more viscous in the mixed slurry compared to PEO6k-silane. PEO20k-silane; however, was too viscous for efficient mixing in a mortar, preventing the homogeneous distribution of LLZO particles in the dry slurry. Consequently, PEO20k-silane was not used for the fabrication of PEO-LLZO films.

The PEO-LLZO CPE is known in literature in several experimental[22,38,359] and computer simulation-based[360,361] studies. Overall, an [O]:[Li] ratio of 15:1 provides the best performance in both simulated and experimental studies for PEO-LLZO CPEs, thus this ratio was used for preparing all PEO.LLZO CPEs.

In contrast, PTHF-LLZO has not been reported in the literature, and no reliable data on the optimal Li-concentration was available. Therefore, as an initial evaluation, PTHF and LLZO were mixed in a 1:1 weight ratio, and different [O]:[Li] ratios (5:1, 10:1, 15:1) were tested to determine the optimal composition (**Figure 30**).

The ionic conductivity of PTHF-LLZO membranes with three different salt concentrations was generally similar; however, the highest ionic conductivity was observed with an [O]:[Li] ratio of 5:1. Based on this result, an [O]:[Li] ratio of 5:1 was used for all PTHF CPEs to calculate the required amount of LiTFSI.

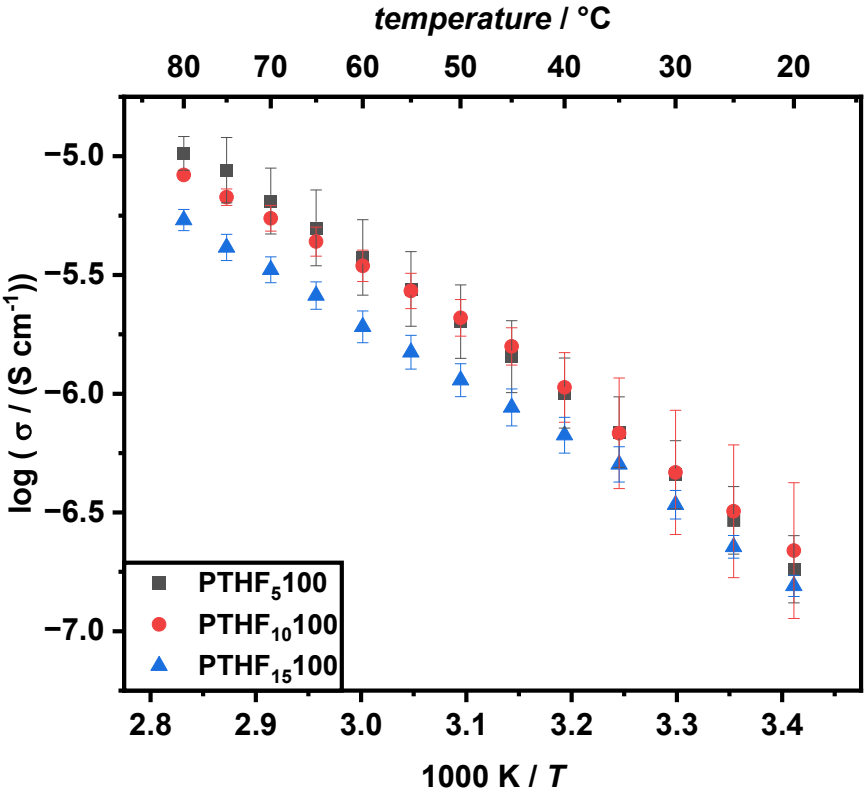

Figure 30 The ionic conductivity of PTHF-LLZO films with a 1:1 mass ratio was measured for [O]:[Li] ratios of 5:1, 10:1, and 15:1. Among these, a ratio of 15:1 exhibited the lowest ionic conductivity at all temperatures tested. Ratios of 5:1 and 10:1 showed similar performance between 20 - 55 °C, but an [O]:[Li] ratio of 5:1 demonstrated the highest conductivity between 60 - 80 °C.

4.4.2.3.1 PEO molecular weight assessment

Since two different molecular weights of PEO were synthesized, the influence on ionic conductivity and transference number was evaluated (**Figure 31**). To investigate this, $PEO_{15}50$ films were prepared using LLZO with a particle size of 350 nm were made. When incorporating 50 % LLZO (in relation to PEO mass), the films remained comparable after doctor blading. However, using larger LLZO particles or increasing the LLZO content resulted in inhomogeneous doctor blading of the PEO10k-silane films, due to increased viscosity compared to PEO6k-silane (Appendix **Figure 129**).

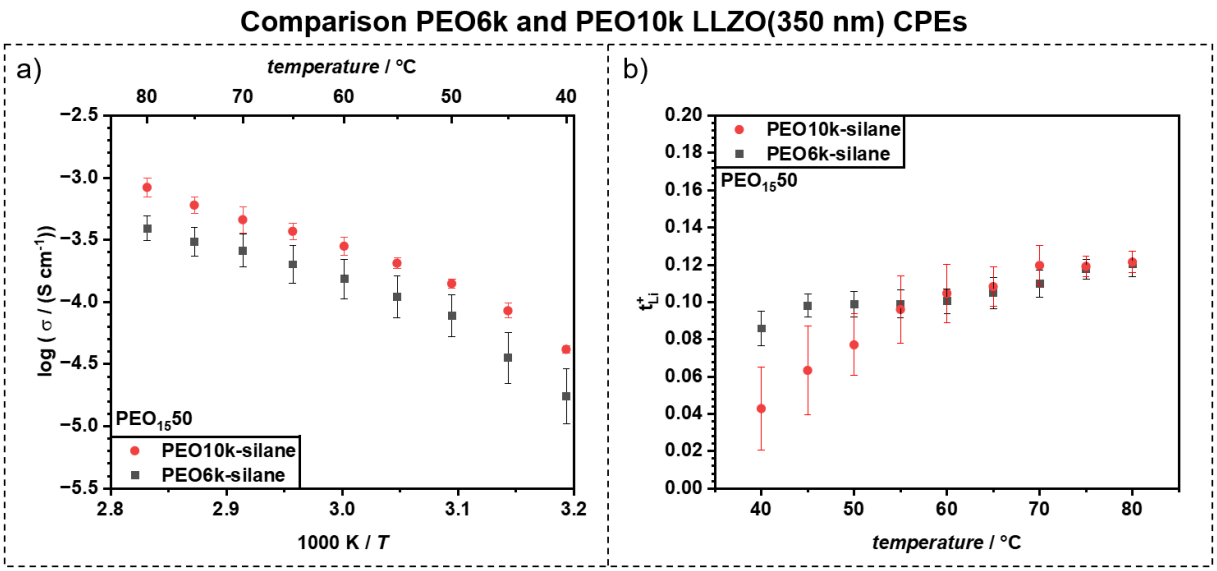

Figure 31 Comparison of the ionic conductivity (a) and transference number (b) of PEO6k- and PEO10k-silane films with LLZO (350 nm). PEO10k has a higher ionic conductivity at all temperatures and a higher transference number at 55 °C and higher temperatures.

PEO10k-silane films showed higher ionic conductivity at all temperatures compared to PEO6k-silane with a value of $4.2 \cdot 10^{-5}$ S cm^{-1} and $1.7 \cdot 10^{-5}$ S cm^{-1} at 40 °C, respectively. This trend persisted at all temperature ranges up to 80 °C, where PEO10k-silane had an ionic conductivity of $8.4 \cdot 10^{-4}$ S cm^{-1}, while PEO6k-silane displayed a value of $3.9 \cdot 10^{-4}$ S cm^{-1}. Nevertheless, PEO10k-silane exhibited a lower t_{Li}^+ from 40 - 55 °C. Above 55 °C, for both films, the t_{Li}^+ was almost identical with a maximum value of 0.121 at 80 °C. As PEO10k-silane had significant deviations, the initial lower t_{Li}^+ may be due to measurement error.

Overall, PEO10k-silane demonstrated a significant improvement in ionic conductivity over PEO6k-silane. As a result, only PEO10k-silane was utilized in further film preparation.

The primary disadvantage of PEO10k-silane was its high viscosity during film preparation, requiring an adaptation of the film fabrication process. To address this, a manual roll-to-roll press with adjustable slit width was purchased to allow precise control over the film thickness of the highly viscous slurry. The slurry was sandwiched between two Mylar® foils and slowly roll pressed to the desired thickness. This method proved to be highly advantageous, allowing for the utilization of LLZO with larger particle size and an increased LLZO content. The roll press setup and an exemplary

$PEO_{15}400$ film with LLZO (6.09 µm average particle size) are shown in the Appendix in **Figure 130** and **Figure 131**, respectively.

4.4.2.3.2 LLZO particle size assessment

Upon adapting the film synthesis process, the effect of particle sizes of LLZO (350 nm and 6.09 µm) and LLZO concentrations on ionic conductivity and transference number between were evaluated using PEO10k-silane. The results are presented in **Figure 32** (350 nm particle size) and **Figure 33** (6.09 µm nm particle size), respectively.

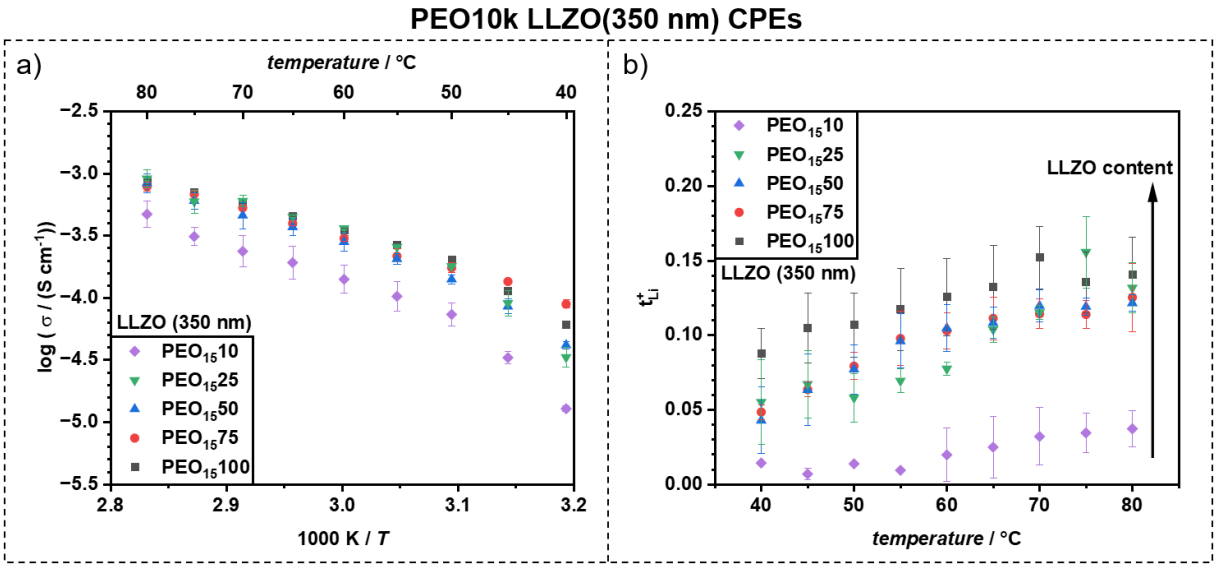

Figure 32 Characterization of PEO10k-LLZO CPEs with LLZO of 350 nm average diameter. Comparison with different LLZO content of a) Ionic conductivity from 40 - 80 °C and b) Li-transference number from 40 - 80 °C. Increasing the LLZO content increases ionic conductivities at lower temperatures while all LLZO concentrations of 25% and higher have similar ionic conductivities. Further, increasing the LLZO content shows a clear benefit to increasing the transference number.

On the one hand, for LLZO with a 350 nm average particle size, no clear trend was observed with increasing the LLZO content. On the other hand, $PEO_{15}10$ had a significantly lower ionic conductivity compared to the other four films. At lower temperatures, e.g., 40 and 45 °C, $PEO_{15}75$ showed the highest ionic conductivity at $8.9 \cdot 10^{-5}$ S cm^{-1} and $1.4 \cdot 10^{-4}$ S cm^{-1}, respectively. However, across all other temperatures, the difference between $PEO_{15}25$-100 became negligible. Conversely, the Li^+ transference number increased with higher LLZO content, reaching a maximum of 0.15 for $PEO_{15}100$ at 70 °C.

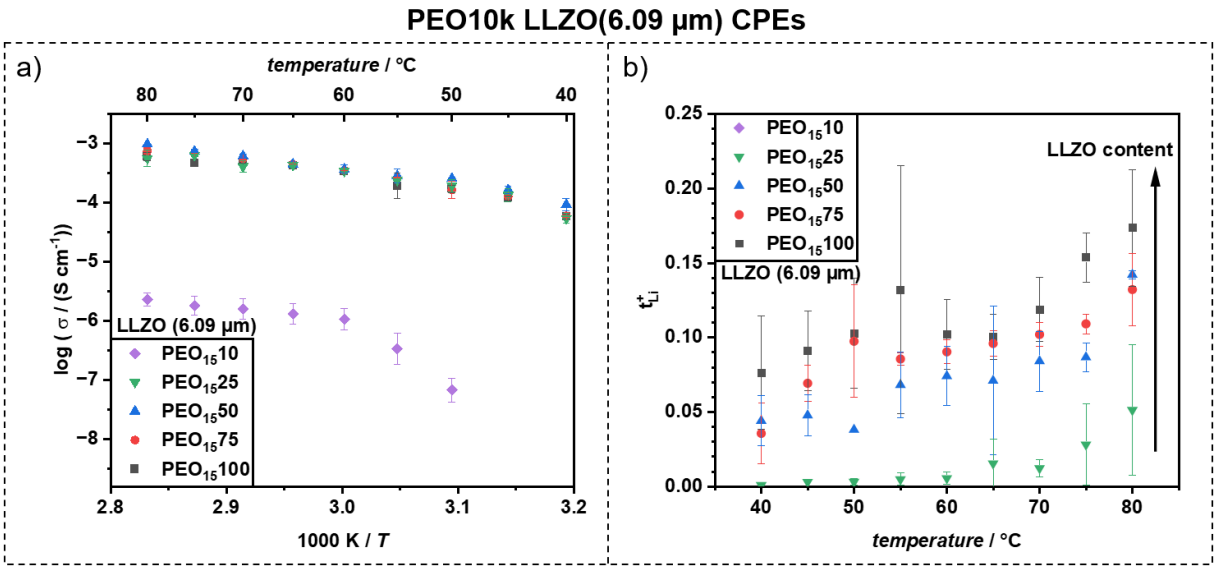

Figure 33 Characterization of PEO10k-LLZO CPEs with LLZO of 6.09 µm average diameter. Comparison with different LLZO content of a) Ionic conductivity from 40 - 80 °C and b) Li-transference number from 40 - 80 °C. Increasing the LLZO content shows no clear trend beyond 25% in increasing the ionic conductivity. Increasing the LLZO content shows a clear benefit to increasing the transference number.

The larger LLZO particles showed similar behavior. However, $PEO_{15}10$ had an even lower ionic conductivity compared to the films containing 350 nm LLZO particles. This was attributed to the comparatively lower surface area of the larger particles, resulting in reduced crosslinking density and poorer film stability.

For the other four films, the ionic conductivity remained identical across at all tested temperatures. Similarly to the films containing smaller LLZO particles, the transference number increased with increased LLZO content ($PEO_{15}10$ could not be measured) resulting in the highest measured Li^+ transference number for PEO of 0.17 for $PEO_{15}100$ at 80 °C.

In **Table 11** the ionic conductivity and Li^+ transference number are compared for all films at 60 °C.

Omitting $PEO_{15}10$ for both particle sizes, no clear trend was observed between ionic conductivity and LLZO content. However, LLZO (6.09 µm) had a slightly higher average ionic conductivity across all LLZO concentrations at 60 °C.

In contrast, the Li^+ transference number t_{Li^+} increased steadily when LLZO content was increased, suggesting that higher LLZO content enhances effective Li^+ conductivity σ_{Li+}.

Table 11 Comparison of PEO10k-LLZO films with 350 nm and 6.09 µm particle size with increasing LLZO content at 60 °C.

Film	LLZO 350 nm		LLZO 6.09 µm	
	σ / S cm^{-1}	t_{Li^+}	σ / S cm^{-1}	t_{Li^+}
$PEO_{15}10$	$1.4 \cdot 10^{-4}$	0.020	$1.1 \cdot 10^{-6}$	-
$PEO_{15}25$	$3.6 \cdot 10^{-4}$	0.078	$3.4 \cdot 10^{-4}$	0.006
$PEO_{15}50$	$2.8 \cdot 10^{-4}$	0.105	$3.7 \cdot 10^{-4}$	0.074
$PEO_{15}75$	$3.0 \cdot 10^{-4}$	0.103	$3.5 \cdot 10^{-4}$	0.090
$PEO_{15}100$	$3.5 \cdot 10^{-4}$	0.126	$3.4 \cdot 10^{-4}$	0.102

To further assess the influence of the particle size, plating-stripping tests were performed in symmetrical Li||Li cells. First, $PEO_{15}100$ containing LLZO (6.09 µm) was sandwiched between two Li-metal electrodes and the current density was increased after 10 cycles to determine the critical current density (CCD) of 0.2 mA cm^{-2} (**Figure 34** a). Afterwards, $PEO_{15}100$ films with both particle sizes were cycled repeatedly at 0.2 mA cm^{-2} until failure (**Figure 34** b).

In the long-term plating-stripping experiments at 0.2 mA cm^{-2}, the film containing 350 nm LLZO particles consistently exhibited a slightly higher overpotential (~0.297 V) compared to the film with 6.09 µm particles (~0.250 V).

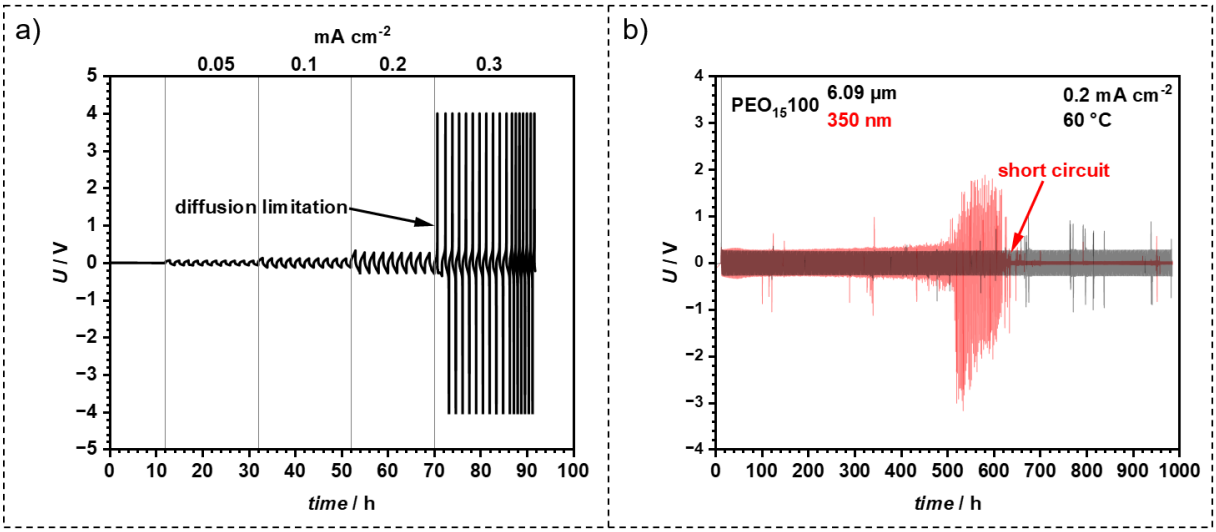

Figure 34 Plating-stripping experiments in symmetrical Li| $PEO_{15}100$|Li CR2032 coin cells at 60 °C. a) Symmetric cycling of $PEO_{15}100$ (LLZO 6.09 µm) with increase in current density after 10 cycles to determine critical current density. b) Symmetric cycling of $PEO_{15}100$ (LLZO 6.09 µm and 350 nm) with steady current density of 0.2 mA cm^{-2} until failure.

The film containing smaller particles showed overpotential peaks starting after 100 h (~ 1.047 V), followed by increasingly noisy overpotential growing after approximately 300 h (~ 0.360 V). After 500 h, overpotentials reaching ~3.155 V indicated the onset of film failure; and ultimately, after 620 h, a short circuit, most likely caused by dendrite penetration, resulted in failure of the CPE.

In contrast, the film with 6.09 µm particles first exhibited overpotential peaks around 660 h (~1.017 V). These peaks aligned with the short opening of the climate chamber for sample exchanges and hence were attributed to temperature fluctuations. $PEO_{15}100$ maintained stable cycling performance, with only a slight increase in overpotential (~0.25 to ~0.28 V), for almost 1000 h, at which point the test was aborted. These results underlined the benefit of adding LLZO, especially with 6.09 µm particles, into a PEO matrix, as stable plating-stripping of PEO-LiTFSI polymer electrolyte systems is not possible under these conditions.[362]

Overall, LLZO with 6.09 µm had the higher average ionic conductivity, the highest lithium transference number, and significantly more stable plating-stripping behavior. Consequently, it was determined that the larger LLZO particles are more suitable for the CPE manufacturing, and all subsequent films were fabricated using LLZO with 6.09 µm average particle size.

With the most suitable PEO molecular weight and the LLZO particle size determined, new films were synthesized using the roll-to-roll press approach. Additionally, since increasing the LLZO content appeared to enhance the Li^+ transference number, the LLZO content was increased beyond the previous maximum of 100%.

4.4.2.3.3 PEO and PTHF CPE Characterization

During the synthesis of the CPE films incorporating various polymers, oxide particles, and concentrations, several key observations were made regarding the film fabrication process. However, due to the influence of numerous variables, these findings could not be reliably quantified, as they affected the overall process.

The rate at which the slurry upon mixing solidified was highly dependent on:

Variable	(faster > slower crosslinking condition)
1. polymer	(hygroscopic > hydrophobic)
2. particle concentration	(higher > lower)
3. particle surface	(oxides > phosphates)
4. temperature	(higher > lower)
5. humidity	(higher > lower)
6. viscosity	(higher > lower)

Overall, the slurry crosslinking time varied significantly, ranging from 3 minutes to several days, depending on the CPE components used. In some cases, particularly at high oxide concentrations (> 200 %), the addition of small amounts of ethyl acetate as a plasticizer was required. Ethyl acetate reduced the viscosity, enhanced the mixability of components, and delayed the onset of crosslinking, thereby facilitating better control during roll pressing. These observations strongly suggest that moisture catalyzed reactions between the alkoxy silane end-groups and hydroxy-groups on the particle surface were the main crosslinking contributor, rather than the selfcondensation of alkoxysilanes. This hypothesis was further supported by EDX and rheological measurements (in Chapter 4.4.2.3.3.2).

Ultimately, for polyether CPES, films containing 25, 50, 100, 200, and 400 % of LLZO (6.09 µm) with PTHF2.9k-silane and PEO10k-silane were successfully produced by roll-pressing. These films were then systematically characterized regarding their thermal, chemical, mechanical, and electrochemical properties.

It is important to note that the simplified naming scheme of the films (e.g., $PEO_{15}100$ having 100 % of the mass of LLZO added in regard to PEO mass) does not correctly reflect the actual wt% of the components in the slurry/CPE, as the weight of LiTFSI is omitted. However, the ceramic content remains a critical factor in correctly classifying a CPE as either as a ceramic-in-polymer (CIP, ceramic < 50 wt%) or a polymer-in-

ceramic (PIC, ceramic > 50 wt%) (refer to Chapter 2.7.4.1). Although the classification of CIP vs. PIC does not directly indicate the interplay of ionic transport mechanisms (i.e., polymer/interface Li-ion transport vs. active particle Li-ion transport), it shows the dominating phase present in the CPE, which must be considered when interpreting experimental results. Hence, **Table 12** provides a comprehensive classification of all PTHF and PEO based CPEs, along with their respective LLZO wt%.

Table 12 Actual wt% of LLZO in the slurry of manufactured PEO and PTHF CPEs with the corresponding classification into CIP or PIC systems.

Film	wt% of LLZO	Classification
PEO_{15}		
25	15.0	CIP
50	26.1	
100	41.4	
200	58.6	PIC
400	73.8	
$PTHF_5$		
25	12.9	CIP
50	22.9	
100	37.3	
200	54.3	PIC
400	70.4	

Even though PEO and PTHF being different polymers with slightly different densities and LiTFSI content, the classification remained consistent for both cases. All films with 100 % and less LLZO mass added were classified as CIP. While films with 200 % and higher LLZO content exceeded > 50 wt% of total mass and were thus considered as PIC. Since additives were introduced in the mg scale, their impact on the overall mass distribution was negligible and did not change the classification.

The thinnest film thickness achieved with sufficient mechanical strength for cell preparation was 16 µm. However, since not all combinations could be successfully roll-pressed to that thickness, 30 µm and 80 µm were generally used as the standard film thickness unless otherwise stated.

4.4.2.3.3.1 Mechanical Characterization

For rheological measurements, films of 200 µm thickness were fabricated and analyzed using oscillatory rheology (**Figure 35** a,b) and tensile strength testing (**Figure 35** c,d).

Frequency sweep tests conducted in the linear regime at room temperature revealed that the storage modulus (G') was consistently greater than the loss modulus (G''), confirming the solid-like and elastic behavior of the composites across all tested frequencies. The phase angle (δ) remained below 30 degrees, indicating good elasticity in all samples. The storage modulus at an angular frequency of 100 rad s^{-1} was measured for all samples, revealing no linear correlation between G' and LLZO content. On the one hand, for PEO, the sample with 50 % LLZO exhibited the lowest storage modulus at $0.3 \cdot 10^5$ Pa, while both 25 % and 100 % LLZO samples had equal G' values of $0.6 \cdot 10^5$ Pa. The 200 % LLZO sample showed the highest G' at $1.7 \cdot 10^5$ Pa. On the other hand, for PTHF, the 200 % LLZO sample displayed the lowest G' at $2.5 \cdot 10^4$ Pa, with the 100 % sample slightly higher at $2.8 \cdot 10^4$ Pa. The 25 % sample showed a significantly higher G' of $4.8 \cdot 10^4$ Pa, while the 50 % sample had the highest G' at $5.8 \cdot 10^4$ Pa. One possible explanation for the observed increase in G' at seemingly arbitrary oxide contents is that an optimal silane concentration and reactive oxide particle surface area may maximize shear strength, ensuring a stable cross-linked network. Since PTHF has a lower molecular weight than PEO, its silane concentration per unit mass is higher, suggesting that PTHF reaches its maximum shear strength at a lower oxide concentration compared to PEO.

Tensile strength tests were performed to evaluate the mechanical properties of the films. Overall, PEO-LLZO films exhibited lower tensile strength than PTHF-based films but demonstrated a higher strain tolerance. The maximum stress for 25 % and 50 % LLZO in PEO was comparable, measuring 1.42 MPa and 1.38 MPa, respectively. In contrast to PTHF, further increases in LLZO content in PEO resulted in a significant reduction in tensile strength, with values of 0.76 MPa for 100 % and 1.02 MPa for 200 %. Regarding strain at break $PEO_{15}50$ exhibited the highest value, reaching 642 %, while $PEO_{15}25$ tore at 433 %. Despite this, the strain at break for the 100 % LZZO sample remained relatively high at 429 %. However, for the 200 % sample, a marked decrease in flexibility was observed, with a maximum strain of only 119 %, indicating increased brittleness at higher oxide concentrations. Additionally, both 100 % and 200 % samples showed necking behavior.

For PTHF-LLZO films, the tensile strength improved with increasing oxide concentration, reaching a maximum of 4.04 MPa at 100 % LLZO. This increase is likely due to the reinforcing effect of the oxide particles, which enhanced stress transfer within the polymer matrix, thereby improving the mechanical properties of the composite. However, beyond 100% LLZO, a decrease in tensile strength was observed, suggesting that further oxide addition may overload the polymer network or result in poor oxide dispersion, which in turn has led to microstructural weaknesses. At 200 % LLZO, the tensile strength slightly decreased to 3.92 MPa, with slight necking observed. In comparison, the 25 % and 50 % LLZO formulations showed significantly lower tensile strengths, at 0.96 MPa and 1.64 MPa, respectively. The elongation at break also varied, with the 100 % LLZO formulation displaying the highest elongation, reaching 151 %.

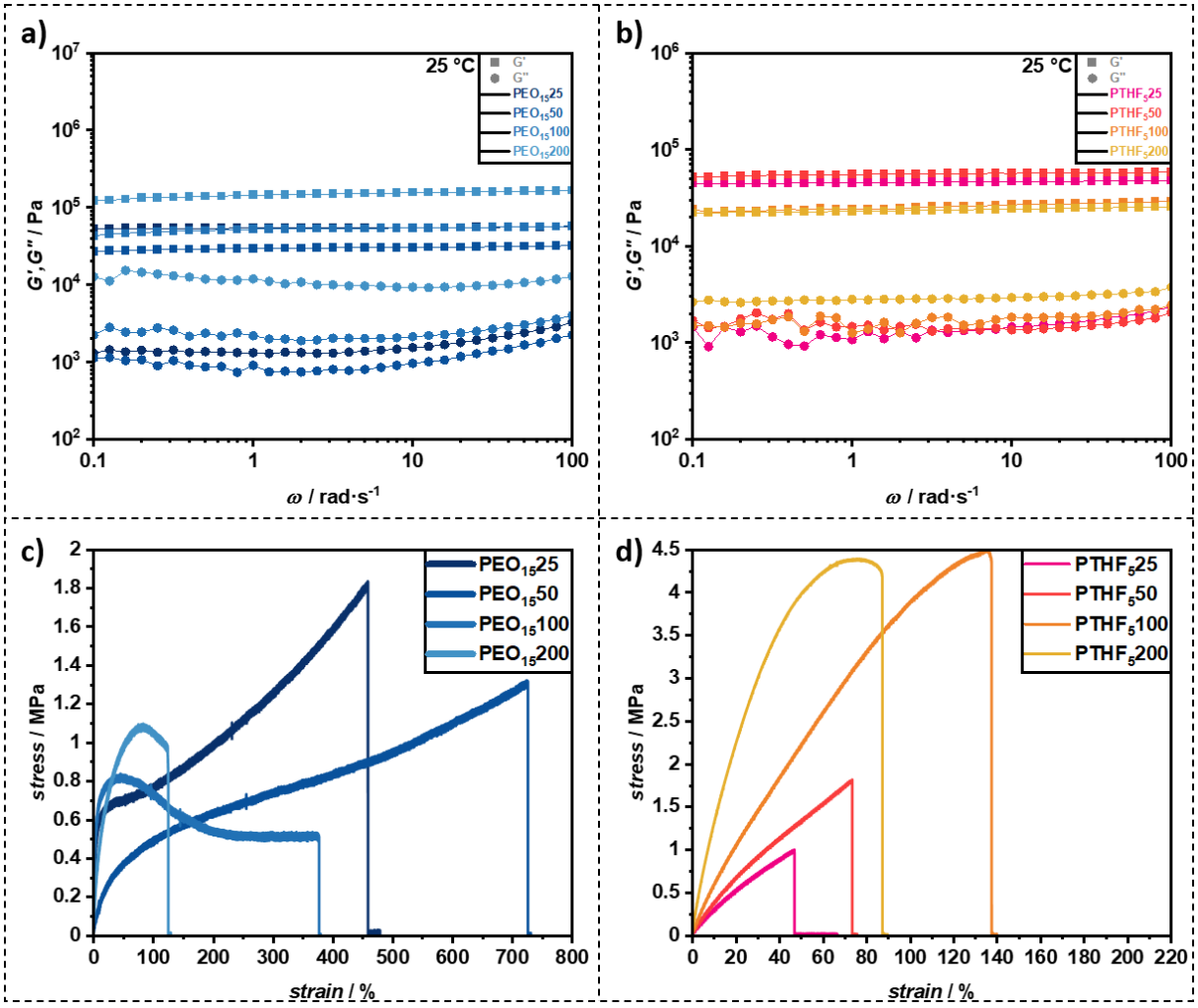

Figure 35 Shear rheology from 0.1 to 100 rad s^{-1} for a) PEO_{15}25-200 and b) $PTHF_5$25-200. Tensile strength measurements of c) PEO_{15}25-200 and d) $PTHF_5$25-200.

Overall, the combined results from shear rheology and tensile strength tests emphasize the importance of optimizing oxide content in polymer electrolytes. These findings highlight the need to balance the polymer and oxide particle content to achieve maximum shear strength while maintaining sufficient flexibility, which is an essential factor for the performance of electrolytes in dynamic environments, such as rechargeable batteries. Moreover, these results suggest the potential to tailor the mechanical properties of polymer-LLZO electrolytes to meet specific application requirements, paving the way for customized electrolyte designs that balance mechanical robustness and electrochemical functionality.

4.4.2.3.3.2 Scanning Electron Microscopy

To assess the morphology and distribution of LLZO particles within the polymer matrix SEM micrographs of the film cross-sections were recorded (**Figure 36**). The film thickness ranged from 25 - 65 µm, demonstrating that the roll-pressing technique was effective in producing thin, self-standing films. The SEM images revealed a uniform distribution of LLZO particles throughout the polymer matrix, indicating successful integration and compatibility between the filler and the host material. In all samples, LLZO particles were evenly dispersed, with no noticeable aggregation or clustering. This homogeneous distribution was crucial, as it enhances both ionic conductivity and mechanical properties of the composite electrolytes. The absence of aggregates reduced the risk of ion-blocking regions, thereby improving overall ionic transport within the electrolyte.

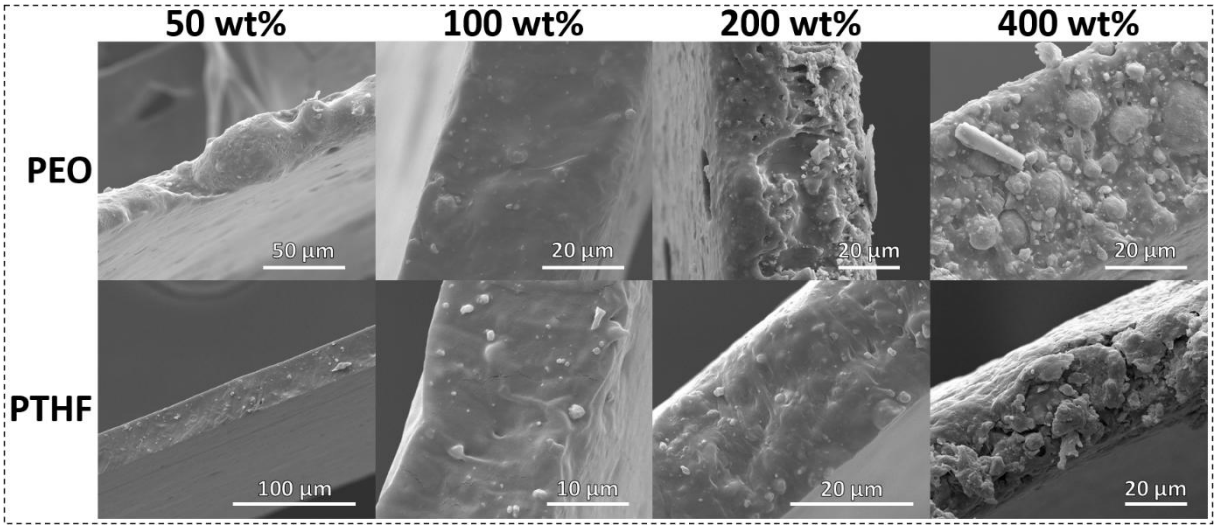

Figure 36 SEM micrographs of the cross-section of PTHF/PEO-LLZO films with 50, 100, 200 and 400 % of LLZO added.

Additionally, the consistent particle distribution suggested that the roll-pressing of a high-viscosity slurry was effective in preventing sedimentation, resulting in a well-dispersed composite. This uniformity not only enhanced the mechanical integrity of the films but also optimized ion conduction by increasing the contact area between the LLZO particles, the polymer matrix, and the electrodes. This improved interface is critical for efficient lithium-ion transport, further reinforcing the suitability of the roll-pressing technique for fabricating high-performance composite polymer electrolytes.

Energy-dispersive X-ray spectroscopy (EDX) maps, derived from SEM images, provided further insight into the elemental distribution within the composite polymer electrolyte films, offering critical information about the interactions between the LLZO particles and the polymer matrix (**Figure 37**). The EDX maps revealed distinct elemental contributions, allowing for a deeper understanding of both the morphology and chemistry of the films.

In the EDX mapping, lanthanum (La), represented in yellow, confirmed the presence of LLZO particles within the polymer matrix. The yellow regions aligned closely with the bright areas in the SEM images, which were identified as LLZO particles, verifying their uniform distribution without any aggregation. This consistent presence of La across the films highlighted the successful integration of LLZO into the polymer matrix, which was essential for enhancing ionic conductivity.

Sulfur (S), depicted in orange, corresponded to the TFSI anion and was clearly separated from the LLZO particles. This spatial separation demonstrated the effective incorporation of the ionic species within the polymer matrix while maintaining distinct boundaries between the LLZO and the polymeric ion-conductive pathways. This differentiation suggested that the LLZO did not interfere with the ionic transport provided by the TFSI, thereby preserving the electrochemical performance of the composite electrolyte.

Silicon (Si), depicted in red, marked the chain ends of the polymer segments. The EDX maps revealed a notable concentration of Si at the surfaces of the LLZO particles, as evidenced by the overlap of La and Si signals. This observation strongly supported the hypothesis that the silane coupling agents primarily interacted with the particle surfaces, enhancing the adhesion between LLZO and the polymer matrix. The high concentration of chain ends near the LLZO particles not only confirmed this interaction but also implied that these localized polymer segments may improve both mechanical

properties and ionic conductivity by fostering a conducive environment for ion transport, which in turn may facilitate enhanced Li-ion mobility, further optimizing the performance of the composite polymer electrolyte.

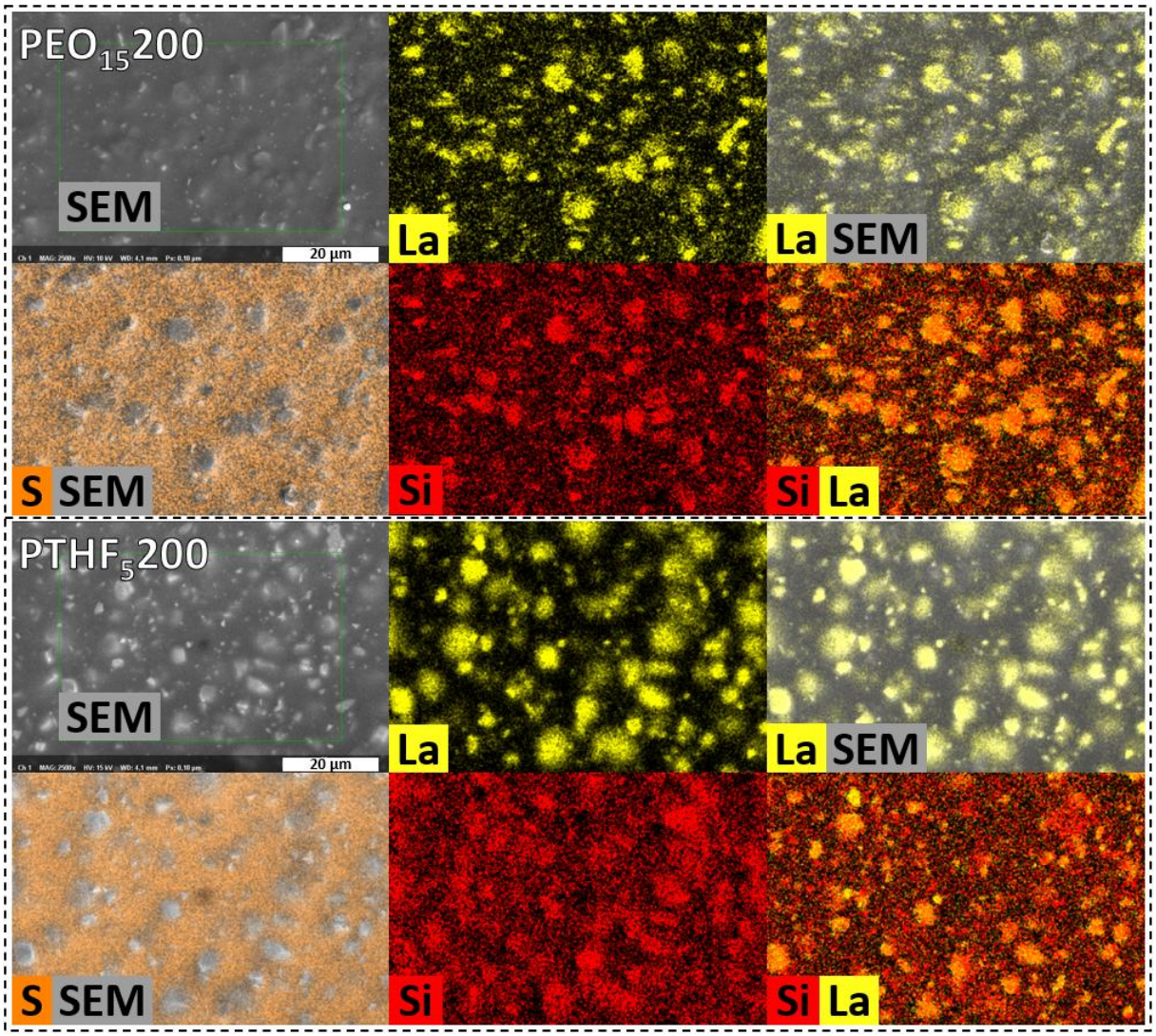

Figure 37 SEM of the flat surface of PEO (top) and PTHF (bottom) with 200 % LLZO. EDX maps of the selected area (green). La (yellow) was chosen for identification of LLZO particles. S (orange) shows the localization of the TFSI-anion. Si (red) shows the end-groups of the respective polymer.

A particularly interesting observation from the EDX maps was the higher concentration of Si found between the LLZO particles in the PTHF-based composite films. This observation aligned with the shear rheology results, suggesting that PTHF contains a higher number of silane groups relative to the reactive surface area available on the LLZO particles. The increased Si concentration in these interstitial regions implied that the silane coupling agents were effectively utilized, potentially saturating the reactive sites on the LLZO surface. This excess silane present between the particles indicated

reduced network formation, influencing both the mechanical properties and the ionic transport behavior of the composite electrolyte.

This finding was consistent with the rheological behavior observed in shear rheology tests, where the PEO-based composite exhibited the highest storage modulus at 200 % LLZO, while the PTHF composite demonstrated the lowest storage modulus under similar conditions. The difference in the mechanical properties could be attributed to the distinct interactions between the polymer matrix and the LLZO particles.

In PEO, the reactive surface area of LLZO was well-matched by the available silane groups, resulting in a strong interfacial interaction that enhanced mechanical stability. This balanced interaction ensured effective stress transfer and reinforcement within the polymer matrix. In contrast, the excess silane groups in PTHF might lead to a more flexible polymer network that was not adequately reinforced by LLZO particles, leading to lower storage modulus values, as observed in the rheology tests. The imbalance between the silane concentration and the reactive surface area LLZO may have hindered effective stress transfer, thereby compromising the mechanical integrity of the composite electrolyte.

These findings emphasized the importance of optimizing the silane content in relation to the reactive surface area of the filler particles. Achieving the right balance could enhance both the mechanical strength and electrochemical performance of the composite polymer electrolytes. Further research will be necessary to investigate the effects of varying silane concentrations on the interfacial properties and overall performance of these materials. Indeed, investigating these effects could lead to improved electrolyte designs, ensuring better mechanical stability, optimized ion transport, and enhanced long-term functionality for applications such as rechargeable batteries.

4.4.2.3.3.3 Thermal Characterization

Thermal characterization of the CPEs (**Figure 38**) showed a decrease in crystallinity for PEO films with increasing LLZO content. This was expected behavior as the LLZO-PEO interface reduces the ability of the polymer chains to align and crystallize. In contrast, PTHF did not exhibit any crystallization. Moreover, a slight decrease in T_g was observed for PEO and PTHF as LLZO concentration increased. For PEO films,

the degradation temperature remained constant at 360 °C, while PTHF films had varying degradation temperatures between 230 and 330 °C. The mass loss observed for both polymers correlated well with the combined wt% of polymer and LiTFSI, further confirming the consistency in the composition of the films.

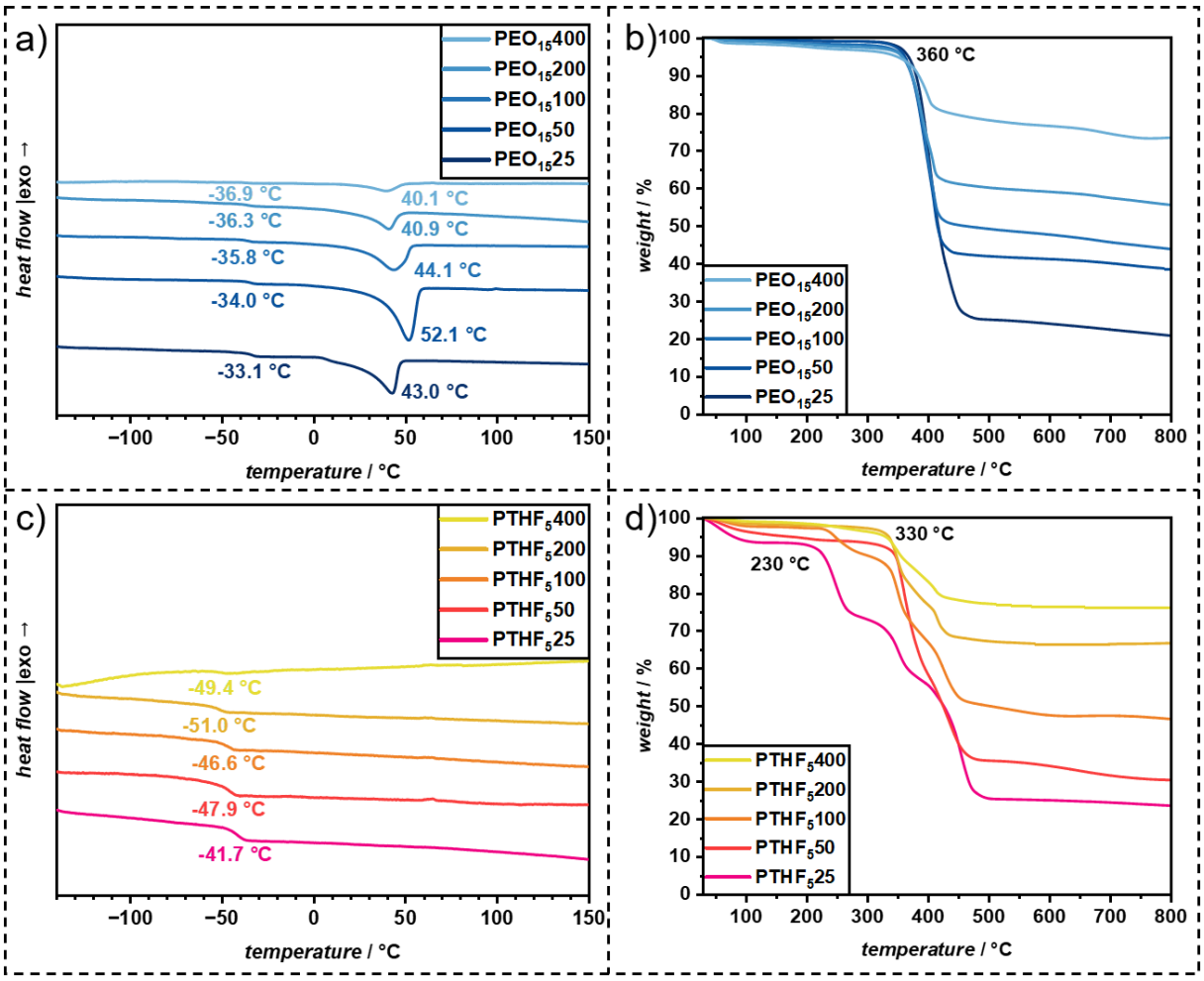

Figure 38 Comparison of thermal properties PEO/PTHF-LLZO films with 25, 50, 100, 200, and 400 % LLZO content. DSC measurements of PEO_{15}25-400 (a) and $PTHF_5$25-400 (c) at a heating rate of 10 K min^{-1}. Depicted is the second heat run. TGA measurements of PEO_{15}25-400 (b) and $PTHF_5$25-400 (d) at a heating rate of 10 K min^{-1} from 30 - 800 °C.

4.4.2.3.3.4 Electrochemical Characterization

Due to the change in the manufacturing procedure, the ionic conductivity and Li^+ transference number of all films were recorded (**Figure 39**) at a film thickness of approximately 100 µm. This characterization was essential to assess the impact of the new fabrication method on the electrochemical performance of the composite polymer electrolytes.

For PTHF-based films, the ionic conductivity was highest for the 25 and 50 % LLZO compositions, measuring 7.06 and $6.02 \cdot 10^{-6}$ S cm^{-1}, respectively at 60 °C. However,

increasing LLZO content beyond this significantly reduced the ionic conductivity, with values of 1.55, 1.28, and $2.52 \cdot 10^{-6}$ S cm^{-1} for 100, 200, and 400 % at 60 °C (**Figure 39** a). Notably, the ionic conductivity of $PTHF_5400$ at 60 °C appeared to be an outlier, showing a higher value than expected which in turn is based on linear extrapolation from measurements at other temperatures. Across all measured temperatures, the ionic conductivity of 25 % and 50 % LLZO films was the highest, showing a clear linear trend from 20 to 80 °C. For PEO-films, at 60 °C, the ionic conductivities for 25 %, 50 %, and 100 % LLZO compositions were similar, at 0.27, 0.26, and $0.24 \cdot 10^{-3}$ S cm^{-1}, respectively (**Figure 39** b). Increasing the LLZO content to 200 % reduced the ionic conductivity slightly to $0.17 \cdot 10^{-3}$ S cm^{-1}, while further increasing it to 400 % caused a significant drop to $0.07 \cdot 10^{-3}$ S cm^{-1}. PEO exhibited non-linear conductivity behavior with a significant loss in ionic conductivity below 50 °C, which correlated with the values of the melting points (ranging from 52 - 40 °C depending on the LLZO content) obtained via differential scanning calorimetry measurements (**Figure 38** a). Due to this temperature-dependent behavior, $PEO_{15}100$ performed best at lower temperatures (20 - 30 °C), reaching $8.44 \cdot 10^{-6}$ S cm^{-1}at 20 °C, while still remaining among the best-performing films at higher temperatures.

The lithium transference number for $PTHF_525$ (0.09) was a significant outlier compared to the other measurements, which ranged from 0.55 - 0.65 (**Figure 39** c). The t_{Li^+} values for higher LLZO contents were comparable to or even slightly higher than those reported in literature.[363] Similarly, for PEO-based films, $PEO_{15}25$ exhibited the lowest t_{Li^+} with 0.06, while the highest value (0.13) was observed for 100 % LLZO. The 50 %, 200 %, and 400 % LZZO samples were exhibiting slightly lower t_{Li^+} values (**Figure 39** d), indicating that moderate LLZO content provided the best balance of Li-ion transport in the polymer matrix.

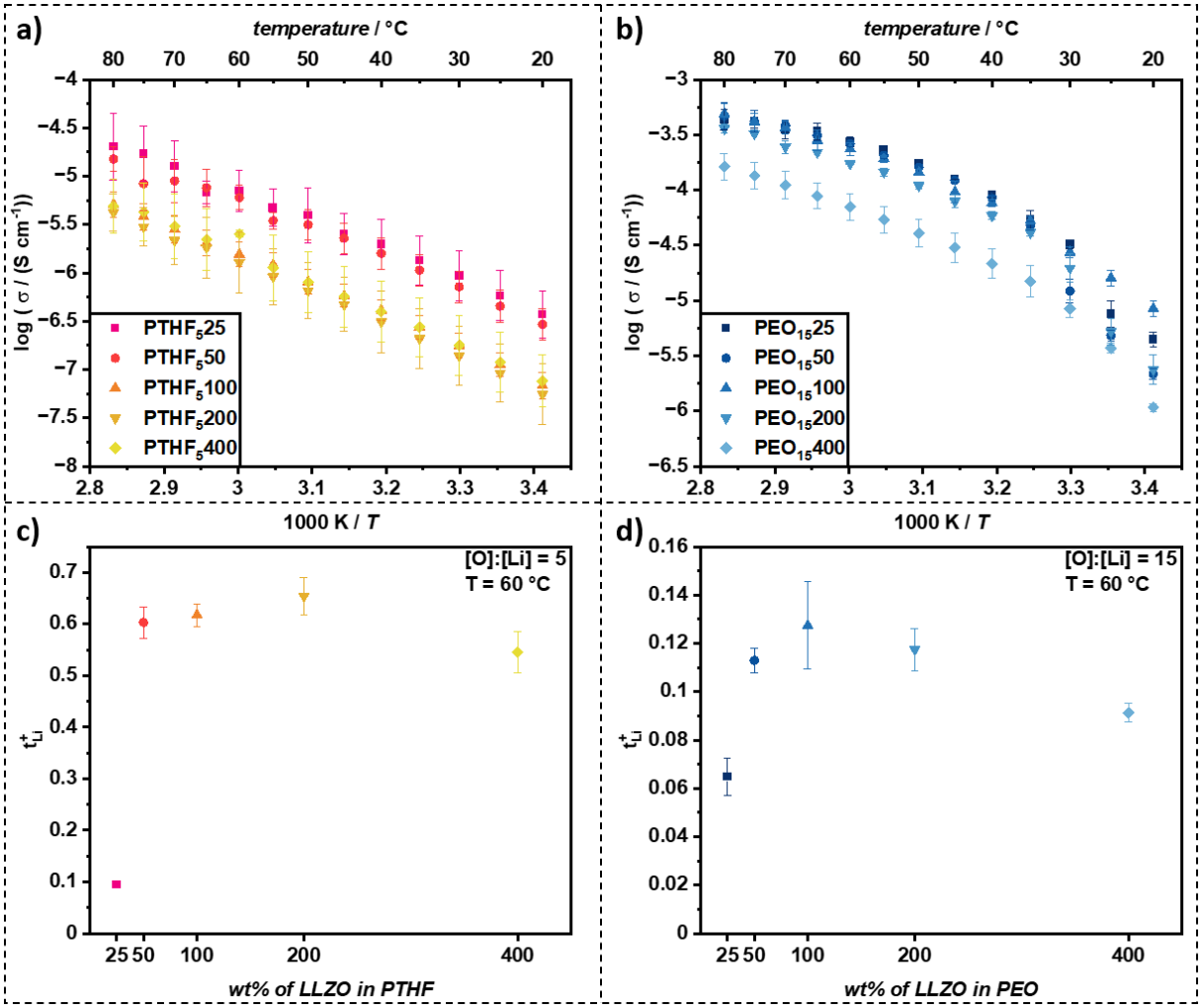

Figure 39 Ionic conductivity Arrhenius plots of a) PTHF and b) PEO mixed with 25, 50, 100, 200, and 400 % of LLZO from 20 - 80 °C. Lithium transference numbers t_{Li}^{+} for c) PTHF and d) PEO mixed with 25, 50, 100, 200 and 400 % of LLZO at 60 °C and a [O]:[Li] ratio of 5:1 for PTHF and 15:1 for PEO.

The symmetrical plating-stripping experiments for PTHF CPEs (**Figure 40**) revealed a low CCD of 0.1 mA cm^{-2} for PTHF$_5$50, PTHF$_5$100, and PTHF$_5$200. At this current density, these samples showed stable overpotentials of ~0.145 V, ~0.174 V, and ~0.186 V, respectively, with values steadily increasing as LLZO content increased. In contrast, PTHF$_5$25 and PTHF$_5$400 did not show any stable plating behavior, indicating poor electrochemical performance. Additionally, the polarization also increased with increasing LLZO content from PTHF$_5$50, PTHF$_5$100, to PTHF$_5$200, suggesting that lower LLZO content was more preferable for PTHF-based CPEs, as higher ceramic loading may hinder effective Li-ion transport.

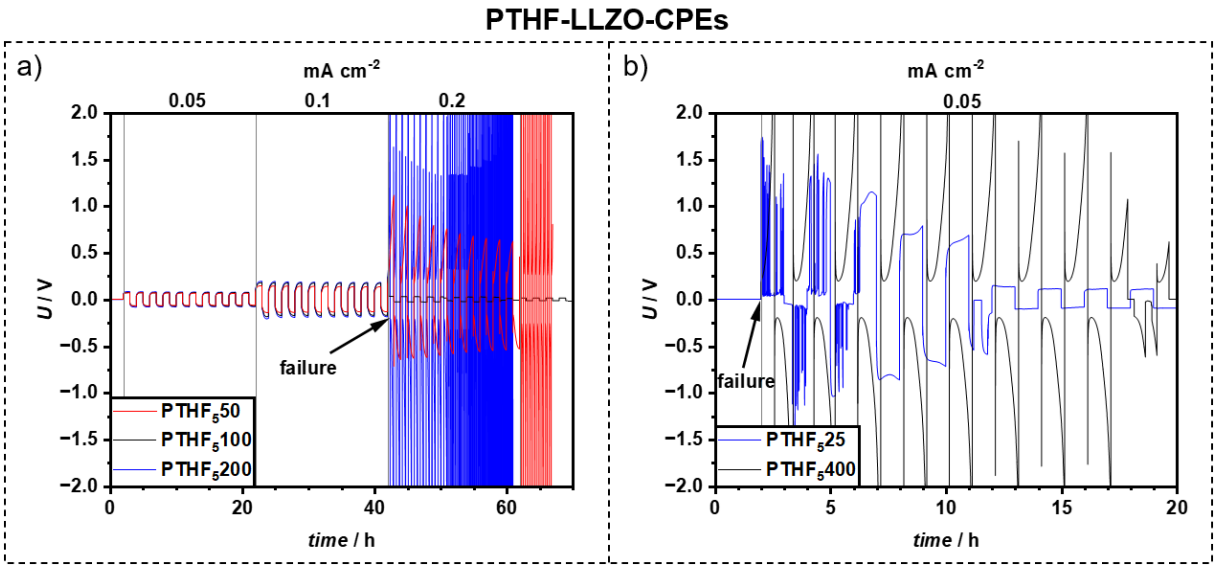

Figure 40 Symmetrical plating-stripping experiments of all PTHF-LLZO films with increasing current density after 10 cycles at 60 °C. Additional plating-stripping graphs are shown in the Appendix **Figure 132**.

Lastly, an impedance spectrum of freshly prepared cells was recorded hourly and analyzed by distribution of relaxation time (DRT) analysis (Appendix **Figure 133** - **Figure 138**). Time constants between 10^{-5} and 10^{-2} s primarily correspond to ion migration through interfaces[364,365] and are referred to as interface resistance. For PEO-based films, the equilibration time decreased as the LLZO content increased from 25 to 100 %, suggesting improved ion transport. Equilibration time increased further once the LLZO content was increased beyond 100 to 400 %. The same trend of a minimum interface resistance was observed for PTHF-films, however, the minimum of overall interface resistance occurred at 50 % LLZO content rather than 100 %.

Moreover, $PEO_{15}25$ and $PEO_{15}50$ indicated the presence of additional diffusion processes by exhibiting additional peaks at $10^{-5.3}$ s. A similar phenomenon was observed for $PTHF_5 25$ and $PTHF_5 400$ exhibiting additional peaks at 10^{-5} s. Although these peaks strongly suggest variations in Li-ion diffusion pathways due to changing LLZO content, a definitive conclusion regarding their origin could not be reached. Further investigations are needed to confirm whether these peaks directly correlate with structural or interfacial modifications.

Overall, among the tested CPEs $PTHF_5 50$ and $PEO_{15}100$ showed the best performance in terms of ionic conductivity, lithium transference number, and interface resistance for their respective polymer matrices. However, despite these improvements, the ionic conductivity of PTHF-based CPEs remained too low for

practical applications, even at 60 °C. During cell assembly, PTHF films were easier to handle and enabled the fabrication of thinner films, making them mechanically advantageous. Given these properties, it would be desirable to enhance the electrochemical performance of PTHF by mixing it with PEO, leveraging the beneficial properties of both polymers. Inevitably, this hybrid strategy could potentially combine the superior mechanical properties of PTHF with the higher ionic conductivity of PEO, creating a more effective composite polymer electrolyte for practical applications.

4.4.2.3.4 Mixed PTHF-PEO CPEs

To evaluate the feasibility of mixed polymer matrices and enhance the performance of PTHF films, three different approaches to PTHF-PEO mixtures were tested. Initially, modified PTHF and PEO were blended in a 1:1 mass ratio, along with their respective LiTFSI equivalents ($PEO_{15}PTHF_5100$). In this formulation, equal masses of both polymers were combined with LLZO, and the resulting film was subsequently assessed for its ionic conductivity and lithium transference number (**Figure 41**).

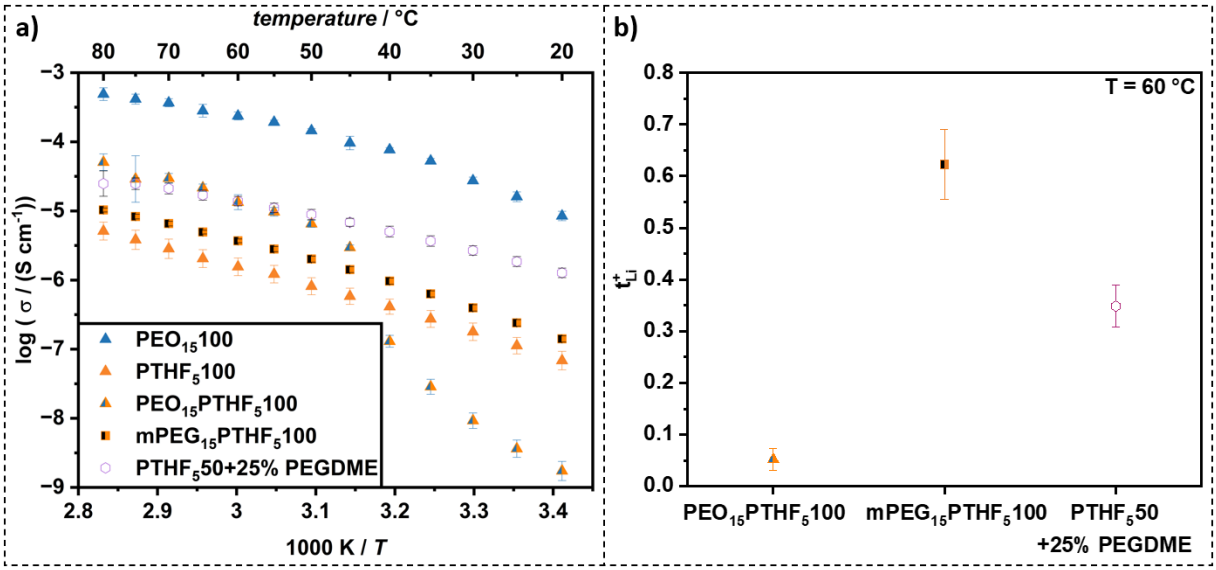

Figure 41 a) Ionic conductivity of PTHF-PEO mixed films from 20 - 80 °C. $PEO_{15}100$ and $PTHF_5100$ are added for comparison. b) Lithium transference numbers for all PTHF-PEO mixed films at 60 °C.

The results showed that incorporating PEO into the PTHF matrix improved its electrochemical properties, especially at higher temperatures. Notably, at temperatures above 45 °C, the performance of the PTHF-PEO mixture closely matched the average of its pure components ($\sigma = 1.3 \cdot 10^{-5}$ S cm^{-1} at 60 °C), indicating a possible synergistic effect, perhaps due to increased mixing of both polymers at

elevated temperatures. However, at temperatures below 40 °C, the blend underperformed compared to both pure PTHF and PEO individually, indicating that the combination may introduce additional resistance or phase incompatibilities at lower temperatures. The lithium transference number measured at 60 °C was 0.05, which was also significantly lower than that of $PEO_{15}100$ and $PTHF_5100$ alone, suggesting that while the polymer blend improved conductivity, it may have negatively impacted Li-ion transport efficiency.

One hypothesis proposed that the lower glass transition temperature in addition to the molecular weight of PTHF allowed it to move more freely within the slurry, enabling it to interact with the particle surface before the partially crystallized PEO at room temperature. This faster surface reaction of PTHF may have hindered the ability of PEO to react with the LLZO surface, leaving unreacted PEO-silane trapped within the PTHF matrix. Additionally, at temperatures below 45 °C, the compartmentalized PEO crystallized, as evidenced by DSC measurements (**Figure 42**), which showed three distinct melting points at 42.5, 30.5, and 16.7 °C, respectively.

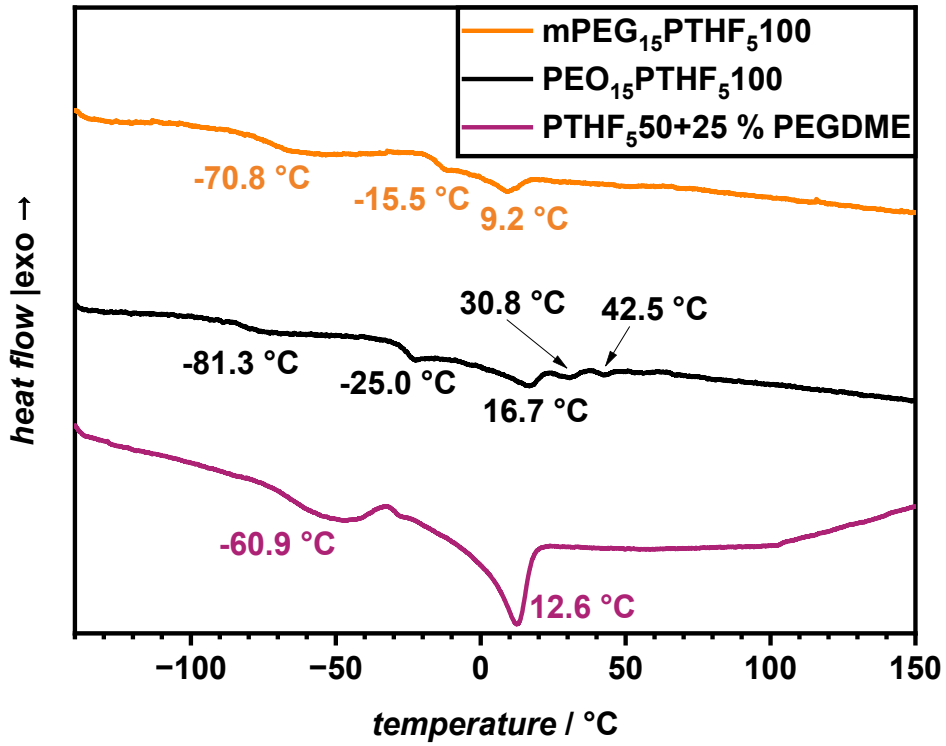

Figure 42 DSC measurements of mixed PEO-PTHF CPEs. $PEO_{15}PTHF_5100$ has two T_g corresponding to both separated polymer phases and multiple melting peaks for compartmentalized PEO-crystals of different sizes. $mPEG_{15}PTHF_5100$ also exhibits two T_g for PTHF and mPEG, respectively while only having one melting point for the mPEG phase. $PTHF_5$50+25 % PEGDME has one T_g and one melting point indicating a mixed phase.

Crystallization reduced the free volume of the polymer matrix, a key factor influencing the ionic conductivity.[366] The gradual crystallization of PEO from 42.5 - 16.7 °C correlated with the sharp decline in ionic conductivity, which dropped even below the values for pure $PTHF_5100$. This behavior was further supported by two additional distinct transport processes, which could be identified in the DRT spectrum between 10^{-5} and 10^{-4} s (Appendix **Figure 139** - **Figure 141**) for the PTHF/PEO mixture, indicating the presence of competing transport pathways within the sample. These findings demonstrated that the partial crystallization of PEO within the PTHF matrix significantly affected ionic conductivity below the melting point of PEO, revealing a complex interplay of temperature-dependent phase interactions between PTHF, PEO, and LLZO particles.

To further investigate mixed polymer systems, monofunctionalized mPEG5000-silane was combined with PTHF2.9k-silane. This modification maintained the same silane concentration but introduced a molecular weight closer to PTHF, improving the mobility of the mPEG chains within the composite slurry and reducing crystallization of mPEG compared to PEO10k-silane. The film was prepared similarly to $PEO_{15}PTHF_5100$, substituting PEO10k-silane with modified mPEG5000-silane to obtain $mPEG_{15}PTHF_5100$. This structure allowed for a core-shell configuration around LLZO particles, as the modified mPEG reacted with only one particle, preventing crosslinking through mPEG and maintaining a simple one-step slurry roll-to-roll process. Additionally, mPEG influenced the particle-PTHF interface by forming a (partial) in-situ coating on the LLZO particles, acting as an interlayer, which had been shown to improve the performance of CPEs.[367] Remarkably, this blend demonstrated a significant improvement in ionic conductivity compared to pure PTHF, more than doubling the conductivity ($\sigma = 3.7 \cdot 10^{-6}$ S cm^{-1} at 60 °C) while demonstrating stable performance across the entire temperature range of 20 - 80 °C. Notably, no decline in conductivity was observed below 45 °C, suggesting that the modified blend maintains its electrochemical efficacy even at lower temperatures.

Moreover, the mPEG-PTHF mixture exhibited Arrhenius behavior similar to pure PTHF, indicating that the thermal activation energy for ionic transport remained consistent. The lithium transference number of the mPEG-PTHF blend (0.62) was almost identical to that of pure PTHF films, suggesting that Li-ion transport primarily

occurred through the PTHF polymer matrix and LLZO particles. Unlike in the PEO-PTHF mixture no competing transport pathways were identified in DRT analysis (Appendix **Figure 141**), reinforcing that the improvements in ionic conductivity were largely attributed to the enhanced interphases from the mPEG coating. If a significant Li^+-conducting mPEG phase were present, it would have significantly lowered the lithium transference number, as observed in $PEO_{15}PTHF_5100$. These findings highlighted the complexity of optimizing electrochemical properties, including ionic conductivity, lithium transference number, and temperature stability. The results suggest that modifying polymer-filler interphases—rather than relying solely on polymer conductivity—plays a critical role in enhancing composite polymer electrolytes.

Blending modified PTHF and PEO directly proved to be ineffective as it resulted in a complete loss of lithium conductivity at lower temperatures, with only a marginal improvement observed when blending modified PTHF and mPEG. Therefore, attention was shifted to using unmodified PEO, specifically Poly(ethylene glycol) dimethyl ether (PEGDME, M_n = 500 g mol^{-1}), as a partial (25 %) replacement for modified PTHF in a $PTHF_550$ film. $PTHF_550$ exhibited the optimal balance of ionic conductivity and lithium transference number among all pure PTHF films. PEGDME, being liquid at room temperature and acting as plasticizer for PTHF, was expected to enhance the ionic conductivity of $PTHF_550$ while also coordinating Li-ions. As anticipated, the ionic conductivity increased by a factor of 2.3 from $6.0 \cdot 10^{-6}$ S cm^{-1} to $13.9 \cdot 10^{-6}$ S cm^{-1} at 60 °C. The improvement was even more pronounced at lower temperatures, where conductivity increased 4.4-fold, from $2.9 \cdot 10^{-7}$ S cm^{-1} to $1.3 \cdot 10^{-6}$ S cm^{-1} at 20 °C, indicating better room-temperature performance than pure $PTHF_550$. Interestingly, the lithium transference number was approximately the average of those of PTHF and PEO (i.e., at 0.35), suggesting that PEGDME contributed more to the ionic conductivity than PTHF, despite its lower content in the polymer matrix. These findings indicated that incorporating plasticizers into the matrix could significantly improve electrochemical performance, although PTHF still did not perform well enough to be suitable for CPE applications. The latter was further confirmed by preliminary plating-stripping tests, where all three PTHF-PEO mixed films failed immediately at a low current density of 0.05 mA cm^{-2} (Appendix **Figure 143**). This result reinforces, one

more time, the challenges of using PTHF-based CPEs, despite improvements in conductivity.

Interestingly, the thermal decomposition temperatures of all mixed CPEs were identical to that of PEO, occurring at 360 °C. The only exception was $PTHF_5$50+PEGDME, which showed an earlier mass loss attributed to the evaporation of PEGDME (boiling point ~240 °C). These results indicated that blending both polymers (i.e., PEO and PTHF) could significantly enhance the thermal stability of the CPE (Appendix **Figure 142**). The findings highlight the potential of polymer mixing strategies to improve both electrochemical and thermal properties, making them more suitable for high-temperature applications.

4.4.2.3.5 PEO-LLZO-CPEs

PEO_{15}50, PEO_{15}100, and PEO_{15}200 exhibited the most promising thermal, mechanical, and electrochemical characteristics. However, while the ionic conductivity of these films was adequate, it was not optimal for high-performance applications. One strategy to enhance their electrochemical performance in a full battery cell was to reduce the film thickness, thereby minimizing internal resistance. To investigate this, two distinct film thicknesses, 30 and 80 µm, were fabricated, leveraging the precise thickness control afforded by the roll-to-roll pressing technique. It was remarkable, that handling of 30 µm CPEs of PEO and LLZO was easily feasible, which strongly indicated the superior mechanical stability of the crosslinked system. This was a significant advancement, as most PEO-LLZO-CPEs reported in the literature typically range from 65 to 300 µm in thicknesses.[21,22,359,367,368] This finding highlights the structural integrity and processability of the optimized PEO-LLZO composite electrolytes, making them more suitable for practical battery applications.

4.4.2.3.5.1 Plating-Stripping Experiments

First, plating-stripping experiments were conducted with both film thicknesses (30 µm and 80 µm) for PEO_{15}50, PEO_{15}100, and PEO_{15}200 (**Figure 43**). This study aimed to evaluate the influence of film thickness on the electrochemical stability and cycling performance of the CPEs.

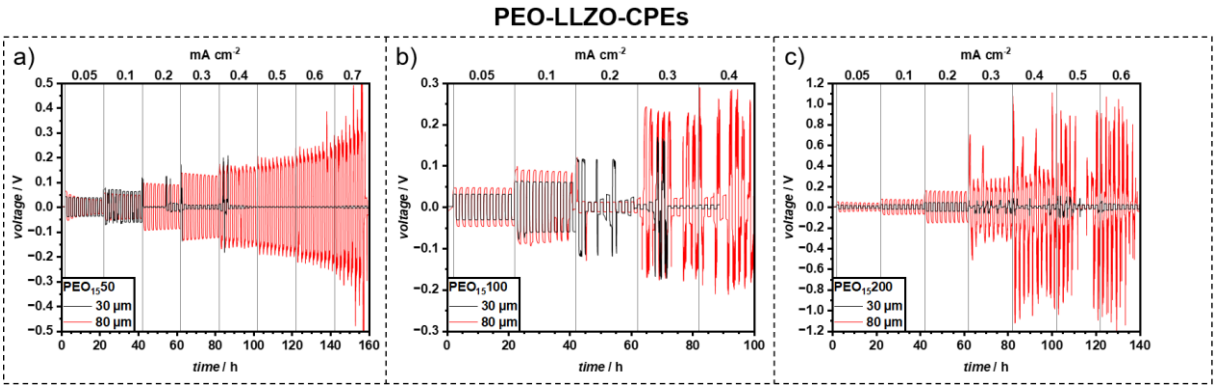

Figure 43 Symmetrical plating-stripping experiments of $PEO_{15}50$ (a), $PEO_{15}100$ (b), and $PEO_{15}200$ (c) films with increasing current density after 10 cycles at 60 °C.

For thicker films, the overpotential should be higher as the films exhibit more resistance, while thicker films are also anticipated to withstand higher current densities. This is mainly due to the failure mode, which most often is dendrite penetration in CPEs.[369] Through thicker films, a dendrite requires more time to fully penetrate, resulting in a slower failure of films compared to thinner films.

$PEO_{15}50$ with 80 µm thickness showed an initial overvoltage of ~0.065 V, which quickly dropped to ~0.034 V at 0.05 mA cm^{-2}, indicating the formation of an SEI. Moreover, this trend of reduction in overpotential was repeated after each incremental current density increase, continuing up to 0.4 mA cm^{-2}, at which point the curve shape indicated strong polarization within the film. One possible explanation for the overpotential reduction is associated with incremental SEI growth following each current density increase, although this hypothesis was not further investigated. In contrast, $PEO_{15}50$ with 30 µm thickness showed a stable overpotential of ~0.036 V at 0.05 mA cm^{-2}, suggesting a lower resistance but also potentially lower tolerance for high current densities compared to the thicker film.

$PEO_{15}100$ showed overpotentials of ~0.031 V (30µm) and ~0.046 V (80µm) at 0.05 mA cm^{-2}, respectively, which aligned with the expectation that thinner films have lower resistance. The same behavior was observed for $PEO_{15}200$, where 30 µm film showed an overpotential of ~0.012 V, while the 80 µm film exhibited 0.038 V at 0.05 mA cm^{-2}, respectively. For both, $PEO_{15}100$ and $PEO_{15}200$, the thinner films showed almost no polarization, while the thicker one indicated slight polarization, as indicated by the shape of the curve. Additionally, while a reduction of overpotential was observed with each cycle, this effect was significantly less pronounced compared to

PEO_{15}50. This general trend indicated that an increase in LLZO concentration reduced overpotentials in comparable films. It should be noted that direct comparison between films is challenging due to the complex nature of interface resistance, interfacial contact, and mechanical properties, all of which are strongly influenced by LLZO concentration.

The results for the observed CCD varied widely across the tested films, as both films of PEO_{15}100 failed rapidly at 0.2 mA cm^{-2}, while both films of PEO_{15}200 withstood a current density of up to 0.3 mA cm^{-2}. PEO_{15}50, however, had the 30 µm film fail at 0.2 mA cm^{-2}, while the 80 µm film showed overvoltage spikes (~0.39 V) at 0.6 mA cm^{-2}, before ultimately failing at 0.7 mA cm^{-2}. Overall, increasing LLZO concentration led to higher overpotential in thicker films compared to the thinner ones. Nevertheless, the CCD results were inconclusive, with no clear trend observed in regard to film thickness and LLZO concentration.

Alternatively, the CCD for PEO_{15}50, PEO_{15}100, and PEO_{15}200 was determined by Linear Sweep Voltammetry (LSV) on the 80 µm films (**Figure 44**). Here PEO_{15}50 and PEO_{15}100 showed a higher CCD of 0.58 mA cm^{-2} with PEO_{15}200 being slightly lower at 0.52 mA cm^{-2}. It has to be noted that CCD values obtained via LSV tend to be higher than those achievable in Li||Li symmetrical cells or full Li-metal batteries. As a result, the LSV CCD measurements often overestimate the practical CCD values of these electrolyte films. The conflicting CCD results from the two measurement techniques, along with the voltage noise observed during plating-stripping experiments, strongly indicated that dendrite penetration of the CPEs was causing short circuits and ultimately leading to the failure of the separator in plating-stripping experiments.

As dendrite penetration is a well-known issue of PEO-based CPEs, two solutions from the literature were adapted. Through the addition of $LiNO_3$[370] and SbF_3[371] to PEO-LLZO-CPEs and PEO Pes, Li and Sun et al. drastically reduced dendrite growth. Consequently, to assess the viability of this approach, $LiNO_3$ and SbF_3 were added to the PEO-LLZO-CPEs.

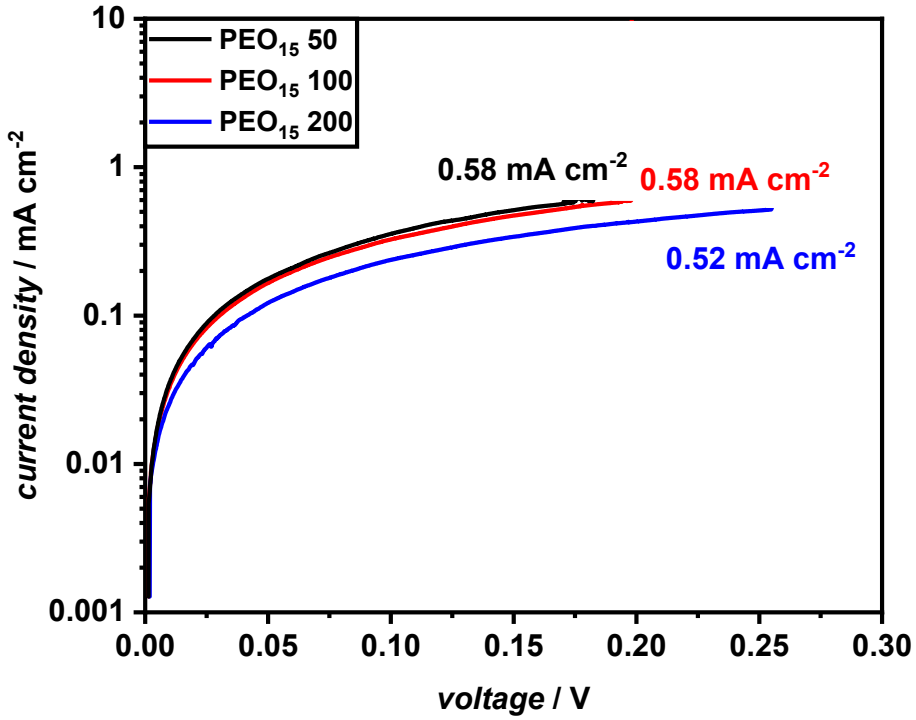

Figure 44 Determination of CCD of PEO_{15}50, PEO_{15}100, and PEO_{15}200 (80 µm) by LSV at $2.0 \cdot 10^{-5}$ V s^{-1}.

For PEO_{15}100, 41.4 mg of $LiNO_3$ and 21.2 mg of SbF_3 were added per 1 g PEO10k-silane, following the optimized concentrations reported in the respective studies (**Figure 45**). To further evaluate the effect of LLZO content, another PEO_{15}200 containing SbF_3 was also synthesized. The ionic conductivity of all three films was identical to their respective counterparts without additives.

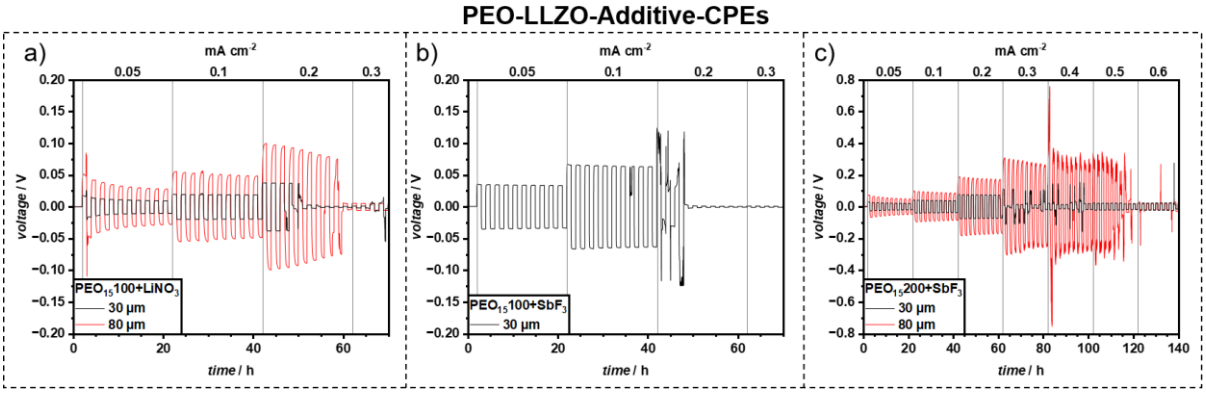

Figure 45 Symmetrical plating-stripping experiments of PEO_{15}100+$LiNO_3$ (a), PEO_{15}100+SbF_3 (b), and PEO_{15}200+SbF_3 (c) films with increasing current density after 10 cycles at 60 °C. For PEO_{15}100+SbF_3 the 80 µm film could not be measured.

The results of the symmetrical plating-stripping tests indicated no benefit to the CCD as $PEO_{15}100$+ $LiNO_3$ and $PEO_{15}100+SbF_3$ both failed at 0.2 mA cm^{-2} for the 30 µm film. In contrast $PEO_{15}100+LiNO_3$ (with 80 µm thickness) exhibited slightly improved durability compared to pure $PEO_{15}100$, however, the dendrite suppression effect reported by Li et al.[370] could not be reproduced for this CPE. Similarly, no measurable enhancement in CCD was observed for $PEO_{15}200+SbF_3$. Since the addition of $LiNO_3$ and SbF_3 did not provide any significant benefit in suppressing dendrites or improving CCD, their use was discontinued in further experiments.

4.4.2.3.5.2 NMC-Compatibility

To evaluate the realistic electrochemical stability of PEO-LLZO CPEs, galvanostatic overcharging was performed at 0.1 C against NMC622, as a high voltage cathode material (**Figure 46**). A characteristic voltage plateau at 4.6 V was observed, reflecting the onset of oxidative decomposition. A typical charge potential for NMC622 is 4.3 V vs. $Li|Li^+$.[139] Thus, the PEO-LLZO-CPEs were deemed to be compatible with NMC622, and $Li|PEO_{15}100|$NMC622 CR2032 cells were built to identify the compatibility of $PEO_{15}100$ with NMC622 in a full cell. A 30 µm-thick film was chosen to minimize internal resistance in initial C-rate capability tests (**Figure 47**).

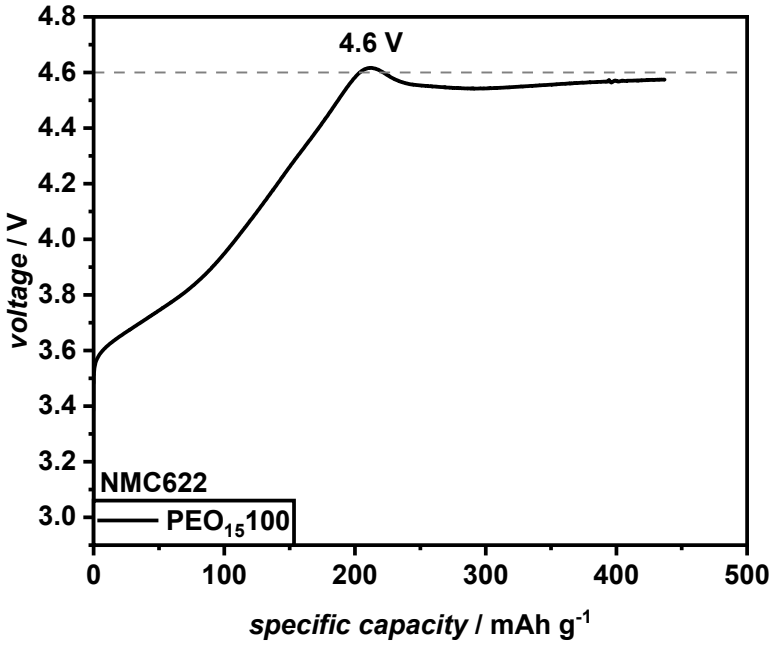

Figure 46 Electrochemical stability of $PEO_{15}100$ against NMC622 determined by galvanostatic overcharging (0.1 C).

In addition to NMC622 with a mass loading of 2 mg cm^{-2} cells (self-made) with a mass loading of 6 mg cm^{-2} (supplied by CustomCells) were used. This comparison was aimed at evaluating the compatibility of $PEO_{15}100$ with thicker cathodes. In solid-state batteries, achieving effective electrolyte-cathode contact within porous cathodes of higher mass loadings is challenging. As a result, solid-state electrolytes (SSEs) are often restricted to low-mass loadings, where direct interfacial contact between the cathode and SSE is sufficient.[372]

After formation in three full charge-discharge cycles at 0.05 C, the specific discharge capacity was determined to be 184.5 mAh g^{-1} and 149.5 mAh g^{-1} for 2 mg cm^{-2} and 6 mg cm^{-2} mass loading, respectively. While for 2 mg cm^{-2} mass loading, the rated capacity of the commercial NMC622 cathodes (175 mAh g^{-1}) was achieved and even slightly exceeded, due to error in the measurements in the cell dimensions. However, as expected, the higher mass loading (6 mg cm^{-2}) resulted in significant capacity loss. Inspired by the benefits of the addition of PEGDME as a plasticizer for $PTHF_5$50, 5 µL of 1 M LiTFSI in tetraethylene glycol dimethyl ether (G4) was added as a catholyte to the 6 mg cm^{-2} mass loading cathode during cell preparation. G4 is similar to the PEO matrix in structure as an oligo ethylene glycol but is liquid at room temperature. Hence, it improved wettability and contact deep into the NMC622 cathode. The discharge capacity could be improved to 186.9 mAh g^{-1} surpassing even the 2 mg cm^{-2} mass loading cell, most likely due to measurement error in cell dimensions. For C-rate tests, the cells were cycled for three cycles each at 0.1 C, followed by 0.25 C, 0.5 C, 1 C, and at 0.1 C again.

At 2 mg cm^{-2} mass loading, 75 % of the initial capacity was maintained at 1 C (175 mA g^{-1} = 1 C), which was comparable to similar solid-state systems.[22] However, as expected, increasing the mass loading to 6 mg cm^{-2} significantly impacted the rate capability, primarily due to the increased current density, which posed greater transport limitations within the thicker cathode.

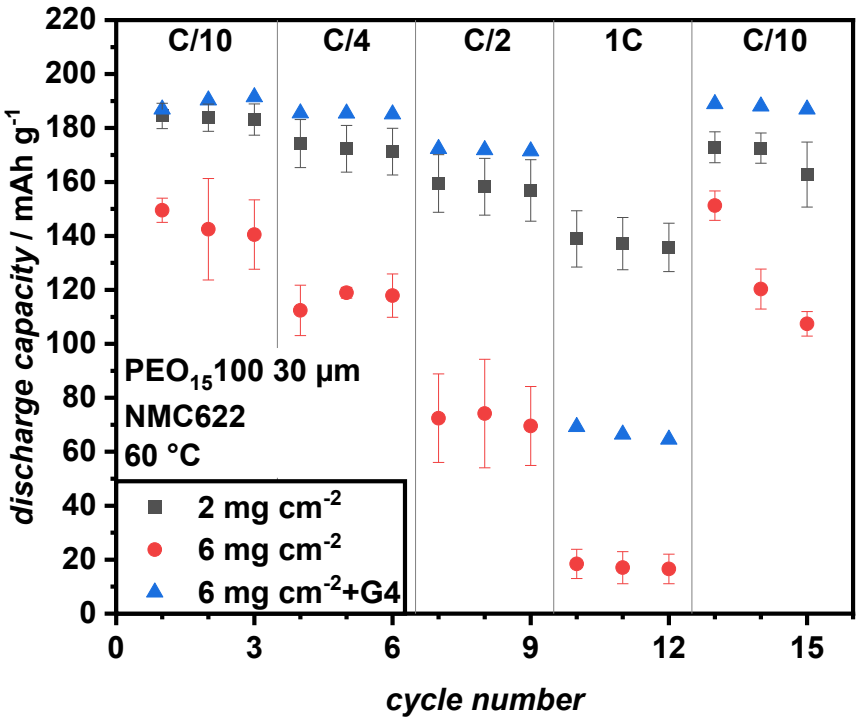

Figure 47 C-rate capability tests of $PEO_{15}100$ (30 µm) with NMC622 with a mass loading of 2 mg cm^{-2}, 6 mg cm^{-2}, and 6 mg cm^{-2} with the addition of 5 µL of 1 M LiTFSI in tetraethylene glycol dimethyl ether (G4) at 60 °C.

The addition of G4 could significantly improve the rate capability allowing the 6 mg cm^{-2} NMC622 cathode to retain 37 % of its initial capacity at 1 C, compared to 12 % for pristine cathode without G4. Additionally, the pristine 6 mg cm^{-2} mass loading NMC622 was unable to recover its initial capacity during the final 0.1 C step, exhibiting significant capacity loss during the three cycles. In contrast, the addition of G4 completely eliminated this issue, demonstrating its effectiveness in stabilizing capacity retention.

For long-term stability assessment, Li|PEO_{15}50/200|NMC622 with 2 mg cm^{-2} mass loading were chosen for constant current cycling tests to assess. These tests aimed to evaluate the stability of the CPEs against NMC622 over an extended period. PEO_{15}50 and PEO_{15}200 were used for testing, as PEO_{15}100 films failed prematurely, preventing meaningful data interpretation. The film failure of PEO_{15}100 was attributed to manufacturing and storage issues, as the air-tight sealing of the film broke during transport, exposing it to moisture for an extended period following the rate capability tests.

With the lower mass loading (2 mg cm^{-2}), the stress on the CPEs due to increased current density was reduced, therefore allowing for a clearer assessment of cathode electrolyte interface (CEI) (**Figure 48**).

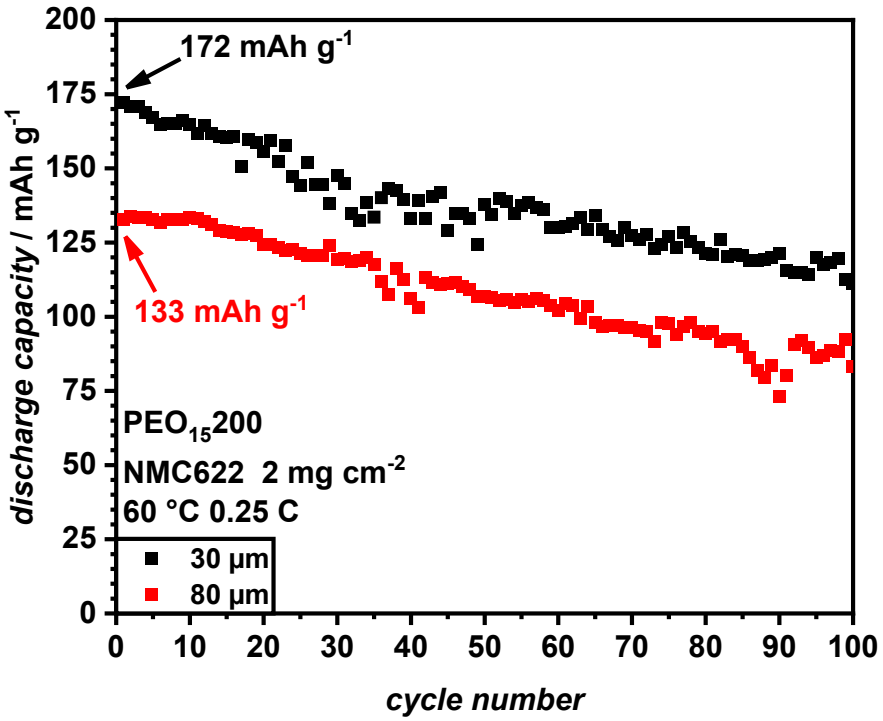

Figure 48 Constant current cycling of $PEO_{15}200$ at 0.25 C of Li|$PEO_{15}200$|NMC622 with 2 mg cm^{-2} mass loading at 60 °C.

As expected, the thinner $PEO_{15}200$ film (30 µm) exhibited a higher initial discharge capacity of 172 mAh g^{-1}, which was close to the calculated maximum capacity of 175 mAh g^{-1}. In contrast, the 80 µm film exhibited a significantly lower initial discharge capacity of 133 mAh g^{-1}. Overall, the discharge capacity of both films fluctuated strongly, indicating parasitic oxidative decomposition of the CPE at the cathode interface. After 100 cycles, the 30 µm membrane retained 65 % of its initial discharge capacity, while the 80 µm retained slightly less at 62 %. For comparison, a study developed by Ma et al. on 60 wt% silane-mPEG coated LLZO in a PEO-LiTFSI. cycled at 0.2 C in a Li||NMC811 cell, reported an initial discharge capacity of 156 mAh g^{-1} maintaining 82 % of its capacity after 100 cycles.[22] While the initial discharge capacity of the 30 µm film in this study was better, the noisy discharge behavior and comparatively lower capacity retention led to the conclusion that the interface instability between the cathode and the PEO-LLZO CPEs was the primary issue. Further

constant current cycling experiments using $PEO_{15}50$ (30 µm) at 0.25 and 1 C confirmed these findings by showing significant capacity loss within just a few cycles (**Figure 49**). This further supports the conclusion that cathode interface instability remains a major limitation in the long-term performance of PEO-LLZO CPEs in Li||NMC cells.

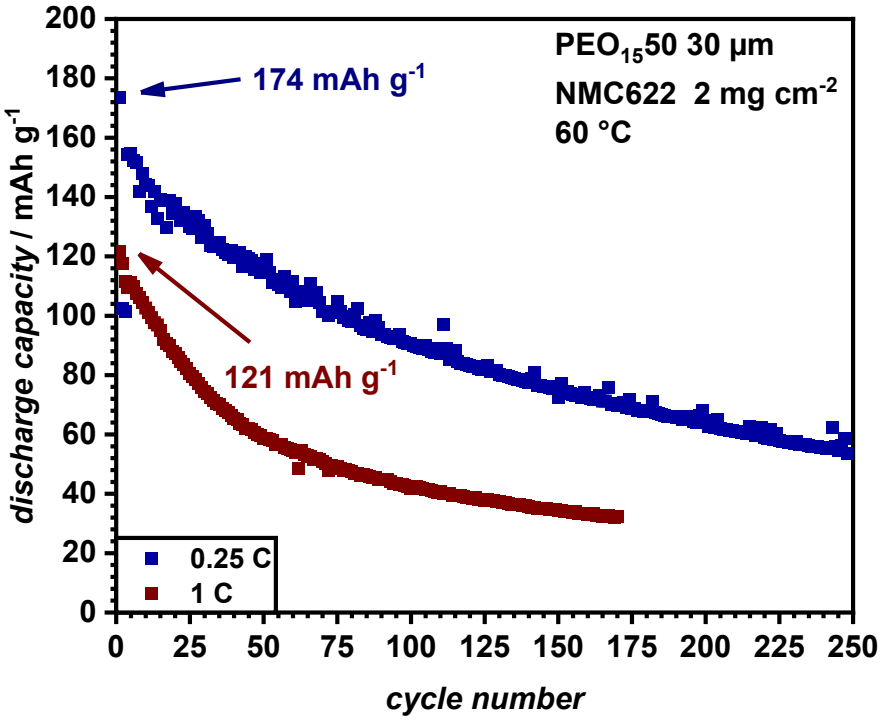

Figure 49 Constant current cycling of $PEO_{15}50$ (30 µm) at 0.25 C and 1 C of Li|$PEO_{15}200$|NMC622 with 2 mg cm^{-2} mass loading at 60 °C.

At 0.25 C, the discharge capacity of 174 mAh g^{-1} was found to be comparable to the previous studies, while at 1 C, the discharge capacity was reduced to 121 mAh g^{-1}. Over 100 cycles, the capacity retention at 0.25 was only 52 %, while at 1 C, it decreased even further to 35 %, indicating severe performance loss. Interestingly, the discharge curves appeared less noisy, particularly at 1 C, yet the capacity retention was even worse than that of $PEO_{15}200$ (30 µm). This suggests that while some improvements in cycling stability were achieved, long-term degradation at higher rates remained a critical issue.

To further assess the practical viability of the CPEs, a 3x3 cm Li|$PEO_{15}200$|NMC622 pouch cell with 6 mg cm^{-2} cathode was assembled to demonstrate its ability safely operate under pressure-free conditions. Indeed, the pouch cell successfully illuminated a red LED (**Figure 50**), confirming the theoretical feasibility of using these films for

stable cycling under these circumstances. However, due to the rapid capacity fading, an in-depth characterization of the pouch cell was not feasible, and no further experiments were conducted.

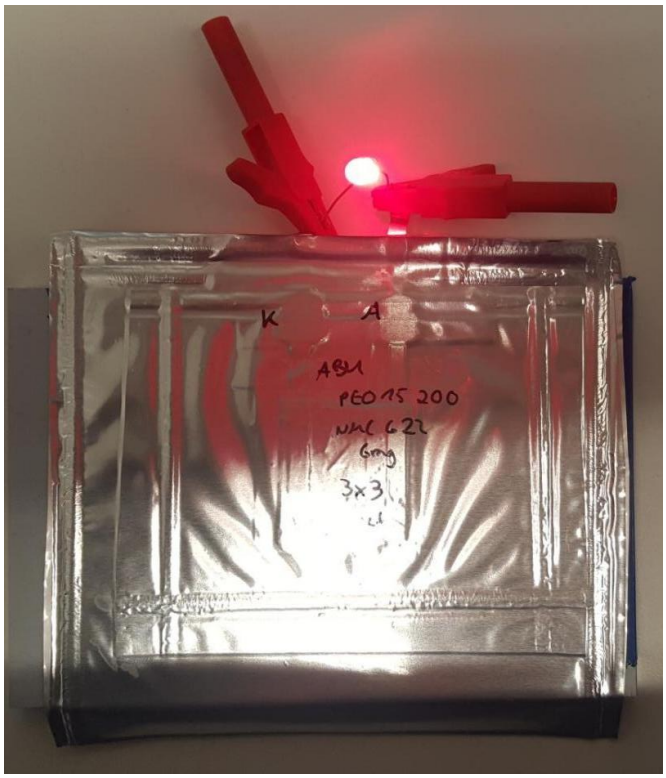

Figure 50 3x3 cm Li|PEO_{15}200|NMC622 6 mg cm^{-2} pouch cell illuminating a red LED. The pouch cell could not be analyzed in-depth due to rapid cell failure through capacity fading.

The rapid capacity fading observed in PEO-based electrolytes when paired with high voltage cathodes (> 4 V vs. Li|Li^+) is well documented and primarily attributed to the oxidative decomposition of PEO, which is catalyzed by the NMC surface. To mitigate this issue, countermeasures such as Al_2O_3 coatings of NMC cathodes have been developed and shown to effectively enhance interface stability.[373]

However, since commercially available coated NMC cathodes were not accessible, further analysis of PEO-CPEs with NMC cathodes were not feasible.

This limitation has highlighted the importance of cathode surface modifications in ensuring the long-term electrochemical stability of PEO-based composite polymer electrolytes.

4.4.2.3.5.3 LFP-Compatibility

Consequently, the cathode material was switched to commercial LFP (maximum voltage of 4.0 V) to mitigate oxidative degradation issues. The LFP cathode, with a

mass loading of 7 mg cm^{-2} (specific capacity = 160 mAh g^{-1}) was supplied by CustomCells). The C-rate capability test was then repeated with the addition of G4 to the cathode. To ensure consistency, new films of $PEO_{15}50$, $PEO_{15}100$, and $PEO_{15}200$ were synthesized in both 30 µm and 80 µm thickness and tested in Li|CPE|LFP full cells (**Figure 51**).

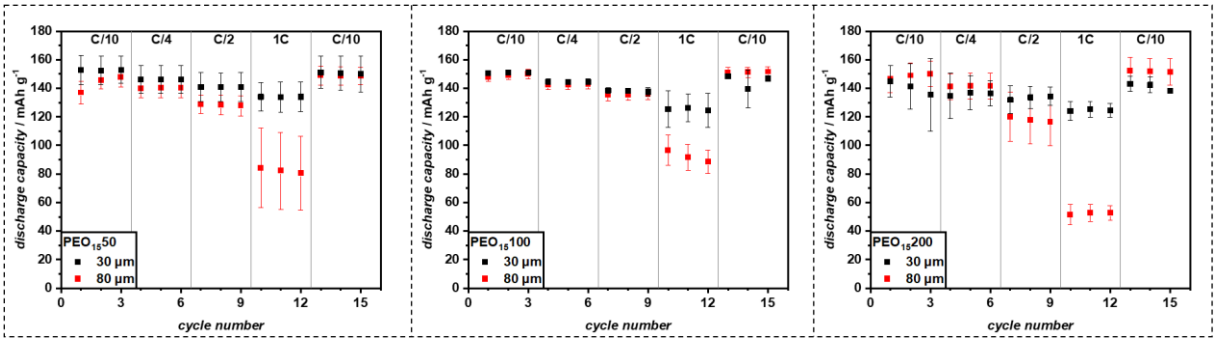

Figure 51 C-rate capability tests of $PEO_{15}50$, $PEO_{15}100$, and $PEO_{15}200$ (30 and 80 µm) with LFP with a mass loading of 7 mg cm^{-2} with the addition of 5 µL of 1 M LiTFSI in tetraethylene glycol dimethyl ether (G4) at 60 °C.

The initial discharge capacity of all three films was slightly lower than the rated capacity of 160 mAh g^{-1} provided by the supplier. A comprehensive summary of the highest measured discharge capacity at 0.1 (16 mA g^{-1}) and 1 C (160 mA g^{-1}) for each film, along their respective thickness, is provided in **Table 13**. This data provides a comparative analysis of the performance variation between different CPE formulations and film thicknesses, allowing for a detailed evaluation of their electrochemical behavior in Li|CPE|LFP full cells.

Table 13 List of the highest average discharge capacity recorded for $PEO_{15}50$, $PEO_{15}100$, and $PEO_{15}200$ at 30 and 80 µm film thickness at 0.1 and 1 C in Li||LFP cells.

Film	Discharge Capacity / mAh g^{-1}			
	30 µm		80 µm	
	0.1 C	1 C	0.1 C	1 C
$PEO_{15}50$	153	134	148	84
$PEO_{15}100$	151	125	149	96
$PEO_{15}200$	144	124	150	52

While for $PEO_{15}50$ and $PEO_{15}100$, the thinner 30 µm films showed a higher discharge capacity values at across all C-rates, $PEO_{15}200$ with the 80 µm film exhibited higher

discharge capacities at 0.1 and 0.25 C. As these measurements had high errors, a definitive correlation between film thickness and performance could not be established On average, the 30 µm films across all LLZO concentrations showed a high capacity retention at 1 C, ranging from 83 to 88 %. For 80 µm films, the capacity retention at 1 C varied significantly, e.g. with 57 % for $PEO_{15}50$, 64 % for $PEO_{15}100$, and 35 % for $PEO_{15}200$. Nevertheless, these capacity retentions still surpassed those of NMC622 cathodes (34 % with 6 mg cm^{-2} + G4), although similar high mass loadings were used. Additionally, due to the increased mass loading, the current density at 0.1 C was equal to 0.15 mA cm^{-2}, which was close to the observed stability limit during the plating-stripping tests. At 1 C, the current density equals 1.5 mA cm^{-2} , far exceeding the stable cycling range of typical PEO-based systems.[362] Hence, it was remarkable that the thinner films (30 µm) performed well in the rate capability tests, even at high C-rates, highlighting their potential for high-power applications.

Following the rate-capability tests, the same cells were used for constant current cycling at 0.25 C and 60 °C to assess long-term stability (**Figure 52**).

Of importance was that 0.25 C corresponded to a current density of 0.375 mA cm^{-2}, exceeding the maximum CCD of 0.3 mA cm^{-2} determined in the plating-stripping tests. However, the fact that several films demonstrated stable cycling under these conditions strongly suggested that the actual CCD of the CPEs may be higher than previously determined.

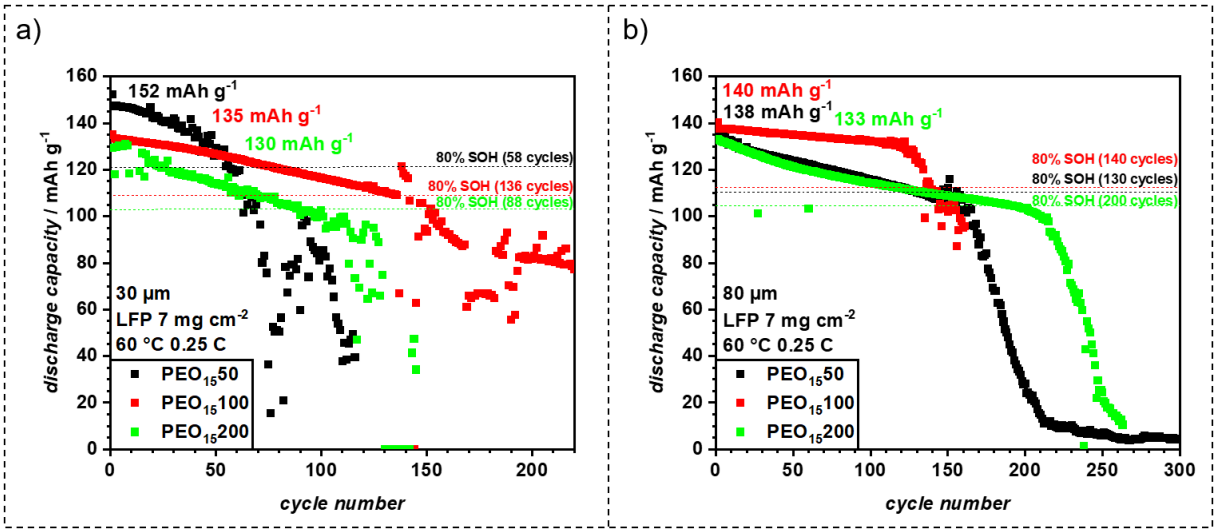

Figure 52 Constant current cycling of $PEO_{15}50$, $PEO_{15}100$, and $PEO_{15}200$ (30 µm (a) and 80 µm (b)) at 0.25 C of Li|CPE|LFP with 7 mg cm^{-2} mass loading at 60 °C. Depicted are the best performing cells for each LLZO concentration. Coulombic efficiency is omitted for clarity. Constant current cycling of all three films containing error data and coulombic efficiency is shown in the Appendix **Figure 144** - **Figure 146**.

Even after undergoing the straining C-rate capability tests, the films exhibited high initial discharge capacities of 152, 135, and 130 mAh g^{-1} for PEO_{15}50, PEO_{15}100, and PEO_{15}200 at 30 µm film thickness, respectively. Similarly, the films at 80 µm thickness showed comparable 138, 140, and 133 mAh g^{-1} discharge capacity for PEO_{15}50, PEO_{15}100, and PEO_{15}200.

During constant current cycling, the 30 µm films failed earlier than the 80 µm films, most likely due to dendrite penetration. Especially, PEO_{15}50 (30 µm) showed strong capacity fading and a noisy voltage profile, reaching 80 % state of health (SOH) after only 58 cycles. PEO_{15}200 (30 µm) showed a slightly better discharge behavior, maintaining 80 % SOH for 88 cycles. PEO_{15}100 (30 µm) displayed the most stable cycling behavior, with minimal noise and a high columbic efficiency (CE) of 99.7 %, reaching 80 % SOH after 136 cycles.

Increasing the film thickness to 80 µm had significant impact on the cycling stability across all formulations. Although, the initial discharge capacity was slightly lower compared to the 30 µm films, the discharge curves exhibited less noise, and in all cases, the number of cycles required to reach 80 % SOH increased. With 130, 140, and 200 cycles until 80 % SOH were reached for PEO_{15}50, PEO_{15}100, and PEO_{15}200 (80 µm), respectively. A clear trend where increasing LLZO content enhances cycling stability was identified. Moreover, PEO_{15}100 (80 µm) improved its CE to 99.8%, further reinforcing the benefits of the crosslinked PEO-LLZO CPEs. Considering the high current density and comparably low film thickness, these results showed a strong improvement of crosslinked PEO-LLZO-CPEs over comparable systems. Cai et al. infiltrated a $Li_{6.4}La_3Zr_2Al_{0.2}O_{12}$ (3D LLZAO) framework with PEO-LiTFSI to obtain a polymer-in-ceramic electrolyte. Their CPE was able to cycle an Li||LFP cell at 0.2 C for approximately 100 cycles, while maintaining 80 % SOH. However, they used a significantly lower mass loading of 1.5 mg cm^{-2}, resulting in a lower current density.[374] Moreover, their CPE preparation method featured a spongey template, which was subsequently infiltrated by LLZAO and a PEO-LiTFSI solution in a poorly scalable and energy intensive process. In contrast, the self-crosslinking PEO-LLZO CPEs developed in this work demonstrated superior electrochemical performance, while also being easier to synthesize and more scalable.

Optimizing the anode interface, particularly for the best performing PEO_{15}100/200, could significantly improve both performance and longevity of the Li||LFP cells.

Possible approaches include the addition of ionic liquids[35], known to improve ionic conductivity and anode stability, or succinonitrile[375], a plasticizer that improves electrolyte stability and flexibility, which might be able to further increase the performance of Li||LFP cells. However, due to time constraints, these enhancements could not be experimentally tested within the scope of this thesis.

4.4.3 Recapitulation

A novel, affordable, and scalable approach for the fabrication of CPEs for Li-metal batteries was systematically developed, analyzed, and optimized. A key breakthrough was the successful synthesis of self-crosslinking polymer-based CPEs in bulk, eliminating the need for solvent-based processing. This advancement is particularly significant, as it reduced energy-intensive processing steps, making the technology more scalable for industrial applications. The successful implementation of this concept led to the filing of a patent for the processing of these electrolyte films, further underscoring its technological and commercial potential.

To enhance the performance of CPEs, an extensive optimization of materials was conducted. Different polymer matrices, including commercially available PEO, PTHF, and PCL, were evaluated alongside inactive oxide fillers such as MoO_3 and active fillers, particularly LLZO. The findings revealed that modifying commercial PEO (M_n = 10,000 g mol^{-1}) with IPTES to obtain a self-crosslinking polymer matrix and combining it with LLZO particles of ~ 6 µm average particle size exhibited the most suitable properties for use in an Li-metal battery. Moreover, tuning the LLZO content from 25 % up to 400 % enabled the formation of a wide range of CPE architectures spanning from ceramics-in-polymer and ceramics-in-polymer character. The films were extensively characterized by DSC, TGA, oscillatory rheology, tensile strength, SEM, EDX, and various electrochemical characterizations including ionic conductivity, Li^+ transference number, plating-stripping tests, critical current density assessment, and constant current cycling of NMC622 and LFP cells with up to 6 and 7 mg cm^{-2} mass loading, respectively. This systematic optimization resulted in a scalable, high-performance CPE system, demonstrating significant potential for next-generation solid-state Li-metal batteries.

Extensive mechanical and thermal characterization validated the robustness of these materials. The LLZO content was proven to have a complex interplay between mechanical strength and flexibility, demonstrating its critical role in optimizing CPE performance. DSC and TGA confirmed that the films remained thermally stable up to 360°C, making them suitable for high-temperature battery environments. Through SEM and EDX the homogeneous distribution of LLZO particles within the polymer matrix, ensuring uniform ion transport pathways. The crosslinking mechanism was

confirmed to occur through a surface reaction between alkoxy silanes and LLZO particles, validating the self-crosslinking approach as a scalable and effective fabrication method.

The research successfully led to the fabrication of thin, flexible, and mechanically stable films with thicknesses below 30 µm. These films are significantly thinner than conventional CPEs, which typically range from 65 to 300 µm, providing advantages in battery performance by reducing internal resistance as demonstrated by excellent capacity retention during rate capability tests. Additionally, the implementation of roll-to-roll processing enhanced film uniformity and handling, further ensuring improved scalability and the manufacturability of these materials for industrial applications.
Stability against lithium metal was a critical aspect, as dendrite growth remains a significant challenge for solid-state batteries. Symmetrical lithium plating-stripping experiments confirmed that the optimized LLZO content significantly improved cycling stability, with some films exceeding 1000 hours of operation without failure.
In terms of electrochemical performance, the developed PEO-LLZO CPEs have demonstrated excellent compatibility with NMC622 cathodes, with a decomposition observed at 4.6 V vs. Li|Li^+. When tested at 60°C, the CPEs demonstrated stable cycling, achieving 75 % capacity at 1 C, indicating their potential for high-performance lithium-metal batteries. Furthermore, the addition of 1 M LiTFSI in tetraethylene glycol dimethyl ether (G4) to infiltrate the porous cathode significantly enhanced the rate capability of high-mass-loading cathodes, thereby improving overall battery efficiency. However, under constant current cycling, the oxidative decomposition of the PEO-matrix led to accelerated capacity fading when in contact with NMC622. Nevertheless, a 3x3 cm pouch cell was successfully fabricated and successfully charged, demonstrating the feasibility of the novel CPEs for operation under ambient pressure.
With high mass loading LFP cathodes, the CPEs exhibited superior performance compared to NMC622, achieving a capacity retention of 88 % at 1 C and 60 °C. Li|CPE|LFP cells maintained 80 % SOH after up to 200 cycles at 60 °C and 0.25 C corresponding to a high current density of 0.375 mA cm^{-2}. Dendrite penetration was identified as the primary failure mode across all cells, indicating the need for improvement at the anode interface.

If solutions to mitigate dendrite growth at the anode and parasitic reactions at the NMC cathodes are developed, these CPEs could enable the advancement of cost-effective and scalable separators for high-energy density Li-metal batteries.

Additionally, an innovative mixed-polymer system was designed and characterized to further optimize the performance of PTHF. While direct blending of PEO and PTHF did not provide significant benefits, the incorporation of PEGDME as a plasticizer significantly improved ionic conductivity at lower temperatures. However, the low ionic conductivity of the system ($13.9 \cdot 10^{-6}$ S cm^{-1} at 60 °C) rendered it unsuitable for Li-metal battery applications. These findings highlight the potential for further material optimizations to refine the electrochemical properties of self-crosslinking CPEs.

5 Conclusion and Outlook

This thesis investigated the implementation of Li-ion conductive particles, both oxide- and sulfide based, into polymer matrices to form hybrid solid-state electrolytes (HSSEs) with enhanced performance. The main challenge of HSSEs, the high interfacial instability and resistance, was tackled through systematic optimizations of particle coatings and fine tuning of polymer properties.
Collaboration with industrial and academic partners was crucial throughout the research.

In the first project, in a collaboration with the industrial partner ARLANXEO, the potential of hydrogenated nitrile butadiene rubber (HNBR) as a matrix for hybrid electrolytes incorporating LATP and Li_6PS_5Cl particles was explored. Initial results showed that incorporating LATP into the HNBR matrix led to particle agglomeration without any significant electrochemical improvement. Hence, LATP particles were coated with PAN to enhance compatibility with the HNBR matrix. Although, the coating process was optimized, the rigid structure of the PAN coatings negatively impacted the ionic conductivity of CPEs. Alternatively, Li_6PS_5Cl was explored as a thiophosphate-based additive. Both mixed and layered hybrid systems of Li_6PS_5Cl and HNBR were manufactured, revealing that the low ionic conductivity of HNBRs overall dominates the Li-ion conductivity leading to poor electrochemical performance. Ultimately, it was determined that HNBR is not suitable as a matrix for composite polymer electrolytes. Additives that significantly boost ionic conductivity may have a positive effect on the CPEs and could leverage the excellent film forming properties, Li^+ transference number, and oxidative stability of HNBR for future hybrid systems based on HNBR.

The second project explored the synthesis of novel sulfur-based polymers as polymer matrices to improve argyrodite compatibility. Argyrodites like Li_6PS_5Cl are known for their high ionic conductivity but degrade rapidly in contact with oxygen-containing polymers due to the oxophilicity of phosphate groups. To address this, several aliphatic polytrithiocarbonates and polythioethers were synthesized and characterized in regard to their thermal stability and electrochemical performance. It was found that polytrithiocarbonates depolymerize into thermodynamically favored cyclic structures upon being in contact with the nucleophilic argyrodite particle surface. Thus, the focus shifted to polythioethers, leading to the optimized synthesis of an amorphous

poly(propylene sulfide). While poly(propylene sulfide) exhibited low mechanical stability and a rigid film formation was not possible, a novel coating procedure using LiTFSI was developed, resulting in coated argyrodite particles with ionic conductivity suitable for room-temperature applications.. However, due to time constraints, it was impossible to assess the electrochemical performance at lower pressures or the protective properties of the coating against air and moisture, leaving avenues for future research. Further research needs to answer the question whether the poly(propylene sulfide) does improve safety of argyrodite based HSSEs.

The third project focused on simplifying and optimizing the coating process of ceramic particles, developing a simple and cost-effective modification of mPEGs modified with surface-active alkoxy silane. mPEG with number average molecular weights of 550 to 5000 g mol^{-1} were modified and their coating properties on LATP nanoparticles were assessed, with mPEG1000 providing the optimal balance of grafting density and homogeneity. The method was successfully adapted to coat LLZO nanoparticles, addressing interfacial degradation issues when combined with PVDF-HFP matrices. In collaboration with Forschungszentrum Jülich, it was proven that the mPEG coating for LLZO drastically increases the air and moisture stability of LLZO, which tends to degrade to Li_2CO_3 adversely affecting the electrochemical performance. Additionally, the agglomeration of LLZO in the CPEs was successfully suppressed, resulting in homogenous films with high CCD. Moreover, the mPEG coated LLZO particles showed excellent performance in PVDF-HFP based CPEs in Li||LFP cells exceeding 1600 cycles at 2 C and over 90 % SOH remaining, laying the foundation for further optimization of LLZO-based CPEs. that do not experience catalytic degradation.

The fourth and last project developed a novel toolbox of bifunctionalized polymers capable of self-crosslinking with various oxidic compounds, producing remarkably thin, self-standing, and homogeneous films. Systematically, PCL, PTHF, and PEO were used in combination with inactive fillers (MoO_3) and active fillers (LLZO) and characterized regarding their thermal, mechanical, and electrochemical performance. Meticulous optimization of parameters such as processing, molecular weight, particle size, and film thickness led to the development of a simple, cheap, and scalable procedure for CPEs of down to 30 µm thickness. These films demonstrated excellent compatibility with high mass loading cathodes. Li||LFP cells with 7 mg cm^{-2} mass

loading were cycled for over 200 cycles at 0.25 C while maintaining 80 % SOH. The simple fabrication process, combined with the potential for additive integration, presents a scalable pathway for high-performance CPE development.

In summary, these results highlight the critical role of interface optimization in HSSEs. Recognizing that many current optimization methods are hindered by complex precursor synthesis and poor scalability, this work put significant emphasis on the use of commercially available materials and industrially applicable procedures. Novel approaches with low cost commercially available polymers and reactants were found and their high capabilities in Li-metal batteries successfully demonstrated.
In conclusion, the development of efficient, scalable, and high-performance composite polymer electrolytes marks a significant step forward in solid-state battery technology, enhancing safety, efficiency, and longevity while maintaining cost-effectiveness—key factors for future commercial applications.

6 Experimental Part

6.1 Instruments and Synthesis Procedures

6.1.1 Nuclear Magnetic Resonance (NMR) Spectroscopy

The ^{1}H-NMR and ^{13}C-NMR spectra were acquired using a Bruker Ascend III 400 MHz spectrometer, with operating frequencies of 400 MHz for proton and 101 MHz for carbon. All samples were dissolved in deuterated solvents, and the chemical shifts are referenced to the residual solvent signals.

6.1.2 Size Exclusion Chromatography (SEC)

6.1.2.1 SEC using THF as Eluent

Size exclusion chromatography was performed in tetrahydrofuran (THF) using a Tosoh Bioscience HLC-8320GPC EcoSEC system, which was equipped with an autosampler, three PSS SDV columns (5 µm, 100 Å, 1,000 Å, 100,000 Å; 8 × 300 mm), and both UV and differential refractive index (RI) detectors. The system operated at a temperature of 35 °C with a flow rate of 1 mL min^{-1}. The system was calibrated with ReadyCal standards, using poly(methyl methacrylate) (PMMA) standards with molecular weights ranging from 800 to 2,200,000 Da, polystyrene (PS) standards from 370 to 2,520,000 Da, and poly(ethylene oxide) standards from 238 to 217,000 Da. Usually, 50 µL of a filtered 2.0 mg mL^{-1} sample solution was injected onto the columns. The eluent contains 0.55 g BHT per 2.5 L HPLC grade THF.

6.1.2.2 SEC using DMAC as Eluent

Size exclusion chromatography was performed in dimethylacetamide (DMAc) using an Agilent Technologies 1260 Infinity II system, equipped with both a refractive index (RI) detector (RID) and a UV detector. The system was calibrated with ReadyCal standards, using poly(methyl methacrylate) (PMMA) standards with molecular weights ranging from 800 to 2,200,000 Da, polystyrene (PS) standards from 370 to 2,520,000 Da, and poly(ethylene oxide) standards from 238 to 217,000 Da. The columns used were a Mixed-C Agilent and Mixed-E Agilent. The eluent consisted of DMAc (HPLC grade) with 0.79 g of LiBr per 2.5 L of solvent. Usually, 50 µL of a filtered

2.0 mg mL^{-1} sample solution was injected onto the columns. The system operated at a temperature of 50 °C with a flow rate of 1 mL min^{-1}.

6.1.3 Attenuated Total Reflection (ATR) Fourier-Transform (FT) Infrared (IR) Spectroscopy (ATR FT-IR)

ATR FT-IR spectra were recorded on a Bruker Alpha II IR from 400 – 4000 cm^{-1} at 22 °C.

6.1.4 Differential Scanning Calorimetry (DSC)

Differential scanning calorimetry was measured on a Netzsch DSC Polyma 214 equipped with liquid nitrogen cooling. Samples of 2 - 10 mg were measured in aluminum pan with a pierced lid in two heating cycles. The measurements were usually performed from -150 to 160 °C at a heating and cooling rate of 10 K min^{-1}.

6.1.5 Thermogravimetric Analysis (TGA)

All thermogravimetric analysis measurements were performed on a TGA 5500 (TA Instruments) in Platinum HT pans under nitrogen atmosphere. Samples are equilibrated at 30 °C and heated to 800 °C at a heating rate of 10 K min^{-1}.

6.1.6 Oscillatory Rheology

Rheological measurements were conducted using a strain-controlled ARES G2 rheometer (TA Instruments) through small amplitude oscillatory shear experiments. The measurements were performed at frequencies ranging from 0.1 to 100 rad/s at temperatures of 25 °C, under a nitrogen atmosphere. A 13 mm parallel plate geometry was used, with a strain of 0.1 %. The samples were prepared from films obtained via the self-crosslinking membrane preparation method, each having a diameter of 13 mm and a thickness of 0.2 mm.

6.1.7 Tensile Strength

Hegewald und Peschke Meß-und Prüftechnik GmbH, Universalprüfmaschine inspekt table 10 kN. Equipped with a 1 kN force transducer. Measurements were performed under ambient conditions with punched out bones of 2.5 cm length and 5 mm width. Films had a thickness of 200 µm.

6.1.8 Electrochemical Impedance Spectroscopy (EIS) and Electrochemical Characterization

6.1.8.1 Evaluation of HNBR for CPEs

For the EIS measurements, coin cells (CR2032 type) were assembled by sandwiching the previously dried films between two stainless steel electrodes (thickness *l* = 100 µm, diameter = 10 mm) in a glovebox. The cells were then preconditioned in a temperature chamber (Binder MK53) at 70 °C for 5 h and chamber cooled to 20 °C. The measurements were performed by increasing the temperature in 10 °C steps from 20 °C to 70 °C, with each temperature being maintained for 2 hours to allow thermal equilibrium to be reached. For the impedance measurements a VMP-300 potentiostat (BioLogic Science Instruments) was used. Impedance spectra were recorded over a frequency range from 1 MHz to 500 mHz with an amplitude of 10 mV at each temperature point. For each film three coin cells were prepared and measured. Subsequently, the mean average ionic conductivity of these three measurements was derived and discussed. The ionic conductivity σ was calculated according to **Equation 7**.

$$\sigma = \frac{l}{R_b * A} \qquad \textbf{Equation 7}$$

with R_b being the bulk electrolyte resistance that can be accessed from the Nyquist plot, *l* the film thickness and *A* the film area.

6.1.8.2 Sulfur-Containing Polymers for Argyrodite-CPEs

Cell assembly and measurements were performed by M.Sc. Philip Heuer from Universität Münster.

All electrochemical measurements were carried out in PEEK lined, airtight press cells with stainless steel current collectors (A = 0.785 cm^2).[376] All measurements were performed with a Biologic-VMP300 and a climate chamber maintained at 25 °C.
For electrochemical impedance spectroscopy 200 mg of $Li_{5.5}PS_{4.5}Cl_{1.5}$ or coated $Li_{5.5}PS_{4.5}Cl_{1.5}$ was placed in between the two steel stamps and uniaxial pressed at 3 t for 3 min. An external pressure of 50 MPa was then applied using a metal frame. The frequency range for impedance measurements was 1 MHz to 100 mHz. The RelaxIs software (rhd instruments) was used for the analyses.

6.1.8.3 Self-Crosslinking Oxide-CPEs

Cell assembly and measurements were conducted by Dr. Annika Buchheit (HI MS).

Ionic conductivity

Electrochemical impedance spectroscopy was used for determination of the ionic conductivity. Therefore, CR2032 coin cells in symmetrical arrangement with stainless steel discs as electrodes with the samples in between were measured on a Multi Autolab M204 with a FRA32M-module (Deutsche Metrohm) and the data were collected with the software NOVA 2.1.4 (Metrohm Autolab B.V.). Logarithmic frequency scans of 50 steps from 1 to 106 Hz with an alternating voltage of 40 mV were performed at all temperature settings 20 to 80 °C, adjusted via climatic chamber (MK 053, Binder GmbH, Germany), temperature fluctuations did not exceed ±0.02 K). Ionic conductivity was calculated according to **Equation 7** (6.1.8.1).

Transference Number

Transference numbers were measured according to Bruce-Vincent method.[377,378] Therefore, symmetrical CR2032 coin cells with lithium electrodes with the electrolyte sandwiched in between were built. The measurements were performed at 60 °C in a climatic chamber (MK 053, Binder GmbH, Germany), temperature fluctuations did not exceed ±0.02 K. Complete transference experiments including polarization and intermediate impedance measurements were performed on an Multi Autolab M204 equipped with FRA32M-module (Deutsche Metrohm) and the data were collected with NOVA software 2.1.4 (Metrohm Autolab B.V.). The cells were equilibrated for 24 h, meanwhile the impedance of the polymer/lithium boundary was monitored in order to ensure the formation of a stable SEI. For determination of transference numbers, a

constant DC voltage of 10 mV (ΔV) was applied to the cell and the time dependent current was monitored, the initial current is denoted as I_0 and the final steady state current is denoted as I_{ss} in the following. The cell impedance was analyzed before and after each single DC polarization step by AC impedance measurements. Therefore, logarithmic frequency scans of 50 steps from 1 to 106 Hz with an alternating voltage of 10 mV were performed. The ohmic part of the electrolyte impedance and the lithium/electrolyte interface impedance is denoted as $R_{el,0}$ and $R_{Li,ss}$ for the sample before polarization and after polarization in steady state, respectively. Calculation of transference numbers were done according to **Equation 8**.

$$t_+ = \frac{R_{el,0} * I_{ss}}{\Delta V - R_{Li,ss} * I_{ss}} \qquad \textbf{Equation 8}$$

LSV/CV

LSV and CV experiments were carried out with an Autolab PGSTAT302 N (Metrohm) potentiostat at 60 °C, data were collected with the software NOVA 2.1.4 (Metrohm Autolab B.V.). Samples were measured in a three-electrode setup in Swagelok cells, whereas Lithium served as the counter and reference electrode. For reductive scan, Nickel was used as working electrode, and for oxidative scan Platinum serves as the working electrode respectively. Reductive scan was performed between OCV and -0.4 V vs. Li│Li^+ or until lithium deposition, oxidative scan was performed between OCV and 7 V vs. Li│Li^+ or the current exceeds 10^{-5} A.

Cell Building

NMC622 cathodes were made according to literature.[356]

NMC622 electrodes consisting of 90 wt.% (1.854 g) NMC622-Powder (BASF TODA Battery Materials LLC), 7 wt.% (0.144 g) Carbon Black (Super C65, Imerys Graphite & Carbon) and 3 wt.% (0.062 g) PVDF (Solef® 5130, Solvay) were produced by first dissolving PVDF in 4 mL (3.883 g) NMP (99.5%, Sigma Aldrich) using an ARM-310 ThinkyMixer (THINKY) for 20 Minutes at 2000 RPM. Carbon Black and NMC622 were subsequently added to the mixture and homogenized with the ThinkyMixer for 20 min. at 2000 RPM and 10 min. at 300 RPM to get rid of any remaining air bubbles within the mixture. The slurry was cast onto previously cleaned aluminum foil (20 µm, Evonik Industries) by using a doctor blade (ZUA 2000 Universal Applicator, ZEHNTER GmbH) with a wet coating thickness of 40 - 50 µm and an Automatic Film Applicator (1133 N, Sheen Instruments) with a speed of 50 mm s^{-1}. The electrode sheets were dried in an

oven (Binder GmbH) at 80 °C for 2 hours before drying under reduced pressure (10^{-3} mbar) over night at 110 °C. This step was followed by calendaring to a thickness of ~34 - 38 µm and punching into circular electrodes using a Hohsen electrode puncher (Hohsen Corp.) with a diameter of Ø = 12 mm and further dried again over night at reduced pressure (10^{-5} mbar) before being used for cell production. The cathodes produced are corresponding to ~2 mg cm^{-2} CAM.

NMC622 (6 mg cm^{-2}) and LFP cathode sheets with a mass loading of 1 mAh cm^{-2} were purchased from Custom Cells GmbH, pre-dried for 12 h at 110 °C and punched to circular discs of 12 mm. 50 µm thick lithium metal foil (Honjo) was used as anode material and punched to circular discs of 14 mm. Cells were built by stacking cathode and anode with a hybrid film of 16 mm in diameter in between in CR2032 coin cells. All cells were built in a dryroom (dewpoint < -60°C).
Galvanostatic cycling experiments were carried out with a battery tester system (Maccor ®, series 4000) at 60 °C in a climatic chamber.

Constant Current Cycling

All constant current cycling experiments were conducted using a coin cell-type two-electrode setup with a Maccor Series 4000 battery test system. The cells were conditioned at 60 °C in a Binder KB 400 climate chamber. Lithium plating and stripping experiments were carried out in symmetrical lithium cells, where an initial conditioning phase at 0.05 mA cm^{-2} for 10 cycles was performed. Subsequently, lithium was plated and stripped at 0.2 mA cm^{-2} either for one hour per cycle over 500 cycles equivalent to 1000 hours or until failure.
For plating and stripping experiments with alternating current densities, an initial 0.05 mA cm^{-2} for 10 cycles were conducted before gradually increasing the current density every 10 cycles in increments of 0.1 mA cm^{-2}, until either a short circuit occurred, or safety limits were reached.
Galvanostatic overcharging (upper voltage limit: 6 V) was performed at 18.0 mA g^{-1} (~0.1 C) for NMC622 cathodes. The voltage plateau observed during testing was used to identify the onset of oxidative decomposition of the polymer electrolyte against the cathode materials.
Full cell cycling experiments were conducted between 3.0 V - 4.3 V vs. $Li|Li^+$ for NMC622 and 2.8 - 4.0 V vs. $Li|Li^+$ for LFP at a charge rate of 0.25 C. For rate

performance evaluations, the charge rate was varied, while the discharge rate remained constant at 0.1 C.
Cells were acclimated at OCV for 12 h at 60 °C. Subsequently for the three forming cycles, cells were charged with constant current - constant voltage protocol with constant voltage for 30 min or < 0.05 C. Discharge cycles were performed under constant current.

6.1.9 Cryo-Transmission Electron Microscopy (TEM)

All Cryo-TEM measurements were performed by M.Sc. Andreas Stihl within the workgroup of Prof. Dr. Felix Schacher at Universität Jena.

Samples were used as a dry powder which was suspended in micropure water at a concentration of 2 mg mL^{-1} and dispersed via brief ultrasonication. The sample was deposited on a carbon support film on a 400-mesh copper grid manufactured by Quantifoil Micro Tools (Großlöbichau, Germany). The films were hydrophilized in an Argon plasma produced by a Diener Electronics (Ebhausen, Germany) plasma oven for 120 s prior to sample deposition. An amount of 10 µL of the suspension was then placed on the film, the excess blotted off using filter paper and allowed to air dry. TEM micrographs were acquired with a 200 kV FEI Tecnai G2 20 (Hillboro, OR, USA) using a 1 k × 1 k Olympus MegaView camera (Münster, Gemany) with the acceleration voltage set to 200 kV.

6.1.10 High-Angle Annular Dark-Field (HAADF) Scanning Transmission Electron Microscopy (STEM) (Project 1)

All HAADF STEM / EDX measurements were performed by Dr. Radian Popescu from Laboratorium für Elektronenmikroskopie at Karlsruher Institut für Technologie.

The size, shape and the chemical composition of nanoparticles was investigated by high-angle annular dark-field (HAADF) scanning transmission electron microscopy (STEM) in combination with energy-dispersive X-ray spectroscopy (EDX) carried out on an FEI Osiris ChemiSTEM microscope at 200 keV electron energy. For performing EDX, the microscope is equipped with a Super-X EDX system comprising four silicon drift detectors (Bruker). EDX spectra are quantified with the FEI software package

"TEM imaging and analysis" (TIA) version 4.7 SP3. Using TIA, element concentrations were calculated on the basis of a refined Kramers' law model, which includes corrections for detector absorption and background subtraction. For this purpose, standard-less quantification, i.e. by means of theoretical sensitivity factors, without thickness correction was applied. The concentration profiles of different chemical elements within a single nanoparticle were determined from EDX spectra measured along a line-scan that passes through its center. EDX line-profiles were recorded by applying a drift-correction routine via cross correlation of several images, which yields a local precision better than 1 nm. The drift-corrected EDX line-profiles were taken with a probe diameter of 0.3 nm and a distance of about 1 nm between two measuring points. The quantification of Si-, O-, S- and N-content from EDX line scans was performed by using the Si-K an S-K series, as well as, the N-K_α and O-K_α lines. Besides the EDX lines of the corresponding elements, i.e. lines of the Si-K and the S-K series, as well as, of the N-K_α and O-$K_\alpha$lines, X-ray lines of Cu-K and Cu-L series from the grid and the C-K_α line from the amorphous carbon substrate are also observed in all EDX spectra.

Alternatively, EDX elemental maps of Si (Si-K_α line), O (O-K_α line), N (N-K_α line) and S (S-K_α line) are recorded and used to investigate their distribution within nanoparticles. The maps are analyzed by using the ESPRIT software (version 1.9) from Bruker.

6.1.11 Scanning Electron Microscope (SEM) and Energy-Dispersive X-ray (EDX) spectroscopy (Project 4)

All EDX measurements were performed by Dr. Erich Müller from Laboratorium für Elektronenmikroskopie at Karlsruher Institut für Technologie.

FEI Helios G4 equipped with a Schottky Thermal Field Emission Cathode. The energy range is 20 eV to 30 keV for secondary and backscattered electron imaging, with beam current ranges of 0.8 pA - 100 nA. The Bruker XFlash 6|60 EDXS detector (60 mm² SDD, slew AP3.3 window) is used for elemental analysis, the Everhart-Thornley (ETD) detector for secondary and backscattered electron detection, and the In-Chamber Electron (ICE) detector for capturing emitted electrons. Additional detectors include a Through-Lens Detector (TLD), Mirror Detector, and In-Column Detector (ICD) for high-quality SEM imaging, as well as the STEM detector with BF, ADF, and HAADF

segments for detailed structural analysis. The system also includes an EBSD (Electron Backscatter Diffraction) and TKD (Transmission Kikuchi Diffraction) detector head for crystal structure analysis, texture, and phase analysis.
Samples were sputtered with gold after being glued with adhesive graphite tabs on an aluminium sample holder.

Additionally, SEM micrographs of cross sections of CPEs were recorded by M.Sc. Alexander Grimm.
Scanning electron microscopy imaging was done using a *Quanta 200 F* from *FEI* with an accelerating voltage of 15 kV. Samples were sputtered with gold for 240 seconds prior to measurement.

6.1.12 Glovebox

6.1.12.1 MBraun

MBraun Unilab glovebox with < 0.1 ppm H_2O, < 0.1 ppm O_2 under inert argon atmosphere.

6.1.12.2 Inert

I-LAB 3-glove glovebox with < 0.1 ppm H_2O, < 0.1 ppm O_2 under inert argon atmosphere. Equipped with a potassium permanganate impregnated activated carbon filter.

6.1.13 Hot-Press

Hot-press model YLJ-HP60-LD purchased from TMAX Battery Equipments. Plate area 12x12 cm with single side heating up to 200 °C. Maximum pressure of 40 MPa. The hot-press is placed inside a glovebox (6.1.12.2).

6.1.14 Roll-to-Roll-Press

Xiamen Tmax Battery Equipments Limited, Lab Manual Roller Press Machine 100 mm diameter and 200 mm width roll dimensions. 0.2 µm tolerance on roll circumference.

6.2 Materials

Chemical	Purity and Information	Supplier
(3-Mercaptopropyl) trimethoxy silan e	99 %	Sigma Aldrich
1,2-Dibromoethane	98 %	Sigma Aldrich
1,8-Diazabicyclo(5.4.0)undec-7-ene	99 %	abcr
1,9-Dibromononane	97 %	Sigma Aldrich
1*H*,1*H*,2*H*,2*H*-Perfluorodecyl triethoxy silane	97 %	Sigma Aldrich
2-(2-Mercaptoethylthio) ethanethiol	90 %	Sigma Aldrich
3-(Triethoxysilyl)propyl isocyanate	95 %	TCI Chemicals
Acetic acid	100 %	Carl Roth
Acetone	99.9 %	VWR
Acetonitrile	99.9 %	VWR
Acrylonitrile	≥99 %, contains 35-45 ppm monomethyl ether hydroquinone as inhibitor	Acros Organics
Azobisisobutyronitrile	98 %	Sigma Aldrich
Benzene-1,3,5-trithiol	98 %	TCI Chemicals
Benzyl mercaptan	96 %	abcr
Bis(trifluoromethane)sulfonimide lithium salt (LiTFSI)	99.95 %, trace metal basis, stored in glovebox	Sigma Aldrich
Bis(triphenylphosphoranylidene)am monium chloride	97 %	Sigma Aldrich
Butane-1,4-dithiol	97 %	Sigma Aldrich
Carbon disulfide	> 99.9 %	Sigma Aldrich
Chloroform	99.9 %	VWR
DCM	99.5 %	VWR
Diethyl ether	99.9 %	VWR
DMF	99,8 %, extra dry, over molecular sieve	Acros Organics
Ethanol	99.9 %	VWR
Ethyl Acetate	99.9 %	VWR
Hexane-1,6-dithiol	97 %	abcr
Hydrochloric acid 32 %		VWR
Li_6PS_5Cl	Ampcera®, 10 µm	MSE Supplies
Methanol	99.9 %	VWR
MoO_3	99.97 %, trace metal basis	Sigma Aldrich
mPEG (M_n = 550, 1,000, 2,000, 5,000 g·mol^{-1})		Sigma Aldrich
Mylar foil	PPI-SP 914 colorless, 100 µm	PPI Adhesive Products
Nonane-1,9-dithiol	95 %	Sigma Aldrich
PCL-diol (M_n = 2,000 g·mol^{-1})		BLD Pharm
PEO (M_n = 6,000, 10,000, 20,000 g·mol^{-1})		Sigma Aldrich
Polyethylene glycol dimethyl ether (500 g mol^{-1})		Sigma Aldrich
Potassium thiocyanate	99 %	Sigma Aldrich
Propylene oxide	99 %	TCI Chemicals
Propylene sulfide	> 98 % stabilized with Butyl Mercaptan	TCI Chemicals

Chemical	Purity and Information	Supplier
PTHF (M_n = 2,900 g·mol^{-1})		Sigma Aldrich
p-Xylene	99.9 %	VWR
Silica nanoparticles	SiO_2, 99.9 %, 200 nm, spherical	US Research Nanomaterials, Inc.
Therban 4367	43 wt% acrylonitrile content, 61 Mooney viscosity	Arlanxeo
THF	99.9 %	VWR
Thiocarbonyldiimidazole	95 %	abcr
Triethylamine	99.5 %	abcr

6.3 Synthetic Procedures and Experimental Data

6.3.1 Evaluation of HNBR for CPEs

6.3.1.1 Film preparation of HNBR-LiTFSI

Therban 4367 (113.4 mg) and LiTFSI (52.8 mg, [N]:[Li]=5:1) are dissolved in 2 mL acetone and stirred at high rpm overnight. The masses are calculated to result in a film thickness of approximately 100 µm. A PTFE ring with 3.7 cm diameter is placed on Mylar® foil and the polymer solution poured into the mold on a leveled surface. An upside-down beaker is put on top of the mold with a small slit for air exchange. The acetone is slowly evaporated for 24 h at r.t. and the film subsequently placed in a vacuum oven at 60 °C and 7 mbar. The film is carefully loosened from the Mylar® foil and placed in a glovebox. Films with 10 mm diameter are punched out and dried in a Büchi oven at 60 °C and 10^{-3} mbar.

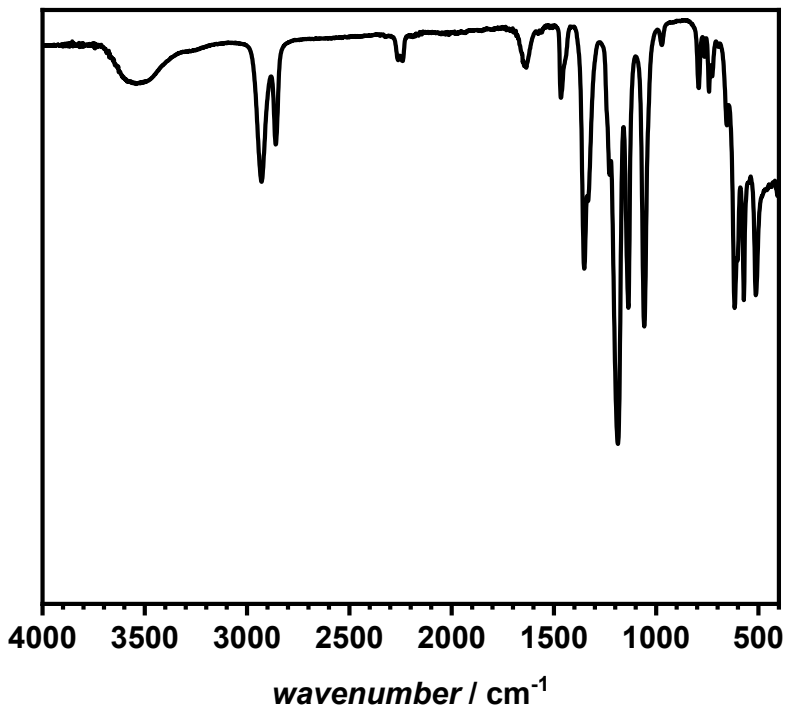

Figure 53 ATR-IR of HNBR-LiTFSI film after drying in a vacuum oven.

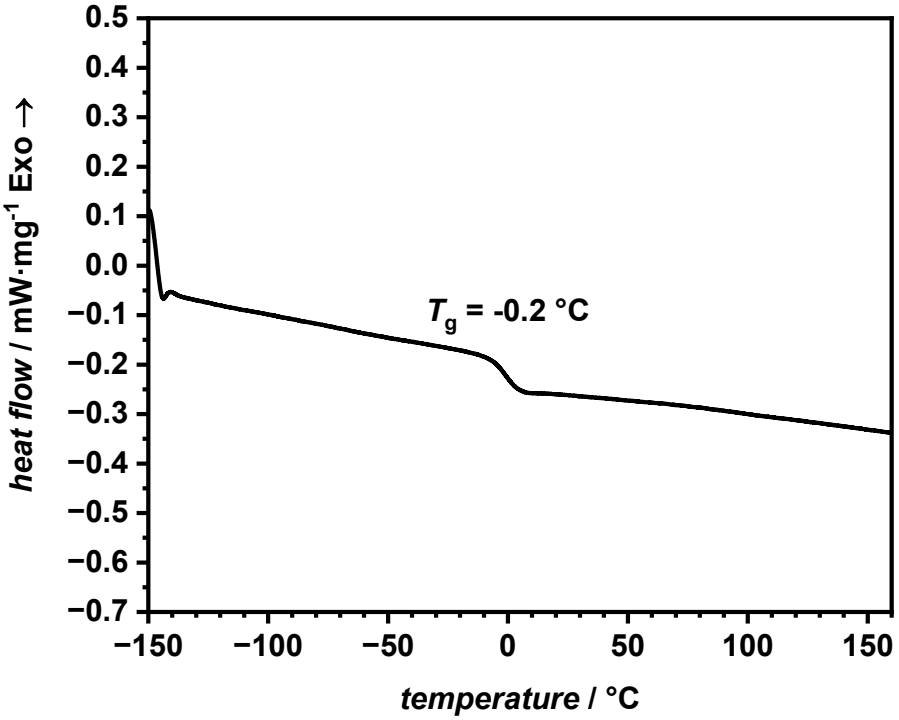

Figure 54 DSC of HNBR-LiTFSI film. Depicted is the 2nd heat run at a heating rate of 10 K min^{-1}.

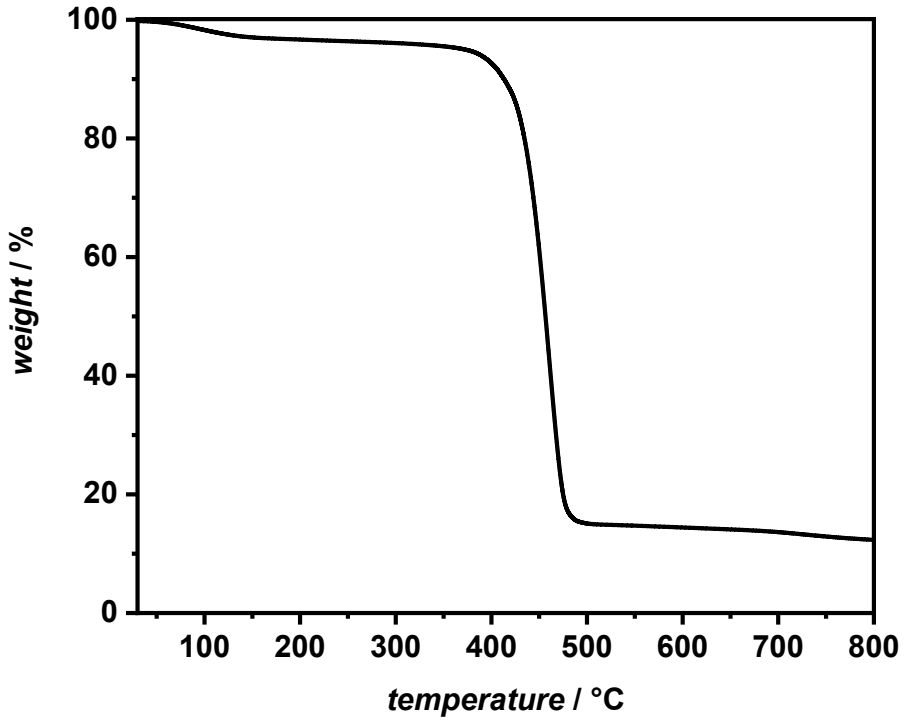

Figure 55 TGA of HNBR-LiTFSI film from 30 - 800 °C at a heating rate of 10 K min^{-1}.

6.3.1.2 Film preparation of HNBR-LATP-LiTFSI CPEs

The HNBR-LATP-LiTFSI CPEs are prepared in the same manner as described in the previous Chapter 6.3.1.1 with the addition of 20% (PAN@)LATP (22.7 mg) calculated from the polymer mass during the stirring overnight. This results in a total oxide content of 12 wt% in the dried film. Additionally, the sample is sonicated shortly for 10 min before pouring the dispersion into the mold.

HNBR-12wt%LATP-LiTFSI:

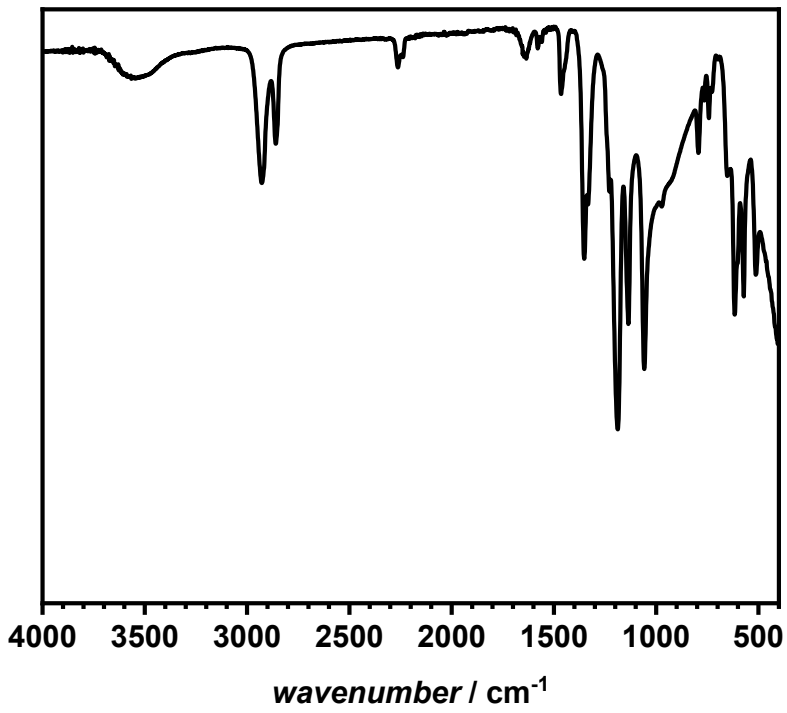

Figure 56 ATR-IR of HNBR-12wt%LATP-LiTFSI film after drying in a vacuum oven.

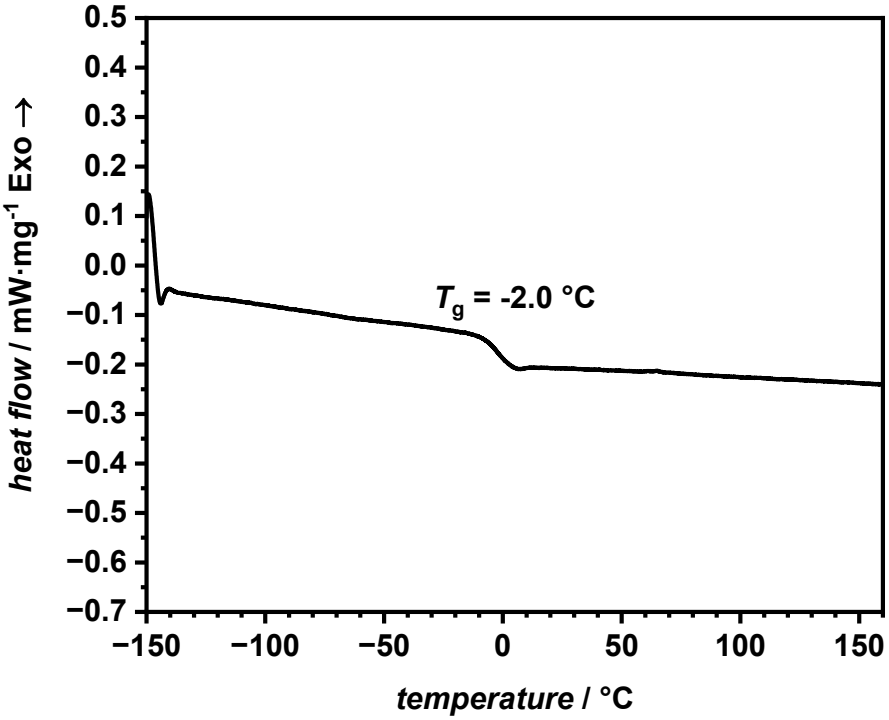

Figure 57 DSC of HNBR-12wt%LATP-LiTFSI film. Depicted is the 2nd heat run at a heating rate of 10 K min^{-1}.

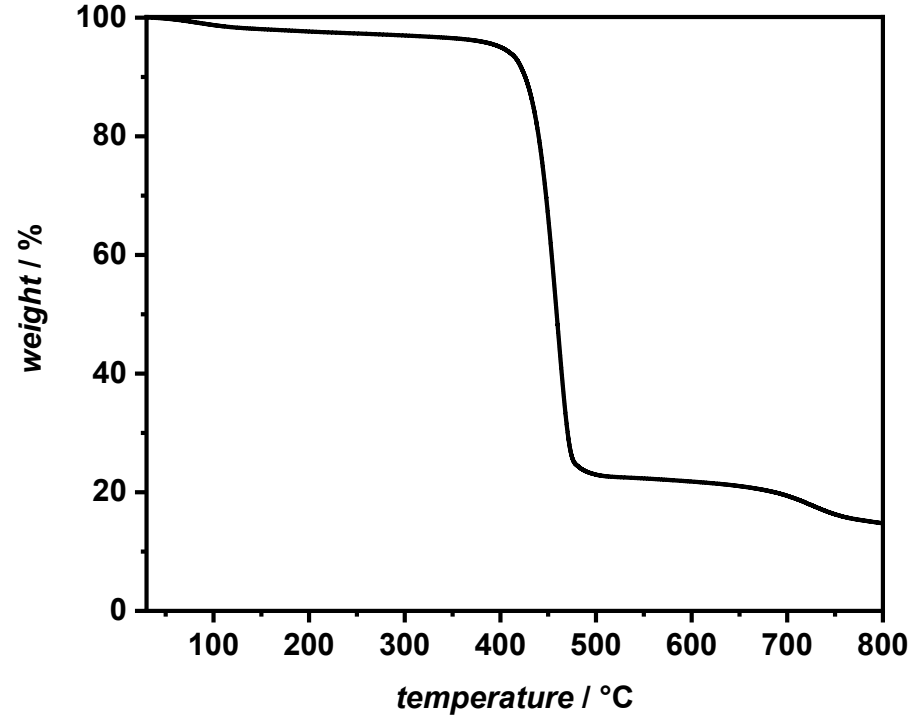

Figure 58 TGA of HNBR-12wt%LATP-LiTFSI film from 30 - 800 °C at a heating rate of 10 K min^{-1}.

HNBR-12wt%PAN@LATP-LiTFSI:

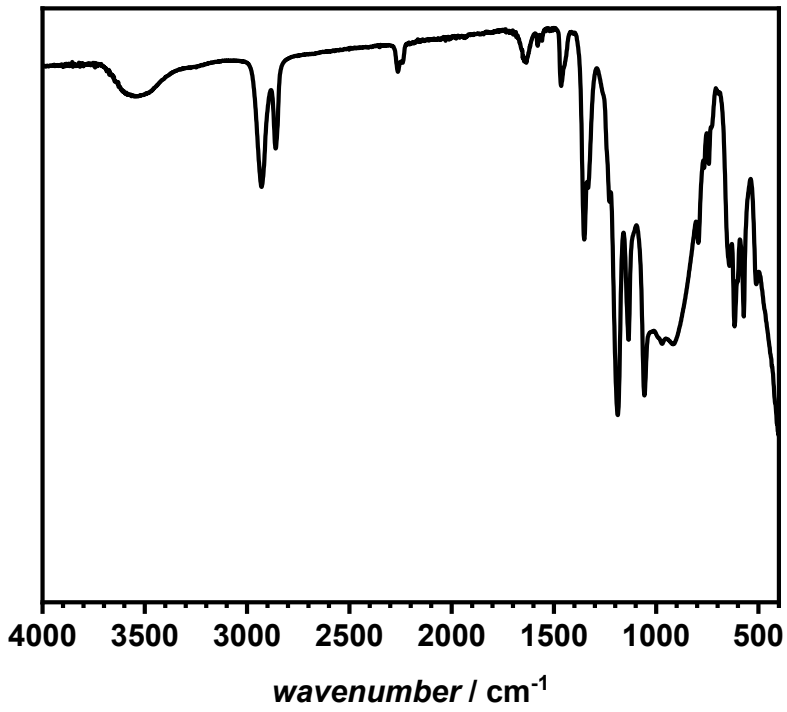

Figure 59 ATR-IR of HNBR-12wt%PAN@LATP-LiTFSI film after drying in a vacuum oven.

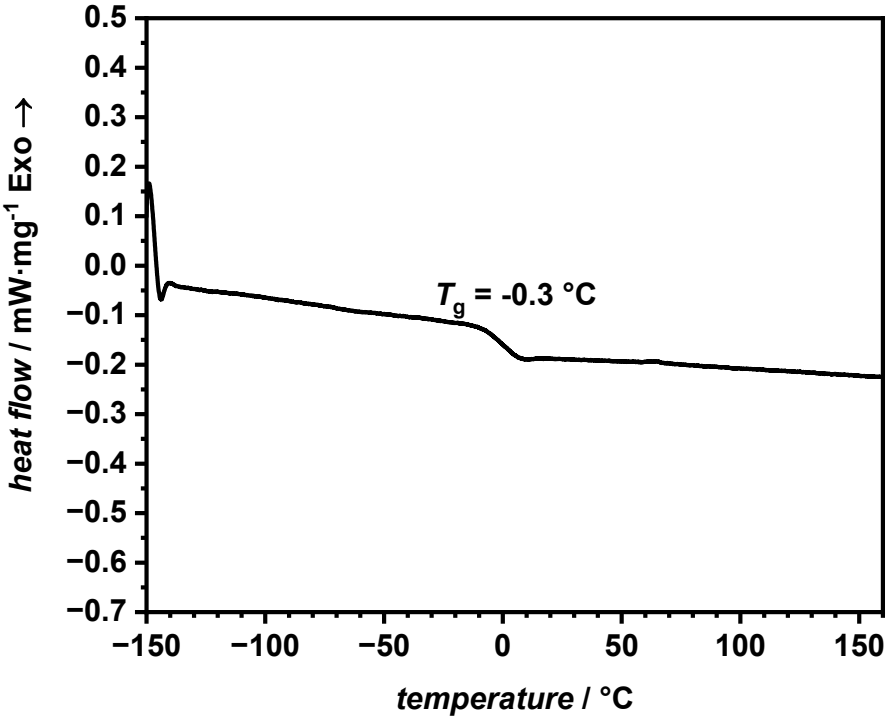

Figure 60 DSC of HNBR-12wt%PAN@LATP-LiTFSI film. Depicted is the 2nd heat run at a heating rate of 10 K min^{-1}.

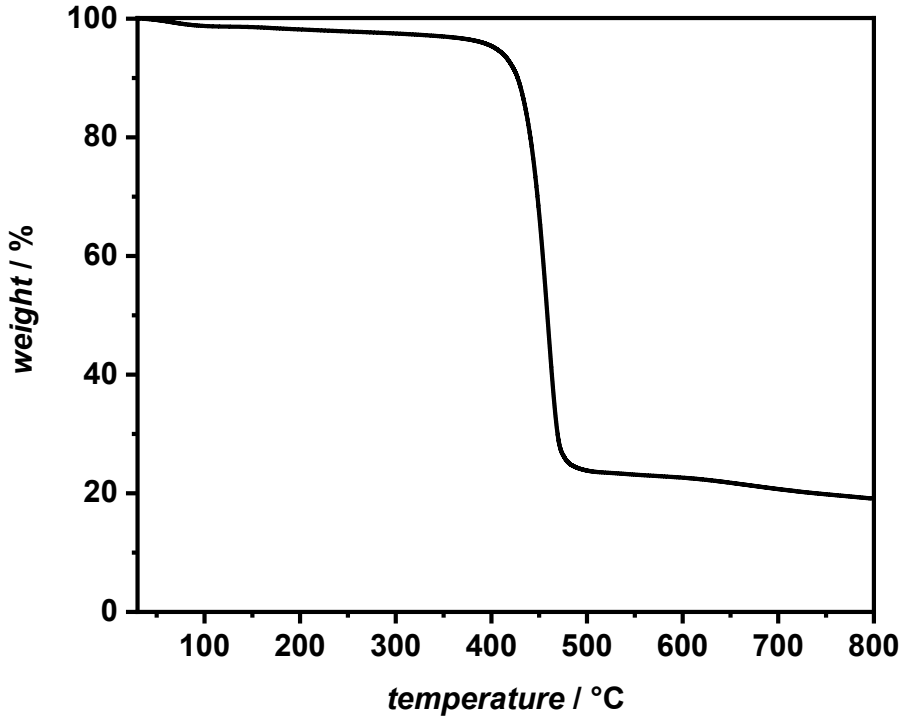

Figure 61 TGA of HNBR-12wt%PAN@LATP-LiTFSI film from 30 - 800 °C at a heating rate of 10 K min^{-1}.

6.3.1.3 SH-TMS coating of nanoparticles (SH@NP)

A mixture of ethanol (57 mL) and water (3 mL) in a flask is acidified with acetic acid to pH 4. Nanoparticles (6 g) are added, and the mixture put in an ultrasonic bath for 3 h. (3-Mercaptopropyl) trimethoxy silane (6.34 g, 6.00 mL, 32.4 mmol) is added and the mixture stirred at 70 °C for 18 h. The crude dispersion is centrifuged, and the silica nanoparticles are spread out on a crystallization dish. The dish is put into a vacuum oven at 120 °C and 7 mbar for 2 h. Afterwards the particles are washed three times with dichloromethane, centrifuged, separated, and dried in a vacuum oven (80 °C, 7 mbar).

SH@SiO$_2$:

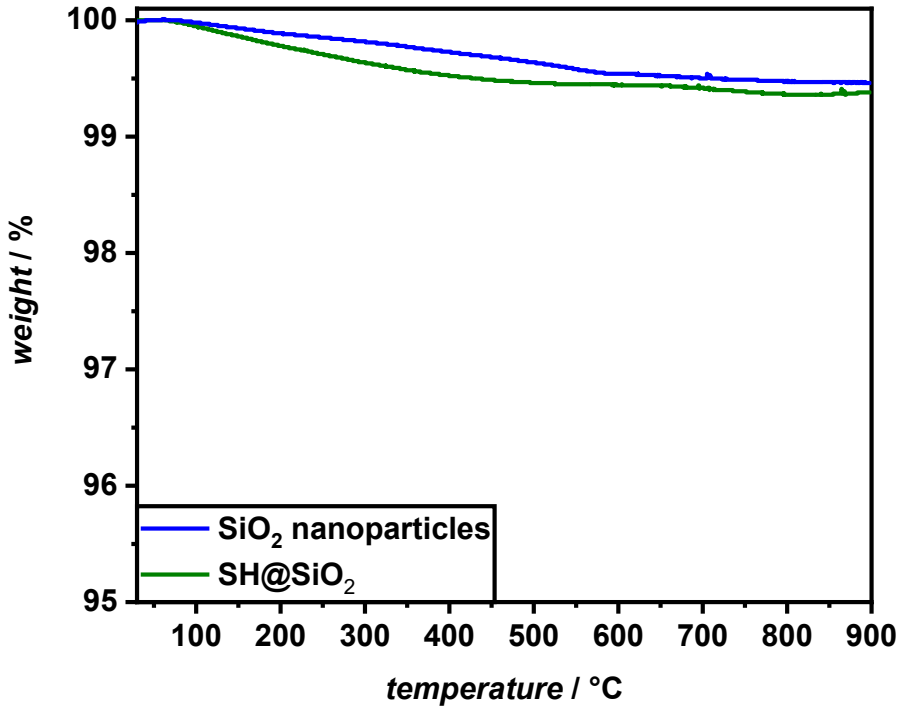

Figure 62 TGA measurements of pure silica nanoparticles and SH@SiO$_2$. SH@SiO$_2$ has a slightly higher mass loss but this within the error of the TGA. There is no discernible difference between the samples as the TGA is not precise enough to provide reproduceable values at mass losses below 0.5 % due to loss of adsorbed gasses and liquids to the surface of the particles.

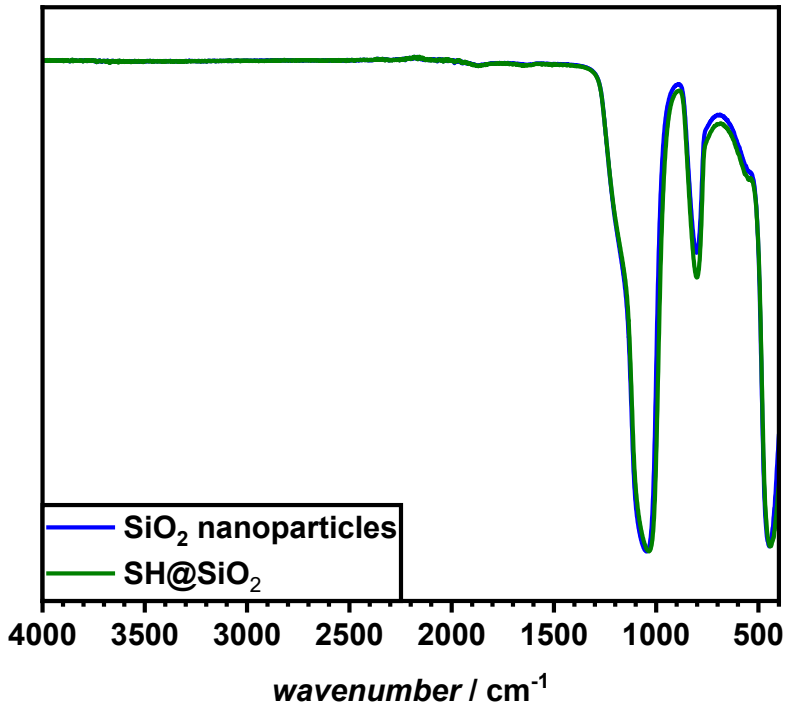

Figure 63 Normalized ATR-IR measurement of the pure silica nanoparticles and SH@SiO_2. There is no difference between the two samples in IR measurements.

6.3.1.4 PAN coating of SH@NP

SH@NP (500 mg) is dispersed in dry DMF (5 mL) and sonicated for 30 min. Acrylonitrile (50/250/500/1,000/2,500 mg, corresponding to 0.1/0.5/1/2/5 times the amount of SH@NP) and AIBN (125 mg) are added to the solution and the dispersion is degassed for 15 min with nitrogen gas. The mixture is heated to 60 °C and stirred for 24 h. The crude dispersion is centrifuged and samples for SEC measurements are taken. Particles are washed with DMF. Dried in a vacuum oven at 100 °C and 7 mbar for 48 h. Yields varied between 430 and 800 mg.

PAN@SiO_2:

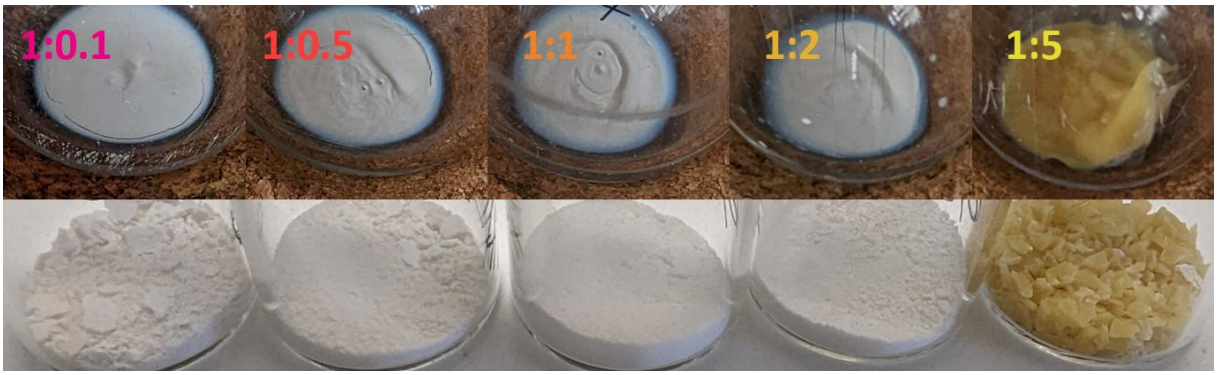

Figure 64 Pictures from PAN@SiO_2 after centrifugation (top) and after grinding in a mortar (bottom): Left to right: 1:0.1, 1:0.5, 1:1, 1:2, and 1:5 SH@SiO_2 particle mass to monomer mass ratio. All samples except 1:5 PAN@SiO_2 are off-white powders after grinding the crude particles in a mortar. 1:5 contains more PAN because assumably the high concentration of acrylonitrile triggered the Trommsdorff-Norrish-effect increasing the reaction rate significantly.

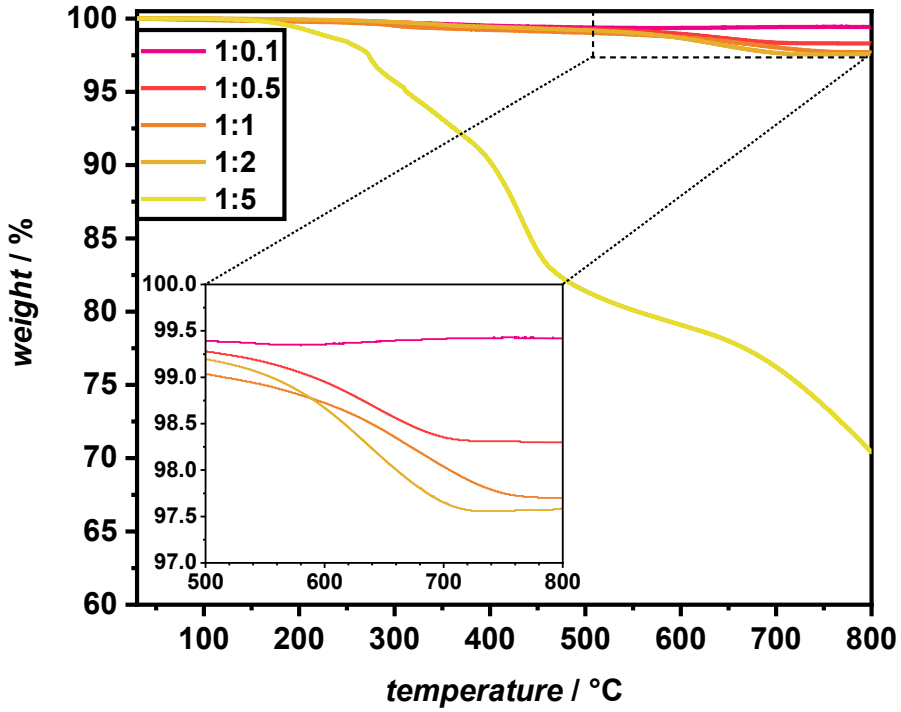

Figure 65 TGA measurements of all coated silica NPs from 30 - 800 °C at a heating rate of 10 K min^{-1}.

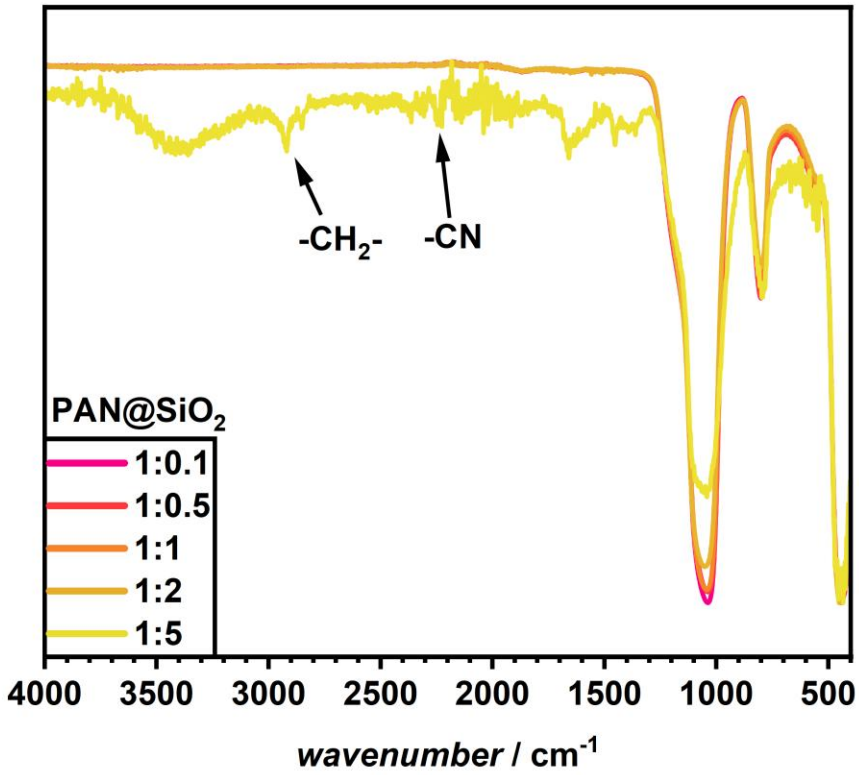

Figure 66 ATR-IR of PAN@SiO_2 1:0.1, 1:0.5, 1:1, 1:2, and 1:5. Only in 1:5 PAN can be identified with the vibrational band of CH_2 at 2,918 cm^{-1}, and CN at 2,242 cm^{-1}. The other samples are identical and show no bands indicating a coating.

Linear fits:

Table 14 Linear fit of the TGA mass loss and polymer chain length in the crude reaction mixture of PAN@SiO_2.

Ratio	M_n^{SEC} /g·mol^{-1}	TGA lowest value /%	TGA mass loss /%
1:0.1	900	99.34	0.66
1:0.5	2,400	98.29	1.71
1:1	4,000	97.63	2.37
1:2	4,900	97.56	2.44
1:5	9,500	63.29	36.71

Linear fit performed with Origin 2023. 1:5 excluded from the linear fit due to the Trommsdorff-Norrish-effect increasing the reaction rate significantly.

Fit function: $f(x) = ax + b$

Values obtained:

$a = 4.51974 * 10^{-4} \pm 8.2642 * 10^{-5}$

$b = 0.41648 \pm 0.28201$

$adjusted\ R^2 = 0.90599$

$Pearson's\ R = 0.96816$

Table 15 Values used to linear fit the coating thickness obtained from TEM pictures and polymer chain length in the crude reaction mixture of PAN@SiO_2.

Ratio	M_n^{SEC} / g·mol^{-1}	Coating thickness from TEM / nm	Error of coating thickness / nm
1:0.1	900	1.725	0.51
1:0.5	2,400	2.943	0.73
1:1	4,000	4.163	0.96
1:2	4,900	5.462	1.19
1:5	9,500	could not be measured in TEM	

Linear fit performed with Origin 2023. 1:5 excluded from the linear fit.

Fit function: $f(x) = ax + b$

Values obtained:

$a = 8.61591 * 10^{-4} \pm 4.18097 * 10^{-5}$

$b = 0.92855 \pm 0.09094$

$adjusted\ R^2 = 0.99065$

$Pearson's\ R = 0.99649$

6.3.1.5 Film preparation of HNBR-Li_6PS_5Cl

The synthesis of HNBR-LiTFSI films is similar to the described procedure in 6.3.1.1

Therban 4367 (390 mg) and LiTFSI (181.5 mg, [N]:[Li]=5:1) are dissolved in 5 mL acetone and stirred at high rpm overnight. The masses are calculated to result in a film thickness of approximately 50 µm. A PTFE ring with 10 cm diameter is placed on Mylar® foil and the polymer solution poured into the mold on a leveled surface. An upside-down beaker is put on top of the mold with a small slit for air exchange. The acetone is slowly evaporated for 24 h at r.t. and the film subsequently placed in a vacuum oven at 60 °C and 7 mbar. The film is carefully loosened from the Mylar® foil and placed in a glovebox.

Mixed HNBR- Li_6PS_5Cl films:

One dried HNBR-LiTFSI membrane is placed on Mylar® foil in a glovebox. 1 g Li_6PS_5Cl is distributed evenly atop the film. The film is folded to encapsule the Li_6PS_5Cl and placed between two sheets of Mylar® foil with the non-sticky side towards the film. The stack is placed in a hot-press and pressed at 80 °C and 40 MPa for 2 minutes. Afterwards, the obtained film is kneaded into a ball and the process is repeated 10 times until a homogeneous film is achieved. Films with 10 mm diameter are punched out and dried in an oven at 60 °C and 10^{-3} mbar.

Layered HNBR- Li_6PS_5Cl films:

One dried HNBR-LiTFSI membrane is placed on Mylar® foil in a glovebox. 1 g Li_6PS_5Cl is distributed evenly atop the film. Another HNBR-LiTFSI film placed on top of the Li_6PS_5Cl layer. A second Mylar® foil with the non-sticky side towards the film is added on top. The stack is placed in a hot-press and pressed at 80 °C and 40 MPa for 2 minutes. Films with 10 mm diameter are punched out and dried in an oven at 60 °C and 10^{-3} mbar.

6.3.2 Sulfur-Containing Polymers for Argyrodite-CPEs

6.3.2.1 Synthesis of P1

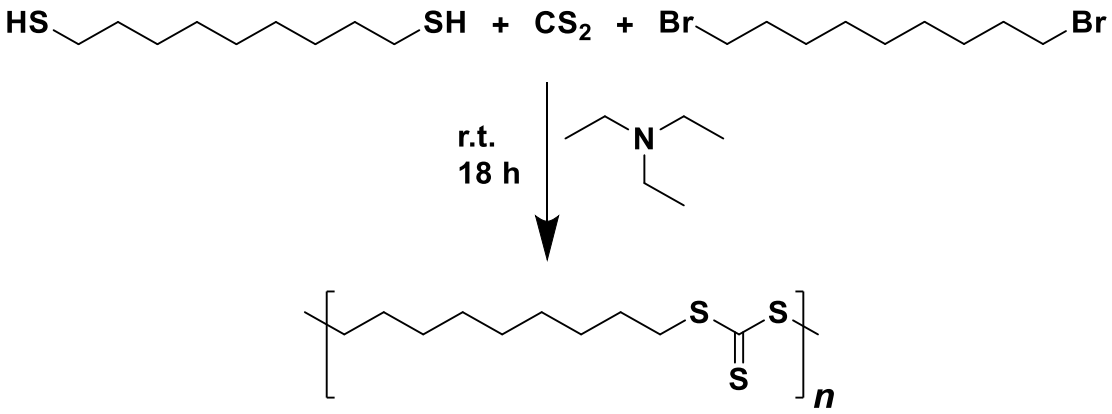

Nonane-1,9-dithiol (500 mg, 2.60 mmol, 1.00 eq.) and triethylamine (579 mg, 793 µL, 5.72 mmol, 2.20 eq.) are mixed in acetone (5 mL). CS_2 (416 mg, 330 µL, 5.46 mmol, 2.10 eq.) is added dropwise while stirring. After 1h 1,9-dibromononane (743 mg, 2.60 mmol, 1.00 eq.) is added dropwise and the mixture stirred for 18 h.

The yellow powder is filtered, washed with water/DCM, and dried under reduced pressure. Yield 1.09 g (89%)

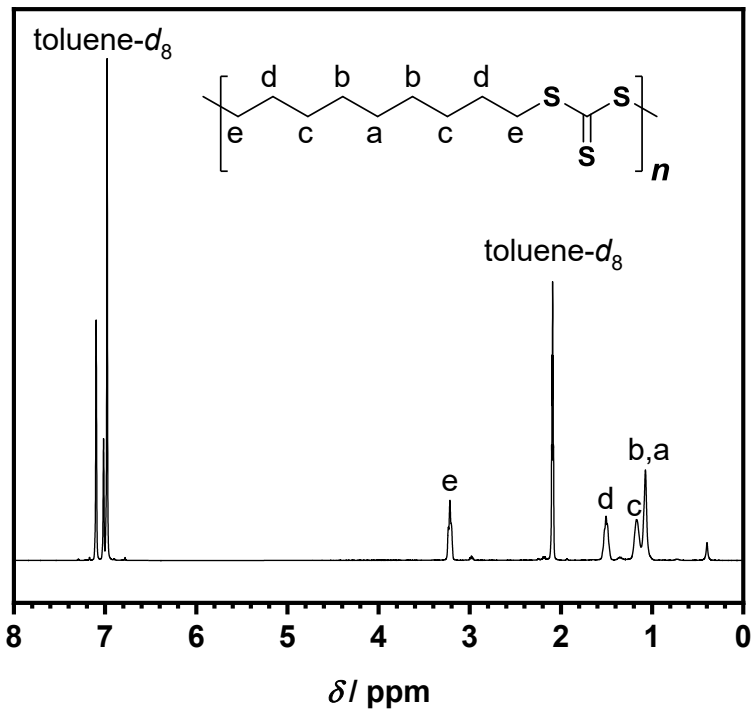

Figure 67 ^{1}H-NMR spectrum of P1 in toluene-d_8.

^{1}H NMR (400 MHz, toluene-d_8) δ / ppm: 3.26 - 3.16 (m, 4H), 1.50 (h, J = 6.3, 5.5 Hz, 4H), 1.22 - 1.13 (m, 4H), 1.11 - 1.04 (m, 6H).

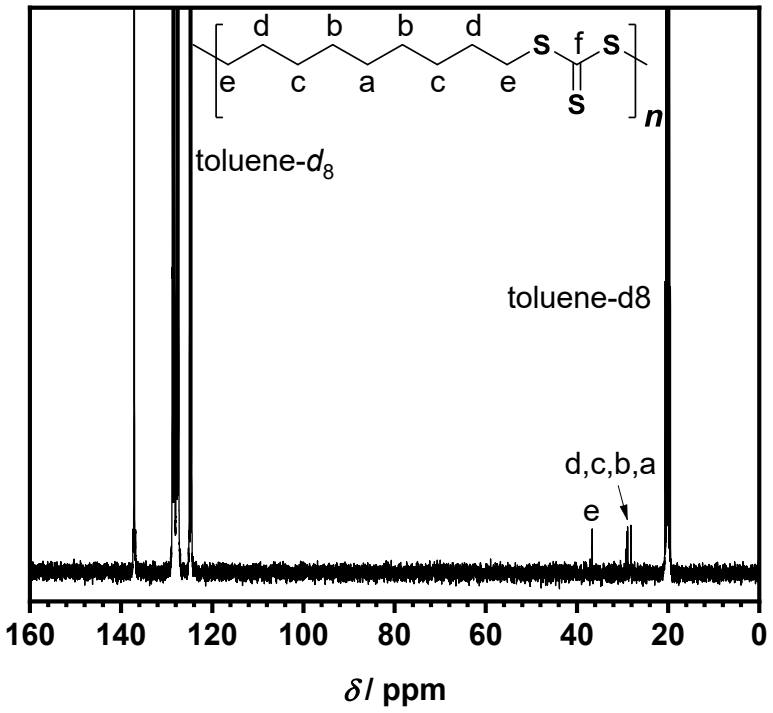

Figure 68 ^{13}C-NMR spectrum of P1 in toluene-d_8. Peak corresponding to f could not be identified.

^{13}C NMR (101 MHz, toluene-d_8) δ / ppm: 36.63, 29.27, 29.03, 28.84, 28.14.

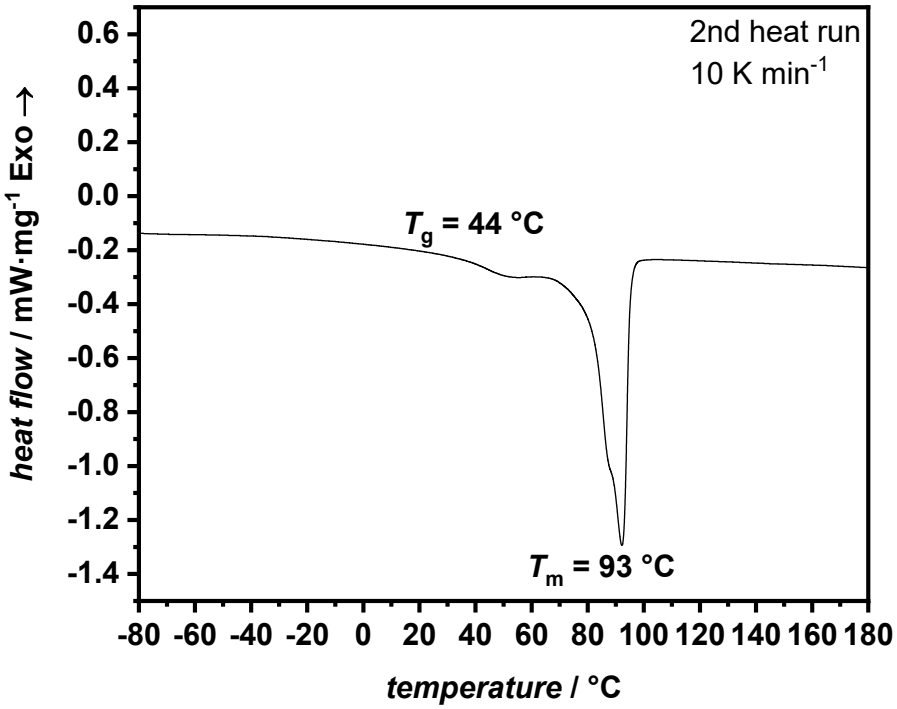

Figure 69 DSC of P1. Depicted is the 2nd heat run at a heating rate of 10 K min^{-1}.

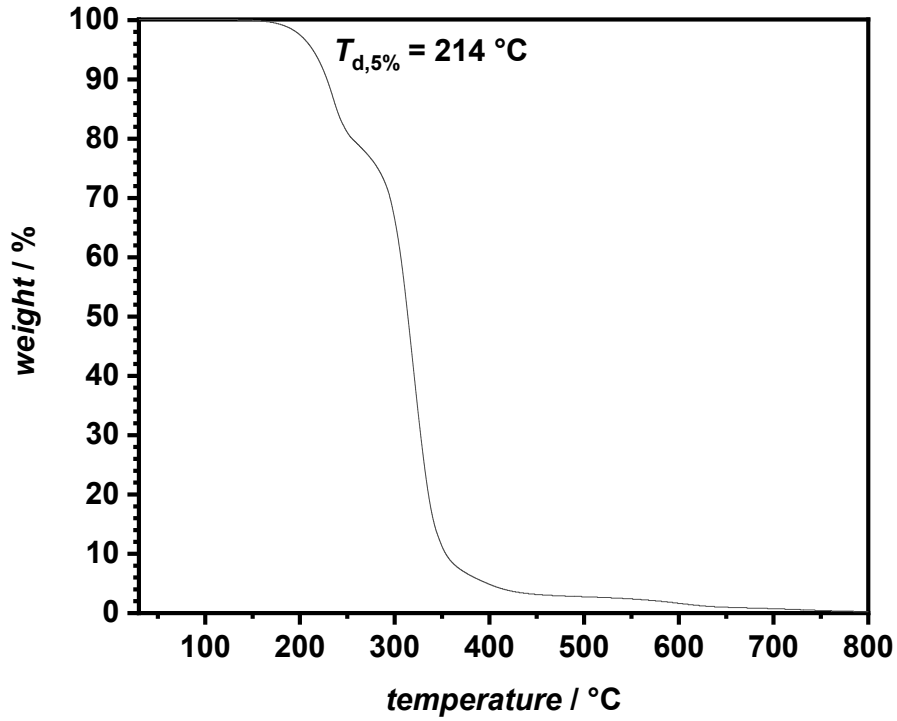

Figure 70 TGA of P1 from 30 - 800 °C at a heating rate of 10 K min^{-1}.

6.3.2.2 Synthesis of P2

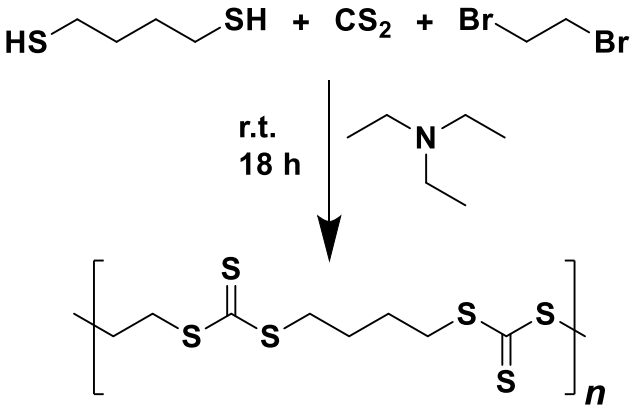

Butane-1,4-dithiol (2.08 g, 2.00 mL, 17.0 mmol, 1.00 eq.) and triethylamine (3.79 g, 5.20 mL, 37.5 mmol, 2.20 eq.) are mixed in acetone (15 mL). CS_2 (2.73 g, 2.16 mL, 35.8 mmol, 2.10 eq.) is added dropwise while stirring. After 1h 1,2-dibromoethane (3.20 g, 1.47 mL, 17.0 mmol, 1.00 eq.) is added dropwise and the mixture stirred for 18 h. The yellow powder is filtered, washed with water/DCM, and dried under reduced pressure. Yield 4.32 g (82%)

$^{1}H/^{13}C$-NMR spectra could not be recorded due to insolubility of the polymer.

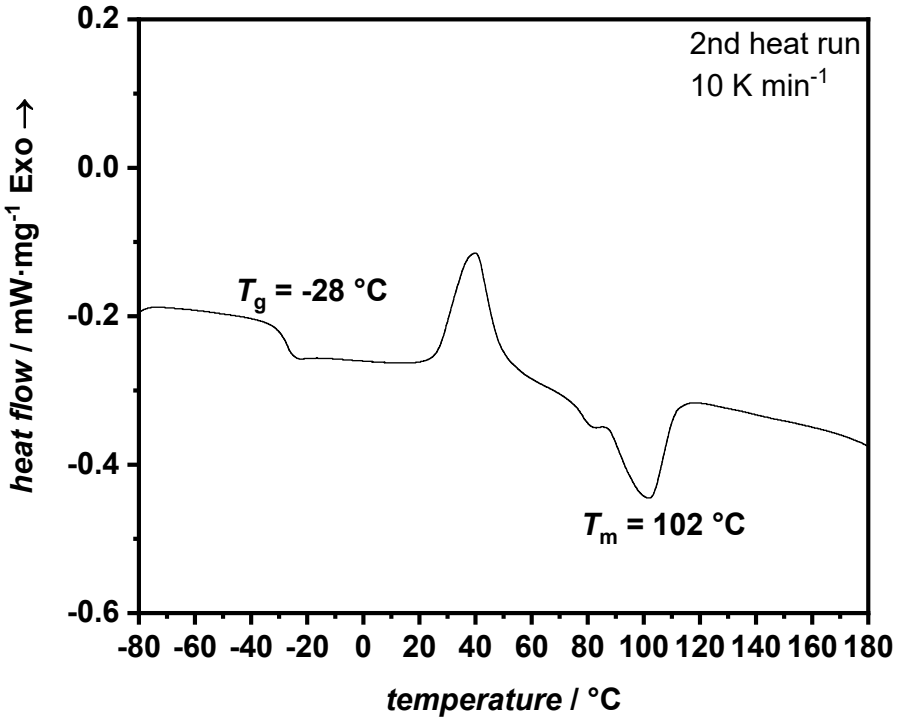

Figure 71 DSC of P2. Depicted is the 2nd heat run at a heating rate of 10 K min^{-1}.

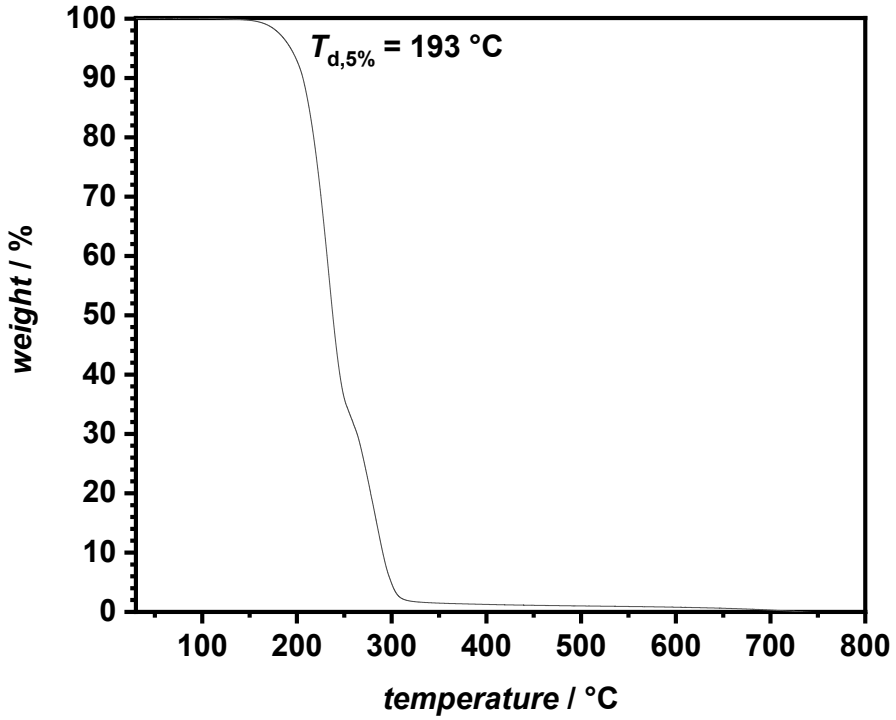

Figure 72 TGA of P2 from 30 - 800 °C at a heating rate of 10 K min^{-1}.

6.3.2.3 Synthesis of P3

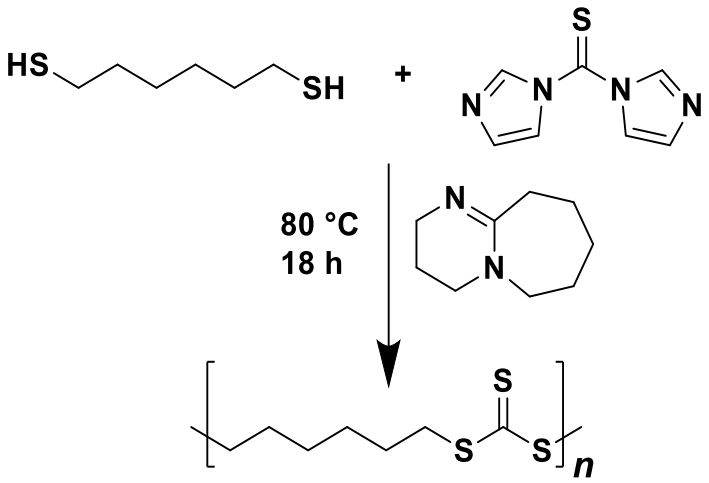

First, in a glovebox, a 5.00 mL crimp vial is charged with thiocarbonyldiimidazole (622 mg, 3.49 mmol, 1.05 eq.) and a stirring bar. After transferring the vial out of the glovebox and purging the reaction vessel with nitrogen for 5 minutes, dry DMSO (4.00 mL), hexane-1,6-dithiol (500 mg, 3.33 mmol, 1.00 eq.), and 1,8-diazabicyclo(5.4.0)undec-7-ene (DBU) (1.02 g, 6.69 mmol, 2.01 eq.) are sequentially added under a continuous nitrogen flow. Yellow solid precipitates immediately. The temperature is increased slowly to 80 °C until everything is dissolved.

Mixture is stirred overnight. The orange solid is filtered and washed with water. Afterwards, the solid is precipitated 2x from hot chloroform into ice-cold methanol. The polymer is dried in a vacuum oven at 45 °C for 24 h. Yield 350 mg (47%)

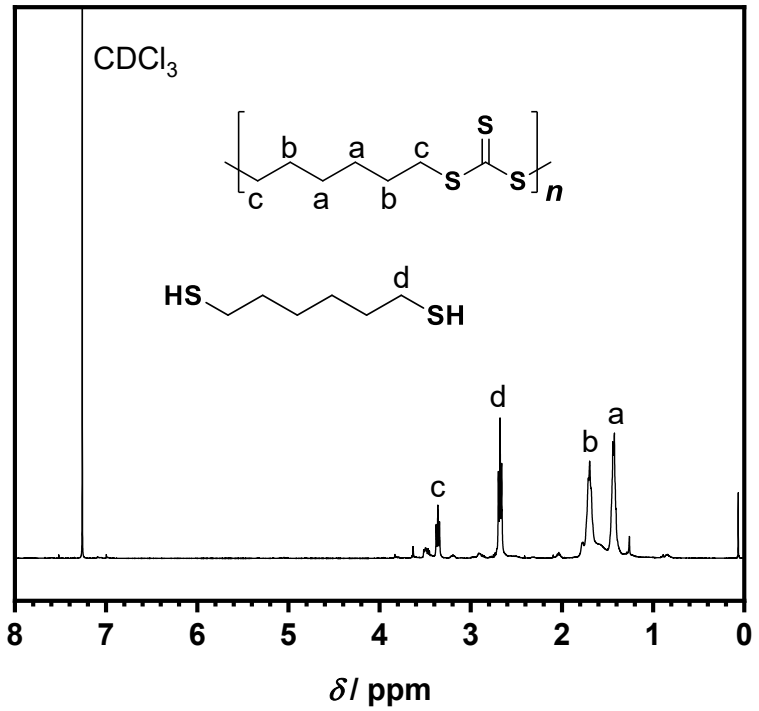

Figure 73 ^{1}H-NMR spectrum of P3 in $CDCl_3$. The observed d peak of the starting material indicates low conversion rates.

^{1}H NMR (400 MHz, $CDCl_3$) δ / ppm: 3.36 (t, J = 6.7 Hz, 2H), 2.68 (t, J = 7.4 Hz, 4H), 1.79 - 1.64 (m, 8H), 1.50 - 1.39 (m, 8H).

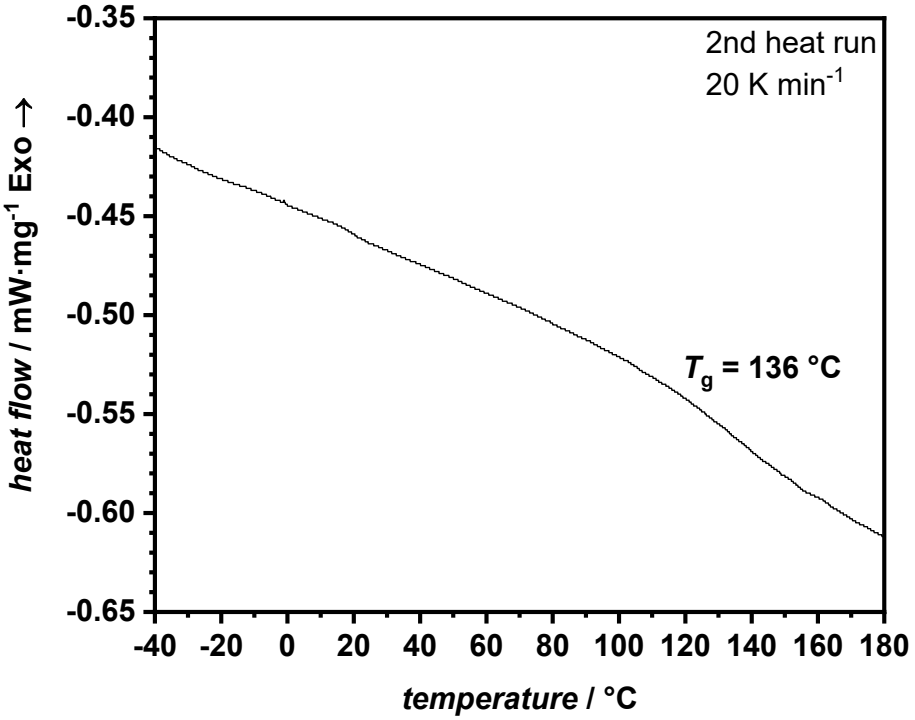

Figure 74 DSC of P3. Depicted is the 2nd heat run at a heating rate of 20 K min^{-1}.

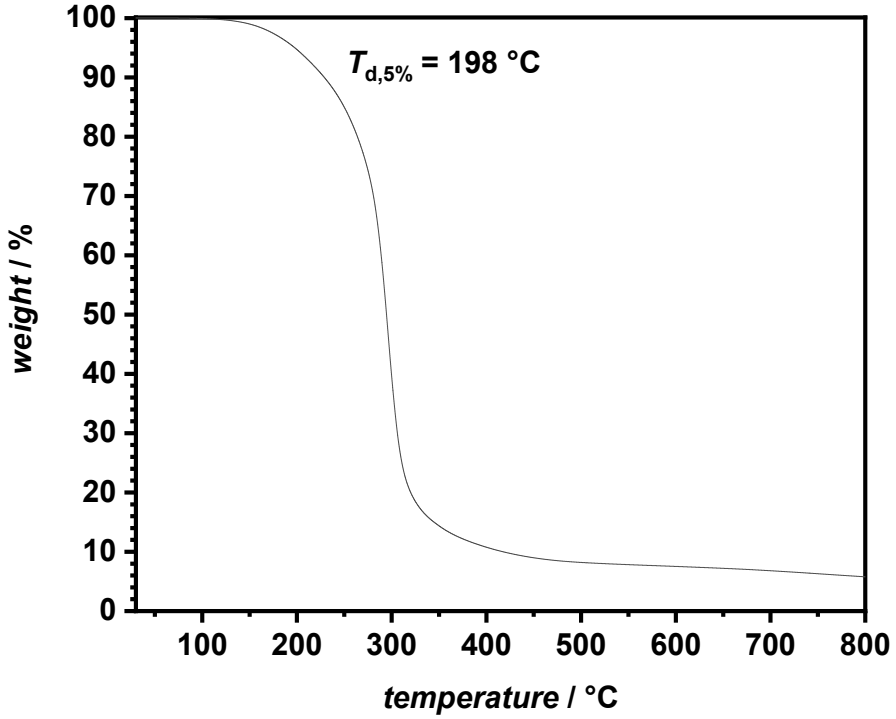

Figure 75 TGA of P3 from 30 - 800 °C at a heating rate of 10 K min^{-1}.

6.3.2.4 Synthesis of P4

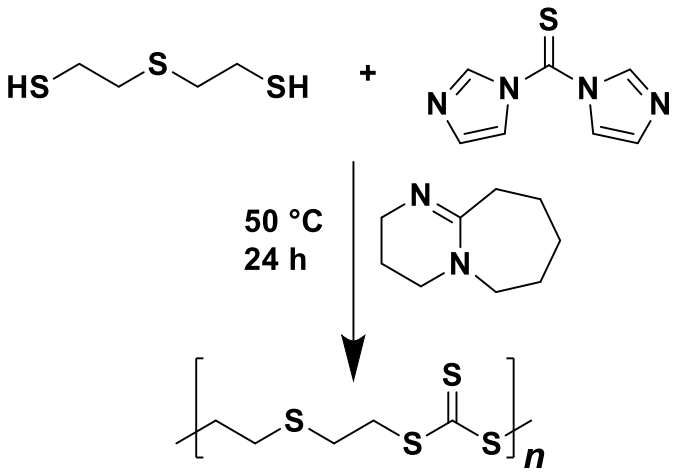

Thiocarbonyldiimidazole (823 mg, 4.62 mmol, 1.00 eq.) and DBU (1.48 g, 9.70 mmol, 2.10 eq.) are added to a crimp vial and dissolved in DMF (4 mL in an ice bath under inert atmosphere. 2-(2-Mercaptoethylthio)ethanethiol (713 mg, 4.62 mmol, 1.00 eq.) is added dropwise slowly under constant stirring. The mixture is stirred and heated to 50 °C for 24h. Solid precipitates and is washed with methanol/DCM/ethyl acetate. Yield 90 mg (10%)

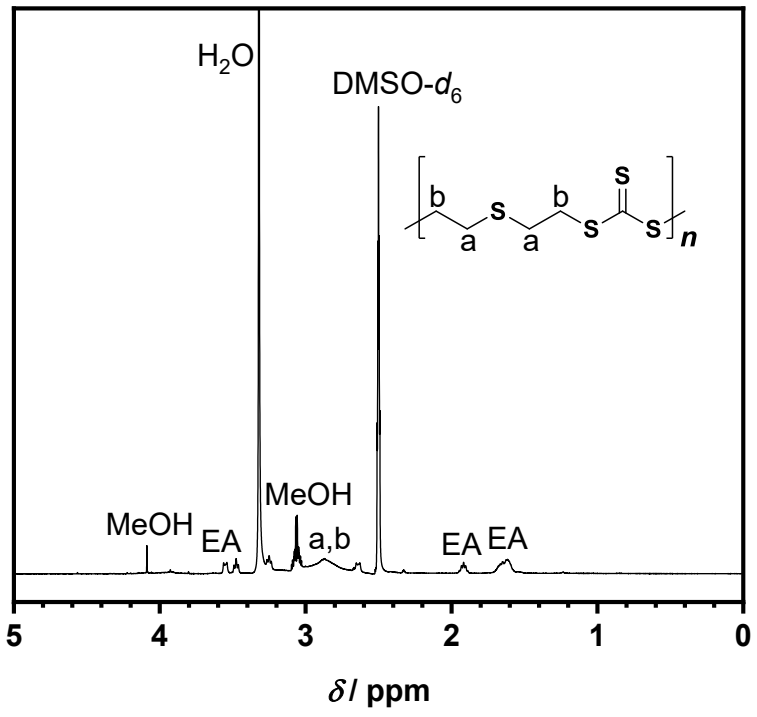

Figure 76 ^{1}H-NMR spectrum of P4 in DMSO-d_6.

^{1}H NMR (400 MHz, DMSO-d_6) δ / ppm: 3.00 - 2.72 (m, 4H).

Due to low yields no further analysis could be carried out.

6.3.2.5 Synthesis of P5

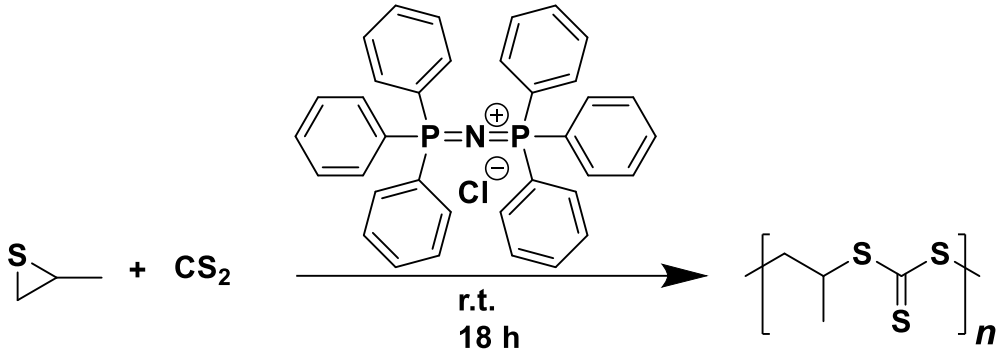

Propylene sulfide (1.29 g, 17.4 mmol, 500 eq.) and CS_2 (2.65 g, 34.8 mmol, 1000 eq.) are degassed with argon and transferred into a glovebox. Bis(triphenylphosphoranylidene)ammonium chloride (PPNCl) (20.0 mg, 34.8 µmol, 1.00 eq.) is also transferred into a glovebox. A flask is dried with a heat gun under vacuum and immediately transferred into the glovebox. Propylene sulfide and CS_2 are added to the flask and subsequently the PPNCl is added. The mixture is stirred for 18 h at r.t. The flask is taken from the glovebox and quenched with 5% HCl. The yellow viscous liquid is precipitated into EtOH. The polymer is washed with ethanol 3x and dried in a vacuum oven at 45 °C.

Table 16 Masses for all synthesis attempts for P5.

Reaction	Propylene sulfide	CS_2	PPNCl	Yield
HSSE133	1.29 g	2.65 g	20.0 mg	2.35 g (59 %)
HSSE137	6.46 g	13.3 g	100 mg	14.9 g (75 %)
HSSE146	23.5 g	48.3 g	364 mg	36.5 g (51 %)

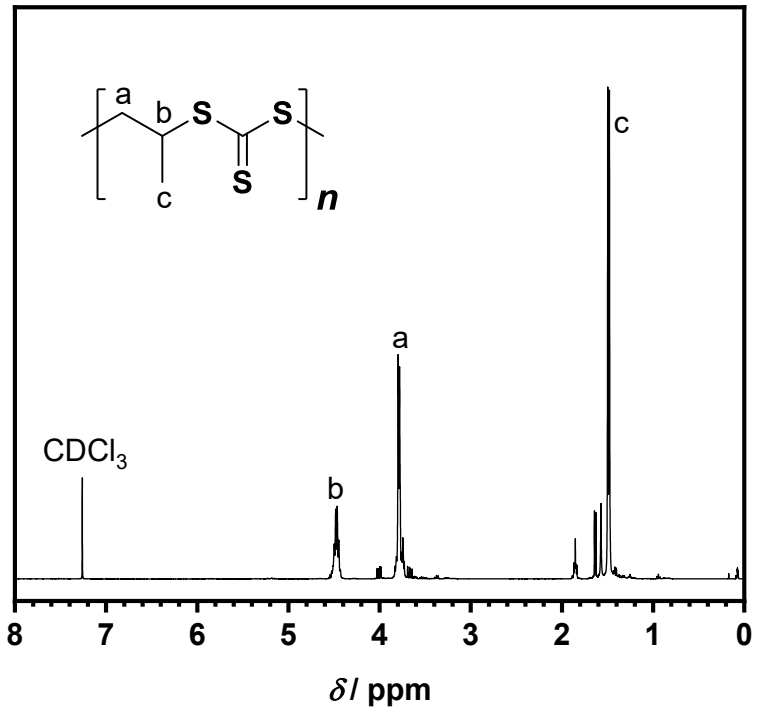

Figure 77 ^{1}H-NMR spectrum of P5 in $CDCl_3$.

^{1}H NMR (400 MHz, $CDCl_3$) δ / ppm: 4.56 - 4.40 (m, 1H), 4.18 - 3.60 (m, 2H), 1.49 (d, J = 7.0 Hz, 3H).

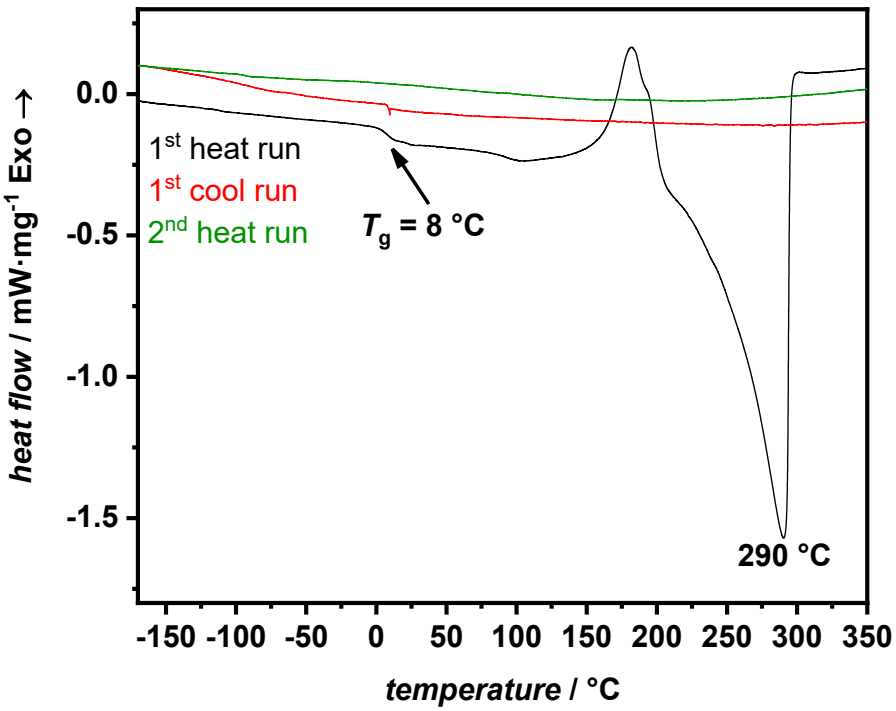

Figure 78 DSC of P5. Depicted all steps at a heating rate of 10 K min^{-1}. Notably, there is no melting peak after the first heat run. This is due to degradation of the polymer above 170 °C triggering a depolymerization reaction.

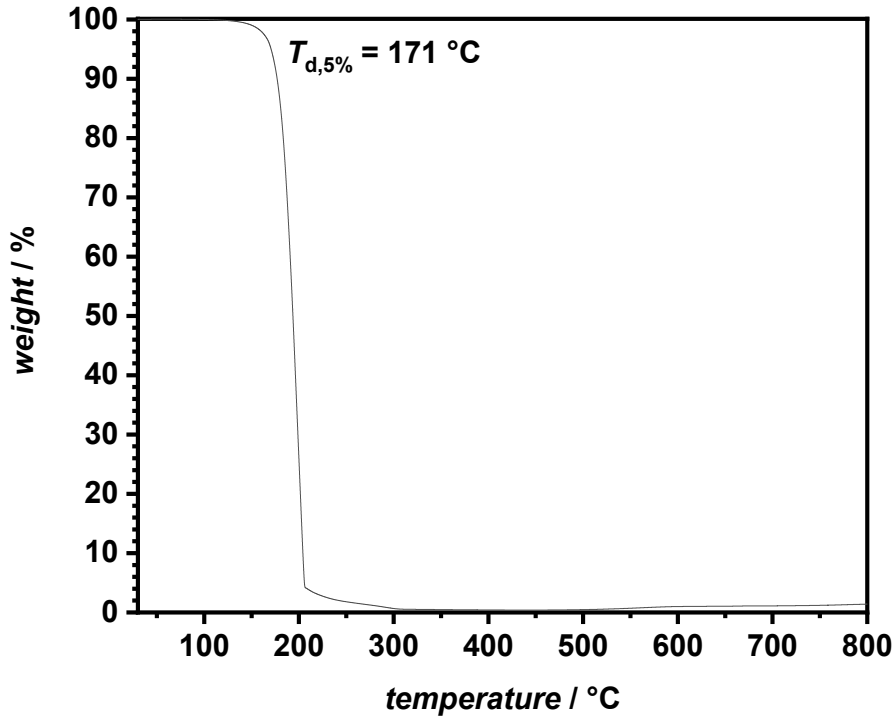

Figure 79 TGA of P5 from 30 - 800 °C at a heating rate of 10 K min^{-1}.

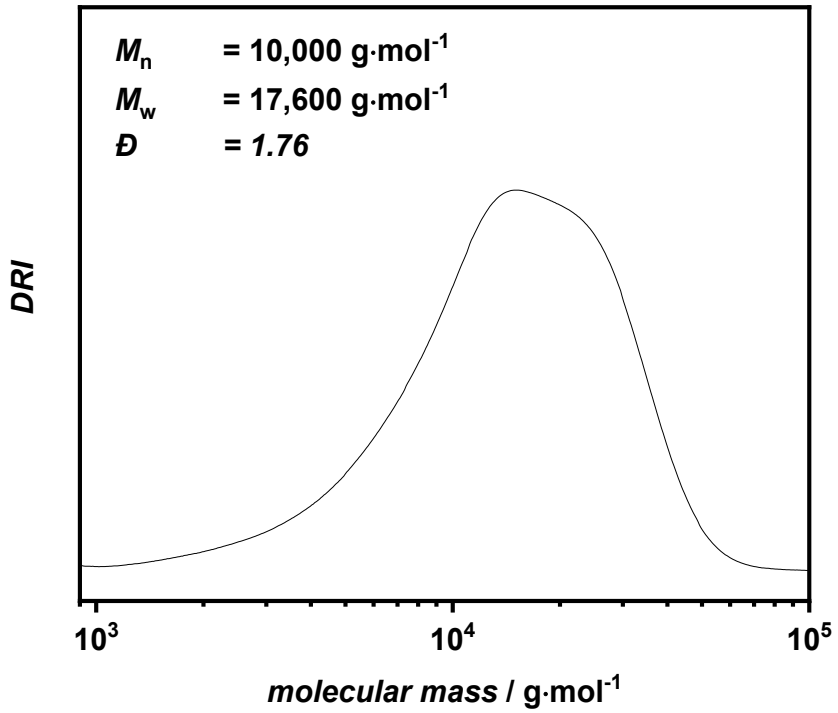

Figure 80 Exemplary THF-SEC of P5 (HSSE146). PMMA standard.

Table 17 List of SEC measurements for all synthesized P5 polymers. Performed in THF-SEC with PMMA standards.

Polymer	M_n / g mol^{-1}	M_w / g mol^{-1}	Đ
HSSE133	8,500	13,900	1.63
HSSE137	9,200	13,100	1.43
HSSE146	10,000	17,600	1.76

6.3.2.6 Synthesis of P6

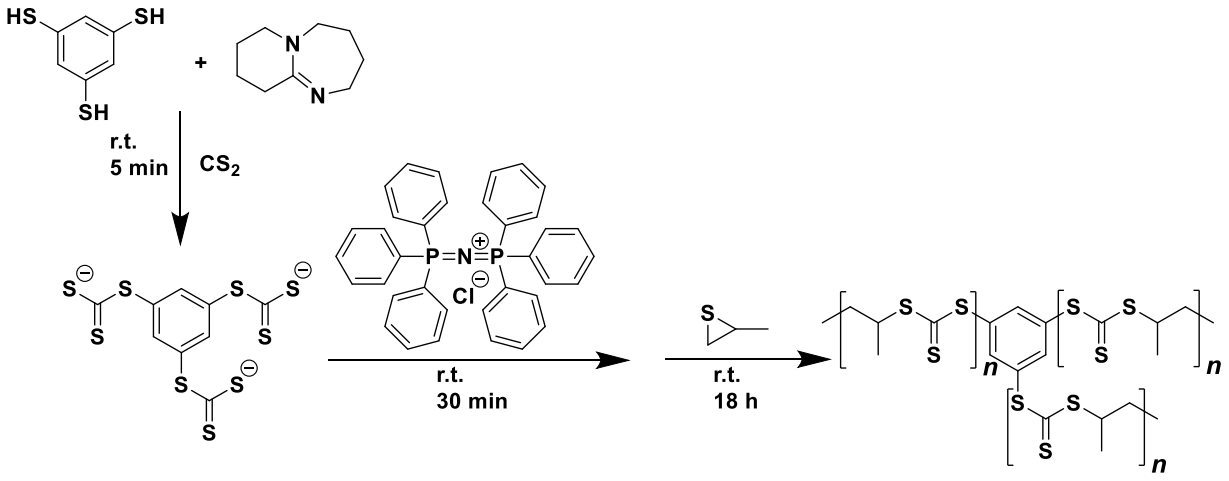

In a glovebox benzene-1,3,5-trithiol (10.0 mg, 57.4 µmol, 1.00 eq.) and DBU (26.2 mg, 172 µmol, 3.00 eq.) are added to a flask. CS_2 (39.3 g, 31.2 mL, 516 mmol, 9000 eq.) is added and the mixture stirred for 5 min. PPNCl (296 mg, 516 µmol, 9.00 eq.) is added and again stirred for 30min. Propylene sulfide (19.1 g, 20.4 mL, 258 mmol, 4500 eq.) is added and the mixture stirred for 18 h. 5% HCl is added to the mixture (20 mL) to quench the reaction. The yellow viscous liquid is precipitated into EtOH. The polymer is washed with ethanol 3x and dried in a vacuum oven at 45 °C.

Table 18 Masses for all synthesis attempts for P6.

Reaction	Benzene-1,3,5-trithiol	DBU	Propylene sulfide	CS_2	PPNCl	Yield
HSSE160	10.0 mg	26.2 mg	6.38 g	13.1 g	98.8 mg	2.73 g (14 %)
HSSE165	10.0 mg	26.2 mg	19.1 g	39.3 g	296 mg	6.46 g (11 %)

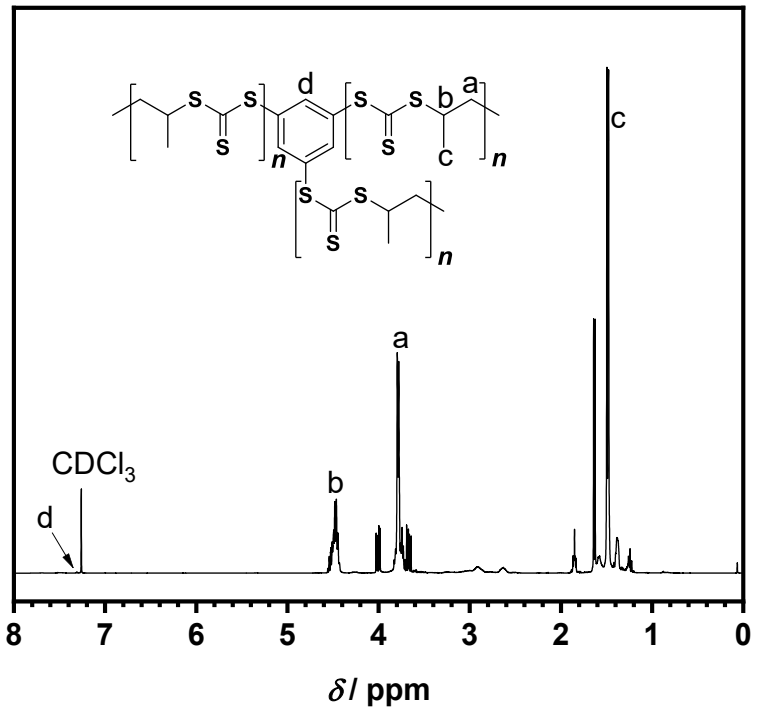

Figure 81 ^{1}H-NMR spectrum of P6 in $CDCl_3$.

^{1}H NMR (400 MHz, $CDCl_3$) δ / ppm: 4.56 - 4.40 (m, 1H), 4.18 - 3.60 (m, 2H), 1.49 (d, J = 7.0 Hz, 3H).

DSC and TGA data is identical to P5.

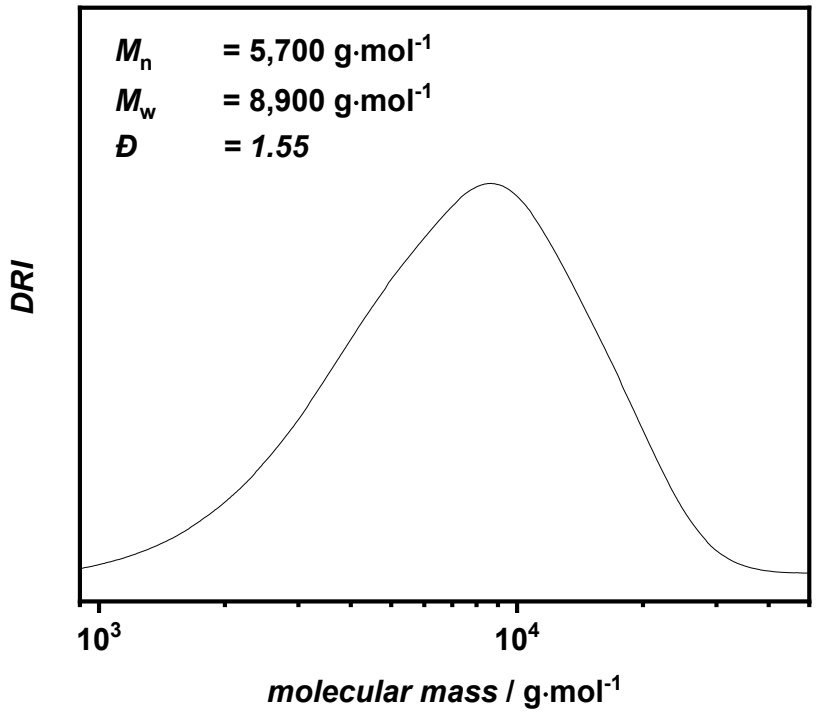

Figure 82 Exemplary THF-SEC of P6 (HSSE160). PMMA standard.

Table 19 List of SEC measurements for all synthesized **P6** polymers. Performed in THF-SEC with PMMA standards.

Polymer	M_n / g mol^{-1}	M_w / g mol^{-1}	Đ
HSSE160	5,700	8,900	1.55
HSSE165	6,300	10,300	1.64

6.3.2.7 Synthesis of P7

Synthesis of propylene sulfide

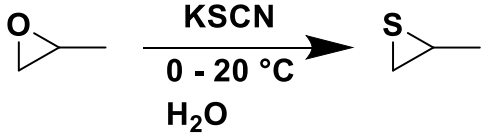

In a 500 ml round-bottomed flask equipped with a magnetic stir bar, potassium thiocyanate (167 g, 1.72 mol, 2.0 eq.) is dispersed into 300 mL water. After the above salt fully dissolved, propylene oxide (50 g, 0.86 mol, 1.0 eq.) is added dropwise to the solution stirred for 2 h at 0 ℃. Then, the solution is stirred overnight at room

temperature. Propylene sulfide is collected by separating the hydrophobic phase from aqueous phase and dried over anhydrous $MgSO_4$. The filtered liquid is used without further purification. Yield 51.7 g (81 %)

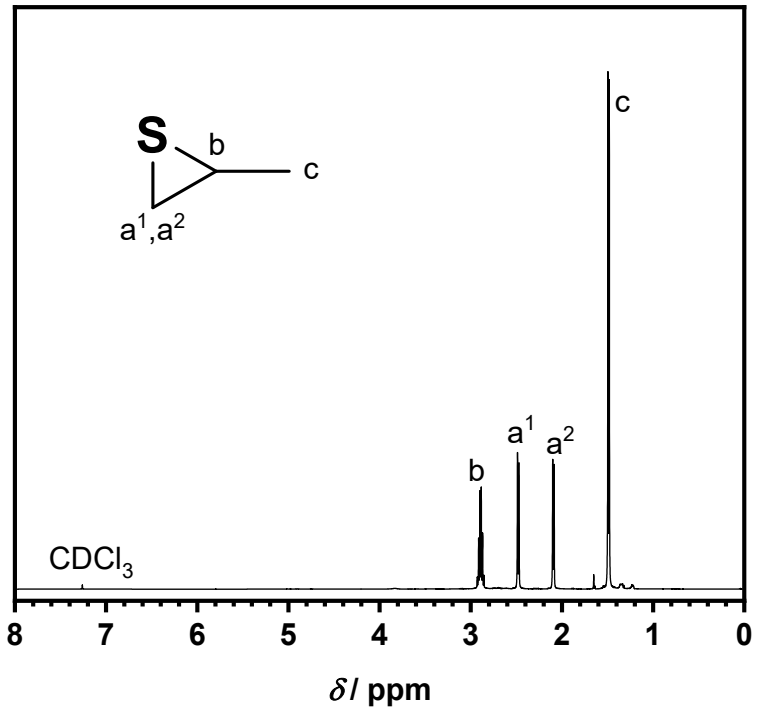

Figure 83 ^{1}H-NMR spectrum of propylene sulfide in $CDCl_3$.

^{1}H NMR (400 MHz, $CDCl_3$) δ / ppm: 2.89 (h, J = 5.8 Hz, 1H), 2.48 (dd, J = 6.3, 1.1 Hz, 1H), 2.09 (dd, J = 5.7, 1.1 Hz, 1H), 1.49 (d, J = 5.8 Hz, 3H).

Polymerization of propylene sulfide (P7)

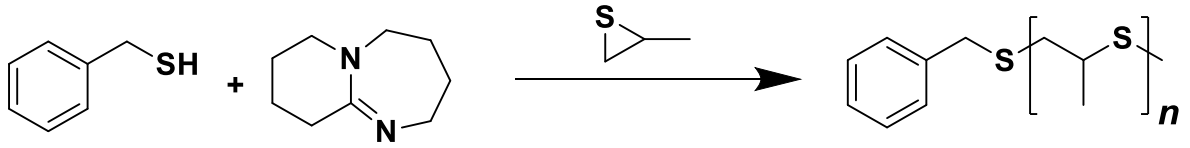

In general, benzyl mercaptan (1 eq.) and DBU (1 eq.) are mixed as an initiator solution and added to propylene sulfide in a closed vial or flask. The reaction is quenched once no more viscosity change is observed with 5 % HCl. The obtained colorless, viscous polymer is dissolved in DCM and precipitated in ethanol 3x. For the exact masses, solvents and conditions refer to **Table 20**. Yield (P7-7) 35.0 g (48 %)

Table 20 Conditions for all attempted polymerization of propylene sulfide to P7. Entries in italics reacted violently resulting in loss of product.

Polymer	Solvent	Benzyl mercaptan	Propylene sulfide equivalents	temperature
P7-1	MeCN 3 mL	10 mg	200	25 °C
P7-2	-	10 mg	200	25 °C
P7-3	THF 3 mL	10 mg	200	25 °C
P7-4	$CHCl_3$ 6 mL	10 mg	2000	25 °C
P7-5	-	200 mg	20	0 °C
P7-6	-	20 mg	200	0 °C
P7-7	-	247 mg	500	0 °C

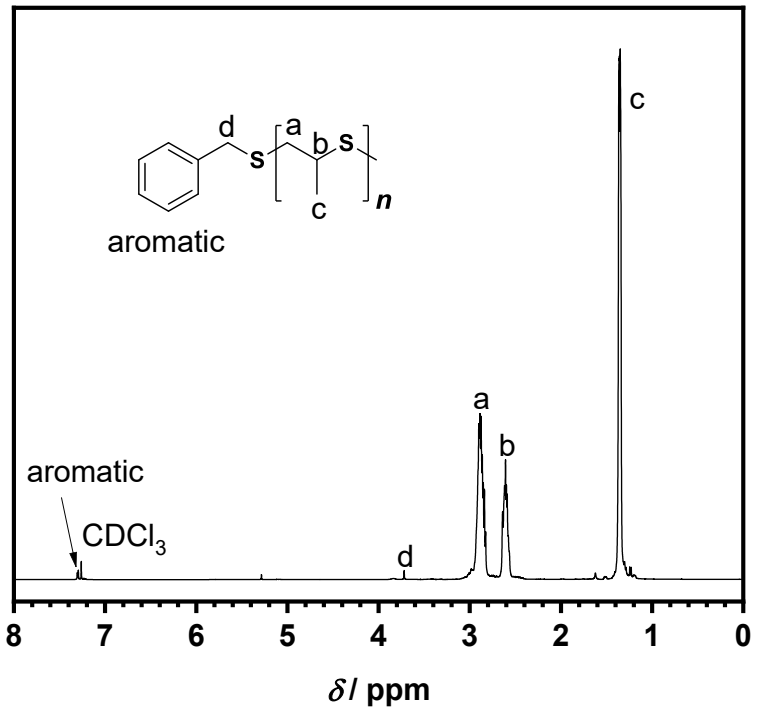

Figure 84 ^{1}H-NMR spectrum of P7 in $CDCl_3$.

^{1}H NMR (400 MHz, $CDCl_3$) δ / ppm: 7.36 - 7.28 (m, 0H), 3.15 - 2.74 (m, 2H), 2.69 - 2.56 (m, 1H), 1.37 (dd, J = 6.7, 3.0 Hz, 3H).

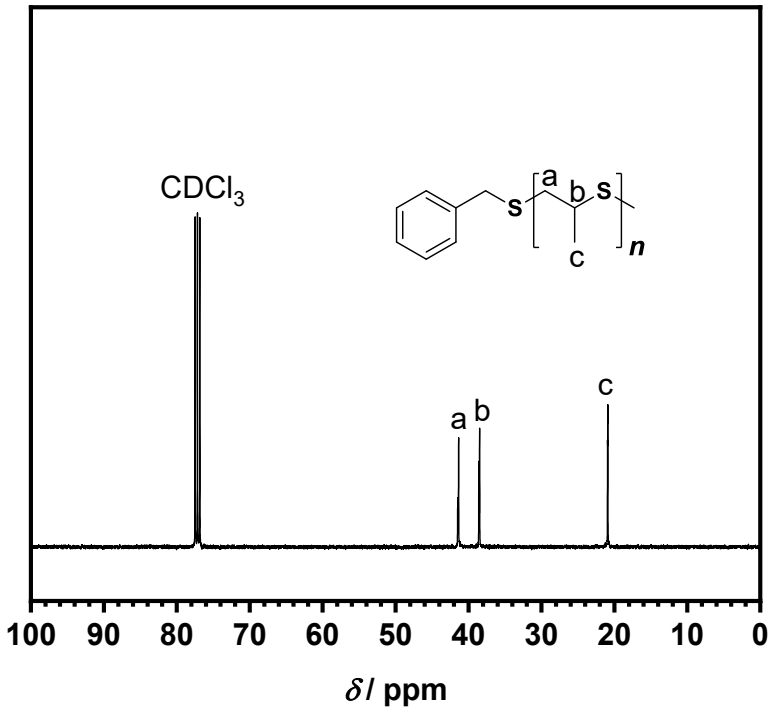

Figure 85 ^{13}C-NMR spectrum of P7 in $CDCl_3$.

^{13}C NMR (101 MHz, $CDCl_3$) δ / ppm: 41.55 - 41.14, 38.64, 21.10.

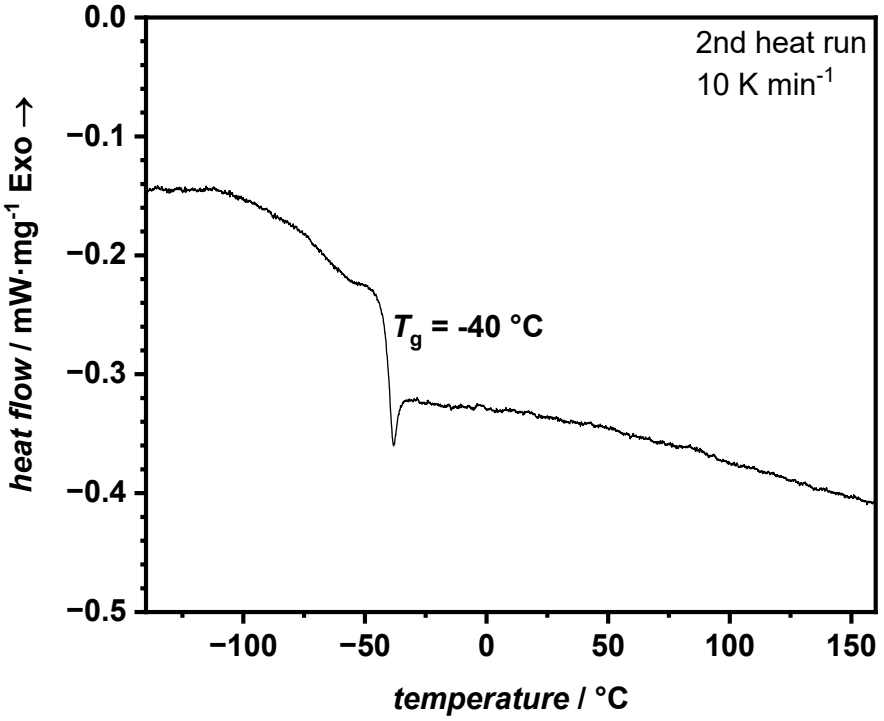

Figure 86 DSC of P7. Depicted is the 2nd heat run at a heating rate of 10 K min^{-1}.

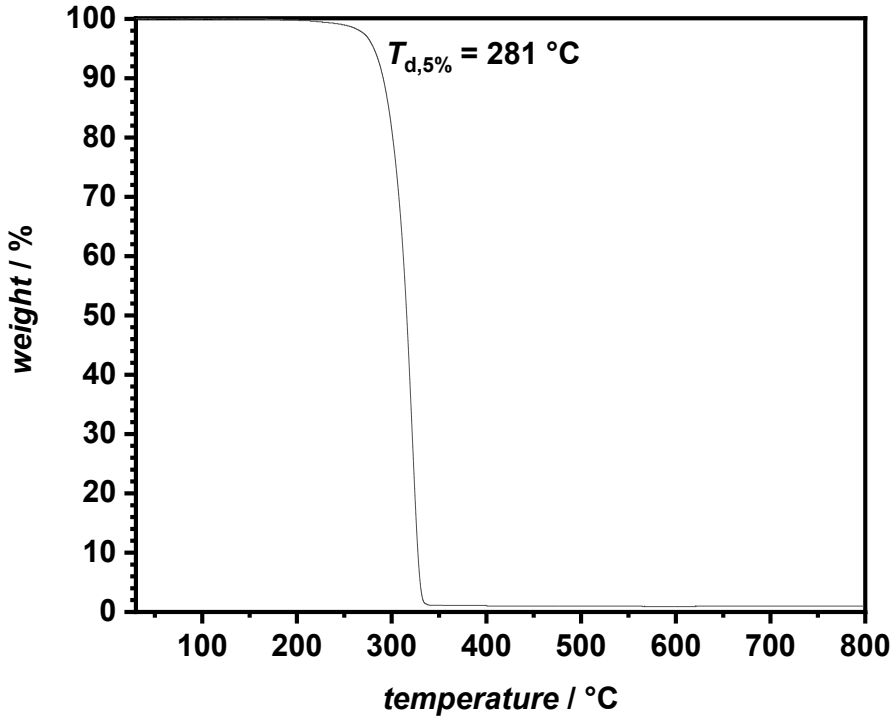

Figure 87 TGA of P7 from 30 - 800 °C at a heating rate of 10 K min^{-1}.

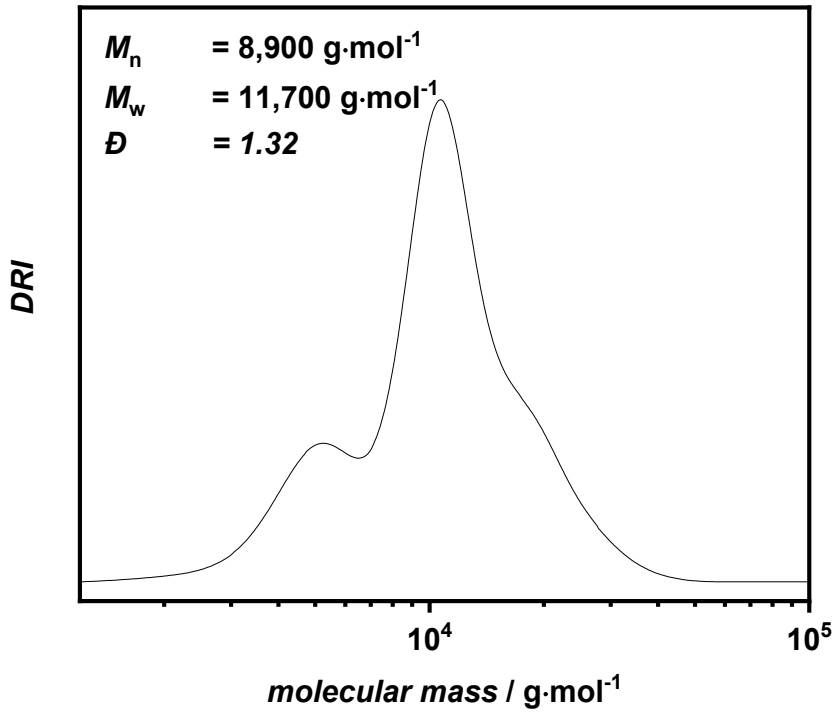

Figure 88 Exemplary THF-SEC of P7 (P7-7). PMMA standard.

Table 21 List of SEC measurements for all synthesized P7 polymers. Performed in THF-SEC with PMMA standards.

Polymer	M_n / g mol^{-1}	M_w / g mol^{-1}	$Đ$
P7-1	8,000	9,500	1.19
P7-2	8,400	11,500	1.36
P7-3	7,600	8,900	1.18
P7-6	9,000	10,400	1.16
P7-7	8,900	11,700	1.32

6.3.2.8 $Li_{5.5}PS_{4.5}Cl_{1.5}$ Synthesis

Synthesis and characterization of $Li_{5.5}PS_{4.5}Cl_{1.5}$ was done by M.Sc. Philip Heuer from Universität Münster according to literature.

All synthesis work and sample treatment for $Li_{5.5}PS_{4.5}Cl_{1.5}$ were performed under an argon atmosphere (< 0.5 ppm H_2O and O_2). Lithium sulfide (Li_2S, Alfa-Aesar, 99.9%), phosphorus pentasulfide (P_2S_5, Merck, 99%), and lithium chloride (LiCl, Alfa-Aesar, 99.9%) were hand ground for 15 minutes to obtain 3 g batches. The mixed materials were then hand pressed into pellets and filled into 8 cm high silica ampoules. The ampoules were prepared with a carbon coating and pre heated at 800 °C for 2 h under vacuum to remove all residual moisture. After precursor placement in the ampoules, they were sealed under vacuum. After 3 days of heating at 450 °C (ramp 100 °C h^{-1}, natural cooling) the powders were ground for 15 min. Following steps were the repetition of pelletizing, sealing inside of a prepared ampoule and annealing the sample at 450 °C (ramp 100 °C h^{-1}, natural cooling) for additional 3 days.[379]

Raman spectroscopy: The obtained powder of $Li_{5.5}PS_{4.5}Cl_{1.5}$ was placed on a Raman sample holder which can be closed airtight to prevent the samples for side reactions and humidity. The measurements were performed with a Bruker Senterra and a 532 nm laser source.

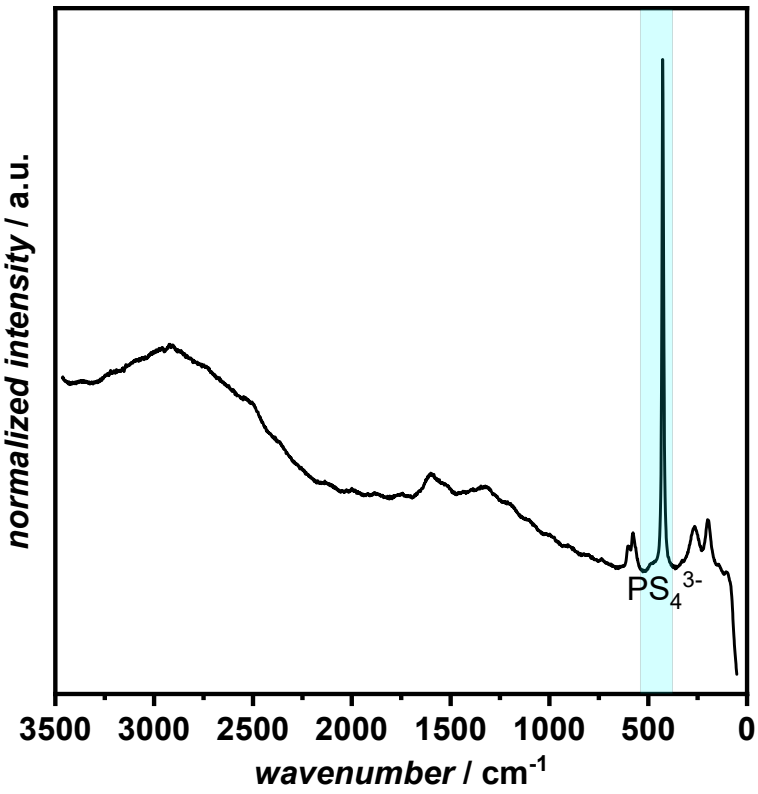

Figure 89 Raman spectrum of $Li_{5.5}PS_{4.5}Cl_{1.5}$. The thiophosphate band is highlighted. Measurement by M.Sc. Philip Heuer.

Powder X-ray diffraction (XRD): Powder X-ray diffraction was performed with a StadiP from STOE in Debye-Scherrer geometry with a Cu-K_α radiation (λ = 1.5451 Å). The $Li_{5.5}PS_{4.5}Cl_{1.5}$ was sealed in 0.5 mm borosilicate capillaries and were measured in 2θ = 3° steps for 120 s in an angle range of 2θ = 10° - 91°.

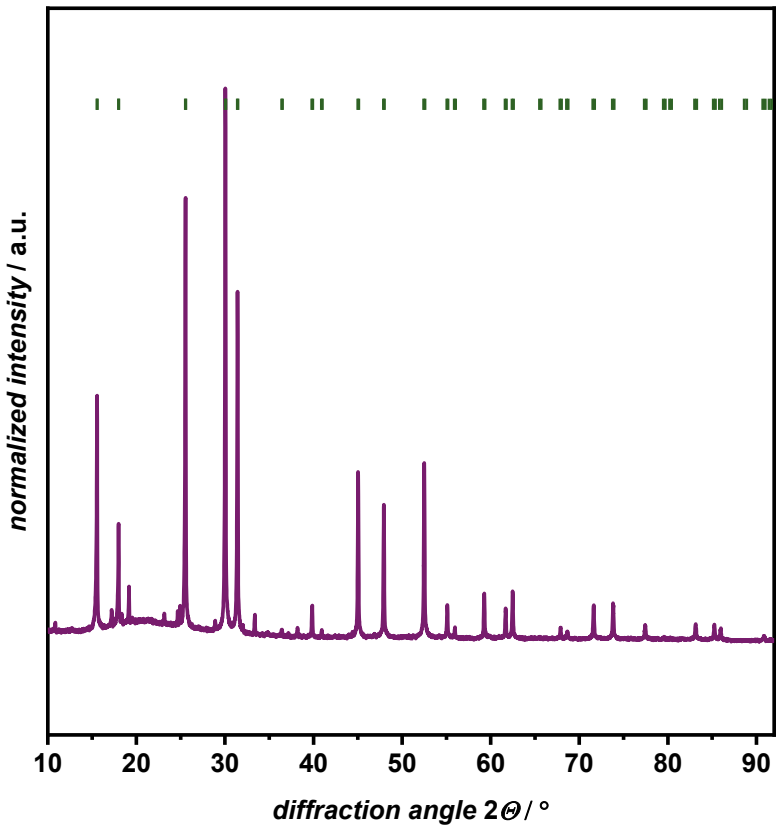

Figure 90 XRD spectrum of $Li_{5.5}PS_{4.5}Cl_{1.5}$. Measurement by M.Sc. Philip Heuer.

6.3.2.9 Preparation of PEs with P5 and P6

P5/P6 (1 g) is dissolved in MeCN (10 mL) and LiTFSI (200 mg) is added. The mixture is stirred for 2 h in a beaker. The solvent is evaporated and the beaker put in a vacuum oven at 45 °C. The dried polymer/salt mix is transferred into a glovebox and sandwiched between two 15x15 cm Mylar® foils. Afterwards, the stack is hot-pressed at 45 °C and 15 MPa for 30 seconds. The film is removed from the hot-press and loosened from the Mylar® foil. 10 mm diameter films are punched out and transferred to an oven and dried at 45 °C and 10^{-3} mbar.

6.3.2.10 Preparation of CPEs with P5

In a glovebox, **P5** (1 g), LiTFSI (200 mg), and $Li_{5.5}PS_{4.5}Cl_{1.5}$ (1 g) are added to a beaker and *p*-xylene (30 mL) is added. The solvent is removed and the mixture sandwiched between Mylar® foils at 45 °C and 15 MPa for 30 seconds. The film is removed from the hot-press and loosened from the Mylar® foil. 10 mm diameter films are punched out and transferred to an oven and dried at 45 °C and 10^{-3} mbar.

6.3.2.11 Preparation of CPEs with P7

In a glovebox, $Li_{5.5}PS_{4.5}Cl_{1.5}$ (1 g), **P7** (100 mg), and LiTFSI (77.4 mg) are added to a mortar with *p*-xylene (2 mL). Mixed in a mortar until most of the solvent evaporated. The paste is transferred into an oven and dried at 40 °C for 24 h.

6.3.3 Coating of LATP/LLZO Particles for Oxide-CPEs

6.3.3.1 Synthesis of triethoxy silane mPEG

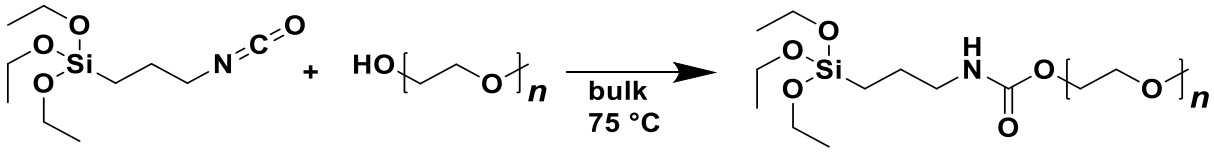

mPEG (20.0 g, 1.00 eq.) and 3-(triethoxysilyl)propyl isocyanate (2 eq.) are added to a round-bottom flask and purged with nitrogen for 15 min. The flask is heated to 75 °C for 24 h while slowly stirring. The polymer is precipitated from THF in ice-cold diethyl ether 3x and dried in vacuum oven overnight at 35 °C 600 mbar. All masses and yields are listed in **Table 22**.

Table 22 Masses and yields for all synthesis mPEG-triethoxy silanes.

Polymer	3-(triethoxysilyl)propyl isocyanate	Yield
mPEG550	17.99 g	17.0 g (59 %)
mPEG1000	9.90 g	20.0 g (80 %)
mPEG2000	4.95 g	17.5 g (78 %)
mPEG5000	1.98 g	20.2 g (96 %)

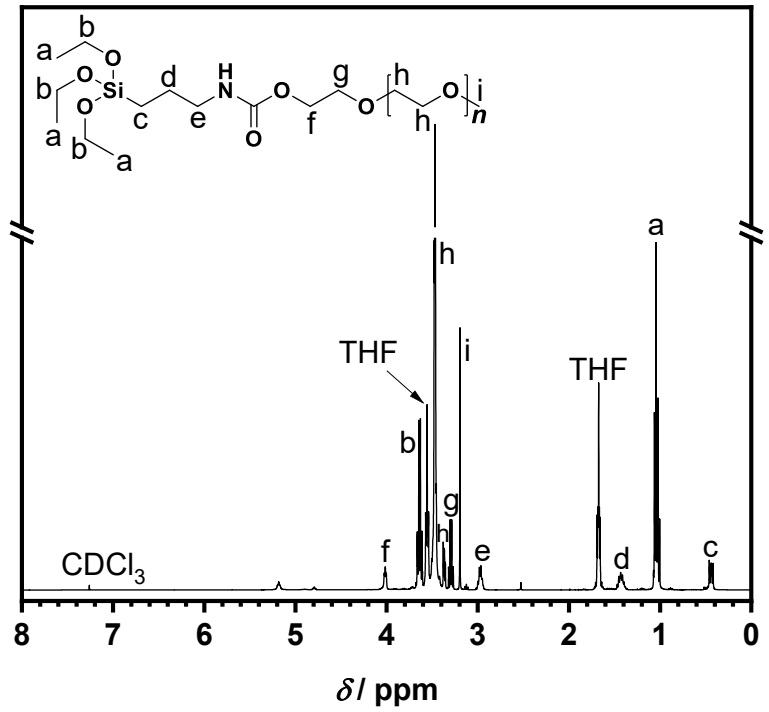

Figure 91 Exemplary ^{1}H-NMR spectrum of mPEG550-silane in $CDCl_3$ with proton assignment.

^{1}H NMR (400 MHz, $CDCl_3$) δ / ppm: 4.01 (t, J = 4.8 Hz, 2H), 3.63 (qd, J = 7.0, 2.1 Hz, 6H), 3.52 - 3.34 (m, 40H), 3.29 (q, J = 7.0 Hz, 2H), 3.19 (s, 3H), 2.97 (q, J = 6.5 Hz, 2H), 1.51 - 1.30 (m, 2H), 1.12 - 0.88 (m, 9H), 0.54 - 0.30 (m, 2H).

The conversion is calculated from the integral ratio of the c and i peak. Since for all mPEG-silanes the i:c ratio is approximately 3:2 full conversion is assumed for calculations.

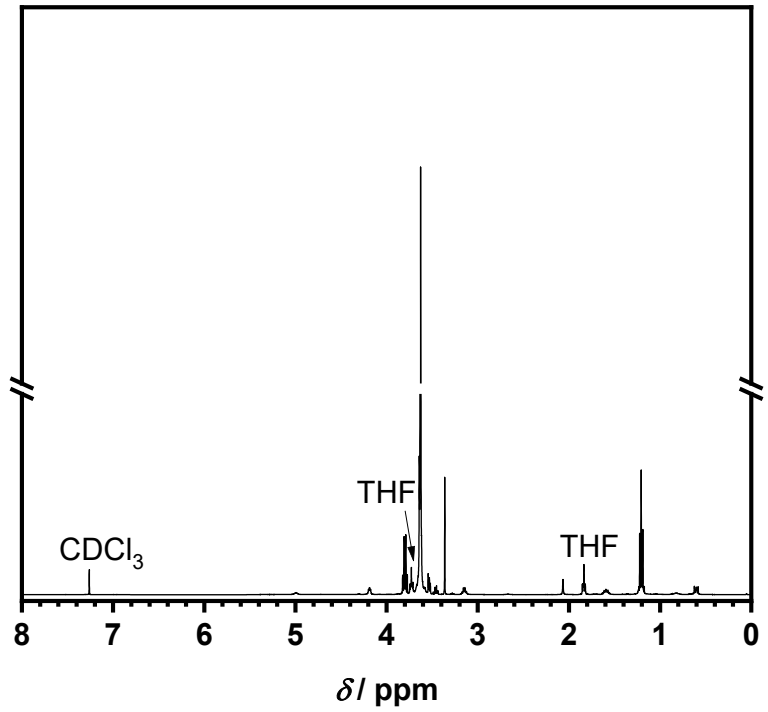

Figure 92 ^{1}H-NMR spectrum of mPEG1000-silane in $CDCl_3$. Refer to mPEG550-silane for proton assignment and chemical shifts.

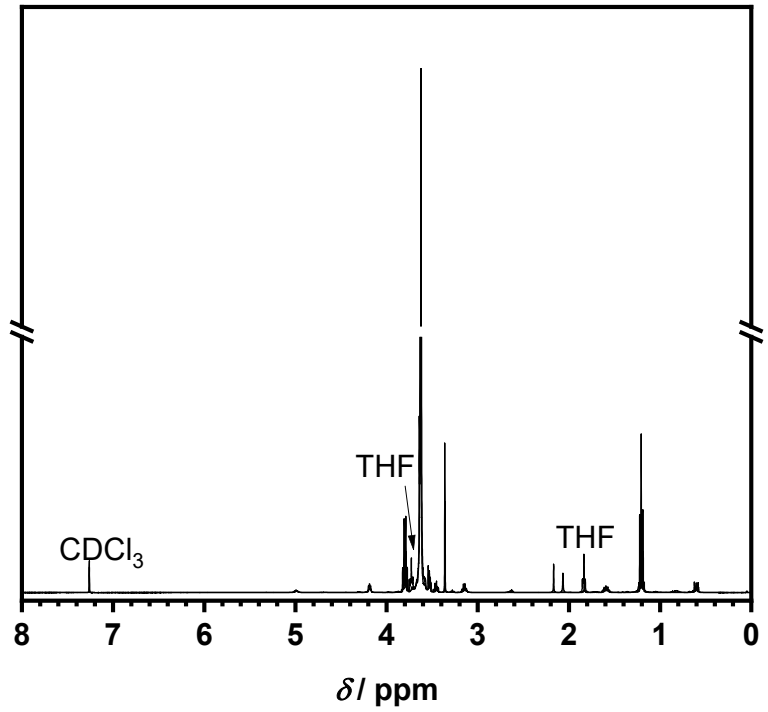

Figure 93 ^{1}H-NMR spectrum of mPEG2000-silane in $CDCl_3$. Refer to mPEG550-silane for proton assignment and chemical shifts.

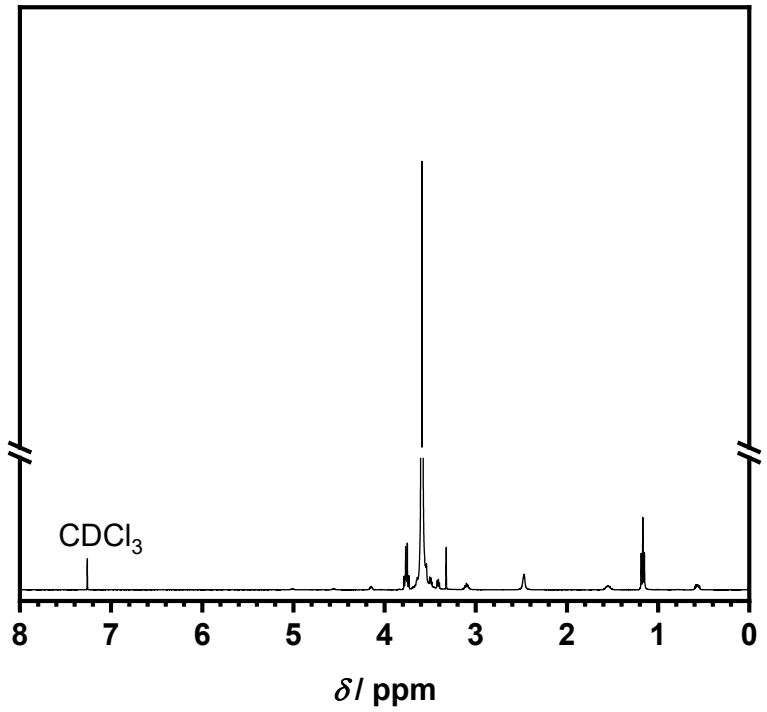

Figure 94 ^{1}H-NMR spectrum of mPEG5000-silane in $CDCl_3$. Refer to mPEG550-silane for proton assignment and chemical shifts.

6.3.3.2 Coating of LATP with triethoxy silane mPEG (mPEG@LATP)

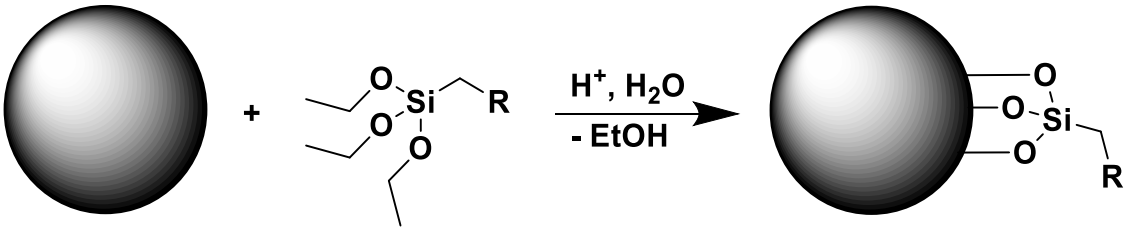

An ethanol/water (10 ml, 95:5 v:v) mixture is acidified with acetic acid to pH=4. LATP powder (1 g) is sonicated in 6 mL of the mixture for 20 min. mPEG-silane (500 mg) is dissolved in 4 ml of the mixture. After sonication the silane solution is added to the dispersion of LATP and stirred for 18 h. Acetone is added and the particles centrifuged and washed with DCM 3x. The coated particles transferred into a beaker and dried in a vacuum oven at 80 °C. Yields between 541 mg and 987 mg

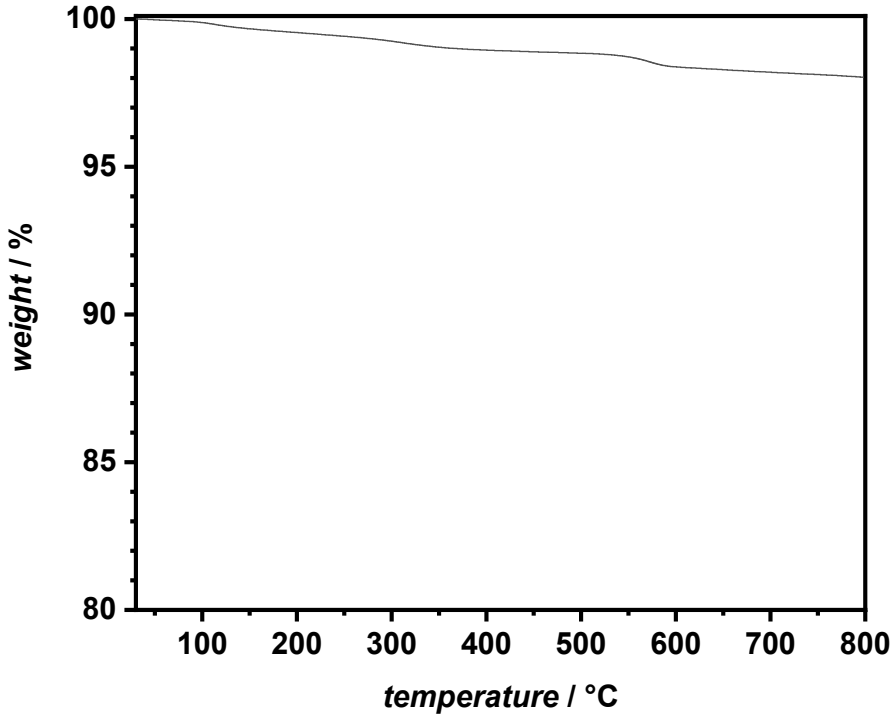

Figure 95 TGA of mPEG550@LATP from 30 - 800 °C at a heating rate of 10 K min^{-1}. The weight equilibrates at 98.1% of the initial value.

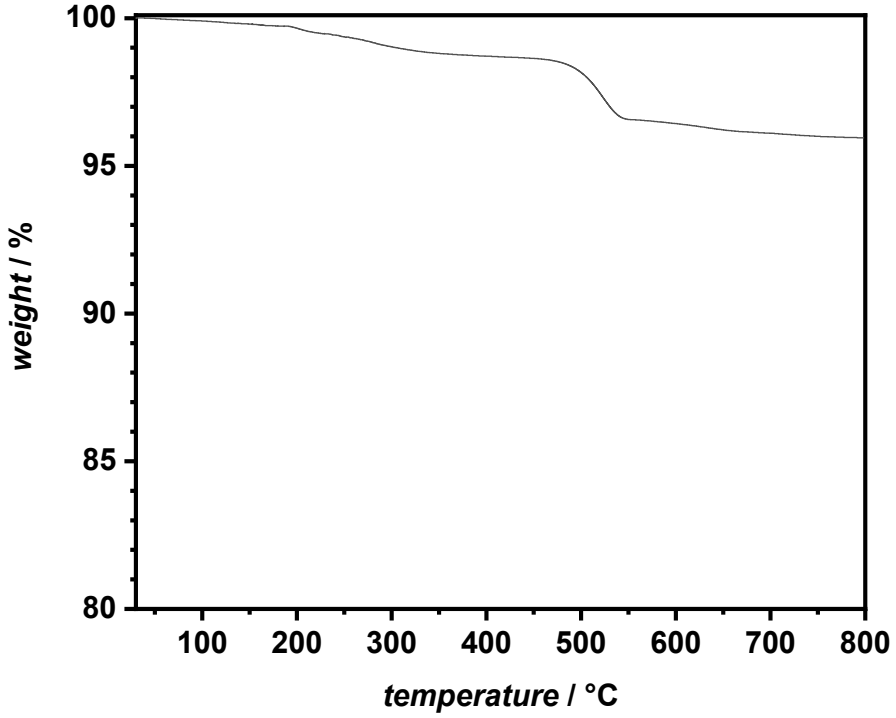

Figure 96 TGA of mPEG1000@LATP from 30 - 800 °C at a heating rate of 10 K min^{-1}. The weight equilibrates at 96.0% of the initial value.

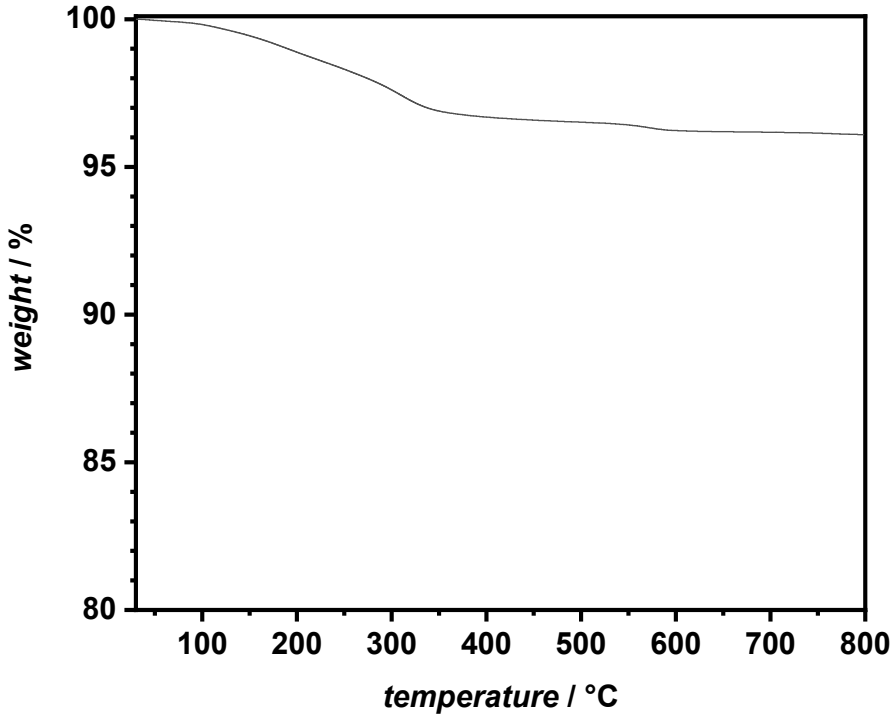

Figure 97 TGA of mPEG2000@LATP from 30 - 800 °C at a heating rate of 10 K min^{-1}. The weight equilibrates at 96.1% of the initial value.

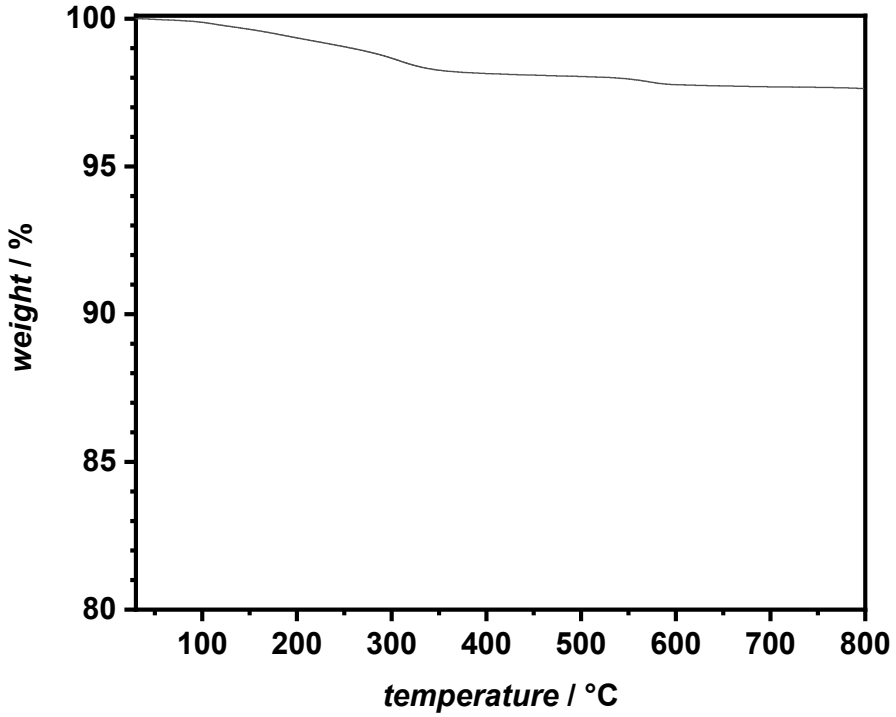

Figure 98 TGA of mPEG5000@LATP from 30 - 800 °C at a heating rate of 10 K min^{-1}. The weight equilibrates at 97.7% of the initial value.

6.3.3.3 Coating of LLZO with 1*H*,1*H*,2*H*,2*H*-perfluorodecyl triethoxy silane (PF@LLZO)

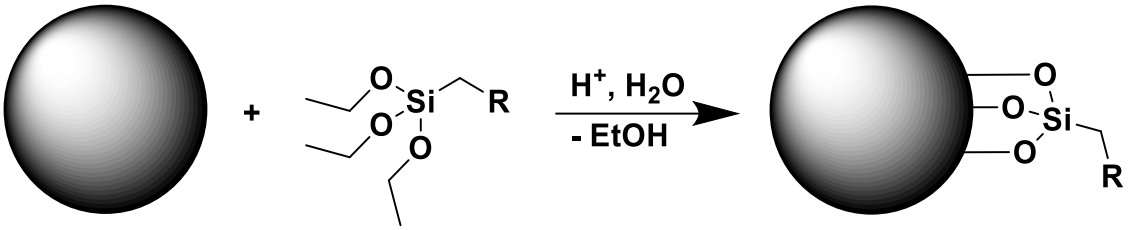

An ethanol/water (50 ml, 95:5 v:v) mixture is acidified with acetic acid to pH=4. LLZO powder (5 g) is sonicated in 30 mL of the mixture for 20 min. 1*H*,1*H*,2*H*,2*H*-perfluorodecyl triethoxy silane (500 mg, 360 µL, 704 µmol) is dissolved in 20 ml of the mixture. After sonication the silane solution is added to the dispersion of LLZO and stirred for 18 h. Acetone is added and the particles centrifuged and washed with DCM 3x. The coated particles transferred into a beaker and dried in a vacuum oven at 80 °C. Yield 5.25 g

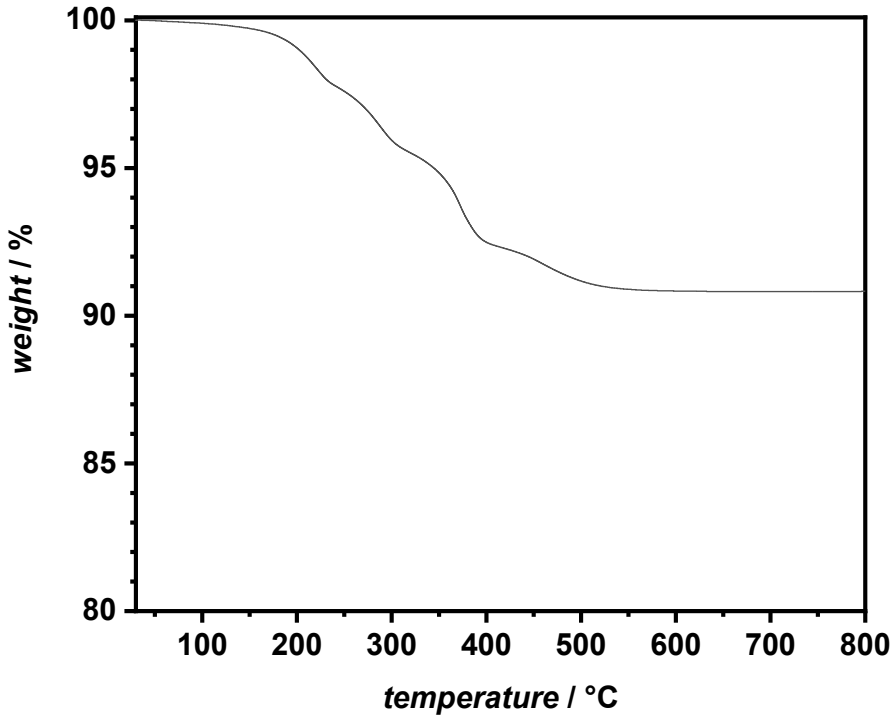

Figure 99 TGA of 1*H*,1*H*,2*H*,2*H*-perfluorodecyl triethoxy silane coated LLZO from 30 - 800 °C at a heating rate of 10 K min^{-1}. The weight equilibrates at 90.8% of the initial value.

6.3.3.4 Coating of LLZO with triethoxy silane mPEG (mPEG@LLZO)

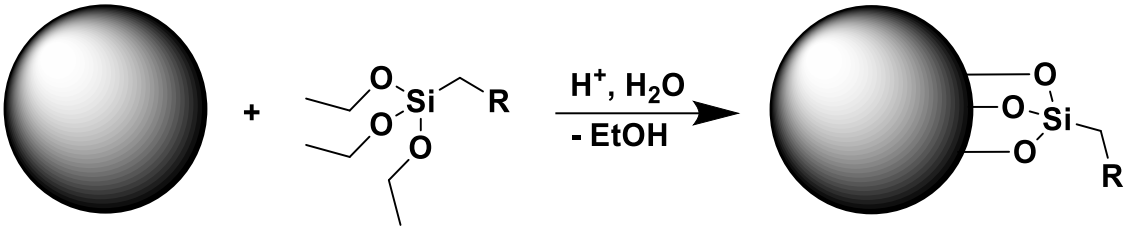

An ethanol/water (20 ml, 95:5 v:v) mixture is acidified with acetic acid to pH=4. LLZO powder (2 g) is sonicated in 12 mL of the mixture for 20 min. mPEG1000-silane (200 mg) is dissolved in 8 ml of the mixture. After sonication the silane solution is added to the dispersion of LLZO and stirred for 18 h. Acetone is added and the particles centrifuged and washed with DCM 3x. The coated particles transferred into a beaker and dried in a vacuum oven at 80 °C. Yield 2.12 g

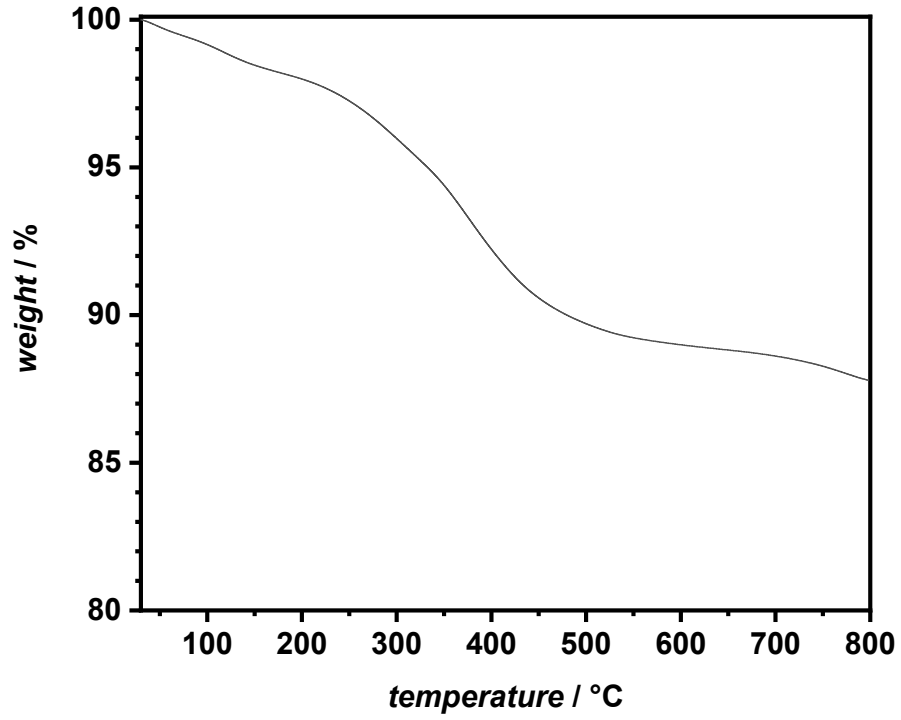

Figure 100 TGA of mPEG1000@LLZO from 30 - 800 °C at a heating rate of 10 K min^{-1}. The weight equilibrates at 87.8% of the initial value.

6.3.4 Self-Crosslinking Oxide-CPEs

6.3.4.1 Modification of polymers with IPTES

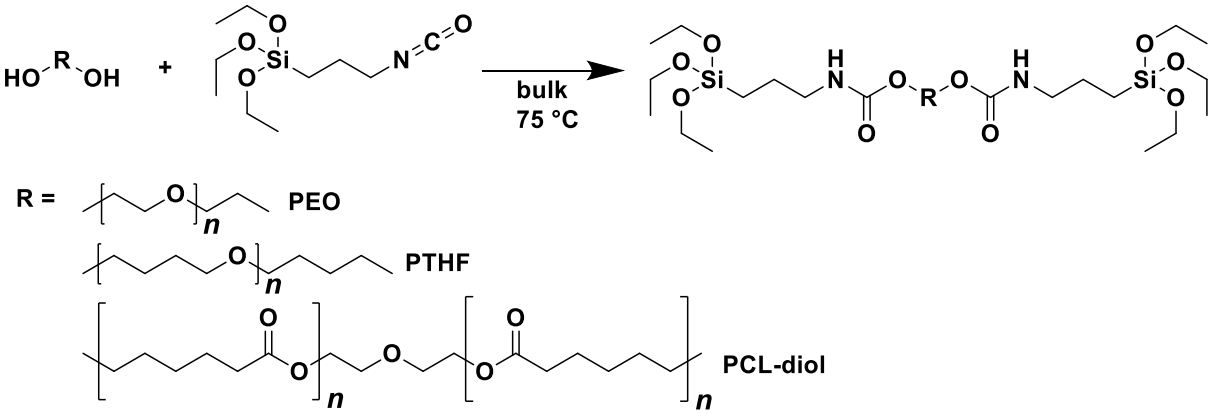

As an example, the synthesis of IPTES-PEO is described. The other polymers were synthesized in the same manner with 2 equivalents of 3-(triethoxysilyl)propyl isocyanate per 1 equivalent of hydroxy groups.

PEO (M_n = 10,000 g·mol^{-1}, 50.0 g, 5.00 mmol, 1.00 eq.) and 3-(triethoxysilyl)propyl isocyanate (4.95 g, 20.0 mmol, 4.00 eq.) are added to a 100 mL flask and purged with nitrogen for 15 min. The flask is heated to 75 °C for 24 h and stirred at a low rate since the molten polymer is highly viscous. THF is added after cooling the flask below 60 °C. Precipitated from THF in ice-cold Et_2O three times. The modified polymer is dried in a vacuum oven overnight at 35 °C 600 mbar. Yields 89 - 97 %

Polymers modified according to this procedure: PEO (6,000, 10,000, and 20,000 g·mol^{-1}), PTHF (2,900 g·mol^{-1}), PCL-diol (2,000 g·mol^{-1})

THF-SEC of the unmodified polymers against PMMA standards are available in the Appendix **Figure 125** - **Figure 128**.

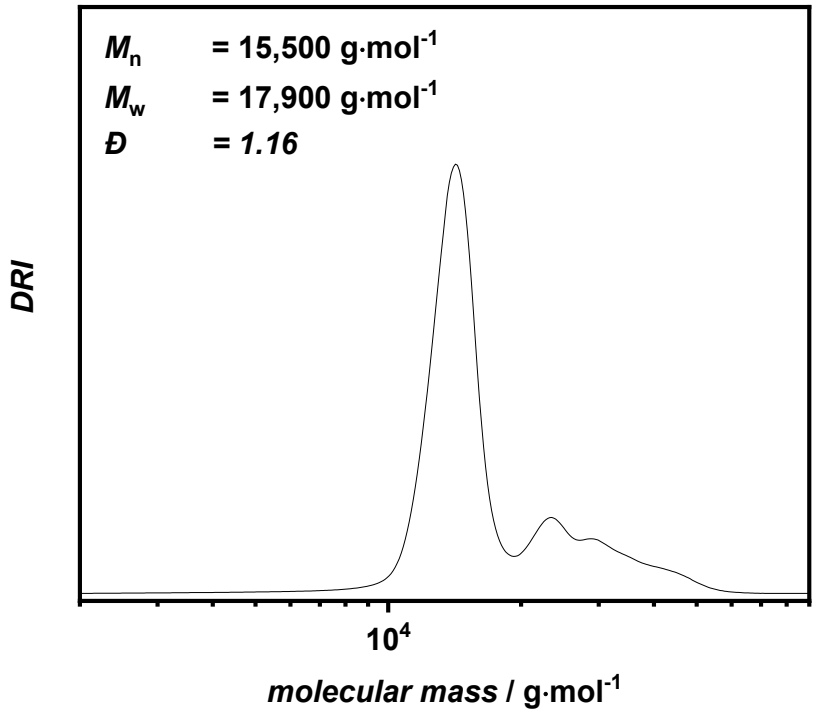

Figure 101 THF-SEC of PEO6k-silane against a PMMA standard.

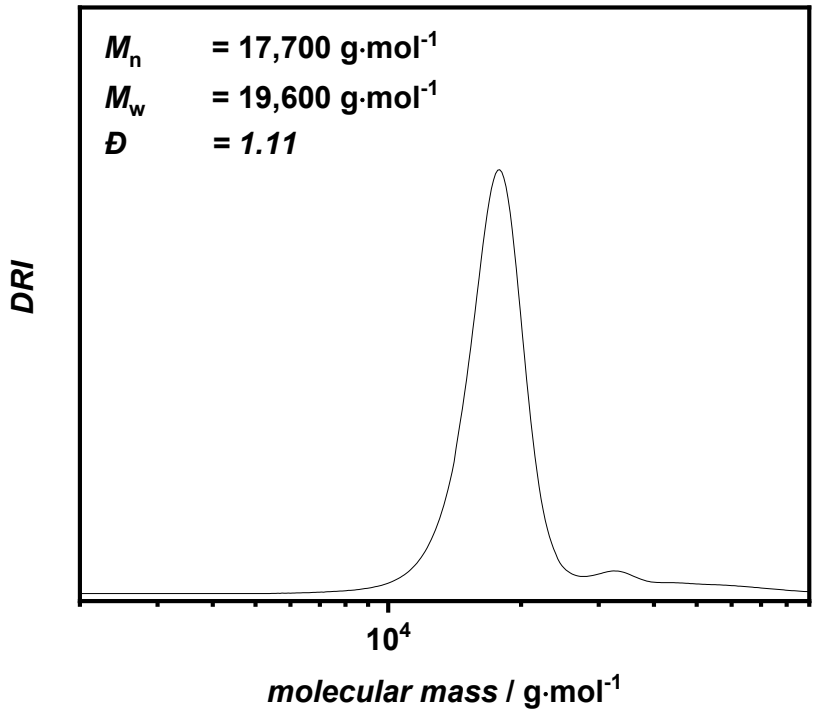

Figure 102 THF-SEC of PEO10k-silane against a PMMA standard.

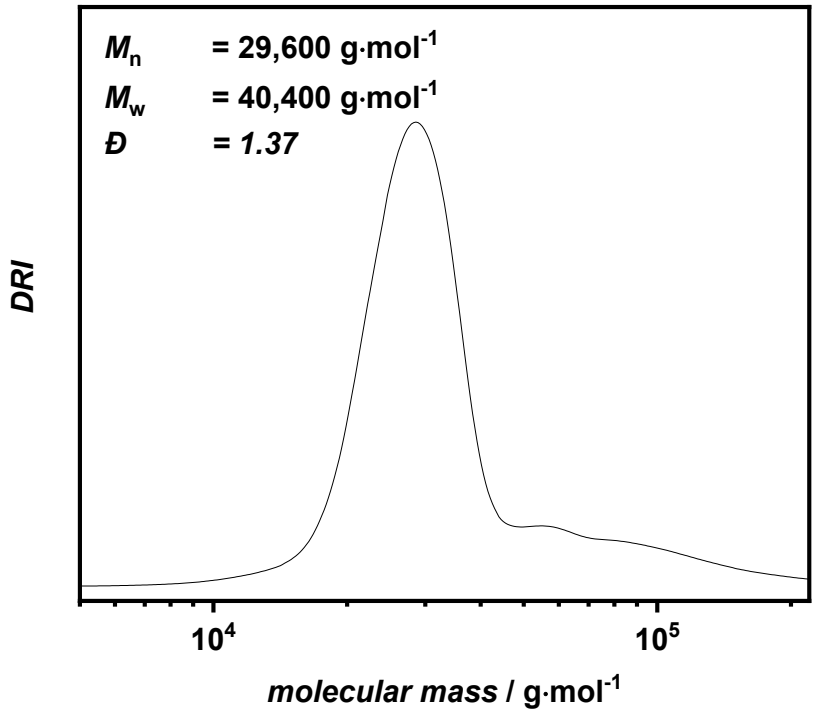

Figure 103 THF-SEC of PEO20k-silane against a PMMA standard.

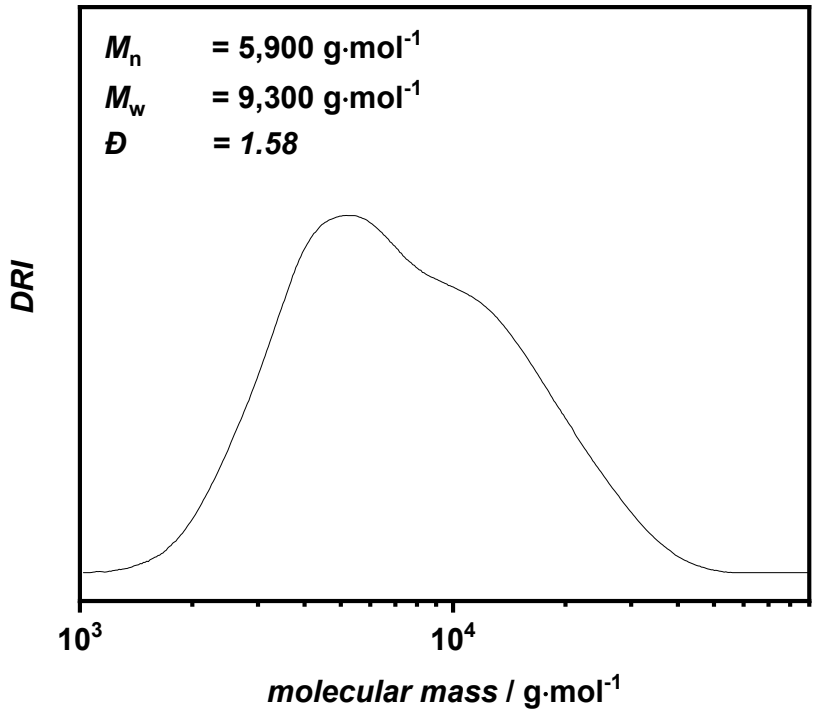

Figure 104 THF-SEC of PTHF2.9k-silane against a PMMA standard.

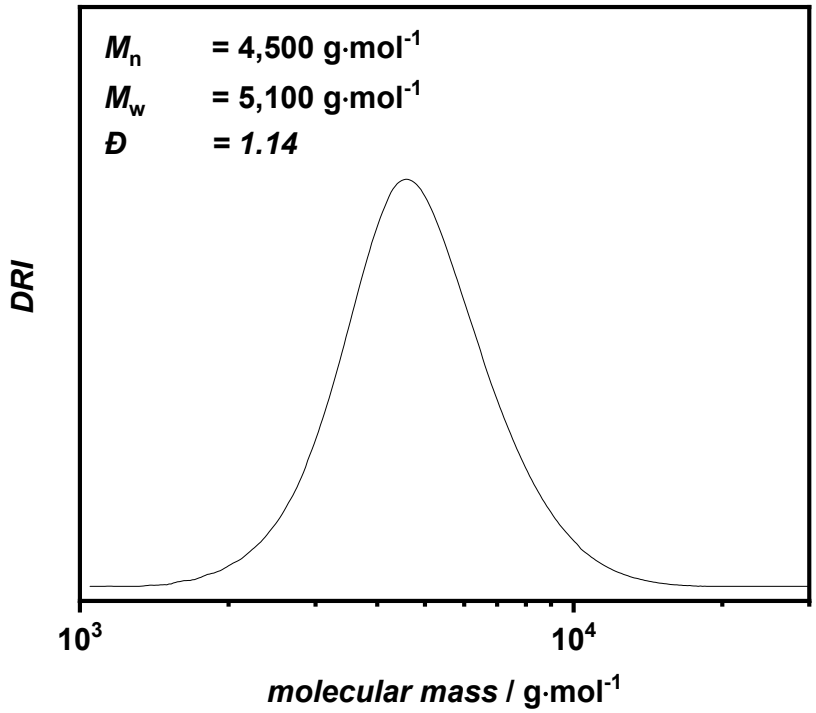

Figure 105 THF-SEC of PCL2k-silane against a PMMA standard.

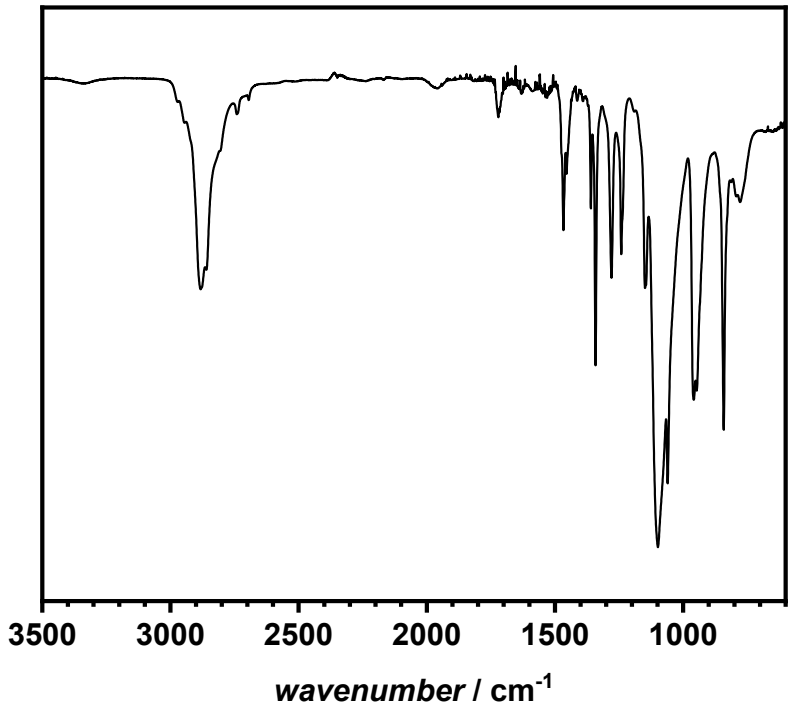

Figure 106 ATR-IR of PEO10k-silane.

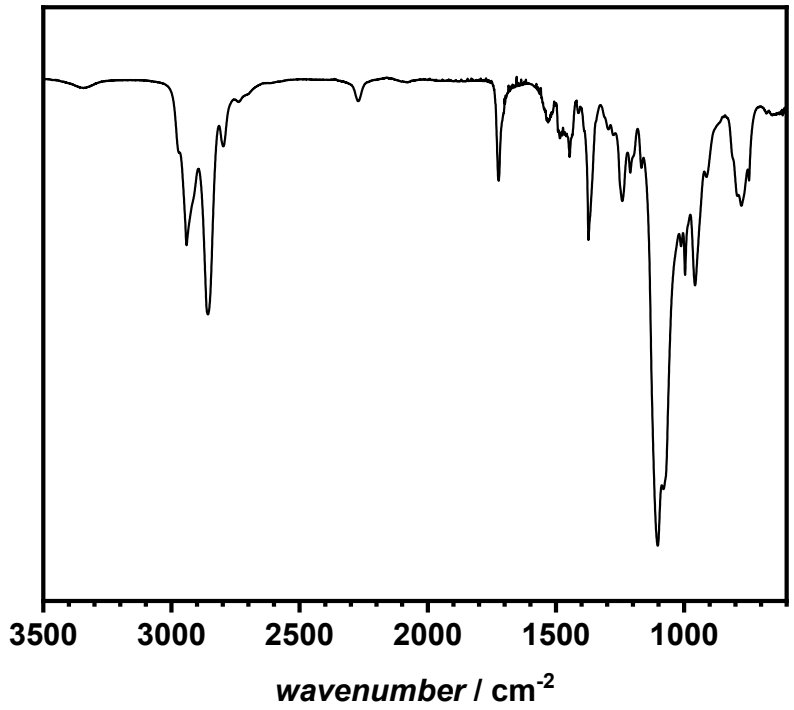

Figure 107 ATR-IR of PTHF2.9k-silane.

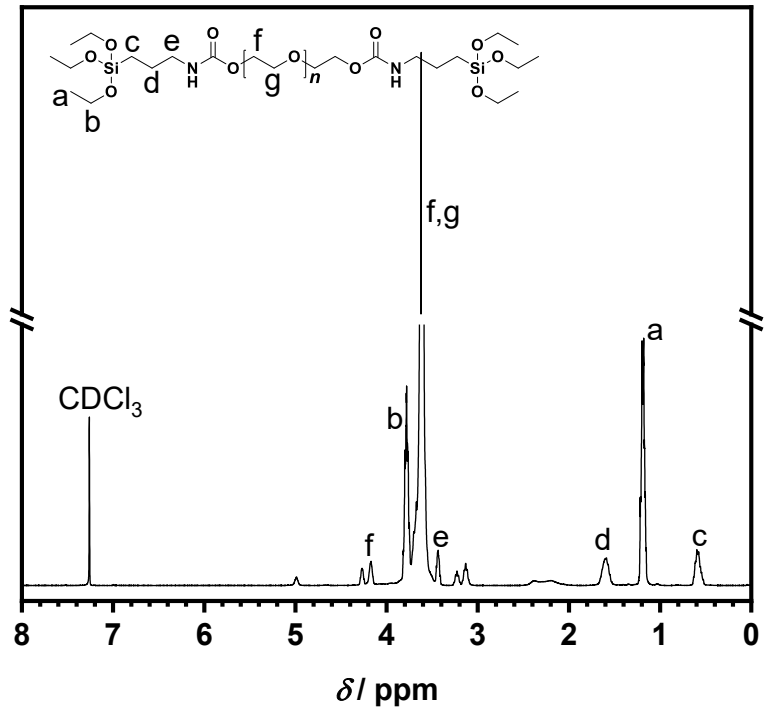

Figure 108 Exemplary ^{1}H-NMR spectrum of PEO6k-silane in $CDCl_3$ with proton assignment.

^{1}H NMR (400 MHz, $CDCl_3$) δ / ppm: 4.49 - 4.07 (m, 2H), 3.86 - 3.73 (m, 6H), 3.72 - 3.38 (m, 200H),3.49 - 3.38 (m, 2H), 1.66 - 1.50 (m, 2H), 1.28 - 1.09 (m, 9H), 0.68 - 0.48 (m, 2H).

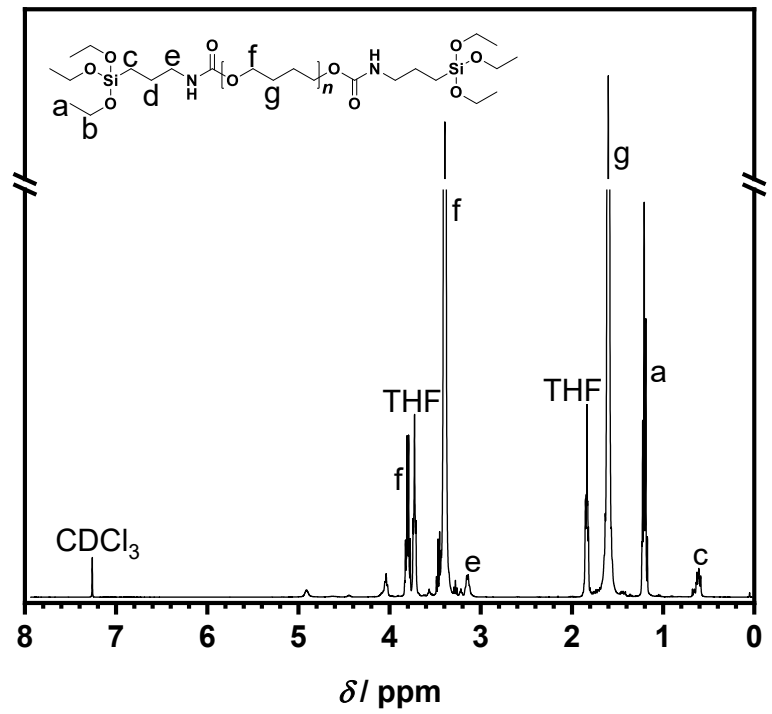

Figure 109 ^{1}H-NMR spectrum of PTHF2.9k-silane in $CDCl_3$ with proton assignment. b is hidden underneath the g peak.

^{1}H NMR (400 MHz, $CDCl_3$) δ / ppm: 3.80 (q, J = 7.0 Hz, 3H), 3.47 - 3.32 (m, 50H), 3.15 (q, J = 7.0 Hz, 2H), 1.63 - 1.53 (m, 50H), 1.29 - 0.95 (m, 9H), 0.73 - 0.50 (m, 2H).

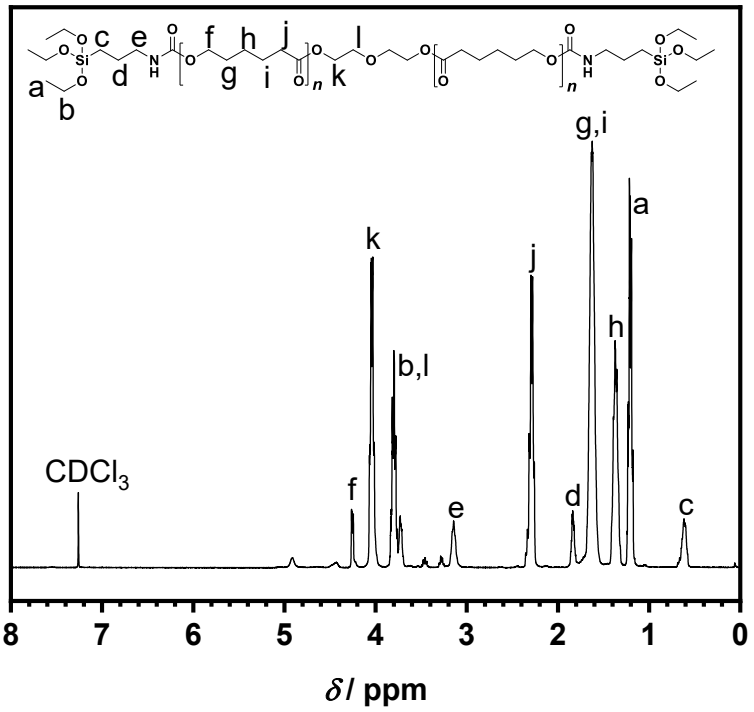

Figure 110 ^{1}H-NMR spectrum of PCL2k-silane in $CDCl_3$ with proton assignment.

^{1}H NMR (400 MHz, $CDCl_3$) δ / ppm: 4.31 - 4.14 (m, 2H), 4.10 - 3.96 (m, 4H), 3.87 - 3.64 (m, 8H), 3.19 - 3.09 (m, 2H), 2.41 - 2.12 (m, 10H), 1.85 - 1.77 (m, 2H), 1.75 - 1.53 (m, 20H), 1.46 - 1.28 (m, 10H), 1.25 - 1.14 (m, 9H), 0.68 - 0.55 (m, 2H).

6.3.4.2 Film preparation

The polymers, LiTFSI, MoO_3/LLZO, and additives are stored in a glovebox. 1 g of polymer, LiTFSI according to the [O]:[Li] ratio (in the index of the film name), and MoO_3/LLZO in ratios of 10, 25, 50, 100, 200 or 400 % in regard to the pure polymer without LiTFSI are weighed in. Additives are weighed in according to the stated amount. All components are taken out of the glovebox and mixed in a mortar until a homogeneous slurry is obtained. Then

a) the slurry is doctor bladed onto a single Mylar® foil in the desired thickness.
b) the slurry is sandwiched between two Mylar® foils and calendared through a manual roll-to-roll press with adjustable slit width. The Mylar® foil has a thickness of 100 µm so the slit width was adjusted to 200+x with x being the desired film thickness.

All films were dried under ambient conditions until a flexible crosslinked film is obtained. Subsequently, the films are dried twice. First, in an oven or Schlenkline (< $5 \cdot 10^{-3}$ mbar) at 60 °C and afterwards on a Highcube (< 10^{-6} mbar) at 60 °C. Films are stored in dry room with a dew point of -60 °C. Flexible and stable films were synthesized in a thickness range of 16 - 200 µm.

Additional information regarding film fabrication (from 4.4.2.3.3):

During the synthesis of the CPE films incorporating various polymers, oxide particles, and concentrations, several key observations were made during the film fabrication process. However, these findings could not be reliably quantified due to the influence of numerous variables, some of which were difficult to control, affecting the overall process.

The rate at which the slurry upon mixing solidified was highly dependent on:

Variable	(faster > slower crosslinking condition)
1. polymer used	(hygroscopic > hydrophobic)
2. particle concentration	(higher > lower)
3. the particle surface	(oxides > phosphates)
4. temperature	(higher > lower)
5. humidity	(higher > lower)
6. viscosity	(higher > lower)

Overall, the slurry crosslinking time varied between 3 minutes and several days, depending on the CPE components used. In some cases, particularly at high oxide concentrations (> 200 %), the addition of small amounts of ethyl acetate as a plasticizer was required. Ethyl acetate reduced viscosity, enhanced the mixability of components, and delayed the onset of crosslinking, thereby facilitating controlled roll pressing. All in all, the influence on the crosslinking rate by these variables highly indicated that a moisture catalyzed reaction between the alkoxy silane end-groups and hydroxy-groups at the particle surface were the main crosslinking contributor and not homocondensation of alkoxysilanes.

7 List of Abbreviations

%	Percentage
[A]	Concentration of A
°C	Degree Celsius
µl	Microliter
µm	Micrometer
a.t.	Ambient temperature
AIBN	2,2′-Azobis(2-methylpropionitrile)
Al_2O_3	Aluminum oxide
AROP	Anionic ring-opening polymerization
ASSB	All-solid-state battery
ATR-IR	Attenuated Total Reflection Fourier-Transform Infrared Spectroscopy
ATRP	Atom transfer radical polymerization
BMS	Battery management systems
C	Capacity or C-rate
CCD	Critical current density
CEI	Cathode electrolyte interface
$CHCl_3$	Chloroform
CIP	Ceramics-in-polymer
cm	Centimeter
CPE	Composite Polymer Electrolytes
CRP	Controlled radical polymerization
CTA	Chain-transfer agents
Đ	Dispersity
Da	Dalton
DBU	1,8-Diazabicyclo(5.4.0)undec-7-ene
DCM	Dichloromethane
DMF	Dimethylformamide
DSC	Differential Scanning Calorimetry
EDX	Energy-dispersive X-ray spectroscopy

EIS	Electrochemical Impedance Spectroscopy
EtOH	ethanol
EV	Alectric vehicle
FB2	FestBatt2
FRP	Free Radical polymerization
g	Gram
G4	1 M LiTFSI in tetraethylene glycol dimethyl ether
h	Hour(s)
HAADF-STEM	High-angle annular dark-field scanning transmission electron microscopy
HI-MS	Helmholtz-Institut Münster
HNBR	Hydrogenated nitrile butadiene rubber
HSSE	Hybrid solid-state electrolyte
I	Current
IPTES	3-(Triethoxysilyl)propyl isocyanate
K	Kelvin
kg	Kilogram
KIT	Karlsruhe Institut für Technologie
LATP	$Li_{1.5}Al_{0.5}Ti_{1.5}(PO_4)_3$
LCO	Lithium cobalt oxide
LDPE	Low-density polyethylene
LE	Liquid electrolyte
LFP	Lithium iron phosphate
Li_2CO_3	Lithium carbonate
Li_3PO_4	Lithium phosphate
LiBOB	Lithium tetraborate
$LiClO_4$	Lithium perchlorate
LiF	Lithium fluoride
Li-ion	Lithium-ion
Li-metal	Lithium-metal
$LiPF_6$	Lithium hexafluorophosphate
LiSICON	Lithium Super Ionic Conductor

LiTf	Lithium triflate
LiTFSI	Lithium bis(trifluoromethanesulfonyl)imide
LLTO	$Li_{3x}La_{(2/3)-x}TiO_3$
LLZO	$Li_7La_3Zr_2O_{12}$ and doped derivatives
LMB	Lithium metal batteries
LSV	Linear Sweep Voltammetry
LTP	$LiTi_2(PO_4)_3$
M	Mega
m(A)	Mass of A
mA	Milliampere
MeCN	Acetonitrile
MeOH	methanol
mg	Milligram
mm	Millimeter
MMA	Methyl methacrylate
M_n	Number average molecular weight
mPEG	Poly(ethylene glycol) methyl ether
mPEG@LATP/LLZO	mPEG coated LATP/LLZO
M_w	Weighted average molecular weight
NaSICON	Sodium (Na) Super Ionic Conductor
NBR	Acrylonitrile-butadiene rubber
NCA	Lithium nickel cobalt aluminium oxide
NiCd	Nickel-cadmium
nm	Nanometer
NMC	Lithium nickel manganese cobalt oxide
NMP	Nitroxide-mediated polymerization
NMR	Nuclear magnetic resonance
NP	Nano particle(s)
p	Conversion
Pa	Pascal
PAN	Polyacrylonitrile

PAN@LATP	PAN coated LATP
PAN@SiO_2	PAN coated silica nanoparticles
PCL	Poly(ε-caprolactone) and poly(ε-caprolactone)-diol
PE	Polymer electrolyte
PEG	Poly(ethylene glycol)
PEO	Poly(ethylene oxide)
PET	Poly(ethylene terephthalate)
PF	1*H*,1*H*,2*H*,2*H*-Perfluorodecyl triethoxy silane
PF@LLZO	PF coated LLZO
PIC	Polymer-in-ceramics
PMMA	Poly(methyl methacrylate)
ppm	Parts per million
PPM	Post-polymerization modification
PS	Polystyrene
PTHF	Polytetrahydrofuran
PVDF-HFP	Poly(vinylidene fluoride-*co*-hexafluoropropylene)
R	Resistance
r.t.	Room temperature
RAFT	Reversible addition-fragmentation chain transfer
RDRP	Reversible-deactivation radical polymerization
RI	Refractive index
S	Siemens
SEC	Size exclusion chromatography
SEI	Solid electrolyte interphase
SEM	Scanning electron microscope
SH@SiO_2	SH-TMS coated silica nanoparticles
SH-TMS	(3-Mercaptopropyl)-trimethoxysilane
SOH	State of health
SSB	Solid-state battery
SSE	Solid-state electrolytes
T	Temperature

TEM	Transmission electron microscopy
T_g	Glass transition temperature
TGA	Thermogravimetric Analysis
THF	Tetrahydrofuran
TiO_2	Titanium dioxide
t_{Li^+}	Lithium transference number
T_m	Melting point (peak temperature for polymers)
U	Potential
UV	Ultra-violet
V	Voltage
v:v	Volume to volume ratio
VTF	Vogel-Tamman-Fulcher
W	Watt
wt%	Weight percentage
X_n	Number-average degree of polymerization
XRD	X-ray diffraction
Δ	Delta
σ	Ionic conductivity

8 List of Figures, Schemes and Tables

8.1 List of Figures

8.2 List of Schemes

8.3 List of Tables

9 List of Publications

Publications within this Dissertation

[3] Liu, X.; Döpping, D.; Scharf, F.; Yao, K.; Stihl, A.; Weiling, M.; Schwab, C.; Touidjine, K. N. K.; Théato, P.; Guillon, O.; Brunklaus, G.; Finsterbusch, M.; Fattakhova-Rohlfing, D. Oligomer Modification Boost Ion Transport in Hybrid Solid-State Electrolytes for Long-life Lithium Metal Batteries. *Adv. Funct. Mater.* **2025**, in preparation

[2] Döpping, D.; Buchheit, A.; Liu, X.; Goeke, A.; Grimm, A. P.; Voll, D.; Wilhelm, M.; Finsterbusch, M.; Winter, M.; Brunklaus, G.; Theato, P. Versatile Solvent-free Synthesis of Composite Polymer Electrolytes for Thin High Performance Solid-State Lithium Metal Batteries. *Small* **2025**, *Accepted Manuscript*. DOI: 10.1002/smll.202504166

[1] Döpping, D.; Schacher, F. H.; Stihl, A.; Voll, D.; Theato, P. Revisiting Polymer Coatings on Nanoparticles: Correlation between Molecular Weight and Coating Thickness in Chain Transfer Polymerizations. *Polym. Chem.* **2025**, *16*, 2075. DOI: 10.1039/D5PY00081E

Other Publications

[4] Döpping, D.; Kern, J.; Rotter, N.; Llevot, A.; Mutlu, H. Biogenic Polymeric Materials from Lignocellulosic Biomass-Derivable 4-Pentenoic Acid and Isosorbide for Potential Biomedical Applications. *ACS Sustainable Chem. Eng.* **2024**, *12* (36), 13401. DOI: 10.1021/acssuschemeng.4c03690

[3] Fu, Q.; Zhao, L.; Luo, X.; Hobich, J.; Döpping, D.; Rehnlund, D.; Multu, H.; Dsoke, S. Electrochemical Investigations of Sulfur-Decorated Organic Materials as Cathodes for Alkali Batteries. *Small* **2024**, *20* (24), 2311800. DOI: 10.1002/smll.202311800

[2] Döpping, D.; Kern, J.; Rotter, N.; Llevot, A.; Theato, P.; Mutlu, H. Synthesis and Characterization of Novel Isosorbide-Based Polyester Derivatives Decorated

with *α*-Acyloxy Amides. *Macromol. Chem. Phys.* **2022**, *223* (13), 2100497. DOI: 10.1002/macp.202100497

[1] Mutlu, H.; Döpping, D.; Huber, B.; Theato, P. Elemental Sulfur Mediated Novel Multicomponent Redox Polycondensation for the Synthesis of Alternating Copolymers Based on 2,4-Thiophene/Arene Repeating Units. *Macromol. Rapid Commun.* **2021**, *42* (6), 2000695. DOI: 10.1002/marc.202000695

Conference Contributions

[4] *Solvent-free Composite Polymer Electrolyte Synthesis Platform*
Poster at MAKRO 2024 (IUPAC World Polymer Congress, 1.-4.07.2024, Warwick University)

[3] *Solvent-free composite polymer electrolyte membrane preparation*
Poster at ESPE23 (European Symposium & Workshop on Polymer Electrolytes for Battery Applications, 25.-27.09.2023, Karlsruhe)

[2] Kern, J.; Mutlu, H.; Döpping, D.; Rotter, N.
Neuartige, synthetische Chitosan-Polymere als Implantatmaterial für die Knorpelrekonstruktion im Kopf-Halsbereich
Conference contribution, *Laryngorhinootologie* **2022**; 101(S 02): S22. DOI: 10.1055/s-0042-1747145, 24.05.2022

[1] *Synthesis and characterization of novel isosorbide based polyester derivatives decorated with α-acyloxy amides*
Poster at MAKRO 2022 (GDCh Fachgruppentagung, 12.-14.09.2022, Aachen)

Patents

[1] Döpping, D.; Theato, P.; Voll, D.; Schmitt, C.
Verfahren zur Herstellung einer Kompositpolymerelektrolytmembran sowie eine durch das Verfahren erhältliche Kompositpolymerelektrolytmembran
deutsche Patentanmeldung: DE102024112955.7

10 Danksagung

Die vorliegende Dissertation markiert den Abschluss von intensiven und lehrreichen 3 Jahren, die ohne die Unterstützung vieler Menschen in dieser Form nicht möglich gewesen wäre. Wissenschaftliche Arbeit ist niemals ein alleiniger Weg, sondern wird maßgeblich durch das Umfeld, die Zusammenarbeit und den Austausch mit anderen geprägt. Daher möchte ich all jenen danken, die mich auf diesem Weg begleitet und unterstützt haben.

Mein besonderer Dank gilt **Prof. Dr. Patrick Théato**, der mir nicht nur die Möglichkeit gegeben hat, meine Promotion in einem spannenden und zukunftsweisenden Projekt zu verfolgen, sondern mir auch das Vertrauen und den Freiraum geschenkt hat, meine eigenen Ideen zu entwickeln und umzusetzen. Diese wissenschaftliche Freiheit und Förderung meiner Selbstständigkeit haben meine persönliche und akademische Entwicklung entscheidend geprägt. Ebenso danke ich **Prof. Dr. Dominic Bresser**, der sich bereit erklärt hat, die Rolle des Korreferenten zu übernehmen und meine Arbeit mit seiner Expertise zu begleiten.

Ein großes Dankeschön geht an **Katharina Kuppinger** und **Klara Urbschat**, die mir in unzähligen Momenten des Laboralltags mit Rat und Tat zur Seite standen. Ihr habt mir geholfen, wenn es mal nicht lief, und den oft stressigen Arbeitsalltag mit eurer Unterstützung und guten Laune bereichert. Auch **Bärbel Seufert-Dausmann**, **Martina Ritter** und **Saskia Block** möchte ich für ihre organisatorische und bürokratische Hilfe danken. Ohne euch wären viele Abläufe deutlich komplizierter gewesen, und ich bin sehr dankbar für eure stets freundliche und geduldige Unterstützung.

Ein ebenso herzlicher Dank gebührt **Dr. Dominik Voll** und **Dr. Christian Schmitt**, die mich in organisatorischen Fragen unterstützt und mir immer mit einem offenen Ohr zur Seite gestanden haben. In den Anfangszeiten meiner Promotion war es insbesondere **Dr. Andreas Butzelaar**, der mir mit seinen Erklärungen und seiner Unterstützung den Einstieg erleichtert hat.

Ein besonderer Dank geht an meinen Laborpartner **Alexander Grimm**. Nicht nur warst du ein verlässlicher und großartiger Kollege im Labor, sondern auch jemand, mit dem man nach Feierabend auf ein wohlverdientes Bier anstoßen konnte – vielen Dank für diese entspannte und freundschaftliche Zusammenarbeit.

Ohne **Dr. Annika Buchheit** wäre diese Arbeit in der jetzigen Form nicht möglich gewesen. Dein unermüdlicher Einsatz, deine Unterstützung bei Messungen, deine

kreativen Ideen und die unzähligen Gespräche haben meine Forschung enorm bereichert. Über die letzten drei Jahre hinweg warst du eine konstante und unersetzliche Hilfe. Nochmals vielen Dank für alles, was du für mich getan hast.

I would also like to thank **Xiaochen Liu** for his frequent support with all LLZO/LATP-related questions. Your expertise and helpfulness have saved me many difficulties. **Philip Heuer** danke ich für die gute Zusammenarbeit, bei den „stinkigen" Angelegenheiten. Ohne dich wäre der holprige Start mit den Argyroditen noch holpriger geworden.

Auch möchte ich mich bei allen FestBatt2-Mitgliedern bedanken, die mich auf diesem Weg unterstützt haben.

Ein besonders großes Dankeschön geht an die **"**Pelikane"**: Nico Zuber**, **Jan Hobich**, **Timo Sehn**, **Pirmin Koch** und **Marten Elzer**. Seit dem ersten Semester seid ihr nicht nur meine Freunde, sondern auch große Unterstützung gewesen. Die gemeinsamen Erlebnisse, das gegenseitige Anspornen in stressigen Zeiten und das Lachen über die kleinen und großen Herausforderungen des Studiums haben meine Zeit an der Universität unvergesslich gemacht.

Ein großer Dank gilt auch **Birgit Huber**, die mich geduldig unterstützt und mir so vieles im SML beigebracht hat. Ebenso danke ich **Hatice Mutlu** für ihre unschätzbare Unterstützung – sowohl akademisch als auch darüber hinaus. Ohne deine Mentorschaft, deine Ratschläge und deine Ermutigung hätte diese Arbeit nicht in dieser Form existiert.

Des Weiteren möchte ich mich auch bei **Dr. Sven Schneider**, **Cornelius Hub**, **Dr. Azra Kocaarslan**, **Dr. Yosuke Akae**, **Dr. Moritz Köhler**, **Dr. Victoria Lee** und **Dr. Meryem Akdemir** bedanken für die tolle Zusammenarbeit und viele lustige Abende.

Mein Dank geht auch an alle weiteren Studenten und Kollegen des **AK Théato** und **AK Wilhelm**, die meine Promotionszeit mit spannenden Diskussionen, Teamgeist und einer großartigen Atmosphäre zu einer wertvollen Erfahrung gemacht haben.

Von Herzen danke ich meiner Familie: **Oliver**, **Viktoria**, **Fabian** und meinen Großeltern. Trotz der räumlichen Distanz habt ihr mich während meines gesamten Studiums bedingungslos unterstützt. Eure Ermutigung, euer Glaube an mich und eure Förderung meines Wissensdursts haben mich immer angetrieben.

Zuletzt **Gianna** – einfach nur danke dafür, dass du du bist.

11 References

(1) Wiseman, J. The Great Energy Transition of the 21st Century: The 2050 Zero-Carbon World Oration. *Energy Res. Soc. Sci.* **2018**, *35*, 227–232. https://doi.org/10.1016/j.erss.2017.10.011.

(2) Schmaltz, T.; Hartmann, F.; Wicke, T.; Weymann, L.; Neef, C.; Janek, J. A Roadmap for Solid-State Batteries. *Adv. Energy Mater.* **2023**, *13* (43), 2301886. https://doi.org/10.1002/aenm.202301886.

(3) Wulandari, T.; Fawcett, D.; Majumder, S. B.; Poinern, G. E. J. Lithium-based Batteries, History, Current Status, Challenges, and Future Perspectives. *Battery Energy* **2023**, *2* (6), 20230030. https://doi.org/10.1002/bte2.20230030.

(4) Pacios, R.; Villaverde, A.; Martínez-Ibañez, M.; Casas-Cabanas, M.; Aguesse, F.; Kvasha, A. Roadmap for Competitive Production of Solid-State Batteries: How to Convert a Promise into Reality. *Adv. Energy Mater.* **2023**, *13* (30). https://doi.org/10.1002/aenm.202301018.

(5) Kim, K. J.; Balaish, M.; Wadaguchi, M.; Kong, L.; Rupp, J. L. M. Solid-State Li–Metal Batteries: Challenges and Horizons of Oxide and Sulfide Solid Electrolytes and Their Interfaces. *Adv. Energy Mater.* **2021**, *11* (1), 2002689. https://doi.org/10.1002/aenm.202002689.

(6) Shan, X.; Song, Z.; Ding, H.; Li, L.; Tian, Y.; Sokolov, A. P.; Tian, M.; Xu, K.; Cao, P.-F. Polymer Electrolytes with High Cation Transport Number for Rechargeable Li–Metal Batteries: Current Status and Future Direction. *Energy Environ. Sci.* **2024**, *17* (22), 8457–8481. https://doi.org/10.1039/D4EE03097D.

(7) Liu, X.; Li, X.; Li, H.; Wu, H. B. Recent Progress of Hybrid Solid-State Electrolytes for Lithium Batteries. *Chem. – Eur. J.* **2018**, *24* (69), 18293–18306. https://doi.org/10.1002/chem.201803616.

(8) Li, Z.; Zhao, Y.; Tenhaeff, W. E. 5 V Stable Nitrile-Bearing Polymer Electrolyte with Aliphatic Segment as Internal Plasticizer. *ACS Appl. Energy Mater.* **2019**, *2* (5), 3264–3273. https://doi.org/10.1021/acsaem.9b00103.

(9) Sedlmeier, C.; Kutsch, T.; Schuster, R.; Hartmann, L.; Bublitz, R.; Tominac, M.; Bohn, M.; Gasteiger, H. A. From Powder to Sheets: A Comparative Electrolyte Study for Slurry-Based Processed Solid Electrolyte/Binder-Sheets as Separators in All-Solid-State Batteries. *J. Electrochem. Soc.* **2022**, *169* (7), 070508. https://doi.org/10.1149/1945-7111/ac7e76.

(10) Verdier, N.; Lepage, D.; Zidani, R.; Prébé, A.; Aymé-Perrot, D.; Pellerin, C.; Dollé, M.; Rochefort, D. Cross-Linked Polyacrylonitrile-Based Elastomer Used as Gel Polymer Electrolyte in Li-Ion Battery. *ACS Appl. Energy Mater.* **2020**, *3* (1), 1099–1110. https://doi.org/10.1021/acsaem.9b02129.

(11) Wu, S.; Wang, C.; Li, S.; Lin, L.; Tong, Q.; Zhu, M.; Weng, J. Coconstruction of Supramolecular Lithium-Conducting Cross-Linked Networks Based on PVDF and Triblock Polymer Nanomicrosphere Solid-State Polymer Electrolytes for Lithium-Metal Batteries. *ACS Appl. Mater. Interfaces* **2024**. https://doi.org/10.1021/acsami.4c03355.

(12) Yi, S. H.; Xu, T. H.; Li, L.; Gao, M. M.; Du, K.; Zhao, H. L.; Bai, Y. Fast Ion Conductor Modified Double-Polymer (PVDF and PEO) Matrix Electrolyte for Solid Lithium-Ion Batteries. *Solid State Ion.* **2020**, *355*, 115419. https://doi.org/ARTN.

(13) Wang, Y.; Chen, Z.; Wu, Y.; Li, Y.; Yue, Z.; Chen, M. PVDF-HFP/PAN/PDA@LLZTO Composite Solid Electrolyte Enabling Reinforced Safety and Outstanding Low-Temperature Performance for Quasi-Solid-State

Lithium Metal Batteries. *ACS Appl. Mater. Interfaces* **2023**, *15* (17), 21526–21536. https://doi.org/10.1021/acsami.3c02678.

(14) Zhang, X.; Liu, T.; Zhang, S.; Huang, X.; Xu, B.; Lin, Y.; Xu, B.; Li, L.; Nan, C.-W.; Shen, Y. Synergistic Coupling between Li6.75La3Zr1.75Ta0.25O12 and Poly(Vinylidene Fluoride) Induces High Ionic Conductivity, Mechanical Strength, and Thermal Stability of Solid Composite Electrolytes. *J. Am. Chem. Soc.* **2017**, *139* (39), 13779–13785. https://doi.org/10.1021/jacs.7b06364.

(15) Tran, H. K.; Truong, B. T.; Zhang, B.-R.; Jose, R.; Chang, J.-K.; Yang, C.-C. Sandwich-Structured Composite Polymer Electrolyte Based on PVDF-HFP/PPC/Al-Doped LLZO for High-Voltage Solid-State Lithium Batteries. *ACS Appl. Energy Mater.* **2023**, *6* (3), 1475–1487. https://doi.org/10.1021/acsaem.2c03363.

(16) Staunton, E.; Andreev, Y. G.; Bruce, P. G. Structure and Conductivity of the Crystalline Polymer Electrolyte β-PEO6:LiAsF6. *J. Am. Chem. Soc.* **2005**, *127* (35), 12176–12177. https://doi.org/10.1021/ja053249v.

(17) Zhai, H.; Xu, P.; Ning, M.; Cheng, Q.; Mandal, J.; Yang, Y. A Flexible Solid Composite Electrolyte with Vertically Aligned and Connected Ion-Conducting Nanoparticles for Lithium Batteries. *Nano Lett.* **2017**, *17* (5), 3182–3187. https://doi.org/10.1021/acs.nanolett.7b00715.

(18) He, L.; Cao, J.-H.; Wang, Y.-K.; Wu, D.-Y. Flexible “Polymer-in-Ceramic” Composite Solid Electrolyte PI–PEO 0.2 –PDA@LATP 0.8 and Its Ionic Conductivity. *Energy Adv.* **2022**, *1* (12), 1028–1034. https://doi.org/10.1039/d2ya00224h.

(19) He, L.; Liang, W.-H.; Cao, J.-H.; Wu, D.-Y. PI-LATP-PEO Electrolyte with High Safety Performance in Solid-State Lithium Metal Batteries. *ACS Appl. Energy Mater.* **2022**, *5* (4), 5277–5286. https://doi.org/10.1021/acsaem.2c00745.

(20) Rong, Y.; Lu, Z.; Jin, C.; Xu, Y.; Peng, L.; Shi, R.; Gu, T.; Lu, C.; Yang, R. Tailoring of Li/LATP-PEO Interface via a Functional Organic Layer for High-Performance Solid Lithium Metal Batteries. *ACS Sustain. Chem. Eng.* **2023**, *11* (2), 785–795. https://doi.org/10.1021/acssuschemeng.2c06404.

(21) Zhang, J.; Zhao, N.; Zhang, M.; Li, Y.; Chu, P. K.; Guo, X.; Di, Z.; Wang, X.; Li, H. Flexible and Ion-Conducting Membrane Electrolytes for Solid-State Lithium Batteries: Dispersion of Garnet Nanoparticles in Insulating Polyethylene Oxide. *Nano Energy* **2016**, *28*, 447–454. https://doi.org/10.1016/j.nanoen.2016.09.002.

(22) Ma, X.; Liu, M.; Wu, Q.; Guan, X.; Wang, F.; Liu, H.; Xu, J. Composite Electrolytes Prepared by Improving the Interfacial Compatibility of Organic-Inorganic Electrolytes for Dendrite-Free, Long-Life All-Solid Lithium Metal Batteries. *ACS Appl. Mater. Interfaces* **2022**, *14* (48), 53828–53839. https://doi.org/10.1021/acsami.2c16174.

(23) Huang, Y.; Zeng, J.; Li, S.; Dai, C.; Liu, J.; Liu, C.; He, Y. Conformational Regulation of Dielectric Poly(Vinylidene Fluoride)-Based Solid-State Electrolytes for Efficient Lithium Salt Dissociation and Lithium-Ion Transportation. *Adv. Energy Mater.* **2023**, *13* (15), 2203888. https://doi.org/10.1002/aenm.202203888.

(24) Butzelaar, A. J.; Röring, P.; Hoffmann, M.; Atik, J.; Paillard, E.; Wilhelm, M.; Winter, M.; Brunklaus, G.; Theato, P. Advanced Block Copolymer Design for Polymer Electrolytes: Prospects of Microphase Separation. *Macromolecules* **2021**, *54* (23), 11101–11112. https://doi.org/10.1021/acs.macromol.1c02147.

(25) Yusim, Y.; Trevisanello, E.; Ruess, R.; Richter, F. H.; Mayer, A.; Bresser, D.; Passerini, S.; Janek, J.; Henss, A. Evaluation and Improvement of the Stability of Poly(Ethylene Oxide)-Based Solid-State Batteries with High-Voltage

Cathodes. *Angew. Chem. Int. Ed.* **2023**, *62* (12), e202218316. https://doi.org/10.1002/anie.202218316.

(26) Grundy, L. S.; Fu, S.; Hoffman, Z. J.; Balsara, N. P. Electrochemical Characterization of PEO/LiTFSI Electrolytes Near the Solubility Limit. *Macromolecules* **2022**, *55* (20), 9030–9038. https://doi.org/10.1021/acs.macromol.2c01655.

(27) Arbi, K.; Bucheli, W.; Jiménez, R.; Sanz, J. High Lithium Ion Conducting Solid Electrolytes Based on NASICON Li 1+x Al x M 2−x (PO 4) 3 Materials (M = Ti, Ge and 0 ≤ x ≤ 0.5). *J. Eur. Ceram. Soc.* **2015**, *35* (5), 1477–1484. https://doi.org/10.1016/j.jeurceramsoc.2014.11.023.

(28) Siyal, S. H.; Li, M.; Li, H.; Lan, J.-L.; Yu, Y.; Yang, X. Ultraviolet Irradiated PEO/LATP Composite Gel Polymer Electrolytes for Lithium-Metallic Batteries (LMBs). *Appl. Surf. Sci.* **2019**, *494*, 1119–1126. https://doi.org/10.1016/j.apsusc.2019.07.179.

(29) Wang, G.; Wei, C.; Liu, X.; Ding, W. Efficient Lithium Dendrite Control and Intimate Li/Garnet Interface Built through a Carbonized Metal–Organic Framework Layer. *ACS Appl. Energy Mater.* **2024**. https://doi.org/10.1021/acsaem.3c03015.

(30) Lu, W.; Xue, M.; Zhang, C. Modified Li7La3Zr2O12 (LLZO) and LLZO-Polymer Composites for Solid-State Lithium Batteries. *Energy Storage Mater.* **2021**, *39*, 108–129. https://doi.org/10.1016/j.ensm.2021.04.016.

(31) Chen, C.; Wang, K.; He, H.; Hanc, E.; Kotobuki, M.; Lu, L. Processing and Properties of Garnet-Type Li_7 La_3 Zr_2 O_{12} Ceramic Electrolytes. *Small* **2023**, *19* (12), 2205550. https://doi.org/10.1002/smll.202205550.

(32) Ahmed, F.; Chen, A.; Altoé, M. V. P.; Liu, G. Argyrodite-Li 6 PS 5 Cl/Polymer-Based Highly Conductive Composite Electrolyte for All-Solid-State Batteries. *Acs Appl. Energy Mater.* **2024**. https://doi.org/10.1021/acsaem.3c02858.

(33) Chen, Y.; Liang, D.; Lee, E. M. Y.; Muy, S.; Guillaume, M.; Braida, M.-D.; Emery, A. A.; Marzari, N.; de Pablo, J. J. Ion Transport at Polymer–Argyrodite Interfaces. *ACS Appl. Mater. Interfaces* **2024**. https://doi.org/10.1021/acsami.4c07440.

(34) Zhou, X.; Ye, Q.; Pang, B.; Wu, Z.; Yang, T.; Zhang, W.; Xia, Y.; Huang, H.; Xia, X.; He, X.; Gan, Y.; Zhang, J. Styrene–Butadiene–Styrene Block Copolymer-Li 5.5 PS 4.5 Cl 1.5 Composite Solid-State Electrolyte Enabling a High-Performance All-Solid-State Lithium Battery. *ACS Appl. Energy Mater.* **2023**, *6* (23), 12120–12127. https://doi.org/10.1021/acsaem.3c02579.

(35) Huang, W.; Bi, Z.; Zhao, N.; Sun, Q.; Guo, X. Chemical Interface Engineering of Solid Garnet Batteries for Long-Life and High-Rate Performance. *Chem. Eng. J.* **2021**, *424*, 130423. https://doi.org/10.1016/j.cej.2021.130423.

(36) Liu, S.; Liu, W.; Ba, D.; Zhao, Y.; Ye, Y.; Li, Y.; Liu, J. Filler-Integrated Composite Polymer Electrolyte for Solid-State Lithium Batteries. *Adv. Mater.* **2023**, *35* (2), e2110423. https://doi.org/10.1002/adma.202110423.

(37) Xie, X.; Wang, Z.; He, S.; Chen, K.; Huang, Q.; Zhang, P.; Hao, S.; Wang, J.; Zhou, W. Influencing Factors on Li-Ion Conductivity and Interfacial Stability of Solid Polymer Electrolytes, Exampled by Polycarbonates, Polyoxalates and Polymalonates. *Angew. Chem. Int. Ed.* **2023**, *62* (13), e202218229. https://doi.org/10.1002/anie.202218229.

(38) Zheng, J.; Tang, M.; Hu, Y.-Y. Lithium Ion Pathway within Li7 La3 Zr2 O12 - Polyethylene Oxide Composite Electrolytes. *Angew. Chem. Int. Ed Engl.* **2016**, *55* (40), 12538–12542. https://doi.org/10.1002/anie.201607539.

(39) He, Z.; Whale, E. A. . Step-Growth Polymerization—Basics and Development of New Materials. In *Polymer Chemistry: A Practical Approach*; Davis, F. J., Ed.;

Oxford University Press, 2004; p 0. https://doi.org/10.1093/oso/9780198503095.003.0009.
(40) Jenkins, A. D.; Kennedy, J. F.; Ferguson, J.; Sparrow, D. J.; Walton, J. G. Step Growth Polymerization. **1982**. https://doi.org/10.1039/9781847556561-00049.
(41) Rogers, M. E.; Long, T. E.; Turner, S. R. Introduction to Synthetic Methods in Step-Growth Polymers. In *Synthetic Methods in Step-Growth Polymers*; John Wiley & Sons, Ltd, 2003; pp 1–16. https://doi.org/10.1002/0471220523.ch1.
(42) Leiske, M. N.; Kempe, K. A Guideline for the Synthesis of Amino-Acid-Functionalized Monomers and Their Polymerizations. *Macromol. Rapid Commun.* **2022**, *43* (2), 2100615. https://doi.org/10.1002/marc.202100615.
(43) Jacobsen, L. L.; Ray, W. H. Unified Modeling for Polycondensation Kinetics. *J. Macromol. Sci. Part C* **1992**, *32* (3–4), 407–519. https://doi.org/10.1080/15321799208021430.
(44) Kricheldorf, H. R. The Role of Self-Dilution in Step-Growth Polymerizations. *Macromol. Rapid Commun.* **2008**, *29* (21), 1695–1704. https://doi.org/10.1002/marc.200800366.
(45) Carothers, W. H. Polymers and Polyfunctionality. *Trans. Faraday Soc.* **1936**, *32*, 39. https://doi.org/10.1039/tf9363200039.
(46) Ignatov, V. N.; Vasnev, V. A.; Vinogradova, S. V. Reactivity of Macromolecules in the Processes of Polymer Formation. Review. *Polym. Sci. USSR* **1987**, *29* (5), 993–1009. https://doi.org/10.1016/0032-3950(87)90107-9.
(47) Cheng, Z.; Liu, Y.; Li, Z.; Song, Y. Condensation Polymers: Synthesis, Properties, and Applications. *E3S Web Conf.* **2021**, *290*, 01025. https://doi.org/10.1051/e3sconf/202129001025.
(48) Gomez-Lopez, A.; Panchireddy, S.; Grignard, B.; Calvo, I.; Jerome, C.; Detrembleur, C.; Sardon, H. Poly(Hydroxyurethane) Adhesives and Coatings: State-of-the-Art and Future Directions. *ACS Sustain. Chem. Eng.* **2021**, *9* (29), 9541–9562. https://doi.org/10.1021/acssuschemeng.1c02558.
(49) Ramakrishnan, T.; Raja Karthikeyan, K.; Tamilselvan, V.; Sivakumar, S.; Gangodkar, D.; Radha, H. R.; Narain Singh, A.; Asrat Waji, Y. Study of Various Epoxy-Based Surface Coating Techniques for Anticorrosion Properties. *Adv. Mater. Sci. Eng.* **2022**, *2022* (1), 5285919. https://doi.org/10.1155/2022/5285919.
(50) Jérôme, C.; Lecomte, P. Recent Advances in the Synthesis of Aliphatic Polyesters by Ring-Opening Polymerization. *Adv. Drug Deliv. Rev.* **2008**, *60* (9), 1056–1076. https://doi.org/10.1016/j.addr.2008.02.008.
(51) Udipi, K.; Davé, R. S.; Kruse, R. L.; Stebbins, L. R. Polyamides from Lactams via Anionic Ring-Opening Polymerization: 1. Chemistry and Some Recent Findings. *Polymer* **1997**, *38* (4), 927–938. https://doi.org/10.1016/S0032-3861(96)00566-6.
(52) Brocas, A.-L.; Mantzaridis, C.; Tunc, D.; Carlotti, S. Polyether Synthesis: From Activated or Metal-Free Anionic Ring-Opening Polymerization of Epoxides to Functionalization. *Prog. Polym. Sci.* **2013**, *38* (6), 845–873. https://doi.org/10.1016/j.progpolymsci.2012.09.007.
(53) Goff, J.; Sulaiman, S.; Arkles, B. Applications of Hybrid Polymers Generated from Living Anionic Ring Opening Polymerization. *Molecules* **2021**, *26* (9), 2755. https://doi.org/10.3390/molecules26092755.
(54) Dechy-Cabaret, O.; Martin-Vaca, B.; Bourissou, D. Controlled Ring-Opening Polymerization of Lactide and Glycolide. *Chem. Rev.* **2004**, *104* (12), 6147–6176. https://doi.org/10.1021/cr040002s.

(55) Bauer, J.; Hüsing, N.; Kickelbick, G. Preparation of Functionalized Block Copolymers Based on a Polysiloxane Backbone by Anionic Ring-Opening Polymerization. *J. Polym. Sci. Part Polym. Chem.* **2002**, *40* (10), 1539–1551. https://doi.org/10.1002/pola.10235.
(56) Nuyken, O.; Pask, S. D. Ring-Opening Polymerization—An Introductory Review. *Polymers* **2013**, *5* (2), 361–403. https://doi.org/10.3390/polym5020361.
(57) Bergeot, V.; Tassaing, T.; Besnard, M.; Cansell, F.; Mingotaud, A.-F. Anionic Ring-Opening Polymerization of ε-Caprolactone in Supercritical Carbon Dioxide: Parameters Influencing the Reactivity. *J. Supercrit. Fluids* **2004**, *28* (2), 249–261. https://doi.org/10.1016/S0896-8446(03)00040-8.
(58) Gao, T.; Xia, X.; Tajima, K.; Yamamoto, T.; Isono, T.; Satoh, T. Polyether/Polythioether Synthesis via Ring-Opening Polymerization of Epoxides and Episulfides Catalyzed by Alkali Metal Carboxylates. *Macromolecules* **2022**, *55* (21), 9373–9383. https://doi.org/10.1021/acs.macromol.2c00656.
(59) Zhang, C.-J.; Zhu, T.-C.; Cao, X.-H.; Hong, X.; Zhang, X.-H. Poly(Thioether)s from Closed-System One-Pot Reaction of Carbonyl Sulfide and Epoxides by Organic Bases. *J. Am. Chem. Soc.* **2019**, *141* (13), 5490–5496. https://doi.org/10.1021/jacs.9b00544.
(60) Stridsberg, K. M.; Ryner, M.; Albertsson, A.-C. Controlled Ring-Opening Polymerization: Polymers with Designed Macromolecular Architecture. In *Degradable Aliphatic Polyesters*; Springer: Berlin, Heidelberg, 2002; pp 41–65. https://doi.org/10.1007/3-540-45734-8_2.
(61) Dreier, P.; Matthes, R.; Barent, R. D.; Schüttner, S.; Müller, A. H. E.; Frey, H. In Situ Kinetics Reveal the Influence of Solvents and Monomer Structure on the Anionic Ring-Opening Copolymerization of Epoxides. *Macromol. Chem. Phys.* **2023**, *224* (1), 2200209. https://doi.org/10.1002/macp.202200209.
(62) Olsén, P.; Odelius, K.; Albertsson, A.-C. Thermodynamic Presynthetic Considerations for Ring-Opening Polymerization. *Biomacromolecules* **2016**, *17* (3), 699–709. https://doi.org/10.1021/acs.biomac.5b01698.
(63) Chen, C.; Gnanou, Y.; Feng, X. Organocatalytic Selective Coupling of Episulfides with Carbon Disulfide for the Synthesis of Poly(Trithiocarbonate)s and Cyclic Trithiocarbonates. *Polym. Chem.* **2022**, *13* (23), 3471–3478. https://doi.org/10.1039/d2py00405d.
(64) Ivin, K. J. Tutorial: Thermodynamics of Ring-Opening Polymerization; Am. Chem. Soc. 199th National Meeting, Boston, April 22–27, 1990, 6th International Symposium on Ring-Opening and Cyclo-Polymerization. *Makromol. Chem. Macromol. Symp.* **1991**, *42–43* (1), 1–14. https://doi.org/10.1002/masy.19910420103.
(65) Klaus, S.; Lehenmeier, M. W.; Anderson, C. E.; Rieger, B. Recent Advances in CO2/Epoxide Copolymerization—New Strategies and Cooperative Mechanisms. *Coord. Chem. Rev.* **2011**, *255* (13), 1460–1479. https://doi.org/10.1016/j.ccr.2010.12.002.
(66) Kiriratnikom, J.; Guo, J.; Cao, X.; Khan, M. U.; Zhang, C.; Zhang, X. Metal-free Terpolymerization of Propylene Oxide, Carbon Dioxide, and Carbonyl Sulfide: A Facile Route to Sulfur-containing Polycarbonates with Gradient Sequences. *J. Polym. Sci.* **2022**, *60* (24), 3414–3419. https://doi.org/10.1002/pol.20220166.
(67) Guo, L.; J. Lamb, K.; North, M. Recent Developments in Organocatalysed Transformations of Epoxides and Carbon Dioxide into Cyclic Carbonates. *Green Chem.* **2021**, *23* (1), 77–118. https://doi.org/10.1039/D0GC03465G.
(68) Moad, G.; Solomon, D. H. *The Chemistry of Radical Polymerization*; Elsevier, 2005.

(69) Mandal, B. M. *Fundamentals Of Polymerization*; World Scientific, 2012.
(70) Davis, F. J. *Polymer Chemistry: A Practical Approach*; OUP Oxford, 2004.
(71) Kostić, M.; Igić, M.; Gligorijević, N.; Nikolić, V.; Stošić, N.; Nikolić, L. The Use of Acrylate Polymers in Dentistry. *Polymers* **2022**, *14* (21), 4511. https://doi.org/10.3390/polym14214511.
(72) Corsaro, C.; Neri, G.; Santoro, A.; Fazio, E. Acrylate and Methacrylate Polymers' Applications: Second Life with Inexpensive and Sustainable Recycling Approaches. *Materials* **2021**, *15* (1), 282. https://doi.org/10.3390/ma15010282.
(73) Armelin, E.; Oliver, R.; Liesa, F.; Iribarren, J. I.; Estrany, F.; Alemán, C. Marine Paint Fomulations: Conducting Polymers as Anticorrosive Additives. *Prog. Org. Coat.* **2007**, *59* (1), 46–52. https://doi.org/10.1016/j.porgcoat.2007.01.013.
(74) Aronovich, D. a.; Boinovich, L. b. Structural Acrylic Adhesives: A Critical Review. In *Progress in Adhesion and Adhesives*; John Wiley & Sons, Ltd, 2021; pp 651–708. https://doi.org/10.1002/9781119846703.ch15.
(75) Behera, S.; Mahanwar, P. A. Superabsorbent Polymers in Agriculture and Other Applications: A Review. *Polym.-Plast. Technol. Mater.* **2020**, *59* (4), 341–356. https://doi.org/10.1080/25740881.2019.1647239.
(76) Ali, U.; Karim, K. J. Bt. A.; Buang, N. A. A Review of the Properties and Applications of Poly (Methyl Methacrylate) (PMMA). *Polym. Rev.* **2015**, *55* (4), 678–705. https://doi.org/10.1080/15583724.2015.1031377.
(77) Pilevar, Z.; Bahrami, A.; Beikzadeh, S.; Hosseini, H.; Jafari, S. M. Migration of Styrene Monomer from Polystyrene Packaging Materials into Foods: Characterization and Safety Evaluation. *Trends Food Sci. Technol.* **2019**, *91*, 248–261. https://doi.org/10.1016/j.tifs.2019.07.020.
(78) Cai, S.; Zhang, B.; Cremaschi, L. Review of Moisture Behavior and Thermal Performance of Polystyrene Insulation in Building Applications. *Build. Environ.* **2017**, *123*, 50–65. https://doi.org/10.1016/j.buildenv.2017.06.034.
(79) Wünsch, J. R. *Polystyrene: Synthesis, Production and Applications*; iSmithers Rapra Publishing, 2000.
(80) Stîngă, F.; Severin, I.; Mitrache, I. A.; Lascu, E. Redesign of the Curing Area of the Tire Manufacturing Process. *Sustainability* **2020**, *12* (17), 6909. https://doi.org/10.3390/su12176909.
(81) Kaiser, A.; Brandau, S.; Klimpel, M.; Barner-Kowollik, C. Acrylonitrile-Butadiene Rubber (NBR) Prepared via Living/Controlled Radical Polymerization (RAFT). *Macromol. Rapid Commun.* **2010**, *31* (18), 1616–1621. https://doi.org/10.1002/marc.201000162.
(82) Gao, Y.; Zhou, D.; Lyu, J.; A, S.; Xu, Q.; Newland, B.; Matyjaszewski, K.; Tai, H.; Wang, W. Complex Polymer Architectures through Free-Radical Polymerization of Multivinyl Monomers. *Nat. Rev. Chem.* **2020**, *4* (4), 194–212. https://doi.org/10.1038/s41570-020-0170-7.
(83) *Fundamentals of Polymerization*; Mandal, B. M., Ed.; World Scientific: Singapore Hackensack, NJ, 2013.
(84) Mayo, F. R. Chain Transfer in the Polymerization of Styrene: The Reaction of Solvents with Free Radicals1. *J. Am. Chem. Soc.* **1943**, *65* (12), 2324–2329. https://doi.org/10.1021/ja01252a021.
(85) Rizzardo, E.; Chong, Y. K.; Evans, R. A.; And, G. M.; Thang, S. H. Control of Polymer Structure by Chain Transfer Processes. *Macromol. Symp.* **1996**, *111* (1), 1–11. https://doi.org/10.1002/masy.19961110103.
(86) Stoiljkovich, D.; Jovanovich, S. Mechanism of the Short Chain Branching in Low Density Polyethylene. *Makromol. Chem.* **1981**, *182* (10), 2811–2820. https://doi.org/10.1002/macp.1981.021821026.

(87) Furuncuoğlu, T.; Uğur, İ.; Değirmenci, İ.; Aviyente, V. Role of Chain Transfer Agents in Free Radical Polymerization Kinetics. *Macromolecules* **2010**, *43* (4), 1823–1835. https://doi.org/10.1021/ma902803p.
(88) Zhou, F.; Liu, W.; Chen, M.; Sun, D. C. A Novel Way to Prepare Ultra-Thin Polymer Films through Surface Radical Chain-Transfer Reaction. *Chem. Commun. Camb. Engl.* **2001**, No. 23, 2446–2447. https://doi.org/10.1039/b107831n.
(89) Gower, M. D.; Shanks, R. A. The Effect of Chain Transfer Agent Level on Adhesive Performance and Peel Master-Curves for Acrylic Pressure Sensitive Adhesives. *Macromol. Chem. Phys.* **2004**, *205* (16), 2139–2150. https://doi.org/10.1002/macp.200400177.
(90) Bilek, M. M. M.; Bax, D. V.; Kondyurin, A.; Yin, Y.; Nosworthy, N. J.; Fisher, K.; Waterhouse, A.; Weiss, A. S.; Dos Remedios, C. G.; McKenzie, D. R. Free Radical Functionalization of Surfaces to Prevent Adverse Responses to Biomedical Devices. *Proc. Natl. Acad. Sci.* **2011**, *108* (35), 14405–14410. https://doi.org/10.1073/pnas.1103277108.
(91) Tjiam, C.; Gomes, V. G. Optimal Operating Strategies for Emulsion Polymerization with Chain Transfer Agent. *Ind. Eng. Chem. Res.* **2014**, *53* (18), 7526–7537. https://doi.org/10.1021/ie4032956.
(92) Kukulj, D.; Davis, T. P.; Gilbert, R. G. Chain Transfer to Monomer in the Free-Radical Polymerizations of Methyl Methacrylate, Styrene, and α-Methylstyrene. *Macromolecules* **1998**, *31* (4), 994–999. https://doi.org/10.1021/ma971323r.
(93) Moghadam, N.; Liu, S.; Srinivasan, S.; Grady, M. C.; Soroush, M.; Rappe, A. M. Computational Study of Chain Transfer to Monomer Reactions in High-Temperature Polymerization of Alkyl Acrylates. *J. Phys. Chem. A* **2013**, *117* (12), 2605–2618. https://doi.org/10.1021/jp3100798.
(94) Ballard, N.; de la Cal, J. C.; Asua, J. M. The Role of Chain Transfer Agent in Reducing Branching Content in Radical Polymerization of Acrylates. *Macromolecules* **2015**, *48* (4), 987–993. https://doi.org/10.1021/ma502575j.
(95) El Rezzi, V. Chain-Transfer Kinetics for Free-Radical Homo- and Coplymerizations of Styrene and Methyl Methacrylate in Supercritical Carbon Dioxide. Doctoral Thesis, 2001. https://doi.org/10.53846/goediss-2107.
(96) Jaramillo-Soto, G.; García-Morán, P. R.; Vivaldo-Lima, E. Effect of Stabilizer Concentration, Pressure and Temperature on Polymerization Rate and Molecular Weight Development in RAFT Polymerization of MMA in scCO2. *Macromol. Symp.* **2010**, *289* (1), 149–154. https://doi.org/10.1002/masy.200900019.
(97) Moghadam, N.; Srinivasan, S.; Grady, M. C.; Rappe, A. M.; Soroush, M. Theoretical Study of Chain Transfer to Solvent Reactions of Alkyl Acrylates. *J. Phys. Chem. A* **2014**, *118* (29), 5474–5487. https://doi.org/10.1021/jp5020669.
(98) Nomura, M.; Minamino, Y.; Fujita, K.; Harada, M. The Role of Chain Transfer Agents in the Emulsion Polymerization of Styrene. *J. Polym. Sci. Polym. Chem. Ed.* **1982**, *20* (5), 1261–1270. https://doi.org/10.1002/pol.1982.170200509.
(99) Corrigan, N.; Jung, K.; Moad, G.; Hawker, C. J.; Matyjaszewski, K.; Boyer, C. Reversible-Deactivation Radical Polymerization (Controlled/Living Radical Polymerization): From Discovery to Materials Design and Applications. *Prog. Polym. Sci.* **2020**, *111*, 101311. https://doi.org/10.1016/j.progpolymsci.2020.101311.
(100) Nicolas, J.; Guillaneuf, Y.; Lefay, C.; Bertin, D.; Gigmes, D.; Charleux, B. Nitroxide-Mediated Polymerization. *Prog. Polym. Sci.* **2013**, *38* (1), 63–235. https://doi.org/10.1016/j.progpolymsci.2012.06.002.

(101) Truong, N. P.; Jones, G. R.; Bradford, K. G. E.; Konkolewicz, D.; Anastasaki, A. A Comparison of RAFT and ATRP Methods for Controlled Radical Polymerization. *Nat. Rev. Chem.* **2021**, *5* (12), 859–869. https://doi.org/10.1038/s41570-021-00328-8.
(102) Siegwart, D. J.; Oh, J. K.; Matyjaszewski, K. ATRP in the Design of Functional Materials for Biomedical Applications. *Prog. Polym. Sci.* **2012**, *37* (1), 18–37. https://doi.org/10.1016/j.progpolymsci.2011.08.001.
(103) Matyjaszewski, K. Current Status and Outlook for ATRP. *Eur. Polym. J.* **2024**, *211*, 113001. https://doi.org/10.1016/j.eurpolymj.2024.113001.
(104) Klumperman, B. Living Radical Polymerization. In *Encyclopedia of Polymer Science and Technology*; John Wiley & Sons, Ltd, 2003. https://doi.org/10.1002/0471440264.pst453.
(105) Lowe, A. B.; McCormick, C. L. Homogeneous Controlled Free Radical Polymerization in Aqueous Media. *Aust. J. Chem.* **2002**, *55* (7), 367. https://doi.org/10.1071/CH02053.
(106) *Handbook of RAFT Polymerization*; Barner-Kowollik, C., Ed.; Wiley-VCH: Weinheim, 2008.
(107) *Functional Polymers by Post-Polymerization Modification: Concepts, Guidelines, and Applications*; Klok, H.-A., Theato, P., Eds.; Wiley-VCH: Weinheim, 2013. https://doi.org/10.1002/9783527655427.
(108) Gauthier, M. A.; Gibson, M. I.; Klok, H.-A. Synthesis of Functional Polymers by Post-Polymerization Modification. *Angew. Chem. Int. Ed.* **2009**, *48* (1), 48–58. https://doi.org/10.1002/anie.200801951.
(109) Günay, K. A.; Theato, P.; Klok, H.-A. Standing on the Shoulders of Hermann Staudinger: Post-Polymerization Modification from Past to Present. *J. Polym. Sci. Part Polym. Chem.* **2013**, *51* (1), 1–28. https://doi.org/10.1002/pola.26333.
(110) Chen, X.; Michinobu, T. Postpolymerization Modification: A Powerful Tool for the Synthesis and Function Tuning of Stimuli-Responsive Polymers. *Macromol. Chem. Phys.* **2022**, *223* (1), 2100370. https://doi.org/10.1002/macp.202100370.
(111) Tiwari, V. K.; Jaiswal, M. K.; Rajkhowa, S.; Singh, S. K. Click Chemistry and Bioorthogonal Chemistry: General Consideration from Discovery to Applications. In *Click Chemistry*; Tiwari, V. K., Jaiswal, M. K., Rajkhowa, S., Singh, S. K., Eds.; Springer Nature: Singapore, 2024; pp 1–42. https://doi.org/10.1007/978-981-97-4596-8_1.
(112) Surana, K.; Jadhav, S.; Khiarnar, R.; Wagh, D.; Mahajan, S.; Sonawane, D. A Recent Concept of Importance: Click Chemistry. *Prog. Chem. Biochem. Res.* **2024**, *7* (4). https://doi.org/10.48309/pcbr.2024.461262.1361.
(113) Soutif, J.-C.; Brosse, J.-C. Chemical Modification of Polymers. *React. Polym.* **1990**, *13* (1–2), 1–26. https://doi.org/10.1016/0923-1137(90)90037-5.
(114) Lin, B.; Zhou, S. Poly(Ethylene Glycol)-Grafted Silica Nanoparticles for Highly Hydrophilic Acrylic-Based Polyurethane Coatings. *Prog. Org. Coat.* **2017**, *106*, 145–154. https://doi.org/10.1016/j.porgcoat.2017.02.008.
(115) Zhang, X.; Lin, G.; Kumar, S. R.; Mark, J. E. Hydrogels Prepared from Polysiloxane Chains by End Linking Them with Trifunctional Silanes Containing Hydrophilic Groups. *Polymer* **2009**, *50* (23), 5414–5421. https://doi.org/10.1016/j.polymer.2009.01.047.
(116) Mai, Y.; Eisenberg, A. Self-Assembly of Block Copolymers. *Chem. Soc. Rev.* **2012**, *41* (18), 5969–5985. https://doi.org/10.1039/C2CS35115C.
(117) Ariga, K.; Hill, J. P.; Lee, M. V.; Vinu, A.; Charvet, R.; Acharya, S. Challenges and Breakthroughs in Recent Research on Self-Assembly. *Sci. Technol. Adv. Mater.* **2008**, *9* (1), 014109. https://doi.org/10.1088/1468-6996/9/1/014109.

(118) Pfeffer, R.; Dave, R. N.; Wei, D.; Ramlakhan, M. Synthesis of Engineered Particulates with Tailored Properties Using Dry Particle Coating. *Powder Technol.* **2001**, *117* (1), 40–67. https://doi.org/10.1016/S0032-5910(01)00314-X.
(119) Karimi, Z.; Karimi, L.; Shokrollahi, H. Nano-Magnetic Particles Used in Biomedicine: Core and Coating Materials. *Mater. Sci. Eng. C* **2013**, *33* (5), 2465–2475. https://doi.org/10.1016/j.msec.2013.01.045.
(120) Torchilin, V. P. Polymer-Coated Long-Circulating Microparticulate Pharmaceuticals. *J. Microencapsul.* **1998**, *15* (1), 1–19. https://doi.org/10.3109/02652049809006831.
(121) Mathiazhagan, A.; Joseph, R. Nanotechnology-A New Prospective in Organic Coating -Review. *Int. J. Chem. Eng. Appl.* **2011**, 225–237. https://doi.org/10.7763/IJCEA.2011.V2.108.
(122) Zhang, X.-T.; Sato, O.; Taguchi, M.; Einaga, Y.; Murakami, T.; Fujishima, A. Self-Cleaning Particle Coating with Antireflection Properties. *Chem. Mater.* **2005**, *17* (3), 696–700. https://doi.org/10.1021/cm0484201.
(123) Caruso, F. Nanoengineering of Particle Surfaces. *Adv. Mater.* **2001**, *13* (1), 11–22. https://doi.org/10.1002/1521-4095(200101)13:1<11::AID-ADMA11>3.0.CO;2-N.
(124) Butt, M. A. Theory Of Adhesion and Its Practical Implications A Critical Review. *J. Fac. Eng. Technol.* **2010**.
(125) Partch, R.; Brown, S. Aerosol and Solution Modification of Particle-Polymer Interfaces. *J. Adhes.* **1998**, *67* (1–4), 259–276. https://doi.org/10.1080/00218469808011111.
(126) Lyu, Q.; Hsueh, N.; Chai, C. L. L. The Chemistry of Bioinspired Catechol(Amine)-Based Coatings. *ACS Biomater. Sci. Eng.* **2019**, *5* (6), 2708–2724. https://doi.org/10.1021/acsbiomaterials.9b00281.
(127) Ahangaran, F.; Navarchian, A. H. Recent Advances in Chemical Surface Modification of Metal Oxide Nanoparticles with Silane Coupling Agents: A Review. *Adv. Colloid Interface Sci.* **2020**, *286*, 102298. https://doi.org/10.1016/j.cis.2020.102298.
(128) Apsey, H.; Hill, D.; Barron, A. R.; Alexander, S. Slippery Alkoxysilane Coatings for Antifouling Applications. *ACS Appl. Mater. Interfaces* **2023**, *15* (13), 17353–17363. https://doi.org/10.1021/acsami.3c00555.
(129) L. M. Gonçalves, J.; J. Castanheira, E.; P. C. Alves, S.; Baleizão, C.; Farinha, J. P. Grafting with RAFT—gRAFT Strategies to Prepare Hybrid Nanocarriers with Core-Shell Architecture. *Polymers* **2020**, *12* (10), 2175. https://doi.org/10.3390/polym12102175.
(130) Kato, K.; Uchida, E.; Kang, E.-T.; Uyama, Y.; Ikada, Y. Polymer Surface with Graft Chains. *Prog. Polym. Sci.* **2003**, *28* (2), 209–259. https://doi.org/10.1016/S0079-6700(02)00032-1.
(131) Vega-Hernández, M. Á.; Cano-Díaz, G. S.; Vivaldo-Lima, E.; Rosas-Aburto, A.; Hernández-Luna, M. G.; Martinez, A.; Palacios-Alquisira, J.; Mohammadi, Y.; Penlidis, A. A Review on the Synthesis, Characterization, and Modeling of Polymer Grafting. *Processes* **2021**, *9* (2), 375. https://doi.org/10.3390/pr9020375.
(132) Matyjaszewski, K.; Dong, H.; Jakubowski, W.; Pietrasik, J.; Kusumo, A. Grafting from Surfaces for “Everyone”: ARGET ATRP in the Presence of Air. *Langmuir* **2007**, *23* (8), 4528–4531. https://doi.org/10.1021/la063402e.
(133) Chevigny, C.; Gigmes, D.; Bertin, D.; Jestin, J.; Boué, F. Polystyrene Grafting from Silica Nanoparticles via Nitroxide-Mediated Polymerization (NMP):

Synthesis and SANS Analysis with the Contrast Variation Method. *Soft Matter* **2009**, *5* (19), 3741. https://doi.org/10.1039/b906754j.
(134) Stamm, M. *Polymer Surfaces and Interfaces: Characterization, Modification and Applications*, 1st ed.; Springer: Berlin, 2008.
(135) Hosseini, M.; Makhlouf, A. S. H. *Industrial Applications for Intelligent Polymers and Coatings*; Springer: Cham, 2016.
(136) Millot, Y.; Hervier, A.; Ayari, J.; Hmili, N.; Blanchard, J.; Boujday, S. Revisiting Alkoxysilane Assembly on Silica Surfaces: Grafting versus Homo-Condensation in Solution. *J. Am. Chem. Soc.* **2023**, *145* (12), 6671–6681. https://doi.org/10.1021/jacs.2c11390.
(137) Suegama, P. H.; de Melo, H. G.; Recco, A. A. C.; Tschiptschin, A. P.; Aoki, I. V. Corrosion Behavior of Carbon Steel Protected with Single and Bi-Layer of Silane Films Filled with Silica Nanoparticles. *Surf. Coat. Technol.* **2008**, *202* (13), 2850–2858. https://doi.org/10.1016/j.surfcoat.2007.10.028.
(138) Yan, H.; Yuanhao, W.; Hongxing, Y. TEOS/Silane Coupling Agent Composed Double Layers Structure: A Novel Super-Hydrophilic Coating with Controllable Water Contact Angle Value. *Appl. Energy* **2017**, *185*, 2209–2216. https://doi.org/10.1016/j.apenergy.2015.09.097.
(139) Overhoff, G. M.; Ali, M. Y.; Brinkmann, J.-P.; Lennartz, P.; Orthner, H.; Hammad, M.; Wiggers, H.; Winter, M.; Brunklaus, G. Ceramic-in-Polymer Hybrid Electrolytes with Enhanced Electrochemical Performance. *ACS Appl. Mater. Interfaces* **2022**, *14* (48), 53636–53647. https://doi.org/10.1021/acsami.2c13408.
(140) Yang, Y.; Yang, Z.; Zhao, Q.; Cheng, X.; Tjong, S. C.; Li, R. K. Y.; Wang, X.; Xie, X. Immobilization of RAFT Agents on Silica Nanoparticles Utilizing an Alternative Functional Group and Subsequent Surface-Initiated RAFT Polymerization. *J. Polym. Sci. Part Polym. Chem.* **2009**, *47* (2), 467–484. https://doi.org/10.1002/pola.23164.
(141) Mohanan, S.; Guan, X.; Liang, M.; Karakoti, A.; Vinu, A. Stimuli-Responsive Silica Silanol Conjugates: Strategic Nanoarchitectonics in Targeted Drug Delivery. *Small* **2024**, *20* (39), 2301113. https://doi.org/10.1002/smll.202301113.
(142) Trovato, V.; Mezzi, A.; Brucale, M.; Rosace, G.; Rosaria Plutino, M. Alizarin-Functionalized Organic-Inorganic Silane Coatings for the Development of Wearable Textile Sensors. *J. Colloid Interface Sci.* **2022**, *617*, 463–477. https://doi.org/10.1016/j.jcis.2022.03.006.
(143) Kuzminska, M.; Carlier, N.; Backov, R.; Gaigneaux, E. M. Magnetic Nanoparticles: Improving Chemical Stability via Silica Coating and Organic Grafting with Silanes for Acidic Media Catalytic Reactions. *Appl. Catal. Gen.* **2015**, *505*, 200–212. https://doi.org/10.1016/j.apcata.2015.08.005.
(144) Cappelletti, G.; Fermo, P. Hydrophobic and Superhydrophobic Coatings for Limestone and Marble Conservation. In *Smart Composite Coatings and Membranes*; Elsevier, 2016; pp 421–452. https://doi.org/10.1016/B978-1-78242-283-9.00015-4.
(145) Chruściel, J. J.; Leśniak, E. Modification of Epoxy Resins with Functional Silanes, Polysiloxanes, Silsesquioxanes, Silica and Silicates. *Prog. Polym. Sci.* **2015**, *41*, 67–121. https://doi.org/10.1016/j.progpolymsci.2014.08.001.
(146) *The Nobel Prize in Chemistry 2019*. NobelPrize.org. https://www.nobelprize.org/prizes/chemistry/2019/popular-information/ (accessed 2024-12-03).
(147) Beard, K. W. *Linden's Handbook of Batteries, Fifth Edition*, 5th edition.; McGraw-Hill Education: New York, N.Y, 2019.

(148) Nzereogu, P. U.; Omah, A. D.; Ezema, F. I.; Iwuoha, E. I.; Nwanya, A. C. Anode Materials for Lithium-Ion Batteries: A Review. *Appl. Surf. Sci. Adv.* **2022**, *9*, 100233. https://doi.org/10.1016/j.apsadv.2022.100233.
(149) Blomgren, G. E. The Development and Future of Lithium Ion Batteries. *J. Electrochem. Soc.* **2016**, *164* (1), A5019. https://doi.org/10.1149/2.0251701jes.
(150) Wang, Q.; Jiang, L.; Yu, Y.; Sun, J. Progress of Enhancing the Safety of Lithium Ion Battery from the Electrolyte Aspect. *Nano Energy* **2019**, *55*, 93–114. https://doi.org/10.1016/j.nanoen.2018.10.035.
(151) Arora, P.; Zhang, Z. (John). Battery Separators. *Chem. Rev.* **2004**, *104* (10), 4419–4462. https://doi.org/10.1021/cr020738u.
(152) Zhu, P.; Gastol, D.; Marshall, J.; Sommerville, R.; Goodship, V.; Kendrick, E. A Review of Current Collectors for Lithium-Ion Batteries. *J. Power Sources* **2021**, *485*, 229321. https://doi.org/10.1016/j.jpowsour.2020.229321.
(153) Kim, T.; Song, W.; Son, D.-Y.; K. Ono, L.; Qi, Y. Lithium-Ion Batteries: Outlook on Present, Future, and Hybridized Technologies. *J. Mater. Chem. A* **2019**, *7* (7), 2942–2964. https://doi.org/10.1039/C8TA10513H.
(154) Wakihara, M. Recent Developments in Lithium Ion Batteries. *Mater. Sci. Eng. R Rep.* **2001**, *33* (4), 109–134. https://doi.org/10.1016/S0927-796X(01)00030-4.
(155) Tarascon, J. M.; Armand, M. Issues and Challenges Facing Rechargeable Lithium Batteries. *Nature* **2001**, *414* (6861), 359–367. https://doi.org/10.1038/35104644.
(156) Long, L.; Wang, S.; Xiao, M.; Meng, Y. Polymer Electrolytes for Lithium Polymer Batteries. *J. Mater. Chem. A* **2016**, *4* (26), 10038–10069. https://doi.org/10.1039/C6TA02621D.
(157) Nishijima, M.; Ootani, T.; Kamimura, Y.; Sueki, T.; Esaki, S.; Murai, S.; Fujita, K.; Tanaka, K.; Ohira, K.; Koyama, Y.; Tanaka, I. Accelerated Discovery of Cathode Materials with Prolonged Cycle Life for Lithium-Ion Battery. *Nat. Commun.* **2014**, *5* (1), 4553. https://doi.org/10.1038/ncomms5553.
(158) Saxena, S.; Xing, Y.; Kwon, D.; Pecht, M. Accelerated Degradation Model for C-Rate Loading of Lithium-Ion Batteries. *Int. J. Electr. Power Energy Syst.* **2019**, *107*, 438–445. https://doi.org/10.1016/j.ijepes.2018.12.016.
(159) Ma, S.; Jiang, M.; Tao, P.; Song, C.; Wu, J.; Wang, J.; Deng, T.; Shang, W. Temperature Effect and Thermal Impact in Lithium-Ion Batteries: A Review. *Prog. Nat. Sci. Mater. Int.* **2018**, *28* (6), 653–666. https://doi.org/10.1016/j.pnsc.2018.11.002.
(160) Wagner, R.; Korth, M.; Streipert, B.; Kasnatscheew, J.; Gallus, D. R.; Brox, S.; Amereller, M.; Cekic-Laskovic, I.; Winter, M. Impact of Selected LiPF6 Hydrolysis Products on the High Voltage Stability of Lithium-Ion Battery Cells. *ACS Appl. Mater. Interfaces* **2016**, *8* (45), 30871–30878. https://doi.org/10.1021/acsami.6b09164.
(161) Hu, M.; Wang, Y.; Ye, D. A Timely Review of Lithium-Ion Batteries in Electric Vehicles: Progress, Future Opportunities, and Challenges. *E3S Web Conf.* **2021**, *308*, 01015. https://doi.org/10.1051/e3sconf/202130801015.
(162) Chen, X. Navigating the Energy Storage Landscape: A Comprehensive Analysis of Lithium-Ion Batteries and Improvements. *Highlights Sci. Eng. Technol.* **2024**, *90*, 129–138. https://doi.org/10.54097/x3ywxs69.
(163) Huang, J.; Li, C.; Jiang, D.; Gao, J.; Cheng, L.; Li, G.; Luo, H.; Xu, Z.-L.; Shin, D.-M.; Wang, Y.; Lu, Y.; Kim, Y. Solid-State Electrolytes for Lithium Metal Batteries: State-of-the-Art and Perspectives. *Adv. Funct. Mater. n/a* (n/a), 2411171. https://doi.org/10.1002/adfm.202411171.

(164) Sharma, S. K.; Sharma, G.; Gaur, A.; Arya, A.; Mirsafi, F. S.; Abolhassani, R.; Rubahn, H.-G.; Yu, J.-S.; Mishra, Y. K. Progress in Electrode and Electrolyte Materials: Path to All-Solid-State Li-Ion Batteries. *Energy Adv.* **2022**, *1* (8), 457–510. https://doi.org/10.1039/d2ya00043a.
(165) Peng, Y.; Xiong, X.; Fan, W.; Gao, W.; Cheng, X.; He, J.; Fu, L.; van Ree, T.; Wang, T.; Wu, Y. Strategies to Regulate the Interface between Li Metal Anodes and All-Solid-State Electrolytes. *Mater. Chem. Front.* **2024**. https://doi.org/10.1039/D3QM01023F.
(166) Heubner, C.; Maletti, S.; Auer, H.; Hüttl, J.; Voigt, K.; Lohrberg, O.; Nikolowski, K.; Partsch, M.; Michaelis, A. From Lithium-Metal toward Anode-Free Solid-State Batteries: Current Developments, Issues, and Challenges. *Adv. Funct. Mater.* **2021**, *31* (51), 2106608. https://doi.org/10.1002/adfm.202106608.
(167) Xu, L.; Tang, S.; Cheng, Y.; Wang, K.; Liang, J.; Liu, C.; Cao, Y.-C.; Wei, F.; Mai, L. Interfaces in Solid-State Lithium Batteries. *Joule* **2018**, *2* (10), 1991–2015. https://doi.org/10.1016/j.joule.2018.07.009.
(168) Minnmann, P.; Strauss, F.; Bielefeld, A.; Ruess, R.; Adelhelm, P.; Burkhardt, S.; Dreyer, S. L.; Trevisanello, E.; Ehrenberg, H.; Brezesinski, T.; Richter, F. H.; Janek, J. Designing Cathodes and Cathode Active Materials for Solid-State Batteries. *Adv. Energy Mater.* **2022**, *12* (35), 2201425. https://doi.org/10.1002/aenm.202201425.
(169) Xian, C.; Wang, Q.; Xia, Y.; Cao, F.; Shen, S.; Zhang, Y.; Chen, M.; Zhong, Y.; Zhang, J.; He, X.; Xia, X.; Zhang, W.; Tu, J. Solid-State Electrolytes in Lithium-Sulfur Batteries: Latest Progresses and Prospects. *Small Weinh. Bergstr. Ger.* **2023**, *19* (24), e2208164. https://doi.org/10.1002/smll.202208164.
(170) Zaman, W.; Hatzell, K. B. Processing and Manufacturing of next Generation Lithium-Based All Solid-State Batteries. *Curr. Opin. Solid State Mater. Sci.* **2022**, *26* (4), 101003. https://doi.org/10.1016/j.cossms.2022.101003.
(171) Song, Z.; Chen, F.; Martinez-Ibañez, M.; Feng, W.; Forsyth, M.; Zhou, Z.; Armand, M.; Zhang, H. A Reflection on Polymer Electrolytes for Solid-State Lithium Metal Batteries. *Nat. Commun.* **2023**, *14* (1), 4884. https://doi.org/10.1038/s41467-023-40609-y.
(172) Li, J.; Cai, Y.; Wu, H.; Yu, Z.; Yan, X.; Zhang, Q.; Gao, T. Z.; Liu, K.; Jia, X.; Bao, Z. Polymers in Lithium-Ion and Lithium Metal Batteries. *Adv. Energy Mater.* **2021**, *11* (15). https://doi.org/10.1002/aenm.202003239.
(173) Guan, X.; Wu, Q. P.; Zhang, X. W.; Guo, X. H.; Li, C. L.; Xu, J. In-Situ Crosslinked Single Ion Gel Polymer Electrolyte with Superior Performances for Lithium Metal Batteries. *Chem. Eng. J.* **2020**, *382*, 122935. https://doi.org/ARTN.
(174) Nair, J. R.; Imholt, L.; Brunklaus, G.; Winter, M. Lithium Metal Polymer Electrolyte Batteries: Opportunities and Challenges. *Electrochem. Soc. Interface* **2019**, *28* (2), 55–61. https://doi.org/10.1149/2.F05192if.
(175) Lu, T.; Guan, L.; Zhan, Q.; Liang, Z.; Liu, C.; Hou, L.; Du, H.; Wei, Y.; Wang, S.; Wang, Q. Designing Polymer Electrolytes for Advanced Solid Lithium-Ion Batteries: Recent Advances and Future Perspectives. *Mater. Chem. Front.* **2023**, *7* (18), 3937–3957. https://doi.org/10.1039/D3QM00315A.
(176) Aziz, S. B.; Woo, T. J.; Kadir, M. F. Z.; Ahmed, H. M. A Conceptual Review on Polymer Electrolytes and Ion Transport Models. *J. Sci. Adv. Mater. Devices* **2018**, *3* (1), 1–17. https://doi.org/10.1016/j.jsamd.2018.01.002.
(177) Ngai, K. S.; Ramesh, S.; Ramesh, K.; Juan, J. C. A Review of Polymer Electrolytes: Fundamental, Approaches and Applications. *Ionics* **2016**, *22* (8), 1259–1279. https://doi.org/10.1007/s11581-016-1756-4.

(178) Molinari, N.; Mailoa, J. P.; Kozinsky, B. Effect of Salt Concentration on Ion Clustering and Transport in Polymer Solid Electrolytes: A Molecular Dynamics Study of PEO–LiTFSI. *Chem. Mater.* **2018**, *30* (18), 6298–6306. https://doi.org/10.1021/acs.chemmater.8b01955.
(179) Nie, M.; Lucht, B. L. Role of Lithium Salt on Solid Electrolyte Interface (SEI) Formation and Structure in Lithium Ion Batteries. *J. Electrochem. Soc.* **2014**, *161* (6), A1001. https://doi.org/10.1149/2.054406jes.
(180) Li, B.; Chao, Y.; Li, M.; Xiao, Y.; Li, R.; Yang, K.; Cui, X.; Xu, G.; Li, L.; Yang, C.; Yu, Y.; Wilkinson, D. P.; Zhang, J. A Review of Solid Electrolyte Interphase (SEI) and Dendrite Formation in Lithium Batteries. *Electrochem. Energy Rev.* **2023**, *6* (1), 7. https://doi.org/10.1007/s41918-022-00147-5.
(181) Kundu, S.; Kraytsberg, A.; Ein-Eli, Y. Recent Development in the Field of Ceramics Solid-State Electrolytes: I—Oxide Ceramic Solid-State Electrolytes. *J. Solid State Electrochem.* **2022**, *26* (9), 1809–1838. https://doi.org/10.1007/s10008-022-05206-x.
(182) DeWees, R.; Wang, H. Synthesis and Properties of NaSICON-Type LATP and LAGP Solid Electrolytes. *ChemSusChem* **2019**, *12* (16), 3713–3725. https://doi.org/10.1002/cssc.201900725.
(183) Wang, C.; Fu, K.; Kammampata, S. P.; McOwen, D. W.; Samson, A. J.; Zhang, L.; Hitz, G. T.; Nolan, A. M.; Wachsman, E. D.; Mo, Y.; Thangadurai, V.; Hu, L. Garnet-Type Solid-State Electrolytes: Materials, Interfaces, and Batteries. *Chem. Rev.* **2020**, *120* (10), 4257–4300. https://doi.org/10.1021/acs.chemrev.9b00427.
(184) Lu, J.; Li, Y. Perovskite-type Li-ion Solid Electrolytes: A Review. *J. Mater. Sci. Mater. Electron.* **2021**, *32* (8), 9736–9754. https://doi.org/10.1007/s10854-021-05699-8.
(185) Tao, B.; Ren, C.; Li, H.; Liu, B.; Jia, X.; Dong, X.; Zhang, S.; Chang, H. Thio-/LISICON and LGPS-Type Solid Electrolytes for All-Solid-State Lithium-Ion Batteries. *Adv. Funct. Mater.* **2022**, *32* (34), 2203551. https://doi.org/10.1002/adfm.202203551.
(186) Wang, Z.; Xu, H.; Xuan, M.; Shao, G. From Anti-Perovskite to Double Anti-Perovskite: Tuning Lattice Chemistry to Achieve Super-Fast Li^+ Transport in Cubic Solid Lithium Halogen–Chalcogenides. *J. Mater. Chem. A* **2018**, *6* (1), 73–83. https://doi.org/10.1039/C7TA08698A.
(187) Zhu, J.; Li, S.; Zhang, Y.; Howard, J. W.; Lü, X.; Li, Y.; Wang, Y.; Kumar, R. S.; Wang, L.; Zhao, Y. Enhanced Ionic Conductivity with Li7O2Br3 Phase in Li3OBr Anti-Perovskite Solid Electrolyte. *Appl. Phys. Lett.* **2016**, *109* (10), 101904. https://doi.org/10.1063/1.4962437.
(188) Dawson, J. A.; Canepa, P.; Famprikis, T.; Masquelier, C.; Islam, M. S. Atomic-Scale Influence of Grain Boundaries on Li-Ion Conduction in Solid Electrolytes for All-Solid-State Batteries. *J. Am. Chem. Soc.* **2018**, *140* (1), 362–368. https://doi.org/10.1021/jacs.7b10593.
(189) Bates, J. Electrical Properties of Amorphous Lithium Electrolyte Thin Films. *Solid State Ion.* **1992**, *53–56*, 647–654. https://doi.org/10.1016/0167-2738(92)90442-R.
(190) Lee, S.-J.; Bae, J.-H.; Lee, H.-W.; Baik, H.-K.; Lee, S.-M. Electrical Conductivity in Li–Si–P–O–N Oxynitride Thin-Films. *J. Power Sources* **2003**, *123* (1), 61–64. https://doi.org/10.1016/S0378-7753(03)00457-9.
(191) Fujita, Y.; Kimura, T.; Deguchi, M.; Motohashi, K.; Sakuda, A.; Tatsumisago, M.; Tsukasaki, H.; Mori, S.; Ikeda, K.; Ohara, K.; Kuwata, N.; Amezawa, K.; Hayashi, A. Structural Investigation of Li_2 O–LiI Amorphous Solid Electrolytes. *J. Phys.*

Chem. C **2023**, *127* (30), 14687–14693. https://doi.org/10.1021/acs.jpcc.3c03876.

(192) Zhang, S.; Zhao, F.; Chen, J.; Fu, J.; Luo, J.; Alahakoon, S. H.; Chang, L.-Y.; Feng, R.; Shakouri, M.; Liang, J.; Zhao, Y.; Li, X.; He, L.; Huang, Y.; Sham, T.-K.; Sun, X. A Family of Oxychloride Amorphous Solid Electrolytes for Long-Cycling All-Solid-State Lithium Batteries. *Nat. Commun.* **2023**, *14* (1), 3780. https://doi.org/10.1038/s41467-023-39197-8.

(193) Okumura, T.; Taminato, S.; Miyazaki, Y.; Kitamura, M.; Saito, T.; Takeuchi, T.; Kobayashi, H. LISICON-Based Amorphous Oxide for Bulk-Type All-Solid-State Lithium-Ion Battery. *ACS Appl. Energy Mater.* **2020**, *3* (4), 3220–3229. https://doi.org/10.1021/acsaem.9b01949.

(194) Famprikis, T.; Canepa, P.; Dawson, J. A.; Islam, M. S.; Masquelier, C. Fundamentals of Inorganic Solid-State Electrolytes for Batteries. *Nat. Mater.* **2019**, *18* (12), 1278–1291. https://doi.org/10.1038/s41563-019-0431-3.

(195) Cao, S.; Song, S.; Xiang, X.; Hu, Q.; Zhang, C.; Xia, Z.; Xu, Y.; Zha, W.; Li, J.; Gonzale, P. M.; Han, Y.-H.; Chen, F. Modeling, Preparation, and Elemental Doping of Li7La3Zr2O12 Garnet-Type Solid Electrolytes: A Review. *J. Korean Ceram. Soc.* **2019**, *56* (2), 111–129. https://doi.org/10.4191/kcers.2019.56.2.01.

(196) Chu, J.; Li, Z.; Wang, J.; Huang, G.; Zhang, X. Optimization Strategies for Key Interfaces of LLZO-Based Solid-State Lithium Metal Batteries. *Mater. Chem. Front.* **2024**. https://doi.org/10.1039/D3QM01111A.

(197) Dong, Y.; Chen, I.-W.; Li, J. Transverse and Longitudinal Degradations in Ceramic Solid Electrolytes. *Chem. Mater.* **2022**, *34* (13), 5749–5765. https://doi.org/10.1021/acs.chemmater.2c00329.

(198) Ghosh, K.; Wasim Raja, M. Engineered Li 7 La 3 Zr 2 O 12 (LLZO) for Pseudo-Solid-State Lithium Metal Batteries (SSLMBs): Tailor-Made Synthesis, Evolution of the Microstructure, Suppression of Dendritic Growth, and Enhanced Electrochemical Performance. *ACS Appl. Energy Mater.* **2023**, *6* (7), 4035–4052. https://doi.org/10.1021/acsaem.3c00291.

(199) Aono, H.; Sugimoto, E.; Sadaoka, Y.; Imanaka, N.; Adachi, G. Ionic Conductivity of the Lithium Titanium Phosphate (Li1 + X M X Ti2 − X (PO 4) 3 , M = Al , Sc , Y , and La) Systems. *J. Electrochem. Soc.* **1989**, *136* (2), 590–591. https://doi.org/10.1149/1.2096693.

(200) Dashjav, E.; Ma, Q.; Xu, Q.; Tsai, C.-L.; Giarola, M.; Mariotto, G.; Tietz, F. The Influence of Water on the Electrical Conductivity of Aluminum-Substituted Lithium Titanium Phosphates. *Solid State Ion.* **2018**, *321*, 83–90. https://doi.org/10.1016/j.ssi.2018.04.010.

(201) Subramanian, M.; Subramanian, R.; Clearfield, A. Lithium Ion Conductors in the System AB(IV)2(PO4)3 (B = Ti, Zr and Hf). *Solid State Ion.* **1986**, *18–19*, 562–569. https://doi.org/10.1016/0167-2738(86)90179-7.

(202) Feng, J. K.; Lu, L.; Lai, M. O. Lithium Storage Capability of Lithium Ion Conductor Li1.5Al0.5Ge1.5(PO4)3. *J. Alloys Compd.* **2010**, *501* (2), 255–258. https://doi.org/10.1016/j.jallcom.2010.04.084.

(203) Wang, S.; Ding, Y.; Zhou, G.; Yu, G.; Manthiram, A. Durability of the $Li_{1+x}Ti_{2-x}Al_x(PO_4)_3$ Solid Electrolyte in Lithium–Sulfur Batteries. *ACS Energy Lett.* **2016**, *1* (6), 1080–1085. https://doi.org/10.1021/acsenergylett.6b00481.

(204) Safanama, D.; Adams, S. High Efficiency Aqueous and Hybrid Lithium-Air Batteries Enabled by Li 1.5 Al 0.5 Ge 1.5 (PO 4) 3 Ceramic Anode-Protecting Membranes. *J. Power Sources* **2017**, *340*, 294–301. https://doi.org/10.1016/j.jpowsour.2016.11.076.

(205) Thokchom, J. S.; Kumar, B. The Effects of Crystallization Parameters on the Ionic Conductivity of a Lithium Aluminum Germanium Phosphate Glass–Ceramic. *J. Power Sources* **2010**, *195* (9), 2870–2876. https://doi.org/10.1016/j.jpowsour.2009.11.037.
(206) Jiménez, R.; Del Campo, A.; Calzada, M. L.; Sanz, J.; Kobylianska, S. D.; Liniova, B. O.; Belous, A. G.; Ragulya, A. V. Improved Conductivity in Tape Casted Li-NASICON Supported Thick Films: Effect of Temperature Treatments and Lamination. *J. Eur. Ceram. Soc.* **2018**, *38* (4), 1679–1687. https://doi.org/10.1016/j.jeurceramsoc.2017.12.017.
(207) Ma, Q.; Xu, Q.; Tsai, C.; Tietz, F.; Guillon, O. A Novel Sol–Gel Method for Large-Scale Production of Nanopowders: Preparation of $Li_{1.5}$ $Al_{0.5}$ $Ti_{1.5}$ (PO_4)$_3$ as an Example. *J. Am. Ceram. Soc.* **2016**, *99* (2), 410–414. https://doi.org/10.1111/jace.13997.
(208) Liu, X.; Tan, J.; Fu, J.; Yuan, R.; Wen, H.; Zhang, C. Facile Synthesis of Nanosized Lithium-Ion-Conducting Solid Electrolyte $Li_{1.4}$ $Al_{0.4}$ $Ti_{1.6}$ $(PO_4)_3$ and Its Mechanical Nanocomposites with $LiMn_2$ O_4 for Enhanced Cyclic Performance in Lithium Ion Batteries. *ACS Appl. Mater. Interfaces* **2017**, *9* (13), 11696–11703. https://doi.org/10.1021/acsami.6b16233.
(209) Huang, L.; Wen, Z.; Wu, M.; Wu, X.; Liu, Y.; Wang, X. Electrochemical Properties of Li1.4Al0.4Ti1.6(PO4)3 Synthesized by a Co-Precipitation Method. *J. Power Sources* **2011**, *196* (16), 6943–6946. https://doi.org/10.1016/j.jpowsour.2010.11.140.
(210) Huang, Y.; Jiang, Y.; Zhou, Y.; Hu, Z.; Zhu, X. Influence of Liquid Solutions on the Ionic Conductivity of $Li_{1.3}$ $Al_{0.3}$ $Ti_{1.7}$ $(PO_4)_3$ Solid Electrolytes. *ChemElectroChem* **2019**, *6* (24), 6016–6026. https://doi.org/10.1002/celc.201901687.
(211) Waetzig, K.; Rost, A.; Langklotz, U.; Matthey, B.; Schilm, J. An Explanation of the Microcrack Formation in Li 1.3 Al 0.3 Ti 1.7 (PO 4) 3 Ceramics. *J. Eur. Ceram. Soc.* **2016**, *36* (8), 1995–2001. https://doi.org/10.1016/j.jeurceramsoc.2016.02.042.
(212) Hallopeau, L.; Bregiroux, D.; Rousse, G.; Portehault, D.; Stevens, P.; Toussaint, G.; Laberty-Robert, C. Microwave-Assisted Reactive Sintering and Lithium Ion Conductivity of Li1.3Al0.3Ti1.7(PO4)3 Solid Electrolyte. *J. Power Sources* **2018**, *378*, 48–52. https://doi.org/10.1016/j.jpowsour.2017.12.021.
(213) Epp, V.; Ma, Q.; Hammer, E.-M.; Tietz, F.; Wilkening, M. Very Fast Bulk Li Ion Diffusivity in Crystalline $Li_{1.5}$ $Al_{0.5}$ $Ti_{1.5}$ $(PO_4)_3$ as Seen Using NMR Relaxometry. *Phys. Chem. Chem. Phys.* **2015**, *17* (48), 32115–32121. https://doi.org/10.1039/C5CP05337D.
(214) Benabed, Y.; Rioux, M.; Rousselot, S.; Hautier, G.; Dollé, M. Assessing the Electrochemical Stability Window of NASICON-Type Solid Electrolytes. *Front. Energy Res.* **2021**, *9*, 682008. https://doi.org/10.3389/fenrg.2021.682008.
(215) Luo, C.; Yi, M.; Cao, Z.; Hui, W.; Wang, Y. Review of Ionic Conductivity Properties of NASICON Type Inorganic Solid Electrolyte LATP. *ACS Appl. Electron. Mater.* **2024**, *6* (2), 641–657. https://doi.org/10.1021/acsaelm.3c01747.
(216) Ishii, K.; Uchikoshi, T.; Miyoshi, S.; Ode, M.; Ohno, T.; Takada, K. Reactivity Evaluation of NASICON-Type Solid Electrolyte LATP, LAGP and Olivine-Type Cathode LCP. *Mater. Lett.* **2022**, *324*, 132736. https://doi.org/10.1016/j.matlet.2022.132736.
(217) Liu, Y.; Sun, Q.; Zhao, Y.; Wang, B.; Kaghazchi, P.; Adair, K. R.; Li, R.; Zhang, C.; Liu, J.; Kuo, L.-Y.; Hu, Y.; Sham, T.-K.; Zhang, L.; Yang, R.; Lu, S.; Song, X.; Sun, X. Stabilizing the Interface of NASICON Solid Electrolyte against Li Metal

with Atomic Layer Deposition. *ACS Appl. Mater. Interfaces* **2018**, *10* (37), 31240–31248. https://doi.org/10.1021/acsami.8b06366.

(218) Zhang, Q.; Jiang, M.; Kungl, H.; Eichel, R.-A. Stabilization the Interface of NASICON-Type Solid Electrolyte and Li Metal by Al Interlayer. *Electrochimica Acta* **2024**, *477*, 143791. https://doi.org/10.1016/j.electacta.2024.143791.

(219) Tolganbek, N.; Bakenov, Z.; Mentbayeva, A. Degradation Prevention of Latp Towards Li Metal and Interface Improvement By Layer-By-Layer Polymer Assembly Technique. *ECS Meet. Abstr.* **2022**, *MA2022-02* (7), 2489–2489. https://doi.org/10.1149/MA2022-0272489mtgabs.

(220) Wang, L.; Wang, L.; Shi, Q.; Zhong, C.; Gong, D.; Wang, X.; Zhan, C.; Liu, G. In-Situ Constructed SnO2 Gradient Buffer Layer as a Tight and Robust Interphase toward Li Metal Anodes in LATP Solid State Batteries. *J. Energy Chem.* **2023**, *80*, 89–98. https://doi.org/10.1016/j.jechem.2023.01.040.

(221) Qin, S.; Zhu, X.; Jiang, Y.; Ling, M.; Hu, Z.; Zhu, J. Growth of Self-Textured Ga3+-Substituted Li7La3Zr2O12 Ceramics by Solid State Reaction and Their Significant Enhancement in Ionic Conductivity. *Appl. Phys. Lett.* **2018**, *112* (11), 113901. https://doi.org/10.1063/1.5019179.

(222) Sun, H.; Kang, S.; Cui, L. Prospects of LLZO Type Solid Electrolyte: From Material Design to Battery Application. *Chem. Eng. J.* **2023**, *454*, 140375. https://doi.org/10.1016/j.cej.2022.140375.

(223) Thompson, T.; Yu, S.; Williams, L.; Schmidt, R. D.; Garcia-Mendez, R.; Wolfenstine, J.; Allen, J. L.; Kioupakis, E.; Siegel, D. J.; Sakamoto, J. Electrochemical Window of the Li-Ion Solid Electrolyte $Li_7 La_3 Zr_2 O_{12}$. *ACS Energy Lett.* **2017**, *2* (2), 462–468. https://doi.org/10.1021/acsenergylett.6b00593.

(224) Liu, Q.; Geng, Z.; Han, C.; Fu, Y.; Li, S.; He, Y.; Kang, F.; Li, B. Challenges and Perspectives of Garnet Solid Electrolytes for All Solid-State Lithium Batteries. *J. Power Sources* **2018**, *389*, 120–134. https://doi.org/10.1016/j.jpowsour.2018.04.019.

(225) Baek, S.-W.; Lee, J.-M.; Kim, T. Y.; Song, M.-S.; Park, Y. Garnet Related Lithium Ion Conductor Processed by Spark Plasma Sintering for All Solid State Batteries. *J. Power Sources* **2014**, *249*, 197–206. https://doi.org/10.1016/j.jpowsour.2013.10.089.

(226) Kim, S.; Hirayama, M.; Taminato, S.; Kanno, R. Epitaxial Growth and Lithium Ion Conductivity of Lithium-Oxide Garnet for an All Solid-State Battery Electrolyte. *Dalton Trans.* **2013**, *42* (36), 13112. https://doi.org/10.1039/c3dt51795k.

(227) Katsui, H.; Goto, T. Preparation of Cubic and Tetragonal Li7La3Zr2O12 Film by Metal Organic Chemical Vapor Deposition. *Thin Solid Films* **2015**, *584*, 130–134. https://doi.org/10.1016/j.tsf.2014.11.094.

(228) Loho, C.; Djenadic, R.; Bruns, M.; Clemens, O.; Hahn, H. Garnet-Type $Li_7 La_3 Zr_2 O_{12}$ Solid Electrolyte Thin Films Grown by CO_2 -Laser Assisted CVD for All-Solid-State Batteries. *J. Electrochem. Soc.* **2017**, *164* (1), A6131–A6139. https://doi.org/10.1149/2.0201701jes.

(229) Biao, J.; Han, B.; Cao, Y.; Li, Q.; Zhong, G.; Ma, J.; Chen, L.; Yang, K.; Mi, J.; Deng, Y.; Liu, M.; Lv, W.; Kang, F.; He, Y. Inhibiting Formation and Reduction of $Li_2 CO_3$ to LiC_x at Grain Boundaries in Garnet Electrolytes to Prevent Li Penetration. *Adv. Mater.* **2023**, *35* (12), 2208951. https://doi.org/10.1002/adma.202208951.

(230) Touidjine, K.; Finsterbusch-Rosen, M.; Kiyek, V.; Ganapathy, S.; Finsterbusch, M.; Guillon, O.; Huijben, M.; Kelder, E.; Wagemaker, M.; Fattakhova-Rohlfing, D. The Impact of Lithium Carbonate on Tape Cast LLZO Battery Separators: A

Balanced Interplay between Lithium Loss and Relithiation. *Energy Storage Mater.* **2024**, *71*, 103487. https://doi.org/10.1016/j.ensm.2024.103487.
(231) Huo, H.; Luo, J.; Thangadurai, V.; Guo, X.; Nan, C.-W.; Sun, X. Li_2CO_3 : A Critical Issue for Developing Solid Garnet Batteries. *ACS Energy Lett.* **2020**, *5* (1), 252–262. https://doi.org/10.1021/acsenergylett.9b02401.
(232) Meng, J.; Zhang, Y.; Zhou, X.; Lei, M.; Li, C. Li2CO3-Affiliative Mechanism for Air-Accessible Interface Engineering of Garnet Electrolyte via Facile Liquid Metal Painting. *Nat. Commun.* **2020**, *11* (1), 3716. https://doi.org/10.1038/s41467-020-17493-x.
(233) Mohammadi, S.; Golmohammad, M.; SharifiRad, A.; Alizadeh, S. M. Surface Modification and Chemical Stability of Garnet LLZO Solid Electrolyte by ZnO Coating through a Facile and Practical Method. *Mater. Chem. Phys.* **2023**, *308*, 128235. https://doi.org/10.1016/j.matchemphys.2023.128235.
(234) Huo, H.; Chen, Y.; Zhao, N.; Lin, X.; Luo, J.; Yang, X.; Liu, Y.; Guo, X.; Sun, X. In-Situ Formed Li2CO3-Free Garnet/Li Interface by Rapid Acid Treatment for Dendrite-Free Solid-State Batteries. *Nano Energy* **2019**, *61*, 119–125. https://doi.org/10.1016/j.nanoen.2019.04.058.
(235) Meier, K.; Laino, T.; Curioni, A. Solid-State Electrolytes: Revealing the Mechanisms of Li-Ion Conduction in Tetragonal and Cubic LLZO by First-Principles Calculations. *J. Phys. Chem. C* **2014**, *118* (13), 6668–6679. https://doi.org/10.1021/jp5002463.
(236) Raju, M. M.; Altayran, F.; Johnson, M.; Wang, D.; Zhang, Q. Crystal Structure and Preparation of Li7La3Zr2O12 (LLZO) Solid-State Electrolyte and Doping Impacts on the Conductivity: An Overview. *Electrochem* **2021**, *2* (3), 390–414. https://doi.org/10.3390/electrochem2030026.
(237) Bernstein, N.; Johannes, M. D.; Hoang, K. Origin of the Structural Phase Transition in Li 7 La 3 Zr 2 O 12. *Phys. Rev. Lett.* **2012**, *109* (20), 205702. https://doi.org/10.1103/PhysRevLett.109.205702.
(238) Rangasamy, E.; Wolfenstine, J.; Allen, J.; Sakamoto, J. The Effect of 24c-Site (A) Cation Substitution on the Tetragonal–Cubic Phase Transition in Li7−La3−A Zr2O12 Garnet-Based Ceramic Electrolyte. *J. Power Sources* **2013**, *230*, 261–266. https://doi.org/10.1016/j.jpowsour.2012.12.076.
(239) Yoon, S. A.; Oh, N. R.; Yoo, A. R.; Lee, H. G.; Lee, H. C. Preparation and Characterization of Ta-Substituted Li7La3Zr2-xO12 Garnet Solid Electrolyte by Sol-Gel Processing. *J. Korean Ceram. Soc.* **2017**, *54* (4), 278–284. https://doi.org/10.4191/kcers.2017.54.4.02.
(240) Liu, C.; Rui, K.; Shen, C.; Badding, M. E.; Zhang, G.; Wen, Z. Reversible Ion Exchange and Structural Stability of Garnet-Type Nb-Doped Li7La3Zr2O12 in Water for Applications in Lithium Batteries. *J. Power Sources* **2015**, *282*, 286–293. https://doi.org/10.1016/j.jpowsour.2015.02.050.
(241) Awaka, J.; Takashima, A.; Kataoka, K.; Kijima, N.; Idemoto, Y.; Akimoto, J. Crystal Structure of Fast Lithium-Ion-Conducting Cubic Li7La3Zr2O12. *Chem. Lett.* **2011**, *40* (1), 60–62. https://doi.org/10.1246/cl.2011.60.
(242) Tang, Y.; Luo, Z.; Liu, T.; Liu, P.; Li, Z.; Lu, A. Effects of B2O3 on Microstructure and Ionic Conductivity of Li6.5La3Zr1.5Nb0.5O12 Solid Electrolyte. *Ceram. Int.* **2017**, *43* (15), 11879–11884. https://doi.org/10.1016/j.ceramint.2017.06.035.
(243) Ma, Z.; Xue, H.-G.; Guo, S.-P. Recent Achievements on Sulfide-Type Solid Electrolytes: Crystal Structures and Electrochemical Performance. *J. Mater. Sci.* **2018**, *53* (6), 3927–3938. https://doi.org/10.1007/s10853-017-1827-6.

(244) Tachez, M.; Malugani, J.; Mercier, R.; Robert, G. Ionic Conductivity of and Phase Transition in Lithium Thiophosphate Li3PS4. *Solid State Ion.* **1984**, *14* (3), 181–185. https://doi.org/10.1016/0167-2738(84)90097-3.
(245) Zhou, J.; Chen, P.; Wang, W.; Zhang, X. Li7P3S11 Electrolyte for All-Solid-State Lithium-Ion Batteries: Structure, Synthesis, and Applications. *Chem. Eng. J.* **2022**, *446*, 137041. https://doi.org/10.1016/j.cej.2022.137041.
(246) Berbano, S. S.; Mirsaneh, M.; Lanagan, M. T.; Randall, C. A. Lithium Thiophosphate Glasses and Glass–Ceramics as Solid Electrolytes: Processing, Microstructure, and Properties. *Int. J. Appl. Glass Sci.* **2013**, *4* (4), 414–425. https://doi.org/10.1111/ijag.12037.
(247) Tufail, M. K.; Ahmad, N.; Yang, L.; Zhou, L.; Naseer, M. A.; Chen, R.; Yang, W. A Panoramic View of Li7P3S11 Solid Electrolytes Synthesis, Structural Aspects and Practical Challenges for All-Solid-State Lithium Batteries. *Chin. J. Chem. Eng.* **2021**, *39*, 16–36. https://doi.org/10.1016/j.cjche.2021.09.021.
(248) Lau, J.; DeBlock, R. H.; Butts, D. M.; Ashby, D. S.; Choi, C. S.; Dunn, B. S. Sulfide Solid Electrolytes for Lithium Battery Applications. *Adv. Energy Mater.* **2018**, *8* (27), 1800933. https://doi.org/10.1002/aenm.201800933.
(249) Roh, J. H.; Hong, S.-T. Li2GeS3: New Structural Type of Lithium Solid Electrolyte for All-Solid-State Batteries. *ECS Meet. Abstr.* **2023**, *MA2023-02* (4), 780. https://doi.org/10.1149/MA2023-024780mtgabs.
(250) Choi, Y. E.; Park, K. H.; Kim, D. H.; Oh, D. Y.; Kwak, H. R.; Lee, Y.-G.; Jung, Y. S. Coatable Li4SnS4 Solid Electrolytes Prepared from Aqueous Solutions for All-Solid-State Lithium-Ion Batteries. *ChemSusChem* **2017**, *10* (12), 2605–2611. https://doi.org/10.1002/cssc.201700409.
(251) Kimura, T.; Kato, A.; Hotehama, C.; Sakuda, A.; Hayashi, A.; Tatsumisago, M. Preparation and Characterization of Lithium Ion Conductive Li3SbS4 Glass and Glass-Ceramic Electrolytes. *Solid State Ion.* **2019**, *333*, 45–49. https://doi.org/10.1016/j.ssi.2019.01.017.
(252) Sahu, G.; Lin, Z.; Li, J.; Liu, Z.; Dudney, N.; Liang, C. Air-Stable, High-Conduction Solid Electrolytes of Arsenic-Substituted Li 4 SnS 4. *Energy Environ. Sci.* **2014**, *7* (3), 1053–1058. https://doi.org/10.1039/C3EE43357A.
(253) Byeon, Y.-W.; Kim, H. Review on Interface and Interphase Issues in Sulfide Solid-State Electrolytes for All-Solid-State Li-Metal Batteries. *Electrochem.* **2021**, *2* (3), 452–471. https://doi.org/10.3390/electrochem2030030.
(254) Morimoto, H.; Yamashita, H.; Tatsumisago, M.; Minami, T. Mechanochemical Synthesis of New Amorphous Materials of $60Li_2S{\cdot}40SiS_2$ with High Lithium Ion Conductivity. *J. Am. Ceram. Soc.* **1999**, *82* (5), 1352–1354. https://doi.org/10.1111/j.1151-2916.1999.tb01923.x.
(255) Warren, Z.; Rosero-Navarro, N. C. Solution-Based Suspension Synthesis of Li2S–P2S5 Glass-Ceramic Systems as Solid-State Electrolytes: A Brief Review of Current Research. *ACS Omega* **2024**, *9* (29), 31228–31236. https://doi.org/10.1021/acsomega.4c03784.
(256) Tatsumisago, M.; Hirai, K.; Minami, T.; Takada, K.; Kondo, S. Superionic Conduction in Rapidly Quenched Li_2S-SiS_2-Li_3PO_4 Glasses. *J. Ceram. Soc. Jpn.* **1993**, *101* (1179), 1315–1317. https://doi.org/10.2109/jcersj.101.1315.
(257) Cao, C.; Li, Z.-B.; Wang, X.-L.; Zhao, X.-B.; Han, W.-Q. Recent Advances in Inorganic Solid Electrolytes for Lithium Batteries. *Front. Energy Res.* **2014**, *2*. https://doi.org/10.3389/fenrg.2014.00025.
(258) Garcia-Mendez, R.; Smith, J. G.; Neuefeind, J. C.; Siegel, D. J.; Sakamoto, J. Correlating Macro and Atomic Structure with Elastic Properties and Ionic Transport of Glassy Li_2 S-P_2 S_5 (LPS) Solid Electrolyte for Solid-State Li Metal

Batteries. *Adv. Energy Mater.* **2020**, *10* (19), 2000335. https://doi.org/10.1002/aenm.202000335.
(259) Bai, X.; Duan, Y.; Zhuang, W.; Yang, R.; Wang, J. Research Progress in Li-Argyrodite-Based Solid-State Electrolytes. *J. Mater. Chem. A* **2020**, *8* (48), 25663–25686. https://doi.org/10.1039/D0TA08472G.
(260) Zhou, L.; Minafra, N.; Zeier, W. G.; Nazar, L. F. Innovative Approaches to Li-Argyrodite Solid Electrolytes for All-Solid-State Lithium Batteries. *Acc. Chem. Res.* **2021**, *54* (12), 2717–2728. https://doi.org/10.1021/acs.accounts.0c00874.
(261) Baktash, A.; Reid, J. C.; Roman, T.; Searles, D. J. Diffusion of Lithium Ions in Lithium-Argyrodite Solid-State Electrolytes. *Npj Comput. Mater.* **2020**, *6* (1), 1–10. https://doi.org/10.1038/s41524-020-00432-1.
(262) Pang, B.; Gan, Y.; Xia, Y.; Huang, H.; He, X.; Zhang, W. Regulation of the Interfaces Between Argyrodite Solid Electrolytes and Lithium Metal Anode. *Front. Chem.* **2022**, *10*, 837978. https://doi.org/10.3389/fchem.2022.837978.
(263) Huang, D.; Liu, G.; Tong, W. Stability of the Argyrodite Electrolyte in Li–In Based All-Solid-State Batteries. *ACS Appl. Energy Mater.* **2024**, *7* (22), 10376–10385. https://doi.org/10.1021/acsaem.4c01873.
(264) Schwietert, T. K.; Arszelewska, V. A.; Wang, C.; Yu, C.; Vasileiadis, A.; de Klerk, N. J. J.; Hageman, J.; Hupfer, T.; Kerkamm, I.; Xu, Y.; van der Maas, E.; Kelder, E. M.; Ganapathy, S.; Wagemaker, M. Clarifying the Relationship between Redox Activity and Electrochemical Stability in Solid Electrolytes. *Nat. Mater.* **2020**, *19* (4), 428–435. https://doi.org/10.1038/s41563-019-0576-0.
(265) Auvergniot, J.; Cassel, A.; Ledeuil, J.-B.; Viallet, V.; Seznec, V.; Dedryvère, R. Interface Stability of Argyrodite Li6PS5Cl toward LiCoO2, LiNi1/3Co1/3Mn1/3O2, and LiMn2O4 in Bulk All-Solid-State Batteries. *Chem. Mater.* **2017**, *29* (9), 3883–3890. https://doi.org/10.1021/acs.chemmater.6b04990.
(266) Yu, C.; Zhao, F.; Luo, J.; Zhang, L.; Sun, X. Recent Development of Lithium Argyrodite Solid-State Electrolytes for Solid-State Batteries: Synthesis, Structure, Stability and Dynamics. *Nano Energy* **2021**, *83*, 105858. https://doi.org/10.1016/j.nanoen.2021.105858.
(267) Indrawan, R. F.; Gamo, H.; Nagai, A.; Matsuda, A. Chemically Understanding the Liquid-Phase Synthesis of Argyrodite Solid Electrolyte Li 6 PS 5 Cl with the Highest Ionic Conductivity for All-Solid-State Batteries. *Chem. Mater.* **2023**, *35* (6), 2549–2558. https://doi.org/10.1021/acs.chemmater.2c03818.
(268) Zhang, Z.; Zhang, L.; Liu, Y.; Yu, C.; Yan, X.; Xu, B.; Wang, L. Synthesis and Characterization of Argyrodite Solid Electrolytes for All-Solid-State Li-Ion Batteries. *J. Alloys Compd.* **2018**, *747*, 227–235. https://doi.org/10.1016/j.jallcom.2018.03.027.
(269) Rajagopal, R.; Subramanian, Y.; Jung, Y. J.; Kang, S.; Ryu, K.-S. Rapid Synthesis of Highly Conductive Li 6 PS 5 Cl Argyrodite-Type Solid Electrolytes Using Pyridine Solvent. *ACS Appl. Energy Mater.* **2022**, *5* (8), 9266–9272. https://doi.org/10.1021/acsaem.2c01157.
(270) Zhang, Z. X.; Zhang, L.; Liu, Y. Y.; Yan, X. L.; Xu, B.; Wang, L. M. One-Step Solution Process toward Formation of Li6PS5Cl Argyrodite Solid Electrolyte for All-Solid-State Lithium-Ion Batteries. *J. Alloys Compd.* **2020**, *812*, 152103. https://doi.org/ARTN.
(271) Sakuda, A.; Hayashi, A.; Tatsumisago, M. Sulfide Solid Electrolyte with Favorable Mechanical Property for All-Solid-State Lithium Battery. *Sci. Rep.* **2013**, *3* (1), 2261. https://doi.org/10.1038/srep02261.

(272) Doux, J.-M.; Yang, Y.; S. Tan, D. H.; Nguyen, H.; A. Wu, E.; Wang, X.; Banerjee, A.; Shirley Meng, Y. Pressure Effects on Sulfide Electrolytes for All Solid-State Batteries. *J. Mater. Chem. A* **2020**, *8* (10), 5049–5055. https://doi.org/10.1039/C9TA12889A.
(273) Keller, M.; Varzi, A.; Passerini, S. Hybrid Electrolytes for Lithium Metal Batteries. *J. Power Sources* **2018**, *392*, 206–225. https://doi.org/10.1016/j.jpowsour.2018.04.099.
(274) Liang, J.; Luo, J.; Sun, Q.; Yang, X.; Li, R.; Sun, X. Recent Progress on Solid-State Hybrid Electrolytes for Solid-State Lithium Batteries. *Energy Storage Mater.* **2019**, *21*, 308–334. https://doi.org/10.1016/j.ensm.2019.06.021.
(275) Qu, H.; Zhang, J.; Du, A.; Chen, B.; Chai, J.; Xue, N.; Wang, L.; Qiao, L.; Wang, C.; Zang, X.; Yang, J.; Wang, X.; Cui, G. Multifunctional Sandwich-Structured Electrolyte for High-Performance Lithium–Sulfur Batteries. *Adv. Sci.* **2018**, *5* (3), 1700503. https://doi.org/10.1002/advs.201700503.
(276) Pervez, S. A.; Ganjeh-Anzabi, P.; Farooq, U.; Trifkovic, M.; Roberts, E. P. L.; Thangadurai, V. Fabrication of a Dendrite-Free All Solid-State Li Metal Battery via Polymer Composite/Garnet/Polymer Composite Layered Electrolyte. *Adv. Mater. Interfaces* **2019**, *6* (11), 1900186. https://doi.org/10.1002/admi.201900186.
(277) Park, H.; Le Mong, A.; Kim, D. Single and Multilayer Composite Electrolytes for Enhanced Li-Ion Conductivity with Restricted Polysulfide Diffusion for Lithium–Sulfur Battery. *Mater. Today Energy* **2023**, *33*, 101274. https://doi.org/10.1016/j.mtener.2023.101274.
(278) Zhou, H.; Wang, Y.; Li, H.; He, P. The Development of a New Type of Rechargeable Batteries Based on Hybrid Electrolytes. *ChemSusChem* **2010**, *3* (9), 1009–1019. https://doi.org/10.1002/cssc.201000123.
(279) Hüttl, J.; Seidl, C.; Auer, H.; Nikolowski, K.; Görne, A. L.; Arnold, M.; Heubner, C.; Wolter, M.; Michaelis, A. Ultra-Low LPS/LLZO Interfacial Resistance – towards Stable Hybrid Solid-State Batteries with Li-Metal Anodes. *Energy Storage Mater.* **2021**, *40*, 259–267. https://doi.org/10.1016/j.ensm.2021.05.020.
(280) Zhou, W.; Wang, Z.; Pu, Y.; Li, Y.; Xin, S.; Li, X.; Chen, J.; Goodenough, J. B. Double-Layer Polymer Electrolyte for High-Voltage All-Solid-State Rechargeable Batteries. *Adv. Mater.* **2019**, *31* (4), 1805574. https://doi.org/10.1002/adma.201805574.
(281) Han, L.; Hsieh, C.-T.; Chandra Mallick, B.; Li, J.; Ashraf Gandomi, Y. Recent Progress and Future Prospects of Atomic Layer Deposition to Prepare/Modify Solid-State Electrolytes and Interfaces between Electrodes for next-Generation Lithium Batteries. *Nanoscale Adv.* **2021**, *3* (10), 2728–2740. https://doi.org/10.1039/D0NA01072C.
(282) Zhang, X.; Xie, J.; Shi, F.; Lin, D.; Liu, Y.; Liu, W.; Pei, A.; Gong, Y.; Wang, H.; Liu, K.; Xiang, Y.; Cui, Y. Vertically Aligned and Continuous Nanoscale Ceramic–Polymer Interfaces in Composite Solid Polymer Electrolytes for Enhanced Ionic Conductivity. *Nano Lett.* **2018**, *18* (6), 3829–3838. https://doi.org/10.1021/acs.nanolett.8b01111.
(283) Sand, S.; Rupp, J.; Yildiz, B. Understanding Polymer Structure and Conductivity in Composite Electrolytes. *ECS Meet. Abstr.* **2023**, *MA2023-01* (6), 1003–1003. https://doi.org/10.1149/MA2023-0161003mtgabs.
(284) Rangasamy, E.; Sahu, G.; Keum, J. K.; Rondinone, A. J.; Dudney, N. J.; Liang, C. A High Conductivity Oxide–Sulfide Composite Lithium Superionic Conductor. *J Mater Chem A* **2014**, *2* (12), 4111–4116. https://doi.org/10.1039/C3TA15223E.

(285) Hood, Z. D.; Wang, H.; Li, Y.; Pandian, A. S.; Parans Paranthaman, M.; Liang, C. The “Filler Effect”: A Study of Solid Oxide Fillers with β-Li3PS4 for Lithium Conducting Electrolytes. *Solid State Ion.* **2015**, *283*, 75–80. https://doi.org/10.1016/j.ssi.2015.10.014.
(286) Park, J.; Jin, H.; Yeon, S.; Kim, H. W.; Ko, M. Oxide-Based Pseudo-Solid-State Hybrid Electrolyte Functionalized by Ionic Liquid for Lithium Metal Batteries. *Energy Technol.* **2023**, *11* (2), 2201153. https://doi.org/10.1002/ente.202201153.
(287) Kim, H. W.; Manikandan, P.; Lim, Y. J.; Kim, J. H.; Nam, S.; Kim, Y. Hybrid Solid Electrolyte with the Combination of Li7La3Zr2O12 Ceramic and Ionic Liquid for High Voltage Pseudo-Solid-State Li-Ion Batteries. *J. Mater. Chem. A* **2016**, *4* (43), 17025–17032. https://doi.org/10.1039/C6TA07268B.
(288) Tu, Z.; Zachman, M. J.; Choudhury, S.; Wei, S.; Ma, L.; Yang, Y.; Kourkoutis, L. F.; Archer, L. A. Nanoporous Hybrid Electrolytes for High-Energy Batteries Based on Reactive Metal Anodes. *Adv. Energy Mater.* **2017**, *7* (8), 1602367. https://doi.org/10.1002/aenm.201602367.
(289) Cheng, E. J.; Liu, M.; Li, Y.; Abe, T.; Kanamura, K. Effects of Porosity and Ionic Liquid Impregnation on Ionic Conductivity of Garnet-Based Flexible Sheet Electrolytes. *J. Power Sources* **2022**, *517*, 230705. https://doi.org/10.1016/j.jpowsour.2021.230705.
(290) Ma, S.; Shen, L.; Liu, Q.; Shi, W.; Zhang, C.; Liu, F.; Baucom, J. A.; Zhang, D.; Yue, H.; Wu, H. B.; Lu, Y. Class of Solid-like Electrolytes for Rechargeable Batteries Based on Metal–Organic Frameworks Infiltrated with Liquid Electrolytes. *ACS Appl. Mater. Interfaces* **2020**, *12* (39), 43824–43832. https://doi.org/10.1021/acsami.0c13437.
(291) Popovic, J.; Hasegawa, G.; Moudrakovski, I.; Maier, J. Infiltrated Porous Oxide Monoliths as High Lithium Transference Number Electrolytes. *J. Mater. Chem. A* **2016**, *4* (19), 7135–7140. https://doi.org/10.1039/C6TA01826B.
(292) Liu, T.; Ren, Y.; Shen, Y.; Zhao, S.-X.; Lin, Y.; Nan, C.-W. Achieving High Capacity in Bulk-Type Solid-State Lithium Ion Battery Based on Li6.75La3Zr1.75Ta0.25O12 Electrolyte: Interfacial Resistance. *J. Power Sources* **2016**, *324*, 349–357. https://doi.org/10.1016/j.jpowsour.2016.05.111.
(293) Aguesse, F.; Manalastas, W.; Buannic, L.; Lopez del Amo, J. M.; Singh, G.; Llordés, A.; Kilner, J. Investigating the Dendritic Growth during Full Cell Cycling of Garnet Electrolyte in Direct Contact with Li Metal. *ACS Appl. Mater. Interfaces* **2017**, *9* (4), 3808–3816. https://doi.org/10.1021/acsami.6b13925.
(294) Jiang, P.; Du, G.; Cao, J.; Zhang, X.; Zou, C.; Liu, Y.; Lu, X. Solid-State Li Ion Batteries with Oxide Solid Electrolytes: Progress and Perspective. *Energy Technol.* **2023**, *11* (3), 2201288. https://doi.org/10.1002/ente.202201288.
(295) Cabana, J.; Kwon, B. J.; Hu, L. Mechanisms of Degradation and Strategies for the Stabilization of Cathode–Electrolyte Interfaces in Li-Ion Batteries. *Acc. Chem. Res.* **2018**, *51* (2), 299–308. https://doi.org/10.1021/acs.accounts.7b00482.
(296) Dong, Y.; Li, J. Oxide Cathodes: Functions, Instabilities, Self Healing, and Degradation Mitigations. *Chem. Rev.* **2023**, *123* (2), 811–833. https://doi.org/10.1021/acs.chemrev.2c00251.
(297) Tang, S.; Guo, W.; Fu, Y. Advances in Composite Polymer Electrolytes for Lithium Batteries and Beyond. *Adv. Energy Mater.* **2021**, *11* (2), 2000802. https://doi.org/10.1002/aenm.202000802.
(298) Khan, K.; Hanif, M. B.; Xin, H.; Hussain, A.; Ali, H. G.; Fu, B.; Fang, Z.; Motola, M.; Xu, Z.; Wu, M. PEO-Based Solid Composite Polymer Electrolyte for High

Capacity Retention All-Solid-State Lithium Metal Battery. *Small* **2024**, *20* (4), e2305772. https://doi.org/10.1002/smll.202305772.
(299) Wang, W.; Alexandridis, P. Composite Polymer Electrolytes: Nanoparticles Affect Structure and Properties. *Polymers* **2016**, *8* (11), 387. https://doi.org/10.3390/polym8110387.
(300) Kuo, C.-W.; Li, W.-B.; Chen, P.-R.; Liao, J.-W.; Tseng, C.-G.; Wu, T.-Y. Effect of Plasticizer and Lithium Salt Concentration in PMMA-Based Composite Polymer Electrolytes. *Int. J. Electrochem. Sci.* **2013**, *8* (4), 5007–5021. https://doi.org/10.1016/S1452-3981(23)14658-X.
(301) Yu, X.; Liu, Y.; Goodenough, J. B.; Manthiram, A. Rationally Designed PEGDA-LLZTO Composite Electrolyte for Solid-State Lithium Batteries. *ACS Appl. Mater. Interfaces* **2021**, *13* (26), 30703–30711. https://doi.org/10.1021/acsami.1c07547.
(302) Feng, J.; Wang, L.; Chen, Y.; Wang, P.; Zhang, H.; He, X. PEO Based Polymer-Ceramic Hybrid Solid Electrolytes: A Review. *Nano Converg.* **2021**, *8* (1), 2. https://doi.org/10.1186/s40580-020-00252-5.
(303) Nkosi, F. P.; Cuevas, I.; Valvo, M.; Mindemark, J.; Mahun, A.; Abbrent, S.; Brus, J.; Kobera, L.; Edström, K. Understanding Lithium-Ion Conductivity in NASICON-Type Polymer-in-Ceramic Composite Electrolytes. *ACS Appl. Energy Mater.* **2024**. https://doi.org/10.1021/acsaem.4c00701.
(304) Meng, N.; Zhu, X.; Lian, F. Particles in Composite Polymer Electrolyte for Solid-State Lithium Batteries: A Review. *Particuology* **2022**, *60*, 14–36. https://doi.org/10.1016/j.partic.2021.04.002.
(305) Tambelli, C. C.; Bloise, A. C.; Rosário, A. V.; Pereira, E. C.; Magon, C. J.; Donoso, J. P. Characterisation of PEO–Al2O3 Composite Polymer Electrolytes. *Electrochimica Acta* **2002**, *47* (11), 1677–1682. https://doi.org/10.1016/S0013-4686(01)00900-8.
(306) Cao, J.; Wang, L.; Shang, Y.; Fang, M.; Deng, L.; Gao, J.; Li, J.; Chen, H.; He, X. Dispersibility of Nano-TiO2 on Performance of Composite Polymer Electrolytes for Li-Ion Batteries. *Electrochimica Acta* **2013**, *111*, 674–679. https://doi.org/10.1016/j.electacta.2013.08.048.
(307) Liu, Y.; Lee, J. Y.; Hong, L. In Situ Preparation of Poly(Ethylene Oxide)–SiO2 Composite Polymer Electrolytes. *J. Power Sources* **2004**, *129* (2), 303–311. https://doi.org/10.1016/j.jpowsour.2003.11.026.
(308) Li, J.; Jing, M.; Li, R.; Li, L.; Huang, Z.; Yang, H.; Liu, M.; Hussain, S.; Xiang, J.; Shen, X. Al_2O_3 Fiber-Reinforced Polymer Solid Electrolyte Films with Excellent Lithium-Ion Transport Properties for High-Voltage Solid-State Lithium Batteries. *ACS Appl. Polym. Mater.* **2022**, *4* (10), 7144–7151. https://doi.org/10.1021/acsapm.2c01034.
(309) Paste, R.; Hanmandlu, C.; Su, P.-Y.; Hou, C.-H.; Chen, H.-A.; Pao, C.-W.; Shyue, J.-J.; Chen, K.-H.; Wu, H.-L.; Lin, H.-C.; Chu, C. W. Intimate Interaction of TFSI− Anions with MoO3−x Oxygen Vacancies Boost Ionic Conductivity of Cathode-Supported Solid Polymer Electrolyte. *Chem. Eng. J.* **2023**, *452*, 139088. https://doi.org/10.1016/j.cej.2022.139088.
(310) Liu, S.; Zhou, L.; Zhong, T.; Wu, X.; Neyts, K. Sulfide/Polymer Composite Solid-State Electrolytes for All-Solid-State Lithium Batteries. *Adv. Energy Mater. 14* (48), 2403602. https://doi.org/10.1002/aenm.202403602.
(311) Chometon, R.; Deschamps, M.; Dugas, R.; Quemin, E.; Hennequart, B.; Deschamps, M.; Tarascon, J.-M.; Laberty-Robert, C. Targeting the Right Metrics for an Efficient Solvent-Free Formulation of PEO:LiTFSI:Li6PS5Cl Hybrid Solid

Electrolyte. *ACS Appl. Mater. Interfaces* **2023**, *15* (50), 58794–58805. https://doi.org/10.1021/acsami.3c11542.

(312) Huo, H.; Jiang, M.; Mogwitz, B.; Sann, J.; Yusim, Y.; Zuo, T.; Moryson, Y.; Minnmann, P.; Richter, F. H.; Veer Singh, C.; Janek, J. Interface Design Enabling Stable Polymer/Thiophosphate Electrolyte Separators for Dendrite-Free Lithium Metal Batteries. *Angew. Chem. Int. Ed.* **2023**, *62* (14), e202218044. https://doi.org/10.1002/anie.202218044.

(313) Hong, S.-B.; Jang, Y.-R.; Jung, Y.-C.; Cho, W.; Kim, D.-W. Sulfide-Based Flexible Solid Electrolyte Enhancing Cycling Performance of All-Solid-State Lithium Batteries. *ACS Appl. Energy Mater.* **2024**. https://doi.org/10.1021/acsaem.4c00547.

(314) Tron, A.; Hamid, R.; Zhang, N.; Paolella, A.; Wulfert-Holzmann, P.; Kolotygin, V.; López-Aranguren, P.; Beutl, A. Film Processing of Li6PS5Cl Electrolyte Using Different Binders and Their Combinations. *J. Energy Storage* **2023**, *66*, 107480. https://doi.org/10.1016/j.est.2023.107480.

(315) Chen, L.; Li, Y.; Li, S.-P.; Fan, L.-Z.; Nan, C.-W.; Goodenough, J. B. PEO/Garnet Composite Electrolytes for Solid-State Lithium Batteries: From “Ceramic-in-Polymer” to “Polymer-in-Ceramic.” *Nano Energy* **2018**, *46*, 176–184. https://doi.org/10.1016/j.nanoen.2017.12.037.

(316) Ahn, J.-H.; Wang, G. X.; Liu, H. K.; Dou, S. X. Nanoparticle-Dispersed PEO Polymer Electrolytes for Li Batteries. *J. Power Sources* **2003**, *119–121*, 422–426. https://doi.org/10.1016/S0378-7753(03)00264-7.

(317) Li, Z.; Aboalsaud, A. M.; Liu, X.; Thankamony, R. L.; Chen, I.-C.; Li, Y.; Lai, Z. Scalable Fabrication of Solvent-Free Composite Solid Electrolyte by a Continuous Thermal-Extrusion Process. *J. Colloid Interface Sci.* **2022**, *628*, 64–71. https://doi.org/10.1016/j.jcis.2022.07.099.

(318) Yang, C.-C.; Lin, S.-J. Preparation of Composite Alkaline Polymer Electrolyte. *Mater. Lett.* **2002**, *57* (4), 873–881. https://doi.org/10.1016/S0167-577X(02)00888-1.

(319) Choi, H.; Kwon, H.; Kim, H.-T. Hybrid Electrolyte of Li 1.3 Al 0.3 Ti 1.7 (PO 4) 3 Nanofibers and Cross-Linked Gel Electrolyte for Li Metal Batteries. *ACS Appl. Energy Mater.* **2023**, *6* (2), 802–811. https://doi.org/10.1021/acsaem.2c03090.

(320) Chandra, A.; Chandra, A.; Thakur, K. Synthesis, Characterization and Polymer Battery Fabrication of Hot-Pressed Ion Conducting Nano-Composite Polymer Electrolytes. *Compos. Part B Eng.* **2014**, *60*, 292–296. https://doi.org/10.1016/j.compositesb.2013.12.071.

(321) Liang, Q.; Chen, L.; Tang, J.; Liu, X.; Liu, J.; Tang, M.; Wang, Z. Large-Scale Preparation of Ultrathin Composite Polymer Electrolytes with Excellent Mechanical Properties and High Thermal Stability for Solid-State Lithium-Metal Batteries. *Energy Storage Mater.* **2023**, *55*, 847–856. https://doi.org/10.1016/j.ensm.2022.12.039.

(322) Fan, L.-Z.; He, H.; Nan, C.-W. Tailoring Inorganic–Polymer Composites for the Mass Production of Solid-State Batteries. *Nat. Rev. Mater.* **2021**, *6* (11), 1003–1019. https://doi.org/10.1038/s41578-021-00320-0.

(323) Lü, H.; Chen, X.; Sun, Q.; Zhao, N.; Guo, X. Uniform Garnet Nanoparticle Dispersion in Composite Polymer Electrolytes. *Acta Phys. Chim. Sin.* **2023**, *0* (0), 2305016. https://doi.org/10.3866/PKU.WHXB202305016.

(324) Overhoff, G. M.; Ali, M. Y.; Brinkmann, J.-P.; Lennartz, P.; Orthner, H.; Hammad, M.; Wiggers, H.; Winter, M.; Brunklaus, G. Ceramic-in-Polymer Hybrid Electrolytes with Enhanced Electrochemical Performance. *ACS Appl. Mater.*

Interfaces **2022**, *14* (48), 53636–53647. https://doi.org/10.1021/acsami.2c13408.
(325) Zhang, Z.; Zhang, L.; Liu, Y.; Wang, H.; Yu, C.; Zeng, H.; Wang, L.; Xu, B. Interface-Engineered Li_7 La_3 Zr_2 O_{12} -Based Garnet Solid Electrolytes with Suppressed Li-Dendrite Formation and Enhanced Electrochemical Performance. *ChemSusChem* **2018**, *11* (21), 3774–3782. https://doi.org/10.1002/cssc.201801756.
(326) Meng, N.; Zhu, X.; Lian, F. Particles in Composite Polymer Electrolyte for Solid-State Lithium Batteries: A Review. *Particuology* **2022**, *60*, 14–36. https://doi.org/10.1016/j.partic.2021.04.002.
(327) *HNBR | ARLANXEO Website / Customer Portal*. https://www.arlanxeo.com/en/families/hnbr (accessed 2024-12-18).
(328) Döpping, D.; Schacher, F. H.; Stihl, A.; Voll, D.; Theato, P. Revisiting Polymer Coatings on Nanoparticles: Correlation between Molecular Weight and Coating Thickness in Chain Transfer Polymerizations. *Polym. Chem.* **2025**, 10.1039.D5PY00081E. https://doi.org/10.1039/D5PY00081E.
(329) Ruhl, J.; Riegger, L. M.; Ghidiu, M.; Zeier, W. G. Impact of Solvent Treatment of the Superionic Argyrodite Li 6 PS 5 Cl on Solid-State Battery Performance. *Adv. Energy Sustain. Res.* **2021**, *2* (2). https://doi.org/10.1002/aesr.202000077.
(330) Kim, M.; Lee, L.; Jung, Y.; Kim, S. Study on Ion Conductivity and Crystallinity of Composite Polymer Electrolytes Based on Poly(Ethylene Oxide)/Poly(Acrylonitrile) Containing Nano-Sized Al2O3 Fillers. *J. Nanosci. Nanotechnol.* **2013**, *13* (12), 7865–7869. https://doi.org/10.1166/jnn.2013.8107.
(331) Chu, P. Sm2O3 Composite PEO Solid Polymer Electrolyte. *J. Power Sources* **2003**, *115* (2), 288–294. https://doi.org/10.1016/S0378-7753(02)00717-6.
(332) Capuano, F.; Croce, F.; Scrosati, B. Composite Polymer Electrolytes. *J. Electrochem. Soc.* **1991**, *138* (7), 1918–1922. https://doi.org/10.1149/1.2085900.
(333) Quartarone, E. PEO-Based Composite Polymer Electrolytes. *Solid State Ion.* **1998**, *110* (1–2), 1–14. https://doi.org/10.1016/S0167-2738(98)00114-3.
(334) Wang, Y.-J.; Pan, Y.; Kim, D. Conductivity Studies on Ceramic Li1.3Al0.3Ti1.7(PO4)3-Filled PEO-Based Solid Composite Polymer Electrolytes. *J. Power Sources* **2006**, *159* (1), 690–701. https://doi.org/10.1016/j.jpowsour.2005.10.104.
(335) Brogioli, D.; Langer, F.; Kun, R.; La Mantia, F. Space-Charge Effects at the Li7La3Zr2O12/Poly(Ethylene Oxide) Interface. *ACS Appl. Mater. Interfaces* **2019**, *11* (12), 11999–12007. https://doi.org/10.1021/acsami.8b19237.
(336) Pantoja, M.; Velasco, F.; Broekema, D.; Abenojar, J.; Del Real, J. C. The Influence of pH on the Hydrolysis Process of γ-Methacryloxypropyltrimethoxysilane, Analyzed by FT-IR, and the Silanization of Electrogalvanized Steel. *J. Adhes. Sci. Technol.* **2010**, *24* (6), 1131–1143. https://doi.org/10.1163/016942409X12586283821559.
(337) *TA Instruments TGA 5500 Brochure*. https://www.tainstruments.com/pdf/brochure/TA-Instruments-DiscoveryTGA-HP750-Brochure-EN.pdf (accessed 2025-01-08).
(338) Lee, J. M.; Park, Y. S.; Moon, J.-W.; Hwang, H. Ionic and Electronic Conductivities of Lithium Argyrodite Li6PS5Cl Electrolytes Prepared via Wet Milling and Post-Annealing. *Front. Chem.* **2021**, *9*, 778057. https://doi.org/10.3389/fchem.2021.778057.
(339) *Ampcera® Argyrodite Li6PS5Cl Sulfide Solid Electrolyte, Pass 150 Mesh (Below 100 um) Coarse Powder*. MSE Supplies LLC. https://www.msesupplies.com/en-

de/products/ampcera-sulfide-solid-electrolyte-argyrodite-li6ps5cl-powder (accessed 2025-01-10).
(340) Mutlu, H.; Ceper, E. B.; Li, X.; Yang, J.; Dong, W.; Ozmen, M. M.; Theato, P. Sulfur Chemistry in Polymer and Materials Science. *Macromol. Rapid Commun.* **2019**, *40* (1), 1800650. https://doi.org/10.1002/marc.201800650.
(341) Keddie, D. J.; Moad, G.; Rizzardo, E.; Thang, S. H. RAFT Agent Design and Synthesis. *Macromolecules* **2012**, *45* (13), 5321–5342. https://doi.org/10.1021/ma300410v.
(342) Bamford, D.; Dlubek, G.; Reiche, A.; Alam, M. A.; Meyer, W.; Galvosas, P.; Rittig, F. The Local Free Volume, Glass Transition, and Ionic Conductivity in a Polymer Electrolyte: A Positron Lifetime Study. *J. Chem. Phys.* **2001**, *115* (15), 7260–7270. https://doi.org/10.1063/1.1402633.
(343) Silva, F. C. A.; Ortega, P. F. R.; Dos Reis, R. A.; Lavall, R. L.; Costa, L. T. Polymer-Ion Interactions in a Pvdf@Ionic Liquid Polymer Electrolytes: A Combined Experimental and Computational Study. *SSRN Electron. J.* **2022**. https://doi.org/10.2139/ssrn.4064376.
(344) Skey, J.; O'Reilly, R. K. Facile One Pot Synthesis of a Range of Reversible Addition–Fragmentation Chain Transfer (RAFT) Agents. *Chem. Commun.* **2008**, No. 35, 4183. https://doi.org/10.1039/b804260h.
(345) Kumagai, S.; Sato, M.; Ma, C.; Nakai, Y.; Kameda, T.; Saito, Y.; Watanabe, A.; Watanabe, C.; Teramae, N.; Yoshioka, T. A Comprehensive Study into the Thermo-Oxidative Degradation of Sulfur-Based Engineering Plastics. *J. Anal. Appl. Pyrolysis* **2022**, *168*, 105754. https://doi.org/10.1016/j.jaap.2022.105754.
(346) Shahid, S.; Agelin-Chaab, M. A Review of Thermal Runaway Prevention and Mitigation Strategies for Lithium-Ion Batteries. *Energy Convers. Manag. X* **2022**, *16*, 100310. https://doi.org/10.1016/j.ecmx.2022.100310.
(347) Zhao, J.-Z.; Yue, T.-J.; Ren, B.-H.; Liu, Y.; Ren, W.-M.; Lu, X.-B. Recyclable Sulfur-Rich Polymers with Enhanced Thermal, Mechanical, and Optical Performance. *Macromolecules* **2022**, *55* (19), 8651–8658. https://doi.org/10.1021/acs.macromol.2c01628.
(348) Rumyantsev, M. Living Polymerizations of Propylene Sulfide Initiated with Potassium Xanthates Characterized by Unprecedentedly High Propagation Rates. *Polym. Chem.* **2021**, *12* (9), 1298–1309. https://doi.org/10.1039/d0py01740j.
(349) Luo, B.; Wu, J.; Zhang, M.; Zhang, Z.; Zhang, X.; Fang, Z.; Xu, Z.; Wu, M. Surface Modification of Garnet Fillers with a Polymeric Sacrificial Agent Enables Compatible Interfaces of Composite Solid-State Electrolytes. *Chem. Sci.* **2023**, *14* (45), 13067–13079. https://doi.org/10.1039/D3SC04710E.
(350) Liu, Y.; Cai, J.; Chang, W.; Tan, Y.; Lai, C.; Peng, Y.; Liu, H. Interface Strategies for Enhancing the Lithium-Ion Transport of Composite Polymer Electrolytes toward High-Performance Solid-State Batteries. *ACS Appl. Energy Mater.* **2024**. https://doi.org/10.1021/acsaem.3c03240.
(351) Lin, B.; Zhou, S. Light-Responsive Nanoparticles with Wettability Changing from Hydrophobicity to Hydrophilicity and Their Application towards Highly Hydrophilic Fluorocarbon Coatings. *Appl. Surf. Sci.* **2015**, *359*, 380–387. https://doi.org/10.1016/j.apsusc.2015.10.111.
(352) Wang, X.; Huang, S.; Guo, K.; Min, Y.; Xu, Q. Directed and Continuous Interfacial Channels for Optimized Ion Transport in Solid-State Electrolytes. *Adv. Funct. Mater.* **2022**, *32* (49), 2206976. https://doi.org/10.1002/adfm.202206976.
(353) Butzelaar, A. J.; Röring, P.; Mach, T. P.; Hoffmann, M.; Jeschull, F.; Wilhelm, M.; Winter, M.; Brunklaus, G.; Théato, P. Styrene-Based Poly(Ethylene Oxide) Side-

Chain Block Copolymers as Solid Polymer Electrolytes for High-Voltage Lithium-Metal Batteries. *ACS Appl. Mater. Interfaces* **2021**, *13* (33), 39257–39270. https://doi.org/10.1021/acsami.1c08841.

(354) Maurel, A.; Armand, M.; Grugeon, S.; Fleutot, B.; Davoisne, C.; Tortajada, H.; Courty, M.; Panier, S.; Dupont, L. Poly(Ethylene Oxide)−LiTFSI Solid Polymer Electrolyte Filaments for Fused Deposition Modeling Three-Dimensional Printing. *J. Electrochem. Soc.* **2020**, *167* (7), 070536. https://doi.org/10.1149/1945-7111/ab7c38.

(355) Buchheit, A.; Hoffmeyer, M.; Teßmer, B.; Neuhaus, K. Characterization of the Particle-Polymer Interface in Dual-Phase Electrolytes by Kelvin Probe Force Microscopy. *J. Electrochem. Soc.* **2021**, *168* (1), 010531. https://doi.org/10.1149/1945-7111/abda59.

(356) Scharf, F.; Krude, A.; Lennartz, P.; Clausnitzer, M.; Shukla, G.; Buchheit, A.; Kempe, F.; Diddens, D.; Glomb, P.; Mitchell, M. M.; Danner, T.; Heuer, A.; Latz, A.; Winter, M.; Brunklaus, G. Synergistic Enhancement of Mechanical and Electrochemical Properties in Grafted Polymer/Oxide Hybrid Electrolytes. *Small* **2024**, *20* (47), 2404537. https://doi.org/10.1002/smll.202404537.

(357) Zhang, B.; Liu, Y.; Liu, J.; Sun, L.; Cong, L.; Fu, F.; Mauger, A.; Julien, C. M.; Xie, H.; Pan, X. “Polymer-in-Ceramic” Based Poly(Ɛ-Caprolactone)/Ceramic Composite Electrolyte for All-Solid-State Batteries. *J. Energy Chem.* **2021**, *52*, 318–325. https://doi.org/10.1016/j.jechem.2020.04.025.

(358) Wang, A.; Pei, D.; Liu, Z.; Huang, S.; Cao, G.; Jin, H.; Hou, S. Exploring High Li + Transference Number Solid-State Electrolytes Based on a Poly(ε-Caprolactone) Polymer Matrix with Efficient Lithium Salt Dissociation for Applications in Lithium-Metal Batteries. *ACS Appl. Energy Mater.* **2023**, *6* (15), 8221–8228. https://doi.org/10.1021/acsaem.3c01341.

(359) Gupta, A.; Sakamoto, J. Controlling Ionic Transport through the PEO-LiTFSI/LLZTO Interface. *Electrochem. Soc. Interface* **2019**, *28* (2), 63–69. https://doi.org/10.1149/2.F06192if.

(360) Cortés, H. A.; Bonilla, M. R.; Marinero, E. E.; Carrasco, J.; Akhmatskaya, E. Anion Trapping and Ionic Conductivity Enhancement in PEO-Based Composite Polymer–Li 7 La 3 Zr 2 O 12 Electrolytes: The Role of the Garnet Li Molar Content. *Macromolecules* **2023**, *56* (11), 4256–4266. https://doi.org/10.1021/acs.macromol.3c00568.

(361) Kim, H.-K.; Barai, P.; Chavan, K.; Srinivasan, V. Transport and Mechanical Behavior in PEO-LLZO Composite Electrolytes. *J. Solid State Electrochem.* **2022**, *26* (9), 2059–2075. https://doi.org/10.1007/s10008-022-05231-w.

(362) Colombo, F.; Bonizzoni, S.; Ferrara, C.; Simonutti, R.; Mauri, M.; Falco, M.; Gerbaldi, C.; Mustarelli, P.; Ruffo, R. Polymer-in-Ceramic Nanocomposite Solid Electrolyte for Lithium Metal Batteries Encompassing PEO-Grafted TiO_2 Nanocrystals. *J. Electrochem. Soc.* **2020**, *167* (7), 070535. https://doi.org/10.1149/1945-7111/ab7c72.

(363) Genier, F. S.; Pathreeker, S.; Adebo, P. O.; Chando, P.; Hosein, I. D. Design of a Boron-Containing PTHF-Based Solid Polymer Electrolyte for Sodium-Ion Conduction with High Na + Mobility and Salt Dissociation. *ACS Appl. Polym. Mater.* **2022**, *4* (10), 7645–7663. https://doi.org/10.1021/acsapm.2c01276.

(364) Iurilli, P.; Brivio, C.; Carrillo, R.; Wood, V. EIS2MOD: A DRT-Based Modeling Framework for Li-Ion Cells. *IEEE Trans. Ind. Appl.* **2022**, *58* (2), 1429–1439. https://doi.org/10.1109/TIA.2021.3134946.

(365) Eckhardt, J. K.; Fuchs, T.; Burkhardt, S.; Klar, P. J.; Janek, J.; Heiliger, C. Guidelines for Impedance Analysis of Parent Metal Anodes in Solid-State

Batteries and the Role of Current Constriction at Interface Voids, Heterogeneities, and SEI. *Adv. Mater. Interfaces* **2023**, *10* (8), 2202354. https://doi.org/10.1002/admi.202202354.

(366) Mu, J.; Liao, S.; Shi, L.; Su, B.; Xu, F.; Guo, Z.; Li, H.; Wei, F. Solid-State Polymer Electrolytes in Lithium Batteries: Latest Progress and Perspective. *Polym. Chem.* **2024**. https://doi.org/10.1039/D3PY01311A.

(367) Kuhnert, E.; Ladenstein, L.; Jodlbauer, A.; Slugovc, C.; Trimmel, G.; Wilkening, H. M. R.; Rettenwander, D. Lowering the Interfacial Resistance in Li6.4La3Zr1.4Ta0.6O12|Poly(Ethylene Oxide) Composite Electrolytes. *Cell Rep. Phys. Sci.* **2020**, *1* (10), 100214. https://doi.org/10.1016/j.xcrp.2020.100214.

(368) Kloker, G.; Pervez, S. A.; Hoefling, A.; Fichtner, M. Improving the Electrochemical Properties of Advanced Cross-Linked Solid Polymer Composite Electrolytes. *ACS Appl. Energy Mater.* **2022**, *5* (11), 13410–13418. https://doi.org/10.1021/acsaem.2c02082.

(369) Su, Y.; Xu, F.; Zhang, X.; Qiu, Y.; Wang, H. Rational Design of High-Performance PEO/Ceramic Composite Solid Electrolytes for Lithium Metal Batteries. *Nano-Micro Lett.* **2023**, *15* (1), 82. https://doi.org/10.1007/s40820-023-01055-z.

(370) Li, L.; Deng, Y.; Duan, H.; Qian, Y.; Chen, G. LiF and LiNO3 as Synergistic Additives for PEO-PVDF/LLZTO-Based Composite Electrolyte towards High-Voltage Lithium Batteries with Dual-Interfaces Stability. *J. Energy Chem.* **2022**, *65*, 319–328. https://doi.org/10.1016/j.jechem.2021.05.055.

(371) Sun, H.; Cheng, J.; Kang, S.; Gao, W.; Xu, R.; Yuan, T.; Cui, L. Eliminating Li Dendrites in PEO-Based Polymer Solid Electrolytes by Doping with SbF 3. *ACS Appl. Energy Mater.* **2023**, *6* (24), 12206–12215. https://doi.org/10.1021/acsaem.3c01875.

(372) Sun, Q.; Tufail, M. K.; Li, W.; Zhao, N.; Bi, Z.; Guo, X. Combination of 3D Current Collectors and *in Situ* Polymerized Electrolytes Enabling High-Mass-Loading Cathodes for Solid-State Lithium Batteries. *Appl. Phys. Lett.* **2023**, *122* (21), 213901. https://doi.org/10.1063/5.0147529.

(373) Zhai, H.; Gong, T.; Xu, B.; Cheng, Q.; Paley, D.; Qie, B.; Jin, T.; Fu, Z.; Tan, L.; Lin, Y.-H.; Nan, C.-W.; Yang, Y. Stabilizing Polyether Electrolyte with a 4 V Metal Oxide Cathode by Nanoscale Interfacial Coating. *ACS Appl. Mater. Interfaces* **2019**, *11* (32), 28774–28780. https://doi.org/10.1021/acsami.9b04932.

(374) Cai, D.; Wang, D.; Chen, Y.; Zhang, S.; Wang, X.; Xia, X.; Tu, J. A Highly Ion-Conductive Three-Dimensional LLZAO-PEO/LiTFSI Solid Electrolyte for High-Performance Solid-State Batteries. *Chem. Eng. J.* **2020**, *394*, 124993. https://doi.org/10.1016/j.cej.2020.124993.

(375) Usta, S.; Çelik, M.; Çetinkaya, T. Enhancement of the Stability Window of PEO for High Voltage All-Solid-State Lithium Batteries. *J. Power Sources* **2023**, *580*, 233404. https://doi.org/10.1016/j.jpowsour.2023.233404.

(376) Zhang, W.; Weber, D. A.; Weigand, H.; Arlt, T.; Manke, I.; Schröder, D.; Koerver, R.; Leichtweiss, T.; Hartmann, P.; Zeier, W. G.; Janek, J. Interfacial Processes and Influence of Composite Cathode Microstructure Controlling the Performance of All-Solid-State Lithium Batteries. *ACS Appl. Mater. Interfaces* **2017**, *9* (21), 17835–17845. https://doi.org/10.1021/acsami.7b01137.

(377) Bruce, P. G.; Vincent, C. A. Steady State Current Flow in Solid Binary Electrolyte Cells. *J. Electroanal. Chem. Interfacial Electrochem.* **1987**, *225* (1–2), 1–17. https://doi.org/10.1016/0022-0728(87)80001-3.

(378) Evans, J.; Vincent, C. A.; Bruce, P. G. Electrochemical Measurement of Transference Numbers in Polymer Electrolytes. *Polymer* **1987**, *28* (13), 2324–2328. https://doi.org/10.1016/0032-3861(87)90394-6.

(379) Ohno, S.; Bernges, T.; Buchheim, J.; Duchardt, M.; Hatz, A.-K.; Kraft, M. A.; Kwak, H.; Santhosha, A. L.; Liu, Z.; Minafra, N.; Tsuji, F.; Sakuda, A.; Schlem, R.; Xiong, S.; Zhang, Z.; Adelhelm, P.; Chen, H.; Hayashi, A.; Jung, Y. S.; Lotsch, B. V.; Roling, B.; Vargas-Barbosa, N. M.; Zeier, W. G. How Certain Are the Reported Ionic Conductivities of Thiophosphate-Based Solid Electrolytes? An Interlaboratory Study. *ACS Energy Lett.* **2020**, *5* (3), 910–915. https://doi.org/10.1021/acsenergylett.9b02764.

12 Appendix

12.1 Additional Data for “Evaluation of HNBR for CPEs”

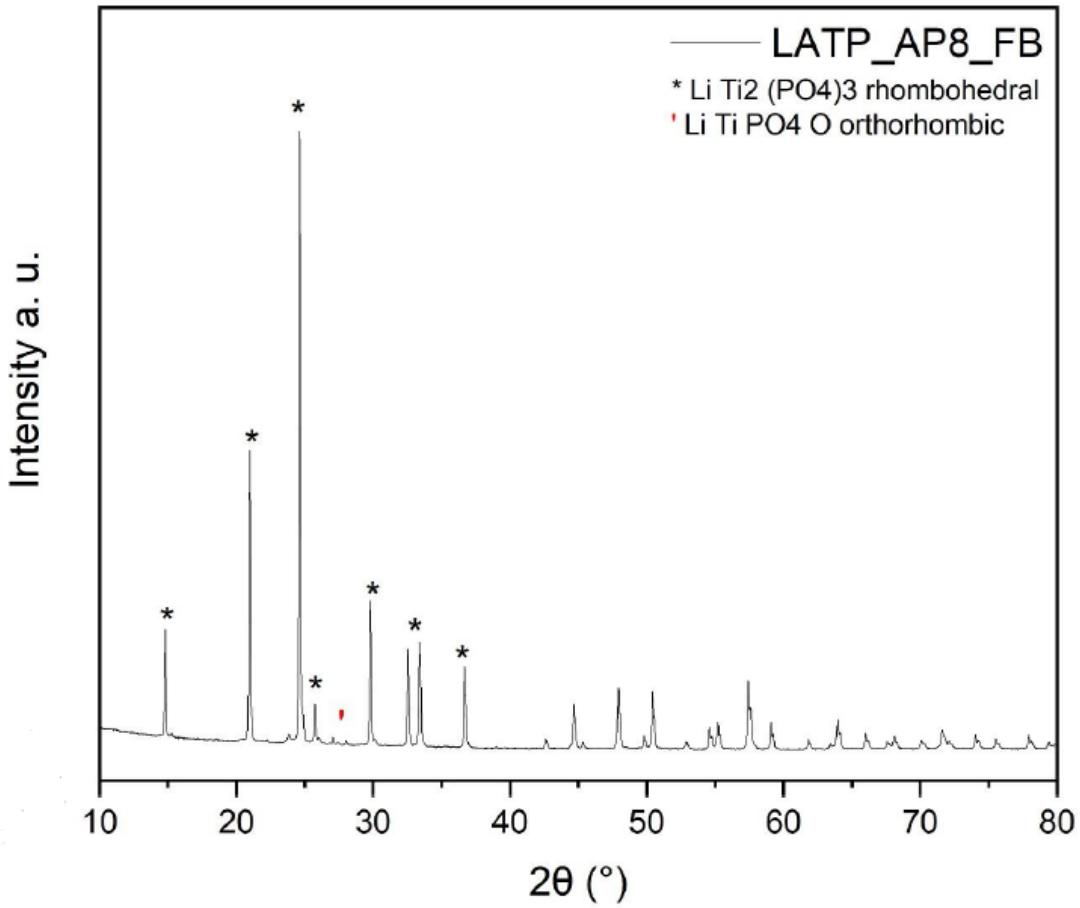

Figure 111 XRD of supplied LATP by Dr. Martin Finsterbusch and M.Sc. Xiaochen Liu. Data provided by Dr. Martin Finsterbusch.

Table 23 PSD in µm of supplied LATP by Dr. Martin Finsterbusch and M.Sc. Xiaochen Liu. Relative density, ICP-OES results, and ionic conductivity at 25 °C are provided below. Data provided by Dr. Martin Finsterbusch.

D(v,0.1)	D(v,0.5)	D(v,0.9)
0.10	0.24	8.01

ICP-OES: $Li_{1.55}Al_{0.49}Ti_{1.59}P_3$

Relative density: 87.1 %

σ (25 °C) = $4.3 \cdot 10^{-4}$ S cm^{-1}

Figure 112 HNBR-LiTFSI film.

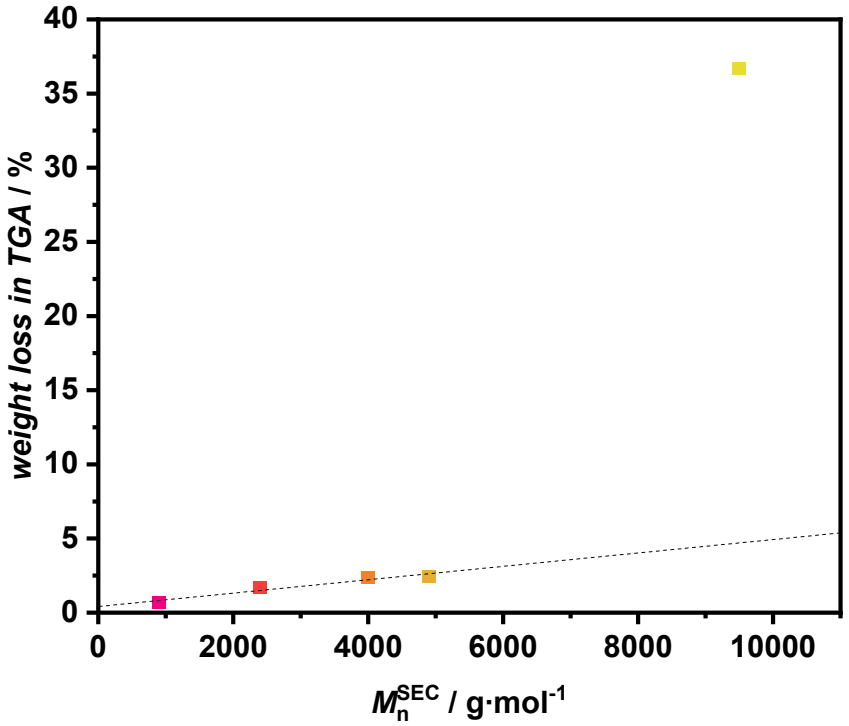

Figure 113 Correlation between M_n determined in DMAC-SEC and mass loss in TGA from PAN@SiO_2 samples. R^2 (0.94) of the linear fit function indicates a strong correlation.

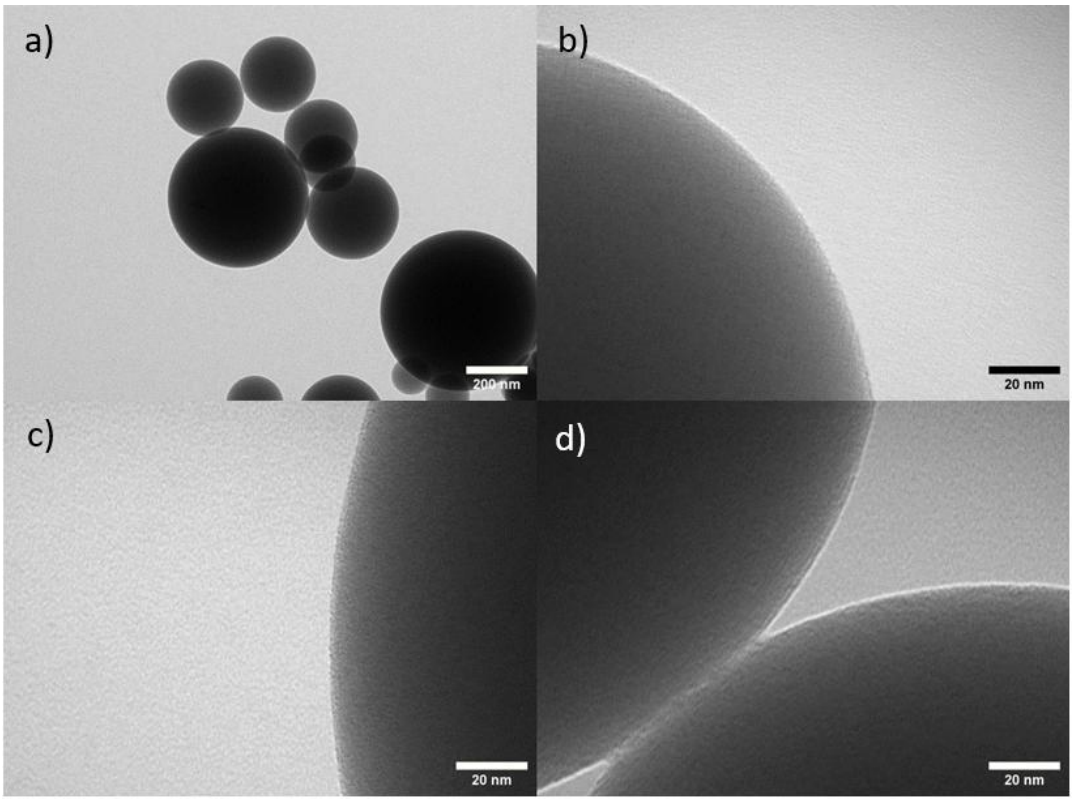

Figure 114 TEM micrographs of PAN@SiO_2 1:0.1. The very thin homogeneous PAN coating can be observed at the particle surface.

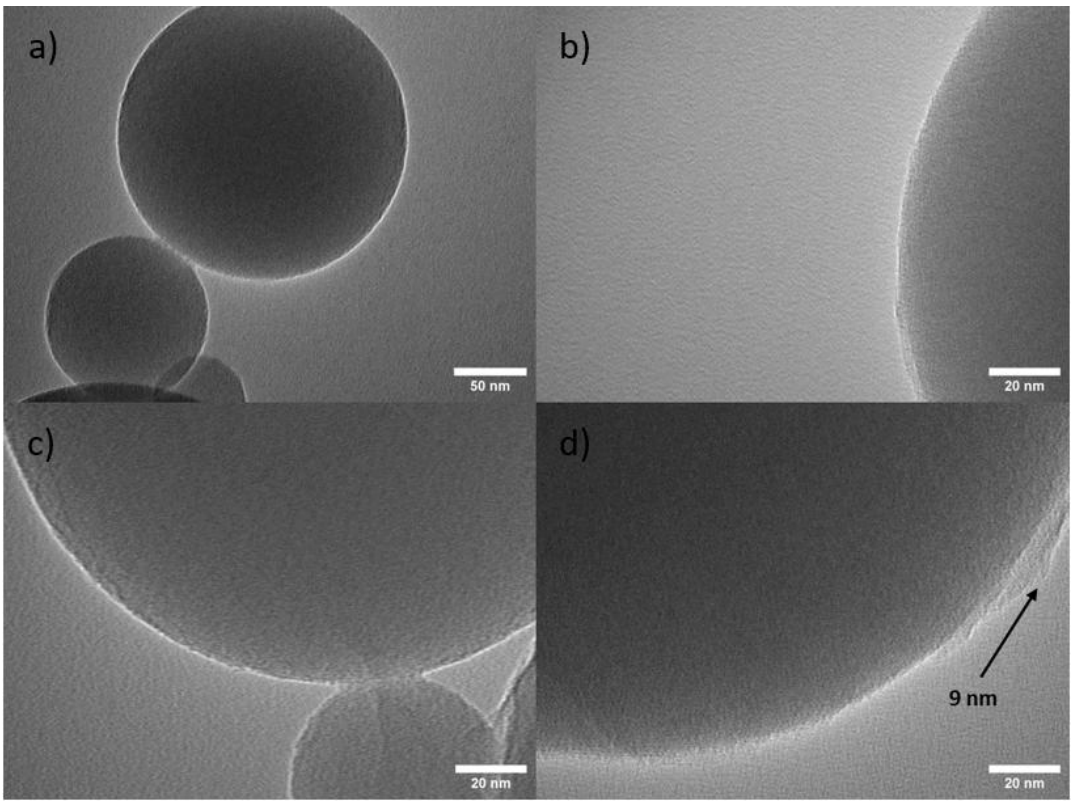

Figure 115 TEM micrographs of PAN@SiO_2 1:0.5. The PAN coating is clearly visible and small agglomerates of PAN can be observed at the surface.

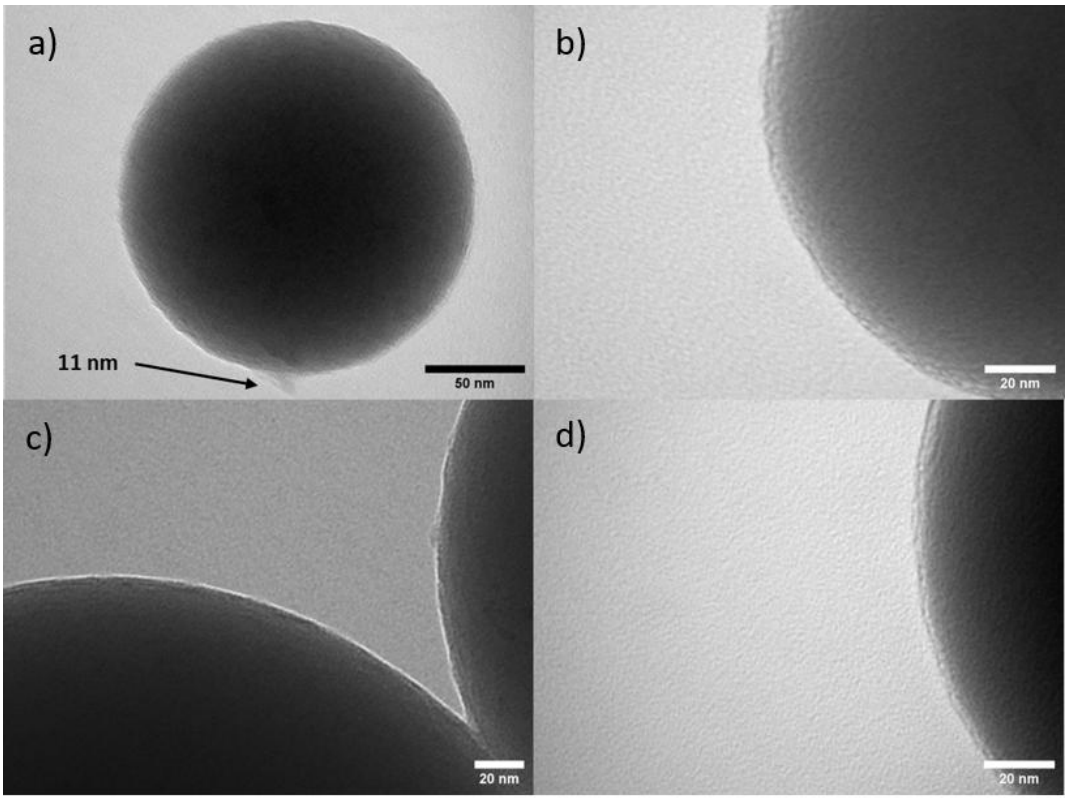

Figure 116 TEM micrographs of PAN@SiO_2 1:1. The amount of PAN agglomerates increases, and the PAN coating thickness increases further.

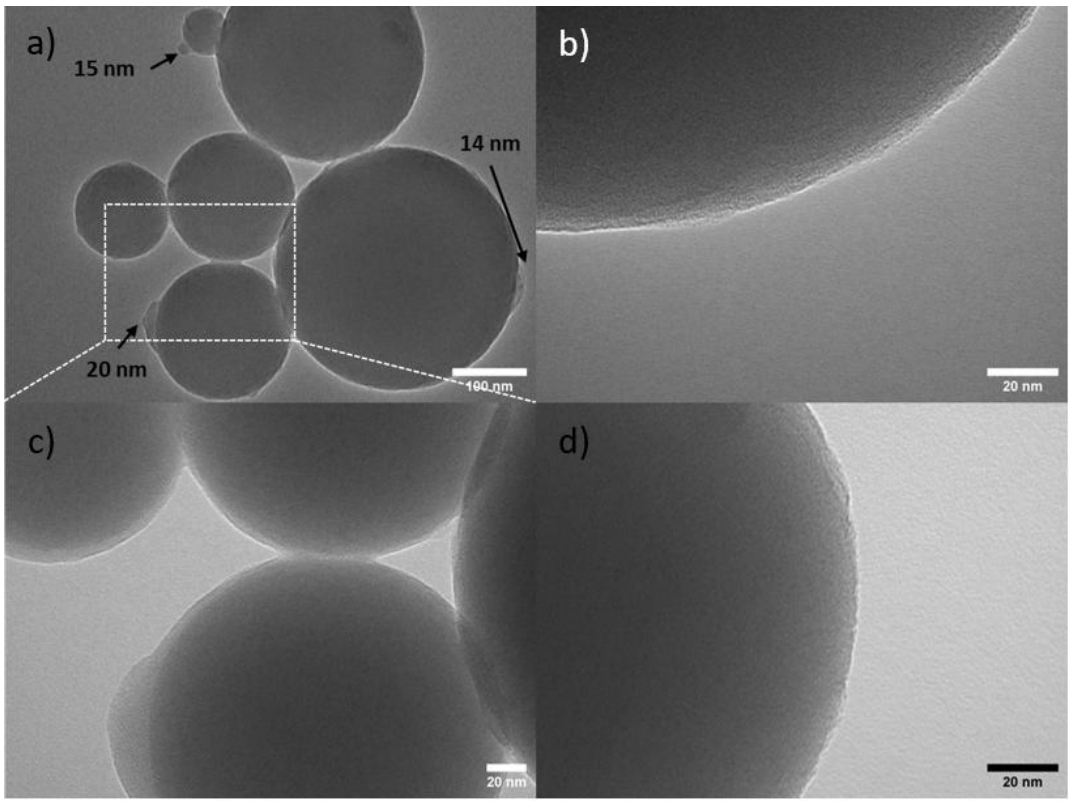

Figure 117 TEM micrographs of PAN@SiO_2 1:2. Large PAN agglomerates form and the PAN coating gets increasingly inhomogeneous.

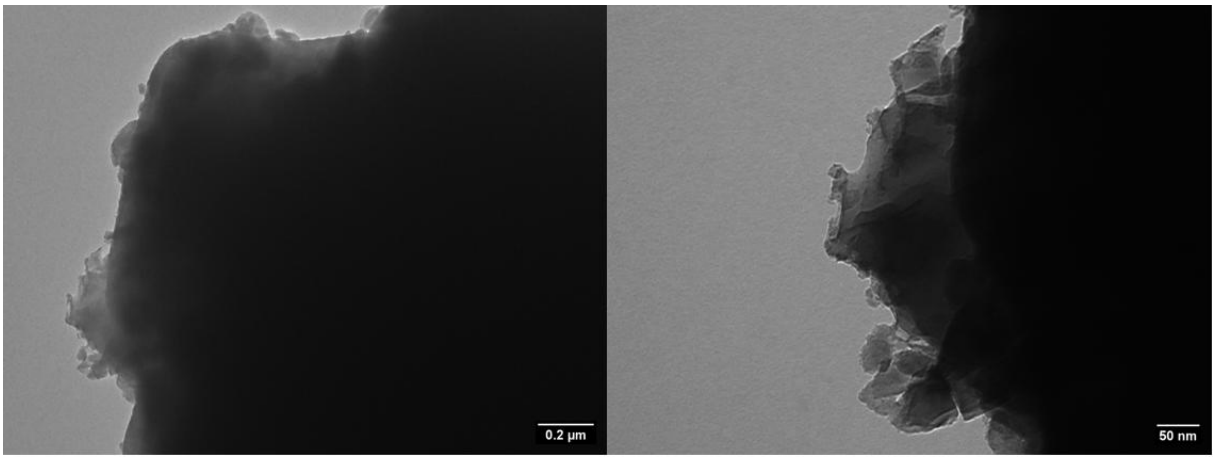

Figure 118 TEM micrographs of pristine LATP. The particles have highly rough contours with crevices.

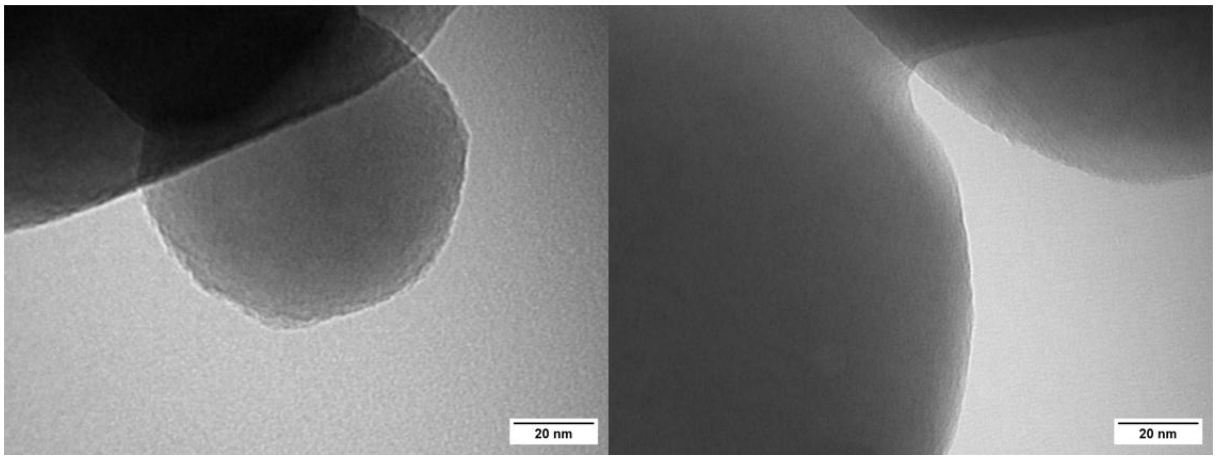

Figure 119 TEM micrographs of SH@LATP. The particles have smooth contours.

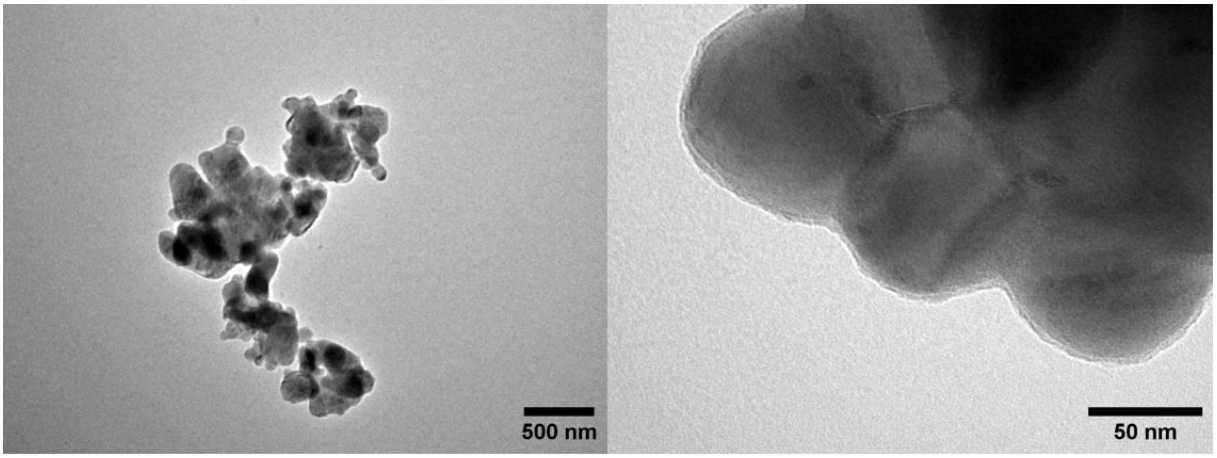

Figure 120 TEM micrographs of PAN@LATP. The particles have a visible smooth amorphous surface coating.

12.2 Additional Data for “Coating of LATP/LLZO Particles for Oxide-CPEs”

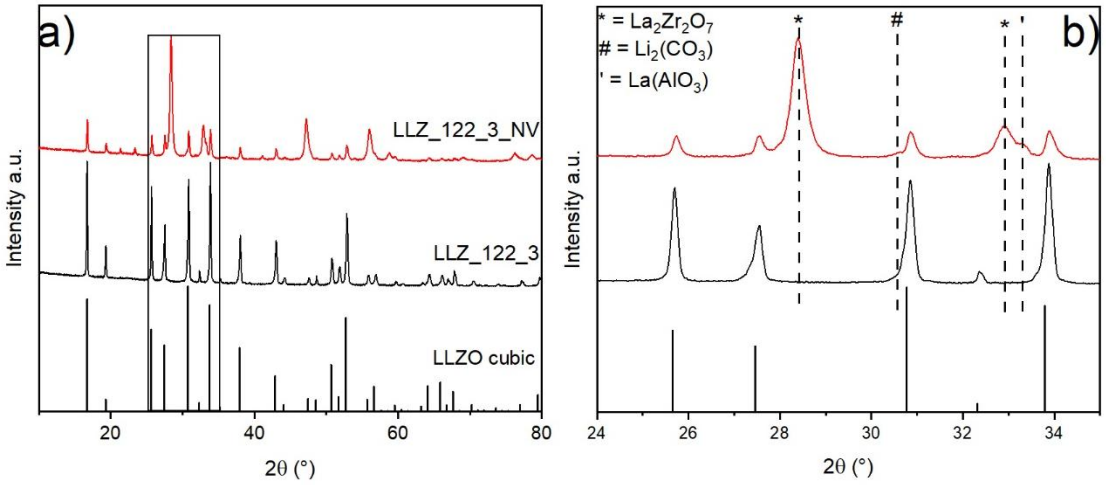

Figure 121 XRD of supplied LLZO by Dr. Martin Finsterbusch and M.Sc. Xiaochen Liu. Data provided by Dr. Martin Finsterbusch.

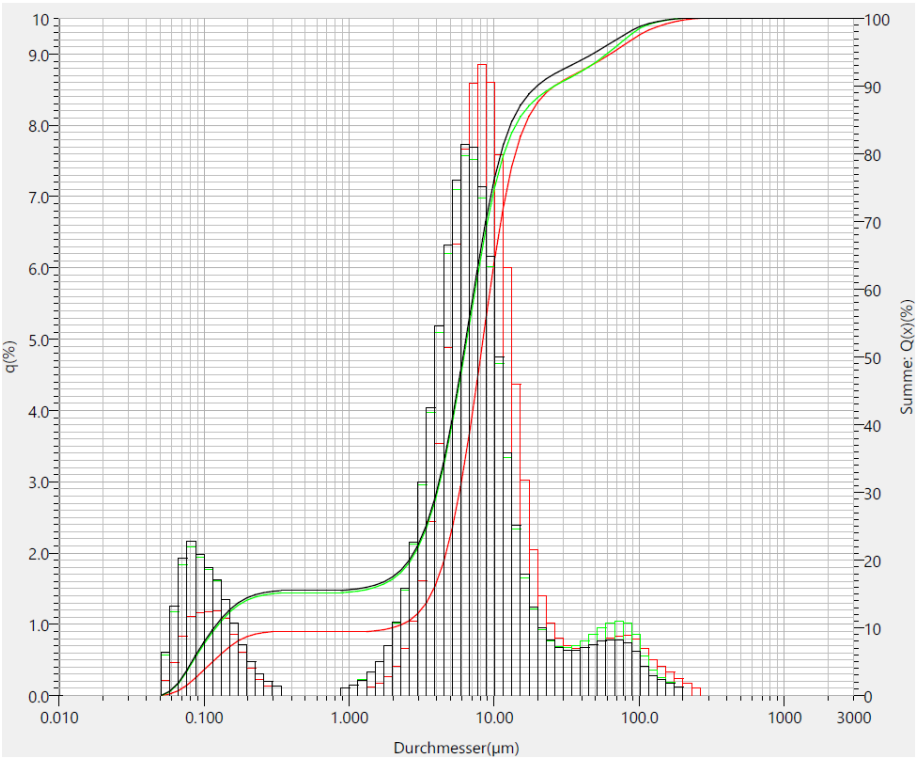

Figure 122 PSD of supplied LLZO 122_3 by Dr. Martin Finsterbusch and M.Sc. Xiaochen Liu. Data provided by Dr. Martin Finsterbusch.

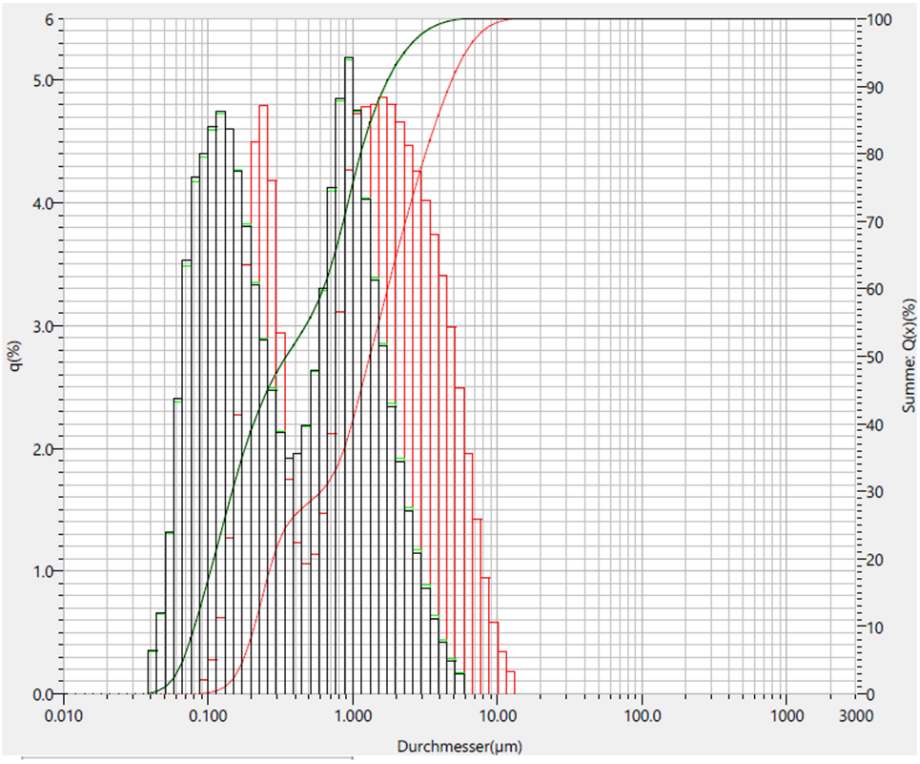

Figure 123 PSD of supplied LLZO 122_3_NV by Dr. Martin Finsterbusch and M.Sc. Xiaochen Liu. Data provided by Dr. Martin Finsterbusch. LLZO 122_3_NV is ball milled and sieved after sintering.

Table 24 PSD in µm of supplied LLZO by Dr. Martin Finsterbusch and M.Sc. Xiaochen Liu. Relative density, ICP-OES results, and ionic conductivity at 25 °C are provided below. Data provided by Dr. Martin Finsterbusch.

LLZO	D(v,0.1)	D(v,0.5)	D(v,0.9)
122_3	0.12	6.09	19.72
122_3_NV	0.08	0.35	1.66

122_3_NV is wet ball milled after sintering and sieved.

ICP-OES: $Li_{7.15}La_3Zr_{1.32}Ta_{0.41}Al_{0.9}Hf_{0.02}$

Relative density: 95.0 %

σ (25 °C) = $6.2 \cdot 10^{-4}$ S cm^{-1}

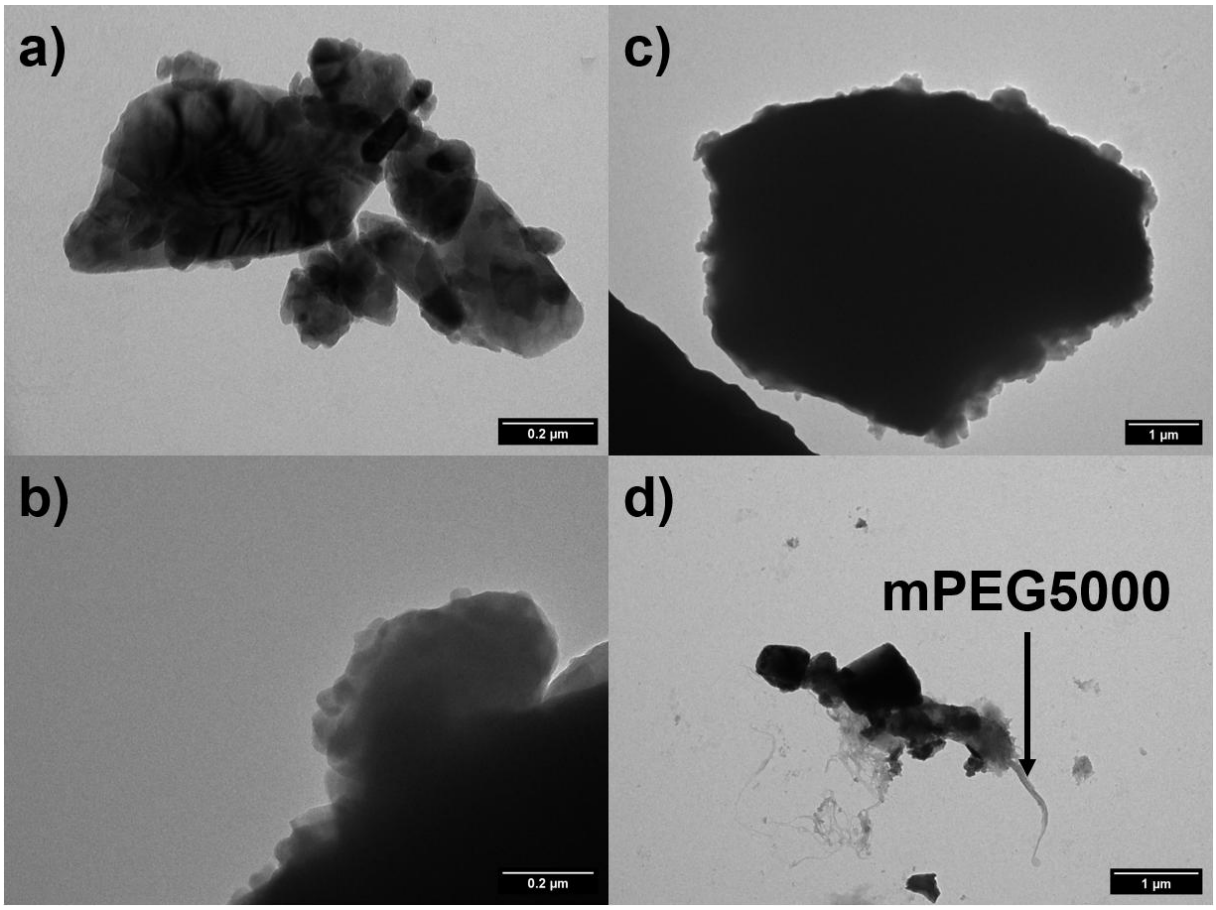

Figure 124 TEM micrographs of a) mPEG550@LATP, b) mPEG1000@LATP, c) mPEG2000@LATP, and d) mPEG5000@LATP.

12.3 Additional Data for “Self-Crosslinking Oxide-CPEs”

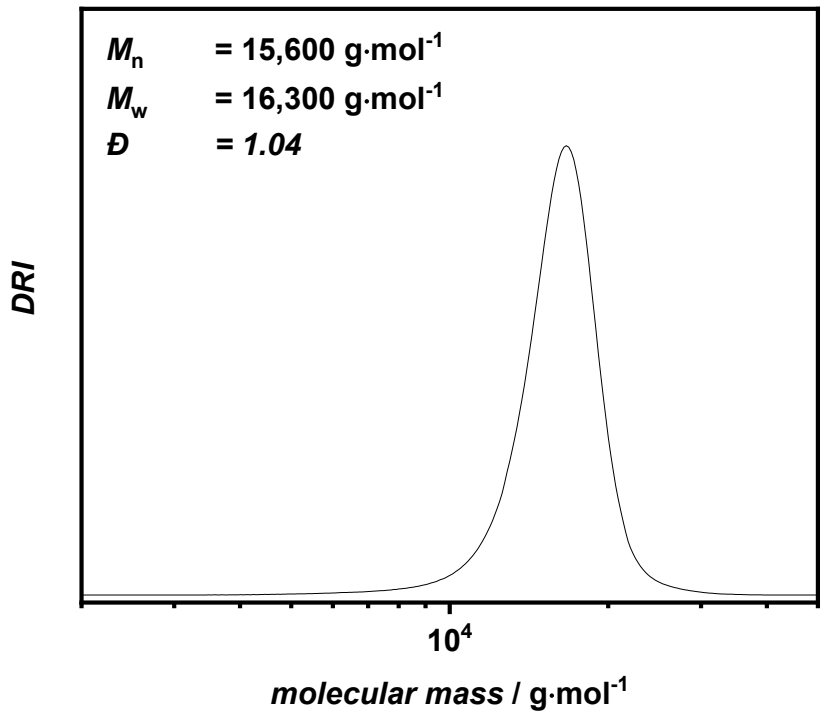

Figure 125 THF-SEC of PEO10k against a PMMA standard.

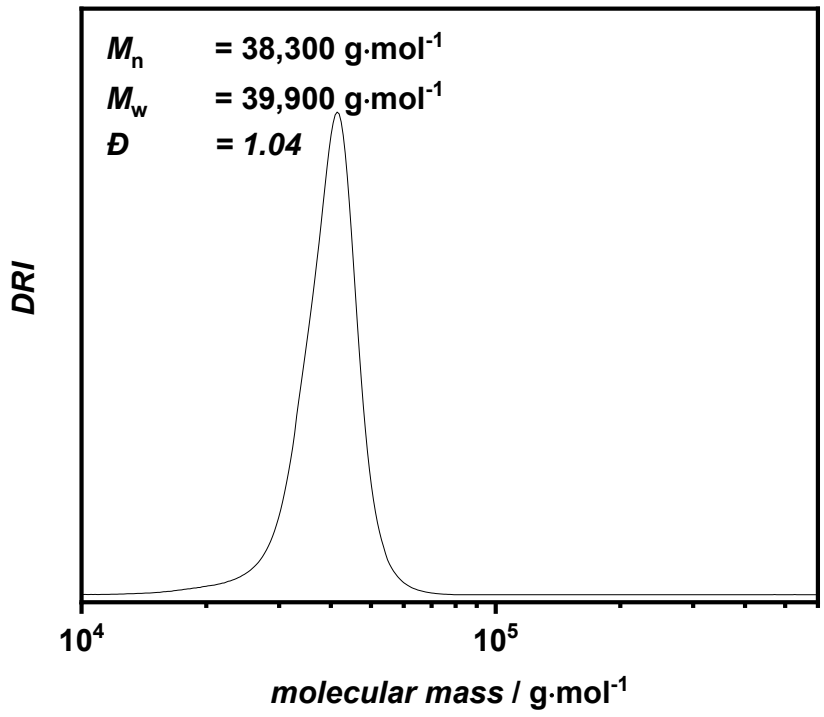

Figure 126 THF-SEC of PEO20k against a PMMA standard.

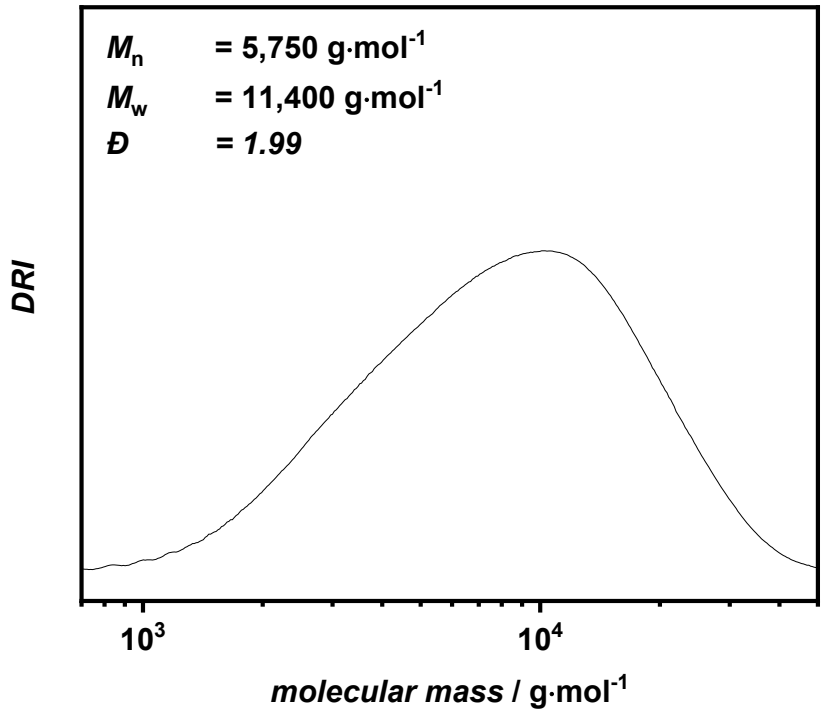

Figure 127 THF-SEC of PTHF2.9k against a PMMA standard.

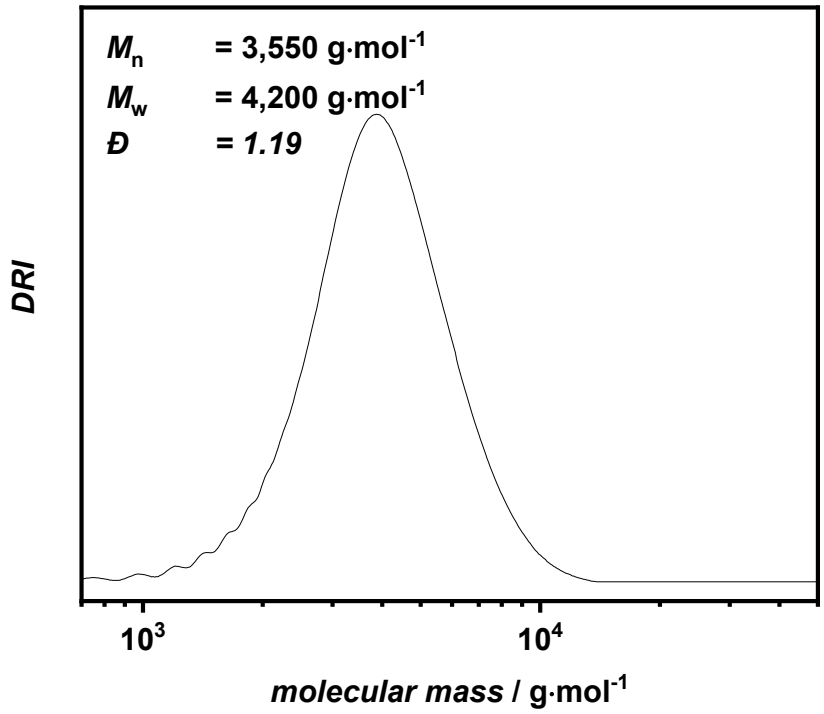

Figure 128 THF-SEC of PCL2k-diol against a PMMA standard.

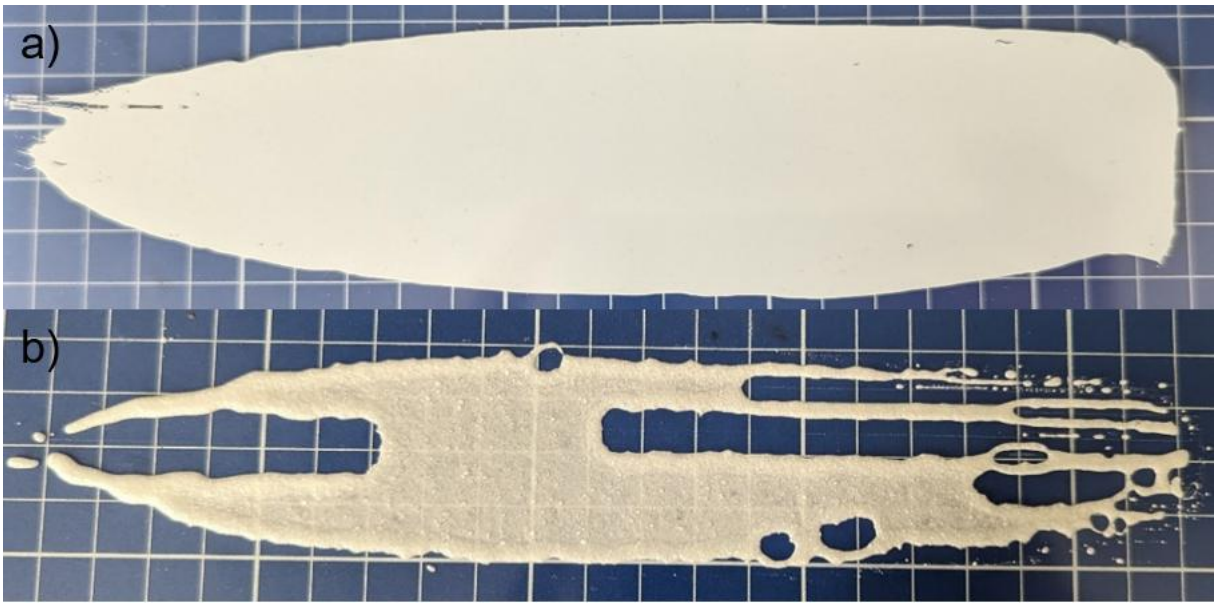

Figure 129 Comparison of doctor bladed films with PEO10k-silane and LLZO. a) with LLZO 350 nm particle size and b) 6.09 µm LLZO particle size.

Figure 130 Picture of the manual roll-to-roll press with adjustable slit width.

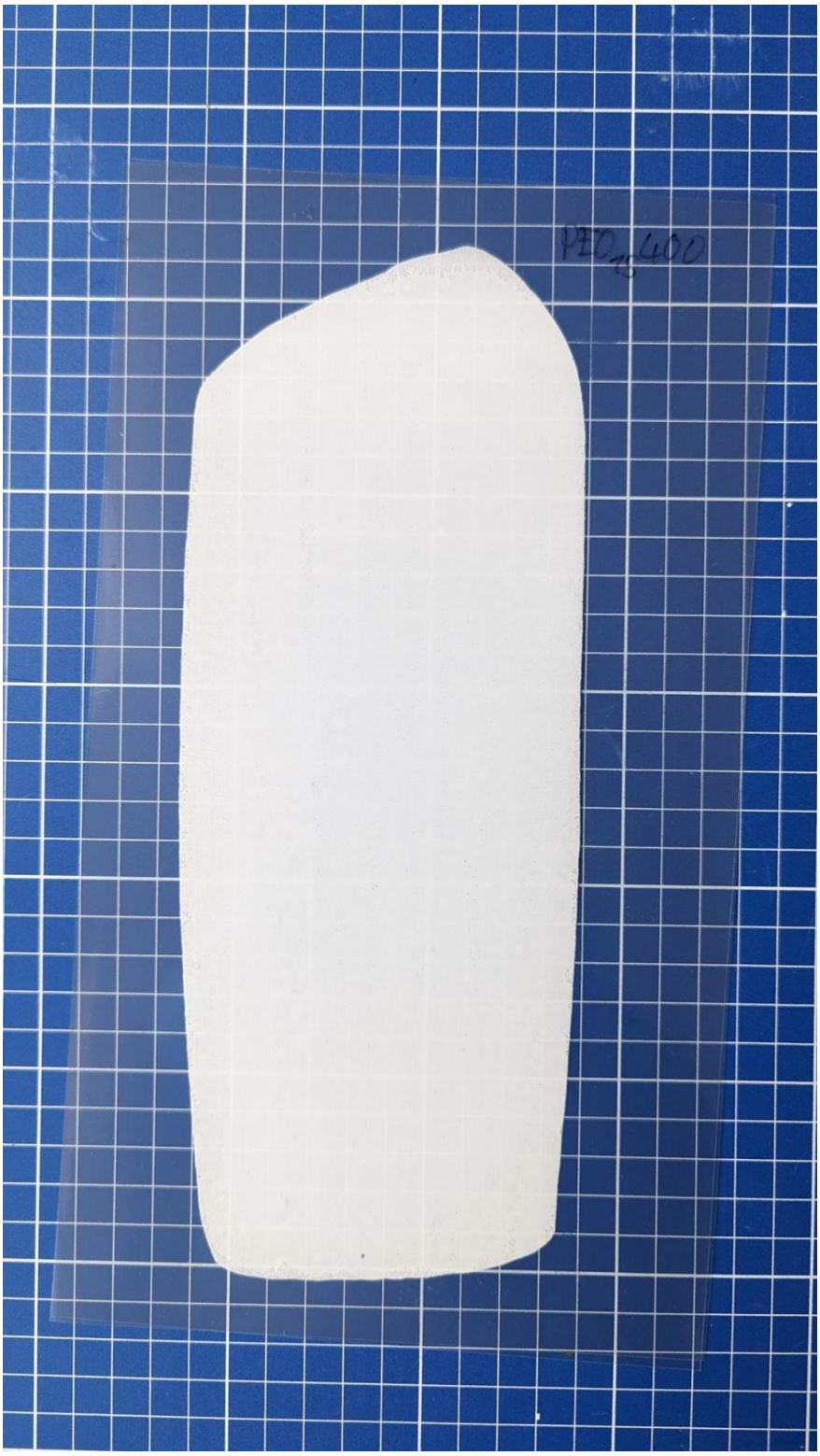

Figure 131 A homogeneous $PEO_{15}400$ film after roll-to-roll pressing in between two Mylar® foils.

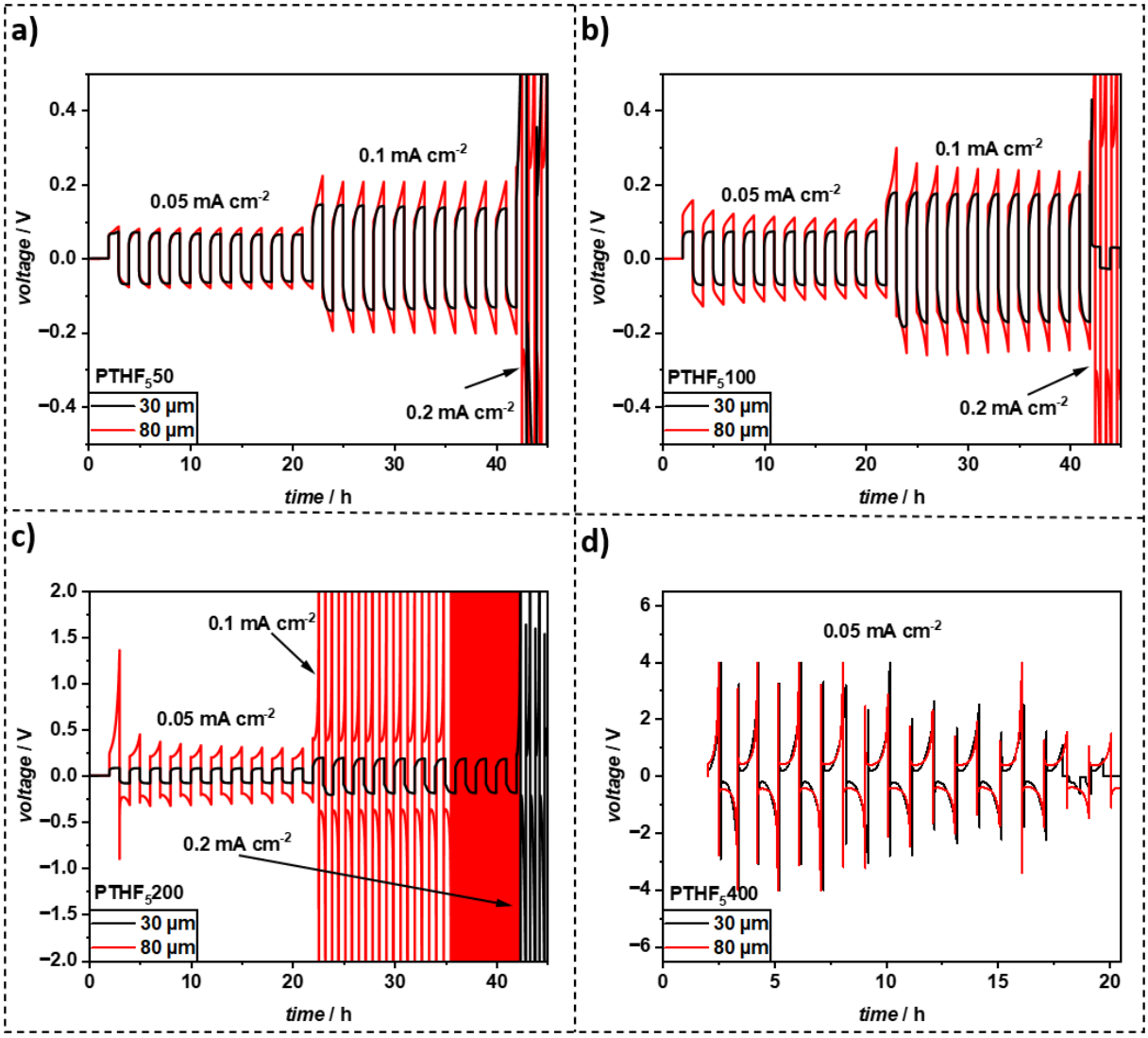

Figure 132 Symmetrical Li||Li plating-stripping experiments of $PTHF_5$50-400-LLZO films (30 µm and 80 µm) with increasing current density after 10 cycles at 60 °C.

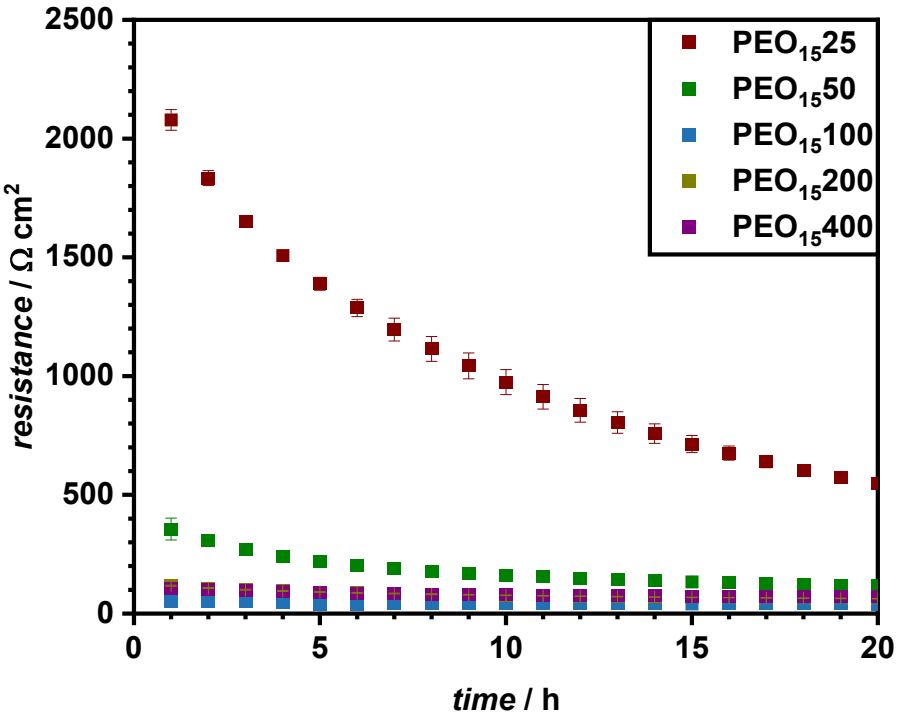

Figure 133 Development of areal resistance of PEO CPEs over 20 h in symmetrical Li||Li cells.

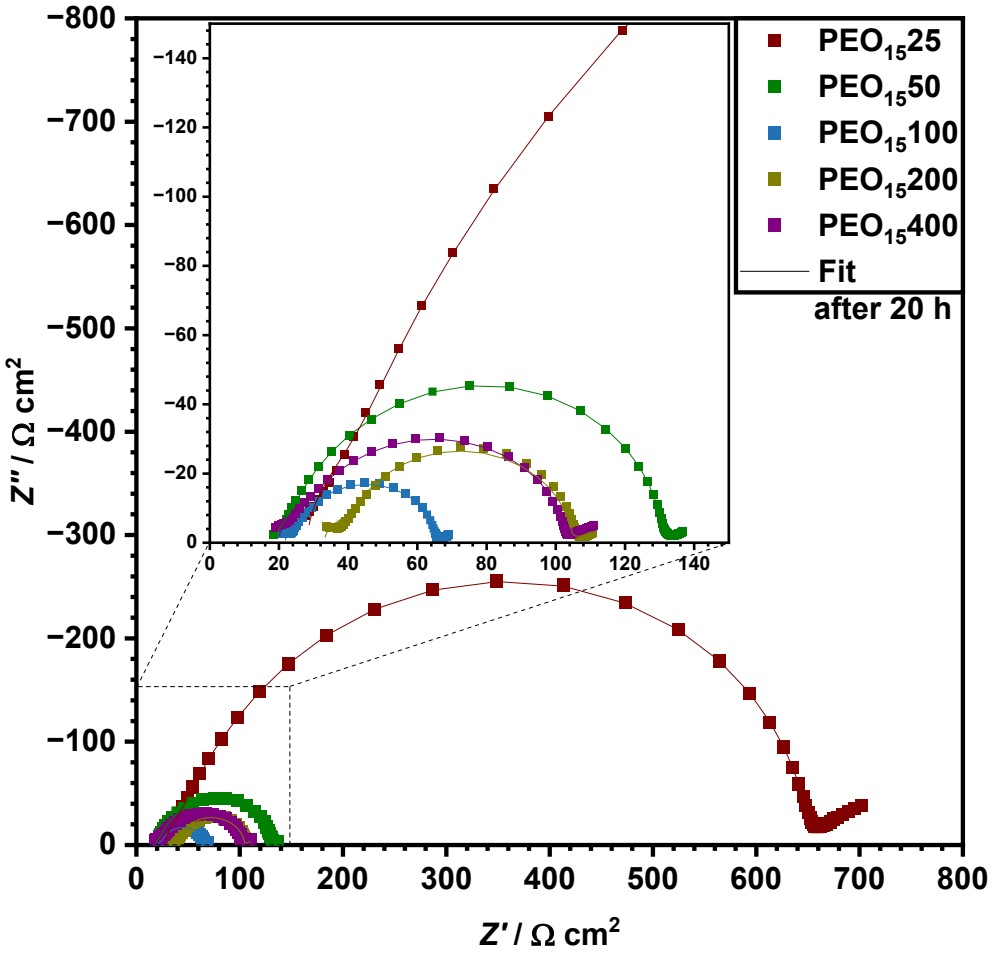

Figure 134 Nyquist plot of PEO CPEs after 20 h in symmetrical Li||Li cells.

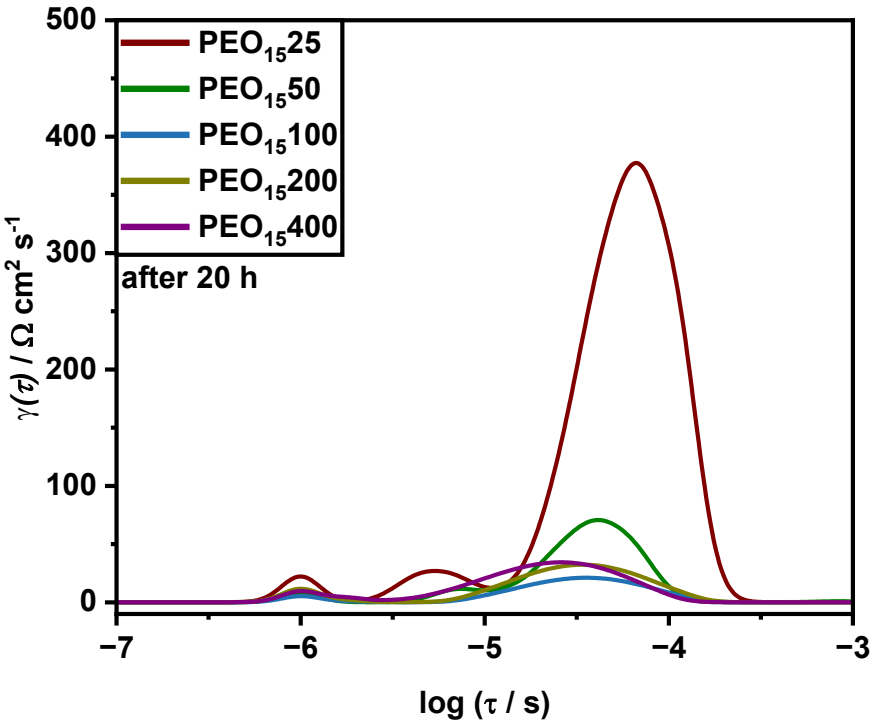

Figure 135 DRT of PEO CPEs after 20 h in symmetrical Li||Li cells.

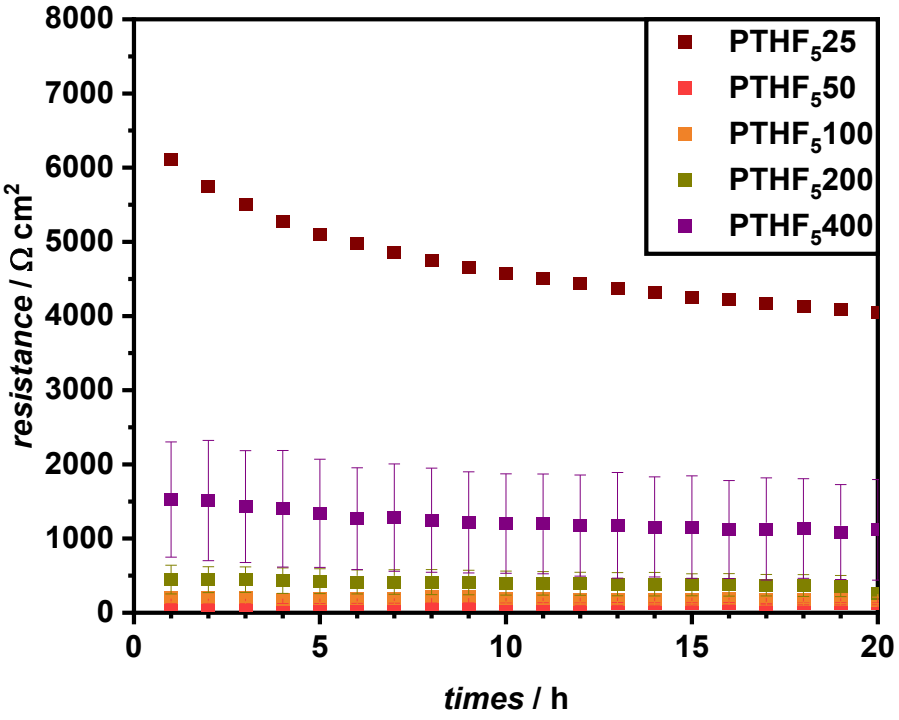

Figure 136 Development of areal resistance of PTHF CPEs over 20 h in symmetrical Li||Li cells.

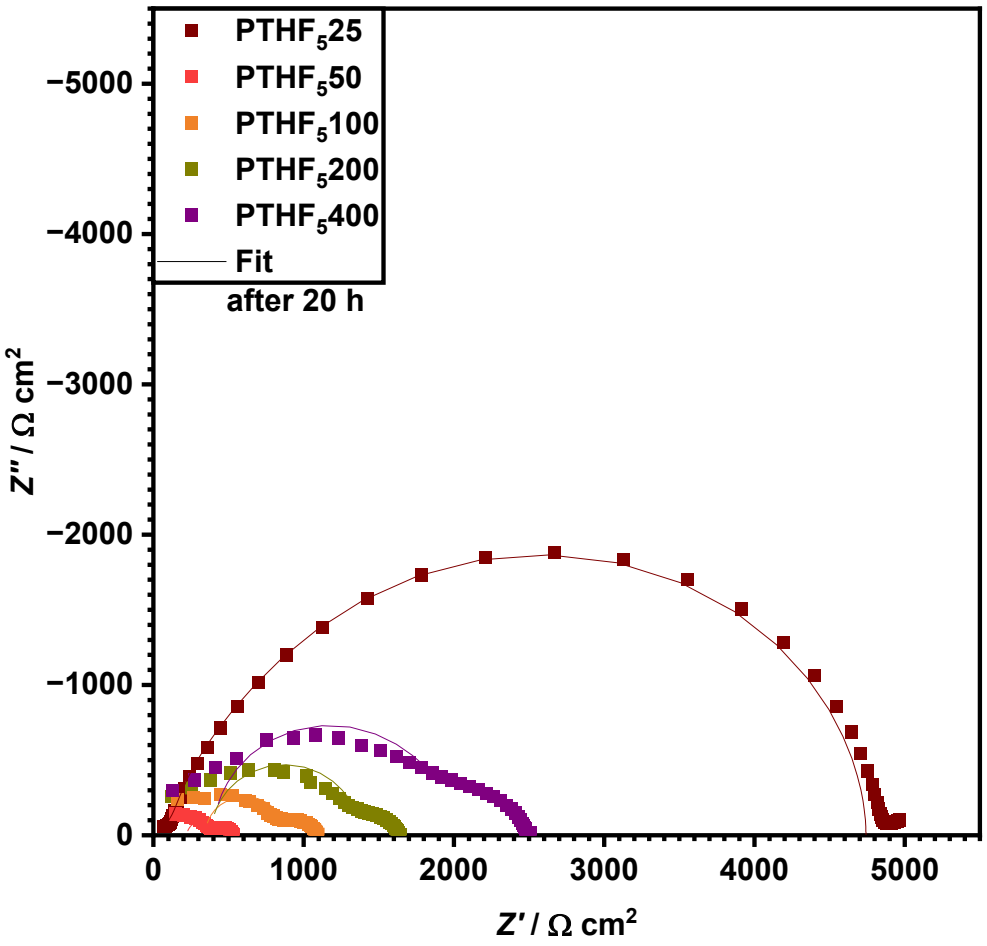

Figure 137 Nyquist plot of PTHF CPEs after 20 h in symmetrical Li||Li cells.

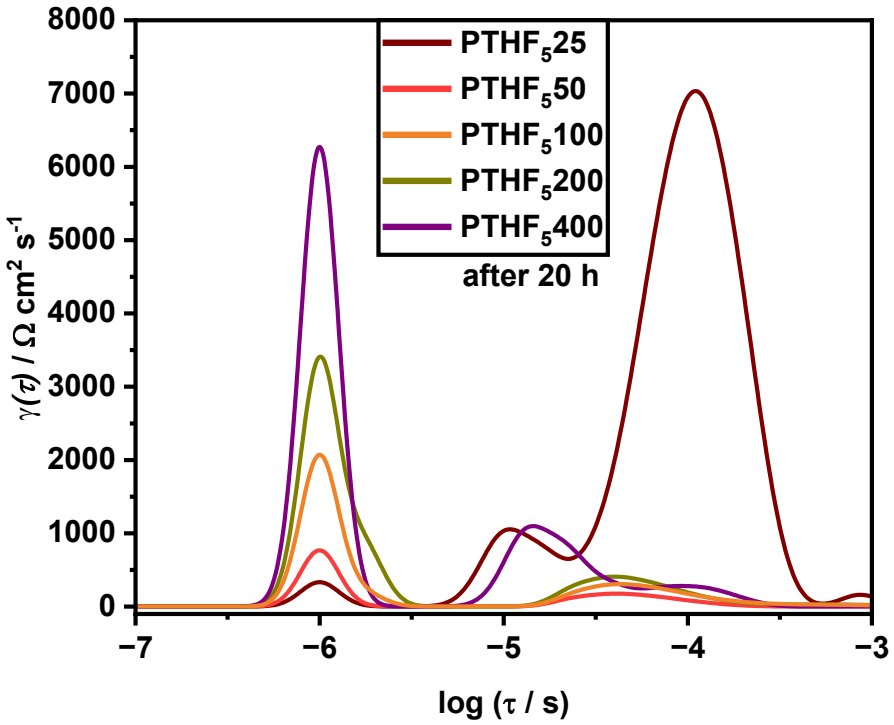

Figure 138 DRT of PTHF CPEs after 20 h in symmetrical Li||Li cells.

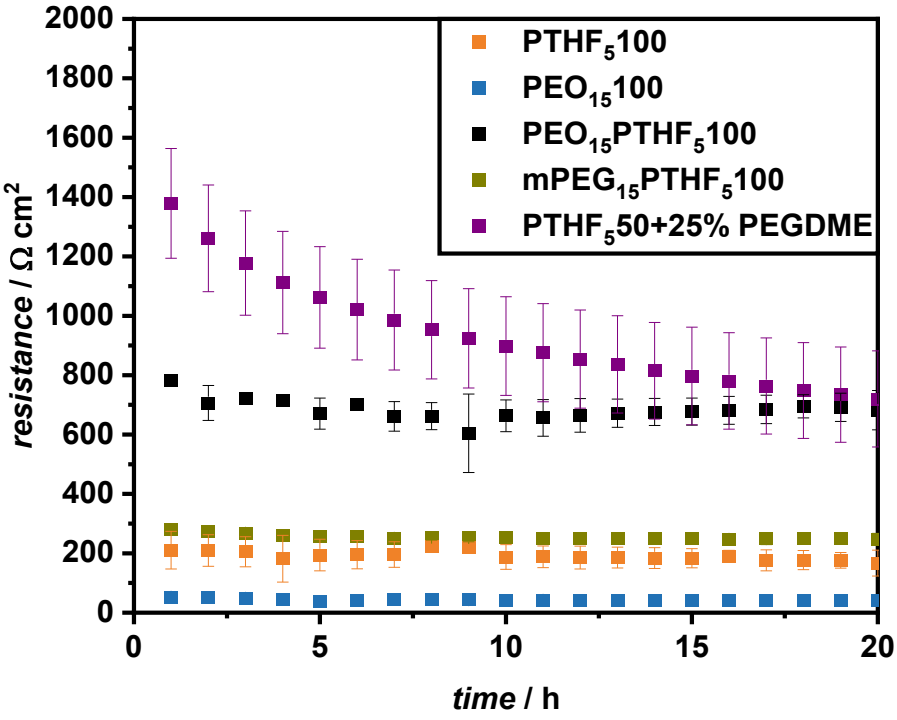

Figure 139 Development of areal resistance of mixed CPEs over 20 h in symmetrical Li||Li cells. $PEO_{15}100$ and $PTHF_5100$ are added as a reference.

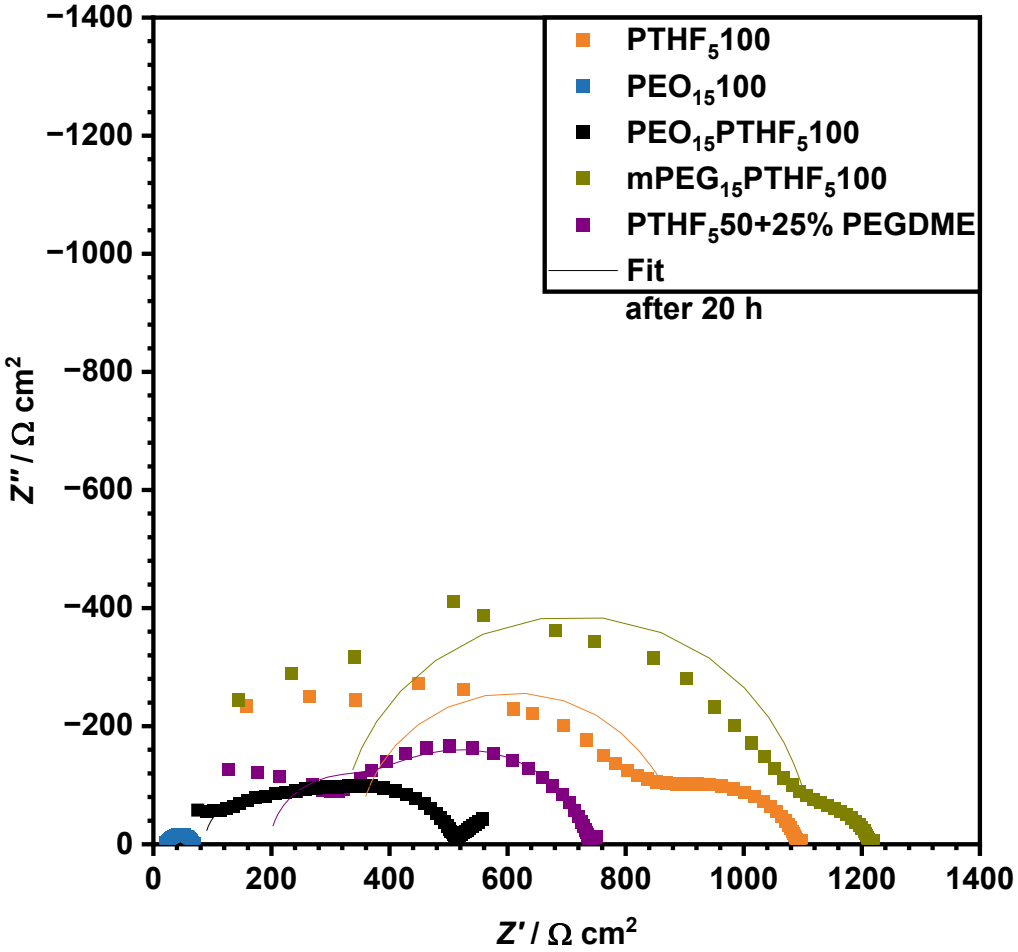

Figure 140 Nyquist plot of mixed CPEs after 20 h in symmetrical Li||Li cells. $PEO_{15}100$ and $PTHF_5100$ are added as a reference.

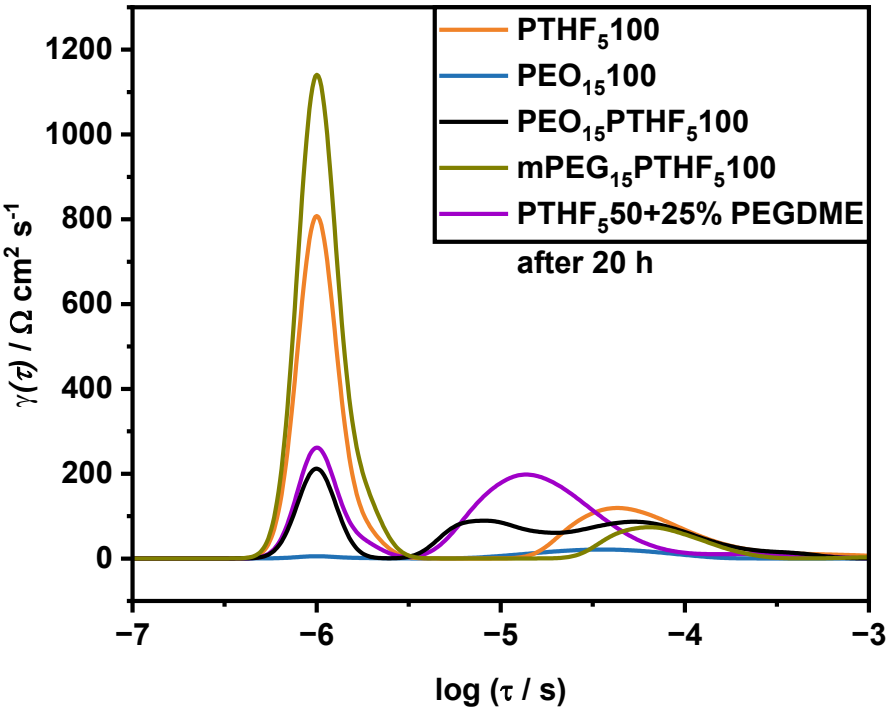

Figure 141 DRT of mixed CPEs after 20 h in symmetrical Li||Li cells. $PEO_{15}100$ and $PTHF_5100$ are added as a reference.

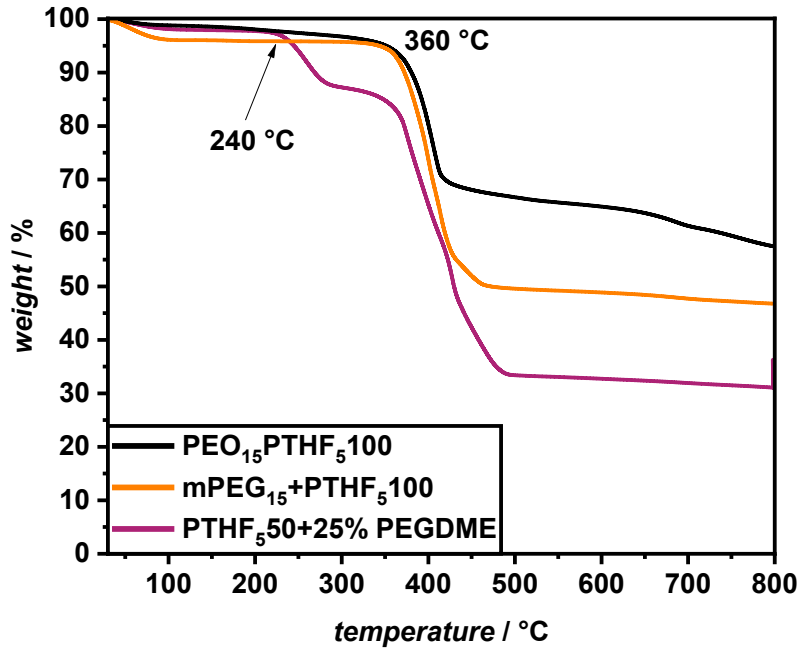

Figure 142 TGA measurements of mixed PTHF films at a heating rate of 10 K min^{-1} from 30 - 800 °C.

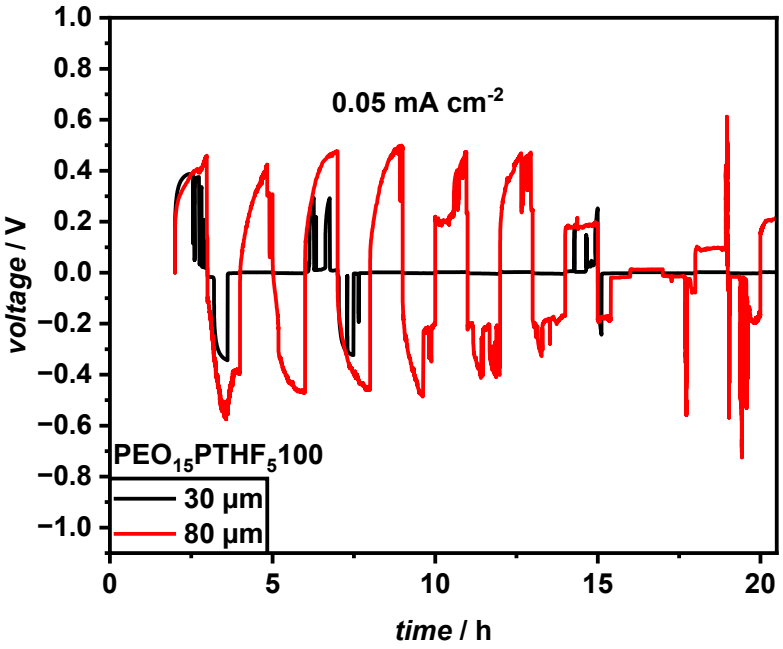

Figure 143 Symmetrical Li||Li plating-stripping experiments of all $PEO_{15}PTHF_5$LLZO (30 µm and 80 µm) with increasing current density after 10 cycles at 60 °C.

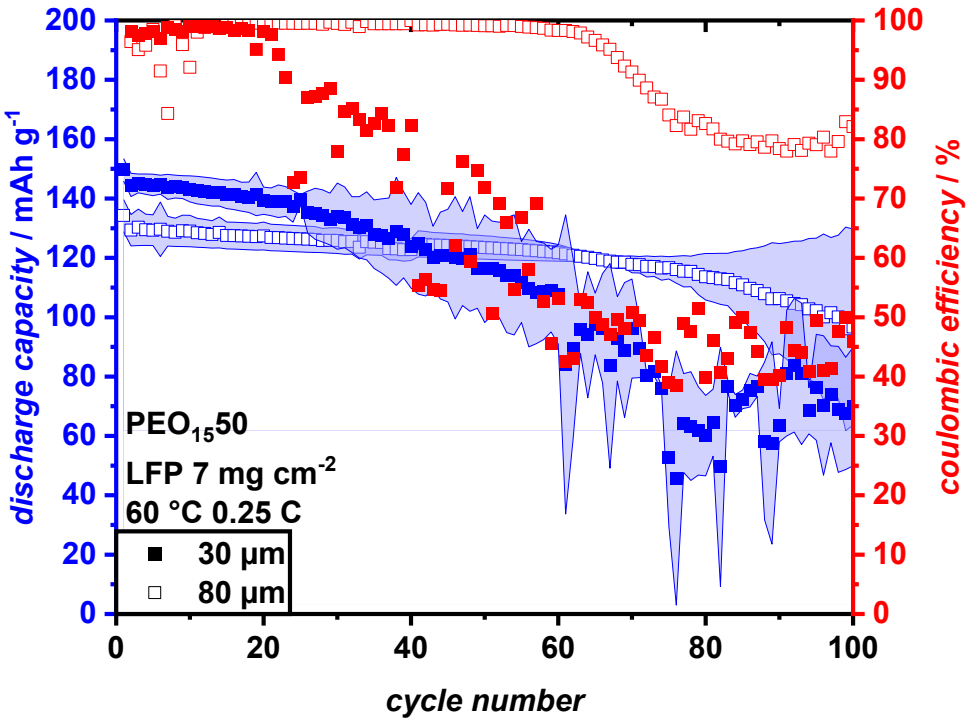

Figure 144 Constant current cycling of PEO_{15}50 (30 µm and 80 µm) at 0.25 C of Li| PEO_{15}50|LFP with 7 mg cm^{-2} mass loading at 60 °C. The discharge capacity includes error bars from 3 cells.

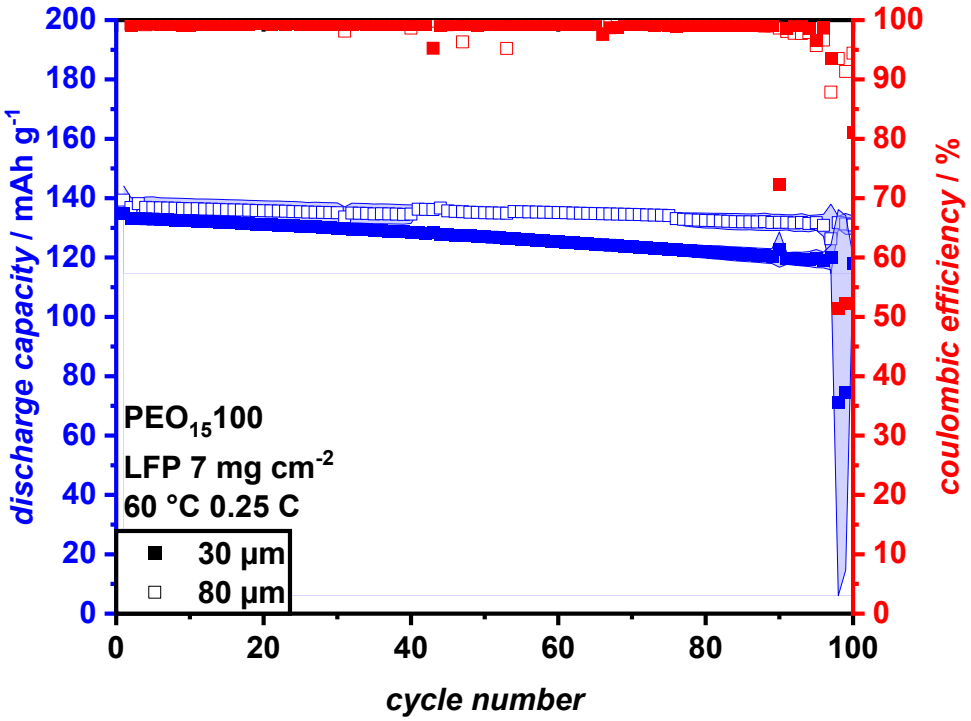

Figure 145 Constant current cycling of $PEO_{15}100$ (30 µm and 80 µm) at 0.25 C of Li| $PEO_{15}100$|LFP with 7 mg cm^{-2} mass loading at 60 °C. The discharge capacity includes error bars from 3 cells.

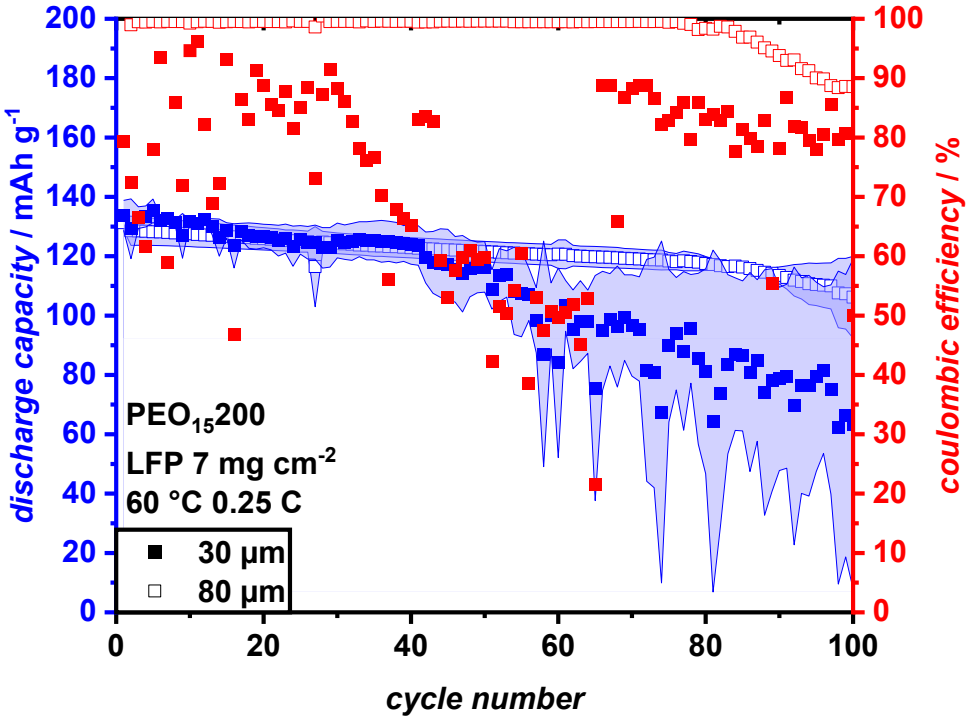

Figure 146 Constant current cycling of $PEO_{15}100$ (30 µm and 80 µm) at 0.25 C of Li| $PEO_{15}200$|LFP with 7 mg cm^{-2} mass loading at 60 °C. The discharge capacity includes error bars from 3 cells.

12.3.1 ATR-IR of prepared CPEs

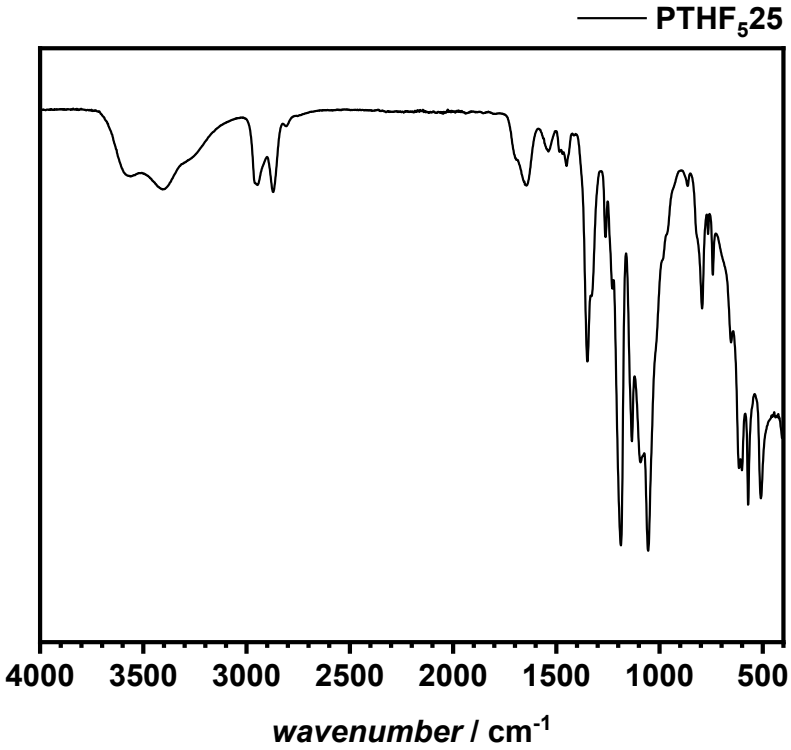

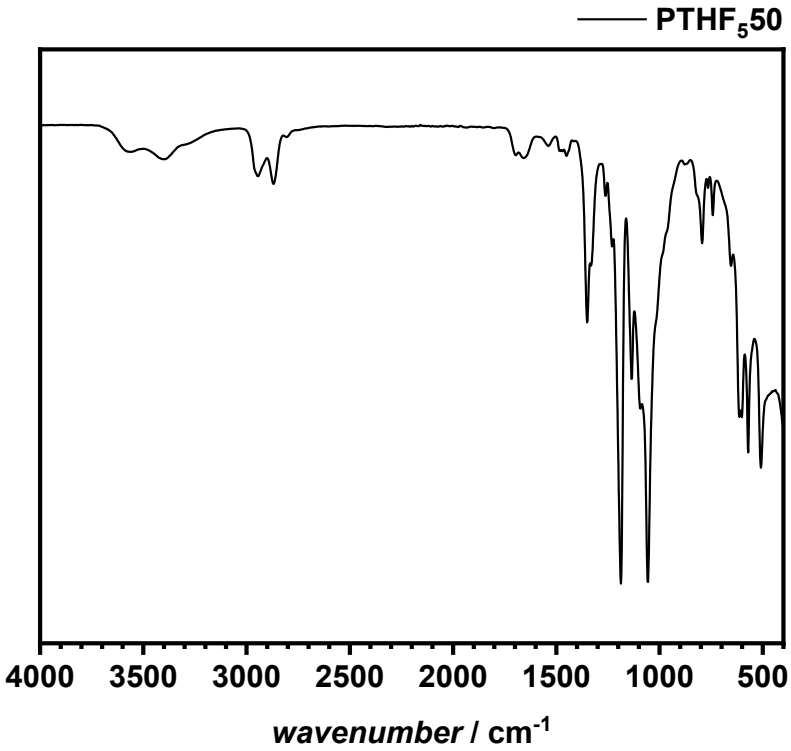

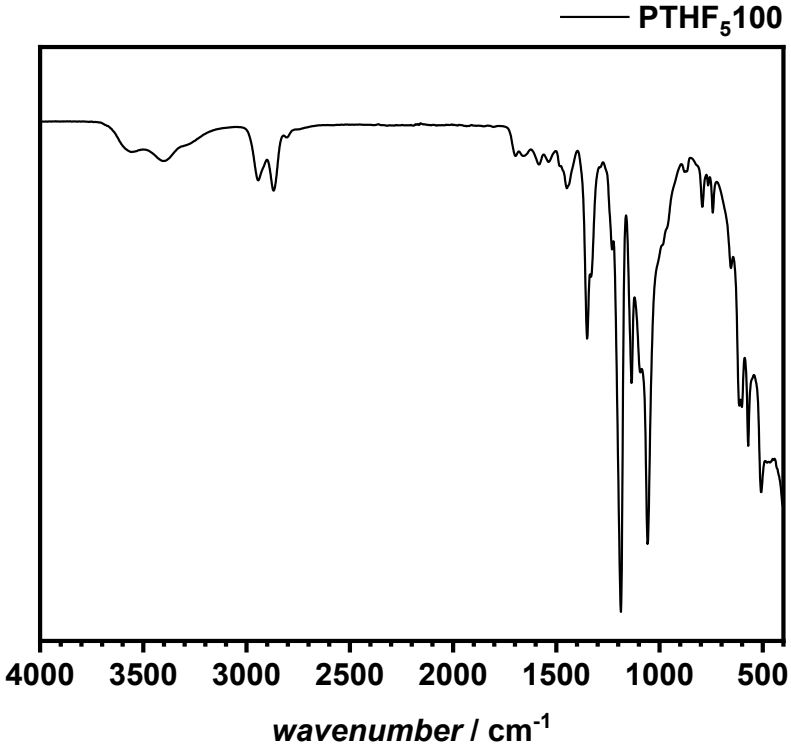
PTHF5100
4000
3500
3000
2500
2000
1500
1000
500
wavenumber / cm-1

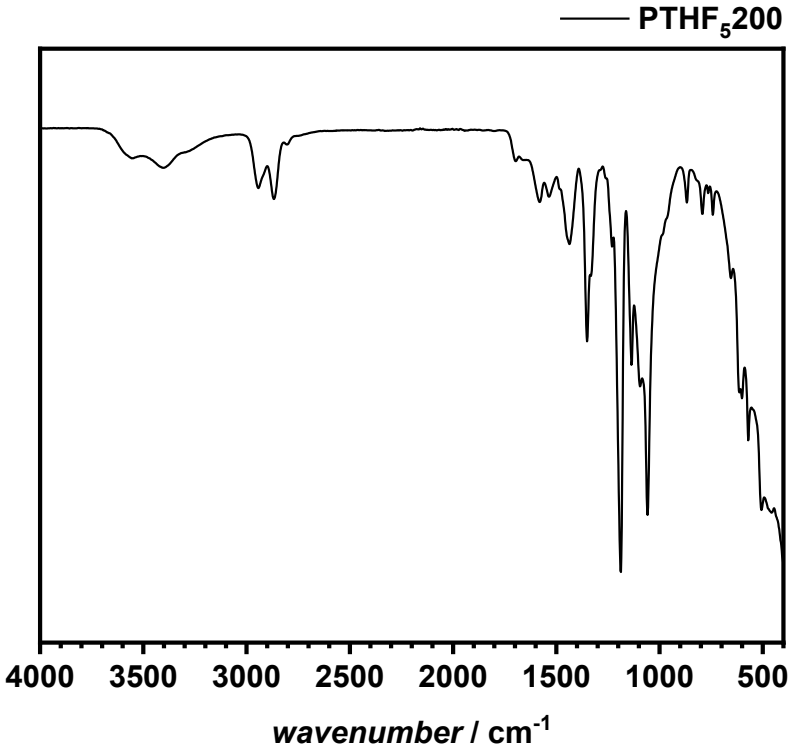
PTHF5200
4000
3500
3000
2500
2000
1500
1000
500
wavenumber / cm-1

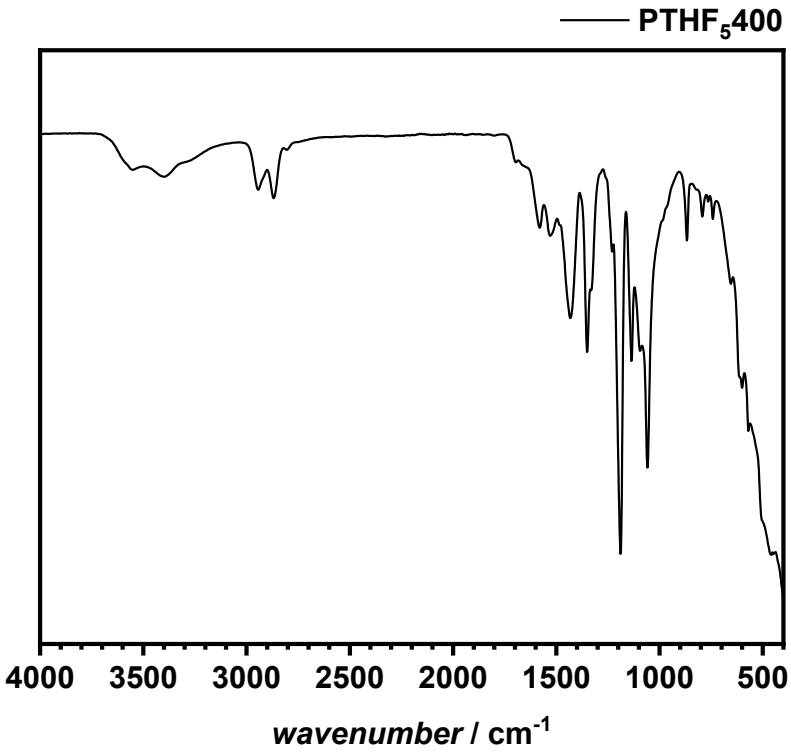
PTHF5400
4000
3500
3000
2500
2000
1500
1000
500
wavenumber / cm-1

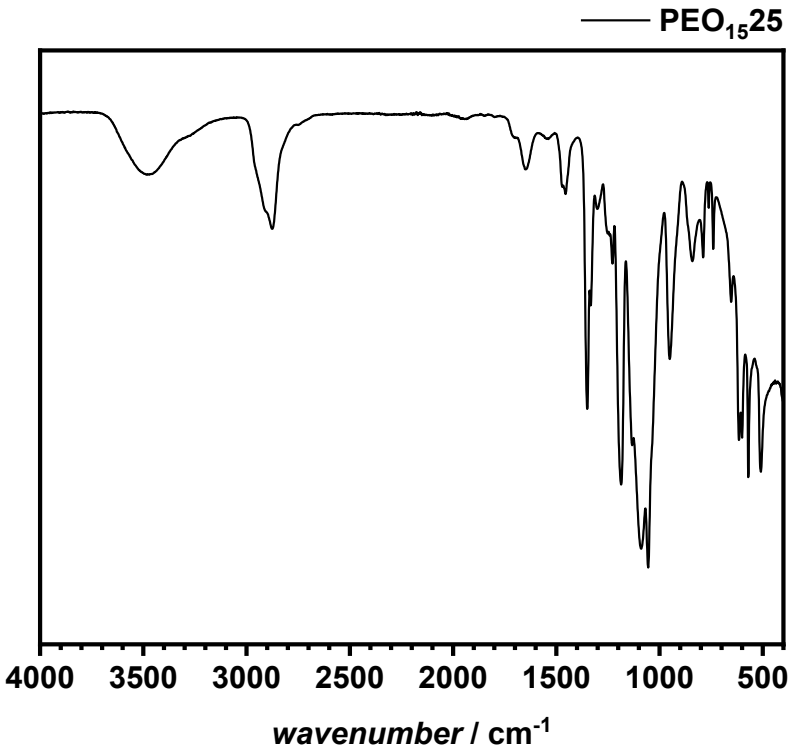
PEO1525
4000
3500
3000
2500
2000
1500
1000
500
wavenumber / cm-1

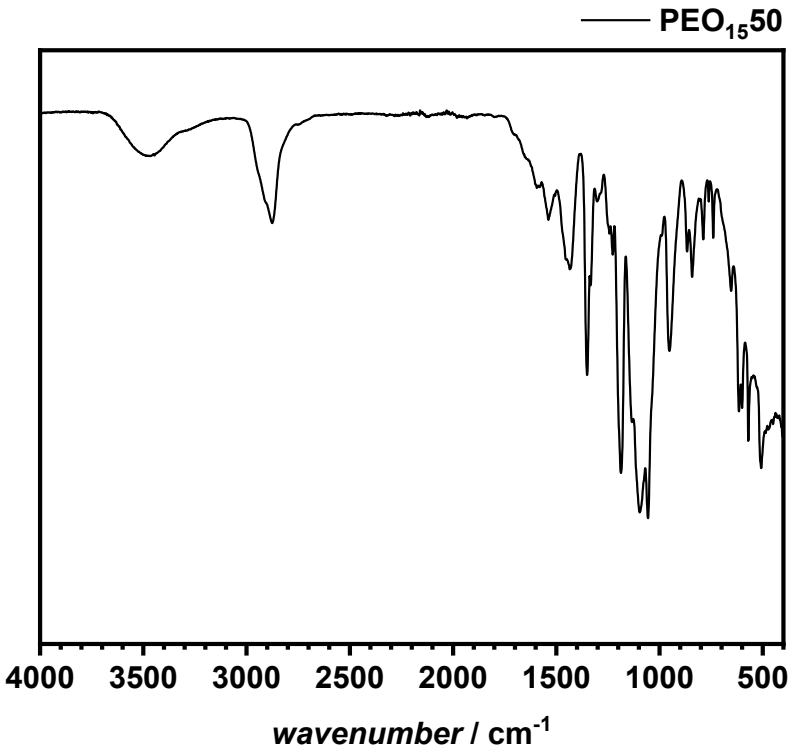
PEO15 50
4000
3500
3000
2500
2000
1500
1000
500
wavenumber / cm-1

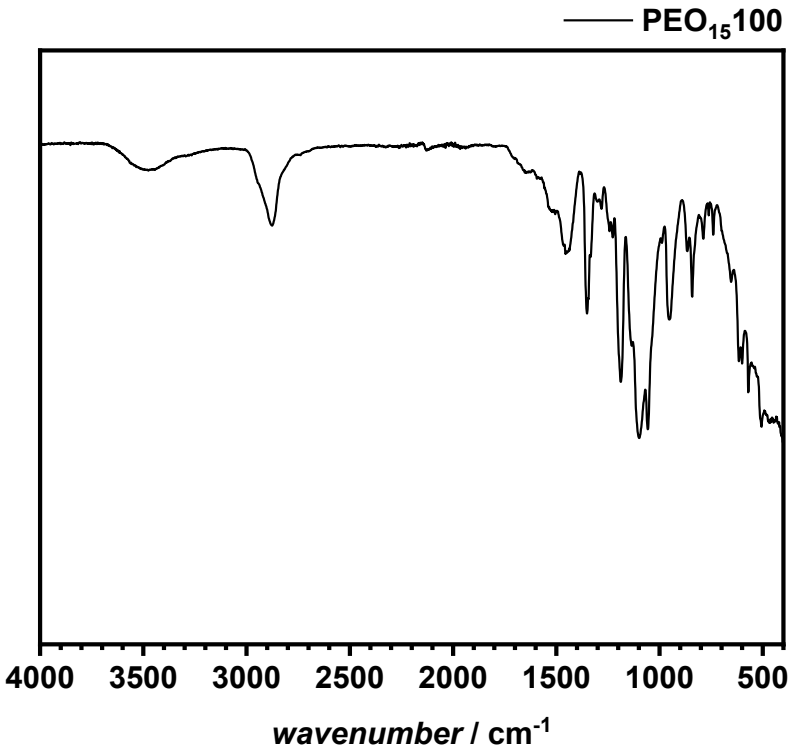
PEO15 100
4000
3500
3000
2500
2000
1500
1000
500
wavenumber / cm-1

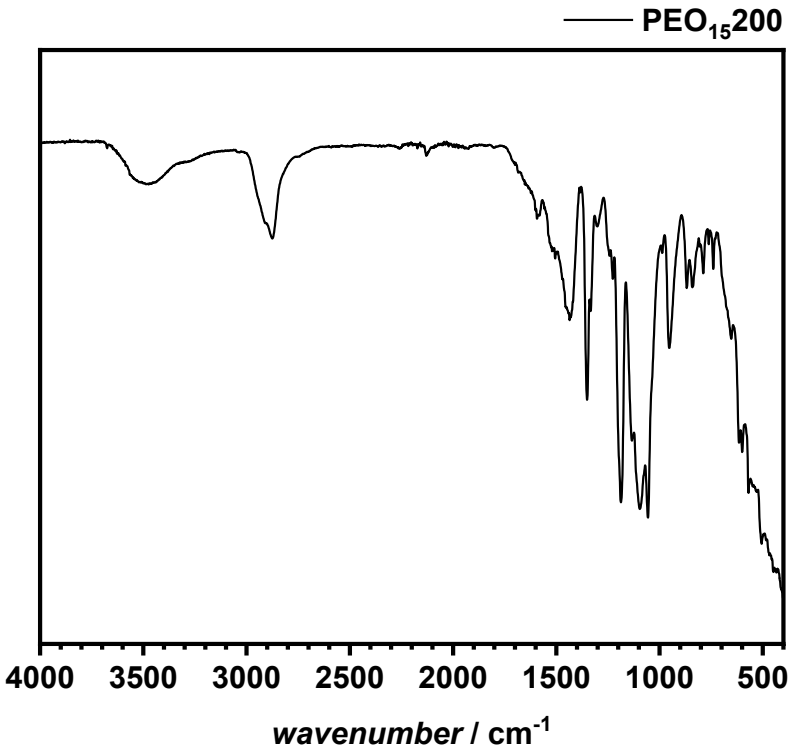
PEO15200
4000
3500
3000
2500
2000
1500
1000
500
wavenumber / cm-1

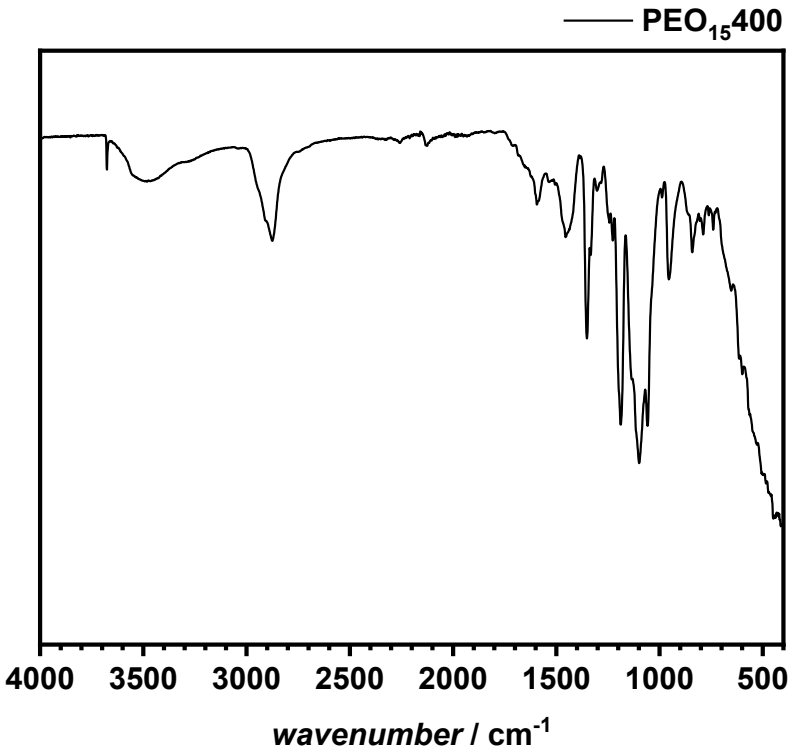
PEO15400
4000
3500
3000
2500
2000
1500
1000
500
wavenumber / cm-1

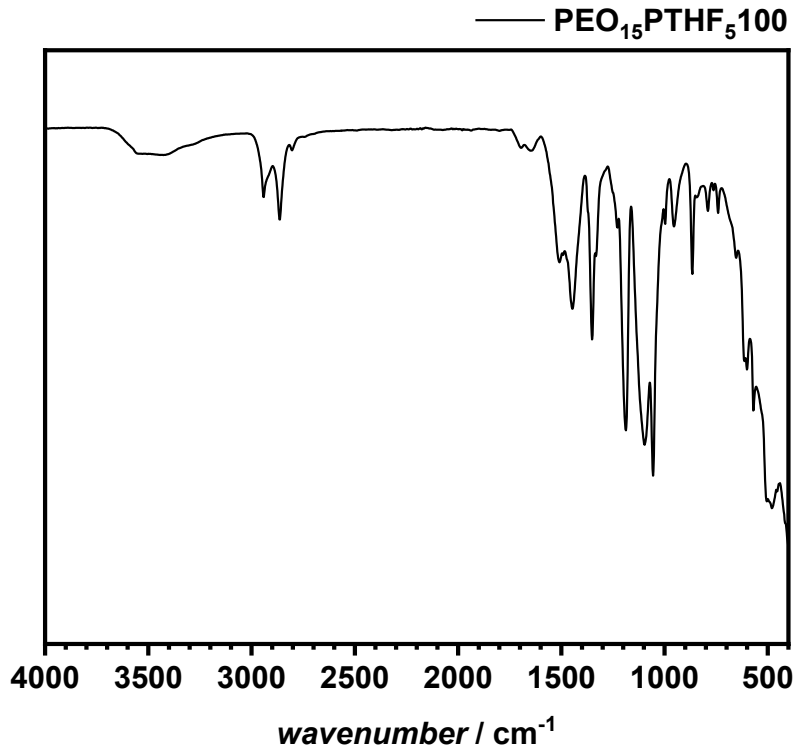
PEO15PTHF5100
4000
3500
3000
2500
2000
1500
1000
500
wavenumber / cm-1

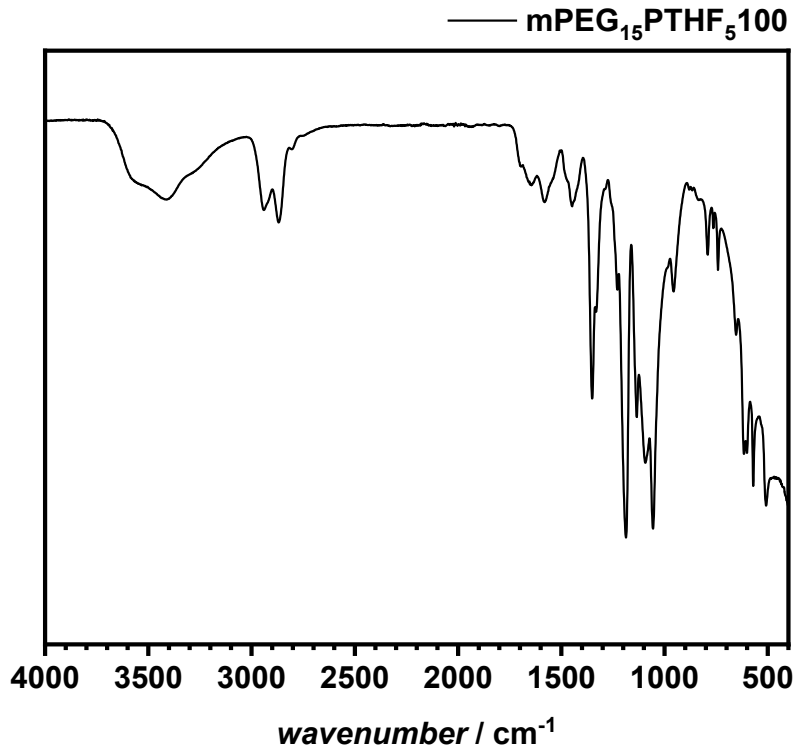
mPEG15PTHF5100
4000
3500
3000
2500
2000
1500
1000
500
wavenumber / cm-1